Carbon burning and hydrodynamic mixing uncertainties in stellar models

Michael Edward Bennett

Doctor of Philosophy

Research Institute for the Environment, Physical Sciences and Applied Mathematics,
University of Keele.

September 2011

Keele
Graduate School

SUBMISSION OF THESIS FOR A RESEARCH DEGREE

Degree for which thesis being submitted

Title of thesis

This thesis contains confidential information and is subject to the protocol set down for the submission and examination of such a thesis.

YES/NO

[please delete as appropriate; if YES the box below should be completed]

Date of submission Original registration date

(Date of submission must comply with Regulation 2D)

Name of candidate

Research Institute

Name of Lead Supervisor

DECLARATION by the candidate for a research degree

I certify that:

(a) the decision to submit this thesis has been taken following consultation with, and having received advice from, my academic and (where appropriate) non-academic (e.g. industrial) supervisor(s)

(b) The thesis being submitted for examination is my own account of my own research

(c) My research has been conducted ethically. Where relevant a letter from the approving body confirming that ethical approval has been given has been bound in the thesis as an Annex

(d) The data and results presented are the genuine data and results actually obtained by me during the conduct of the research

(e) Where I have drawn on the work, ideas and results of others this has been appropriately acknowledged in the thesis

(f) Where any collaboration has taken place with one or more other researchers, I have included within an 'Acknowledgments' section in the thesis a clear statement of their contributions, in line with the relevant statement in the Code of Practice (see Note overleaf).

(g) The greater portion of the work described in the thesis has been undertaken subsequent to my registration for the higher degree for which I am submitting for examination

(h) Where part of the work described in the thesis has previously been incorporated in another thesis submitted by me for a higher degree (if any), this has been identified and acknowledged in the thesis

(i) The thesis submitted is within the required word limit as specified in the Regulations

Total words in submitted thesis (including the text and footnotes, but excluding references and appendices) _____

Signature of candidate ……Date ……

I have read the thesis*/I have read part of the thesis*/I have not read the thesis*, and I am aware that the student intends to submit.

Signature of lead supervisor …… Date ……

Please print name .....

Delete the following box if it does not apply:

I have read the thesis*/I have read part of the thesis*/I have not read the thesis*, and I am aware that the student intends to submit.

Signature of non-academic supervisor ……

Please print name .....

On behalf of …… (non-academic sponsor)

The copy of the thesis lodged in the University Library shall be subject to an embargo on access for a period of ….. years.

Signature of lead supervisor ……

Signature of non-academic supervisor ……

Signature of research student …… Date ……

***Delete as appropriate**

Note

Extract from Code of Practice: If the research degree is set within a broader programme of work involving a group of investigators – particularly if this programme of work predates the candidate's registration – the candidate should provide an explicit statement (in an 'Acknowledgments' section) of the respective roles of the candidate and these other individuals in relevant aspects of the work reported in the thesis. For example, it should make clear, where relevant, the candidate's role in designing the study, developing data collection instruments, collecting primary data, analysing such data, and formulating conclusions from the analysis. Others involved in these aspects of the research should be named, and their contributions relative to that of the candidate should be specified (*this does not apply to the ordinary supervision, only if the supervisor or supervisory team has had greater than usual involvement*).

Cc: Director of Postgraduate Research

Abstract

The aim of this thesis is to investigate uncertainties in the input physics of stellar models that are relevant for the evolution of stars and the related nucleosynthesis, in particular the s-process. Nuclear reaction rates and mixing prescriptions in particular can modify significantly the yields of heavy elements in stellar models. The s-process, which is a slow neutron-capture process that can occur in massive stars and asymptotic giant branch (AGB) stars, is an important driver for uncertainty studies because the output yields of heavy nuclides in these astrophysical sites are sensitive to the interior conditions and the input physics.

In this work, two uncertainties are considered. The first is the ^{12}C + ^{12}C nuclear reaction rate which, despite considerable experimental efforts, remains uncertain at temperatures relevant for hydrostatic carbon burning in massive stars. We show that changes to this reaction rate affect the stellar structure and nucleosynthesis of massive stars and, consequently, the final yields. A comparison of these yields with the Solar system abundances enabled us to constrain the ^{12}C + ^{12}C reaction rate in the relevant temperature range.

The second of these uncertainties is the treatment of convective-radiative interfaces in 1D stellar models, which are particularly important for modelling thermal pulses in AGB stars. The s-process during thermal pulses is sensitive to the treatment of mixing across convective-radiative interfaces. A possible link between full 3D hydrodynamics models of convective-radiative interfaces and 1D stellar models was investigated by considering a diffusion approximation. A technique for calculating diffusion coefficients from the output of hydrodynamics models was developed and an exploration of the diffusive approach for convective-boundary mixing is presented,

along with the successes and limitations of this approach.

Acknowledgements

Over the course of this work, there were many people whose advice and support were fundamental to the completion of this work. In particular, Raphael Hirschi, the lead supervisor, provided a colossal level of advice with regards to the scientific method and whose availability, patience and optimism were often beyond the call of duty. Raphael also generated the fifteen stellar models used in this work with the Geneva Stellar Evolution Code (GENEC), which formed the basis for the study into the evolution and nucleosynthesis of massive stars presented in this work. In addition, I would like to thank Marco Pignatari and Falk Herwig for their hard work in developing the post-processing code (MPPNP) used in this work and for numerous lively discussions and constructive criticism, often conducted with overseas communication, which was fundamental to this work. I would also like to thank all members of the NuGrid collaboration, in particular Chris L. Fryer, Gabe Rockefeller and Frank X. Timmes, for their continued development and verification of MPPNP. I would also like to thank Michael Wiescher for taking the time to provide important advice concerning the nuclear physics aspect of this work.

A considerable portion of this thesis required extensive use of computer resources and software packages. I am therefore grateful for the support of Dr Barry Smalley, not just for installing python, but also for his incredibly dry sense of humour in the face of digital oblivion and for enforcing the all-important coffee rota. I would also like to thank Sam Toon for enabling and managing the use of the KHAOS cluster at Keele University and Frank X. Timmes for access to the Saguaro 2 computer cluster at the Arizona State University Advanced Computing Center. The analysis of mixing in stellar convection is based on data taken from hydrodynamics simulations performed by

Paul Woodward and his group at the LCSE, University of Minnesota, in collaboration with Falk Herwig of the University of Victoria.

This thesis would not have been possible without the continued support of colleagues, friends and family. Many thanks go to the Bennett family, in particular to my niece Molly for giving me her plasticine snail, which kept me smiling during the writing-up stage. I would like to thank Norshaliza Yusof, Urs Frischknecht and Sam Jones for many interesting discussions and comments over the course of the PhD. My thanks go to Robert Hadzik, for being like a brother to me over so many years, John Bradley, Matthew Crowther, Peter Griffiths and Rhodri Saunders for innumerable beers and pool matches and Steven Vaughan and James Duggan for keeping me level-headed and allowing me to indulge in city-life. I am grateful for the thoughtful friendship of Emily and Dean Reynolds, Juliet Yates, Helen Ireland, Grace Cash, Naomi Bowers, David Hayden and many other Keelites who have contributed to the precious experiences I have had here at Keele University. I am also grateful to Nick McMullen, Dave Gibbons, Hannah Merry and Will Beasley for shameless and decadent explorations of musical and digital creativity.

Last of all, I would like to thank Lauren Fuzi for her friendship, spirit and inspiration. Our times together helped develop my sense of awe at nature's wonders and mysteries and have helped me keep my eyes focused on the stars.

Contents

List of Figures

List of Tables

1 Introduction

> "Nothing exists except atoms and empty space; everything else is opinion." – Democritus

An important unanswered question often posed to scientists and philosophers is "what are we made of?", which refers to the origin and nature of matter which makes up the constituent building blocks of everything that is experienced around us. A physical theory attempting to solve this question must correctly explain the physical processes involved in the origin, transmutation and transport of matter, the direct consequences of those processes and quantitatively predict the current state of matter in the universe. The solution to such an important problem is a significant driver for studies in many subjects, such as cosmology, astrophysics and nuclear physics, and provides a remarkable synergy between subjects that relate to very small and very large spatial scales.

The origin of all matter can be attributed to the Big Bang and according to Big Bang nucleosynthesis models, the Big Bang accounts for almost all of the observed hydrogen, helium and lithium (Tytler et al., 2000; Steigman, 2007, and references therein). Most of the other elements in the periodic table are formed in stars (Burbidge et al., 1957; Cameron, 1957). Nuclear reactions in stellar interiors process primordial matter that consequently, through many generations of stars, enriches the universe in heavy elements. Therefore, a question can be asked: "what processes are responsible for the transmutation of primordial matter into its current form and the subsequent transport of matter from stellar interiors into the interstellar environment?".

Unfortunately, direct observations of stellar interiors cannot usually be made

since the light emitted from the star is characteristic of the stellar surface. However, exceptions to this are observations of rare Wolf-Rayet (WR) stars (where strong mass loss during their evolution reveals underlying layers of the star) and observations of asymptotic giant branch (AGB) and post-AGB stars that have undergone dredge-up episodes (where elements synthesized in the interior are mixed to the surface). Applications of asteroseismic techniques can be applied to spectroscopic and photometric data to directly infer interior properties. In addition, neutrino and gravitational wave astronomy could reveal the interior details of massive stars undergoing supernova explosions. In any case, indirect methods, such as theoretical modelling, are necessary to consider, which in their application require a detailed understanding of the interior processes. Computational stellar models are important tools to link knowledge of the underlying input physics with observable quantities, which allow specific observations, such as the acquisition of photometric or spectroscopic data, to verify predictions made by the models. However, the scope by which models can make predictions is based on many underlying assumptions and simplifications, which are often made in order to enable the calculation of previously unfeasible problems or reduce computational expense (observations can constrain stellar models by limiting uncertainties in the underlying input physics).

The identification and characterisation of uncertainties in models of stellar evolution and nucleosynthesis is the main focus for this work, specifically aimed at two astrophysical scenarios: hydrostatic carbon burning in massive stars and hydrogen-ingestion flashes in thermally-pulsing AGB stars. In the former case, the reaction rate for the carbon burning reaction, $^{12}\mathrm{C} + {}^{12}\mathrm{C}$, is a highly uncertain rate that could potentially disrupt the slow neutron-capture process (s-process) occurring during massive star evolution. In the latter case, the mixing of hydrogen-burning ashes during

a hydrogen-ingestion flash and the ensuing nucleosynthesis is dependent on the treatment of convective–radiative interfaces, which remains a considerable uncertainty in stellar models. The hydrogen-ingestion flash could represent an additional site for neutron-capture nucleosynthesis that differs from that of the ^{13}C pocket s-process.

Since many s-process elements can be observed, observations of elemental or isotopic abundances that are known to be produced during the s-process can constrain uncertainties in those phenomena. These phenomena can be investigated by utilising computer programs that calculate changes in the abundances of nuclides in the stellar interior dependent on the environment and mixing processes involved.

In order to take advantage of current advances in computing hardware, parallelism has been exploited and parallel routines have been implemented in a post-processing code. In a post-processing code, the majority of the nucleosynthesis calculations of the stellar model are performed by a separate program operating on stellar model output. One of the advantages of using the post-processing approach is the ability to apply a simple parallel scheme in order to improve the performance of the code, which would otherwise be a significant technical challenge. This enables the calculation of more demanding nucleosynthesis problems.

This thesis is arranged as follows. Chapter 2 presents the nuclear astrophysics concepts relevant for stellar models, including s-process nucleosynthesis, and Chapter 3 introduces the stellar models. In Chapter 4, the uncertainty study concerning the ^{12}C + ^{12}C reaction and the consequences on massive star evolution and nucleosynthesis is presented. The investigation into mixing over convective–radiative interfaces and diffusion, as applied to helium-shell-flash convection in AGB stars, is presented in Chapter 5. Finally, the summary, conclusions and further work can be found in Chapter 6. It should be noted that the majority of the content from Chapter 4 and parts of

Chapter 3 have been published as a journal paper in the Monthly Notices of the Royal Astronomical Society (see appendix D for a copy of the manuscript).

2 Nuclear astrophysics of stars

In this chapter, some theories of nuclear astrophysics and stellar evolution are outlined, with some core principles and nomenclature specified for clarity. The following text is based on Krane (1987), Rolfs & Rodney (1988) and Iliadis (2007), unless specified otherwise, which the keen reader is recommended to peruse for further information.

2.1 The Solar system abundances

Although the periodic table indicates the existence of a large number of unique elements, a quantitative analysis of abundances is more valuable for determining the effects of stellar nucleosynthesis, as they provide an important observational constraint on the nucleosynthesis processes occurring in stars. These abundances are determined primarily from Solar spectra and meteorite analyses. Figure 2.1 shows the Solar system abundances of Anders & Grevesse (1989). As indicated by Fig. 2.1, the Solar system abundances contain a rich variety of nuclides whose abundances vary by approximately ten orders of magnitude[1].

It is possible to define the mass fraction abundance of an isotope i as

$$X_i \equiv \frac{\rho_i}{\rho} = \frac{A_i n_i}{N_A \rho} = Y_i A_i \tag{2.1}$$

[1]More recent evaluations of the Solar system abundances, such as those of Lodders et al. (2009) and Asplund et al. (2009), show differences from that of Anders & Grevesse (1989) (in particular a lower metal content; see §3.1.5 for more details). However, the general features of the abundances curve discussed in §2.1 remain robust between different sets of Solar system abundance compilations.

where ρ_i, n_i and A_i are the mass density, number density and mass number of isotope i, N_A is Avogadro's number, Y_i is the number fraction and ρ is the total density of the stellar plasma. By definition, $\sum_i^N X_i = 1$, where N is the total number of nuclear species in the star. The sum of mass fractions for hydrogen isotopes and for helium isotopes are denoted as X and Y respectively. All other elements can be considered as 'metals', which are often specified as a single quantity Z, where $Z = 1 - X - Y$. The 'metallicity' of a body is then a measure of the fraction with which that body is formed up by metals, which can be specified relative to the Solar metallicity $Z_\odot$. The values of X, Y and Z, and mass fraction abundances of specific isotopes, X_i, quantify the composition of the Sun and are $X = 0.70683 \pm 0.025$, $Y = 0.27431 \pm 0.06$ and $Z = 0.01886 \pm 0.085$ for the Anders & Grevesse (1989) abundances. Abundances are also occasionally specified as the number of atoms per 10^6 silicon atoms or on a logarithmic scale relative to the number of hydrogen atoms $[A_i] = \log(N_i/N_H) + 12.00$. The uncertainties of X, Y and Z relate to systematic errors in the observations and Solar model uncertainties. The range of reported values for X, Y and Z, for the photosphere, vary by $\approx 1\%, 2\%$ and 30% respectively in the literature (see for instance Asplund et al., 2009).

The various features present in Fig. 2.1 can be described as follows:

- The most abundant nuclei are hydrogen and helium, with a general decline in abundances with increasing atomic mass. The reason for this is that as the atomic number increases, the Coulomb barrier increases. This suggests that the formation of heavier nuclei through charged particle reactions is increasingly inhibited. In addition, the binding energy per nucleon beyond the iron-group (the peak at ^{56}Fe in Fig. 2.1) decreases.

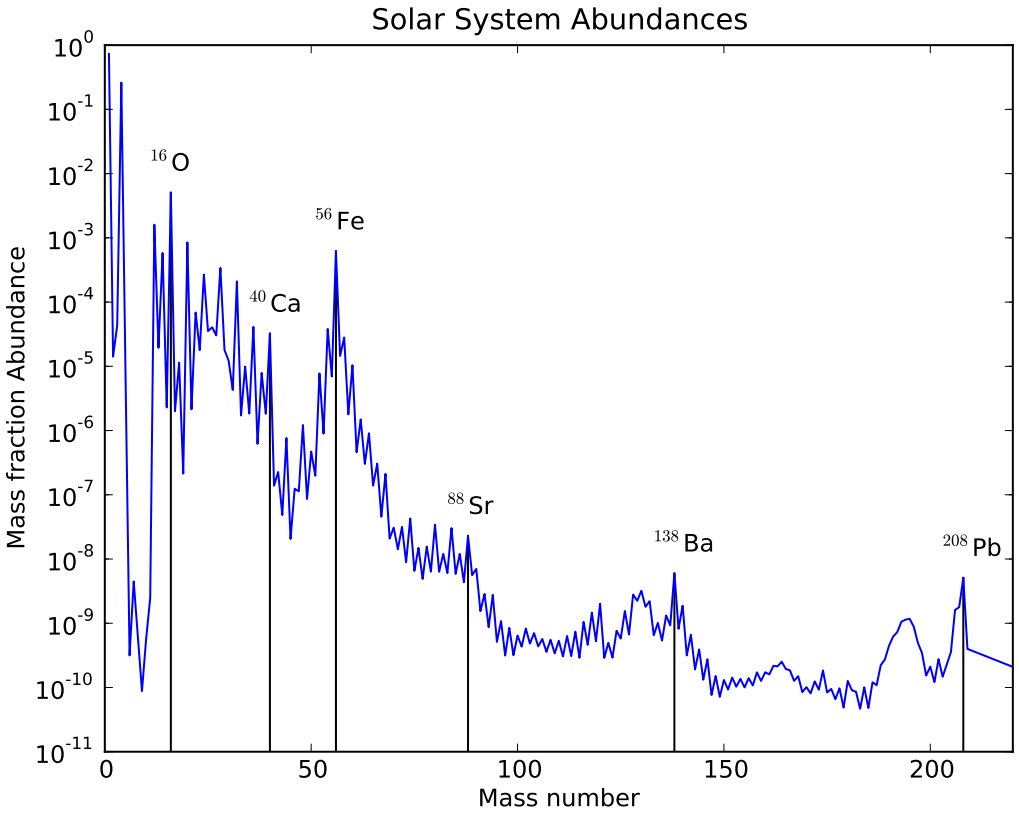

Figure 2.1: Solar system abundances from Anders & Grevesse (1989), where the abundances for nuclides with equal mass number are summed so that each particular mass number has a single point. The location where some specific nuclides lie is indicated by the straight black lines, which are neutron magic nuclei (except for ^{56}Fe). The features in the curve, such as the various peaks and troughs, can be understood by a combination of nuclear physics and stellar astrophysics knowledge. See text for details.

- A zig-zag pattern is present over the whole abundances curve. This is due to the pairing of neutrons and protons in nuclei, a consequence of the Pauli-exclusion principle, which favours stability in the case of even nuclei; the binding energy due to pairing is largest for even nuclei with both an even number of neutrons and an even number of protons, followed by nuclei with an odd number of nucleons, followed by even nuclei with both an odd number of neutrons and an odd number of protons. More tightly bound nuclei are generally built up in nucleosynthesis processes because nuclear reactions that destroy these nuclei are relatively inefficient.

- Lithium, beryllium and boron nuclei are fragile since the number of protons or neutrons in these nuclei are between the magic numbers 2 and 8. Photodisintegration occurs rapidly on these nuclei, depleting them heavily. The small abundance attributed to these nuclei is predominantly due to spallation reactions in the interstellar medium.

- Carbon, nitrogen and oxygen nuclei are much less fragile than the preceding nuclei and represent the next largest abundances after hydrogen and helium. Similarly, many light nuclides between carbon and iron are abundant. These nuclei are primarily formed through charged-particle reactions in hydrostatic burning stages in stars (see §2.3).

- There is a large peak at $A \simeq 56$, by iron, cobalt and nickel. This feature is present because the binding energy per nucleon reaches a maximum at these nuclides and decreases with increasing atomic mass beyond these nuclides. These nuclei are heavily produced in massive stars, where advanced stages of burning allow the formation of iron-group nuclei through charged particle reactions,

as well as in type Ia supernovae. Beyond iron-group nuclei, the increasing Coulomb barrier and the increased susceptibility to photodisintegration makes it extremely difficult to form heavier nuclei through charged-particle reactions. Since neutron capture reactions are not hindered by the Coulomb barrier, neutron capture nucleosynthesis accounts for the majority of heavy isotopes beyond the iron-group (see §2.4 for more details on s-process nucleosynthesis).

- Three peaks are evident at locations indicated in Fig. 2.1 by ^{88}Sr, ^{138}Ba and ^{208}Pb. These are nuclei with magic neutron numbers ($N = 50, 82$ and 126 respectively). These peaks arise due to slow neutron-capture nucleosynthesis processes (also known as the s-process). Nuclei with magic numbers of neutrons, such as ^{88}Sr, ^{138}Ba and ^{208}Pb, are much more stable against neutron-capture reactions and tend to be slowly built up during s-process nucleosynthesis.

- Each s-process peak has a corresponding adjacent peak at lower atomic mass. These peaks arise from the rapid neutron-capture nucleosynthesis process (the r-process). In this process, the neutron-capture nucleosynthesis favours production of neutron-rich, unstable isotopes, which are built-up at nuclides with magic numbers of neutrons near the neutron drip line. These nuclides have a total atomic mass which is less than the stable nuclides at the same neutron magic numbers. At the end of the neutron-capture process, the unstable nuclides beta-decay to stable nuclides, which will consequently have a lower atomic mass than those at the s-process peak.

The above features of the curve can be explained by combining knowledge of nucleosynthesis in stellar plasmas with the nuclear physics that governs the mechanism for the nuclear reactions occurring during nucleosynthesis. In order to further

understand the origin of nuclei, it is necessary to understand nuclear reactions and the physical impact of those reactions on stellar systems.

2.2 Thermonuclear reactions

2.2.1 Nuclear interactions and the Q-value

In this work, nuclear interactions are specified as follows:

$$\mathrm{X(A,B)Y} \tag{2.2}$$

where A is the projectile, X is the target, Y is the product and B is an ejectile. This notation is convenient to specify certain types of reactions. For example, (n,γ), (n,p) and (n,α) refer to various neutron-capture reactions. Any leptons involved in the reaction are normally omitted.

Upon collision with X, the nuclei A and X undergo a nuclear interaction where a variety of possible outcomes are possible. Scattering occurs if Y=X and B=A. In this case the nuclei have exchanged energy and/or momentum but otherwise remain chemically similar to their prior state. If Y and B are in their ground states, the collision is elastic. If Y and/or B is in an excited state, the collision is inelastic. If there is no projectile (A), the situation corresponds to a nuclear decay.

A nuclear reaction occurs if Y $\neq$ X and/or B $\neq$ A. A nuclear reaction that removes nucleons from X, which are emitted as separate outgoing particles, is known as a knockout reaction. If the outgoing particle becomes part of Y, it is known as a transfer reaction. Knockout reactions can also be referred to as spallation.

Nuclear reactions can also be described by the mechanism that governs the process. In direct reactions, only a few nucleons are involved in the reactions, with the remainder acting as spectators. The opposite case is the compound reaction, whereby the projectile and the target merge briefly before the outgoing particles are ejected. Between these two extremes are resonant reactions, in which the incoming particle forms a "quasibound" state before the outgoing particle is ejected. Nuclear reaction rates are often enhanced if the energetics of the fusion reaction in question correspond to energies required to form resonant states.

It is possible to define the Q-value, which is the energy liberated in a nuclear reaction (or energy taken if the Q-value is negative), as

$$Q = (m_{\text{initial}} - m_{\text{final}})c^2 \tag{2.3}$$

$$= (m_{\text{X}} + m_{\text{a}} - m_{\text{Y}} - m_{\text{b}})c^2, \tag{2.4}$$

where m is the mass. The reaction is exoergic if $Q > 0$ and endoergic if $Q < 0$. In the case of endoergic reactions, the energy is expended in the form of nuclear mass or binding energy of the reaction products. The Q-value is an important quantity as it determines the amount of energy supplied to the stellar environment per reaction. The energy generation rate (with units J s^{-1} kg^{-1}) by a reaction in a stellar environment can be specified as

$$\epsilon_{\text{nuc},ij} = \frac{Q}{\rho}\left(\frac{dn_i}{dt}\right)_j \tag{2.5}$$

where n_i is the number density of nuclide i produced by the reaction (with nuclide j) and ρ is the mass density of the stellar plasma. The total nuclear energy generation rate in a star is calculated as the sum of the energy generation rates for all reactions.

Note that if the reaction ejects neutrinos, these particles interact very weakly with baryonic matter at stellar densities and can remove energy from the star. Therefore, the net energy production of a star must take into account the energy taken away by neutrinos.

2.2.2 The cross section and reaction rate

In a nuclear reaction, the initial kinetic energy, E_{initial}, is a variable quantity. In the case of a stellar plasma, a distribution of energies exist. Therefore, the probability of a particular nuclear reaction occurring as a function of energy is important to determine the total amount of energy supplied by nuclear reactions to the stellar environment. The cross section, σ, is such a quantity, which has units of area. It is defined as the number of interactions, N_R, per unit time divided by the product of the number of incident particles, N_b, per unit area per unit time and the number of target nuclei, N_t, within the beam,

$$\sigma \equiv \frac{(N_R/t)}{[N_b/(tA)]N_t}, \tag{2.6}$$

which can be determined from experiments. Alternatively, one can write Eq. 2.6 as

$$\sigma = \frac{R}{n_{\mathrm{X}} n_{\mathrm{A}} v} \tag{2.7}$$

where $R = N_R/(Vt)$ is the reaction rate, $n_{\mathrm{X}} = N_t/V$ is the number density of target nuclei, $n_{\mathrm{A}} = N_b/V$ is the number density of projectiles and v is the relative velocity of A and X. Generally, σ is a function of kinetic energy, but it can also be specified as a function of relative velocity. If $P(v)dv$ is the probability that the stellar plasma will

have a relative velocity between v and $v + dv$, then by definition

$$\int_0^\infty P(v)dv = 1. \tag{2.8}$$

The reaction rate can be generalised for a distribution of relative velocities as

$$R = n_{\rm X} n_{\rm A} \int_0^\infty v P(v) \sigma(v) dv \equiv n_{\rm X} n_{\rm A} \langle \sigma v \rangle_{\rm X,A} \tag{2.9}$$

where $\langle \sigma v \rangle_{\rm X,A}$ is the reaction rate per particle pair. For identical pairs of nuclei (A=X), the total number density of pairs is given by $N_X^2/2$. The general expression for the rate can therefore be specified as

$$R = \frac{n_{\rm X} n_{\rm A} \langle \sigma v \rangle_{\rm X,A}}{1 + \delta_{\rm X,A}} \tag{2.10}$$

where $\delta_{\rm X,A}$ is the Kronecker delta ($\delta = 1$ if X = A; $\delta = 0$ otherwise). In a stellar plasma, the kinetic energy available to nuclei is present as thermal motion. Nuclear reactions in stars are therefore referred to as thermonuclear reactions. In most cases, the stellar plasma is nondegenerate and the relative velocities are nonrelativistic. If this is the case, the relative velocities can be described by a Maxwell-Boltzmann distribution

$$P(v)dv = 4\pi v^2 \left(\frac{\mu_{\rm X,A}}{2\pi kT} \right)^{3/2} \exp\left(\frac{-\mu_{\rm X,A} v^2}{2kT} \right) dv \tag{2.11}$$

where $\mu_{\rm X,A} = m_{\rm X} m_{\rm A}/(m_{\rm X} + m_{\rm A})$ is the reduced mass, T is the temperature and k is the Boltzmann constant. Since $E = \mu_{\rm X,A} v^2/2$ and $dE/dv = \mu_{\rm X,A} v$,

$$P(v)dv = P(E)dE = \frac{2}{(kT)^{3/2}} \left(\frac{E}{\pi} \right)^{1/2} \exp\left(\frac{-E}{kT} \right) dE. \tag{2.12}$$

The reaction rate per particle pair is therefore

$$\langle \sigma v \rangle_{\mathrm{X,A}} = \int_0^\infty v\sigma(E)P(E)dE \tag{2.13}$$

$$= \left(\frac{8}{\pi \mu_{\mathrm{X,A}}}\right)^{1/2} \frac{1}{(kT)^{3/2}} \int_0^\infty E\sigma(E) \exp\left(\frac{-E}{kT}\right) dE. \tag{2.14}$$

In the literature, the reaction rates are often tabulated as $N_A\langle \sigma v \rangle$ in units of cm^3 s^{-1} mol^{-1} and can be written as

$$N_A\langle \sigma v \rangle_{\mathrm{X,A}} = \frac{3.7318 \times 10^{10} \mu_{\mathrm{X,A}}}{T_9^{3/2}} \int_0^\infty E\sigma(E) \exp\left(\frac{-11.605E}{T_9}\right) dE \tag{2.15}$$

where the centre-of-mass energy E is in units of MeV, $T_9 = T/(10^9\mathrm{K})$, N_A is Avogadro's number and $\mu_{\mathrm{X,A}}$ is in atomic mass units (u).

With a tabulated rate per particle pair, $N_A\langle \sigma v \rangle_{\mathrm{X,A}}$, determined from nuclear physics experiments or from theory, changes in abundances due to the reaction can now be predicted using

$$\left(\frac{dn_{\mathrm{X}}}{dt}\right)_{\mathrm{A}} = -\lambda_{\mathrm{A}} n_{\mathrm{X}} = -n_{\mathrm{X}} n_{\mathrm{A}} \langle \sigma v \rangle_{\mathrm{X,A}}, \tag{2.16}$$

where λ_{A} is the decay constant for the reaction. Reaction terms can be included for a variety of reactions. For neutron capture nucleosynthesis, the rate of change of abundance of a nucleus n_A with mass number A is

$$\left(\frac{dn_A}{dt}\right) = -n_n n_A \langle \sigma v \rangle_A + n_n n_{A-1} \langle \sigma v \rangle_{A-1} \tag{2.17}$$

where n_n is the neutron density and the reaction rates, $\langle \sigma v \rangle_A$, refer to neutron-capture reactions on nucleus A. With the addition of charged-particle reactions, weak interac-

tions (such as β-decays and electron captures) and photodisintegration, the determination of dn/dt for all nuclei forms a system of coupled equations. This is referred to as the nuclear reaction network, which can be solved numerically, and can be stated as

$$\frac{dn_i}{dt} = \sum_j \pm N_i \lambda_j n_j + \sum_{j,k} \pm \frac{N_i}{N_j! N_k!} R_{jk} n_j n_k + \sum_{j,k,l} \pm \frac{N_i}{N_j! N_k! N_l!} R_{jkl} n_j n_k n_l, \tag{2.18}$$

where the indices i, j, k and l cover all isotopes (Arnett & Thielemann, 1985) and the R terms are given by Eq. 2.7. The first term of Eq. 2.18 refers to beta-decays, electron-captures and photodisintegration, the second terms refers to two-body reactions and the third term refers to three-body reactions. The values N_i, N_j, N_k and N_l are the number of particles of each type involved in a single nuclear reaction, which accounts for reactions involving identical nuclei.

An evaluation of the nuclear reaction network requires knowledge of the reactions rates (such as $\langle \sigma v \rangle$), which is often tabulated in the literature. The reaction rates are either determined from nuclear physics experiments (see for instance Angulo et al., 1999) or from theoretical models (see for instance Rauscher & Thielemann, 2001).

2.2.3 The Gamow window

The reaction rate per particle pair described by Eq. 2.14 is calculated by assuming that the stellar plasma can be described as an ideal gas with a velocity/energy distribution governed by the Maxwell-Boltzmann distribution. For the most part, this approximation is adequate for input into stellar models. However, fusion via Coulomb

tunnelling is not taken into account in Eq. 2.14. In order to account for this, one can consider a cross-section of the form,

$$\sigma(E) \equiv \frac{1}{E} \exp(-2\pi\eta) S(E), \tag{2.19}$$

where $G \equiv \exp(-2\pi\eta)$ is the Gamow factor and η is known as the Sommerfeld parameter. G is an approximation of the transmission coefficient for fusion via s-wave capture through the Coulomb barrier, a quantity that describes the probability of penetration through the Coulomb barrier (the transmission coefficient is defined as the ratio of particle flux found in the inner region of a Coulomb barrier to the particle flux external to the barrier). G can also be expressed in the form, $G = \exp(-[E_G/E]^{1/2})$, where

$$E_G = \left(\pi\alpha Z_A Z_X\right)^2 \cdot 2\mu_{\mathrm{X,A}} c^2. \tag{2.20}$$

In Eq. 2.20, E_G is the Gamow energy, Z_A and Z_X are the atomic (or proton) numbers of the projectile and the target respectively and $\alpha = e^2/(4\pi\epsilon_0\hbar c) = 1/137$ is the fine structure constant. E_G is a measure of the difficulty of penetrating the Coulomb barrier, in units of energy. The presence of Z_A and Z_X in Eq. 2.20 indicates that as the charge numbers increase, the Coulomb barrier increasingly prohibits charged particle reactions from occurring.

The definition given in Eq. 2.19 removes the dependence on $1/E$ and G from the rate. The S-factor, $S(E)$, varies much less than $\sigma(E)$ and incorporates the nuclear structure effects of the reaction rate. Equation 2.14 can now be written as

$$\langle\sigma v\rangle_{\mathrm{X,A}} = \left(\frac{8}{\pi\mu_{\mathrm{X,A}}}\right)^{1/2} \frac{1}{(kT)^{3/2}} \int_0^\infty S(E) \exp\left(\frac{-E}{kT}\right) \exp(-2\pi\eta) dE \tag{2.21}$$

and the integral is dependent on $S(E)$ and two factors, $\exp(-E/kT)$, which is a Maxwell-Boltzmann distribution, and $\exp(-2\pi\eta)$, which is the Gamow factor. The reaction rate is largest when the product of these two factors is the largest. This occurs at a position

$$E_0 = \left[\left(\frac{1}{4\pi\epsilon_0}\right)^2 \left(\frac{\pi}{\hbar}\right)^2 \left(Z_A Z_X e^2\right)^2 \left(\frac{\mu_{\mathrm{X,A}}}{2}\right) kT^2\right]^{1/3} = \left(\frac{E_G (kT)^2}{4}\right)^{1/3}. \tag{2.22}$$

The product forms a peak known as the Gamow window at a position E_0, which corresponds to the energy where non-resonant fusion reactions are most effective. As Z_A and Z_X increase, E_0 increases and the area under the Gamow window decreases. Therefore, for a given mixture of reactions occurring in a plasma, one can expect that the reactions involving a larger Coulomb barrier will require higher temperatures to burn and that at any given temperature the reactions with smaller Coulomb barriers will have the larger reaction rate and contribute most towards the total energy budget.

It is also possible to consider the Gamow window for resonant reactions. For a single narrow and isolated resonance, the cross-section can be described by the one-level Breit-Wigner formula,

$$\sigma_{\mathrm{BW}}(E) = \frac{\pi\hbar^2}{2\mu_{\mathrm{X,A}}E} \frac{(2J+1)(1+\delta_{\mathrm{X,A}})}{(2j_{\mathrm{X}}+1)(2j_{\mathrm{A}}+1)} \frac{\Gamma_a \Gamma_b}{(E_r - E)^2 + \Gamma^2/4} \tag{2.23}$$

$$= \frac{\pi\hbar^2\omega}{2\mu_{\mathrm{X,A}}E} \frac{\Gamma_a \Gamma_b}{(E_r - E)^2 + \Gamma^2/4} \tag{2.24}$$

where j_{X} and j_{A} are the spins of the target and projectile, J and E_r are the spin and energy of the resonance, Γ_a and Γ_b are the partial widths of the entrance and exit channel, Γ is the total resonance width and $\omega \equiv (2J+1)(1+\delta_{\mathrm{X,A}})/[(2j_{\mathrm{X}}+1)(2j_{\mathrm{A}}+1)]$.

Substitution into Eq. 2.14 gives

$$\langle \sigma v \rangle_{\mathrm{X,A}} = \frac{(2\pi)^{1/2}\hbar^2}{(\mu_{\mathrm{X,A}} kT)^{3/2}} \omega \int_0^\infty \frac{\Gamma_a \Gamma_b}{(E_r - E)^2 + (\Gamma^2/4)} \exp\left(\frac{-E}{kT}\right) dE. \tag{2.25}$$

Since the resonance is a narrow resonance, the exponential Maxwell-Boltzmann term and the partial widths Γ_a and Γ_b are approximately constant over the energy range of the resonance. The energy term in the exponential can be replaced with the resonance energy, E_r. This leaves

$$\langle \sigma v \rangle_{\mathrm{X,A}} = \frac{(2\pi)^{1/2}\hbar^2}{(\mu_{\mathrm{X,A}} kT)^{3/2}} \omega \Gamma_a \Gamma_b \exp\left(\frac{-E_r}{kT}\right) \int_0^\infty \frac{1}{(E_r - E)^2 + (\Gamma^2/4)} dE. \tag{2.26}$$

$$= \frac{(2\pi)^{1/2}\hbar^2}{(\mu_{\mathrm{X,A}} kT)^{3/2}} \omega \Gamma_a \Gamma_b \exp\left(\frac{-E_r}{kT}\right) \cdot \frac{2\pi}{\Gamma} \tag{2.27}$$

$$= \left(\frac{2\pi}{\mu_{\mathrm{X,A}} kT}\right)^{3/2} \hbar^2 (\omega\gamma) \exp\left(\frac{-E_r}{kT}\right), \tag{2.28}$$

where evaluation of the definite integral requires the assertion that $\arctan(2E_r/\Gamma) = \pi/2$, where $E_r \gg \Gamma/2$ (this is valid, as $E_r \sim$ MeV and $\Gamma \sim$keV or less for a narrow resonance), and $(\omega\gamma) \equiv \omega\Gamma_a\Gamma_b/\Gamma$. $(\omega\gamma)$ is known as the resonance strength, as its value is proportional to the area under the resonance cross-section curve.

For a number of resonances, Eq. 2.28 can be rewritten as

$$N_A \langle \sigma v \rangle_{\mathrm{X,A}} = \frac{1.5399 \times 10^{11}}{\left(\frac{A_\mathrm{A} A_\mathrm{X}}{A_\mathrm{A} + A_\mathrm{X}} T_9\right)^{3/2}} \sum_i (\omega\gamma)_i \exp\left(\frac{-11.605 E_i}{T_9}\right) \tag{2.29}$$

where the subscript i is over resonances and A_A and A_X are the atomic mass numbers of the projectile and the target nuclei respectively. $(\omega\gamma)_i$ and E_i are in units of MeV. The total reaction rate can then be specified as the sum of the resonant and nonresonant

contributions.

It should be noted that in the case of broad resonances, the assumptions of constant partial widths and a constant Maxwell-Boltzmann term are not applicable. In these cases, the reactions rates cannot be determined analytically and must be evaluated numerically.

2.2.4 Temperature sensitivity

The sensitivity of nuclear reaction rates to the temperature can be determined by considering the Gamow window at position E_0. For both the resonant and non-resonant cases, the reaction rate at E_0 is

$$\langle \sigma v \rangle_{\mathrm{X,A}} \propto \exp\left(- \left[\frac{E_G}{E_0} \right]^{1/2} + \left[\frac{E_0}{kT} \right] \right). \tag{2.30}$$

Substitution of E_0 (Eq. 2.22) into Eq. 2.30 gives

$$\langle \sigma v \rangle_{\mathrm{X,A}} \propto \exp\left(-3 \left[\frac{E_G}{4kT} \right]^{1/3} \right). \tag{2.31}$$

By setting $\beta = (E_G/4kT)^{1/3}$, it is possible to show that $\langle \sigma v \rangle_{\mathrm{X,A}} \propto T^{\beta}$. Table 2.1 provides typical values for β for some important charged-particle reactions. The central temperature, T_c, and Gamow energy, E_G, are also specified. The large value for β in each case indicates that for typical stellar burning temperatures, the sensitivity to temperature is large and small perturbations in temperature can cause large changes in the reaction rate.

Table 2.1: Values of β for some important reactions relevant to hydrostatic burning stages in stars. The reaction, central temperature (T_c) and Gamow energy for the reaction (E_G) is also specified.

Burning stage	Reaction	T_c (GK)	E_G (MeV)	β
Hydrogen (pp-chain)	p(p,d)	0.015	0.494	4.6
Hydrogen (CNO bicycle)	^{14}N(p,g)^{15}O	0.06	45.2	13.0
Helium	$\alpha(2\alpha,\gamma)^{12}$C	0.1	169	17.0
Carbon	^{12}C(^{12}C,α)^{20}Ne	0.9	7680	29.1
Oxygen	^{16}O(^{16}O,α)^{28}Si	2	32400	36.1

2.3 Nuclear reactions and stellar evolution

A star that supports itself against gravitational contraction by means of energy release from nuclear reactions will eventually deplete its available fuel. Once this occurs, the star will contract over a Kelvin-Helmholtz timescale in thermal equilibrium. As the star contracts, the radius decreases and the temperature rises due to the equation of state of the stellar plasma and, after some time, may lead to the ignition of a new source of fuel. Upon ignition of a new fuel source, there will be short period of stellar restructuring until hydrostatic equilibrium is established.

Since the temperature sensitivity of nuclear reactions is very high, temperature perturbations can cause very large increases in the rate. Stable burning therefore requires (and does indeed occur in) hydrostatic equilibrium, maintaining the burning temperature at a 'simmering' value. The mechanisms responsible for damping temperature perturbations so that hydrostatic equilibrium can be maintained are convective and radiative energy transport. For hydrostatic burning, stars must follow an evolutionary scenario, where numerous burning episodes follow on from each other, from one source of fuel to the next, with each burning stage occurring at a slowly varying tem-

perature. The interplay between nuclear reactions and thermodynamic processes play a key role in determining the stellar structure and composition at each evolutionary stage.

The initial composition of a protostar is comprised of light elements left over from big bang nucleosynthesis, mainly hydrogen and helium, and any metals that were generated in previous generations of stars that polluted the nascent molecular cloud. Since the initial abundances of the protostar are dependent on its environment, one can differentiate between the nucleosynthesis processes that are independent of the initial metal content (primary processes) and those that are metallicity-dependent (secondary processes). Since hydrogen and helium dominate the initial composition, the primary processes resulting from these nuclei and the products from previous primary processes determine the general course of stellar evolution. Secondary processes however can have a significant influence on stellar evolution. The evolutionary sequence is heavily dependent on the initial mass of the star, since it sets the initial amount of fuel for stellar burning and increases the action of gravitational contraction, which itself influences many interior properties.

For a typical massive star, with an initial mass of, say, $15M_{\odot}$, the evolutionary sequence can be briefly summarised as follows:

- Hydrogen burning is the first main hydrostatic burning stage to occur, resulting in the net production of ^{4}He from ^{1}H through the CNO tricycle and pp-chain reactions where, unlike lower mass stars, the CNO tricycle is largely dominant. The CNO elements act as a catalyst; the sum of C, N and O is constant but the relative amounts change in favour of the production of ^{14}N at the expense of ^{12}C and ^{16}O. This is due to the presence of the bottleneck reaction ^{14}N(p,γ)^{15}O,

which is the CNO reaction with the lowest cross-section. During this stage, the NeNa and MgAl cycles occur, which do not contribute greatly to the energy generation but strongly affect the production of those nuclides. Of particular importance is the synthesis of ^{26}Al by the MgAl cycle, which can be detected in the interstellar medium indirectly by γ-ray spectroscopy (e.g., Diehl et al., 2006). The lifetime for hydrogen burning in a $15M_{\odot}$ is $\simeq 1.5 \times 10^{7}$ yrs, which is much shorter than for a $1M_{\odot}$ star ($\sim 10^{10}$ yrs).

- Helium burning occurs through the interaction of three α particles, resulting in the formation of ^{12}C. Helium burning is also the site for the weak s-process (see §2.4.1). Another important reaction occurring during this stage is the $^{12}\mathrm{C}(\alpha,\gamma)^{16}\mathrm{O}$ reaction, which modifies the final $^{12}\mathrm{C}/^{16}\mathrm{O}$ ratio and competes with neutron sources for α-particles, which are a key ingredient for the neutron-source reactions. The $^{12}\mathrm{C}/^{16}\mathrm{O}$ ratio has repercussions for the carbon burning stage and the subsequent advanced burning stages. The lifetime for helium burning is about a factor of 10 less than the hydrogen burning stage due to the lower Q-value of the 3α reaction (0.606 MeV per nucleon, c.f. 6.56 MeV per nucleon during hydrogen burning), at a few million years.

- Carbon burning occurs through the $^{12}\mathrm{C} + {}^{12}\mathrm{C}$ reaction in a small, central convective core and in a number of subsequent convective shells. In higher mass stars, the central burning occurs in radiative conditions and the number of carbon burning shells decreases, although the size of the convective shells are much larger. The $^{12}\mathrm{C} + {}^{12}\mathrm{C}$ reaction produces mainly ^{20}Ne and ^{24}Mg with small amounts of ^{23}Na and ^{25}Mg. Central carbon burning marks the start of the advanced stages of evolution, where the timescale for the evolution is

governed by the severity of the neutrino losses instead of the radiative losses. The lifetime is therefore significantly reduced to a value $\sim 10^{3-4}$ years. Carbon burning does not occur in lower mass stars ($M_{ini} \simeq 7M_{\odot}$) because the interior temperatures are not high enough to ignite ^{12}C and the formation of a CO white dwarf occurs instead.

- Neon burning is characterised by photodisintegration of the abundant ^{20}Ne nuclei, forming ^{16}O and providing a source of α particles. These are captured onto other nuclei, such as ^{16}O and ^{20}Ne, to form ^{24}Mg and ^{28}Si. The most abundant species following this stage are ^{16}O, which has been largely preserved from the helium-burning stage, ^{24}Mg and ^{28}Si. The lifetime is $\sim 1 - 10$ years.

- Oxygen burning occurs through ^{16}O + ^{16}O reactions, primarily forming ^{28}Si and ^{32}S, with relatively small amounts of ^{31}P. This is the last burning stage to be fuelled directly through charged particle fusion reactions and their subsequent energy release; the last burning stage (silicon burning) occurs by photodisintegration. The lifetime of oxygen burning is similar to or less than that of neon burning, at $\sim 0.1 - 1$ year. The temperatures during oxygen burning ($\sim 1 - 2$ GK) are high enough for heavy elements to be photodisintegrated into lighter elements, destroying elements heavier than iron formed through neutron-capture reactions.

- Silicon burning is similar in nature to that of neon-burning, whereby ^{28}Si is photodisintegrated into constituent particles (mainly α particles and protons), which are subsequently captured onto any remaining ^{28}Si and other light nuclei to form a variety of products up to the iron-group (Fe, Ni, Co), which represent the most stable elements in nature. Nucleosynthesis proceeds through the for-

mation of two quasiequilibrium (QSE) clusters: one featuring isotopes between ^{12}C and ^{44}Ti and those between ^{48}Cr and ^{60}Zn. The lifetime for silicon burning is $\sim 1 - 10$ days.

Following silicon burning, the stellar environment will not encounter a new source of fuel and will start to collapse, eventually leading to a supernova explosion. The stellar plasma in the deep interior of the star following silicon burning enters a phase of nuclear statistical equilibrium (NSE) that operates in a similar way to silicon burning; numerous photodisintegration reactions occur involving all isotopes up to the iron-group.

It should be noted that following each burning stage there is the development of a shell burning stage, with the exception of silicon burning where a shell may or may not appear. During shell burning, the core continues to contract until it is supported by degeneracy pressure or until a new fuel is ignited.

2.4 Nucleosynthesis processes

Nucleosynthesis processes can be represented schematically in an isotope chart (also known as a Segré chart), which locates isotopes according to their proton and neutron numbers (Z and N respectively). An example of an isotope chart is shown in Fig. 2.2. Black squares indicate stable isotopes that follow a valley of stability which is given by $Z \simeq N$ for light isotopes and skews towards more neutron-rich nuclei as Z increases.

Specified on the chart are arrows referring to the main nucleosynthesis processes responsible for the production of nuclides in the diagram. The direction of the arrows in Fig. 2.2 points towards nuclides that show a net production at the expense of lighter

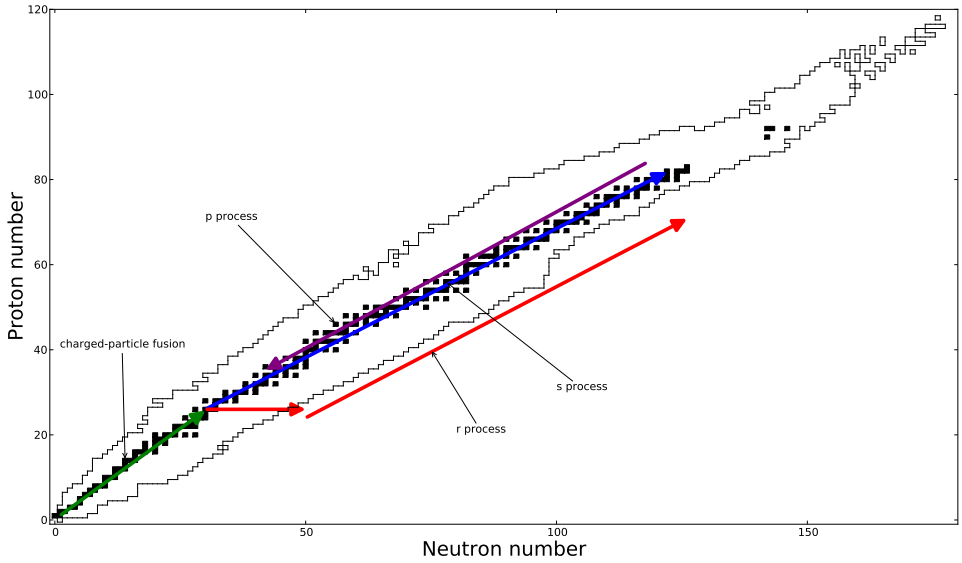

Figure 2.2: The chart of isotopes, with arrows indicating possible stellar processes responsible for the nucleosynthesis of isotopes across the chart (see text for details). Experimentally known isotopes, as specified in the Karlsruher Nuklidkarte (2007 edition) compilation, are bordered by thin black lines and stable isotopes are indicated by the black squares.

elements (or heavier elements in the case of the p-process). Figure 2.2 indicates that charged-particle fusion reactions cannot proceed beyond the iron-group nuclei and that the main processes responsible for the production of heavy elements are the slow (s) and rapid (r) neutron-capture processes. Photodisintegration reactions (the p process) are responsible for the production of some proton-rich/neutron-poor isotopes.

For any given nuclide, a large variety of reactions could possibly occur, but the reaction rate for the various reactions is often small enough to be considered negligible. Therefore, the s- and r-processes are satisfactorily described by the timescale of neutron captures ($\tau_{n\gamma}$) and their interplay with β-decays (with timescale τ_β). As an example

of neutron-capture nucleosynthesis, one can consider a sample of stable isotope ${}^{A}\mathrm{X}_{Z}$ that represents the heaviest, most-stable isotope for element X that is subjected to a neutron flux forming nuclei ${}^{A+1}\mathrm{X}_{Z}$. If the flux is such that the time to capture a neutron is long with respect to β-decays (i.e., $\tau_{n\gamma} \gg \tau_{\beta}$), then the unstable nuclide created (with $A+1$ nucleons) is more likely to β-decay rather than capture another neutron. In this case the nucleosynthesis path across the isotope chart follows the valley of stability. This scenario corresponds to the s-process, where a slow and steady neutron source operates over long timescales.

If the flux is such that the time to capture a neutron is much shorter with respect to the β-decay (i.e., $\tau_{n\gamma} \ll \tau_{\beta}$), another neutron-capture is more likely to occur before β-decay occurs. This will lead to the production of another unstable isotope, ${}^{A+2}\mathrm{X}_{Z}$, often with a much shorter β-decay half-life. Therefore, for a given $\tau_{n\gamma}$, successive neutron captures will occur until the isotopes involved in the path have a comparable τ_{β}. This may cause the production of nuclei at the neutron drip-line, where successive neutron captures will create nuclei too unstable to exist in a bound state. This scenario corresponds to the r-process, where a rapid burst of neutrons over a short timescale causes the production of very neutron-rich nuclei. Once the neutron source is extinguished, the unstable nuclides undergo successive β-decays to the valley of stability.

For a given quantity of nuclei involved in reactions, there will be a fraction of nuclei ${}^{A+1}\mathrm{X}_{Z}$ that are destroyed via β-decay, with the remainder capturing neutrons. This fraction is known as the branching ratio, β, and can be defined as

$$\beta \equiv \frac{\tau_{\beta}}{\tau_{n\gamma} + \tau_{\beta}}. \tag{2.32}$$

Branching ratios are important to consider for unstable isotopes that lie between two

stable isotopes for a given element. Such isotopes exist due to the pairing effect of nucleons. An example of such branching is displayed in Fig. 2.3 (Dillmann et al., 2008, Fig. 1.), where the branching point nucleus ^{79}Se leads to a splitting of the s-process path depending on the branching ratio. The branching ratio is further complicated by the presence of isomeric states in ^{79}Se. Isomeric states are nuclear energy levels that, upon being populated, exhibit different lifetimes and preferential decay paths. In the case of ^{79}Se, the β^- decay lifetime of the $\frac{1}{2}^-$ isomeric state is $\sim$ 3.92 mins, in stark contrast to the ground state, which has a lifetime of 2.8×10^5 yrs. Therefore, β^--decays to ^{79}Br will occur dominantly via ^{79}Se populated by the isomeric state. Transitions to and from isomeric states need to be included in nuclear reaction networks in order to determine the correct branching ratios.

Overall, the proportion of elements above iron created by the s- and r-processes is approximately 50:50, but there are particular isotopes that are identified to be formed predominantly by a single process. These are referred to as s-only, r-only or p-only depending on the process responsible for its production. For example, ^{80}Kr is an s-only isotope because it is 'shielded' by the stable isotope ^{80}Se. That is, there is no r-process contribution to the abundance of ^{80}Kr because β-decays from neutron-rich nuclei will create ^{80}Se. Therefore, observations of s-only (r-only) isotopes are important tracers of the s-process (r-process). Examples of useful observational tracers for the s- and r-processes are Ba (since ^{134}Ba and ^{136}Ba are shielded by Xe isotopes) and Eu (since none of the stable isotopes are shielded) respectively. Note that the two stable Eu isotopes, ^{151}Eu and ^{153}Eu are not strictly r-only isotopes, but their production by the s-process is very low.

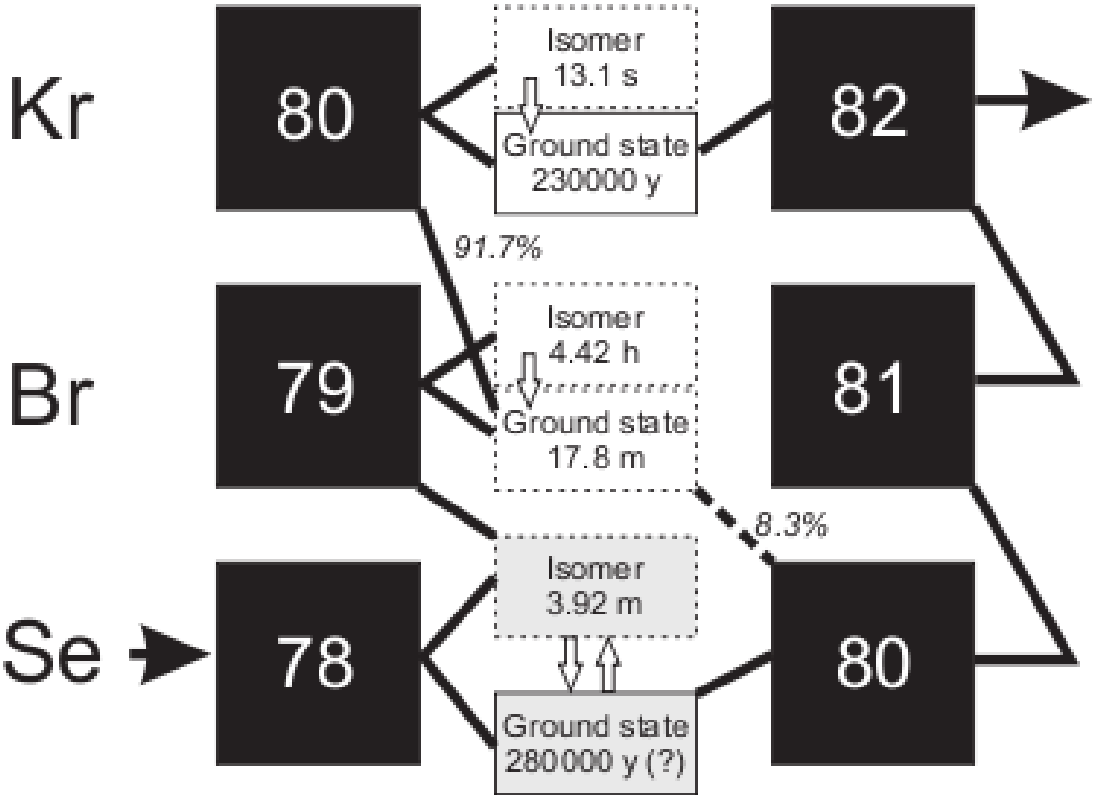

Figure 2.3: A small section of the chart of isotopes showing the s-process path around the branching point nucleus ^{79}Se. The black arrows/lines indicate the dominant nucleosynthesis paths during the s-process, whereas white arrows indicate dominant transitions between different internal nuclear states (between isomeric and ground states) for a particular isotope. The half-lives specified here are terrestrial values, which is relatively uncertain for ^{79}Se (at a value of $2.80 \pm 0.36 \times 10^5$ yr).

2.4.1 The classical s-process

Following Burbidge et al. (1957), early work in s-process nucleosynthesis was conducted in order to identify the neutron sources responsible for the abundances of heavy elements and the sites of operation (Clayton et al., 1961, and references therein). The procedure was typically to solve equations of the form of Eq. 2.17 analytically. For neutron-captures, Eq. 2.17 can be rewritten as

$$\left(\frac{dn_A}{dt}\right)_A = -n_n v_T n_A \langle\sigma\rangle_A + n_n v_T n_{A-1} \langle\sigma\rangle_{A-1} \tag{2.33}$$

where the substitution $\langle\sigma v\rangle_A = \langle\sigma\rangle_A v_T$ is justified because the thermal velocity, v_T, and the average cross-section, $\langle\sigma\rangle_A$ do not vary much over the neutron irradiation; the neutron-captures often occur during the hydrostatic burning of another fuel, with slowly varying (approximately constant) temperature. It is now possible to define the neutron exposure, in units of cm^{-2} (often converted into units of 10^{-27} cm^{-2}, or millibarns^{-1} [mb^{-1}]), as

$$\tau_n \equiv v_T \int n_n(t) dt \tag{2.34}$$

which reduces Eq. 2.33 to

$$\left(\frac{dn_A}{d\tau_n}\right)_A = -n_A \langle\sigma\rangle_A + n_{A-1} \langle\sigma\rangle_{A-1} = -\psi_A + \psi_{A-1}. \tag{2.35}$$

Equation 2.35 can then be solved analytically or numerically for the region $56 < A < 209$, with $\psi_{55} = 0$ and $\psi_{210} = 0$, with the initial conditions

$$n_a(0) = \begin{cases} n_{56}(0) & A = 56 \\ 0 & A > 56. \end{cases}$$

From Eq. 2.35, it can be seen that if $n_A > \frac{\langle\sigma\rangle_{A-1}}{\langle\sigma\rangle_A} n_{A-1}$, then $dn_A/dt < 0$ and n_A will decrease, and if $n_A < \frac{\langle\sigma\rangle_{A-1}}{\langle\sigma\rangle_A} n_{A-1}$, $dn_A/dt > 0$ and n_A will increase. That is, the equation has the property that given some period of exposure, ψ will take values that minimize the differences between them. For large values of cross-sections (applicable to nonmagic nuclei), the ψ values are larger than their differences and $\psi_A \approx \psi_{A-1}$ (Clayton, 1968, ch. 7-3). This is known as the local approximation, which does not apply for magic nuclei.

The effect of the local approximation was verified in observations of the abundances in the envelopes of red giants stars as measured by Suess & Urey (1956). Fig. 2.4 shows $\langle\sigma_A\rangle n_A = \psi_A$ as a function of atomic mass for their abundance measurements (Clayton et al., 1961, Fig. 19). The fitted curve corresponds to $\langle\sigma_A\rangle n_A = 2160\psi_{n_c=2.8} + 990\psi_{n_c=6.9} + 45\psi_{n_c=34} + 3.6\psi_{n_c=100}$, where n_c is the neutron-captures per iron seed, defined by

$$n_c = \frac{\sum_{56}^{209}(A-56)(n_A)}{n_{56}}. \tag{2.36}$$

The values of n_c quoted correspond to values of $\tau_n = 0.1, 0.2, 0.6$ and 1.1 mb^{-1}. Although the particular values chosen are arbitrary, they indicate that the best solution corresponds to a distribution of different exposures rather than a single exposure. The series of plateaus between magic nuclei demonstrates the applicability of the local approximation. This is also true for the Solar system abundances; Fig. 2.5 shows a similar fitting curve overlaid with the Solar system abundance values (Seeger et al., 1965, Fig. 1). The analytical solution plotted in Fig. 2.5 is given by an exponential distribution of exposures, $\rho(\tau_n)$ (see Eq. 2.37). The close fit with the observational data after

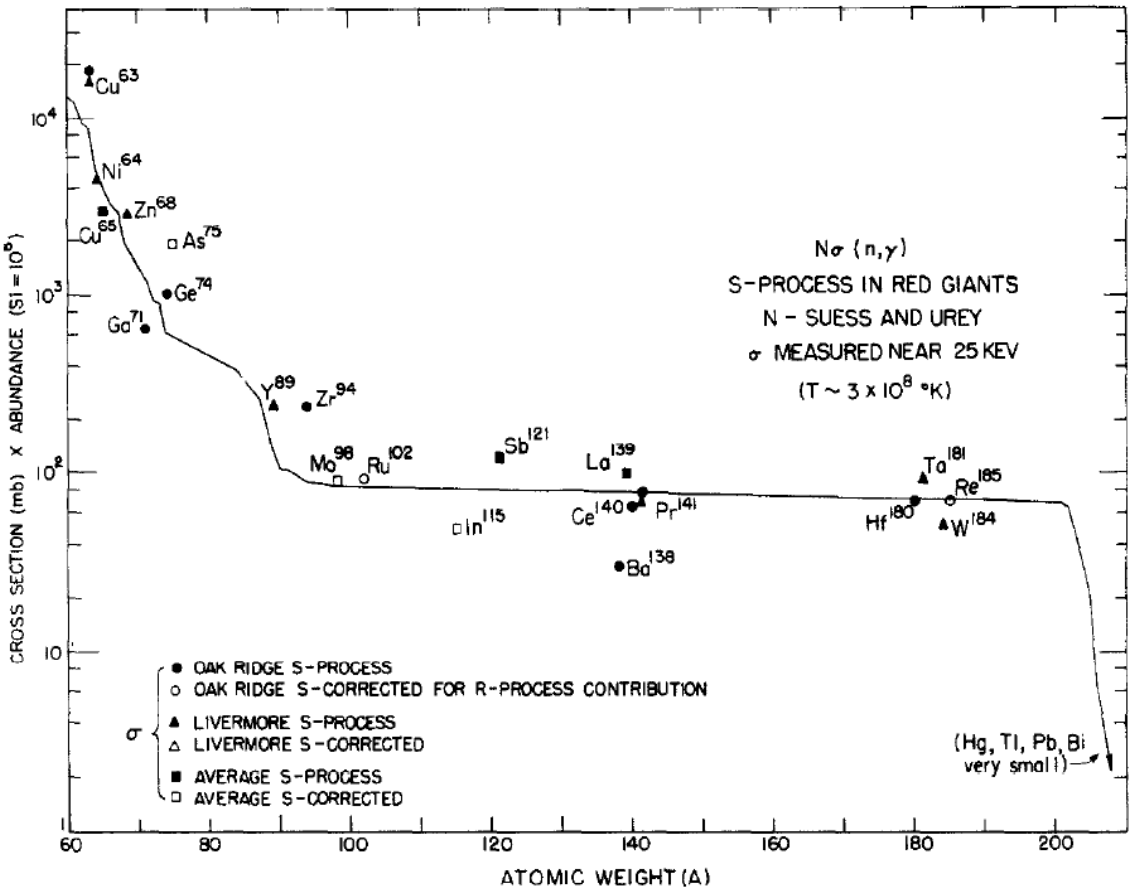

Figure 2.4: The product of the cross-section for neutron capture and the abundance as a function of atomic mass using data from observations of red giant stars (Suess & Urey, 1956, Fig. 19.). A correction is applied for some isotopes that have a contribution from other processes.

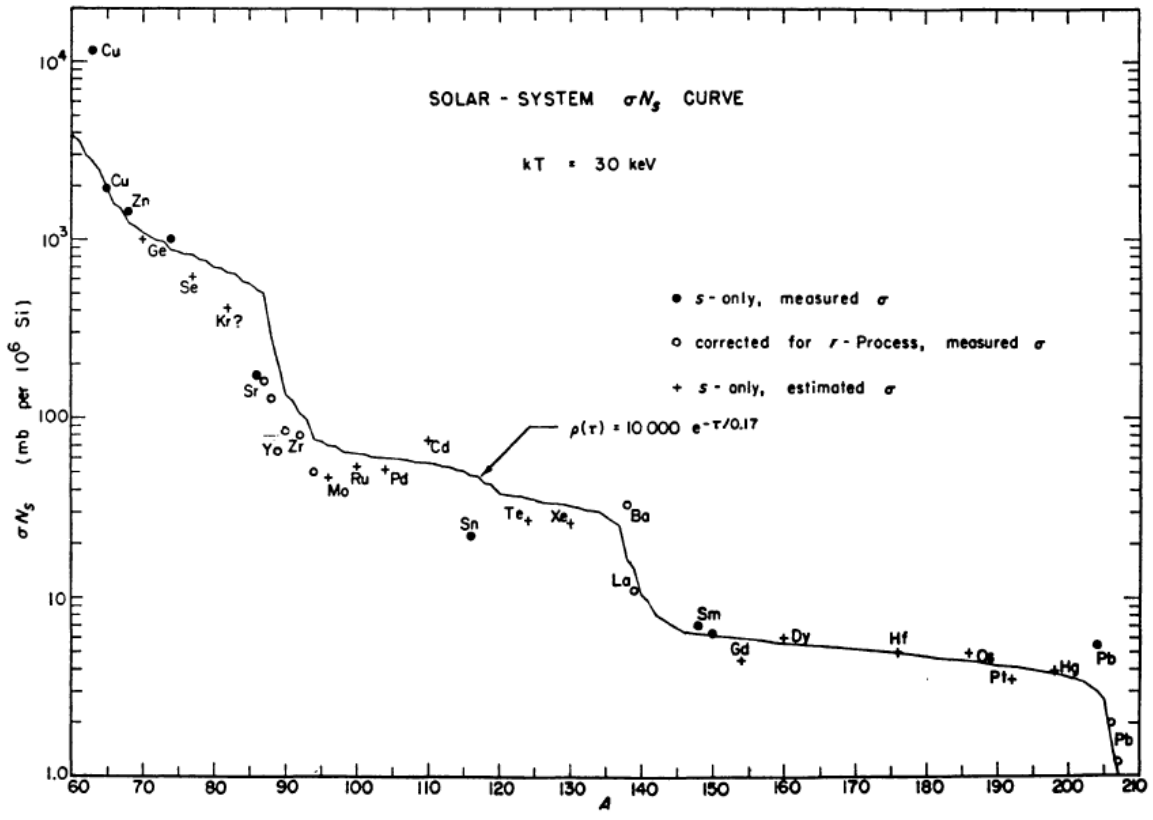

Figure 2.5: The product of the cross-section for neutron capture and the abundance as a function of atomic mass using Solar system abundance determinations (Seeger et al., 1965, Fig. 1.). A correction is applied for some isotopes that have a contribution from other processes (such as the r-process).

considering neutron parameters that do not vary with time in a stellar environment strongly-enhanced the robustness of the s-process idea and the local approximation. However, there was degeneracy associated with whether a distribution of exposures was due to different neutron exposures in different sites or the presence of uncertainties in stellar physics (such as mixing effects).

Although considerable uncertainties still remain in present s-process models (see §2.4.2), the identification of multiple sites for the s-process, their quantitative evaluation and comparisons with observations strongly supported the s-process idea, as did observations of the unstable element Tc (Merrill, 1952), which provided direct evidence of s-process nucleosynthesis in S-type stars (the half-life of ^{99}Tc is 2.1×10^5 yrs, which is smaller than the main sequence lifetime. Therefore, its presence in S-type stars suggests that the s-process responsible for the observed isotopes is relatively recent or ongoing in the stars' evolutionary history). The isotopes ^{13}C and ^{22}Ne, activated by (α,n) reactions, were suggested as the main sources of neutrons (Cameron, 1955, 1960) and were consequently verified in early computer models of helium cores in massive stars and the thermally-pulsing phase of asymptotic giant branch (AGB) stars. The ^{13}C neutron source is produced by the ^{12}C(p,γ)^{13}N(β^-)^{13}C reaction chain, where the ^{12}C is mainly primary (because ^{12}C is synthesised during helium burning via the 3α reaction), whereas the ^{22}Ne neutron source is formed via the ^{14}N$(\alpha,\gamma)^{18}$F$(\beta^+)^{18}$O$(\alpha,\gamma)^{22}$Ne reaction chain and is mainly secondary (because ^{14}N is produced at the expense of ^{12}C and ^{16}O during the CNO bicycle and the abundances of CNO isotopes during hydrogen burning is dependent on the metallicity). Peters (1968) verified that although the s-process in the helium core of massive stars can create a distribution of neutron exposures in stars with different initial masses (and due to mixing in a shrinking, convective helium core), the maximum exposures are too small to account for the whole Solar sys-

tem abundance distribution and that repeated cycling of material through numerous stars could occur. Couch et al. (1974) also verified, using updated models based on polytropic stellar structure (Arnett, 1972a), that the helium-core s-process could not account for the whole Solar system distribution, but contributed to nuclei in the mass region $60 < A < 80$. However, Couch et al. (1974) also suggested that the s-process occurring in AGB stars via the ^{13}C neutron source during thermal pulses (Scalo & Ulrich, 1973; Ulrich, 1973) could reproduce, in combination with the weak neutron exposure in massive stars, the s-process contribution to the Solar system abundances. Indeed, the distribution estimated from models of thermally pulsing lower-mass stars produced soon after were shown to naturally exhibit an exponential distribution of exposures with resulting abundances that follow a Solar system-like distribution (Iben, 1975b,a; Gallino et al., 1988). Independent work by Lamb et al. (1977), using updated reaction rates and models, yielded similar conclusions on the s-process during helium-core burning in massive stars.

It emerged that a complete picture of the s-process neutron exposures could be explained by three main components, a weak, a strong and a main component (Truran & Iben, 1977; Käppeler et al., 1982, 1989; Käppeler, 1999, and references therein). Each component has an exponential distribution of exposures of the form

$$\rho(\tau_n) = \frac{f n_{56}}{\tau_0} \exp\left(-\frac{\tau_n}{\tau_0}\right). \tag{2.37}$$

By assuming that $\langle\sigma\rangle_A n_A$ is a smooth curve determined using

$$\langle\sigma\rangle_A n_A = \int_0^\infty \rho(\tau_n)\psi_A(\tau_n)d\tau_n, \tag{2.38}$$

a solution can be obtained, which is found by substituting for $\rho(\tau_n)$ in Eq. 2.38:

$$\langle\sigma\rangle_A n_A = \frac{f n_{56}}{\tau_0} \prod_{i=56}^{A} [1 + (\langle\sigma\rangle_i \tau_0)^{-1}]^{-1} \tag{2.39}$$

where f is the fraction of total ^{56}Fe subject to neutron irradiation and τ_0 is a parameter that forms an estimate of the mean neutron exposure. Fig. 2.6 shows $\langle\sigma\rangle_A n_A$ for a two-component solution as a function of atomic mass, which demonstrates the need for multiple components to describe the Solar system abundances (Käppeler, 1999, Fig. 16). The two components are plotted using Eq. 2.39 with $f = 0.04\%$ and $\tau_0 = 0.3$ mb^{-1} for the main component and $f = 1.6\%$ and $\tau_0 = 0.07$ mb^{-1} for the weak component. The lines are compared with the Solar system abundances for s-only nuclei, showing a remarkable fit (the variance is only 3%). However, the two-component model underestimates the abundance of ^{208}Pb, giving rise to the requirement of a third component. This strong component is responsible for converting a small fraction of iron-seed nuclei into ^{208}Pb (Clayton & Rassbach, 1967; Truran & Iben, 1977). The two-component model also exhibits 'breaks' in the main component at specific nuclei. These can be attributed to branching points in the s-process path, which are not taken into account in the classical model since it is assumed that the $\tau_{n\gamma} \gg \tau_\beta$. Branching points in the s-process path must therefore be taken into account in order to determine an accurate abundances curve. The typical parameters for the s-process components are listed in Table 2.2, which show how the parameters vary for each distribution (values taken from Iliadis, 2007).

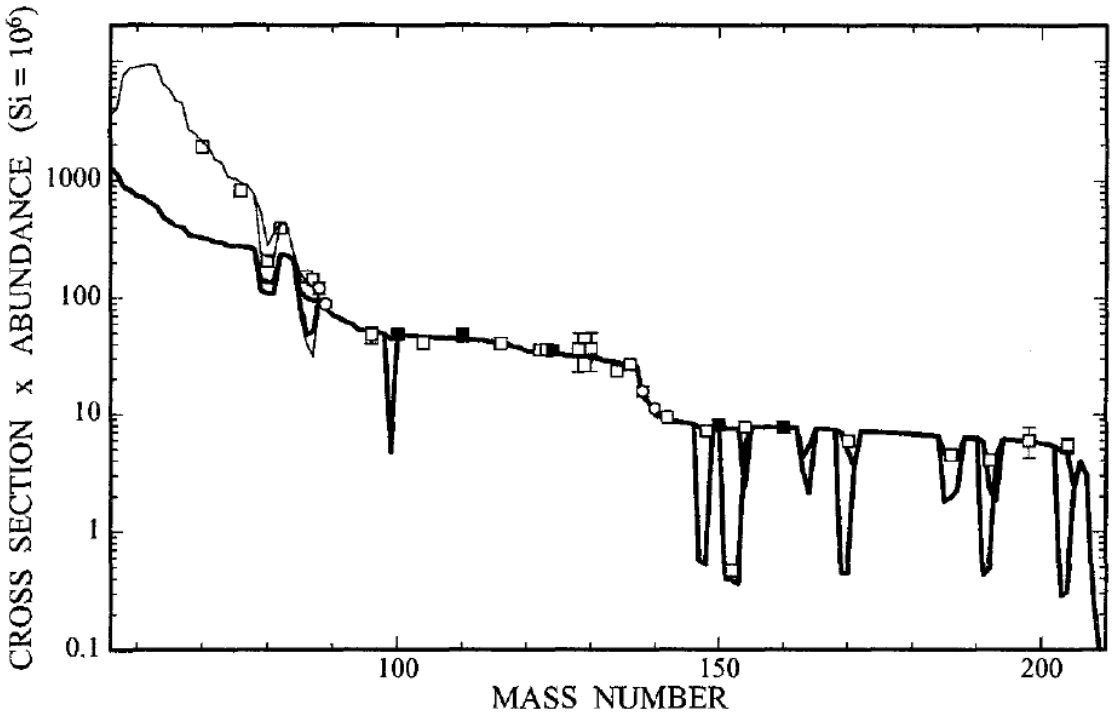

Figure 2.6: The product of the cross-section for neutron capture and the abundance ($\langle\sigma\rangle_A n_A$) as a function of atomic mass for a two-component model, compared with s-only isotopes. The main component is indicated by the bold line and the weak component is indicated by the thinner line (Käppeler, 1999, Fig. 16).

Table 2.2: Typical parameters for s-process components. Specified for each component are the stellar site, the percentage fraction of seed nuclei destroyed via neutron captures (f), the mean neutron exposure (τ_0) and the neutron captures per iron seed (n_c).

Component	Stellar site	f (%)	τ_0 (mb^{-1})	n_c
Weak	Massive stars	1.6	0.07	3
Main	Low/intermediate mass AGB stars	0.06	0.3	10
Strong	Low mass, low metallicity AGB stars	10^{-4}	7	140

2.4.2 Recent s-process models

Considering the empirical nature of the s-process studies and the assumptions present in the formulation, the ability of the classical s-process theory to account for the Solar system abundances to within a small error is a considerable success. However, detailed studies for specific nuclei indicated the need for a more rigorous treatment of the s-process. The classical s-process model overpredicts the abundances of ^{142}Nd, ^{136}Ba and ^{116}Sn, which were revealed through improved experimental data (Käppeler et al., 1989) and for nuclei at or near to the magic number peaks in atomic mass, where the local approximation is not applicable, the classical s-process is considered unreliable. This is a consequence of assumptions such as $\tau_{n\gamma} \gg \tau_{\beta}$, which is not true for all nuclei, and the constant neutron density during the s-process as a function of time. For example, the branching-point nuclei ^{85}Kr and ^{79}Se are known to exhibit different branching ratios dependent on the neutron irradiation. Consequently, observations of the ^{80}Kr/^{80}Se and ^{86}Sr/^{86}Kr ratios, combined with accurate cross-sections, can probe the interior conditions present during the s-process (see for example, Walter et al. 1986a,b).

2.4.2.1 The weak s-process component

S-process nucleosynthesis models either calculate the full nucleosynthesis during the stellar model or by taking profiles from existing stellar evolution models and 'post-processing' with a separate network code. The calculations may be made using a single 1D spherical shell (or 'zone'), which represents well the relevant s-process site (such as the bottom of a convection zone), or using many zones, including those involved in neutron-capture nucleosynthesis. In regards to the massive-star s-process, the models following the early works by Peters (1968), Couch et al. (1974) and Lamb

et al. (1977) were made in order to assess potential uncertainties and explore s-process nucleosynthesis in different sites other than the helium-core. For reaction rates, the $^{12}C(\alpha,\gamma)^{16}O$ and $^{22}Ne(\alpha,n)^{25}Mg$ rates were often studied due to their importance in the s-process nucleosynthesis and the high uncertainties associated with their cross-section determinations (Arnett & Thielemann, 1985; Busso & Gallino, 1985; Raiteri et al., 1991). The $^{12}C(\alpha,\gamma)^{16}O$ rate is important because it affects the $^{12}C/^{16}O$ ratio at the end of helium-burning, which consequently affects the central carbon- and oxygen-burning stages, and competes with the ^{22}Ne neutron source for α-particles, which are an ingredient for the $^{22}Ne(\alpha,n)^{25}Mg$ neutron source reaction. Changing the $^{22}Ne(\alpha,n)^{25}Mg$ reaction rate (via a modified cross-section) affects the neutron density during the neutron irradiance and the total neutron exposure, since the ^{22}Ne isotope is only partially burnt. In addition to the $^{12}C(\alpha,\gamma)^{16}O$ reaction, recent models have also looked at the effect of variations in 3α (Tur et al., 2007, 2009) and (n,γ) reactions (Heil et al., 2008; Pignatari et al., 2010). The latter is particularly important because, unlike the local approximation, a 'propagation effect' in the nucleosynthesis can occur, where the change in a single neutron-capture rate can modify the abundances of many isotopes along the whole s-process path. Accurate cross section data for neutron-capture reactions on seed nuclei are therefore important in constraining stellar models.

In addition to the helium-core burning stage, carbon-core and carbon-shell burning stages were also determined to exhibit neutron irradiances due to unburnt ^{22}Ne left over from helium-core burning (Arnett & Thielemann, 1985; Arcoragi et al., 1991; Raiteri et al., 1991). Typical parameters for these stages are specified in Table 2.3. It should be noted that the neutron exposures exhibited in these stages differ from the classical prediction given in Table 2.2 because only a fraction of the isotopes will be included in the stellar wind or the supernova ejecta, which are the mechanisms in which

Table 2.3: Typical parameters for s-process sites in massive stars. Specified for each burning stage are the typical burning temperature during the s-process, T, the neutron exposure (τ_n) and the maximum neutron density (n_n^{max}).

Burning Stage	T (GK)	τ_0 (mb^{-1})	n_n^{max} (cm^{-3})
Helium-core	0.25	0.2	10^{5-7}
Carbon-core	0.5	0.2	10^{7}
Carbon-shell	0.9	0.06	10^{10-11}

the star can enrich the interstellar medium with neutron-capture elements. The central carbon core was identified to have a neutron exposure (as a result of the ^{13}C(α,n)^{16}O neutron source) of the same order as the helium core, but the isotopes created by the burning remain in the core and are not ejected into the interstellar medium by the stellar wind or the supernova explosion. This is because the carbon burning occurs either in radiative conditions or in a relatively small convective core. The helium- and carbon-shell burning stages were found to exhibit low neutron exposures and therefore contribute only a negligible amount to the total heavy elements. In the case of helium-shell burning, the temperature is too low for the neutron sources to become efficient and are considered negligible. In the case of carbon-shell burning however, the neutron density is quite large, with a value $\sim 10^{11}$ neutrons cm^{-3}, despite the low neutron exposure. This affects branching point nuclei and modifies the abundances of specific isotopes within the region $70 < A < 90$, in addition to some heavy isotopes (e.g. ^{180}Ta and ^{180}W) (Käppeler et al., 1989, and references therein).

For further details of the weak s-process, see §4.1.2.

2.4.2.2 The main s-process component

With regards to AGB stars, early models suggested that the ^{22}Ne neutron source is effective during thermal pulses in intermediate mass ($3M_{\odot} < M_{ini} < 9M_{\odot}$) AGB stars (Iben, 1975b,a). However, the ^{22}Ne neutron source is marginal relative to the ^{13}C neutron source, hence the ^{13}C(α,n)^{16}O reaction is the main neutron source for the main component, which is effective during the interpulse phase in lower mass ($M_{ini} < 3M_{\odot}$) AGB stars (Busso et al., 1988; Gallino et al., 1998; Busso et al., 2001). Typical neutron parameters are $n_n \sim 10^{9-10}$ cm^{-3} $\tau_n \sim 0.14$ mb^{-1} (Hollowell & Iben, 1988). Thermal pulses also provide a natural explanation for the exponential distribution of exposures required to describe the main component (Ulrich, 1973; Scalo & Ulrich, 1973). This distribution is of the form

$$\rho(\tau_n) = \exp\left(\frac{\tau_n \ln(r)}{\Delta\tau_n}\right) \tag{2.40}$$

where r is the fractional overlap between successive helium-shell flash convection zones and $\Delta\tau_n$ is the exposure per pulse (analogous to τ_0 in the classical model). However, thermal pulses and the formation of the ^{13}C neutron source are difficult to model accurately and require parameterised models (see for example Busso et al., 1999; Herwig, 2005, and references therein). Consequently, thermal pulses and the mechanism for s-process nucleosynthesis in AGB stars remains an open problem in nuclear astrophysics.

In any case, one can consider two possible thermal pulse scenarios that can occur during the evolution of thermally pulsing AGB stars. Fig. 2.7 shows these scenarios in terms of the convection zone structure and sites of nucleosynthesis (Suda et al., 2004, Fig. 3). These scenarios are the helium-flash with hydrogen-ingestion scenario (Hollowell & Iben, 1988) (panel a), and the 'standard' radiative scenario (panel b). The standard radiative case is thought to occur in most AGB stars, whereas the hydrogen-

ingestion case can occur in the very-late thermal pulse (VLTP) of an AGB star (Herwig, 2005) or in low metallicity ([Fe/H] $\lesssim -2.5$) AGB stars (Suda et al., 2004). Both scenarios start with the ignition of helium off-center in the star, which develops into a helium-shell flash convection zone. The convection zone grows in size until, during the peak of the flash, it approaches the bottom of the slowly-advancing hydrogen-burning shell and convective envelope.

In the case of the standard radiative case, this convection zone does not penetrate the bottom of the hydrogen-burning shell due to the presence of an entropy barrier between the helium- and hydrogen-shell. Following the peak of the thermal pulse, the envelope expands and cools. As this occurs, the bottom of the convective envelope moves deeper into the star (in mass coordinate), bringing into the envelope ashes from the previous thermal pulse. Mixing of this form is known as third dredge-up (TDU). After TDU, the envelope continues to move higher in mass coordinate, leaving behind a mixture of protons and ^{12}C. The protons capture onto the ^{12}C, forming ^{13}N, which $\beta-$decays to ^{13}C (an incomplete CNO cycle). The ^{13}C is then responsible for a neutron irradiance in the pocket until the next thermal pulse. The s-process products are then mixed into the helium-shell flash convection zone during the next thermal pulse and are mixed into the envelope at the next TDU episode. This is the mechanism by which Solar metallicity AGB stars contribute to the main s-process component of the Solar system abunbdances.

In the case of the hydrogen-ingestion scenario, the entropy barrier between the helium- and hydrogen-shell is much lower and the helium-shell flash convection zone can penetrate into the hydrogen-burning shell. In this case, protons are mixed down into helium-shell flash convection zone. Since the temperatures in the interior are already large enough to instigate hydrogen burning, the hydrogen mixes down into the

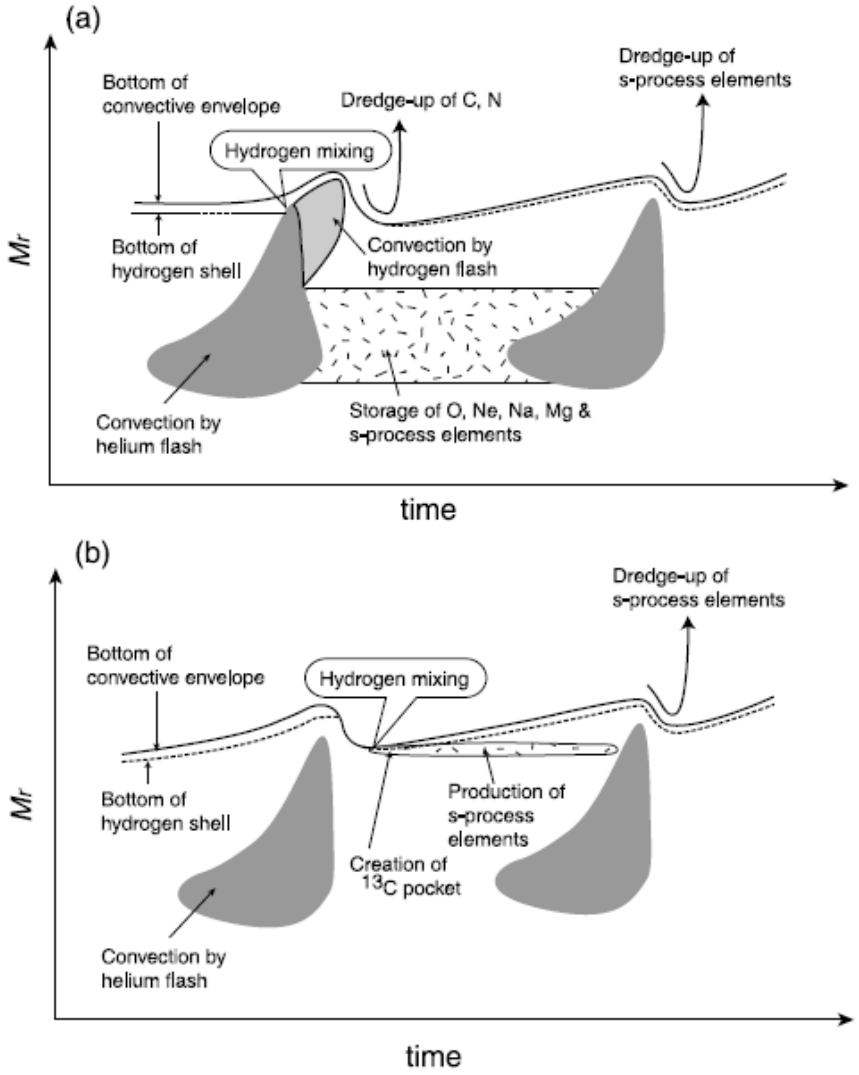

Figure 2.7: Two possible scenarios for convection zone evolution during the thermally-pulsing phase of AGB stars between two consecutive thermal pulses (Suda et al., 2004, Fig. 3). Panel a) represents the case where a hydrogen-ingestion occurs following the helium-flash, which is characterised by the penetration of the bottom of the convective envelope by the helium-shell flash convection zone. This is relevant for low metallicity AGB stars and for the very-late thermal pulse (VLTP) in post-AGB stars. Panel b) represents the scenario where the helium-shell flash convection zone does not penetrate the bottom of the convective envelope, which is characteristic of standard AGB star evolution. See text for details.

helium-shell flash convection zone until the timescale for burning is comparable to the timescale for convective mixing. This results in a hydrogen-ingestion flash, splitting the helium-shell flash convection zone into two convection zones; one driven by helium-burning and one driven by hydrogen burning. The hydrogen burning zone then extends outwards in mass, bringing with it additional fuel from the radiative hydrogen-burning zone above. TDU then occurs as normal, mixing mainly carbon and nitrogen into the envelope. The ^{13}C neutron source is formed in the helium-shell flash convection zone by proton captures onto ^{12}C, causing a neutron irradiance in the convective shell which synthesizes nuclides up to the Sr-Y-Zr peak. These nuclides may then be included into the next thermal pulse and deposited in the envelope by TDU, in a similar way to the radiative case.

2.4.2.3 Sakurai's object

Sakurai's object, which is a $0.6M_{\odot}$ born-again post-AGB star that has experienced a VLTP, has observed abundances that are highly non-Solar. The abundance signature is characteristic of a hydrogen-ingestion flash of the kind seen in panel a) of Fig. 2.7 (Asplund et al., 1999; Herwig, 2005; Herwig et al., 2011). Fig. 2.8 shows the observed abundances of Sakurai's object relative to the Solar system abundances (Asplund et al., 1999, table 2). The enhancement of carbon, nitrogen and oxygen is caused by the incomplete CNO burning occurring during the hydrogen-ingestion flash and the production of the light s-process elements, Sr, Y and Zr, is caused by the s-process in the helium-flash convection zone. This may suggest that the hydrogen-ingestion flash is the site for the light-element primary process (LEPP; see §2.4.2.4 and Herwig et al., 2011). The low abundance of Mg suggests that the main neutron source for the

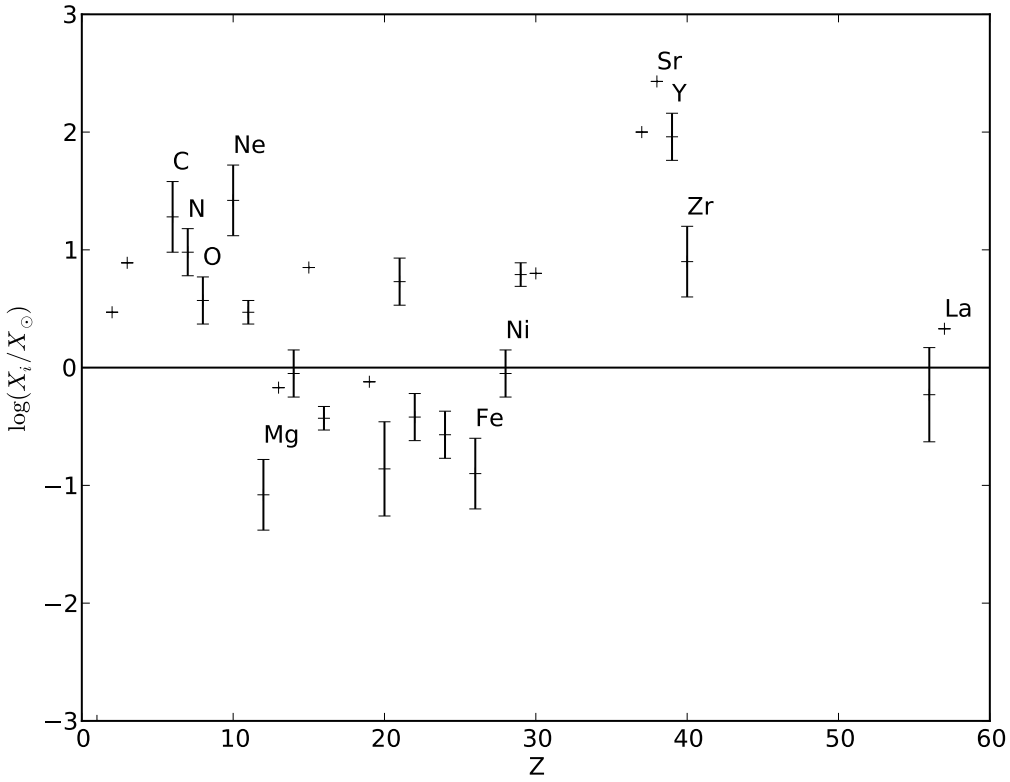

Figure 2.8: Elemental abundances of Sakurai's object relative to the Solar system abundances (Asplund et al., 1999, table 2). No error was provided for abundances that were derived from a single spectral line.

s-process is ^{13}C, since the product of the ^{22}Ne neutron source reaction is ^{25}Mg.

The abundances (in addition to the light curve; see for example Miller Bertolami & Althaus, 2007) of Sakurai's object allow observational constraints to be placed on thermal pulse models including hydrogen-ingestion flashes. The abundances of Sakurai's object can be approximately reproduced in 1D stellar models provided that the mixing between the helium-shell flash convection zone and the hydrogen-ingestion flash convection zone is assumed to be more efficient than that predicted by MLT (Herwig

et al., 2011). A more adequate treatment of the mixing between convective–radiative interfaces, such as those provided by multidimensional simulations, may provide additional insight into the mixing processes relevant for thermally pulsing AGB stars and allow for a more accurate reproduction of the abundances of Sakurai's object (Herwig et al., 2006, 2011).

2.4.2.4 Light Element Primary Process (LEPP)

Galactic chemical evolution models using updated s-process yields from stellar models and observations of r-process-rich stars demonstrate a deficiency of Sr, Y and Zr relative to the Solar system abundances (Travaglio et al., 2004; Serminato et al., 2009). Travaglio et al. (2004) therefore inferred the existence of an additional nucleosynthesis process other than the s-and r-processes which produces a non-negligible fraction of the Solar Sr, Y and Zr and possibly some of the heavier elements between the Sr-Y-Zr and Ba-La peaks (see Fig. 2.1), such as Mo, Ru, Cd and Pd. This process is called the LEPP, which is thought to be of primary nature. The exact origin of the LEPP is unknown at present, but has been observed in r-process enriched metal-poor stars (François et al., 2007; Montes et al., 2007). The possibility of the LEPP being composed of two contributions: one at Solar metallicity (the 'Solar LEPP') and one at low metallicity (the 'stellar LEPP') has also been discussed (Montes et al., 2007).

Since the stellar LEPP requires a nucleosynthesis process that operates at low metallicity, there are very few iron seeds for the s-process and low mass stars have been unable to contribute yet to the galactic chemical evolution because of their long lifetimes. The additional Sr, Y and Zr could therefore arise from an alternative nucleosynthesis process that occurs in low metallicity massive stars. Consequently, two

additional solutions for the overabundances of Sr, Y and Zr have been proposed, which are the "weak r-process" (Kratz et al., 2007; Cowan et al., 2011) and the "α-process" (Qian & Wasserburg, 2007, 2008; Arcones & Montes, 2011). A source for the LEPP could also be the s-process in low-metallicity, fast-rotating massive stars, where primary ^{14}N formed during hydrogen-shell burning mixes into the helium-core, consequently forming the ^{22}Ne neutron source (Pignatari et al., 2008).

Uncertainties present in existing s-process calculations may also account for the discrepancy in Sr, Y and Zr, such as uncertainties in the $^{12}\mathrm{C}(\alpha,\gamma)^{16}\mathrm{O}$ and 3α rates (Tur et al., 2009) and overshooting (Pumo et al., 2010). In addition, the abundances derived in more recent compilations of the Solar abundances (Asplund et al., 2009; Lodders et al., 2009) are smaller than those used (Anders & Grevesse, 1989) in the galactic chemical evolution models (Travaglio et al., 2004; Serminato et al., 2009). In any case, the source of the additional production of elements between Sr and Pd remains unresolved.

3 Stellar evolution models and nucleosynthesis post-processing

Computer simulations of stars provide an important link between observations and theory; any stellar model, with its particular prescriptions of input physics, must correctly replicate stars in accordance with existing observations. Therefore, uncertainties in the input physics can be constrained by observations, although the precision with which constraints can be made depends not only on the uncertainties of observations, but also on systematic errors present in the numerical algorithms of the underlying model. These errors are a consequence of the assumptions and simplifications applied in order to enable the calculation of difficult problems within a realistic time frame with the available resources. Any uncertainty studies must therefore consider these sources of uncertainty in order to make reliable constraints.

In the next chapter, an uncertainty study is undertaken in order to constrain the $^{12}C + {}^{12}C$ rate. The investigation will proceed by generating a grid of massive star models with different initial masses (at Solar metallicity) in order to compare the output yields with the Solar system abundances. Because uncertainties in the stellar models are important in order to evaluate the validity of the output yields, this chapter outlines the choices of input physics considered in the Geneva Stellar Evolution code (GENEC) and the NuGrid[1] Multi-Zone Post-Processing tool (MPPNP), which are used in this work. Because of the complex nature of the computer programs used, the main focus is on the uncertainties in the stellar physics prescriptions. For a detailed specification of the numerical algorithms used in GENEC, see Hirschi (2004) and Eggenberger et al.

[1] http://forum.astro.keele.ac.uk:8080/nugrid

(2008). For further details regarding the post-processing code, see Herwig et al. (2008) and Pignatari et al. (2012, in prep.).

The description of the stellar physics in this chapter is also based on Maeder (2009) and Weiss et al. (2004), except where otherwise specified.

3.1 Stellar structure and the Geneva Stellar Evolution Code (GENEC)

Stellar evolution models, such as GENEC, are computed by solving the equations of stellar structure. These can be formulated as follows:

$$\frac{\partial P}{\partial m} = -\frac{Gm}{4\pi r^4} \tag{3.1}$$

$$\frac{\partial r}{\partial m} = \frac{1}{4\pi r^2 \rho} \tag{3.2}$$

$$\frac{\partial T}{\partial m} = -\frac{GmT}{4\pi r^4 P}\nabla \tag{3.3}$$

$$\frac{\partial L}{\partial m} = \epsilon_{\rm nuc} - \epsilon_{\nu} + \epsilon_{\rm grav}. \tag{3.4}$$

These equations are the hydrostatic equilibrium equation, the continuity equation, the radiative transfer equation and the thermal equilibrium equation, respectively (see for example Kippenhahn & Weigert, 1990). In this 1D shellular formulation, the thermal pressure, P, radius r, temperature T and luminosity, L, are specified with respect to the Lagrangian mass coordinate m, since variations with mass are typically smoother than variations with radius. $\epsilon_{\rm nuc}$, ϵ_{ν} and ϵ_{grav} are the energy generation rates due to

nuclear reactions, neutrino losses and gravithermal energy. $\nabla \equiv d\ln T/d\ln P$, which is

$$\nabla = \nabla_{rad} = \frac{3}{16\pi acG}\frac{\kappa LP}{mT^4} \tag{3.5}$$

in the case where radiation dominates the energy transport. If convection occurs, $\nabla = \nabla_{\rm conv}$ and the gradient requires evaluation from a theory of convection, such as Mixing-Length Theory (MLT). G, a and c are the gravitational constant, radiation constant and speed of light in a vacuum respectively. A solution of the set of equations requires knowledge of the nuclear reaction rates (in order to evaluate the energy generation rate by thermonuclear reactions, $\epsilon_{\rm nuc}$), the opacities, κ, to determine the radiation transport and the equation of state to determine the density, ρ, for a given T and P.

The ϵ_{nuc} term on the right-hand side (RHS) of Eq. 3.4 is calculated using equation Eq. 2.5, which requires the determination of dn/dt. This can be rewritten in terms of the mass fraction abundance specified in Eq. 2.1;

$$\frac{\partial X_i}{\partial t} = \frac{A_i}{N_A\rho}\left(\frac{\partial n_i}{\partial t}\right), \tag{3.6}$$

where the index over all known isotopes is replaced with i to avoid confusion with the atomic mass number A or Avogadro's number N_A. Additional terms describing the mixing can be written as terms of $\partial X_i/\partial t$, such as the following diffusive-mixing formulation:

$$\frac{\partial X_i}{\partial t} = \frac{\partial}{\partial m}\left[(4\pi r^2\rho)^2 D\frac{\partial X_i}{\partial m}\right]_{mix} + \left(\frac{\partial X_i}{\partial t}\right)_{nuc}. \tag{3.7}$$

In this case, the diffusion coefficient, D, is calculated depending on whether the region is convective or radiative. No mixing is calculated for radiative regions, whereas for convective regions, D can be set to the value calculated by MLT ($D = \frac{1}{3}v_c\ell$ where v_c

is the average velocity of convective elements and ℓ is the mixing length). Convective boundaries are determined using a convection criterion, which is an important physical input as it has a critical impact on mixing processes in stars.

3.1.1 Convection Criteria

Convection criteria are determined from the stability of the stellar plasma against small perturbations in density (see for example Weiss et al., 2004, Ch. 14). A perturbation in density may arise from a perturbation in the radial position of matter, since the density of the stellar plasma varies as a function of radius. Alternatively, a temperature perturbation can lead to a change in the density due to pressure equilibrium, which is linked to the equation of state. In any case, a density perturbation results in a change in the net force (due to buoyancy) on a 'mass element'. If the mass element is stable against convection, the resultant force causes oscillatory motion or the motion is damped and the net force returns to zero. If this is not the case the resultant force can lead to an exponentially increasing acceleration of the mass element. The general criterion for convective instability is based on density perturbations and is of the form

$$\left(\frac{d\rho}{dr}\right)_{\delta m} < \left(\frac{d\rho}{dr}\right)_{\text{unpert}}, \tag{3.8}$$

where the left-hand side (LHS) is the density gradient as a function of radius for the perturbed mass element and the RHS is the same quantity, but for the unperturbed surroundings. The density gradients are generally negative, such that if the density gradient for the pertubation is shallower than the density gradient for the surroundings, the stellar plasma is stable against convection. One can consider an equation of state

of the form

$$P^{\alpha} = \frac{\rho}{\mu^{\phi}} k T^{\delta} \tag{3.9}$$

where μ is the mean molecular weight of the stellar plasma, k is the Boltzmann constant and α, ϕ and δ are powers of order unity (note that $\alpha = \phi = \delta = 1$ for an ideal gas Maeder, 2009, Ch. 5). α and δ can be assumed to vary slowly with radius, but this assumption is not valid for ϕ since stratified layers of matter (that are approximately discontinuous) can exist in the stellar interior. By making ρ the subject in Eq. 3.9 and differentiating with respect to r, one obtains

$$\frac{\partial \rho}{\partial r} = \rho \left(\alpha \frac{\partial \ln P}{\partial r} + \phi \frac{\partial \ln \mu}{\partial r} - \delta \frac{\partial \ln T}{\partial r} \right). \tag{3.10}$$

The pressure scale height, H_P, is defined as

$$H_P = -\frac{\partial r}{\partial \ln P}, \tag{3.11}$$

which can be implemented into Eq. 3.10 to give

$$\frac{\partial \rho}{\partial r} = -\frac{\rho}{H_P} \left(\alpha + \phi \frac{\partial \ln \mu}{\partial \ln P} - \delta \frac{\partial \ln T}{\partial \ln P} \right). \tag{3.12}$$

One can now consider the various terms of the RHS of Eq. 3.12 as applied to the interior mass element ('int') and to the unperturbed surroundings ('ext'). $\alpha_{\rm int} = \alpha_{\rm ext} = \alpha$ and $\delta_{\rm int} = \delta_{\rm ext} = \delta$ since they are slowly varying with radius. $H_{P,{\rm int}} = H_{P,{\rm ext}} = H_P$ due to pressure equilibrium. Perturbations in density are small such that $\rho_{\rm int} = \rho_{\rm ext} = \rho$. Consequently,

$$\left(\frac{\partial \rho}{\partial r} \right)_{\delta m} = -\frac{\rho}{H_P} \left(\alpha - \delta \frac{\partial \ln T_{\rm int}}{\partial \ln P} \right) \tag{3.13}$$

and

$$\left(\frac{\partial \rho}{\partial r}\right)_{\text{unpert}} = -\frac{\rho}{H_P}\left(\alpha + \phi\frac{\partial \ln \mu_{\text{ext}}}{\partial \ln P} - \delta\frac{\partial \ln T_{\text{ext}}}{\partial \ln P}\right) \tag{3.14}$$

where possible variations of μ inside the mass element are not considered. Substitution of Eq. 3.13 and 3.14 into Eq. 3.8 gives

$$\frac{\partial \ln T_{\text{ext}}}{\partial \ln P} > \frac{\partial \ln T_{\text{int}}}{\partial \ln P} + \frac{\delta}{\phi}\frac{\partial \ln \mu_{\text{ext}}}{\partial \ln P} \tag{3.15}$$

It is then possible to define 'nabla' gradients of the form

$$\nabla_{\text{unpert}} \equiv \frac{\partial \ln T_{\text{ext}}}{\partial \ln P}, \nabla_{\delta m} \equiv \frac{\partial \ln T_{\text{int}}}{\partial \ln P}, \nabla_{\mu} \equiv \frac{\partial \ln \mu_{\text{ext}}}{\partial \ln P} \tag{3.16}$$

to give Eq. 3.8 in terms of 'nabla' gradients. Two cases can be considered: the first is the case where the composition is uniform ($\nabla_{\mu} = 0$),

$$\nabla_{\delta m} < \nabla_{\text{unpert}}. \tag{3.17}$$

In a radiative zone the temperature gradient is given by the radiative gradient ($\nabla_{\text{unpert}} = \nabla_{\text{rad}}$), whereas the motion of the mass element is adiabatic such that $\nabla_{\delta m} = \nabla_{\text{ad}}$. Hence

$$\nabla_{\text{ad}} < \nabla_{\text{rad}} \tag{3.18}$$

in a convection zone. This is called the Schwarzschild criterion. By taking into account a non-uniform chemical composition, the convection criterion becomes

$$\nabla_{\text{ad}} < \nabla_{\text{rad}} - \frac{\phi}{\delta}\nabla_{\mu} \tag{3.19}$$

where $\alpha_{\rm ad} \simeq \alpha_{\rm rad}$, $\delta = \delta_{\rm ad} = \delta_{\rm rad}$ and $\nabla_\mu \equiv \frac{\partial \ln \mu}{\partial \ln P}$ is a correction to the temperature gradient based on the chemical composition gradient. This is called the Ledoux criterion. Note that there is only a single ∇_μ term because the mass element is assumed to have a homogeneous composition (i.e., $\nabla_{\mu,\rm ext} = 0$).

Fig. 3.1 (Mocák et al., 2011, Fig. 6) shows a schematic representation of the convection criteria and the resulting convective phenomena that result from different values of the ∇ terms (see also Maeder, 2009, Ch. 6). If a mass element is stable against convection according to the Ledoux criterion but unstable according to the Schwarzschild criterion, semiconvection arises. In semiconvection, a convective eddy that sinks due to a perturbation in density will be hotter than the surrounding medium and therefore radiate. As the temperature lowers in the convective mass element, the temperature decreases and the density increases further, causing the mass element to sink further. This results in a slow mixing that differs from convection. If the stellar interior is instead unstable against convection according to the Ledoux criterion but stable according to the Schwarzschild criterion, thermohaline convection arises. In this case, a mass element can have a larger μ and a larger temperature than the surrounding medium. It will therefore radiate, increasing the density and causing the mass element to sink. This is also a slow mixing that differs from that of convection.

The choice of whether to use the Schwarzschild or Ledoux criterion is a long-standing problem in stellar astrophysics. Uncertainties also arise from the particular treatments of semiconvection and thermohaline convection. In GENEC, the Schwarzschild criterion is used and mixing due to semiconvection and thermohaline convection are not considered. An alternative description of the above criteria is made

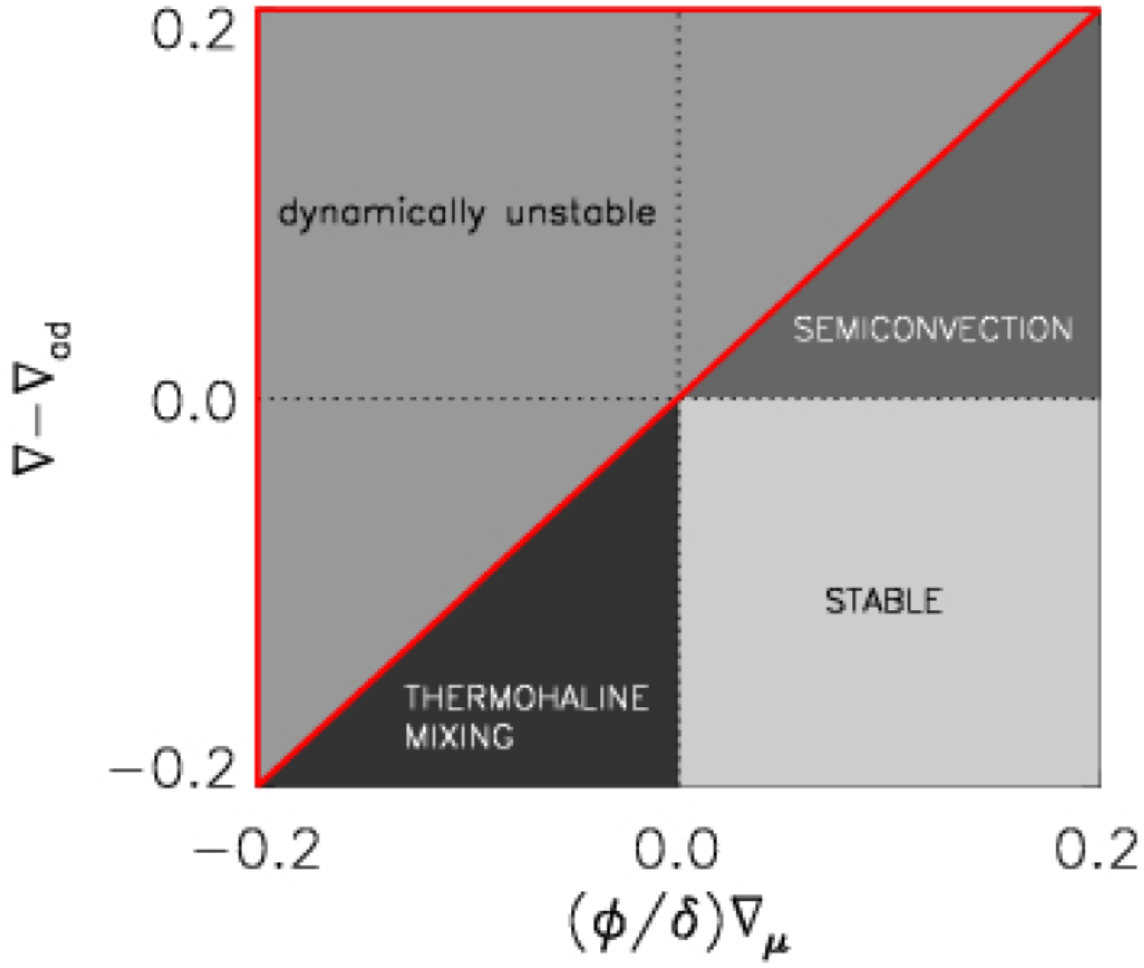

Figure 3.1: Schematic representation of convective mixing processes that occur for different values of $\nabla_{\rm ad}$, $\nabla_{\rm rad}$ (which is equal to ∇) and $\frac{\phi}{\delta}\nabla_\mu$. Taken from Mocák et al. (2011, Fig. 6).

considering the Brunt-Vőisőlő frequency,

$$N^2 = \frac{g\delta}{H_P}\left(\nabla_{ad} - \nabla_{rad} + \frac{\phi}{\delta}\nabla_\mu\right), \tag{3.20}$$

which is a solution of the equation of motion due to a density perturbation caused by a spatial perturbation, $(r - r_0)$, from an equilibrium position r_0. The equation of motion is

$$\rho_{\delta m}\, r + g(\rho_{\delta m} - \rho_{unpert}) = 0. \tag{3.21}$$

The Brunt-Vőisőlő frequency provides the number of times per second a buoyant mass element crosses r_0 (due to harmonic oscillation) and both the Schwarzschild and Ledoux criteria are determined for the case where $N^2 < 0$, where for the Schwarzschild criterion the ∇_μ term is ignored.

3.1.2 Convective core overshooting

Overshooting is a phenomenon associated with additional mixing beyond the convection boundary governed by the convection criterion, which remains a considerable uncertainty in stellar models. The physical description assigned to the overshooting phenomenon is that ascending or descending convective plumes will have a non-zero velocity when crossing the convective boundary into the adjacent radiative zone and hence penetrate into the radiative layer. This additional mixing is not accounted for in local MLT. Zahn (1991) also differentiates between overshooting and penetrative convection, where in the latter case the temperature gradient in the overshooting region is affected by the intruding convective plumes. Overshooting is then assigned to cases where a relatively inefficient mixing process takes place over the Schwarzschild

boundary that changes the composition and transports angular momentum, but does not change the temperature gradient in the region.

Overshooting is normally specified as an extension of the convective boundary (as set by the Schwarzschild criterion) by an additional distance equal to $\alpha_{\rm ov} H_P$, where $\alpha_{\rm ov}$ is a free parameter and H_P is the pressure scale height. In this case, it is often assumed that mixing in the overshoot region is instantaneous (Zahn, 1991). An alternative prescription is to use a modified diffusion coefficient, $D_{\rm ov}$, for mixing in the overshoot region (see Eq. 3.7), of the form

$$D_{\rm ov} = D_0 \exp\left(\frac{-2z}{f H_P}\right) \tag{3.22}$$

where D_0 is the convective diffusion coefficient calculated at the Schwarzschild boundary, f is a free parameter and $z = |r - r_{\rm edge}|$, which is the radial distance into the overshoot region, where r is the radius of the star and $r_{\rm edge}$ is the radial position of the Schwarzschild boundary (Freytag et al., 1996). In GENEC, no overshooting is included except for hydrogen- and helium-burning cores, where an extension of the convective core is applied with $\alpha_{\rm ov} = 0.2$ (Maeder, 1992). This choice of $\alpha_{\rm ov}$ is supported by observations (Demarque et al., 1994; Kozhurina-Platais et al., 1997).

The overshooting causes a convective core to be larger, which mixes additional fuel into the core and increases the luminosity of a star at a given temperature. The mixing of additional fuel also increases the main-sequence lifetime. Its interplay with mass loss consequently decreases the width of the main sequence for O-type stars and increases the width for B-type stars and later spectral types (Maeder & Meynet, 1987). In addition, overshooting during helium-burning mixes more ^{4}He into the core, increasing the availability of α-particles during helium burning. This consequently reduces

the $^{12}C/^{16}O$ ratio and modifies the s-process abundances, since the resulting increase of α-captures onto the ^{22}Ne neutron source increases the s-process efficiency. Combined with a change in the helium burning lifetime, changes in the average overabundances (the overproduction factor for an isotope is defined as the mass fraction abundance divided by the initial abundance) of s-only nuclides at the end of helium burning can be up to a factor of 6 for a change in f from 10^{-5} to 0.035 (Costa et al., 2006; Pumo et al., 2010).

Eldridge & Tout (2004) investigated overshooting using a correction to the convection criterion of the form

$$\nabla_{\rm rad} > \nabla_{\rm ad} - \delta \tag{3.23}$$

where in this case

$$\delta = \frac{\delta_{\rm ov}}{2.5 + 20\xi + 16\xi^2}. \tag{3.24}$$

In Eq. 3.24, $\delta_{\rm ov}$ is a different overshooting parameter to $\alpha_{\rm ov}$, which has a value of 0.12, and ξ is the ratio of gas pressure to radiation pressure. A scheme of this form was reported to give an extension of the convective boundary of $0.3H_P$ for massive stars. Eldridge & Tout (2004) found that including overshooting decreased the limiting mass for creation of a CO or ONeMg white dwarf. This effect may provide a satisfactory solution to the differing predicted masses of Cepheid variables as determined from stellar models (with no overshooting) and observations (Neilson et al., 2010, and references therein). However, this is true only in combination with applications of mass loss and rotation in stellar models. Observational constraints will be important in order to constrain the effects of the various phenomena in addition to free parameters such as $\alpha_{\rm ov}$, and multidimensional simulations can be used to investigate mixing across convective–radiative interfaces (see §5).

3.1.3 Mass loss

Massive stars lose significant amounts of mass over their lifetimes, which pollutes the interstellar medium with matter of a different composition to that of molecular cloud from which the star formed. Mass loss takes place during hydrogen burning, when the evolution timescale is very long, and during helium-core burning, when the opacity of the expanded envelope during this phase is higher; the advanced stages (carbon burning onwards) are too short for a significant amount of mass to be lost. For stars with initial masses larger than $\approx 30 M_{\odot}$, the stellar wind is large enough to expose an increasingly helium-rich envelope (or a bare helium-burning core for the largest masses) and consequently form a Wolf-Rayet star (with a displacement on the HR diagram towards the blue). Mass loss also affects the interior evolution since it lessens the rate of gravitational energy production ($\epsilon_{\rm grav}$) and a lower energy generation rate is sufficient to support the star against gravitational contraction.

In GENEC, several mass loss rates are used depending on the effective temperature, $T_{\rm eff}$, and the evolutionary stage of the star. For O-type massive stars, where $\log T_{\rm eff} > 3.9$, mass loss rates are taken from Vink et al. (2001). These mass loss rates take into account the bi-stability jump between fast and slow winds. For $3.7 < \log T_{\rm eff} < 3.9$, the mass loss rates are taken from de Jager et al. (1988). For $\log T_{\rm eff} < 3.7$, a scaling law of the form

$$\dot{M} = -1.479 \times 10^{-14} \times \left(\frac{L}{L_{\odot}} \right)^{1.7} \tag{3.25}$$

is used, where $\dot{M}$ is the mass loss rate in Solar masses per year, L is the total luminosity and $L_{\odot}$ is the Solar luminosity. During the Wolf-Rayet (WR) phase, mass loss rates

by Nugis & Lamers (2000) are used.

3.1.4 Neutrino losses

Neutrino losses are critical for the evolution of massive stars beyond helium burning. During the advanced stages, neutrino losses start to dominate over radiative losses and the timescale for core burning reduces significantly. In fact, massive star evolution during the advanced stages of evolution can be described as a neutrino-mediated Kelvin-Helmholtz contraction of a carbon-oxygen core (Woosley et al., 2002; El Eid et al., 2009). A reduction in the neutrino losses, ϵ_ν, for example, allows a star to be supported by a smaller energy generation rate (due to nuclear reactions; $\epsilon_{\rm nuc}$), which will affect the consumption of fuel and the lifetime of the burning stage. The formation processes for neutrinos in stellar interiors can be summarized as follows:

i) pair annihilation $\quad {\rm e}^+ + {\rm e}^- \rightarrow \nu + \bar{\nu}$

ii) ν-photoproduction $\quad \gamma + {\rm e}^\pm \rightarrow {\rm e}^\pm + \nu + \bar{\nu}$

iii) plasmon decay $\quad \gamma^* \rightarrow \nu + \bar{\nu}$

iv) bremsstrahlung on nuclei $\quad {\rm e}^\pm + Z \rightarrow {\rm e}^\pm + Z + \nu + \bar{\nu},$

where each process is dominant for different regions of the temperature-density plane (Esposito et al., 2003). In the cores of massive stars, with typical densities of $\rho_c \leq 10^5 {\rm gcm}^{-3}$ and $T_c \geq 10^8$ K, the dominant neutrino loss mechanisms are ν-photoproduction

and pair annihilation processes (Itoh et al., 1996), with pair annihilation dominating ν-photoproduction as the source of neutrinos for temperatures higher than $T \geq 10^9$ K. A small proportion of neutrinos are also formed from Bremsstrahlung and plasmon decay (see also Table 4.2), but these production mechanisms are dominant only for high density conditions typical of white dwarfs. Neutrino loss rates in GENEC are calculated using fitting formulae from Itoh et al. (1989), which are the same as those of the more recent evaluation from Itoh et al. (1996) for pair and photoneutrino processes.

3.1.5 Initial composition, metallicity and opacities

The dependence on metallicity, linked with the choice of initial abundances, affects numerous physical mechanisms in stars. A lack of metals inhibits the role of secondary processes, such as the CNO tricycle during the hydrogen burning phase and the s-process. The s-process is affected because the number of iron-seed nuclei and the abundance of the secondary neutron source ^{22}Ne is reduced. A lower metallicity also lowers the contribution of metals to the opacity, which lowers the mass loss.

Only Solar metallicity models are considered in this work. However, different choices of Solar abundances are available in the literature. In GENEC, the initial abundances used were those of Grevesse & Noels (1993), which are consistent with the opacity tables used (OPAL; Rogers et al., 1996). The OPAL tables are valid for $3.75 \leq \log T \leq 8.7$. For lower temperatures, opacities from Ferguson et al. (2005) are used. Updated initial abundances generally have a lower content of metals, in particular carbon, nitrogen, oxygen and neon (Lodders, 2003; Lodders et al., 2009; Asplund et al., 2009). The use of different choices of initial composition affects the s-process during carbon shell burning, since most of the CNO elements are converted to the ^{22}Ne neutron

source. Stellar models using the Lodders (2003) initial abundances, for example, have been shown to cause a decrease in the elemental overproduction factors of Ge, Kr and Sr by factors of 2.0, 3.6 and 2.1 respectively (Pignatari et al., 2010). However, lower metal abundances in the Sun may be at variance with helioseismic observations (for example, see discussion in Asplund et al., 2009). In order to remain consistent, calculations made relative to Solar abundances (such as the overproduction factors calculated throughout §4) use the Grevesse & Noels (1993) abundances.

3.1.6 Rotation

Inclusion of rotation in stellar models enhances the mixing due to meridional currents, secular and dynamical shears. Rotating models frequently exhibit larger convective cores, having similar effects to that of overshooting (the stars are more luminous at a given temperature). The additional mixing due to rotation is known to account for ^{14}N enhancements observed in O and B stars (Heger et al., 2000; Meynet & Maeder, 2000). The changes in properties are such that, to first order, the properties of rotating massive stars can be assumed to evolve similarly to larger-mass non-rotating stars.

Since ^{14}N is an ingredient in the production of the ^{22}Ne neutron source, rotation can affect the s-process during helium-core burning (Pignatari et al., 2008). The effect on the s-process is akin to an increase in the overshooting parameter. In fact, models including the effects of rotation use a smaller overshooting parameter ($\alpha_{\rm ov} = 0.1$ Hirschi et al., 2004). In this work, rotation is not included, but the effect of rotation (in terms of the mixing of nuclides in the interior) is more limited in the advanced stages because of the short timescale for evolution.

3.1.7 Nuclear reaction networks

In the post-processing approach used in this work, the stellar model and the post-processing tool have separate nuclear reaction networks. The isotopes used in each network are discriminated depending on whether they are involved in reactions important for energy generation (featured in both the stellar model and the post-processing tool) or not (featured only in the post-processing tool). GENEC uses a skeleton network of 31 isotopes, which is the same network used in previous GENEC models (e.g., Hirschi et al., 2004, 2005, see also Table 3.1 and Fig. 3.2.). This network is a combination of fundamental isotopes relevant for pp-chain reactions, the CNO tricycle and helium burning and a network similar to the $\alpha 7$ network of Hix et al. (1998), enacted during the advanced burning stages, which reduces the computational expense associated with a larger network without causing significant errors in energy generation rates.

In GENEC the reaction rates are chosen to be those of the NACRE compilation; Angulo et al. (1999) for the experimental rates and from their website[2] for theoretical rates. However, there are a few exceptions. The rate of Mukhamedzhanov et al. (2003) was used for ^{14}N(p, γ)^{15}O below 0.1GK (which is the temperature range available in the reference) and the lower limit NACRE rate was used for temperatures above 0.1GK. This combined rate is very similar to the more recent LUNA rate (Imbriani et al., 2005) at relevant temperatures. The Fynbo et al. (2005) rate was used for the 3α reaction and the Kunz et al. (2002) rate was used for ^{12}C(α, γ)^{16}O. The ^{22}Ne(α, n)^{25}Mg rate was taken from Jaeger et al. (2001) and used for the available temperature range ($T \leq 1$ GK). Above this range, the NACRE rate was used. The ^{22}Ne(α, n)^{25}Mg rate competes

[2]http://pntpm3.ulb.ac.be/Nacre/nacre.htm

Table 3.1: Nuclear network used for the stellar model calculations

Isotope	A	Z	Isotope	A	Z
^{1}H	1	1	^{18}F	18	9
^{2}H	2	1	^{19}F	19	9
^{3}He	3	2	^{20}Ne	20	10
^{4}He	4	2	^{22}Ne	22	10
^{7}Be	7	4	^{24}Mg	24	12
^{8}B	8	5	^{25}Mg	25	12
^{12}C	12	6	^{26}Mg	26	12
^{13}C	13	6	^{28}Si	28	14
^{13}N	13	7	^{32}S	32	16
^{14}N	14	7	^{36}Ar	36	18
^{15}N	15	7	^{40}Ca	40	20
^{15}O	15	8	^{44}Ti	44	22
^{16}O	16	8	^{48}Cr	48	24
^{17}O	17	8	^{52}Fe	52	26
^{18}O	18	8	^{56}Ni	56	28
^{17}F	17	9			

with $^{22}\mathrm{Ne}(\alpha,\gamma)^{26}\mathrm{Mg}$ for $\alpha-$particles. For this rate, the NACRE rate was used.

3.2 Nucleosynthesis post-processing and the Multi-zone Post-Processing Network Tool

As GENEC calculates burning and mixing separately (an operator-split scheme), the post-processing approach can be exploited to calculate large nuclear reaction networks typically involved in s-process calculations. This approach involves post-processing the stellar model output in order to calculate the large nuclear reaction networks separately from the stellar model, with the aim of enabling methods to reduce the computational expense of the calculation. For example, parallel computation is implemented in the

post-processing tool. Another advantage of this approach is the ability to experiment with different nuclear reaction networks without recalculating the stellar model. However, the specific nuclear reactions considered in the post-processing tool must not contribute a significant amount of energy to the total energy budget of the star, otherwise the ramifications of the change on the stellar structure are not calculated. Care must also be made to preserve consistency by ensuring that the same reactions used in the stellar evolution code are also used in the post-processing code. This is true also for the mixing regime; mixing of isotopes in both programs must follow the same approach to maintain consistency.

The Multi-zone Post-Processing Network tool (Parallel-variant; MPPNP) is a post-processing tool that solves the set of nuclear reaction rates (Eq. 2.18) for all considered isotopes, including charged-particle reactions, neutron-captures, photodisintegration and β-decays. This system of equations for the rate of change of abundances of isotopes is solved using an implicit finite differencing method combined with the Newton-Raphson scheme, with the output temperature, density and the distribution of convection (and radiation) zones from GENEC as input.

Additional features have been included to enhance the calculations or save on unnecessary computations. Sub-timesteps are inserted where appropriate to improve convergence in the case where the timescale of reactions is smaller than the stellar evolution timestep. Also, the nuclear network is dynamic, adding or removing isotopes from the network depending on the stellar conditions (up to the maximal network defined in Table 3.2). This is useful in reducing the number of computations associated with nuclear reactions where the change in abundance of a given nuclide is zero or negligible. The same (adaptive) mesh used in GENEC was used for the post-processing calculations.

The operation of MPPNP can be summarized as follows. Upon initialisation, the reaction rates and input parameters are read into memory. The post-processing code then reads from a stellar model the temperature and density (and the initial composition if it is the first time step) as a function of Lagrangian mass coordinate and then performs the nuclear network calculations in order to determine the change in abundances at each time step for each spherical shell. Once the change in abundances has been determined, the modifications are applied and a mixing subroutine is invoked to account for mixing (which requires knowledge of the diffusion coefficients used by the stellar model). Following this step, the program performs any necessary output operations, then repeats the procedure over all available/specified time steps. If the post-processing code is interrupted during the run, a restart capability is available that allows the post-processing code to resume from a 'checkpoint', which is written into a file periodically during the run.

3.2.1 Nuclear network calculation

The system of coupled equations given by Eq. 2.18 can be rewritten using vector/matrix notation (in bold face) of the form

$$\dot{\mathbf{Y}} = \mathbf{F}, \tag{3.26}$$

where $\mathbf{F}$ is a matrix of 'fluxes', whose matrix elements correspond to the reaction rates multiplied by the abundances of nuclei involved in the reaction (RHS of Eq. 2.16).

The change in a variable $\Delta\mathbf{Y}$ over some time Δt can be written as

$$\Delta\mathbf{Y} = \dot{\mathbf{Y}}\Delta t, \tag{3.27}$$

where $\dot{\mathbf{Y}}$ is a function providing the rate of change of $\mathbf{Y}$ in time. If values of $\mathbf{Y}$ are sampled at a series of points defining time steps with index n, the equation can be written as

$$\frac{\mathbf{Y}^{n+1} - \mathbf{Y}^{n}}{\Delta t} = \dot{\mathbf{Y}}^{n}, \tag{3.28}$$

where the RHS is evaluated at time step n. This is called the explicit method. In this case, knowledge of all quantities at n ($\dot{\mathbf{Y}}^{n}$ and $\mathbf{Y}^{n}$) and the Δt term can allow a solution for $\mathbf{Y}^{n+1}$. If the method is repeated, then given some boundary condition for $\dot{\mathbf{Y}}^{n}$ and $\mathbf{Y}^{n}$, values of $\mathbf{Y}^{n+1}$ can be determined for all n. A fully implicit scheme evaluates the RHS at $n+1$, giving

$$\frac{\mathbf{Y}^{n+1} - \mathbf{Y}^{n}}{\Delta t} = \dot{\mathbf{Y}}^{n+1}. \tag{3.29}$$

The fully implicit scheme is often used in stellar models due to the stiffness of the set of equations describing the nuclear reaction network. The solution of Eq. 3.29 requires a more sophisticated calculation since the values of quantities at $n+1$ are unknown. It can be solved for $\mathbf{Y}^{n+1}$ using a Newton-Raphson scheme. This can be specified as

$$\mathbf{Y}_{i+1}^{n+1} = \mathbf{Y}_{i}^{n+1} - \frac{f(\mathbf{Y}_{i}^{n+1})}{f'(\mathbf{Y}_{i}^{n+1})}, \tag{3.30}$$

where the additional index i is introduced here to indicate iterations of refinement. Given a trial solution, $\mathbf{Y}_{i=0}^{n+1}$, Eq. 3.30 returns a value for $\mathbf{Y}_{i+1}^{n+1}$. The functions $f(\mathbf{Y}_{i}^{n+1})$

and $f'(\mathbf{Y}_i^{n+1})$ are given by

$$f(\mathbf{Y}_i^{n+1}) = \mathbf{Y}_i^{n+1} - \mathbf{Y}_i^n - \Delta t \dot{\mathbf{Y}}_i^{n+1} = 0 \tag{3.31}$$

$$f'(\mathbf{Y}_i^{n+1}) = \frac{\partial f(\mathbf{Y}_i^{n+1})}{\partial \mathbf{Y}_i^{n+1}} = \mathbf{1} - \Delta t \frac{\partial \dot{\mathbf{Y}}_i^{n+1}}{\partial \mathbf{Y}_i^{n+1}} = \mathbf{1} - \Delta t \mathbf{J}_i^{n+1}, \tag{3.32}$$

where $\mathbf{J}_i^{n+1}$ is the Jacobian matrix and $\mathbf{1}$ is the unit matrix. Eq. 3.30 can therefore be rearranged to give

$$\mathbf{Y}_{i+1}^{n+1} = \mathbf{Y}_i^{n+1} - \left[\mathbf{1} - \Delta t \mathbf{J}_i^{n+1}\right]^{-1} \left[\mathbf{Y}_i^{n+1} - \mathbf{Y}_i^n - \Delta t \dot{\mathbf{Y}}_i^{n+1}\right] \tag{3.33}$$

$$\mathbf{Y}_{i+1}^{n+1} = \mathbf{Y}_i^{n+1} - \mathbf{B}\mathbf{A}. \tag{3.34}$$

where $\mathbf{B} = \left[\mathbf{1} - \Delta t \mathbf{J}_i^{n+1}\right]^{-1}$ and $\mathbf{A} = \left[\mathbf{Y}_i^{n+1} - \mathbf{Y}_i^n - \Delta t \dot{\mathbf{Y}}_i^{n+1}\right]$. In MPPNP, Eq. 3.34 is solved for the $\mathbf{Y}_{i+1}^{n+1}$ at a given time step $n+1$ using $\mathbf{Y}_i^n$ as the trial solution, where $\dot{\mathbf{Y}}_i^{n+1}$ and $\mathbf{J}_i^{n+1}$ are evaluated using Eq. 3.26. Several iterations of the Newton-Raphson scheme may be required for a satisfactory solution of $\mathbf{Y}^{n+1}$.

The calculation of $\mathbf{B}$ requires a matrix inversion, which is the most computationally expensive task out of the required operations. In MPPNP, three solver routines are available to perform the matrix inversion and the resulting matrix multiplication with $\mathbf{A}$. The currently implemented solvers are LU decomposition with back-substitution and Gauss-Jordan elimination, with the inclusion of routines from Press et al. (1992, Ch.2) and freely available LAPACK routines. Two LAPACK routines are available that are optimised for Intel and AMD processor systems respectively, with support for shared-memory parallel computation. The LAPACK routines are therefore used for most applications of MPPNP, with the other solvers occasionally applied for debugging purposes.

3.2.2 The nuclear reaction network

The solution of Eq. 3.34 involves the fluxes given by **F** in Eq. 3.26, which are in turn calculated using the Maxwellian-averaged cross sections for all involved reactions. Since the number of floating point operations required in the matrix inversion scales with the number of isotopes $\sim n_{var}^3$, the inclusion of a factor of 10 more isotopes in the nuclear reaction network increases the workload of the program by a factor ~ 1000. Since large networks become computationally expensive, parallelism was implemented (see appendix A for a full description of the parallel implementation and the relevant background theory).

The isotopes included in the network for MPPNP are specified in Table 3.2 and are shown in Fig. 3.2 (including the skeleton network used by GENEC). Five isomeric states are also included, which are treated as separate nuclei from their ground state equivalents. These are $^{26}\mathrm{Al}^m$, $^{85}\mathrm{Kr}^m$, $^{115}\mathrm{Cd}^m$, $^{176}\mathrm{Lu}^m$ and $^{180}\mathrm{Ta}^m$

3.2.3 Reaction rates

MPPNP supports different formats for reactions (both tables and formulae). At each time step, the tabulated rates are interpolated linearly in log-space for a given temperature, whereas formulae, which are often provided for theoretical rates, are calculated directly in the Fortran subroutines. Much like isotopes, individual reactions in the nuclear network can be toggled on or off in MPPNP. Reactions can also be multiplied by a constant factor, which may be useful for performing sensitivity studies for numerous reaction rates. Apart from the 3α reaction, all reactions considered in the nuclear network are either nuclear decays or two-body reactions. The 3α reaction can

Table 3.2: Nuclear network used for post-processing calculations

Element	A_{min}	A_{max}	Element	A_{min}	A_{max}	Element	A_{min}	A_{max}
n	1	1	Br	74	87	Yb	160	180
H	1	2	Kr	76	90	Lu	165	182
He	3	4	Rb	79	91	Hf	166	185
Li	7	7	Sr	80	94	Ta	169	186
Be	7	8	Y	85	96	W	172	190
B*	8	11	Zr	86	98	Re	175	191
C	11	14	Nb	89	99	Os	179	196
N	13	15	Mo	90	102	Ir	181	197
O	14	18	Tc	93	105	Pt	184	202
F	17	20	Ru	94	106	Au	185	203
Ne	19	22	Rh	98	108	Hg	189	208
Na	21	24	Pd	99	112	Tl	192	210
Mg	23	28	Ag	101	113	Pb	193	211
Al	25	29	Cd	102	118	Bi	202	211
Si	27	32	In	106	119	Po	204	210
P	29	35	Sn	108	130			
S	31	38	Sb	112	133			
Cl	34	40	Te	114	134			
Ar	35	44	I	117	135			
K	38	46	Xe	118	138			
Ca	39	49	Cs	123	139			
Sc	43	50	Ba	124	142			
Ti	44	52	La	127	143			
V	47	53	Ce	130	146			
Cr	48	56	Pr	133	149			
Mn	51	57	Nd	134	152			
Fe	52	61	Pm	137	154			
Co	55	63	Sm	140	158			
Ni	56	68	Eu	143	159			
Cu	60	71	Gd	144	162			
Zn	62	74	Tb	147	165			
Ga	65	75	Dy	148	168			
Ge	66	78	Ho	153	169			
As	69	81	Er	154	175			
Se	72	84	Tm	159	176			

* ^{9}B is not included.

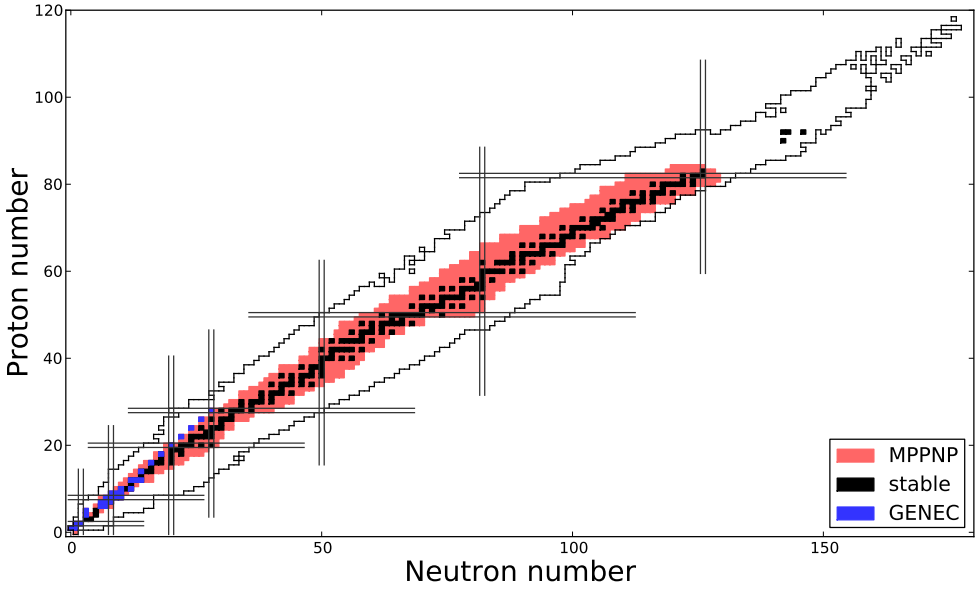

Figure 3.2: Chart of isotopes indicating the nuclear reaction networks used in this work: GENEC (blue squares) and MPPNP (pale red squares). The network used by MPPNP includes all stable isotopes, which are indicated by black squares. The outer boundary to each side of the valley of stability indicates the position of all currently known isotopes, including heavy transuranic isotopes. Parallel grid lines indicate values of Z or N that are magic as specified in the nuclear shell model.

be calculated by considering a two-body collision between an α-particle and a 2-α 'particle'.

The reaction rates in MPPNP were set to those used in the skeleton network of GENEC for the same reactions. Additional reactions are taken from the default setup of MPPNP and are specified as follows: charged particle reactions are from Angulo et al. (1999) and Iliadis et al. (2001). β-decays and electron captures are from Oda et al. (1994), Fuller et al. (1985) and Aikawa et al. (2005). Neutron captures are from the Karlsruhe astrophysical database of nucleosynthesis in stars (KADONIS) (Dillmann et al., 2006). The ^{16}O neutron poison is effective at capturing neutrons, forming ^{17}O, which can either resupply the 'recycled' neutrons via the ^{17}O(α,n)^{20}Ne or undergo the competing reaction ^{17}O$(\alpha, \gamma)^{21}$Ne. For ^{17}O(α, n)^{20}Ne the NACRE reaction is used and for ^{17}O$(\alpha, \gamma)^{21}$Ne the correction of the Caughlan & Fowler (1988) rate by Descouvemont (1993) is applied. For reactions not found in these references, reaction rates from the Reaclib database[3] were used, which incorporates a compilation of experimental rates and theoretical rates from NON-SMOKER (Rauscher & Thielemann, 2000, 2001).

[3]http://nucastro.org/reaclib.html

4 Carbon burning uncertainties and their effects on massive star evolution and nucleosynthesis

In this chapter, an analysis of the uncertainties in the $^{12}C + ^{12}C$ reaction rate is presented, along with the consequences that changes to the rate have on the stellar models of massive stars. Massive stars are chosen in particular for this analysis because they undergo hydrostatic carbon burning episodes during their evolution. As outlined in §2.4.1 and 2.4.2, massive stars are responsible for the weak s-process component of the Solar system abundances, which represents a key observable of the chemical feedback of massive stars. This can be used to constrain the input physics relevant for massive star evolution and nucleosynthesis. Specifically, this chapter presents constraints to the $^{12}C + ^{12}C$ rate, which were made by considering the changes to the yields of massive stars upon comparison with the Solar system abundances.

In §4.1 the main properties of massive stars will be recalled, focusing on carbon burning stages and the s-process occurring in massive stars. In §4.2 the $^{12}C + ^{12}C$ reaction is described and the uncertainties are summarised. In §4.3 the stellar evolution models produced by GENEC and the carbon burning rates used in the work are specified. The following sections specify the changes to the output of the stellar models, starting with changes to the stellar structure and evolutionary properties, which are found in §4.4. Changes to the nucleosynthesis are then outlined in §4.5 and the yields are presented in §4.6. Finally, the changes to the yields and the constraints to the $^{12}C + ^{12}C$ are discussed in §4.7.

4.1 Carbon burning in massive stars

Massive stars play a key role in the evolution of galaxies and are the progenitors of luminous blue variables, Wolf-Rayet stars, supernovae, neutron stars and black holes. They are a significant source of heavy elements and UV radiation which, in addition to stellar winds and supernovae, represent major sources of heating, cooling and mixing processes that occur in the interstellar medium (Zinnecker & Yorke, 2007) (Maeder, 2009, ch. 27). However, work on massive stars presents significant challenges to observational and theoretical astrophysics. Massive stars are rare, evolve quickly and massive young stellar objects (YSOs) are often obscured by dust from their parent molecular cloud (see for instance Churchwell, 2002; Chen et al., 2009; Churchwell et al., 2009; Furness et al., 2010). In addition, important physical parameters of massive stars, such as mass-loss and rotation rates, can be difficult to measure or interpret from data, particularly in Wolf-Rayet stars (Crowther, 2007). Theoretically, difficulties originate from the fact that massive stars undergo further evolutionary sequences compared to stars of lower mass, featuring advanced burning stages that exhibit a stellar structure that becomes increasingly more complex over time, which is dependent on many factors, including rotation, convection, initial composition and in particular nuclear reactions (Woosley et al., 2002).

Massive stars are defined as those stars with an initial main-sequence mass high enough to start carbon burning in the core. This mass limit, known as the M_{up} parameter, is the limit that separates supernova progenitors and white dwarf progenitors, providing an important constraint on stellar models (see for instance Smartt et al., 2009; Williams et al., 2009). Stars with main-sequence masses, M_{MS}, between about $7 \leq M_{MS} \leq 11 M_{\odot}$ are known as intermediate-mass stars or super asymptotic giant

branch (SAGB) stars because they ignite carbon off-center (Siess, 2007). However, these mass limits depend on overshooting and other uncertainties in the models. The final fate of stars that have $M_{MS} > 11M_{\odot}$ is a type II supernova, which is the domain of interest in this work.

4.1.1 Carbon burning

Carbon burning marks the first of the advanced burning stages in massive stars. At the end of helium core burning, the composition of the star is largely ^{12}C and ^{16}O, with the initial ratio of ^{12}C to ^{16}O at this stage largely governed by the 3α and $^{12}\mathrm{C}(\alpha,\gamma)^{16}\mathrm{O}$ reactions occurring during helium-core burning. Carbon burning occurs at a temperature ~ 0.7 GK and occurs through three dominant carbon burning reactions. These are

$$^{12}\mathrm{C}(^{12}\mathrm{C},\alpha)^{20}\mathrm{Ne}, \qquad Q = +4.617 \tag{4.1}$$

$$^{12}\mathrm{C}(^{12}\mathrm{C},\mathrm{p})^{23}\mathrm{Na}, \qquad Q = +2.240 \tag{4.2}$$

$$^{12}\mathrm{C}(^{12}\mathrm{C},\mathrm{n})^{23}\mathrm{Mg}, \qquad Q = -2.599. \tag{4.3}$$

Therefore, carbon burning mainly produces ^{20}Ne and ^{24}Mg, since $\sim 99\%$ of ^{23}Na synthesised through the p-channel is destroyed via efficient $^{23}\mathrm{Na}(\mathrm{p},\alpha)^{20}\mathrm{Ne}$ and $^{23}\mathrm{Na}(\mathrm{p},\gamma)^{24}\mathrm{Mg}$ reactions. Carbon-core burning, which is convective for stars with initial mass $M \lesssim 20M_{\odot}$ and radiative for $M \gtrsim 20M_{\odot}$ (Hirschi et al., 2004), is followed by convective carbon-shell burning episodes at temperatures $\sim 0.8-1.0$ GK. The number of episodes and the spatial extent of each shell differs between massive stars of different initial mass

as the development of the carbon shells is sensitive to the spatial ^{12}C profile at the end of helium-core burning; the formation of a convective carbon-shell often lies at the same spatial coordinate as the top of the previous convective shell (Arnett, 1972b; El Eid et al., 2004). The presence of a convective carbon core depends on the CO core mass as both the neutrino losses and energy generation rate depend on the density, which decreases with increasing CO core mass (Arnett, 1972b; Woosley & Weaver, 1986; Limongi et al., 2000). Consequently, mechanisms that affect the CO core mass or the carbon burning energy budget, such as rotation (Hirschi et al., 2004) and the ^{12}C abundance following helium burning (El Eid et al., 2009), will affect the limiting mass for the presence of a convective core.

4.1.2 Weak s-process nucleosynthesis

The s-process in massive stars occurs mainly during helium-core burning, but can also occur during carbon burning stages. Additional neutron-capture nucleosynthesis also occurs in the helium-shell via the ^{22}Ne neutron source, but this process is marginal compared to the s-process operating in the helium-core or the carbon shells (see for example The et al., 2007). Beyond carbon burning, the temperature becomes high enough in the interior ($\sim$ 2 GK) for photodisintegration reactions to destroy heavy nuclides. Because the s-process can probably occur during both central and shell carbon-burning, one can expect that changes in the ^{12}C + ^{12}C rate affect the stellar structure and nucleosynthesis and therefore also the s-process.

The ^{22}Ne neutron source, which is formed via the ^{14}N$(\alpha,\gamma)^{18}$F$(\beta^+)^{18}$O$(\alpha,\gamma)^{22}$Ne reaction chain during helium burning, is the main neutron source (Peters, 1968; Couch et al., 1974; Lamb et al., 1977). As the temperature approaches 0.25 GK near the

end of helium-burning, ^{22}Ne(α, n)^{25}Mg reactions become efficient (Busso & Gallino, 1985; Raiteri et al., 1991). During this phase a $25M_{\odot}$ star, for example, has a neutron density $n_n \sim 10^6$ cm^{-3} and a neutron exposure $\tau_n \sim 0.2$ mb^{-1} (see for instance Pignatari et al., 2010, and references therein). The ^{22}Ne source becomes efficient in a convective environment and heavy elements formed through neutron captures are mixed out from the centre of the star. Some of these abundances will be modified by further explosive nucleosynthesis later in the evolution, but will otherwise survive long enough to be present in the supernova ejecta and contribute to the total yields of the star. Consequently, ^{22}Ne in massive stars is the dominant neutron source responsible for the classical weak-s-process component (Truran & Iben, 1977; Prantzos et al., 1987; Käppeler et al., 1989; Raiteri et al., 1991).

The main neutron source during carbon core burning is ^{13}C, which is formed through the ^{12}C(p, γ)^{13}N(β^+)^{13}C reaction chain (Arnett & Truran, 1969). During carbon-core burning this neutron source, via the ^{13}C(α, n)^{16}O reaction, becomes efficient which results in an s-process in the carbon-core with a typical neutron density $n_n = 10^7$ cm^{-3} (Arnett & Thielemann, 1985; Chieffi et al., 1998). The abundance of ^{13}C is dependent on the ^{13}N(γ,p)^{12}C reaction, which dominates the depletion of ^{13}N at temperatures above 0.8 GK. The ^{22}Ne neutron source is the dominant neutron source when the temperature rises above such a temperature, although the ^{13}C neutron source may also provide an important contribution to the total neutron exposure (Clayton, 1968; Arcoragi et al., 1991). In any case, the carbon-core s-process occurs primarily in radiative conditions with a relatively small neutron exposure and any heavy elements synthesised via the ensuing neutron-captures usually remain in the core (see however the discussion on overlapping convection zones in §4.4.4); photodisintegrations and the supernova explosion process will ensure that these elements are not present in the final

ejecta and do not contribute to the final yields of the star (see for example, Chieffi et al., 1998).

Any remaining ^{22}Ne present at the end of helium-core burning is later reignited during carbon-shell burning resulting in an s-process with a higher neutron density and a lower neutron exposure ($n_n \sim 10^{11-12}$ cm^{-3} and $\tau_n \sim 0.06$ mb^{-1}; Raiteri et al., 1991). The increased neutron density is responsible for changing the branching ratios of unstable isotopes (see Eq. 2.32), which is particularly important for branching isotopes, such as ^{69}Zn, ^{79}Se and ^{85}Kr, since they inhabit positions in the isotope chart of nuclides where different s-process paths across the valley of stability are available (Käppeler et al., 1989). The increase in neutron density is responsible for opening the s-process path so that the carbon-shell burning contribution to specific isotopes, such as ^{70}Zn, ^{80}Se and ^{86}Kr, may be relevant (see for example Raiteri et al., 1991; The et al., 2007).

4.2 The ^{12}C + ^{12}C reaction

During carbon-burning, the α- and p-channels dominate, with the n-channel contributing less than 2% of all ^{12}C + ^{12}C reactions (Dayras et al., 1977). An important parameter concerning the ^{12}C + ^{12}C reaction is the branching ratio between different exit channels, β_x, which is defined as

$$\beta_x \equiv \frac{\sigma_x}{\sigma_{\rm tot}}, \tag{4.4}$$

where σ_x is the cross-section for the x-exit channel and $\sigma_{\rm tot} = \sum_x \sigma_x$. The choice of branching ratio for the α- and p-exit channels is 13:7, which is valid within the energy range $4.42 < E_{\rm com} < 6.48$ MeV (Aguilera et al., 2006). It is assumed in this work

that the branching ratio is preserved to lower centre of mass energies and hence be preserved at lower temperatures during carbon burning. For the n-exit channel, we use the branching ratio from Dayras et al. (1977), which decreases significantly with decreasing temperature.

The ^{12}C + ^{12}C reaction has been studied for over four decades (Betts & Wuosmaa, 1997, and references therein), but despite the considerable effort, reaction rate determinations at Gamow peak energies ($E_0 \simeq 1.5$ MeV, or $T \simeq 0.5$ GK) are still relatively unknown (Strieder, 2010), with the cross-section at lower energies determined from extrapolations of higher energy data. The main reasons for this are associated with a number of experimental and theoretical difficulties. These are outlined below.

4.2.1 ^{12}C + ^{12}C experiments

The cross-section for the ^{12}C + ^{12}C reactions is very low ($\sigma \ll 1$ nbarn) at Gamow peak energies. The low count rates due to the small cross-section therefore require a significant amount of beam time. In addition, nuclear experiments require a significant reduction in the background level of radioactivity. Recent experiments with γ-ray spectroscopy have encountered background γ-rays from natural radioactivity and from hydrogen and deuterium impurities in the carbon target (Barrón-Palos et al., 2006; Spillane et al., 2007). The measurement of secondary gamma radiation associated with the particle decay is also handicapped by natural and cosmic ray induced background radiation (Costantini et al., 2009; Strieder, 2010). Impurities in the target interact with the beam creating γ-rays at $E_\gamma \simeq 2.36$ MeV (from hydrogen impurities) and $E_\gamma = 3.09$ MeV (from deuterium impurities), which interfere with the γ-ray lines of interest at $E_\gamma = 1634$ keV and $E_\gamma = 440$ keV (Costantini et al., 2009). The lines of interest

originate from transitions from the first excited state to the ground state of ^{20}Ne and ^{23}Na respectively, through the α- and p-exit channels of the compound, excited nucleus ^{24}Mg. In addition, particle measurements are difficult because of the limited energy resolution of the particle detectors which makes a separation of the particle groups extremely difficult at the low count rate conditions.

Nevertheless recent experiments suggest an increase in the low energy S-factor indicating the possibility of narrow resonances at lower energies (Barrón-Palos et al., 2006; Aguilera et al., 2006; Spillane et al., 2007). Some of these are seen in Fig. 4.1 (Strieder, 2008, Fig. 2), which gives experimental values of the S-factor for ^{12}C + ^{12}C fusion for α- and p-exit channels, compared with previous experimental data (High & Čujec, 1977; Kettner et al., 1980; Aguilera et al., 2006; Barrón-Palos et al., 2006; Spillane et al., 2007). Although some of the data points show a large S-factor, the uncertainty in the experimental results is also very large. Consequently, the ^{12}C + ^{12}C rate at Gamow peak energies is normally determined from extrapolations of higher energy data.

4.2.2 Theoretical ^{12}C + ^{12}C rates

Due to the lack of experimental data, published ^{12}C + ^{12}C reaction rates for use in stellar models (for example, Caughlan & Fowler, 1988), use extrapolations of higher energy data to lower energies, which represents a source of uncertainty for the evaluation of the rate at Gamow peak energies. Other sources of uncertainties include the branching ratios and the background and resonance contributions to the astrophysical S-factor. These other sources of uncertainty originate from the relatively unknown nuclear mechanisms underlying the resonance features of the compound ^{24}Mg nucleus

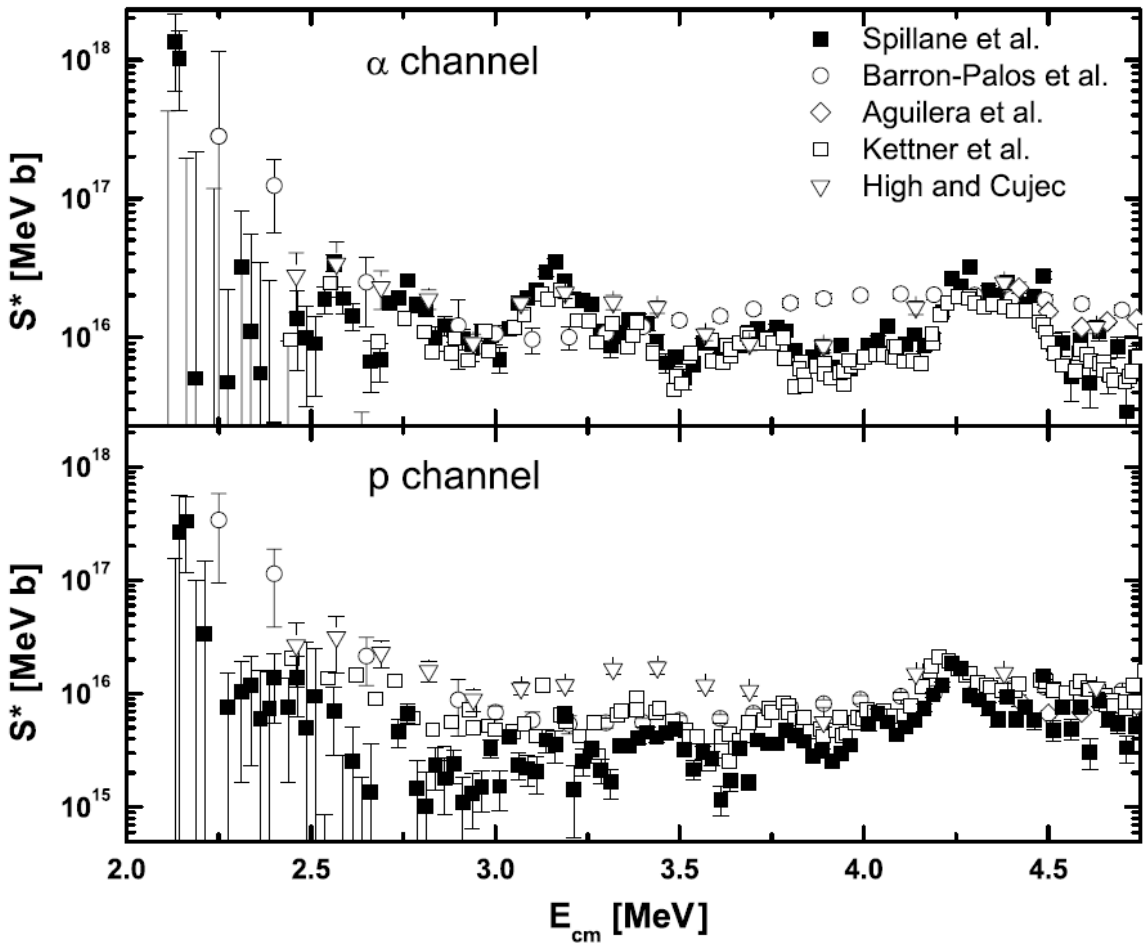

Figure 4.1: Experimental data for the S-factor of ^{12}C + ^{12}C fusion for the α- and p-exit channels (Strieder, 2008, Fig. 2).

and the consequences this has on the fusion of ^{12}C + ^{12}C nuclei.

The ^{12}C + ^{12}C S-factor is known to contain a complex resonance structure associated either with scattering states in the ion-ion potential or with quasimolecular states of the compound nucleus ^{24}Mg. A theory that predicts the location and strength of the resonant-part has not yet been proposed (Strieder, 2008), but resonance characteristics can be determined either by coupled-channel calculations or optical model potentials based on, for example, α-particle condensates or cluster structures (Xu et al., 2010; Betts & Wuosmaa, 1997, and references therein). Resonances have consequently been predicted by both approaches at energies $\sim$ 2 MeV (Michaud & Vogt, 1972; Perez-Torres et al., 2006). Dynamic reaction theories are also being developed. They have been tested successfully for fusion of spherical nuclei like ^{16}O + ^{16}O (Diaz-Torres et al., 2007) but the theoretical treatment of fusion reactions of two deformed ^{12}C nuclei requires a non-axial symmetric formalism for a fully reliable treatment (Diaz-Torres, 2008).

An additional source of uncertainty is the evaluation of Coulomb barrier penetration in the pycnonuclear regime (characterised by stellar temperatures and high densities; $\rho \geq 10^9$ gcm^{-3}), where the stellar plasma effects on ^{12}C + ^{12}C reactions need to be considered in detail (Cussons et al., 2002; Itoh et al., 2003; Gasques et al., 2005; Yakovlev et al., 2006; Chugunov et al., 2007; Chugunov & Dewitt, 2009). These effects are important when considering denser and more degenerate objects, such as white dwarfs and neutron stars, but are less important in the thermonuclear regime typical of hydrostatic burning in stellar interiors.

A resonance with strength $(\omega\gamma) \simeq 3.4 \times 10^{-7}$ eV has been invoked to correct the ignition depth of neutron star superbursts (Cooper et al., 2009), which are believed to be caused by ignition of carbon-burning reactions causing a thermonuclear runaway

in the crust of a neutron star. Type Ia supernovae should also exhibit changes to the ignition characteristics, but ignition conditions (other than central density) are insensitive to changes in the carbon burning rate (Cooper et al., 2009; Iapichino & Lesaffre, 2010).

Alternatively, the reaction rate may not be dominated by resonances at lower energies due to a fusion hindrance reported in heavy-ion reactions that may be relevant for the $^{12}C + ^{12}C$ reaction (see for instance Jiang et al., 2004, 2007). The consequences of the hindrance phenomenon in astrophysical scenarios was examined by Gasques et al. (2007), where it was demonstrated that hindrance is much more significant in the pycnonuclear regime than the thermonuclear regime, but does exhibit a noticeable effect on the yields of massive stars. The reduced rate, by approximately a factor of 10-100 at carbon burning temperatures (see Fig. 4.2), increases the temperature with which carbon burning occurs and therefore affects the nucleosynthesis. Changes in the yields were generally rather small, but some specific isotopes, such as ^{26}Al, ^{40}Ca, ^{46}Ca, ^{46}Ti, ^{50}Cr, ^{60}Fe, ^{74}Se, ^{78}Kr and ^{84}Sr, exhibited larger changes most likely due to the increased neutron density exhibited by the burning of neutron sources at higher temperatures.

A selection of experimental results for the S-factor of $^{12}C + ^{12}C$ fusion is displayed in Fig. 4.2 together with five different theoretical rates (Strieder, 2008, Fig. 3). The theoretical rates in Fig. 4.2 demonstrate the large uncertainty associated with S-factor determinations at Gamow peak energies (see Aguilera et al. (2006) for a more details).

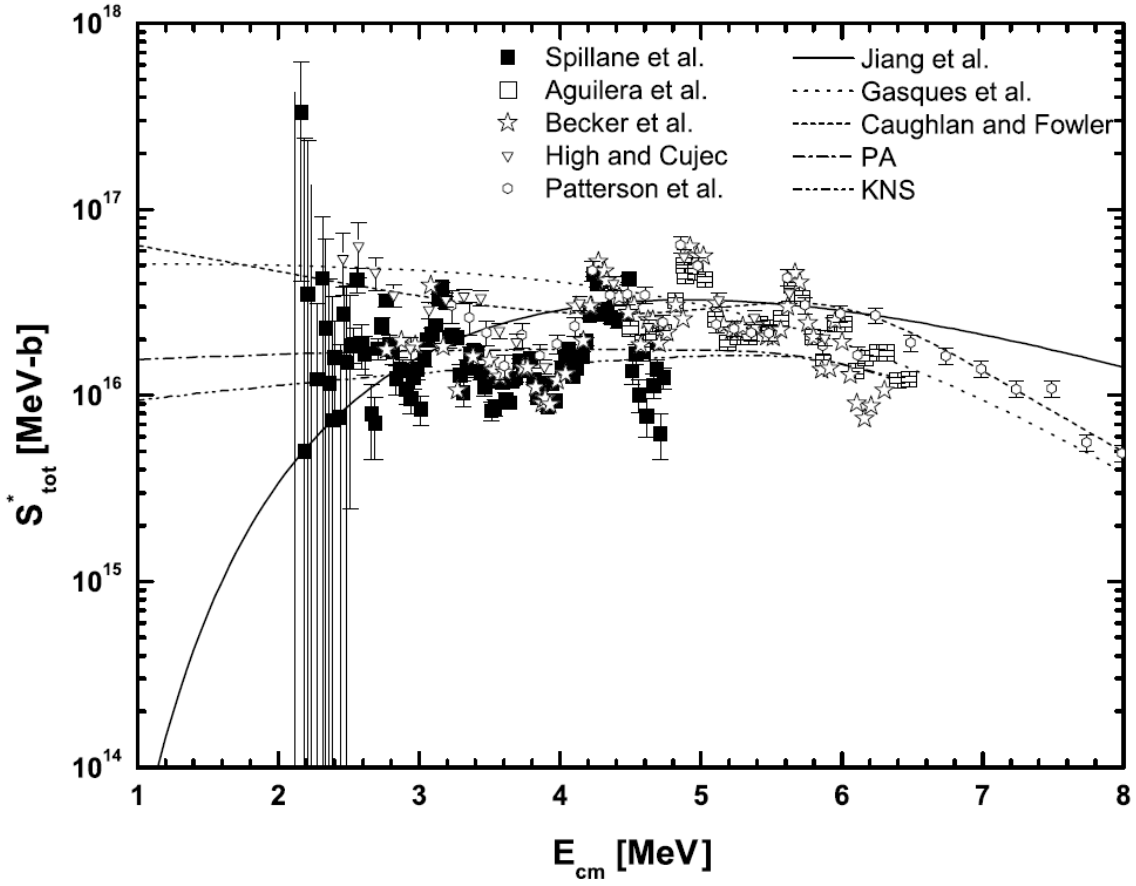

Figure 4.2: Experimental and theoretical determinations of the total S-factor for ^{12}C + ^{12}C fusion (Strieder, 2008, Fig. 3). Experimental data from Patterson et al. (1969); High & Čujec (1977); Becker et al. (1981); Aguilera et al. (2006); Spillane et al. (2007) are used together with S-factors from Caughlan & Fowler (1988); Gasques et al. (2005); Jiang et al. (2007). Theoretical S-factors using the proximity-adiabatic (PA) and Krappe-Nix-Sierk (KNS) nuclear potentials are also displayed (see Aguilera et al., 2006, and references therein).

4.2.3 Preliminary studies of $^{12}C + ^{12}C$ rate uncertainties

Uncertainties in the $^{12}C + ^{12}C$ rate were investigated in preliminary studies, which demonstrated that changes to the total $^{12}C + ^{12}C$ rates within a factor of 10 affect the convection zone structure and nucleosynthesis of a 25 $M_{\odot}$ star at Solar metallicity (Bennett et al. 2010a; see also appendix D). The main conclusions were an increase in the carbon-burning shell contribution to the s-process abundances by two different scenarios. The first, applicable to the case where the rate was increased by a factor of 10, was due to the presence of large carbon-burning shells that 'overlapped'. In this situation, the second carbon-burning shell was polluted with ashes from the first carbon-burning shell, modifying the overall composition. The second scenario, applicable to the case where the rate was reduced by a factor of 10, was an increase in neutron density associated with the neutron source, ^{22}Ne, burning at a higher temperature in the convective shell. The overall increase in the abundances of most isotopes with $60 < A < 90$ was approximately 0.1 to 0.4 dex. Strongly enhanced rates were also investigated (Bennett et al. 2010b; see also appendix D), which show that the presence of a larger convective core has a significant impact on the total yields, since the convective core adds an additional neutron exposure towards the total contribution of s-process yields; abundances of many heavy nuclides increased by up to ~ 2 dex. However, no comparison could be made with observations as a 25 $M_{\odot}$ stellar model (at Solar metallicity) was the only one considered.

4.3 Massive star models

Three carbon burning rates are considered in this work (which were also used by Bennett et al. 2010b; see also §D). These are the Caughlan & Fowler (1988) 'standard' rate (ST) and two enhanced rates: an 'upper limit' rate (CU) and an intermediate rate (CI), the latter of which is a geometric mean of the ST and CU rates. The resonance in the CU rate has a strength $(\omega\gamma) = 6.8 \times 10^{-5}$ eV at a centre-of-mass energy $E_{\rm com} = 1.5$ MeV. This choice of resonance originates from a preliminary particle spectroscopy experiment on ^{12}C + ^{12}C obtained at the CIRCE radioactive beam facility in Caserta/Napoli, Italy (Terrasi et al., 2007; Costantini et al., 2009). Although the CI rate was determined via a geometric mean, a resonance that would replicate the peak at 1.5 MeV for this rate would have a magnitude of $(\omega\gamma) \simeq 3.4 \times 10^{-7}$ eV. The top panel of Fig. 4.3 shows the Maxwellian-averaged cross-sections of the reaction rates as a function of temperature. The bottom panel shows the reaction rates relative to the ST rate. As indicated by the figure, the peak of the CU and CI rates is at ~ 0.5 GK and is a factor of approximately $50,000$ and 250 times the ST rate at that temperature respectively.

The GENEC models used in this work are non-rotating stellar models at Solar metallicity, using the input physics prescriptions given in §3.1. Five masses were considered for each carbon-burning rate, which are 15, 20, 25, 32 and 60 $M_\odot$, for a total of 15 stellar models. These will be referred to as XXYY where XX is the initial mass of the star in Solar masses and YY denotes the rate.

The models were calculated for as far into the evolution as possible, which for most models is after or during the silicon-burning stage. The models that ceased before silicon burning were the 15CI, 15CU, 60CI and 60CU models, which proceeded

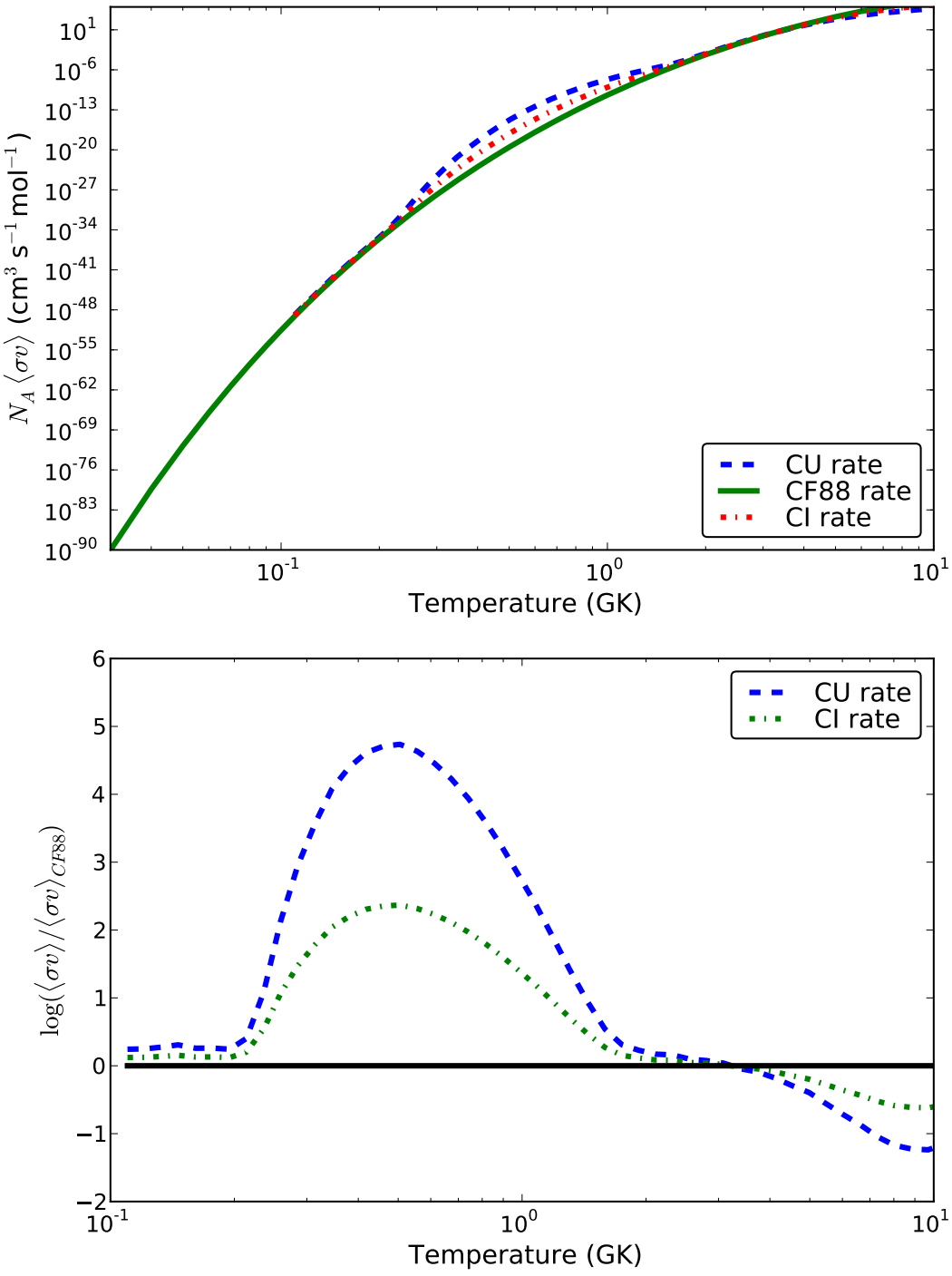

Figure 4.3: *Top panel:* Maxwellian-averaged cross-sections for ^{12}C + ^{12}C rates used in (Bennett et al. 2010b) and also in this study. The three rates are the Caughlan &

to oxygen-shell burning, and the 20CI and 20CU models, which proceeded to just after the oxygen-shell burning stage. The s-process yields are not significantly affected by hydrostatic burning stages following oxygen burning because most of the isotopes produced via the s-process will be destroyed by photodisintegration and the choice of remnant mass for the supernova explosion, which defines the boundary between matter that falls back onto the remnant and matter that forms supernova ejecta, reduces the impact of nucleosynthesis that neon, oxygen and silicon burning stages would have on the total yields (see also §4.6.2). However, it must be noted that there will be explosive burning processes during the supernova explosion and photodisintegration occurring at the bottom of the convective carbon, neon and oxygen shells during the advanced stages, which will affect the abundances (see for example Rauscher et al., 2002; Tur et al., 2009). In this work the contribution of explosive burning and photodisintegration to the total yields is not considered.

Since the $^{12}C + ^{12}C$ reactions do not become efficient until after helium-core burning, the CU and CI models for a particular choice of initial mass were started just before the end of helium-core burning using the ST model data as initial conditions, reducing some of the computational expense.

4.4 Effects on stellar structure and evolution

4.4.1 Surface evolution

The evolution of each stellar model during hydrogen- and helium-burning is given entirely by the ST models, as the CI and CU models were started using the profile

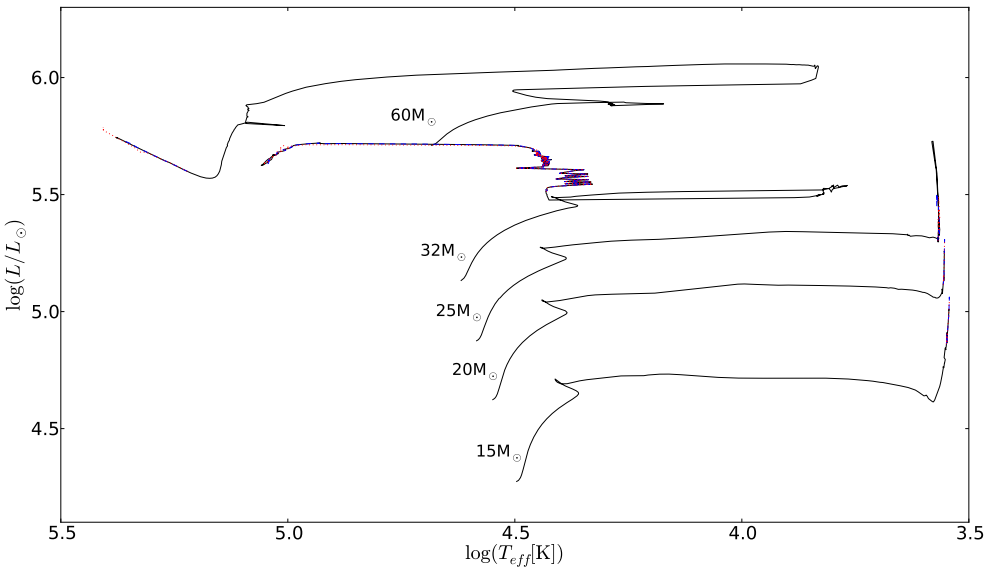

Figure 4.4: Hertzsprung-Russell diagram for all models. Full black lines refer to ST model tracks, dashed blue lines refer to CI model tracks and the dotted red lines refer to the CU model tracks. The tracks indicate that the enhanced rates do not affect the surface evolution, since changes in the carbon-burning rate do not affect the surface properties. The tracks exhibited by the 32 $M_\odot$ and 60 $M_\odot$ models show evolution towards the WR phase, which is explained by mass loss.

just before the end of helium burning. Figure 4.4 shows the Hertzsprung-Russell (HR) diagram for all models, which shows that the evolutionary tracks for all models follow their course in the HR diagram primarily during the hydrogen- and helium-burning phases and are not modified by enhanced rates. The reason for this is that the surface evolution of the stellar models is unaffected by changes in the carbon-burning rate, which is a consequence of the small timescale for burning associated with advanced burning stages in massive stars; the envelope has insufficient time to react significantly to changes in core properties.

Overall, the ST models are very similar to those previously published by the

Geneva group, such as the non-rotating stars of Meynet & Maeder (2003) and Hirschi et al. (2004). The 15, 20 and 25 $M_{\odot}$ model stars evolve towards the red and remain as red supergiants (RSGs) during the advanced stages of evolution. The 32 and 60 $M_{\odot}$ model stars evolve towards the Humphreys-Davidson limit at $\log T_{\rm eff} \sim 3.8$ and evolve as Wolf-Rayet (WR) stars.

The 32 $M_{\odot}$ proceeds to the WR phase during helium-burning. This is because the mass loss is strong enough for the star to expel the entire hydrogen envelope during helium-burning, with the composition of the remaining envelope rich in helium. The lower opacity of the helium-rich envelope lowers the radius and favours evolution towards the blue (Maeder, 2009, §27.3.2). The deviations from the ST track for the CI or CU tracks for this mass are slightly larger than for other masses. These deviations are generally of the order of 0.1% with a maximum deviation of 0.01 in $\log T_{\rm eff}$ ($\simeq 2$ per cent), which occurs during the rapid transit to the blue during helium burning.

The 60 $M_{\odot}$ star becomes a WR star just after hydrogen-burning. At the end of the hydrogen-burning phase, the star enters the first 'loop' towards the blue (at $\log T_{\rm eff} \simeq 4.4$), which occurs because of mass loss being high enough to expose the helium-rich outer layer. Following the first loop to the blue, helium-burning is ignited. During this phase the core shrinks, lowering the core fraction, q, favouring evolution to the red (Maeder, 2009, §27.3.2). However, the star approaches the Humphreys-Davidson limit in the HR diagram during the evolution and the mass loss becomes high enough to, eventually, peel away the envelope, exposing the helium-burning core ($q \simeq 75$ per cent during helium-burning). The star consequently evolves towards the blue (at $\log T_{\rm eff} \simeq 5.0$).

4.4.2 Central evolution

Unlike the surface evolution, the interior evolution of the star is modified significantly by the enhanced carbon burning rates and changes to the central evolution of the star are important in order to assess changes to the main burning regimes.

Figure 4.5 shows $T_c - \rho_c$ diagrams for the 15, 20 and 25 $M_\odot$ models, separated into panels by initial mass. The enhanced rate models in all cases (including the 32 and 60 $M_\odot$ models) ignite carbon burning at lower temperatures and densities, which consequently affects the evolution of the central properties of the star. This is seen, for example, in the top and middle panels of Fig. 4.5, where the curves for the CI and CU cases deviate away from that of the ST case towards the higher temperature (at a given density) side of the curve (see also column 7. in Table 4.1 and Fig. 4.7 and 4.8). The tendency to deviate in this direction is caused by the presence of a convective core. This is verified in the bottom panel for the case of the 25CU model whereby the 'kink' at carbon ignition is larger than that of the 25ST and 25CI models, since the CU model is the only 25 $M_\odot$ model to have a convective core (see also Fig. 4.10). The deviation towards the higher temperature and lower density side of the ST track occurs for the duration the convective core is present. When the star moves onto carbon shell burning, the core cools and the track returns to the standard curve.

The changes seen in Fig. 4.5 and 4.6 can be understood in terms of the change in the ignition conditions, which depend on the energy generation rate. The total energy generation rate of the ^{12}C + ^{12}C reaction is given by (Woosley et al., 2002):

$$\epsilon_{\rm nuc}(^{12}{\rm C}) \approx 4.8 \times 10^{18} Y^2(^{12}{\rm C}) \rho \lambda {\rm erg\,g^{-1}s^{-1}} \tag{4.5}$$

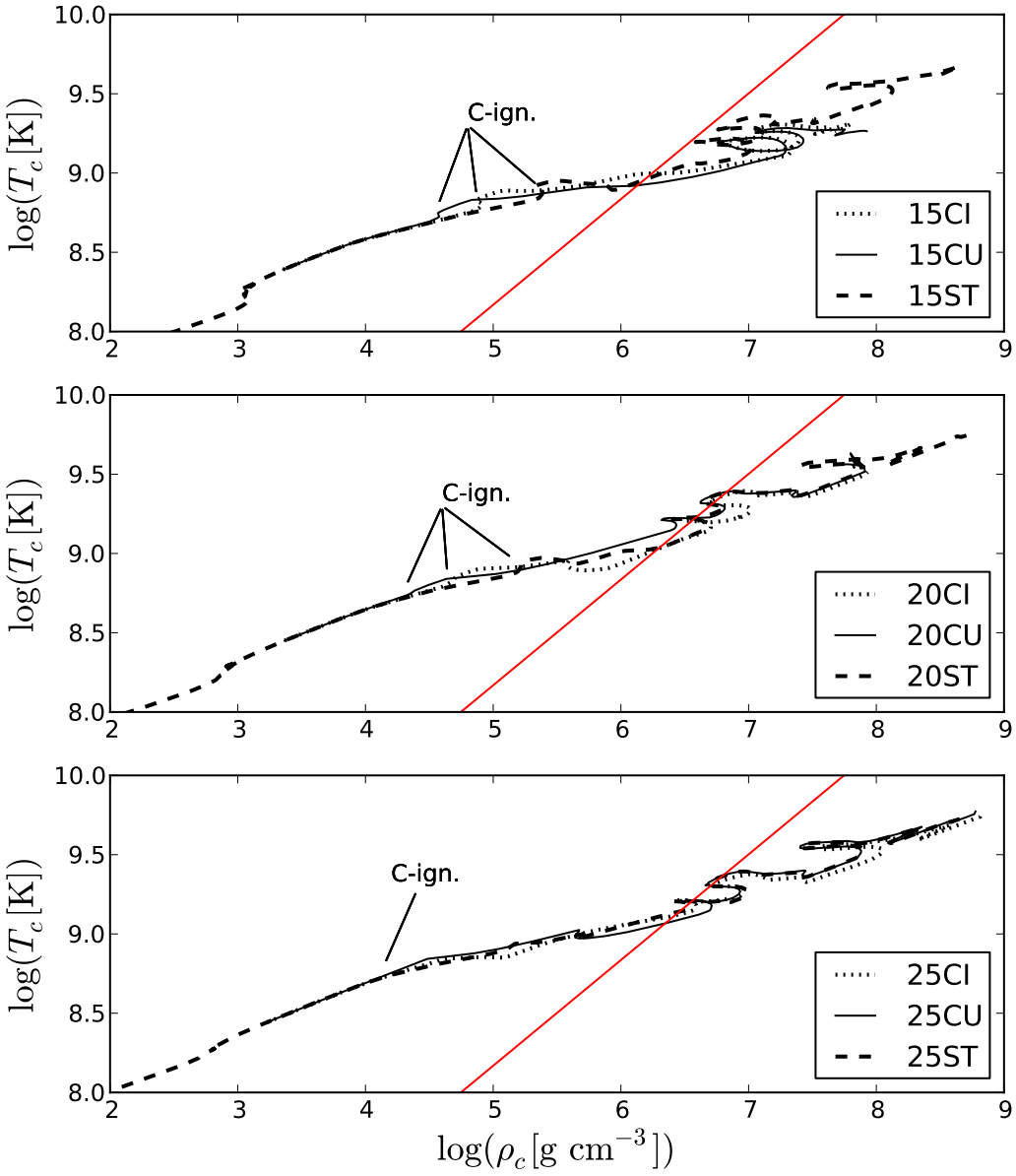

Figure 4.5: $T_c - \rho_c$ diagram for all 15 (top panel), 20 (middle panel) and 25 $M_\odot$ (bottom panel) models. The straight line in each panel indicates the location in the diagram where the ideal gas pressure is equal to the electron degeneracy pressure; $P_{gas} = P_{e,deg}$. Ignition points for convective core carbon burning are indicated by the annotation.

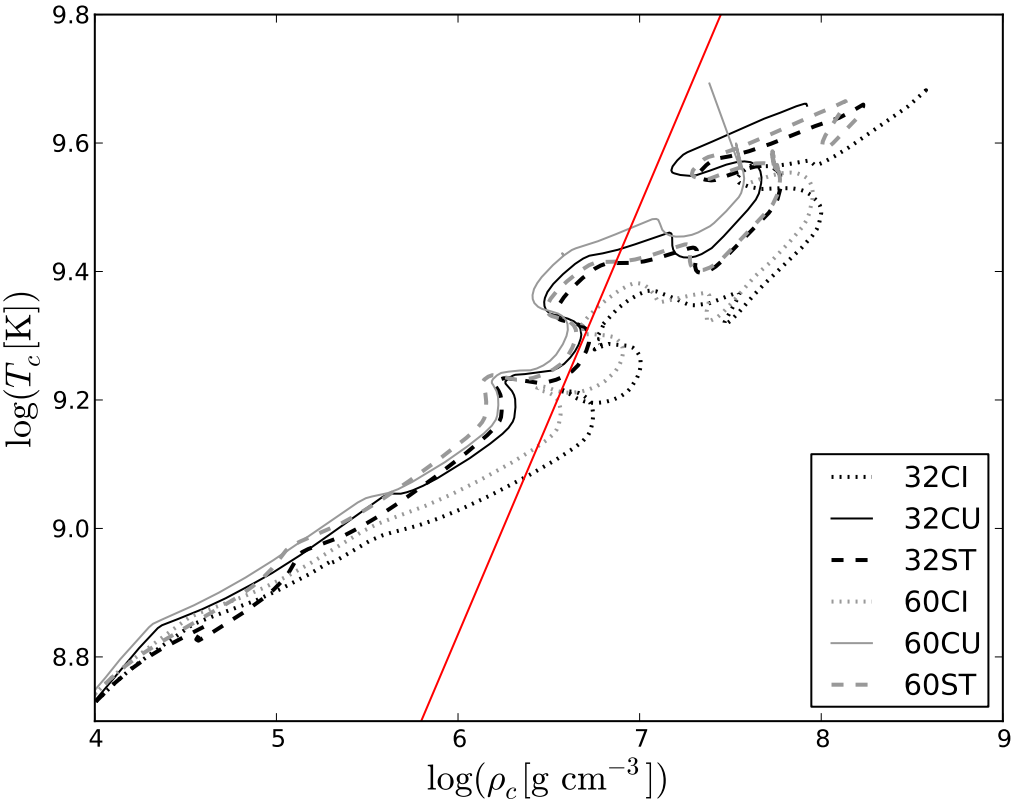

Figure 4.6: $T_c - \rho_c$ diagram for all 32 and 60 $M_\odot$ models. The straight line indicates the location in the diagram where the ideal gas pressure is equal to the electron degeneracy pressure; $P_{gas} = P_{e,deg}$.

where $Y(^{12}\mathrm{C})$, is the number abundance of ^{12}C (dimensionless), ρ is the density (g cm^{-3}) and λ is a nuclear reaction rate factor (cm^3 s^{-1} g^{-1}). The numerical factor in Eq. 4.5, which has units of erg g^{-1}, is the typical energy released by carbon burning reactions per gram of reacting carbon. For a given density and abundance, an increased ^{12}C + ^{12}C rate increases the energy generation rate from nuclear reactions. The effect this has on the ignition conditions (temperature and density) for core carbon burning are displayed in Fig. 4.7 and 4.8 (the ignition point is defined as the point in time when the central mass fraction abundance of ^{12}C is 0.3 per cent lower than its maximum value). An increased rate allows a star to reach the required energy output to support the star against gravitational contraction at a lower temperature (and also lower density). Note also the dependence on initial mass, with ignition conditions favouring higher temperatures and lower densities with increasing initial mass. In the case of lower ignition temperatures and densities, the convective core ignites more promptly in the CI and CU models.

Figure 4.5 shows the impact that the enhanced carbon burning rates have on the central evolution during carbon burning. However, despite the deviations, many of the models at a particular mass are similar, especially the 25 $M_\odot$ models. Figure 4.6 shows $T_c - \rho_c$ diagrams for the 32 and 60 $M_\odot$, which are also quite similar. In the case of Fig. 4.6, the 32 and 60 $M_\odot$ models exhibit significant mass loss during the hydrogen- and helium-burning stages such that the total mass during the advanced burning stages is very similar ($\sim 13M_\odot$). Combined with the fact that the helium cores at this stage are qualitatively similar, the models from this point onwards evolve similarly, with the 32CI and 60CI models entering the more degenerate region of the diagram. Consequently, the tracks follow similar paths dependent on the choice of ^{12}C + ^{12}C reaction rate.

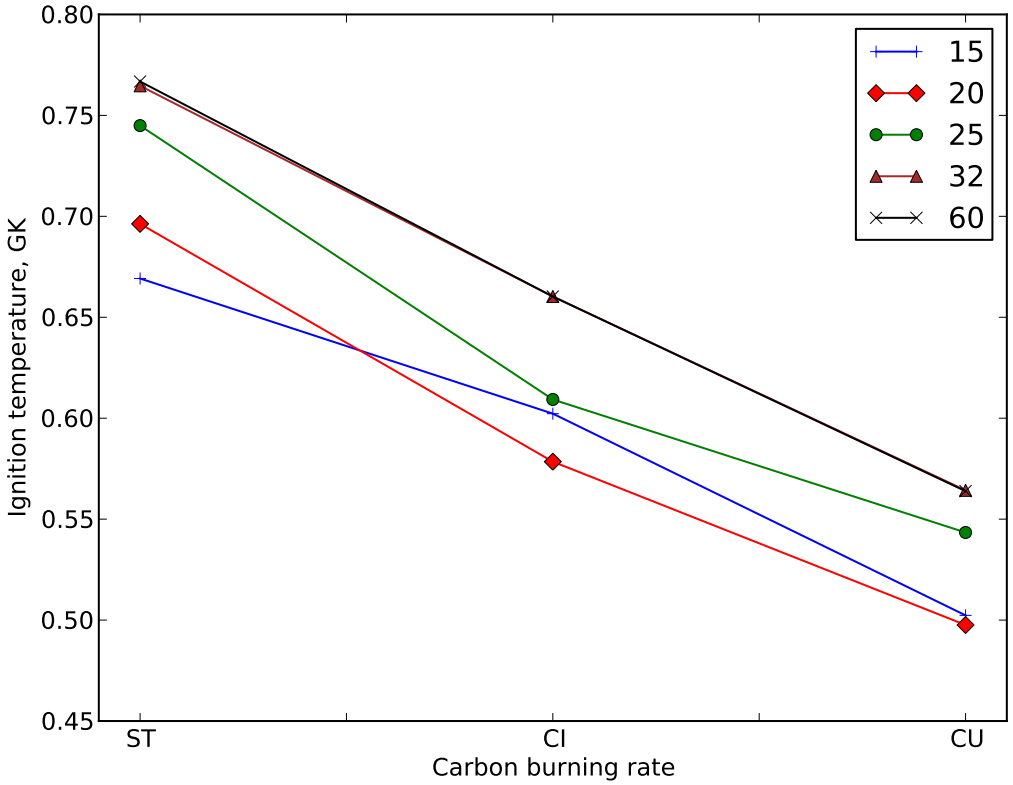

Figure 4.7: Ignition temperatures for core carbon burning for all models.

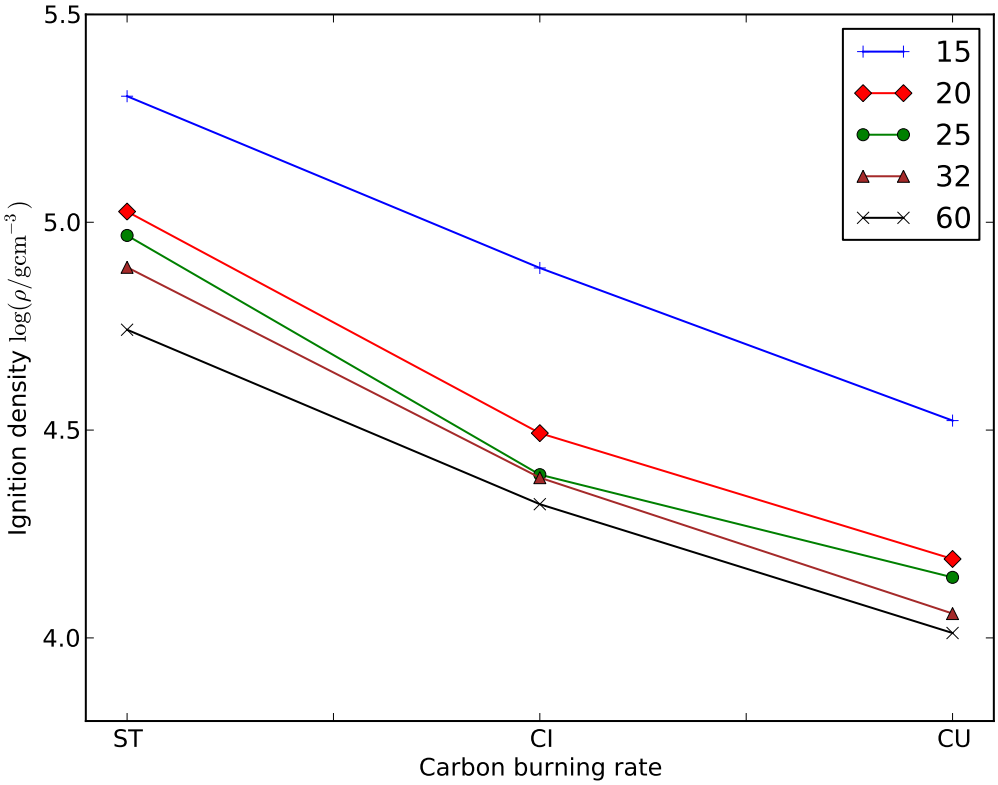

Figure 4.8: Ignition densities for core carbon burning for all models.

4.4.3 Stellar structure

The structure of the interior can be conveniently displayed in terms of Kippenhahn diagrams, which are presented in Fig. 4.9, 4.10 and 4.11. The shaded regions correspond to convection zones and the intermediate, unshaded, regions correspond to radiative zones. Overall, Fig. 4.9, 4.10 and 4.11 show that the convection zone structure of the carbon-burning stage is heavily modified by the increased rates, particularly for the CU models where a convective carbon-core is present over the entire initial mass range considered. The presence of a convective carbon-core is important for nucleosynthesis as the convective mixing provides more fuel for carbon-burning and the carbon-core s-process compared to the radiative case. The mass loss increases significantly with initial mass, but does not change much with the $^{12}C + {}^{12}C$ rate. Small deviations in the mass loss, which are less than 1%, are due to the increased lifetime of the core carbon burning stage in the CI and CU models (see Table 4.3).

The ST models indicate an upper mass limit for the presence of a convective carbon core with a value between 20 and 25 $M_{\odot}$, which is consistent with previous models (Heger et al., 2000; Hirschi et al., 2004). For model 25CI a strong convective shell is ignited slightly off-centre (at a mass coordinate of $0.436 M_{\odot}$) and model 25CU exhibits a large convective carbon core. In all CU models the carbon-core burning stage is convective, which, in models 25CU, 32CU and 60CU, replaces the radiative cores. In Model 25CI the first carbon shell ignites close to the centre and models 20CI and 15CI have larger convective cores. Considering these facts and the presence of a convective core in every CU model, one can hypothesise that the limiting mass for the presence of a convective carbon core increases with the carbon burning rate, which will consequently represent a source of uncertainty for the presence of a convective core

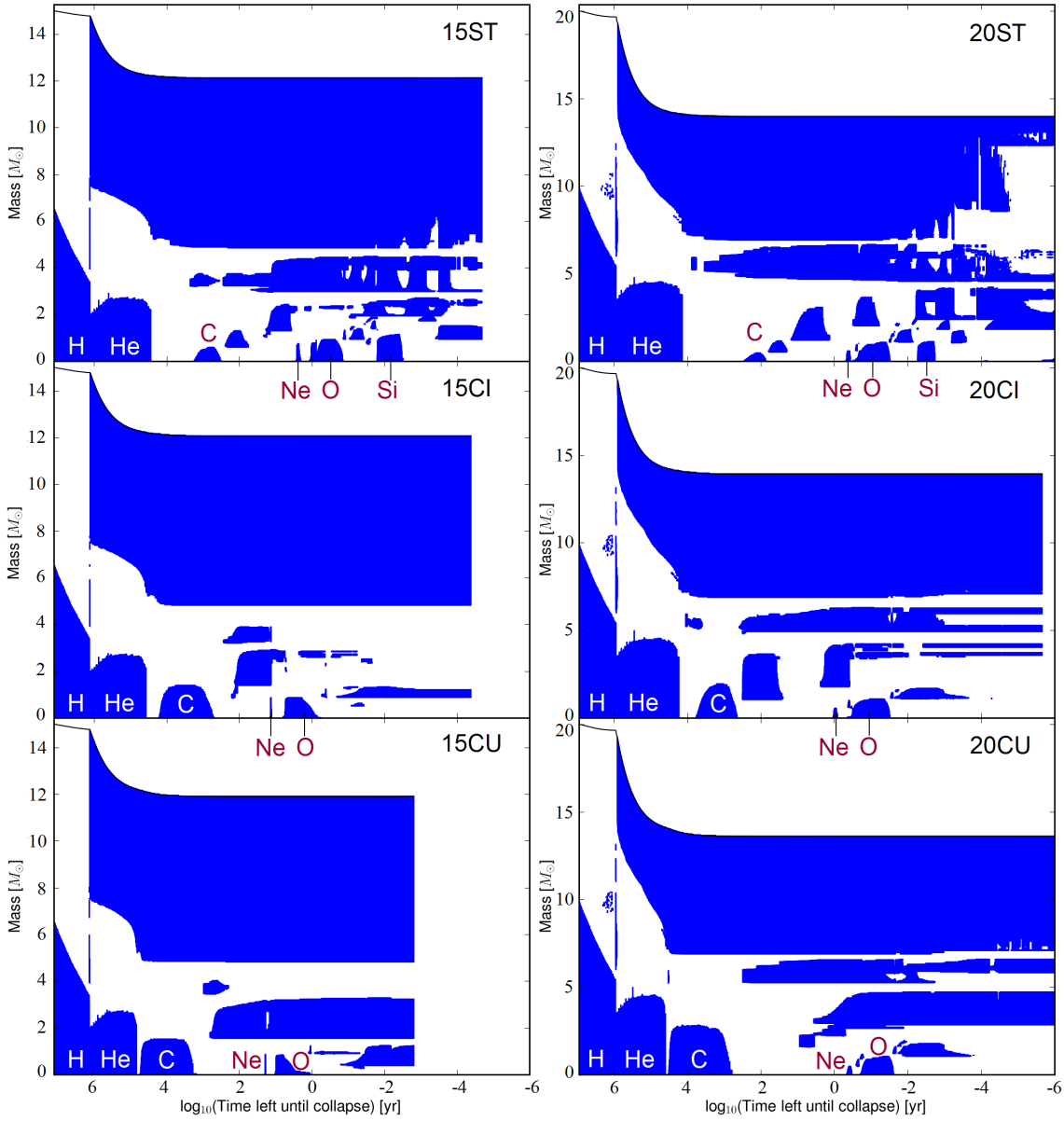

Figure 4.9: Kippenhahn diagrams for all 15 and 20 $M_\odot$ models. Shaded regions correspond to convection zones. The major central burning regimes are indicated by the text. The total mass is given by the thin black line at the top of each diagram.

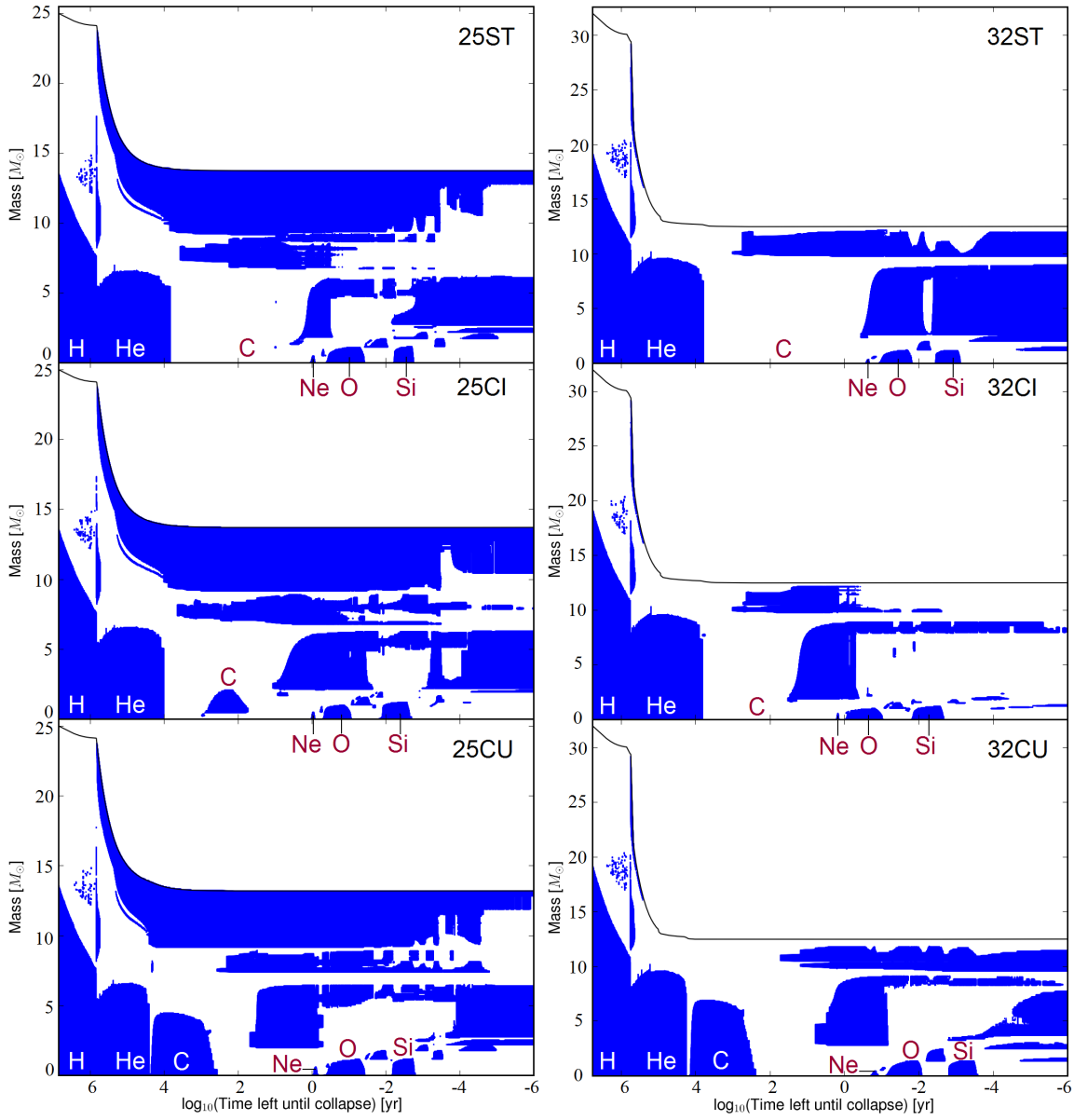

Figure 4.10: Kippenhahn diagrams for all 25 and 32 $M_\odot$ models. Shaded regions correspond to convection zones. The major central burning regimes are indicated by the text. The total mass is given by the thin black line at the top of each diagram.

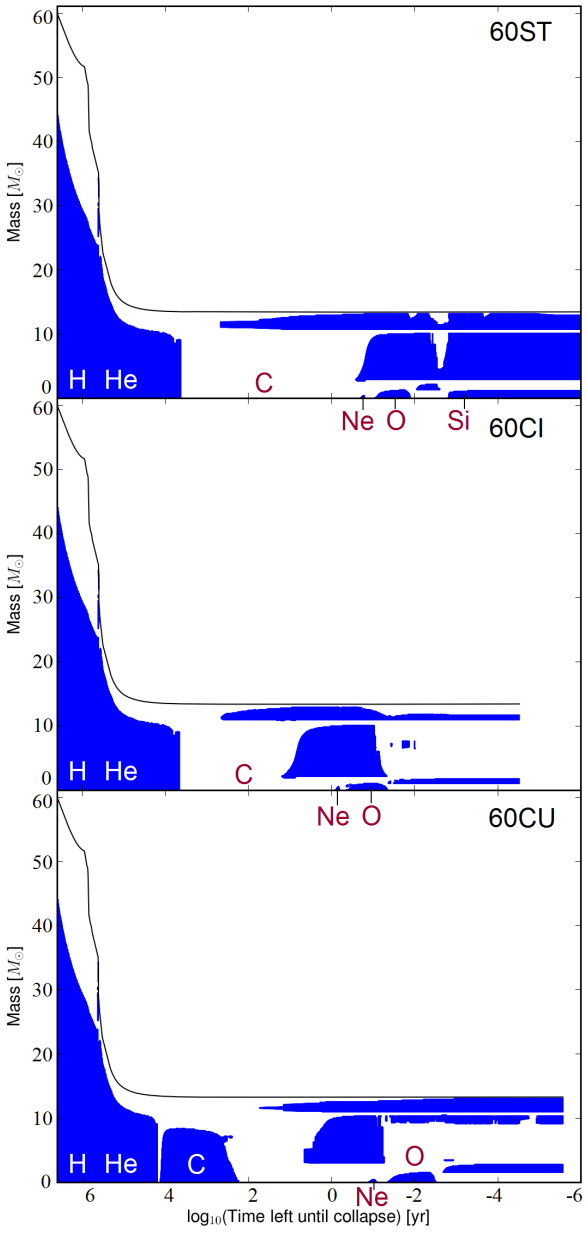

Figure 4.11: Kippenhahn diagrams for the 60 $M_\odot$ models. Shaded regions correspond to convection zones. The major central burning regimes are indicated by the text. The total mass is given by the thin black line at the top of each diagram.

near to the limiting mass of $\sim 22 M_{\odot}$. A firm verification of the limiting mass for the CI case would however require a finer grid of stellar models between 20 and 25 $M_{\odot}$.

The sizes, in mass, of the carbon-burning zones (column 6 in Table 4.1) are generally larger in CI and CU models. This affects the ^{12}C abundance profile within the star and consequently the number of carbon-burning shells during the evolution. The Kippenhahn diagrams for the 15 and 20 $M_{\odot}$ models (Fig. 4.9) demonstrate this effect well; the 15ST and 20ST models have many carbon burning shells where the ignition of a successive shell lies at a position that corresponds to the maximum coordinate reached by the previous convective shell.

Table 4.1: Stellar structure properties for carbon-burning cores and shells at the onset of convection. Shells are labelled in chronological order. $\tau_{\rm conv}$ is the lifetime of the convection zone, $M_{\rm low}$ and $M_{\rm upp}$ are lower and upper mass coordinates for the location of the zone. ΔM is the size of the zone in mass, T and ρ are the temperature and density of the zone at $M_{\rm low}$ and $X_{^{12}{\rm C}}$ and $X_{^{16}{\rm O}}$ are the ^{12}C and ^{16}O mass fraction abundances within the convection zone.

Model	Core/Shell	$\tau_{\rm conv}$ (yr)	$M_{\rm low}$ ($M_\odot$)	$M_{\rm upp}$ ($M_\odot$)	ΔM ($M_\odot$)	T (GK)	ρ (g cm^{-3})	$X_{^{12}{\rm C}}$	$X_{^{16}{\rm O}}$
15ST	Core	1458	0	0.588	0.588	0.717	2.367×10^5	0.2947	0.6296
	1	187.2	0.604	1.293	0.689	0.773	1.816×10^5	0.3002	0.6332
	2	17.92	1.302	2.435	1.134	0.904	1.936×10^5	0.0862	0.5041
15CI	Core	15720	0	1.381	1.381	0.589	7.409×10^4	0.3104	0.6400
	1	150.1	1.396	2.907	1.511	0.758	1.139×10^5	0.0472	0.4883
15CU	Core	51890	0	1.517	1.517	0.486	3.011×10^4	0.3192	0.6458
	1	594.2	1.536	3.270	1.734	0.531	3.557×10^4	0.3185	0.6453
20ST	Core	219	0	0.466	0.466	0.783	1.587×10^5	0.2320	0.6441
	1	41.55	0.507	1.157	0.650	0.843	1.390×10^5	0.2150	0.6332
	2	13.40	1.024	3.088	1.884	0.873	1.109×10^5	0.2438	0.6516
	3	0.228	2.021	3.319	1.298	1.132	1.447×10^5	0.0469	0.5350
20CI	Core	5418	0	1.921	1.921	0.626	4.155×10^4	0.2636	0.6647
	1	290.9	1.047	3.631	2.584	0.781	7.203×10^4	0.0675	0.5481
	2	1.985	1.784	4.137	2.354	0.872	6.615×10^4	0.0488	0.5380
20CU	Core	32280	0	2.771	2.771	0.498	1.553×10^4	0.2861	0.6794
	1	10.05	2.158	2.609	0.450	0.712	4.792×10^4	0.0147	0.5275
	2	3.714	2.815	4.696	1.880	0.592	2.706×10^4	0.2861	0.6794
25ST	1	3.734	1.819	5.928	4.109	0.946	1.017×10^5	0.1449	0.6306
25CI	1	925.4	0.436	2.075	1.640	0.718	3.656×10^4	0.1830	0.6554
	2	12.69	2.111	6.208	4.097	0.516	3.893×10^4	0.2492	0.6975
25CU	Core	22520	0	4.452	4.452	0.510	1.191×10^4	0.2586	0.7038
	1	34.77	1.954	6.429	4.475	0.735	3.622×10^4	0.0191	0.5656

Table4.1 – continued

Model	Core/Shell	$\tau_{\rm conv}$ (yr)	$M_{\rm low}$ ($M_\odot$)	$M_{\rm upp}$ ($M_\odot$)	ΔM ($M_\odot$)	T (GK)	ρ (g cm^{-3})	$X_{^{12}\rm C}$	$X_{^{16}\rm O}$
32ST	1	0.373	2.586	8.948	6.361	1.059	7.925×10^4	0.1346	0.6869
32CI	1	33.06	1.869	8.789	6.920	0.773	3.290×10^4	0.1507	0.6973
32CU	Core	13780	0	6.897	6.897	0.539	1.001×10^4	0.2164	0.7399
	1	5.679	2.774	9.077	6.303	0.710	2.390×10^4	0.0269	0.6265
60ST	1	0.260	2.900	10.12	7.221	1.073	7.159×10^4	0.1360	0.6794
60CI	1	15.04	2.171	10.04	7.866	0.793	3.080×10^4	0.1541	0.6911
60CU	Core	12900	0	8.326	8.326	0.542	9.210×10^3	0.2205	0.7341
	1	4.276	2.975	10.39	7.412	0.721	2.207×10^4	0.0309	0.6207

4.4.4 Overlapping carbon shells

As the rate is increased, the tendency for convective shells to 'overlap' (where the lower bound in mass of the convective region extends below the upper bound of the previous convection zone) is increased. All CU models, except the 15CU model, show this overlap, which occurs between a convective carbon core and the first convective carbon shell. The amount of overlap between the carbon core and the first carbon shell, and the first and second carbon shells, in the 20CI model (in Fig. 4.9) is also much larger than that in the 20ST model. This overlap effect occurs because successive carbon-shell burning episodes, caused by ignition of residual ^{12}C fuel left over from previous burning stages, can occur at a lower temperature and density or with a lower abundance of ^{12}C fuel (see column 9. of Table 4.1). This effect has been noted previously by Chieffi et al. (1998) and in the preliminary studies (Bennett et al. 2010a,b; see also appendix D).

The presence of the residual ^{12}C is caused by the gradual shrinking of the carbon-core near the end of the burning stage. This occurs in model 20CI and all CU models, except model 15CU where the shell is located at the top of the previous convective carbon core. The convective carbon shell in the 20CU model (see Fig. 4.9), however, shows an interesting structure. In this case a carbon shell is ignited at a position that overlaps with the core and then shortly after an additional shell is ignited at the point corresponding to the top of the previous core. Because of the unusual structure, the lifetime given in Table 4.1 for the 20CU model, shell 1, is defined from the onset of convection to the time it shrinks back up into the second shell.

The presence of overlap with a carbon core has a significant impact on the composition of the shell at the onset of convection. Indeed, carbon-core burning ashes, including s-process nuclides, will mix out to a position above the remnant mass and be

present in the supernova ejecta. As mentioned above, overlapping shells have previously been noted in the literature, but the consequences of overlapping shells of this nature are not well studied. The nucleosynthetic consequences of overlap will be discussed in §4.6.3.

4.4.5 Lifetimes

The lifetime of convection zones is generally longer in the CI and CU models. This could be perceived as counter-intuitive, since with an enhanced rate one would expect that the ^{12}C fuel would be expended more rapidly. However, the burning takes place in lower temperature and density conditions, which affect the neutrino losses. Table 4.2 shows the energy generation terms for nuclear reactions ($\epsilon_{\rm nuc}$) and neutrino losses (ϵ_{ν}) at the centre of the star when the mass fraction of ^{12}C is half the amount available just prior to carbon-core burning. The proportion of neutrinos formed by various neutrino processes are also specified in Table 4.2, which are given as fractions, f, of the total neutrino losses (in per cent). These processes are pair annihilation ($f_{\rm pair}$), ν-photoproduction ($f_{\rm phot}$) and the rest ($f_{\rm rest}$), which are bremsstrahlung and plasmon decay processes (see §3.1.4). Neutrino formation through the last two processes is negligibly small at carbon burning temperatures.

As shown by Table 4.2, the energy generation rate from nuclear reactions and the neutrino losses are reduced in the CI and CU models, although an increase is seen in models 25CU, 32CU and 60CU from their CI counterparts. This increase is due to the presence of the convective carbon core in place of a radiative one, where there is an increased availability of ^{12}C fuel from mixing. During carbon burning, the timescale for burning is governed primarily by the neutrino losses (as is true for all advanced burning

stages) and these losses generally increase monotonically with increasing temperature. Therefore, a reduction in the neutrino-losses has the consequence of increasing the lifetime of carbon-burning stages. Only the carbon shells in models 32CU (see Fig. 4.10) and 60CU (see Fig. 4.11) do not show this behaviour. This can be explained by the presence of a previous convective carbon core in those models, which reduces the abundance of carbon fuel available for burning in these shells. Systematic trends during shell burning are less clear because of the rather complicated evolution of the shell structure, but convective shells often form at lower temperatures in CI and CU models (see column 7 in Table 4.1), similar to the situation in the core. For carbon core burning, on the other hand, there is a clear increase in the lifetime with increasing rate, which is shown in Fig. 4.12.

The main neutrino processes during carbon burning are those caused by pair annihilation and ν-photoproduction processes (Woosley et al., 2002; Itoh et al., 1996). It is worth noting that the decrease in temperature in the CI and CU models is responsible for a larger proportion of neutrinos formed by ν-photoproduction rather than pair annihilation. This trend at larger carbon-burning rates is opposite to the trend with initial mass, which favours higher temperatures and production of neutrinos by pair annihilation with increasing initial mass.

Despite the changes to the stellar structure during carbon burning, the evolution of the advanced burning stages in the core following carbon-burning seems only slightly affected in terms of the convection zone structure, as seen in Fig. 4.9, 4.10 and 4.11, but exhibit burning stages with different lifetimes. The burning lifetimes for the hydrostatic burning stages are presented in Table 4.3, which are defined for each stage as the difference in age from the point where the principal fuel for that stage (^{1}H for hydrogen burning, ^{4}He for helium burning, etc.) is depleted by 0.3 per cent from its maximum

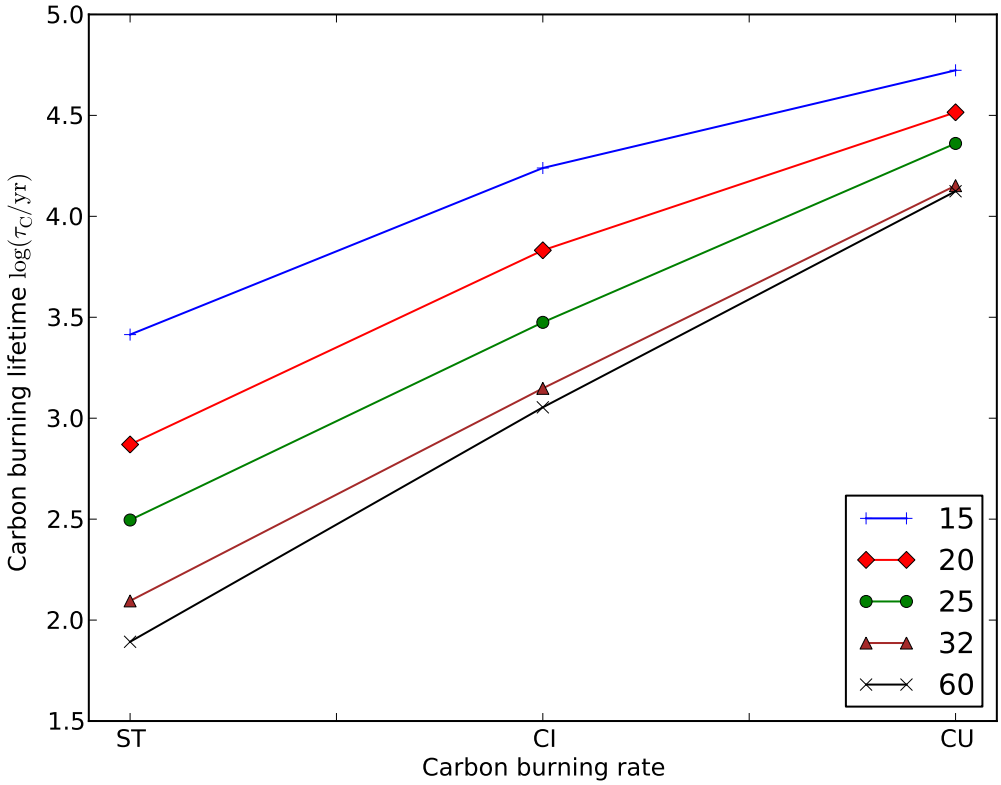

Figure 4.12: Carbon core burning lifetimes.

Table 4.2: Energy generation and neutrino parameters during core carbon burning. For each model the central values of temperature, T, density, ρ, energy generation rates for nuclear burning, $\epsilon_{\rm nuc}$, and neutrino losses, ϵ_ν, and percentage fractions of the total neutrinos formed by pair annihilation ($f_{\rm pair}$), ν-photoproduction ($f_{\rm phot}$) and other processes ($f_{\rm rest}$) are specified. These parameters are determined at the time when the mass fraction of ^{12}C is half of the value just prior to carbon burning.

Model	T (GK)	ρ (g cm^{-3})	$\epsilon_{\rm nuc}$ (erg g^{-1} s^{-1})	ϵ_ν (erg g^{-1} s^{-1})	$f_{\rm pair}$ (%)	$f_{\rm phot}$ (%)	$f_{\rm rest}$ (%)
15ST	0.830	2.141×10^5	4.762×10^7	-1.542×10^7	89.665	10.253	0.082
15CI	0.686	7.659×10^4	6.822×10^6	-1.454×10^6	70.007	29.861	0.132
15CU	0.566	3.772×10^4	2.277×10^6	-1.448×10^5	19.800	79.902	0.298
20ST	0.883	1.679×10^5	1.663×10^8	-5.910×10^7	95.651	4.327	0.022
20CI	0.723	5.356×10^4	1.529×10^7	-5.260×10^6	87.461	12.508	0.031
20CU	0.588	2.477×10^4	3.727×10^6	-2.643×10^5	41.935	57.943	0.122
25ST	0.859	1.439×10^5	5.176×10^7	-4.435×10^7	95.061	4.917	0.022
25CI	0.690	3.942×10^4	2.603×10^6	-2.975×10^6	83.475	16.490	0.035
25CU	0.603	1.889×10^4	4.975×10^6	-4.533×10^5	58.913	41.026	0.061
32ST	0.904	1.313×10^5	1.360×10^8	-1.234×10^8	97.310	2.680	0.010
32CI	0.711	3.532×10^4	3.682×10^6	-5.995×10^6	89.439	10.543	0.018
32CU	0.621	1.510×10^4	5.725×10^6	-9.148×10^5	74.347	25.625	0.028
60ST	0.919	1.106×10^5	1.900×10^8	-1.954×10^8	98.053	1.941	0.006
60CI	0.725	3.260×10^4	5.863×10^6	-9.442×10^6	92.247	7.741	0.012
60CU	0.625	1.375×10^4	6.244×10^6	-1.096×10^6	77.670	22.309	0.021

value to the age where the mass fraction of that fuel depletes below a value of 10^{-5}, except for carbon burning and neon burning, where this value is 10^{-3}, and oxygen burning, where this value is 10^{-2}. These criteria are necessary to ensure a lifetime is calculated in those cases where residual fuel is unburnt (such as during oxygen burning in the 15CU model, where the ^{16}O mass fraction abundance that remains unburnt following the end of core oxygen burning is $\sim 3.177 \times 10^{-3}$) and to ensure that the burning stages are correctly separated (for example, the mass fraction abundance of ^{12}C at neon ignition for model 60ST is 4.123×10^{-5}). The lifetime of the advanced stages is relatively sensitive to the mass fraction abundances of isotopes defining the lifetime.

Carbon burning lifetimes are longer for the CI and CU rates, but lifetimes for the other advanced stages do not show a general trend with the carbon burning rate. This lack of trend also applies to the central properties, as seen in Fig. 4.5, where the tracks are modified by the enhanced rate models but the modifications do not follow a general pattern. In fact, there are examples of $T_c - \rho_c$ tracks, e.g. the 25CI and 25CU models in Fig. 4.5, where following the deviation caused by carbon ignition the track returns to that of the ST rate (especially for the 15, 20 and 25 $M_\odot$ models). The main property determining the variations in the lifetime is the central temperature, which is linked with the neutrino loss rates.

Table 4.3: Lifetimes for all core burning stages in all models (in yrs). Lifetimes are provided for hydrogen burning ($\tau_{\rm H}$), helium burning ($\tau_{\rm He}$), carbon burning ($\tau_{\rm C}$), neon burning ($\tau_{\rm Ne}$), oxygen burning ($\tau_{\rm O}$) and silicon burning ($\tau_{\rm Si}$). The total lifetime is given by ($\tau_{\rm Total}$).

Model	$\tau_{\rm H}$	$\tau_{\rm He}$	$\tau_{\rm C}$	$\tau_{\rm Ne}$	$\tau_{\rm O}$	$\tau_{\rm Si}$	$\tau_{\rm Total}$
15ST	1.137×10^{7}	1.255×10^{6}	2.595×10^{3}	1.253	1.233	1.685×10^{-2}	1.268×10^{7}
15CI	1.137×10^{7}	1.255×10^{6}	1.735×10^{4}	14.296	4.745	–	1.269×10^{7}
15CU	1.137×10^{7}	1.255×10^{6}	5.288×10^{4}	12.918	8.815	–	1.272×10^{7}
20ST	7.926×10^{6}	8.396×10^{5}	7.409×10^{2}	0.193	0.293	1.302×10^{-2}	8.799×10^{6}
20CI	7.926×10^{6}	8.396×10^{5}	6.786×10^{3}	0.655	0.542	–	8.803×10^{6}
20CU	7.926×10^{6}	8.396×10^{5}	3.275×10^{4}	0.265	0.253	–	8.825×10^{6}
25ST	6.492×10^{6}	6.519×10^{5}	3.131×10^{2}	0.634	0.603	4.322×10^{-3}	7.168×10^{6}
25CI	6.492×10^{6}	6.519×10^{5}	2.984×10^{3}	0.539	0.597	1.097×10^{-2}	7.169×10^{6}
25CU	6.492×10^{6}	6.519×10^{5}	2.296×10^{4}	0.505	0.515	1.746×10^{-2}	7.186×10^{6}
32ST	5.287×10^{6}	5.346×10^{5}	1.245×10^{2}	0.111	0.167	8.997×10^{-3}	5.840×10^{6}
32CI	5.287×10^{6}	5.346×10^{5}	1.406×10^{3}	0.726	1.123	1.173×10^{-2}	5.840×10^{6}
32CU	5.287×10^{6}	5.346×10^{5}	1.419×10^{4}	0.148	0.111	5.458×10^{-3}	5.852×10^{6}
60ST	3.549×10^{6}	3.935×10^{5}	7.808×10^{1}	0.090	0.119	8.624×10^{-3}	3.955×10^{6}
60CI	3.549×10^{6}	3.935×10^{5}	1.132×10^{3}	0.425	0.505	–	3.955×10^{6}
60CU	3.549×10^{6}	3.935×10^{5}	1.331×10^{4}	0.112	0.071	–	3.966×10^{6}

The last column of Table 4.3 shows that the total lifetime of the star increases slightly with an enhanced carbon burning rate, because of the longer carbon burning lifetime. Since the total lifetime increases by $\approx 1 - 5 \times 10^4$ years, the strong mass loss characteristic of massive stars, which can increase by up to $\sim 10^{-5} M_\odot$ yr^{-1}, increases the mass lost by up to $0.5 M_\odot$.

4.4.6 Core masses

The changes in lifetimes, mass loss and position of shell burning episodes in mass coordinate will affect the core masses. The core masses are shown in Table 4.4, which are evaluated at the end of oxygen burning for all models. In column 3 of Table 4.4, we see that the carbon burning rate does not affect the helium core mass (the helium core mass is defined as the mass coordinate where the mass fraction abundance of ^{4}He is 0.75 at the interface between the hydrogen and helium-rich layers). There is only a tiny difference for the 25 $M_\odot$ case because of the small structure re-arrangement of the hydrogen burning shell. In column 4, we see that with an increasing carbon burning rate, the CO core mass is larger (the CO core mass is defined as the mass coordinate where the ^{4}He mass fraction abundance is 10^{-3}). The reason is the following. With an increased rate, carbon burning occurs at lower temperatures where the energy production dominates over neutrino cooling and this leads to a stronger carbon core burning in a larger convective zone. The carbon burning core therefore produces more energy, which leads to a less energetic helium-burning shell that is radiative rather than convective, which is the case for the ST models. When the He-shell is radiative the burning front depletes completely the helium available at one mass coordinate and then moves upwards leading to a more massive CO core whereas with a convective

He-shell, the bottom of the shell stays at the same mass coordinate since the helium in the convective shell is never completely exhausted due to mixing. Note also that the 32 and 60 $M_{\odot}$ models do not exhibit a value for $M_{\alpha}^{75\%}$. This is because the mass loss is strong enough in these WR stars to expel the majority of their helium-rich envelopes and the ^{4}He abundance is not high enough to satisfy the criterion for $M_{\alpha}^{75\%}$. In these cases, the helium core mass is taken as the final mass, $M_{\rm Final}$ (see column 2 of Table 4.4).

As shown in Fig. 4.9, 4.10 and 4.11, the size of the convective cores during neon, oxygen and silicon burnings is only slightly affected by the changes in carbon burning rate. The changes to the oxygen-free core, ($M_{\rm O-free}$, see last column of Table 4.4), which are calculated at the end of core oxygen burning, occur due to the changes to the carbon burning convective history. Specifically, the changes in $M_{\rm O-free}$ with carbon burning rate are caused by changes in the position of the lower boundary of the last convective carbon shell, which is affected by the presence of a convective carbon core. Generally, the changes to the $M_{\rm O-free}$ do not present a clear pattern.

4.5 Effects on nucleosynthesis

4.5.1 S-process parameters

Several indicators for the neutron capture nucleosynthesis are considered. The s-process is typically characterised by the neutron density, n_n, the neutron captures per iron seed,

Table 4.4: Core masses at the end of oxygen burning, in Solar masses. For each model, the final total mass ($M_{\rm Final}$), helium core mass ($M_{\alpha}^{75\%}$), CO core mass ($M_{\rm CO}$) and the oxygen-free core mass ($M_{\rm O-free}$) are specified. Note that the 32 and 60 $M_{\odot}$ models expel most of their helium-rich envelopes, consequently becoming WR stars.

Model	$M_{\rm Final}$	$M_{\alpha}^{75\%}$	$M_{\rm CO}$	$M_{\rm O-free}$
15ST	12.132	4.791	2.805	0.921
15CI	12.069	4.791	2.923	0.867
15CU	11.907	4.791	3.239	0.849
20ST	13.974	6.826	4.494	1.083
20CI	13.916	6.826	4.491	1.099
20CU	13.602	6.826	4.696	1.040
25ST	13.738	9.199	6.301	1.081
25CI	13.710	9.092	6.384	0.980
25CU	13.202	9.092	6.544	1.124
32ST	12.495	12.495	9.146	1.187
32CI	12.495	12.495	9.146	0.984
32CU	12.493	12.493	9.425	1.334
60ST	13.428	13.428	10.701	1.242
60CI	13.423	13.423	10.446	0.990
60CU	13.278	13.278	10.929	1.519

n_c, and the neutron exposure, τ_n. n_c is defined as follows:

$$n_c = \frac{\sum_i^n (A_i - 56)(X_i - X_i^{\rm init})}{X_{^{56}\rm Fe}}, \tag{4.6}$$

where $X_i^{\rm init}$ is the initial mass fraction abundance of isotope X_i with atomic mass A_i and $X_{^{56}\rm Fe}$ is the intial mass fraction abundance of ^{56}Fe, which is the dominant seed isotope for s-process nucleosynthesis. τ_n is defined as $\tau_n = \int v_T n_n dt$ (Clayton, 1968). These definitions are, however, of limited use in the multi-zone calculations used here. The reason for this is that in the multi-zone stellar models, convective mixing affects the neutron irradiance experienced by a given mass element (The et al., 2007). Stellar matter, including the neutron sources, seeds and poisons, is mixed into and out of the bottom of the convection zone, where the temperature is highest and where the majority of the s-process occurs. Consequently, an evaluation of n_c or τ_n at a particular mass coordinate will be different to that experienced by a given mass element.

Therefore, in order to evaluate relevant parameters to describe the neutron irradiance, convective mixing needs to be taken into account in the evaluation of the parameter. This can be achieved for the neutron exposure by considering the initial and final abundances of ^{54}Fe, an isotope that is slowly destroyed by neutron captures in the s-process sites considered here. It cannot be used during or after oxygen burning where temperatures are high enough to photodisintegrate heavy elements (Woosley & Weaver, 1995). An estimate of the neutron exposure using ^{54}Fe can be made using the following formula (Woosley & Weaver, 1995; The et al., 2000),

$$\tau_{54} = -\frac{1}{\sigma}[\ln X_{\rm i}(^{54}\rm Fe) - \ln X_{\rm f}(^{54}\rm Fe)], \tag{4.7}$$

where σ is the ^{54}Fe(n,γ)^{55}Fe reaction rate ($\sigma = 29.6 \pm 1.3$ mb, Dillmann et al., 2006) and $X_{\rm i}(^{54}{\rm Fe})$ and $X_{\rm f}(^{54}{\rm Fe})$ are the mass fraction abundances of ^{54}Fe before and after the neutron exposure respectively. A better estimate of n_c can be obtained by using mass-averaged abundances for X_i, $X_i^{\rm init}$ and $X_{^{56}{\rm Fe}}$ over the maximum size of the convective region,

$$n_{c,{\rm av}} = \frac{\sum_i^n (A_i - 56)(\langle X_i \rangle - \langle X_i^{\rm init} \rangle)}{\langle X_{^{56}{\rm Fe}} \rangle}. \tag{4.8}$$

This takes into account any changes to the size of the convective region during the burning stage where the s-process nucleosynthesis occurs.

4.5.2 Core helium burning

The s-process starts in the helium core. Although changes to the ^{12}C + ^{12}C do not affect helium burning, the s-process during helium burning contributes greatly to the s-process abundances. The triple-α and $^{12}{\rm C}(\alpha,\gamma)^{16}{\rm O}$ reactions occurring during helium burning affect the amount of ^{12}C fuel available at the beginning of carbon-burning. In addition, the $^{12}{\rm C}(\alpha,\gamma)^{16}{\rm O}$ reaction changes the abundance of ^{12}C and its ratio with ^{16}O (Arnett & Thielemann, 1985). The $^{12}{\rm C}/^{16}{\rm O}$ ratio is also dependent on the amount of overshooting employed in the models (Maeder & Meynet, 1987).

The $^{12}{\rm C}/^{16}{\rm O}$ ratios at the end of helium core burning are 0.509, 0.436, 0.384, 0.297 and 0.322 for models 15ST, 20ST, 25ST, 32ST and 60ST respectively (slight variations in the $^{12}{\rm C}/^{16}{\rm O}$ ratio in Table 4.1 for models with different rates are due to the differing durations of the radiative burning of carbon before the convective episodes start). The increase in the ratio for model 60ST with respect to model 32ST is due to the higher density/lower temperature conditions during central helium burning, favouring more

production of ^{12}C by 3α reactions and less destruction of ^{12}C to ^{16}O by ^{12}C$(\alpha,\gamma)^{16}$O reactions. This is due to the strong mass loss in the $60M_{\odot}$ models

A comparison of the s-process parameters at the end of helium burning for different authors is presented in Table 4.5 for the 15, 20 and $25M_{\odot}$ models. In general, the s-process parameters evaluated for the helium burning s-process in this work agree with those in the existing literature and validate the use of the average quantities specified in §4.5.1. The overproduction factor of ^{80}Kr (last column of Table. 4.5), however, is the lowest amongst the other authors. This can be attributed to use of different nuclear reactions, especially the ^{12}C$(\alpha,\gamma)^{16}$O, ^{22}Ne$(\alpha$,n$)^{25}$Mg reactions and (n,γ) reactions around the vicinity of the branching-point nuclide ^{79}Se. In this work, the rates are taken from Kunz et al. (2002), Jaeger et al. (2001) and Dillmann et al. (2006) for the ^{12}C$(\alpha,\gamma)^{16}$O, ^{22}Ne$(\alpha$,n$)^{25}$Mg and (n,γ) reactions respectively.

The characteristic distribution of nuclides produced by the weak s-process includes nuclides with $60 < A < 90$ (those nuclides that lie between the iron-group nuclides and the Sr-Y-Zr peak). This distribution is similar for all models, but the overproduction factors for nuclides with $60 < A < 90$ are larger overall in models with increasing initial mass (see Fig. 4.13 for the 25ST case). This is because more ^{22}Ne neutron source is burnt by the end of helium burning with increasing mass. This distribution can be regarded as an initial distribution, which is modified by neutron-capture nucleosynthesis occurring during carbon-core burning and, if there are overlapping convection zones, carbon-shell burning (see §4.5.3.2 for more details).

Table 4.5: Comparison of s-process parameters at the end of helium burning among different authors. For each publication (and model) the average neutron captures per iron seed (n_c), mean neutron exposure ($\langle\tau\rangle$), ^{22}Ne mass fraction abundance ($X_{^{22}\mathrm{Ne}}$) and ^{80}Kr overproduction factor ($X_{^{80}\mathrm{Kr}}/X_{^{80}\mathrm{Kr}\odot}$) are specified.

Author	n_c	$\langle\tau\rangle$ (mb^{-1})	$X_{^{22}\mathrm{Ne}}$ ($\times10^{-2}$)	$X_{^{80}\mathrm{Kr}}/X_{^{80}\mathrm{Kr}\odot}$
	$15M_\odot$			
Kaeppeler et al. (1994)	1.80	0.09	1.65	21
The et al. (2000) (A)	3.38	0.10	1.33	117
The et al. (2007) (15N)	1.19	0.06	1.50	15
This work, (15ST)	1.64	0.09	1.51	12
	$20M_\odot$			
Kaeppeler et al. (1994)	3.66	0.15	1.32	116
The et al. (2000) (A)	5.48	0.16	1.04	598
The et al. (2007) (20N)	2.34	0.10	1.12	56
This work, (20ST)	3.07	0.14	1.10	30
	$25M_\odot$			
Raiteri et al. (1991a)	5.67	0.21	0.96	481
Kaeppeler et al. (1994)	5.41	0.20	1.00	475
The et al. (2000) (A)	6.70	0.22	0.76	1100
The et al. (2007) (25N)	3.52	0.15	0.77	174
Pignatari et al. (2010) (Model 1)	4.95	0.20	1.14	169
This work, (25ST)	4.28	0.18	0.77	75

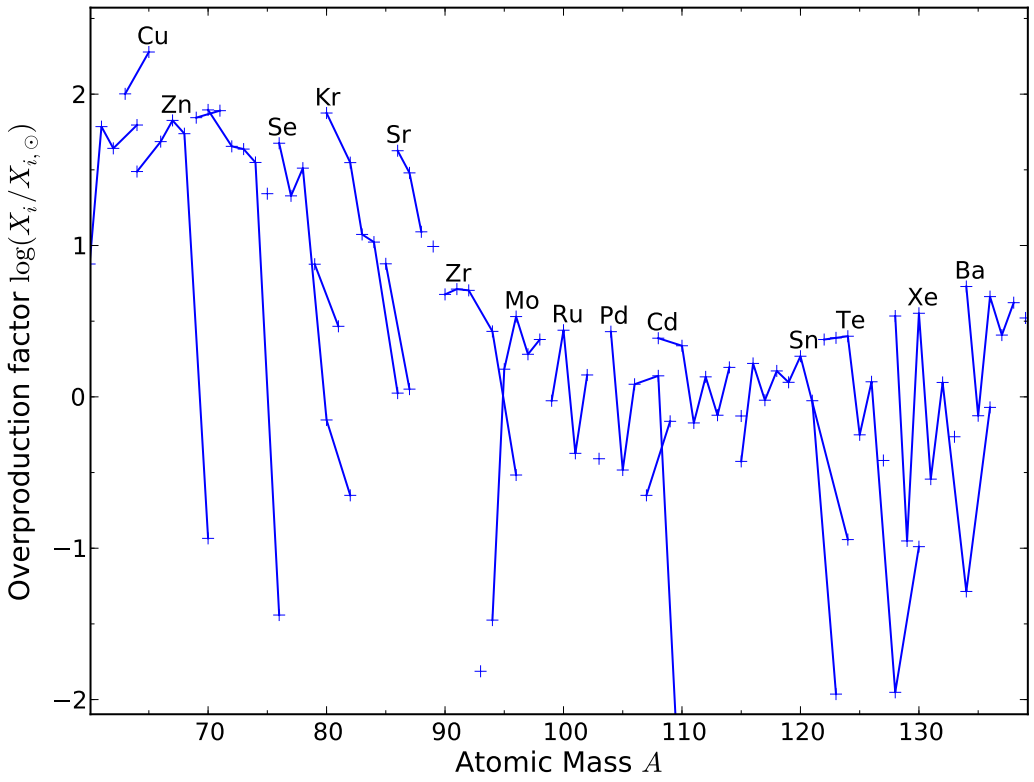

Figure 4.13: Central overproduction factors for the end of core helium burning for model 25ST. The plot shows an increase in nucleosynthesis of isotopes between $60 < A < 90$ in the CI and CU models, which is between the iron-group nuclei and the Sr-Y-Zr peak at an atomic mass ≈ 90.

4.5.3 Carbon core burning

4.5.3.1 Lighter elements

The main products of carbon-burning are ^{20}Ne and ^{24}Mg, with non-negligible amounts of ^{23}Na. The most abundant isotope following carbon burning is ^{16}O, which is left over from core helium-burning. Changes to the nucleosynthesis of these isotopes directly from ^{12}C + ^{12}C reactions will be minimal for any fixed amount of ^{12}C fuel since the branching ratio implemented in the model is not temperature dependent. However, the lower burning temperatures affect other reactions that occur during the carbon burning stages and the amount of ^{12}C fuel available for burning can vary as a consequence of the modified convection zone structure. In particular, the presence of larger convective cores and shells in the enhanced rate models affect the nucleosynthesis. With regards to core-carbon burning, the additional transport of ^{12}C fuel down into the centre causes more ^{12}C fuel to be burnt over the star's lifetime in the enhanced rate models, producing more ^{20}Ne, ^{23}Na and ^{24}Mg. Subsequent neutron captures on these isotopes produce some additional ^{21}Ne, ^{22}Ne and ^{25}Mg. Although more of these nuclides are produced, the larger convective cores in the enhanced rate models causes the newly formed isotopes to be spread over a larger volume (dilution). Therefore, no clear trend is seen in the production of light elements with increasing carbon burning rate.

^{16}O is depleted less with increasing carbon burning rate because of a reduction in the destruction of ^{16}O by ^{16}O$(\alpha,\gamma)^{20}$Ne reactions at lower temperature, except in the 32CU and 60CU models where a large convective core mixes ^{16}O into the centre, depleting it more with respect to the radiative cores of the corresponding ST and CI models. ^{23}Na has a comparable or slightly reduced abundance than ^{24}Mg in the

ST models, but is more dominant in the CI and CU models. This is because of the constant branching ratio of the $^{12}C + {}^{12}C$ exit channels with temperature, since at lower temperature the connecting $^{23}Na(p,\alpha)^{20}Ne$ and $^{23}Na(p,\gamma)^{24}Mg$ reactions are reduced.

4.5.3.2 Heavier elements

Heavier elements (with $A > 60$) are produced almost exclusively by neutron-capture nucleosynthesis. Table 4.6 lists, for all models, the neutron exposure, τ_{54}, the neutron captures per iron seed, $n_{c,\mathrm{av}}$, the mass fraction abundances of the isotopes ^{54}Fe and ^{88}Sr and the isotopic ratios of $^{70}Ge/^{70}Zn$, $^{80}Kr/^{80}Se$ and $^{86}Sr/^{86}Kr$. ^{88}Sr, like ^{54}Fe, is also a useful s-process indicator as it has a neutron-magic nucleus and is slowly built-up over the course of the s-process. The isotopic ratios are also specified as changes to the ratios demonstrate deviations to the main s-process path at branching point nuclides (^{69}Zn, ^{79}Se and ^{85}Kr for $^{70}Ge/^{70}Zn$, $^{80}Kr/^{80}Se$ and $^{86}Sr/^{86}Kr$ respectively). If the neutron density increases, the s-process path opens to allow the production of more neutron-rich isotopes, lowering these isotopic ratios.

Table 4.6: S-process tracers, neutron capture parameters and isotopic ratios at the end of helium-core burning, carbon-core burning and convective carbon-shell burning. $n_{c,\mathrm{av}}$ is the neutron captures per iron seed averaged over the convective region and τ_{54} is the neutron exposure calculated using Eq. 4.7. Isotopes (such as ^{88}Sr and ^{54}Fe) represent average mass fraction abundances at the end of the burning stage, except for radiative burning where the central values are taken. The s-process parameters for a shell that persists to the presupernova stage use final abundances that are evaluated at start of oxygen burning, which removes the effects of photodisintegration occurring during the late evolutionary stages from the evaluation of the s-process parameters.

Model	Shell	^{88}Sr	^{54}Fe	$n_{c,\mathrm{av}}$	τ_{54} (mb^{-1})	^{70}Ge/^{70}Zn	^{80}Kr/^{80}Se	^{86}Sr/^{86}Kr
15ST	He-core	2.005×10^{-7}	5.750×10^{-6}	1.641	0.088	115.913	2.690	4.247
15ST	C-core	1.556×10^{-6}	7.721×10^{-7}	6.601	0.062	1165.633	5.107	46.001
15ST	1	1.000×10^{-6}	1.089×10^{-6}	4.740	0.048	1036.915	3.668	20.178
15ST	2	6.629×10^{-7}	1.266×10^{-6}	3.903	0.042	335.818	0.701	2.708
15CI	C-core	1.009×10^{-4}	9.137×10^{-8}	29.270	0.134	901.882	4.284	45.048
15CI	1	2.803×10^{-5}	6.958×10^{-7}	6.005	0.059	862.687	3.172	23.268
15CU	C-core	2.182×10^{-4}	3.716×10^{-8}	46.293	0.165	743.822	4.080	44.065
15CU	1	5.046×10^{-5}	2.163×10^{-6}	19.423	0.055	638.189	0.765	1.726
20ST	He-core	3.817×10^{-7}	1.070×10^{-6}	3.069	0.143	928.859	3.588	7.503
20ST	C-core	1.286×10^{-6}	1.615×10^{-7}	8.080	0.062	1315.250	4.012	30.741
20ST	1	1.064×10^{-6}	2.303×10^{-7}	6.605	0.043	1245.114	2.605	17.583
20ST	2	9.403×10^{-7}	3.382×10^{-7}	4.934	0.033	518.314	0.774	4.205
20ST	3	8.762×10^{-7}	4.292×10^{-7}	0.119	0.001	487.403	0.696	3.802
20CI	C-core	5.197×10^{-5}	8.818×10^{-8}	27.796	0.084	970.039	4.200	41.853
20CI	1	2.424×10^{-5}	3.828×10^{-7}	5.920	0.023	975.182	2.873	20.450
20CI	2	2.160×10^{-5}	3.869×10^{-7}	2.737	0.012	347.183	0.366	3.352
20CU	C-core	1.727×10^{-4}	4.802×10^{-9}	60.722	0.182	779.749	4.104	36.648
20CU	1	7.074×10^{-5}	5.484×10^{-7}	4.073	0.019	494.139	2.019	22.567
20CU	2	1.194×10^{-5}	6.573×10^{-7}	4.651	0.027	151.579	0.348	4.048

Table 4.6 – Continued

Model	Shell	^{88}Sr	^{54}Fe	$n_{c,\mathrm{av}}$	τ_{54} (mb^{-1})	^{70}Ge/^{70}Zn	^{80}Kr/^{80}Se	^{86}Sr/^{86}Kr
25ST	He-core	6.153×10^{-7}	3.539×10^{-7}	4.280	0.180	2220.036	3.755	11.329
25ST	C-core	1.472×10^{-6}	7.918×10^{-8}	8.271	0.045	1432.597	4.385	35.554
25ST	1	9.499×10^{-7}	1.482×10^{-7}	5.632	0.028	87.609	0.109	0.515
25CI	C-core	4.092×10^{-5}	1.411×10^{-9}	48.421	0.179	970.416	4.576	59.426
25CI	1	1.772×10^{-5}	6.313×10^{-8}	23.538	0.045	1063.729	4.066	38.990
25CI	2	1.111×10^{-6}	1.564×10^{-7}	5.543	0.028	315.357	0.280	1.401
25CU	C-core	1.475×10^{-4}	1.509×10^{-9}	73.339	0.184	804.018	4.072	36.419
25CU	1	9.824×10^{-5}	1.347×10^{-7}	15.755	0.015	698.157	1.283	10.094
32ST	He-core	1.097×10^{-6}	1.192×10^{-7}	5.623	0.217	3380.614	3.900	16.340
32ST	C-core	1.788×10^{-6}	5.333×10^{-8}	6.239	0.024	1640.445	3.640	28.449
32ST	1	1.315×10^{-6}	8.625×10^{-8}	3.016	0.010	75.996	0.130	1.014
32CI	C-core	1.825×10^{-5}	3.955×10^{-9}	38.296	0.110	1042.993	4.740	60.126
32CI	1	2.045×10^{-6}	6.562×10^{-8}	5.220	0.017	1021.836	1.646	9.944
32CU	C-core	1.007×10^{-4}	8.498×10^{-10}	77.718	0.167	837.791	3.949	39.032
32CU	1	7.633×10^{-5}	3.346×10^{-8}	16.738	0.011	509.651	0.428	4.911
60ST	He-core	1.524×10^{-6}	6.404×10^{-8}	6.489	0.238	1741.270	1.125	12.267
60ST	C-core	1.701×10^{-6}	5.297×10^{-8}	5.862	0.023	1743.568	3.246	25.865
60ST	1	1.335×10^{-6}	7.814×10^{-8}	2.779	0.009	69.670	0.146	1.136
60CI	C-core	1.491×10^{-5}	4.808×10^{-9}	33.897	0.104	1072.384	4.619	52.637
60CI	1	1.622×10^{-6}	5.837×10^{-7}	3.800	0.029	871.777	0.921	5.676
60CU	C-core	1.076×10^{-4}	6.551×10^{-10}	81.743	0.172	837.512	3.877	36.865
60CU	1	8.908×10^{-5}	2.512×10^{-8}	17.940	0.010	455.999	0.370	4.862

According to Table 4.6, all CI and CU models show a depletion of ^{54}Fe and production of ^{88}Sr relative to the ST case, indicating that a higher neutron exposure is present in the convective carbon core. For all CI and CU models, irrespective of mass, the neutron exposure is high enough to allow an increasing production of isotopes beyond the Sr-Y-Zr peak, which is quantified in a higher neutron captures per iron seed. An example of this nucleosynthesis for the $25M_{\odot}$ model is seen in Fig. 4.14, which shows the central overproduction factors for heavy, stable isotopes in the star at the end of carbon burning. The distribution of synthesised isotopes is extended, with increasing rate, beyond the Sr-Y-Zr peak to include isotopes up to the Ba-La peak at $A \approx 140$. This is an anomalous distribution compared to the weak s-process component, which is different to the distribution of the previous helium burning core (see Fig. 4.13).

The neutron density in the carbon core decreases from a typical value of $\sim 10^8$ cm^{-3}, which is maintained throughout the burning, to $\sim 10^7$ cm^{-3} in the models with an increasing carbon burning rate. In the 25CU, 32CU and 60CU models the neutron density is enhanced over the CI cases because of the presence of the convective core; the mixing into and out of the centre acts to maintain a supply of neutron sources at the centre. Concerning the ST case, the neutron exposures for the cores are similar in magnitude to that of the helium burning core (~ 0.06 mb^{-1}), but are lower for the most massive stars considered here (~ 0.02 mb^{-1} for the 32ST and 60ST models). For the CI and CU rates the neutron exposures are significantly enhanced, typically exceeding 0.1 mb^{-1}. This is mainly due to the rising efficiency of the ^{13}C neutron source at lower temperatures, coupled with the increased lifetime of the core carbon burning stage.

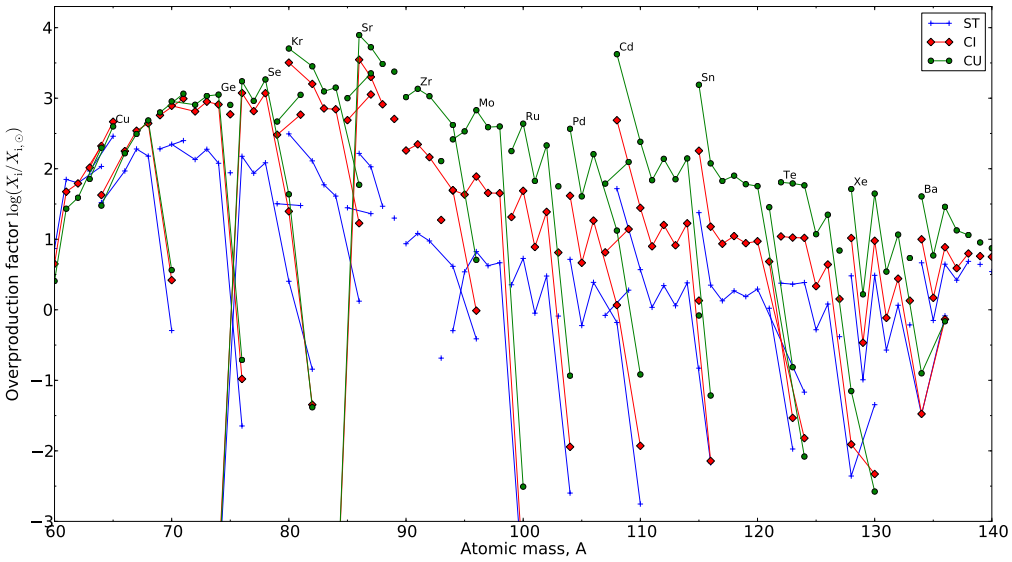

Figure 4.14: Central overproduction factors for most stable isotopes at the end of carbon-core burning for the $25M_{\odot}$ models. The plot shows a significant increase in nucleosynthesis of isotopes between $60 < A < 140$ in the CI and CU models, which is beyond the Sr-Y-Zr peak.

4.5.4 Carbon shell burning

Nucleosynthesis in the carbon shells is characterised by the s-process with a high neutron density but lower neutron exposure compared to carbon core, with ^{22}Ne being the dominant neutron source. In the ST models, the neutron densities vary from $\sim 10^8$ cm^{-3} for early convective shells (models 15ST and 20ST), and increase to a typical value of $\sim 10^{10}$ cm^{-3} in the final carbon burning shell. In the CI and CU models, the neutron density is $\sim 10^7$ cm^{-3} in early shells, similar to the values obtained during core carbon burning, and then rises to $\sim 10^{8-9}$ cm^{-3}. The lifetimes for the carbon shell burning stages vary quite differently from model to model, but are generally increasing with increasing rate. For example, in the 15CU case, the lifetimes of the last carbon shell in Table 4.1 for the 15ST, 15CI and 15CU models are 17.92, 150.1 and 594.2 years respectively. The carbon shell in model 15CU consequently exhibits a strong neutron exposure of similar magnitude to the carbon core (see Table 4.6). It should be noted however that in almost every instance of a carbon burning shell, the neutron exposure is smaller than that of the carbon core in the same model. This asserts the fact that carbon shells are characterised by a lower neutron exposure and higher neutron density (with ^{22}Ne as the main neutron source), although the degree with which this is true is reduced with an increasing carbon burning rate. That is, the general trend with increasing rate is a decrease in the neutron density and an increase in the neutron exposure in the carbon shells.

The above can be verified by considering the ratios of isotopes involved at branching points, since the lower neutron density will close the s-process path to the synthesis of more neutron-rich isotopes at branching points. The last three columns of Table 4.6 show the isotopic ratios at the end of the core and shell carbon burning stages for

^{70}Ge/^{70}Zn, ^{80}Kr/^{80}Se and ^{86}Sr/^{86}Kr, with values for the end of helium core burning specified for reference. For most models, the ratios increase in the last carbon shell with increasing carbon burning rate, favouring production of the s-only isotopes ^{70}Ge, ^{80}Kr and ^{86}Sr, due to the lower neutron density in the carbon-shells in the CI and CU models. However, the ratios are sensitive to the convection, since shell overlap causes the shells to be polluted with carbon core s-process ashes. Consequently, the 25CU, 32CU and 60CU models instead show a decrease in the ratios. Considering that the ratios in the initial composition are 3.271, 6.124 and 0.036 for ^{70}Ge/^{70}Zn, ^{80}Kr/^{80}Se and ^{86}Sr/^{86}Kr, the presence of lower isotopic ratios than these in the shells indicates that the branching is indeed affected during the carbon shell s-process and that the decrease is not associated purely with the mixing of carbon core matter with helium burning ashes.

4.6 Final yields

4.6.1 Calculations

The yields calculations were made in the same manner as that of Hirschi et al. (2005), which considers two contributions to the yields: the stellar wind and the supernova explosion. The wind yield for nuclide i for a star with initial mass m (in $M_{\odot}$) is calculated using:

$$mp_{im}^{\mathrm{wind}} = \int_0^{\tau(m)} \dot{M}(m,t)[X_i^S(m,t) - X_i^0]dt \tag{4.9}$$

where $\tau(m)$ is the final age of the star, $\dot{M}(m,t)$ is the mass loss rate, X_i^S is the surface mass-fraction abundance and X_i^0 is the initial mass-fraction abundance. The majority

of the matter lost through the stellar wind occurs during hydrogen and helium burning. The composition of the wind is similar to that of the initial composition, except for the $32M_{\odot}$ and $60M_{\odot}$ models where the mass loss is significant enough to include some of the hydrogen burning ashes. Table 4.4 shows that the total mass lost over the stellar evolution due to the stellar wind increases significantly with initial mass ($\approx$ 20 per cent lost for the 15 $M_{\odot}$ models to $\approx$ 80 per cent lost for the 60 $M_{\odot}$ models).

The presupernova yields are calculated using:

$$mp_{im}^{\mathrm{preSN}} = \int_{M_{\mathrm{rem},m}}^{m_{\tau}} [X_i(m_r) - X_i^0] dm_r \tag{4.10}$$

where m_{τ} is the total mass of the star at $\tau(m)$, $M_{\mathrm{rem},m}$ is the remnant mass, X_i^0 is the initial mass fraction abundance of element i and $X_i(m_r)$ is the mass fraction abundance at mass coordinate m_r. The total yields are then just the sum of the wind and the presupernova yields.

The point in the evolution in which the yields are taken in this work is at the end of central oxygen burning. After central oxygen burning, the material outside the remnant mass is not affected much by the pre-explosive evolution. The only potential contribution that may affect the s-process abundances is during the early collapse, when the neutron density may increase significantly (for example, in the carbon shell Pignatari et al., 2010) as well as partial or complete photodisintegration at the bottom of the carbon, neon and oxygen shells.

With regards to explosive burning, the supernova explosion is responsible for destroying and recreating a portion of the ejecta, which includes p-process rich and, to a smaller extent, s-process rich layers, possibly having a relevant impact on the total yields of s-process nuclides (see for instance Rauscher et al., 2002; Tur et al., 2009).

However, the explosive burning process is sensitive to uncertainties in the supernova explosion mechanism for the range of initial masses considered here (Fryer, 2009). The uncertainties associated with the supernova explosion, namely the explosion energy, the ignition mechanism and the amount of fall-back, are important especially for the 15, 20 and 25 $M_{\odot}$ models. These uncertainties would also affect the amount of matter locked up in the remnants. In this work, the choice of remnant masses for the models is taken from the analytical fits of Fryer et al. (2011, in prep.) for Solar metallicity stars, which derive from energy-driven explosions (see for instance Fryer, 2009). These remnant masses take into account the additional matter that falls back onto the remnant following the initial explosion. They are given by

$$M_{\mathrm{rem},m} = \begin{cases} 1.1 + 0.2e^{(m-11)/4} - 3e^{0.4(m-26)} & 11 < m \leq 30M_{\odot} \\ 18.35 - 0.3m & 30 < m < 50M_{\odot} \end{cases} \tag{4.11}$$

which gives remnant masses of 1.61, 2.73, 5.71 and 8.75 $M_{\odot}$ for initial masses, m, of 15, 20, 25 and 32 $M_{\odot}$ respectively. For the 60 $M_{\odot}$ models a remnant mass was calculated by scaling with the CO core mass ratio for the ST models,

$$M_{\mathrm{rem},60M_{\odot}} = M_{\mathrm{rem},32M_{\odot}} \left(\frac{M_{\mathrm{CO},60M_{\odot}}}{M_{\mathrm{CO},32M_{\odot}}} \right), \tag{4.12}$$

giving a remnant mass of 10.24 $M_{\odot}$. The resultant remnant masses are such that for the 15 $M_{\odot}$ models, the oxygen shell is partially included in the supernova ejecta. For the other models however, the remnants are large and the ejecta includes the upper portion of the carbon shell and the overlying layers only. The remnant masses here are larger in comparison with those used in previous studies of explosive nucleosynthesis (Limongi et al., 2000; Rauscher et al., 2002). This is due to the use, in those studies,

of piston-driven models that are known to underestimate the amount of fall-back onto the supernova remnant (Young & Fryer, 2007). The large remnant masses may cause the explosive nucleosynthesis to occur predominantly in the layers that falls back onto the remnant and will not be ejected.

In addition to the yields, the ejected masses, E_{im} can be calculated, which are the exact analogues of Eq. 4.9 and 4.10, but without the inclusion of the X_i^0 term. If the total mass of matter ejected is $M_{\mathrm{ej},m} = m_\tau - M_{\mathrm{rem},m}$, the overproduction factors averaged over the ejecta are calculated using

$$\langle \mathrm{OP} \rangle_{im} = \frac{E_{im}}{M_{\mathrm{ej},m} X_i^0} \tag{4.13}$$

Full yield tables for the models are provided in appendix C.

4.6.2 Total yields for each star

The overproduction factors averaged over the ejecta for the s-only isotopes are shown in Fig. 4.15, which represents well the general abundance distribution for stable isotopes created by the models. A considerable amount of s-process nucleosynthesis occurs for all CU models by up to 3 dex, which is either because of overlap between the carbon shells and the carbon core (for models 20CI, 25CU, 32CU and 60CU) or because of strong neutron exposures in the carbon shells (models 15CU and 20CU). The 20CI model features a strong overlap between the convective carbon core and the successive carbon shells, which is not seen in model 20CU and therefore has more significant production than model 20CU. In fact, for the CI rate, only the 20 $M_\odot$ model shows a significantly enhanced production over the ST rate. The 15CI model also shows some

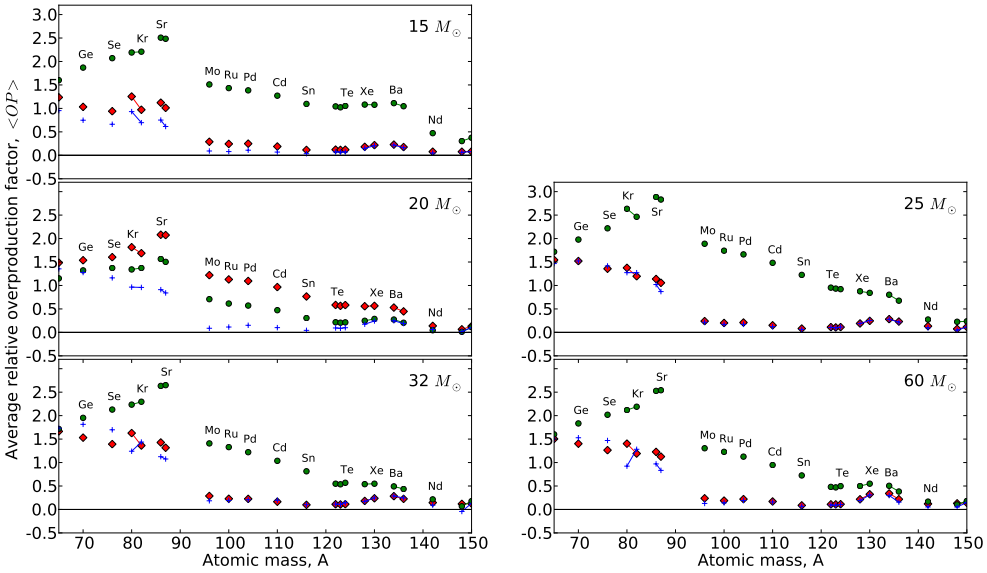

Figure 4.15: The overproduction factors averaged over the total ejected mass for s-only nuclides as a function of atomic mass. The ST, CI and CU rates are indicated by the blue crosses, red diamonds and green circles respectively. Isotopes of the same element are connected by adjoining lines.

production, but the distribution of isotopes is very similar when compared to the ST rate. This is in contrast to the 20CI model, which shows an extended distribution of production featuring heavier nuclides.

Since the heavy elements representing the weak component have $60 < A < 90$, the photodisintegration occurring in this phase, according to Fig. 4.16, does not drastically affect the abundances of the s-process nuclides. However, the change in stellar structure due to the enhanced carbon burning rate could affect the production of p-only isotopes, which could represent an observable consequence of the carbon burning rate.

Photodisintegration occurs at the bottom of the carbon, neon and oxygen shells just before the supernova explosion because of the increasing temperature of the in-

terior. The photodisintegration reactions deplete the heavy nuclides and synthesize p-process isotopes and other neutron-poor isotopes, which affect the s-process yields of the star. The presupernova yields containing the signature of this process can be calculated at the end of both oxygen burning and silicon burning and compared. Fig. 4.16 shows the presupernova yields per unit mass for all standard models at the end of core oxygen burning relative to the end of silicon burning, where the shaded area represents the region bound by $-0.2 < \log(y_{im}^{\rm preSN}(\text{Siend})/y_{im}^{\rm preSN}(\text{Oend})) < 0.2$. Model 25ST shows only minor changes in the yields, but models 20ST, 32ST and 60ST show a small effect which primarily modifies the abundances of the most neutron-poor or neutron-rich isotopes of a particular isotopic chain. The neutron-poor isotopes, such as the p-only isotopes, are synthesised from photodisintegrated heavier nuclei. For example, the second panel of Fig. 4.16 (model 20ST) shows a strong production of p-only isotopes, such as ^{120}Te, ^{124}Xe and ^{130}Ba. The difference in relative yield is large for these isotopes ($\sim 2-3$ dex), since their initial abundance is low. Model 15ST shows yields that are more significantly affected by photodisintegration; in particular, the top panel of Fig. 4.16 shows a consistently lower yield of approximately 0.2 dex. This is because there is an inclusion of a small portion of the oxygen shell in the ejecta, where the composition is depleted more significantly in heavy nuclides by photodisintegration.

4.6.3 Evaluation of the weak component

A first order approximation of the weak s-process component can be made by taking the sum of the yields for each stellar model, taking into account the number of stars

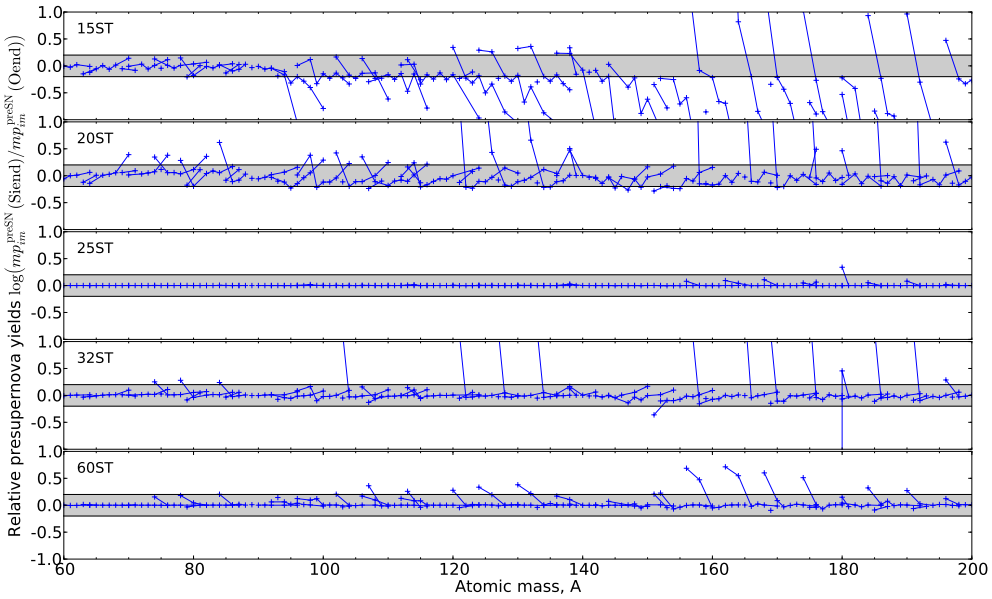

Figure 4.16: The presupernova yields evaluated at the end of silicon burning relative to those calculated at the end of oxygen burning. The shaded regions correspond to yields that deviate by more than 0.2 dex. The deviations in the yields for model 15ST are caused by a portion of the oxygen shell being included in the ejecta.

with that initial mass formed. The weak component is evaluated using

$$y_{\mathrm{weak},i} = \frac{\sum_m r_m E_{im}}{\sum_m M_{\mathrm{ej},m} r_m}, \tag{4.14}$$

where r_m is a weighting factor determined by the integration of the Salpeter initial mass function (IMF), $dN/dm = \xi_0 m^{-2.35}$, over a certain range. Yields from the 15, 20, 25, 32 and 60 $M_\odot$ models were applied to stars within the initial mass ranges of 12.5-17.5, 17.5-22.5, 22.5-28.5, 28.5-46 and 46-80 $M_\odot$ respectively, giving values of r_m equal to 39.75, 19.89, 13.45, 14.59, 12.32 % respectively (with $\xi_0 = 0.304$). Consequently, the 15 and 20 $M_\odot$ models dominate as the main contributors to the evaluation of the weak component (≈ 60 % of all stars in the total massive star mass range considered here). Stars with initial masses less than 12.5 $M_\odot$ or greater than 80 $M_\odot$ are assumed to have a zero contibution to the weak s-process component.

The ^{13}C neutron source during carbon core burning is mainly primary whereas the ^{22}Ne source is secondary[1], since it depends on the initial ^{14}N abundance from the CNO cycle. If a Solar metallicity star of a given mass is the dominant site for the production of particular primary and secondary nuclides, A and B, the overproduction factor for A is expected to be approximately twice that of B (Truran & Cameron, 1971). Although this is a rather crude approximation regarding the detailed nature of chemical evolution within galaxies and/or star clusters and the nucleosynthesis processes themselves (Tinsley, 1979), the weak s-process in massive stars is expected to hold reasonably to this approximation because the dominant neutron sources, seeds

[1]The products of nucleosynthesis processes in stars, to first order, can be described as being primary or secondary depending on whether the processes responsible for the production depend on the initial metallicity. The production of primary nuclides does not vary much with metallicity whereas secondary nuclides will be produced in proportion to their initial seed nuclei.

and poisons of the weak s-process are secondary. It can be expected therefore that the overproduction factors for the weak s-process nuclides reproduce the Solar system abundances when the overproduction factor is approximately twice that of ^{16}O (Tur et al., 2009). In any case, this rule of thumb can be used as a guide to indicate the typical Solar production of s-process nuclides (Rauscher et al., 2002; Pignatari et al., 2010).

The overproduction factors of the weak component, $y_{\mathrm{weak},i}/X_{i,\odot}$, for nuclides with atomic masses $50 < A < 150$, are displayed in Fig. 4.17. Concerning the CU rate, the overproduction factors are very large (up to 2.56 dex for ^{86}Sr) with respect to the ST model, with significant s-process production of nuclides up to the Ba-La peak at $A \approx 140$. The resulting s-process distribution, peaked at the Sr-Y-Zr, is not characteristic of the weak s-process component, stopping at $A \approx 90$. The s-process nuclides with $90 < A < 110$ have overproduction factors that are comparable to ^{16}O multiplied by two. Such differences for the CU case compared to the classical weak s-process component occur because of the ^{13}C neutron source.

For the CI case, the overabundances of many nuclides are similar to the ST case, except for nuclides that are close to the Sr-Y-Zr peak or with higher atomic mass (Mo, Ru, Cd, and Pd for example). S-process isotopes of Kr and Sr have overproduction factors that are higher than the ^{16}O multiplied by two line. The abundances of the heavier nuclides Y, Zr, Mo, Ru, Cd and Pd show an enhanced production, which is 0.5 to 1.0 dex lower the Kr-Sr peak. Overall, the resulting s-process distribution is approximately flat from Ni to Sr.

Fig. 4.18 shows the overproduction factors for the weak components of the CI and CU cases plotted relative to the ST case. The peak of the relative production of s-process nuclides lies at ^{87}Sr in both cases and declines smoothly with increasing mass

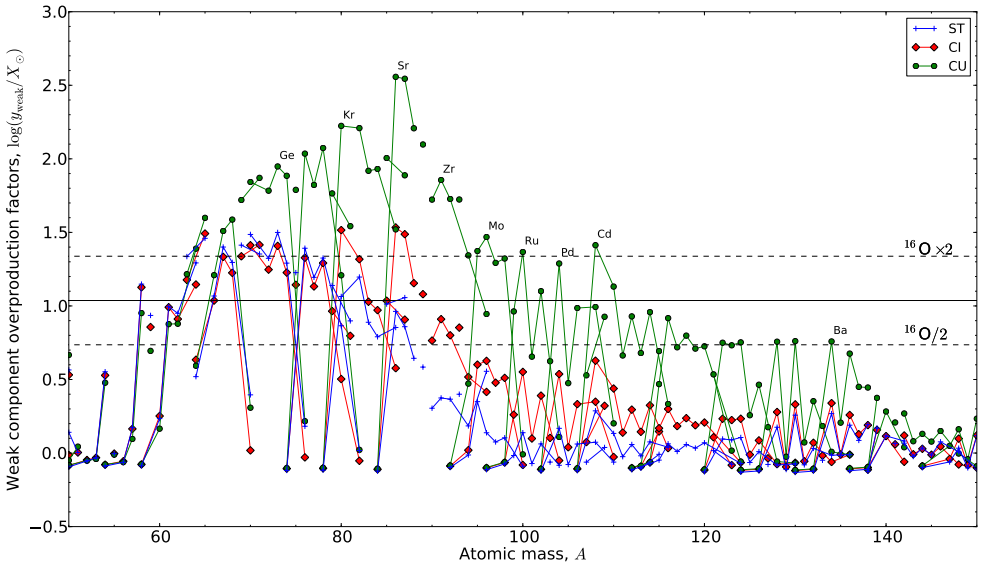

Figure 4.17: The overproduction factors of the predicted weak component for each rate, focusing on isotopes with atomic mass $50 < A < 150$. Isotopes of the same element are connected by adjoining lines. The solid black line indicates the overproduction factor ^{16}O and the two dashed lines corresponds to the overproduction factors of ^{16}O multiplied and divided by two. Changes to the overproduction factor of ^{16}O are negligibly small with changes to the carbon burning rate. The isotopic chains for Ge, Kr, Sr, Zr, Mo, Ru, Pd, Cd and Ba in the CU model are labelled for clarity.

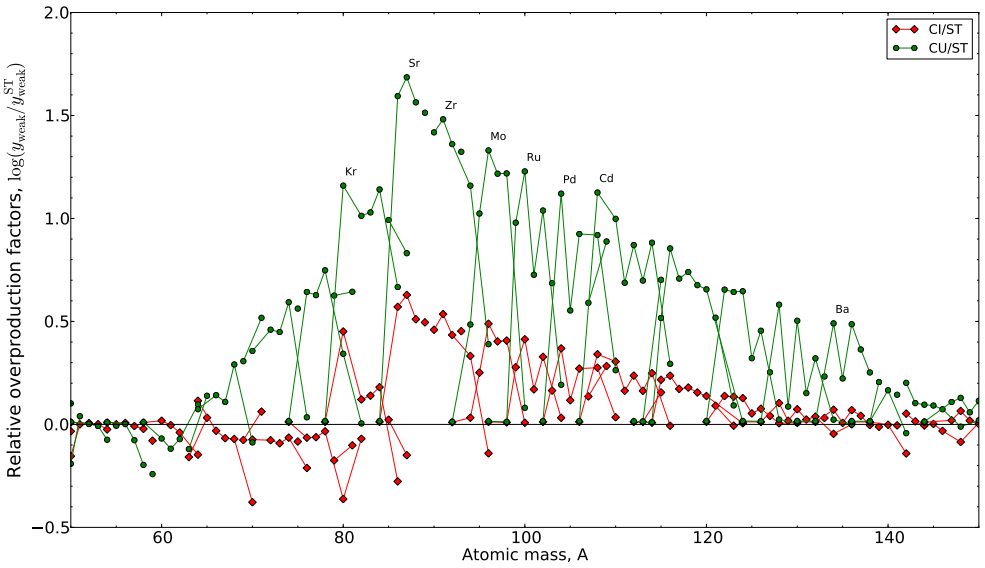

Figure 4.18: The overproduction factors of the predicted weak component for the CI and CU rates plotted relative to the ST rate. Isotopes are connected by adjoining lines. The isotopic chains for Kr, Sr, Zr, Mo, Ru, Pd, Cd and Ba in the CU model are labelled for clarity.

number, although the overproduction factor for ^{86}Sr is slightly larger than the ^{87}Sr for all cases (see Fig. 4.17). For the CU case, the overabundance of ^{87}Sr is 1.7 dex larger than the ST case. The enhancement stops at Ba, with 0.5 dex more production and declines rapidly, with a production of heavier nuclides similar to that of the ST case. For the CI case however, the peak production at ^{87}Sr is 0.6 dex larger than the ST case and tends to 0.0 at Ba.

The overproduction factors of Sr, Y, Zr, Mo, Ru, Pd and Cd are enhanced in the carbon-core s-process (for example, see Fig. 4.14). In the CU case, this occurs for all models other than model 15CU. In the CI case, the overlap between the convective carbon core and the carbon shell only occurs for model 20CI. Removing the 20 $M_{\odot}$ models from the evaluation of the weak component allows for a comparison between the predicted weak component with and without the occurrence of an overlap. Fig. 4.19 shows the predicted weak component (CI - no20) using the 15, 25, 32 and 60 $M_{\odot}$ models using initial mass ranges of 12.5-20.0, 20.0-28.5, 28.5-46 and 46-80 $M_{\odot}$ in the IMF calculation. The overproduction factors for the CI - no20 case show a reduction in Sr isotopes to values just less than the ^{16}O$\times$2 line and a significant reduction in Y, Zr, Mo, Ru, Pd and Cd isotopes to values similar to the ST case and a reduction in Br and Rb isotopes to values close to the ^{16}O/2 line. The branching at ^{95}Zr is also affected, which mainly affects the relative overproduction factors of ^{96}Zr and ^{95}Mo.

4.7 Discussion

The results in the previous section show that with an increased carbon burning rate, the contribution of the neutron-capture processes during hydrostatic burning stages to

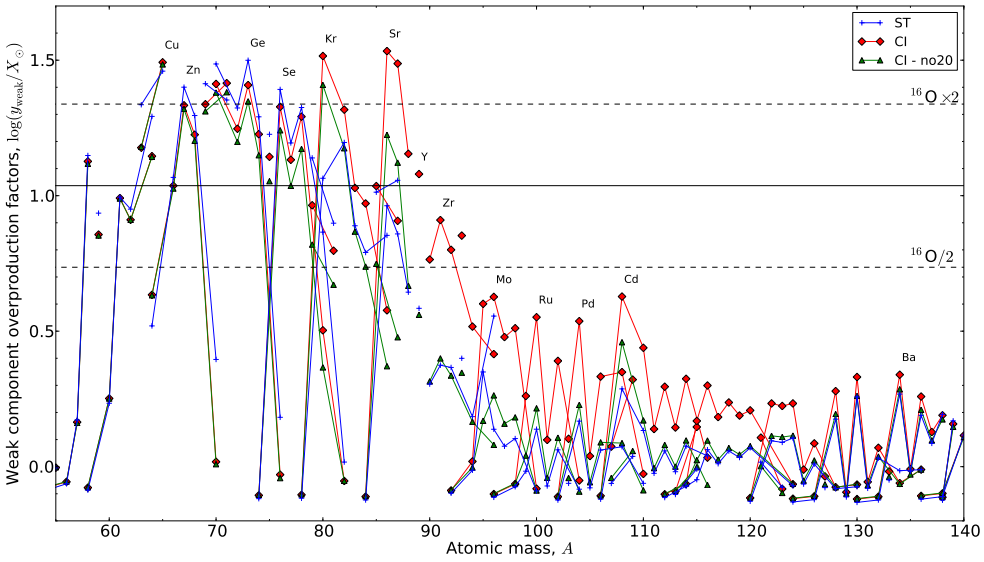

Figure 4.19: The overproduction factors of the predicted weak component relative to the Solar system abundances with the $20M_\odot$ models removed from the calculation (CI - no20). The weak components for the ST and CI case including the 20 $M_\odot$ models are included for comparison. Isotopes of a given element are connected by adjoining lines. The isotopic chains for Cu, Ge, Se, Kr, Sr, Y, Zr, Mo, Ru, Pd, Cd and Ba in the CU model are labelled for brevity.

the yields of massive stars is modified significantly.

The CU case exhibits a strong production of isotopes between the iron-group nuclides and the Ba-peak nuclides with regards to current massive star models (see Fig. 4.17). This production originates from the s-process production in a convective carbon core in which mixing has caused the ashes of carbon burning to be transported out from the centre of the star where it will be present in the supernova ejecta. This overlap was found in all but one of the CU models (15CU). Fig. 4.17 shows that the yields of the CU case are inconsistent with the weak s-process contribution to the Solar system abundances (see for example the anomolously high abundance of Sr-Y-Zr peak and Ba-La peak nuclides compared to those with $60 < A < 90$). Therefore, a strong resonance with $(\omega\gamma) \sim 6.8 \times 10^{-5}$ eV at a centre-of-mass energy $E_{\rm com} = 1.5$ MeV in the ^{12}C + ^{12}C reaction rate is unlikely to be present in the reaction rate, according to the models used in the present analysis.

For the CI case, an extended distribution is found but the overproduction factors are not as high as the CU case (see Fig. 4.18). The main nucleosynthesis differences occur at the Sr-Y-Zr peak and beyond, which is a signature dominated by the presence of overlap of a carbon shell with the convective carbon core. The large overproduction of Kr and Sr could suggest that the CI carbon burning rate is too high. In any case, it is unlikely that a Solar metallicity model should demonstrate a strong overlap between the convective carbon core and the carbon-shell of the kind experienced in model 20CI. However, considering the present uncertainties in the stellar models such as the reaction rates (for example, the critical reactions ^{12}C$(\alpha,\gamma)^{16}$O and ^{22}Ne$(\alpha$,n$)^{25}$Mg), the initial composition and the treatment of convective–radiative boundaries, the abundance of Sr is not a significant enough constraint to assert that the CI rate would be inconsistent with the Solar system abundance distribution.

The carbon core s-process and the mixing of heavy nuclei out from the centre could provide an alternative nucleosynthesis scenario for the LEPP (see §2.4.2.4). It is tempting to underline the similarity between the LEPP signature and the anomalous carbon burning s-process component present in the CU models and partly in the CI models. However, we recall that the LEPP process should be primary if the Solar LEPP and (low metallicity) stellar LEPP are indeed the same process (see for example Montes et al., 2007). Although the carbon-core s-process features a primary neutron source, ^{13}C, the seed nuclei, ^{56}Fe, are secondary. Consequently, an s-process component using iron seeds in these conditions cannot reproduce the stellar LEPP abundances at low metallicity. Therefore, the carbon core s-process component is unlikely to represent the site for the stellar LEPP component at low metallicity. In addition, when the number of seeds is lowered, the neutron captures per iron seed increases (see Eq. 4.6) and the distribution of s-process nuclides extends to higher atomic mass.

5 Hydrodynamic mixing and the link between 3D and 1D models

In the previous chapter, constraints were made to the $^{12}C + ^{12}C$ rate by comparing the yields of 1D stellar evolution models with the Solar system abundance distribution. The yields, however, are dependent on the s-process production during carbon-core burning, which would likely be affected by the treatment of the convective boundary of the convective core. The impact this could have on the s-process production may be analogous to the situation in the helium-core (see for example Costa et al., 2006). Indeed, mixing across convective–radiative interfaces occurs in the advanced stages of massive star evolution, which can be described as turbulent entrainment according to the simulations by Meakin & Arnett (2007). The treatment of convective–radiative interfaces is therefore an important uncertainty to consider in stellar models. Multidimensional stellar models are required for a sufficiently detailed treatment of entrainment at convective–radiative boundaries (see for example Herwig et al., 2006; Meakin & Arnett, 2007). However, there exists a disparity in timescales between that of stellar structure during the evolution ($\sim 10^{14}$s) and convection ($\sim 10^{4}$s). Therefore, a full multidimensional treatment of convection and convective–radiative interfaces cannot be included directly into stellar evolution models without incurring an unrealistic computational expense.

Nevertheless, stand-alone hydrodynamics models of specific sites may provide insight into possible improvements that could be applied to the treatment of convective–radiative interfaces. The link between 1D and 3D stellar models can aid in the development of alternative theories of convection and mixing in stellar interiors (Meakin et al.,

2011, and references therein). In addition, existing prescriptions for time-dependent mixing used in 1D stellar evolution models (which are often diffusive in nature) can be fine-tuned to better replicate the mixing found at convective–radiative interfaces. This is the aim of the following investigation.

Uncertainties in mixing prescriptions are especially important for models of thermally-pulsing AGB stars, since the behaviour of convective boundaries affects the qualitative as well as quantitative nature of thermal pulse evolution (see also §2.4.2.2). The following chapter therefore concerns the analysis of 3D hydrodynamics simulations in order to investigate one of the key uncertain convective-boundary situations, namely the entrainment of hydrogen during a hydrogen-ingestion flash in a thermally-pulsing AGB star (Herwig et al., 2006, 2011).

5.1 Diffusive mixing in 1D stellar models

A link can be established between the treatment of mixing in 1D stellar evolution models and 3D hydrodynamics simulations by considering diffusion. One can recall from §3.1 that convective mixing of nuclides in 1D stellar evolution calculations is often treated as a diffusive process, with a diffusion coefficient for convective mixing calculated using MLT:

$$D_{\mathrm{MLT}} = \frac{1}{3}\bar{v}\ell, \tag{5.1}$$

where $\bar{v}$ is the time average velocity of convective eddies and ℓ is the mean free path. The diffusion coefficients are normally large ($\sim 10^{12-16}$ cm^2 s^{-1}) such that the mixing can be regarded as instantaneous. One can also recall from §3.1.2 that overshoot mixing across a convective–radiative interface can be treated either by increasing the size of the

convection zone by a distance $d = \alpha_{\rm ov} H_P$ (where H_P is the pressure scale height and $\alpha_{\rm ov}$ is a free parameter) or by using a diffusive approximation with an exponentially declining diffusion coefficient of the form

$$D_{ov} = D_0 H_P \exp\left(\frac{-2z}{f H_P}\right), \tag{5.2}$$

where D_0 is a background diffusion coefficient (in the convection zone), z denotes the distance from the edge of the convective boundary and f is a free parameter. The diffusion coefficient specified in Eq. 5.2 is guided by multidimensional models of convective boundaries (Freytag et al., 1996). Although mixing in the convection zone and over the convective–radiative interface is complicated, the end result (a change in composition) is often similar in diffusion and advection scenarios. Therefore, diffusion algorithms may be justified for use in 1D stellar models. One can investigate whether a tailored set of diffusion coefficients can be used to describe any arbitrary mixing process and, if so, what input diffusion coefficients would be necessary to replicate it.

Diffusion is described using Fick's second law. In 1D, it is given by:

$$\frac{\partial X}{\partial t} = \frac{\partial}{\partial x}\left(D \frac{\partial X}{\partial x}\right) \tag{5.3}$$

where X is the diffusing entity, which is normally a concentration or mass fraction abundance, x is the spatial coordinate, t is the temporal coordinate and D is a diffusion coefficient, in units of $m^2 s^{-1}$. This formula is applicable provided there is no bulk fluid motion (advection). It can also be used for the case of interdiffusion of two fluids, provided that the diffusion coefficients are 'mutual' (that is, they can be used to describe the diffusion of both fluids). A larger diffusion coefficient corresponds to an increase

in the proportion of material being diffused per unit time. Diffusion can be simulated using a finite differencing method to calculate $\partial X/\partial t$ for all t provided that $D(x,t)$ and $X(x,0)$ are known. Alternatively, the equation can be solved for $D(x,t)$ if $X(x,t)$ is known. Such diffusion coefficients, if obtained from 3D hydrodynamics models, could perhaps be useful for modelling convective-boundary mixing in 1D stellar evolution models using existing diffusive mixing implementations.

Finite difference methods for solving boundary value problems, such as diffusion, are well known (see for example Press et al., 1992, Ch. 19.2). In this work, two computer programs are used: one that simulates diffusion using an implicit finite differencing scheme and one that calculates diffusion coefficients from abundance profiles. These programs were written in the FORTRAN programming language, using the tridiagonal solver routine specified in Press et al. (1992, Ch. 2.4). The implicit diffusion simulator was written with the purpose of testing diffusive mixing of abundance profiles for which a convenient analytic solution is difficult (if not impossible). The diffusion coefficient calculator can then use the output of the diffusion simulator in order to test whether the program is capable of extracting diffusion coefficients accurately (see appendix B for a full description of equations used by both programs and the test cases). The diffusion coefficient calculator was then applied to a case using variable diffusion coefficients (of the form given by Eq. 5.3) and to radially-averaged output of 3D hydrodynamics simulations of hydrogen-ingestion to calculate diffusion coefficients. The diffusion coefficients are then compared between these two test cases to see if convective-boundary mixing in the hydrogen-ingestion flash model can be described using overshoot mixing with Eq. 5.2.

5.2 Diffusion simulations using a variable diffusion coefficient

In order to further test the ability of the diffusion coefficient calculators and to investigate the ability of the diffusion coefficient calculator to determine diffusion coefficients for models describing convective-boundary mixing, an initial abundance profile given by a step function was diffused with a variable diffusion coefficient over space (but constant in time). An abundance profile of this form represents abundances inside and outside the convection zone. An exponentially decreasing function is used, motivated by the exponentially declining coefficient given by Eq. 3.22, which is often used to describe overshoot mixing in 1D stellar evolution models. Using an initial profile of the form

$$X(x,0) = \begin{cases} 0, & 0 \leq x \leq 5\text{km} \\ 1, & 5 < x \leq 10\text{km} \end{cases}, \tag{5.4}$$

the implicit diffusion simulator was run using the following input diffusion coefficients:

$$D_{\text{in}}(x) = \begin{cases} 10^6, & 0 \leq x \leq 5\text{km} \\ 10^6 \exp(460.517019 - 92.103403x), & 5 < x \leq 10\text{km} \end{cases}. \tag{5.5}$$

In this simulation, the domain given by $0 < x < 5$km represents the convection zone, which has a large and constant value of the diffusion coefficient. The domain given by $5 < x < 10$km is the radiative zone, where no convection is taking place. Overshoot mixing is then described by using an exponentially reducing diffusion coefficient in the radiative zone.

The diffusion coefficient rapidly declines over the spatial domain, which has a

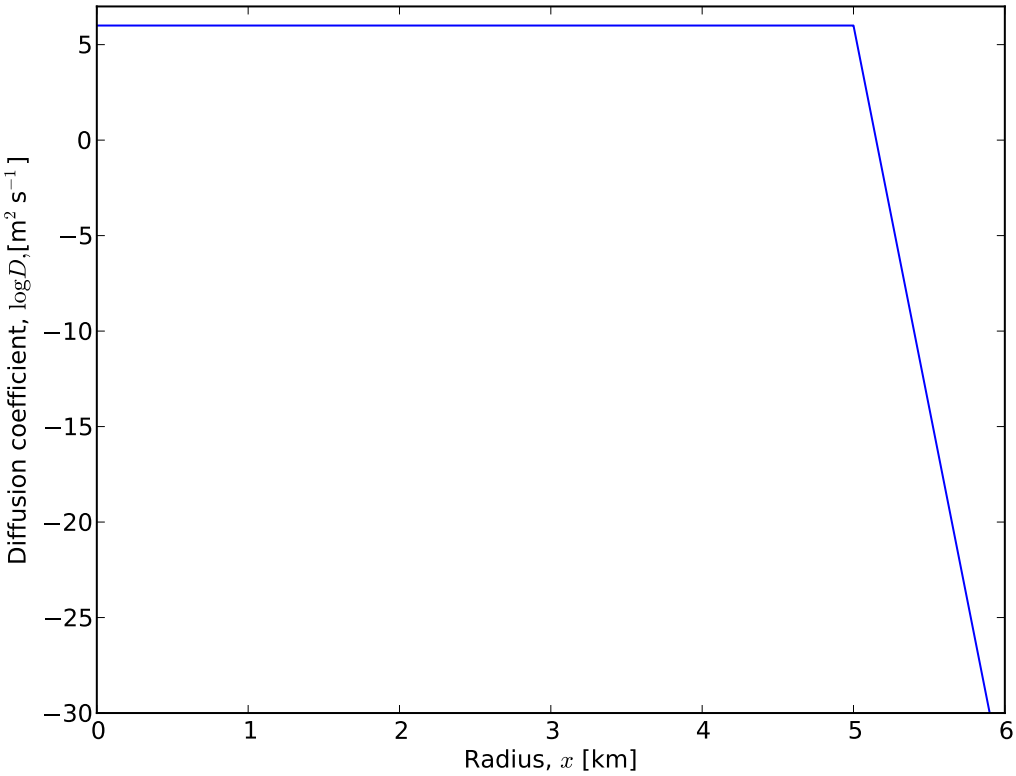

Figure 5.1: Exponentially reducing input diffusion coefficients, as given by Eq. 5.5.

total size of 10 km. The parameters for the diffusion coefficients are chosen such that $D_{\rm in}(5) = 10^6$ and $D_{\rm in}(5.1) = 10^2$ m^2 s^{-1}. This corresponds to a value of

$$f = \frac{0.0217}{H_P}, \tag{5.6}$$

in Eq. 5.2, where the pressure scale height, H_P, is given in km. H_P is normally of the order of a few kilometres in stellar interiors. For example, for a value of H_P equal to 2.28 km (Herwig et al., 2011), $f \simeq 0.01$.

Abundance curves for this run are displayed in Fig. 5.2, with resolution parameters of $\Delta t = 100$ s and $\Delta x = 10$ m. The exponentially declining diffusion coefficient causes the profile to be asymmetrical about the interface. Initially, over the first timestep (see the $t = 100$s curve in Fig. 5.2) a large abundance of matter located within the domain $5.0 < x < 5.1$km is quickly diffused and efficiently spread out over the convective region, which has a constant diffusion coefficient. The abundance profile maintains a similar shape throughout the run, but the timescale with which the profile moves into the region of high abundance increases exponentially. This is verified by the roughly equidistant spacing of the profiles for successive timesteps increasing by a factor of 10. The use of the f parameter in Eq. 5.2 can therefore be set in stellar models to be that necessary to cause the required extension of the convective boundary over the required timescale for mixing in order to reproduce a corresponding observable quantity. That is, should a user wish to model overshooting with a particular characteristic mixing length over a particular characteristic timescale, an f parameter can be specified for that case.

The abundance profiles for the test case, with knowledge of the diffusion coefficients, can now be used with the diffusion coefficient calculator to test whether the

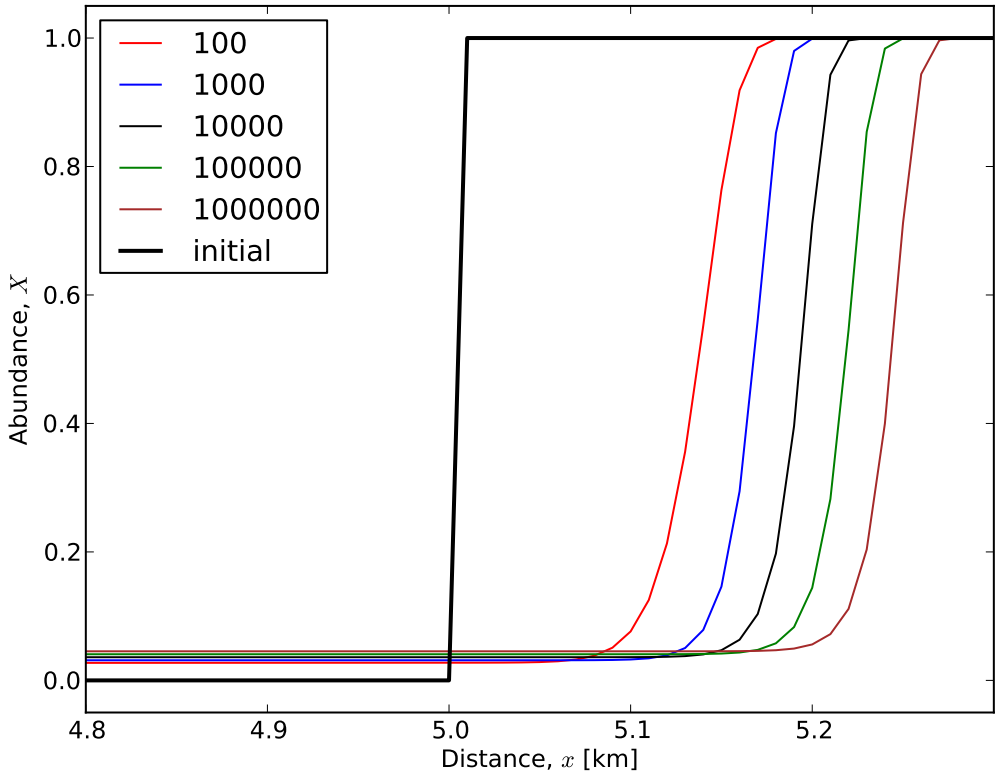

Figure 5.2: Abundance profiles for diffusion of a step function using an exponentially reducing diffusion coefficient. The time, t, for each timestep considered is provided in the legend. The resolution parameters are $\Delta t = 10$ s and $\Delta x = 10$ m.

coefficients can be recovered using the reverse process. Diffusion coefficients calculated using the diffusion calculator for this case are shown in Fig. 5.3. We recall from appendix B that there are two methods for calculating the diffusion coefficients: an 'instantaneous evaluation', in which no assumptions were made about diffusion coefficients, and a 'constant D evaluation', which assumes that the diffusion coefficient is constant over the time domain considered in the calculation. Both diffusion coefficient calculators were unable to calculate coefficients over the whole spatial domain because the abundance changes are zero beyond 5.215 km. If this is the case, the calculated coefficients are zero. The coefficients evaluated for this case show similarities to the previous case (given in §B.3.2) in that the diffusion coefficients tend to underestimate the solution and converge towards the correct solution over time. Fig. 5.4 shows the ratio between the evaluated coefficients and the input diffusion coefficient profile at the interface at $t = 1000, 2000, 3000$ and 4000 s. A constant D evaluation is also shown over timesteps 100 to 200 ($t = 1000$ s to 2000 s). In the domain given by $0 \leq x \leq 5$ km, the evaluated coefficient has converged to the input diffusion coefficient, which is slightly lower than the input coefficient by 0.2% by $t = 5000$ s. The constant D evaluation shows a lower diffusion coefficient by 1.5% in this region. Where the input diffusion coefficient drops exponentially, the deviation increases for each evaluation but can contain sporadic changes in the coefficient as the diffusion continues into the region of high abundance and the changes in abundance are no longer zero. The maximum error is exhibited by the constant D evaluation at a value of 75% at the right-hand most point, but in this region the diffusion coefficients are very low and the changes in abundance are small. The maximum error for the instantaneous evaluations can be quantified as varying between -0.025 and 0.025 dex (or $\pm 5.9\%$).

To summarise, for a mixing model that describes the changes in composition due

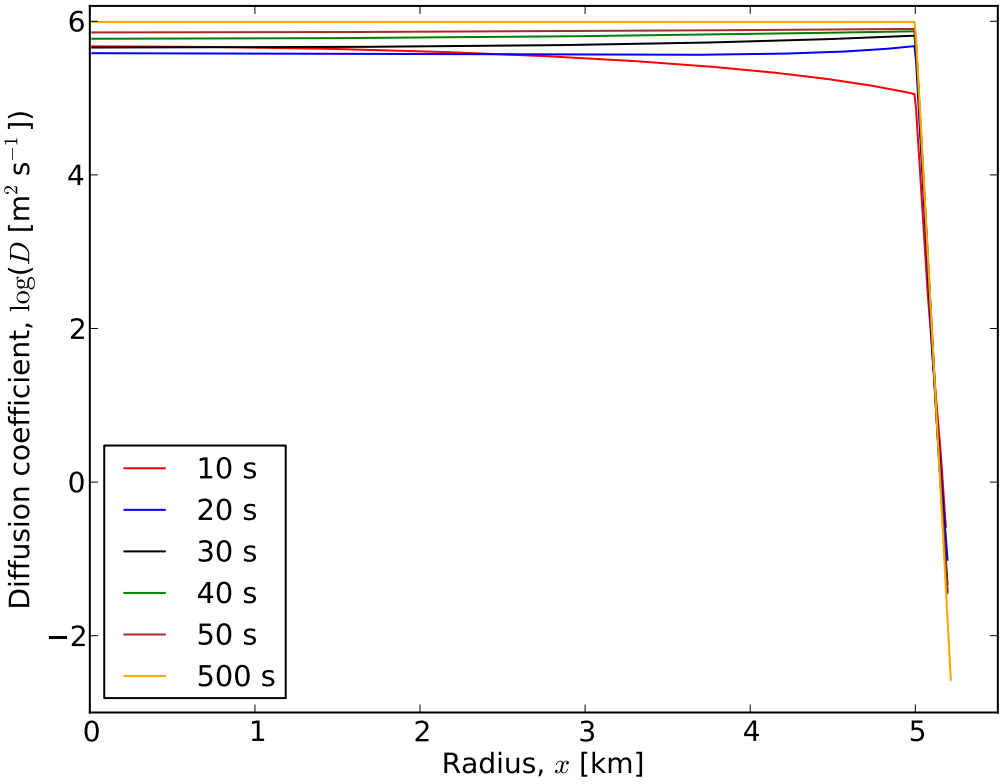

Figure 5.3: Instantaneous diffusion coefficients for diffusion of a step function using an exponentially reducing diffusion coefficient. The time, t, for each timestep considered is provided in the legend. The resolution parameters are $\Delta t = 10$ s and $\Delta x = 10$ m.

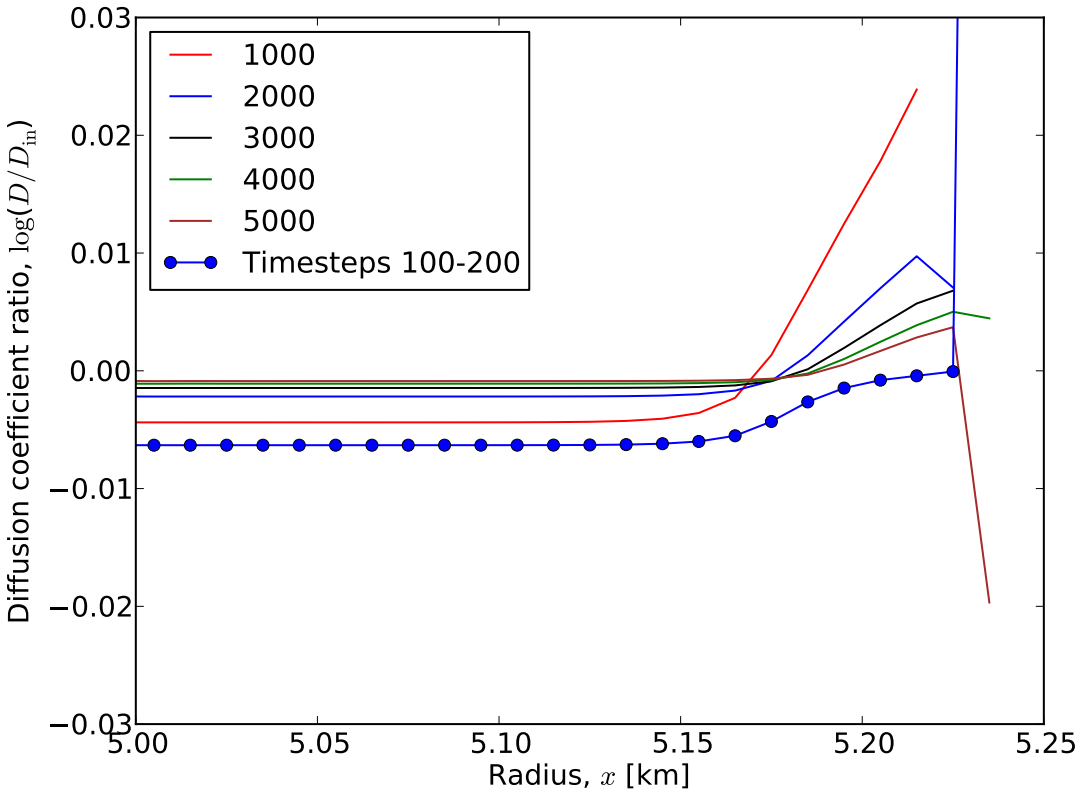

Figure 5.4: The ratio between input and output diffusion coefficients at the interface for the exponentially reducing diffusion coefficient. The resolution parameters are $\Delta t = 10$ s and $\Delta x = 10$ m. For the instantaneous evaluations, the time t, in seconds, for each timestep is provided in the legend. A curve for a constant D evaluation is also shown using timesteps 100-200 ($t = 1000$ s to 2000 s), which is given by the blue circles.

to diffusion with the diffusion coefficients given by an exponentially declining function typical of overshooting prescriptions (Eq. 5.2), the diffusion coefficient calculator is able to recover the input diffusion coefficients at the percentage level of accuracy in the spatial domain of prime interest. This is generally smaller than the physics uncertainties that are to be investigated using the diffusion coefficient calculators. The accuracy of the evaluated coefficients are dependent on the time and spatial resolutions and deviations from the input coefficient are seen at early timesteps and, particularly in the case of the constant D assumption, boundary effects (see also appendix B).

5.3 Diffusion coefficients from hydrodynamics simulations

The diffusion calculators discussed in the previous sections are now applied to output data from a hydrodynamics model. The hydrodynamics model data is taken from simulations of the convective–radiative interface during a hydrogen-ingestion flash using the Piecewise Parabolic Method (PPM; Colella & Woodward, 1984; Herwig et al., 2011). The simulations use 4π geometry on a three-dimensional grid, with two fluids that have different molecular weights. The duration of the simulations covers 20 convective turn-over timescales. The primary goal of the simulations is to investigate the properties of stellar shell convection and the entrainment at convective boundaries stabilized by a molecular weight gradient. They were also used recently to investigate the hydrogen-ingestion flash in Sakurai's object (Herwig et al., 2011, see also appendix D).

Radially-averaged output data from PPM includes volume fraction profiles. The

volume fraction, V_f, is defined as the fraction of volume within a 1D spherical shell of volume V that contains a particular fluid. The volume fraction, like mass fraction abundances or concentration, can be considered as a diffusing entity in the case of the interdiffusion of two fluids, where the diffusion coefficients of the matter are expected to be a property of the mixing of the two fluids.

Two fluids are considered, which are labelled 'H+He' and 'conv'. The fluids represent a hydrogen and helium rich fluid and a convective fluid, which is rich in helium, carbon and oxygen, which is the case for He-shell flash convection in AGB stars. However, the fluids differ only by their mean molecular weights, which are set at 0.667 and 1.51 for the H+He and conv fluids respectively, and the abundances of particular nuclides in the fluids are not treated. This is because the nuclear processes are not treated in detail; the energy that powers the helium-shell flash is added as a constant volume heating at the bottom of the convectively unstable layer. These simplifications are necessary trade-offs in such simulations due to the computational expense of performing 3D simulations.

The initial composition of the H+He fluid is given by

$$X_{\mathrm{H+He}}(x,0) = \begin{cases} 0, & 0 \leq x < 30\mathrm{Mm} \\ 1, & x \geq 30,\mathrm{Mm} \end{cases} \tag{5.7}$$

which inhabits the radiative zone, although a transition layer of size $\Delta x = 0.5$ Mm placed at $x = 30$ Mm is added to smooth the initial discontinuity. The conv fluid fills the remaining spatial domain (the convection zone) below the interface:

$$X_{\mathrm{conv}}(x,0) = \begin{cases} 1, & 0 \leq x < 30\mathrm{Mm} \\ 0, & x \geq 30\mathrm{Mm} \end{cases} . \tag{5.8}$$

At $x = 9.5$ Mm, which is the lower boundary of the convection zone, an artificial source of heating with a constant value of $4.2 \times 10^7 L_\odot$ is placed, which corresponds to the typical luminosity of the helium-shell flash when hydrogen-ingestion takes place. This heating corresponds to the helium burning that drives the flash.

Radially-averaged profiles for a PPM run are displayed in Fig. 5.5 and 5.6 for four timesteps throughout the simulation. The profiles fall-off rapidly with distance away from the convective boundary during the simulation. The spatial domain is a cubic grid with 1536^3 cells and resolution parameters $\Delta t = 60.14$ s and $\Delta x = 22.79$ km. After the radial averaging is performed, the mixing of the two fluids over a 1D spatial coordinate can be treated as an interdiffusion of two fluids. However, in the simulation, convective plumes from the conv fluid approach the convective–radiative interface and mixing occurs between the H+He fluid and the conv fluid. The mixing is facilitated by Kelvin-Helmholtz instabilities which occur due to horizontal shear. It is to be expected therefore that any diffusion coefficients calculated from the profiles may exhibit inaccuracies due to the advective nature of the mixing at the convective boundary.

5.3.1 Calculated diffusion coefficients

The diffusion coefficient calculators were applied to the 1D radially-averaged abundance profiles of the PPM models. If the current 1D prescriptions are correct, one would expect an approximately constant diffusion coefficient in the convection zone and an exponentially declining coefficient over the convective–radiative interface. The steepness of the diffusion coefficient profile can then be used to extract a value for the f parameter.

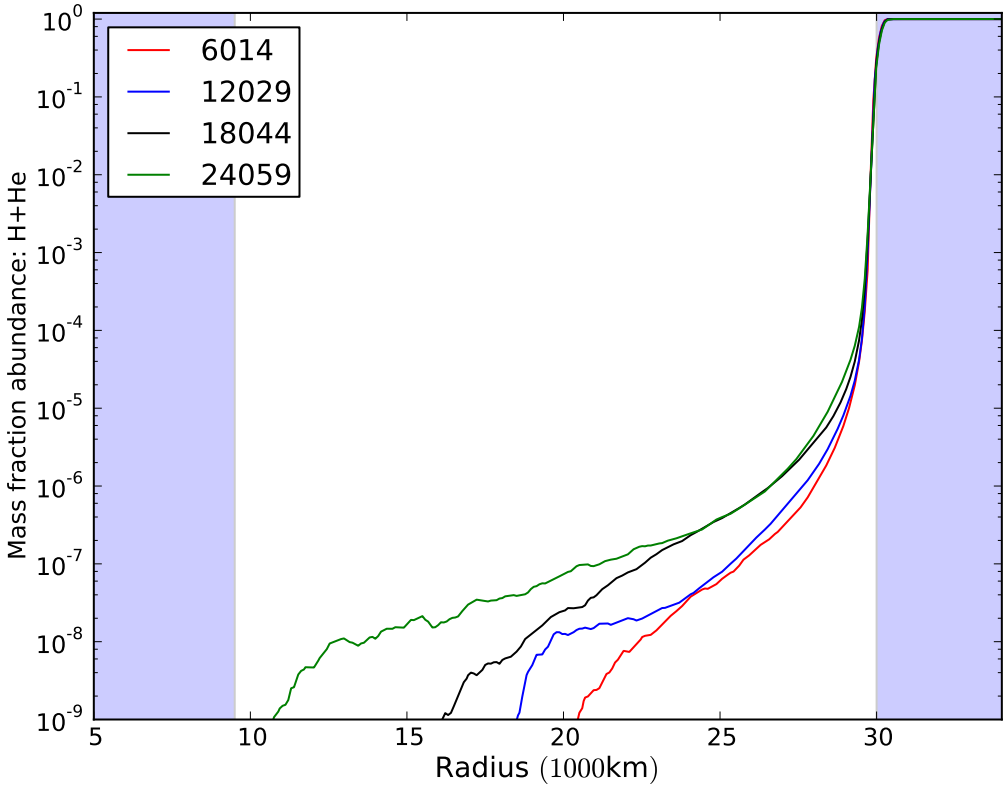

Figure 5.5: Abundance profiles for the H+He fluid over the total spatial domain of the simulation. Shaded regions correspond to radiative zones. The legend gives the time, t, in seconds.

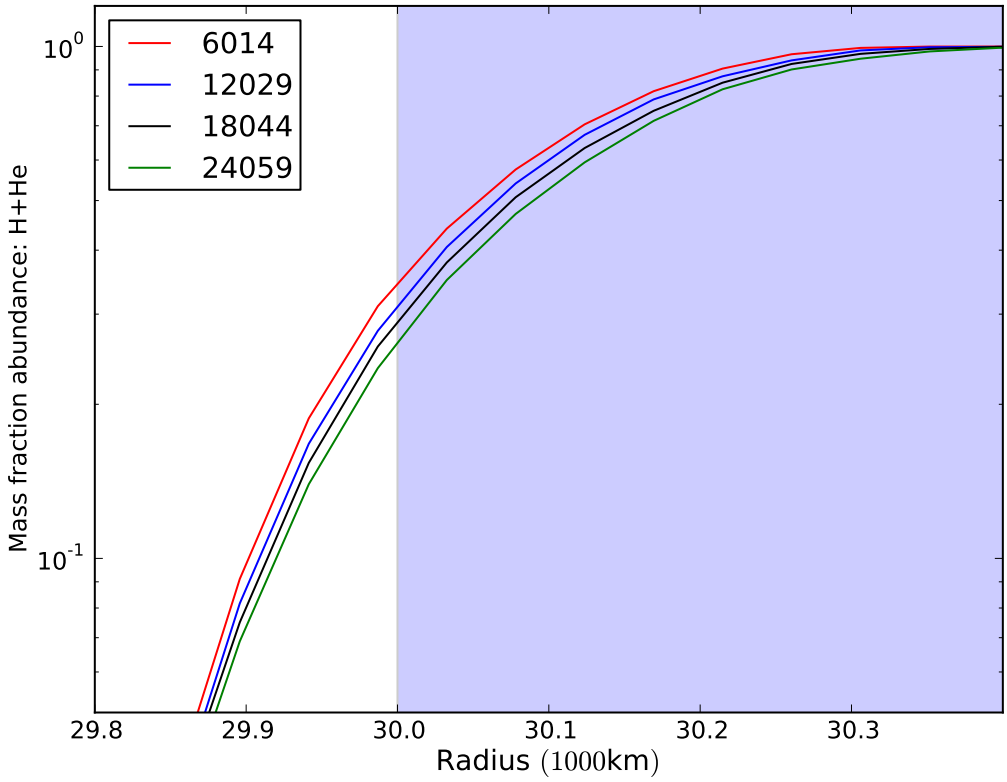

Figure 5.6: Abundance profiles for the H+He fluid around the convective–radiative interface, which is a zoomed in equivalent of Fig. 5.5. The shaded region corresponds to the radiative zone. The legend gives the time, t, in seconds.

Solutions for instantaneous diffusion coefficients are shown in Fig. 5.7. The instantaneous diffusion coefficient evaluations are very noisy and also patchy in places due to evaluated diffusion coefficients that are negative (which are not shown in Fig. 5.7). This occurs because the abundance changes in the convection zone are poorly described by a diffusion process and changes to the abundance due to advection are not described properly by a diffusion framework. However, in 1D stellar evolution simulations this is normally not problematic since convective mixing inside the convection zone is usually much faster than the thermal and nuclear processes involved. The negative diffusion coefficients refer to changes in abundances that are opposite to what would be expected for diffusion. This is seen, for example, in cases where the abundance of H+He fluid below the top of the convective boundary decreases with time for one or more timesteps. Below the interface, the calculated diffusion coefficients vary by three orders of magnitude at values between approximately 10^{12} and 10^{15} cm^2 s^{-1}, but decrease to a value of approximately 10^9 cm^2 s^{-1} at the interface.

In order to mitigate the effects of noisy data, the diffusion coefficients can be evaluated using the constant D assumption. These are displayed in Fig. 5.8 over 50-timestep domains. The evaluations represent a form of 'averaging' where an increased number of mesh points are used to evaluate the diffusion coefficients, although strictly-speaking the evaluation performed in this way is not equivalent to a mean of calculated diffusion coefficients over the temporal domain considered. The calculated coefficients may therefore represent a better approximation of the time-averaged picture of mixing on which MLT is based than the instantaneous evaluations. Domains of 50 timesteps are chosen because the duration of this time domain is comparable to the typical turnover timescale of the convective motions ($\tau \sim 3000$ s), although larger domain choices give similar results.

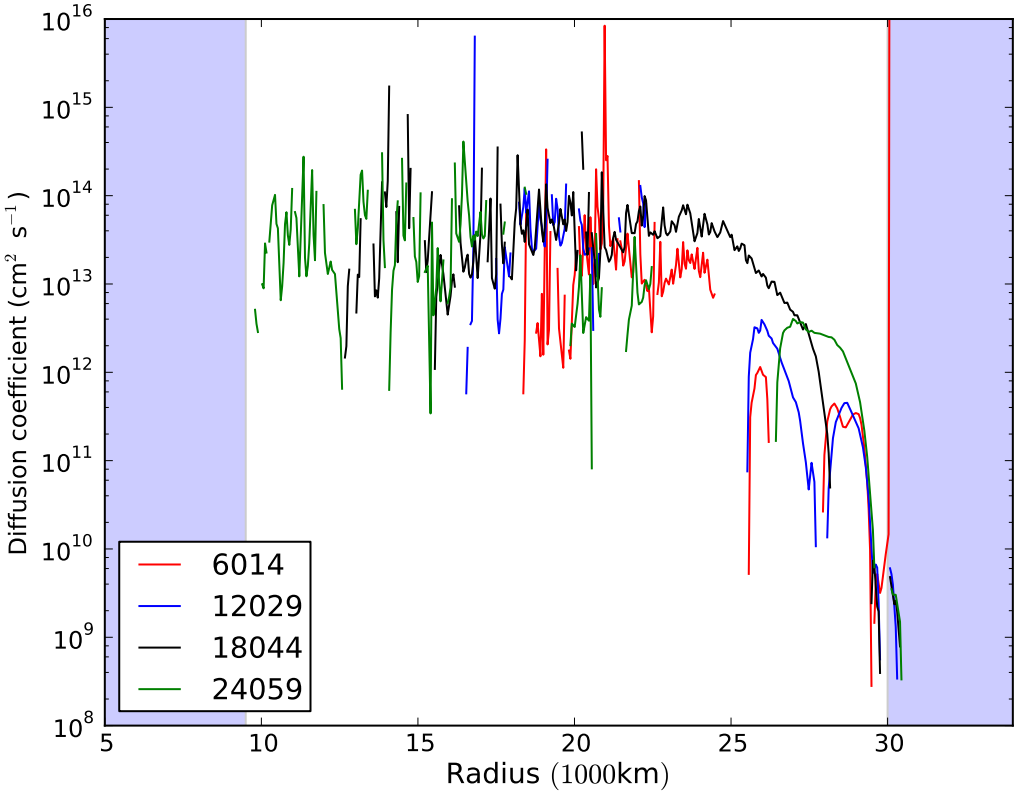

Figure 5.7: Instantaneous diffusion coefficient calculations for the H+He fluid for four timesteps. Shaded regions correspond to radiative zones. The legend gives the time, t, in seconds.

The evaluated diffusion coefficients shown in Fig. 5.8 are therefore smoother and vary in a similar way to the instantaneous evaluations in Fig. 5.7. That is, the lines are patchy due to negative diffusion coefficients and the diffusion coefficients below the interface vary by three orders of magnitude, although the range is a factor of 10 lower than for the instantaneous diffusion coefficients (between 10^{11} and 10^{14} cm^2 s^{-1}). In addition, 'boundary' deviations of the form seen in previous tests (see Fig. B.12) are seen, which occur near to the bottom of the convection zone and occasionally throughout the convection zone. This is due to the low abundance of H+He fluid in the convection zone, which yields a lower numerical precision. Nevertheless, the evaluated diffusion coefficients are of a similar order of magnitude as those predicted for convection zones from MLT. The boundary deviations could also be responsible for the decline towards the interface, but the evaluations of the diffusion coefficients are consistent with the instantaneous evaluation, which tends not to suffer from this particular type of error.

A close-up of the upper interface region in Fig. 5.8 can be seen in Fig. 5.9. The variations in the calculated diffusion coefficients are less than that seen further into the convection zone, which span approximately one order of magnitude (between 10^{11} to 10^{12} cm^2 s^{-1}). The diffusion coefficients then tend to a value of 10^8 cm^2 s^{-1} before negative diffusion coefficients are determined. The decreasing diffusion coefficients with increasing radius are expected because convective plumes approaching the interface will reduce their radial velocities and increase their tangential/perpendicular velocities, which will inhibit mixing (see also Fig. 5.10). Inside the radiative zone, the diffusion coefficients are approximately 5×10^9 cm^2 s^{-1} with a rough variation of approximately 20%, decreasing with increasing radius to about 10^9 cm^2 s^{-1}. The diffusion coefficients in the radiative zone represent non-convective-mixing, which is induced by turbulence

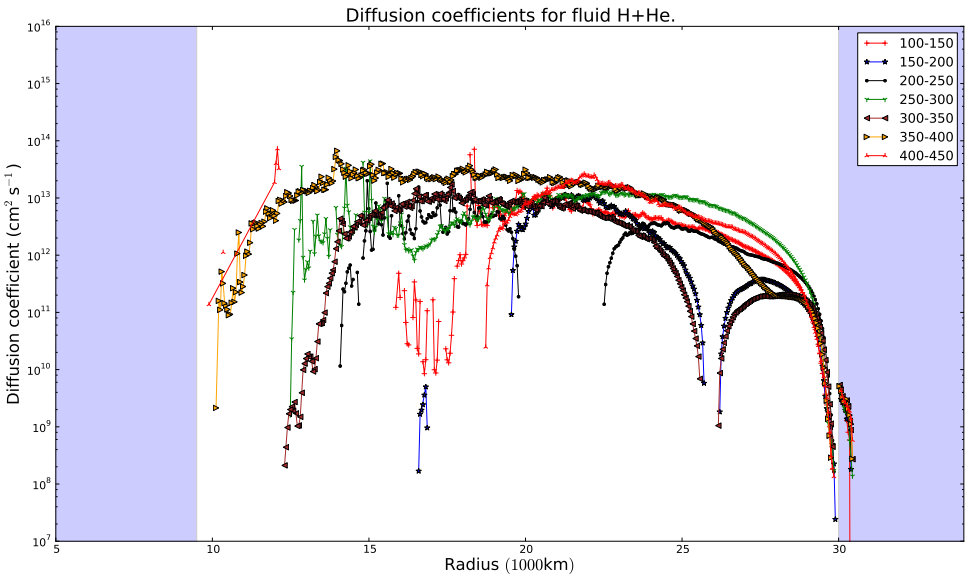

Figure 5.8: Diffusion coefficients calculated assuming constant D using timestep domains of 50 timesteps. Shaded regions correspond to radiative zones.

from internal gravity waves.

5.3.2 Resolution effects

The diffusion coefficients calculated for the previous case may be subject to errors of the type seen in the preliminary tests (see appendix B). Fig. 5.11 shows a plot of the diffusion coefficients calculated using the constant D assumption using a domain over timesteps 320 to 480 for different spatial resolutions. Fig. 5.11 shows that the calculated diffusion coefficients are converging on a solution, which is towards smaller coefficients as the resolution increases. The changes in the coefficients demonstrate that changes to the convective-boundary mixing due to the different spatial resolution of

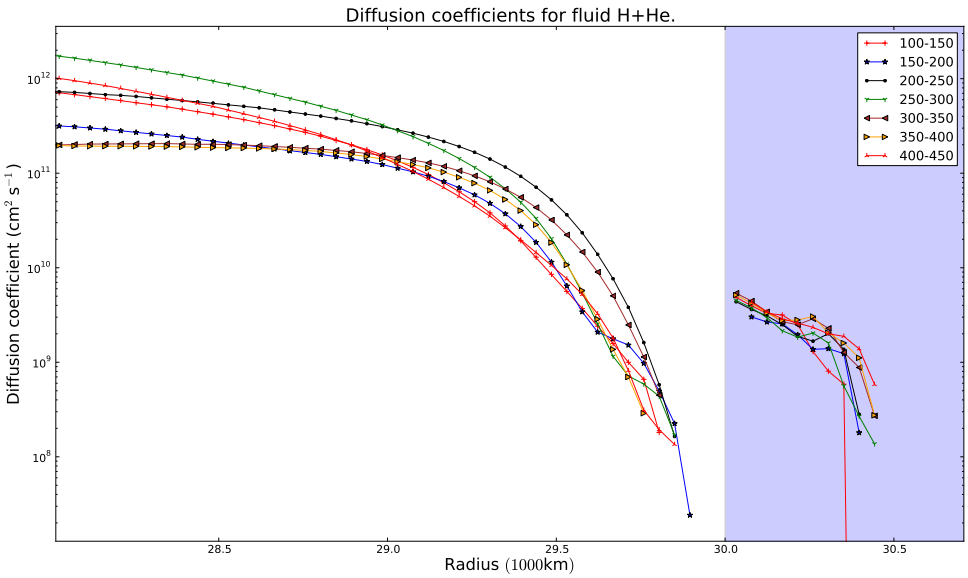

Figure 5.9: As Fig. 5.8, but zoomed into the interface region.

the input models affects the evaluated diffusion coefficients. Higher resolution runs will be required in order to see if the diffusion coefficients have been computed adequately. In any case, the diffusion coefficients calculated for the 1536^3 grid provide a good first indication of the correct order of magnitude.

However, Fig. 5.11 also shows some diffusion coefficients that were evaluated to be negative. For the plot, these values are made positive and plotted with a separate symbol. All of the negative diffusion coefficients, which lie at the interface, have a value which is intermediate between the positive coefficient values in the convection zone and radiative zone close to the interface. The negative diffusion coefficients are a result of an increase in abundance in a spatial location where, by diffusion, the abundance is expected to decrease (or vice versa). The diffusion coefficients in Fig. 5.11 for the 1536^3 case therefore demonstrate that the mixing occurring over the interface may be

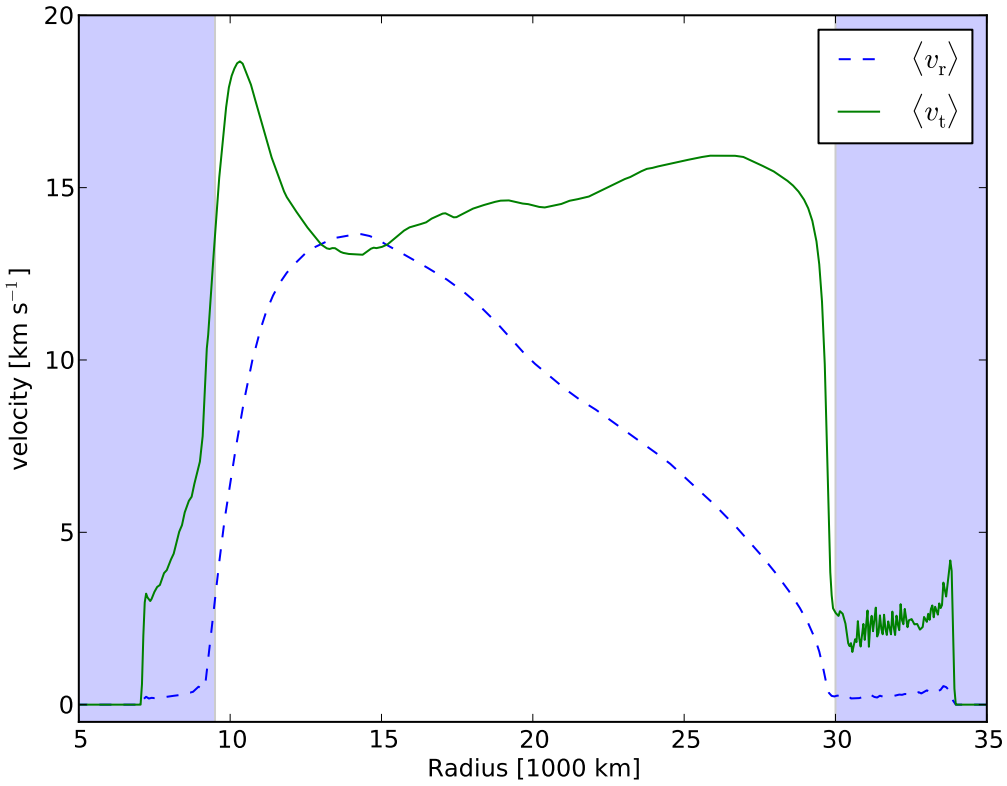

Figure 5.10: Average radial ($\langle v_\mathrm{r} \rangle$) and tangential ($\langle v_\mathrm{t} \rangle$) velocity distributions at timestep 300 ($t = 18042$ s). Shaded regions correspond to radiative zones.

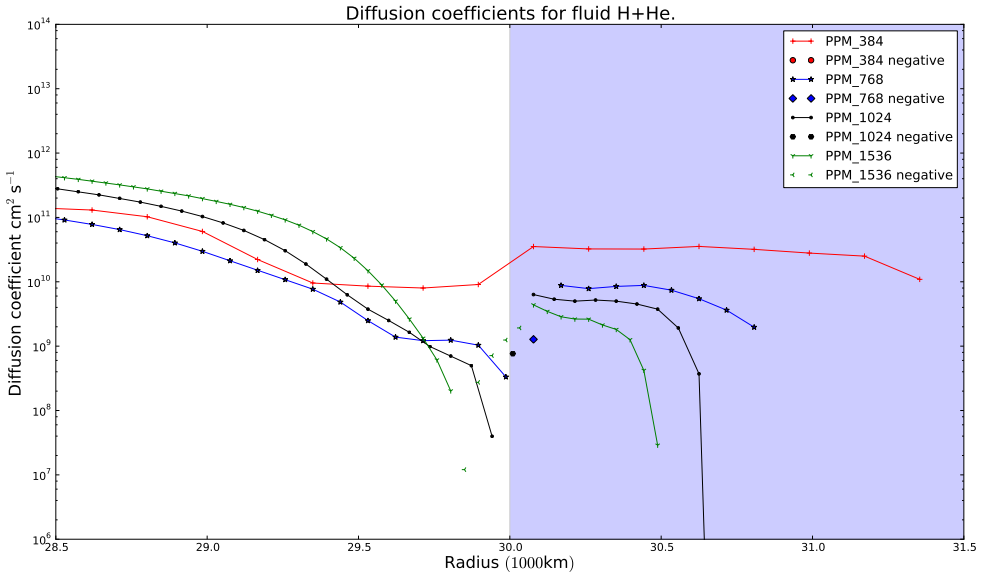

Figure 5.11: Diffusion coefficients using the constant D assumption with different spatial resolutions. Positive diffusion coefficients are connected with solid lines, whereas negative diffusion coefficients are made positive and plotted with a different symbol. The resolution is specified in the legend as the number of spatial mesh points used over one side of the cubical domain.

better described using and alternative mixing scheme, such as advection.

5.4 Discussion

It was demonstrated that the diffusion calculators are capable of recovering the input coefficients of diffusion simulations for conditions similar to those encountered at the boundaries of stellar shell-flash convection zones. This was verified for the case of a constant diffusion coefficient (see appendix B) and for the case of a variable diffusion coefficient of the kind used in overshoot mixing precriptions in 1D stellar models (see §5.2). However, the input data from the hydrodynamics model carries the signature of advective gusts and turbulent entrainment at the convective–radiative interface. Despite the fact that the hydrogen-ingestion and subsequent convective mixing are not diffusive processes, diffusion coefficients calculated from radially-averaged profiles show a common structure. This structure is characterised by a decrease in the diffusion coefficient towards the convective boundary, which is a consequence of the decrease in the radial-component of the velocity of convective plumes before reaching the interface. Beyond the interface, a declining diffusion coefficient is seen, but this coefficient could differ from that of an exponential law. These features indicate that the exponentially-declining coefficients given by Eq. 5.2 may not be suitable for describing convective–radiative interfaces in AGB stars.

Negative diffusion coefficients at the interface indicate that the transfer of matter across the interface occurs with an advective character that is poorly replicated with diffusion. Since the radial velocity of convective plumes decreases as the plumes approach the convective–radiative interface, an increase in the velocity of matter trav-

elling parallel to the interface is larger. Therefore, the fluid instabilities present at the interface are more akin to those of a Kelvin-Helmholtz instability (shear turbulence) than the Rayleigh-Taylor instability, which is characterised by buoyancy-driven structures. Since diffusion is a process characterised by a radial flux of matter due to the presence of an abundance gradient, diffusion may not be appropriate for use at the interface. The diffusion coefficient profiles however indicate that the final outcome of the mixing to each side of the interface may be adequately described using diffusion.

The Kelvin-Helmholtz nature of the convective-boundary mixing is suggested when considering the average velocity distribution of stellar plasma. In Fig. 5.10, averaged radial ($\langle v_{\rm r} \rangle$) and tangential ($\langle v_{\rm t} \rangle$) velocity distributions are shown. The radial component of the average velocity decreases with increasing radius, whereas the perpendicular component increases slightly. This indicates that convective plumes are influenced (due to pressure) by the convective–radiative boundary before they approach the convective–radiative interface. At the interface, the tangential component of the average velocity is much higher than the radial one. This is in accordance with the description that mixing at the convective–radiative interface is driven by Kelvin-Helmholtz instabilities due to horizontal shear and is provides a situation that is more akin to turbulent entrainment than to ballistic penetration by overshooting (as previously found by Meakin & Arnett, 2007). Meakin & Arnett (2007) also suggested that, depending on the nature of the convective–radiative interface, an extension of the convective boundary may be described in a 1D stellar model using an entrainment law of the form

$$\dot{M}_E = (4\pi r_i^2 \rho_i)\sigma_H f_A \times 10^{-n \log \mathrm{Ri}_B}, \tag{5.9}$$

where $\dot{M}_E$ is the rate of change of entrained mass, σ_H is the rms turbulence velocity,

Ri_B is the Richardson number (which is a measure of 'stiffness' for the convective boundary) and f_A and n are free parameters. ρ_i and r_i are the density and radius at the position of the interface. The negative coefficients at the boundary could therefore reflect the need for an advection term in the diffusion equation:

$$\frac{\partial X_i}{\partial t} = \frac{\partial}{\partial x}\left(D\frac{\partial X_i}{\partial x}\right) + \nabla \cdot (uX_i), \tag{5.10}$$

where u is an average velocity. Further studies will be needed to determine whether an advection term could improve the analysis of convective–radiative interfaces in stellar interiors, such as for the case of a hydrogen-ingestion flash.

6 Summary, conclusions and further work

In this thesis, two commonly encountered regimes in s-process research, massive star and AGB evolution, were investigated in order to test the applicability of a nucleosynthesis post-processing code to investigate uncertainties in 1D stellar models. It is often encountered in the literature that the main sources of uncertainty are associated with reaction rates, which are difficult to determine in beam experiments, and computer simulations of mixing phenomena, which are difficult to model and are computationally expensive. Consequently, the current work was guided into two projects, which looked at particular features of each of these sources of uncertainty.

6.1 The ^{12}C + ^{12}C reaction rate in massive stars

Massive stars, which undergo advanced stages of hydrostatic burning, represent an important source of heavy elements in the universe and consequently represent an important test-bed for uncertainty studies in stellar models. The ^{12}C + ^{12}C reaction rate, which features low-energy resonances that are not predicted by nuclear theory, is a highly unconstrained rate that is important for the evolution of massive stars, as well as being relevant for stellar evolution of SAGB stars, neutron star structure, superbursts and type Ia supernovae. Ongoing nuclear physics experiments will help to constrain the ^{12}C + ^{12}C rate at relevant astrophysical energies for use in stellar models, but these experiments are of considerable difficulty and until experimental rates can be accurately obtained at low energies, constraints from astronomical observations will remain critical.

Uncertainties in the rate were shown to affect both the stellar structure and nucleosynthesis of massive stars, with the main factor being the ignition and burning of ^{12}C fuel at a lower temperature. The decrease in temperature changes the neutrino losses and the energy generation rate. Consequently, the core carbon-burning stage has a longer lifetime. There are fewer convective shell burning episodes in the less massive stars and carbon burning convection zones are enhanced in size. Enhanced rate models were often found to have convective carbon-burning cores instead of radiative ones. The interior composition of light elements is affected by changes to the $^{12}C + {}^{12}C$ rate, but this was not significant enough to affect significantly the advanced burning stages following carbon burning.

The heavy elements that are synthesized by s-process nucleosynthesis, however, are affected significantly by changes to the carbon burning rate. The lower central temperature in the increased carbon burning rate models causes the neutron sources to be activated with smaller rates, lowering the neutron density. The increased lifetime of the carbon burning stage causes an increase in the neutron exposure. In addition, there is the possibility of shell overlap in the models with larger convection zones, which can cause the shell-burning convection zones to be polluted with the ashes of carbon-core burning or previous carbon-shell burning episodes. This overlap causes the carbon-core s-process to partially contribute towards the yields of the star, changing the weak-component.

The weak-component predicted by the enhanced rate models allows constraints to be applied to the $^{12}C + {}^{12}C$ reaction rate. For the case of a large resonance (CU case), massive stars were found to have much higher overproduction factors and a modified abundance distribution. Therefore, that rate could be ruled out. For the intermediate case (CI case), the abundance distribution was enhanced in nuclides with

$80 < A < 120$, due to the inclusion of the carbon-core s-process to the yields of the $20M_{\odot}$ model. This enhancement is anomalous compared to the weak s-process component. However, considering uncertainties in the nuclear reaction rates and the treatment of convective–radiative interfaces, the enhancement is not severe enough to allow a definitive constraint to be made to the rate. Consequently, the intermediate rate used in this work can be considered as a tentative 'upper limit' to the rate, since any further increases to the rate will increase the likelihood of carbon-core s-process nuclides being included in the final yields of the star, making the weak s-process component differ further from that of the Solar system abundance distribution.

The predicted weak component was obtained using five choices of initial mass and a Salpeter IMF. In order to constrain smaller changes to the reaction rate, more accurate predictions of the weak-component will be required. This could be achieved by using the yields as input for a galactic chemical evolution model. A finer grid of models in mass, around $m = 20M_{\odot}$, will allow a better determination of the limiting mass for a convective carbon core. In addition, photodisintegration reactions at the bottom of convective shells and the s-process nucleosynthesis that occurs during the propagation of the supernova shockwave were not considered in this work. These will need to be included in the stellar models for quantitative studies, particularly for nuclides that lie at, or just above, the iron-group (such as nickel, zinc and copper), which are heavily produced during the explosion.

Other uncertainties, such as overshooting, the initial composition and other nuclear reaction rates will also have a large impact on the stellar yields. Additional uncertainty studies will help to make more stringent constraints on the $^{12}C + {}^{12}C$ rate and on the s-process sites. Rotation and overshoot mixing uncertainties will be important to consider in low-metallicity massive stars, especially given that the abundance

signature of the carbon-core s-process bears similarities to the LEPP abundance signature. In particular, uncertainties in the 3α and $^{12}C(\alpha,\gamma)^{16}O$ reactions, which are efficient during helium burning, affect the abundance of ^{12}C available for carbon burning. It is likely that these uncertainties will affect the s-process during carbon-core burning in addition to the s-process during helium burning. Other important reaction rate uncertainties include $^{22}Ne(\alpha,n)^{25}Mg$ and $^{17}O(\alpha,\gamma)^{21}Ne$. The first reaction affects the neutron density and the second competes with the $^{17}O(\alpha,n)^{20}Ne$ for α-particles, affecting the efficiency of the ^{16}O neutron poison (since ^{17}O is formed from (n,γ) reactions on ^{16}O) and the recycling of neutrons during the s-process.

Additional uncertainties directly pertaining to the $^{12}C + {}^{12}C$ reaction rate that were not explored in this work are the branching ratios for the $\alpha-$, p- and n-exit channels. The branching ratios used in this work were assumed to be applicable down to carbon burning temperatures, but changes to the branching ratios could affect the s-process yields during carbon-core and carbon-shell burning since the direct by-products of the $^{12}C + {}^{12}C$ reactions are $\alpha-$particles and protons, which are captured by other nuclides, including the neutron source isotopes.

With regards to the development of MPPNP, the post-processing technique can also be applied to a range of different astrophysical scenarios, including type I and II supernovae, novae and accreting binary stars. By including reaction rates with MPPNP, the only requirements, in principle, for the use of the post-processing technique are the temperature and density of matter as a function of time and an initial composition. In addition, Monte Carlo simulations can be applied to a single stellar model, with the aim of quantifying nuclear physics and stellar model uncertainties. Further development of MPPNP in this regard will be conducted by the NuGrid collaboration to perform additional uncertainty studies.

6.2 Convective-boundary mixing during the hydrogen-ingestion flash in AGB stars

In 1D stellar models, diffusion is used to approximate convective mixing. Overshoot mixing across convective–radiative interfaces is particularly important for the interaction between adjacent hydrogen and helium convection zones during hydrogen-ingestion flashes and also affects the formation of the ^{13}C neutron source after helium-shell flashes in thermally-pulsing AGB stars. Improvements in the evaluation of the mixing over convective–radiative interfaces is important to test the robustness of the s-process mechanism in thermally pulsing AGB stars and consequently the main s-process component of the Solar system abundances.

Improvements in the treatment of convection in stellar evolution models awaits a computational method that can calculate accurately the motion of fluid elements in a convection zone in 3D. Although such models exist in hydrodynamics simulations, their application to stellar evolution models features fundamental barriers associated with a disparity in the timescales of convection and stellar evolution. In addition, full 3D hydrodynamics models are too computationally expensive to be included directly in stellar evolution models using current technology. Nevertheless, existing hydrodynamics simulations of convection can be used to constrain overshoot mixing across convective–radiative interfaces, which can be used to guide and improve the input physics of 1D stellar models. In this work, the radially-averaged output from the hydrodynamics code PPM was analyzed in order to calculate diffusion coefficients that represent the mixing of matter across the boundary. This required the development of computer programs that can calculate the diffusion coefficients when provided with a

known abundance as a function of time and space.

An implicit diffusion simulator was developed in order to provide test cases for the diffusion coefficient calculators. A comparison with the input coefficients verified that the diffusion coefficient calculators can reproduce the input diffusion coefficients used in the diffusion simulators using constant or variable diffusion coefficients. The variable coefficient case was that of an exponentially declining function that is often used for the treatment of overshooting in stellar interiors. However, the calculated diffusion coefficients from the 3D hydrodynamics model showed a different shape to that expected from the overshooting case, characterised by a decrease in the diffusion coefficient within the convection zone and negative coefficients at the convective–radiative interface. In the convection zone, the declining coefficients reflect the decreasing velocity of convective eddies with increasing radius towards the convective boundary. This is already expected to be the case from 3D hydrodynamics simulations, but is currently not treated in 1D stellar evolution codes. The negative diffusion coefficients evaluated at the convective–radiative interface can be attributed to a different physical situation to that of overshoot mixing; the calculated diffusion coefficients could demonstrate the fact that there is the presence of convective-boundary mixing associated more with Kelvin-Helmholtz instabilities and shear turbulence rather than Rayleigh-Taylor instabilities and penetrative convection.

In this work, a numerical approach was taken to investigate mixing over a convective–radiative interface in a 3D hydrodynamics simulation of hydrogen-ingestion. The resolution test showed that the calculated diffusion coefficients could converge to a more accurate coefficient profile, but the negative diffusion coefficients may demonstrate the need for a more detailed theoretical treatment to describe the convective-boundary mixing in 1D stellar models (as demonstrated by Meakin & Arnett, 2007).

Although higher resolution simulations would be desirable, further analysis could be made regarding advection in the simulations and the diffusion coefficient calculators. Advection has also been known to occur in the interdiffusion of two liquids in the case where the diffusion coefficient is dependent on the abundance. In this case, the advection can result in the displacement of the interface between the two fluids, known as the Kirkendall effect (see for example Crank, 1975). An abundance-dependent diffusion coefficent and the Kirkendall effect may provide a means for taking into account the displacement of a convective–radiative interface, which could be included into 1D stellar models.

In addition, one could explore the link between 1D and 3D codes for other convective boundaries. In this work, the lower convective boundary was not treated, but the velocity distribution in Fig. 5.10 indicates that mixing should occur at the lower convective boundary. Since this region is attributed to the source of heating in the hydrodynamics simulations, mixing across the lower convective boundary could affect the heating rate due to nuclear burning. In this work, the initial abundance of the two fluids does not trace mixing across the lower boundary, but further simulations could be made to trace the mixing in this region. Such models may also be beneficial for investigating the combination of both mixing and nuclear burning and the interaction between the two processes.

6.3 Final thought

1D stellar models, together with observations, will continue to further our understanding of stellar structure and nucleosynthesis. Uncertainty studies help to achieve this

by providing new constraints on existing input physics, such as nuclear reaction rates and mixing prescriptions. Such studies require the development of new or improved computer programs to calculate nucleosynthesis (such as MPPNP) or analyze mixing (such as PPM and the diffusion programs). Continued development on computational tools for nuclear astrophysics will therefore be critical in further improving the accuracy of 1D stellar models and furthering our understanding of the origin of the heavy elements in the Galaxy and in the Solar system.

A Parallel programming and computation

A.1 The motivation for parallelisation

Modern supercomputers utilise parallel architectures in order to split the work of a computational problem into many parts, which can be solved separately. As physical limits are approached in the development of uniprocessors, development of parallel architectures is favoured, eventually leading to the availability of 'multi-core' machines in the commercial domain. These machines typically implement a method of shared-memory programming, where multiple processors access the same pool of data to perform computations independently. Distributed-memory resources are also popular choices for parallel systems since they can be set-up using existing network capabilities, although they also exist as purpose-built cluster networks.

MPPNP calculates stellar nucleosynthesis by solving a nuclear reaction network over the spatial domain of a star, as described by the stellar model. This spatial domain is split into a series of concentric, spherical shells (the 1D approximation), with each shell harbouring a unique network calculation depending on the abundances of isotopes within the shell and the stellar parameters, such as temperature and density (as functions of radius). The post-processing task is computationally expensive, as the nuclear network calculation requires the computation of the inverse of a large matrix for each shell. Therefore, exploiting parallelism is not only a generic performance enhancement, it makes post-processing of very large reaction networks in a reasonable timeframe feasible.

In this work, several parallel-computing resources were used. These are the

KHAOS cluster at Keele University, Saguaro 2 at the University of Arizona and numerous multicore desktop machines available at Keele University. The KHAOS cluster has 43 dual dual-core machines (172 cores), which were used mainly for testing and Saguaro 2 has 570 dual quad-core machines (4560 cores), which were used for the majority of the main calculations. Each core operates at a maximum frequency of approximately 2.4 GHz and the machines on both clusters are networked using Infiniband interconnects. A typical full post-processing run on either system takes approximately 2 weeks to calculate using 64 cores for each run, depending on the number of nuclear reaction networks calculated by the model. In addition, many of the digital computers available in the Keele Astrophysics Laboratory have at least 4 cores (Intel or AMD) either in the form of arrays of dual-core or quad-core processors. These machines are ideal for testing parallel implementations since most tests will require a minimum of 2 processors to operate (a 'master' processor, which operates the task scheduler and handles input and output, and a 'slave' processor, which performs the majority of the useful calculations). It is worth noting that it is possible to assign more processors to a task than there is available processors. For example, if two processors are assigned to a task and operated on a uniprocessor machine, two 'virtual processors' are invoked, which both run on the single physical processor which, for all intensive purposes, operates identically to that of a real parallel machine, albeit without the performance enhancement.

The choice of parallelisation can be summarised as utilising a dynamic first-in first-out (FIFO) scheduler farming over 1D spherical shells using the message-passing interface (MPI) in Fortran. The main reasons for this particular choice are simplicity and efficiency. Since MPPNP utlises a unique network calculation for each shell, independent of the other shells, no communication of information over different shells

is required and the algorithm becomes 'embarrassingly parallel' and therefore a simple parallel algorithm can be implemented. The FIFO scheduler is a dynamic and non-deterministic scheduler that provides a useful mechanism for the distribution of work and provides a basis for more sophisticated schedulers or load-balancing algorithms. MPPNP is designed with the intention to run on cluster networks, which represent typical resources available at universities and academic facilities and MPI is ideal for providing parallel capability for Fortran programs over distributed computing resources.

Section A.2 deals with the general theory of parallel systems and the implementation of parallel programming into MPPNP. The theory of parallel programming is extensive and a complete recall of the theory is beyond the scope of this work, but there are fundamental concepts that are relevant for the design choices and performance of the post-processing code. The above is also true for the field of complexity theory, which looks at the nature of different logic problems with respect to their solution via computational means. For this purpose, an extensive amount of content is recalled from Zomaya (1996), with additional content recalled from Wilkinson & Allen (2004) and Gropp et al. (1999). Section A.3 applies the theory to MPPNP in order to determine performance characteristics of the parallel implementation.

A.2 Parallel theory

There are numerous properties of computational systems that need to be considered when determining the performance of a parallel system. Parallel systems and algorithms can be designed and operated in many different ways and therefore an unbiased,

universal scheme for performance analysis is necessary. Analysis of parallel programming is based on an idealised, abstract system. Once an abstract model has been chosen and measures are in place to estimate the consumption of hardware resources, more realistic scenarios of resource consumption can be described.

A.2.1 Parallel models and classification

The performance of a parallel system is strongly dependent on both the hardware configuration and the choice of the parallel algorithms. Therefore, in order to determine a general theory of parallel programming, it becomes necessary to treat both the hardware and software as generally as possible by considering abstract models of computation.

A.2.1.1 The Turing machine

The simplest model of an abstract machine is the Turing machine, which consists of three basic components: a finite state machine, a read-write head and an infinite memory store, organised into cells, with each cell holding a single alphanumeric character or symbol (Zomaya, 1996, p. 93). Upon reading a character from memory, the Turing machine can decide whether or not to overwrite a character. Then, depending on the symbol in the cell and the state of the machine, the Turing machine can move the read-write head to the next, or previous, memory location. If this process is unique for a particular state of the machine, then the Turing machine is deterministic (DTM). If several options are possible, the Turing machine is nondeterministic (NDTM). The DTM is a machine that solves 'tractable' problems, which are directly computable by

an algorithm, and the NDTM is a machine that solves 'decision' problems, or searches.

A NDTM can be modeled using a 'branching tree', i.e. the final solution is determined by searching through a tree of possibilites; each branch representative of a boolean 'OR' condition. Therefore, the NDTM is regarded as a machine that operates by repeatedly making 'guesses' at the solution to a problem until some acceptance with criteria is determined, giving a solution. The NDTM can also be modeled in terms of DTMs provided there is unbounded parallelism (Zomaya, 1996, p. 94), which is the assertion that a DTM can make any number of copies of itself. Whenever the DTM approaches an 'OR' branch of the tree, the DTM makes a copy of itself and each DTM computes each respective branch of the tree. If a copy fails to determine a solution at the end of the tree, the DTM terminates. If a DTM is successful, then all other DTMs are stopped. This means that a single NDTM is equivalent to an exponential number of DTMs working in parallel or a single DTM operating over an exponentially longer duration than the single NDTM. In addition, any result determined by a NDTM can be *verified* by a DTM.

The Turing machine is in general too abstract and idealistic, however, for use in describing the behaviour of modern computers, but it is useful for studying the complexity of algorithms (see section A.2.4.2).

A.2.1.2 The Random Access Machine (RAM)

An alternative abstract model is the Random Access Machine (RAM) (Zomaya, 1996, p. 11, 106-107), which consists of a single processor, an infinite memory unit, a read-only tape and a write-only tape (see Fig. A.1 for a typical schematic of a RAM). The memory consists of an infinite number of registers, $R_0, R_1, R_2, \ldots$, that can each hold

an integer of arbitrary size. The RAM operates a single program that consists of a sequence of instructions read from tape. The basic instruction set of a RAM consists of the following:

- $R_i \leftarrow$ constant (Load memory with an integer constant)
- $R_i \leftarrow R_i * R_k$ (Perform binary arithmetic, such as addition and subtraction)
- $R_i \leftarrow R_{R_j}$ (Indirect load)
- $R_{R_i} \leftarrow R_j$ (Indirect store)
- Goto label m

The RAM can operate as a DTM or NDTM and can also be used for the measurement of complexity. This measurement is made by assuming each instruction takes a unit time and that the space used is the maximum number of memory cells needed for any computational step. Thus one can define the 'work' performed by the RAM as the number of instructions multiplied by the time per instruction. The time required to access memory is assumed to be negligible.

The parallel version of the RAM is the Parallel Random Access Machine (PRAM) (Zomaya, 1996, p. 11-12, 107). This machine consists of a set of synchronous processors connected to a shared memory, which can be accessed by more than one processor at a time (see Fig. A.2). The PRAM model assumes that instructions take the same time to compute on all processors (they are synchronised) and that there is no interconnection network between processors. Therefore the effect of communications on the parallel performance is ignored. Nevertheless, the PRAM model is useful as a basis for theoretical analysis; generally, any algorithm that cannot operate well on a PRAM cannot operate satisfactorily on any other parallel system.

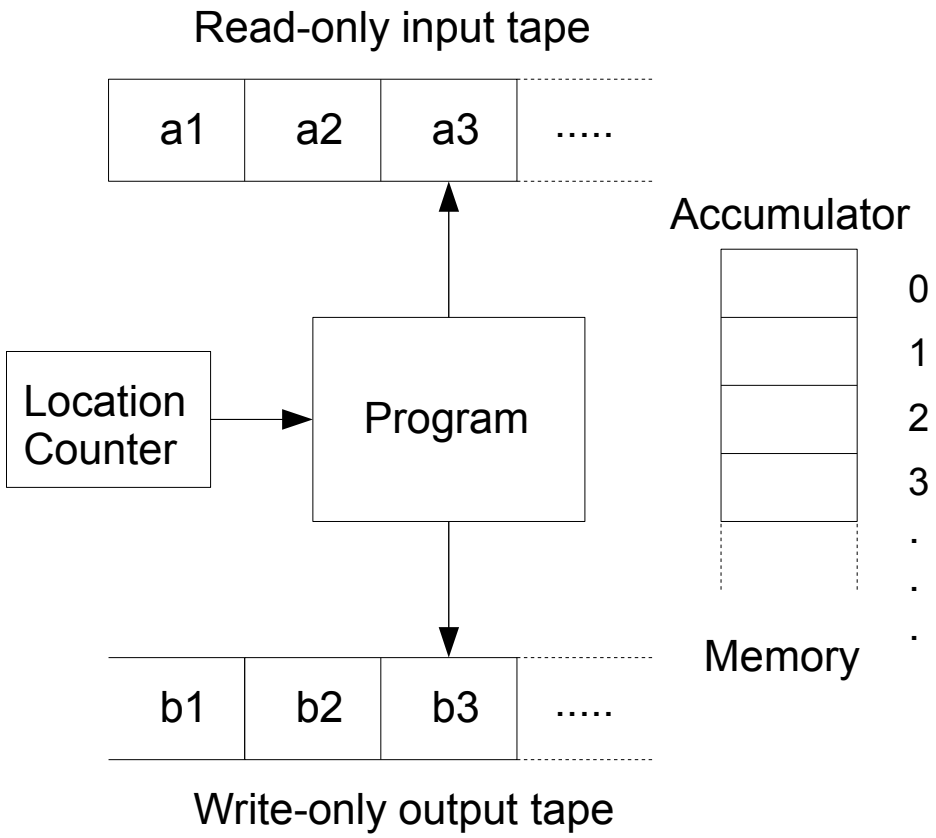

Figure A.1: Schematic representation of a Random Access Machine (RAM). *ai* represents input cell number (i) and *bi* represents output cell number (i).

A.2.1.3 Flynn's taxonomy

Different parallel systems can be conveniently classed, following Flynn's taxonomy, into 4 categories depending on the concurrency of the instructions and the number of data

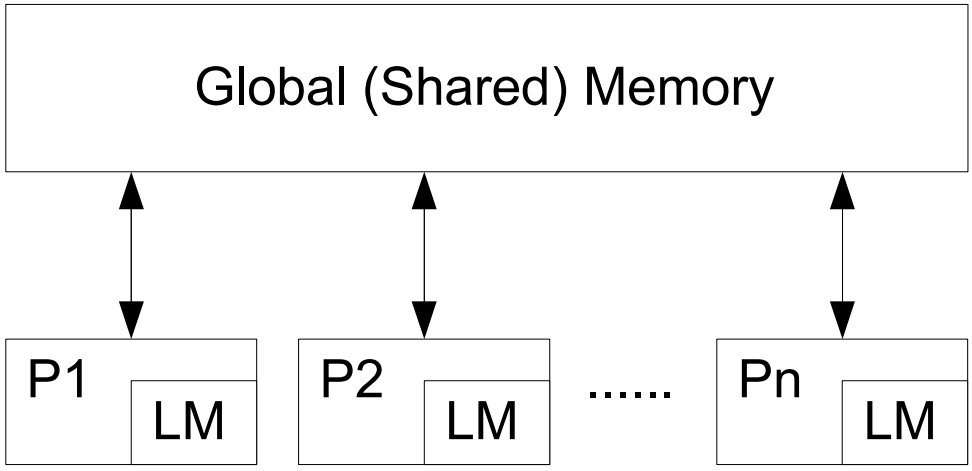

Figure A.2: Schematic representation of a Parallel Random Access Machine (PRAM). Pi represents processor (i) and LM represents local memory

pipelines available (Zomaya, 1996, p. 7-9, 112-113).

- **SISD: Single Instruction, Single Data.** Any computer that uses a single, serial processor to operate on a single pool of data comes under this category. The von Neumann architecture, on which almost all modern computers are based, is the classical example of a SISD system and most traditional uniprocessor personal computers are SISD systems.

- **SIMD: Single Instruction, Multiple Data.** If a system utilises more than one processing unit, but still uses a single control unit to assign tasks to processors in a serial manner, then it falls under this category. The tasks can be performed in parallel on numerous processors sharing a single memory space,

or alternatively, access memory local to the processor. Examples of SIMD systems are vector processors and graphics processing units.

- **MISD: Multiple Instruction, Single Data.** In a MISD computer, each processor has a control unit and shares a common memory unit. In this system a multitude of tasks are operated on the same data (or task replication), which is desirable in systems where fault tolerance is important. An example of a MISD system is the systolic array, which is a processor formed by a mesh of processing units that pass the results of the computation to neighbouring units for further processing.

- **MIMD: Multiple Instruction, Multiple Data.** A significant variety of different parallel architectures come under this category, which include multiple numbers of processors, control units and utilisation of multiple memory locations or shared memory resources. Examples of these are cluster networks and modern supercomputers.

Alternative schemes exist, such as SPMD (Single Program, Multiple Data) and MPMD, which distinguishes between architectures that operate parallelism using one or multiple programs, and Schwartz's scheme, which compares architectures based on whether the machine accesses shared memory (paracomputers) or local memory with communications via a fixed interconnected network (ultracomputers).

A.2.2 Implementation of parallelism

There are a large variety of parallel models available. Here, two main implementations will be discussed relevant to cluster networks: the shared-memory model and message-

passing model. One reason to discuss these two particular models is that there exists easily-available commercial software for both of these models, such as OpenMP, High Performance Fortran and MPI (see, for instance, Chapman et al., 2007; Gropp et al., 1999), that can operate using the Fortran programming language, the language in which MPPNP has been written (see, for instance, Metcalf & Reid, 1990).

In the shared-memory model, the processing units access a single, shared repository of data, with simultaneous access to files controlled by a locking mechanism, although higher level programming languages can hide the use of locks. This type of parallelism is generally easier to use and program, but can suffer significantly from communication overhead. An additional problem is that most cluster networks follow a distributed computing model, whereby memory is distributed over the network. However, in this situation, a hybrid model with both shared-memory and message-passing elements can be implemented.

In the message-passing model, the processing units access their own local memory store and information is communicated between processing units via the sending and receiving of messages. Since processing units operate independently when they are not communicating, it is possible for the processing units to have different states at different times. Therefore, synchronization is also a key aspect of message-passing. This can be performed by the message passing itself (via blocking communications) or by the use of independent blocks. It is generally harder to program and utilise message-passing programs over shared-memory programs, but they allow for convenient parallel computing over distributed networks and are portable over different system configurations.

As MPPNP will operate on distributed computing resources, the Message Passing Interface (MPI) is used, which is a library that is designed to upgrade the functionality

of the existing programming languages Fortran and C/C++ (Gropp et al., 1999) to allow message-passing operations. MPI programs require a minimum of six functions to operate, but there are a total of 125 functions available (Gropp et al., 1999, p. 21). The six functions are as follows:

MPI_INIT invokes the environment for which other MPI calls can operate. It is typically the first call of any program.

MPI_COMM_RANK is an enquiry function that determines how many processes (for example, the number of processors) are operating the program and assigns them a context, which is the group of processes, and a rank for each process. This allows each process to be identified individually. The default communicator is `MPI_COMM_WORLD`, which defines a single context that includes all processes, but contexts can be specified by the user.

MPI_COMM_SIZE returns the total number of processes operating within a context. Knowledge of the total number of processors is necessary for most programs.

MPI_SEND is the first of the two most common message-passing functions. `MPI_SEND` is the basic building block of any parallel program and its function is to communicate information between processes. The arguments of the function control the content of the message, the destination and any additional information relating to the message.

MPI_RECV . MPI uses synchronous communications. Therefore, any send function must correspond with an associated receive function that controls who receives

the message and designates variables for which the content of the message will be inserted.

MPI_FINALIZE terminates the MPI environment.

Although any parallel program can be written using only these six functions, there are various additional functions, for example, that handle collective communications, such as `MPI_BCAST`, for broadcasting messages, and `MPI_REDUCE`, which is used to collectively operate on variables spread over multiple processes.

A.2.3 Speed-up

Parallelisation typically manifests by taking some fraction of the program, P, and distributing the computations contained in P over p processors so that the total time to process the total workload is shorter.

The maximum speed-up factor, S, is defined as

$$S(p, n) = \frac{t_s}{t_p} \tag{A.1}$$

where t_s is the time to execute a serial version of the program and t_p is the time to execute the parallel program (see, for instance, Wilkinson & Allen, 2004, p. 6-12)). S is a function of the number of processors, p, and the number of items of data being processed, n. For the moment, only the p dependence of S will be considered. If the program can be parallelised efficiently such that the speed-up is exactly linear with the number of processors, $t_p = t_s/p$. Therefore,

$$S(p) = \frac{t_s}{t_s/p} = p \tag{A.2}$$

and the maximum speed-up is simply the number of processors. This represents an ideal situation, since the speed-up is very rarely linear; side-effects such as communications, idle processor time, the start-up cost, differing processor performance and memory contention can affect the speed-up. In addition, there will be serial computations outside the scope of the parallel implementation.

A.2.3.1 Amdahl's law

By considering a fraction of the program, f, which must run in serial, the relations $P = 1 - f$ and

$$t_p = ft_s + Pt_s/p = ft_s + (1 - f)t_s/p \tag{A.3}$$

are obtained. Substituting Eq. A.3 into Eq. A.1 yields Amdahl's law

$$S(p) = \frac{t_s}{ft_s + (1 - f)t_s/p} = \frac{p}{1 + f(p - 1)} \tag{A.4}$$

As $f \to 0$, $S \to p$ and Eq. A.2 is obtained in the limit of $f = 0$. By using l'Hopital's rule on Eq. A.4, it is trivial to determine $S(p \to \infty)$

$$S(p \to \infty) = \frac{1}{f} \tag{A.5}$$

Eq. A.5 shows that the upper limit of the performance of a parallel processor is limited by the serial component of the program. For example, a program which is 5% serial has a maximum speed-up of 20, regardless of the number of processors available. An efficient parallel implementation will ensure that f is as small as possible to increase the potential speed-up. This can be accomplished by either parallelising as much code

as possible or by parallelising at a finer level of granularity (see section A.2.6).

A.2.3.2 Gustafson's law

Eq. A.4 and A.5 caused Amdahl to promote the development of serial processors over parallel ones in the late 1960s. However, Gustafson showed that the limits of parallel processing need not be as severe as those shown by Amdahl's law. Amdahl's law is based on the assumption of a fixed problem size (or alternatively, constant t_s), which generally need not be the case. Gustafson instead proposed to keep the parallel execution time, t_p, fixed, which results in a scaled speed-up factor that varies with the problem size. Specifying t_s in terms of t_p,

$$t_s = ft_p + p(1-f)t_p \tag{A.6}$$

is obtained. Therefore,

$$S(p) = \frac{ft_p + p(1-f)t_p}{t_p} = p + (1-p)f \tag{A.7}$$

Fig. A.3 shows the speed-up for both Amdahl's law and Gustafson's law for the case of $p = 20$. Fig. A.3 verifies that assuming a fixed problem-size restricts the potential speed-up of a parallel system; one can improve the overall performance by assigning more work. This effect can also be observed in Fig. A.4, which shows the speed-up as a function of the number of processors for a serial fraction of 5%.

Fig. A.4 is an example of a scaling relation, which is a plot of the reciprocal of t_p as a function of p (note that $S \propto 1/t_p$). The scaling relation is a useful measure of the performance of a parallel program as it indicates how close the parallelisation is

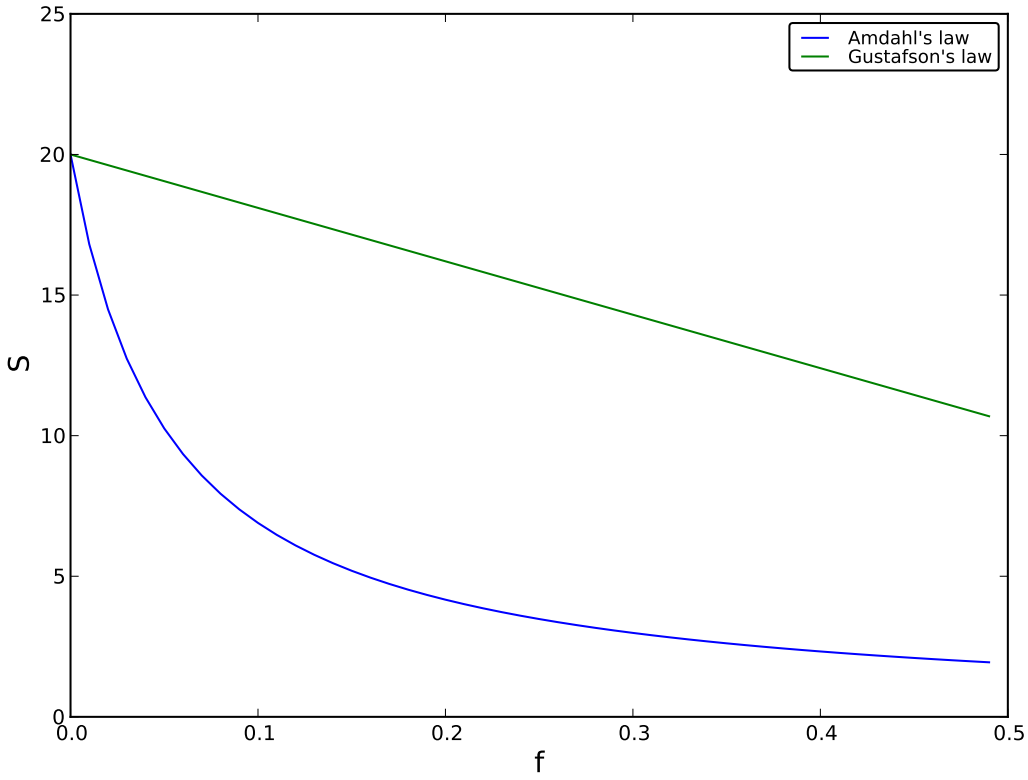

Figure A.3: Gustafson's law and Amdahl's law for the speed-up, S, plotted with respect to the serial fraction of the code, f, for the case of 20 processors.

to the ideal case and differences in the choice of different algorithms can be compared directly. The scaling of MPPNP is discussed in sec. A.3.

A.2.3.3 Communications

In the message-passing model, data stored by parallel processors are in local memory and are shared via communications when required. Such communications can be in the form of passing variables between processors, or by synchronization routines,

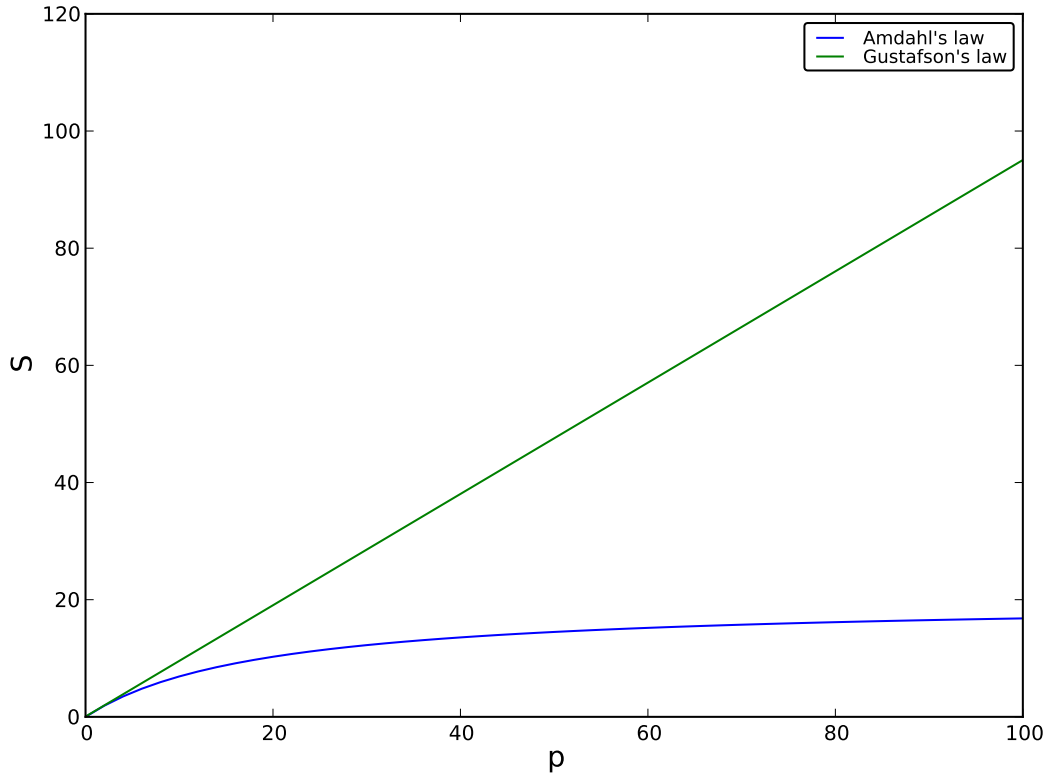

Figure A.4: Gustafson's law and Amdahl's law for the speed-up, S, plotted as a function of the number of processors, p, for the case of a serial fraction of 5%.

and excessive communication can become a major performance issue. The effect of communications on the total execution time is specified as

$$t_p = t_{\text{comm}} + t_{\text{comp}} \tag{A.8}$$

where t_{comm} is the communication time and t_{comp} is the computation time. t_{comm} is a function of p and n and therefore varies between different parallel programs. The ratio

$$R = \frac{t_{\text{comm}}}{t_{\text{comp}}} \tag{A.9}$$

can be used to determine whether the communications will dominate the total execution time.

A.2.4 Time complexity

The speed-up of a system is a function of the number of processors and the number of items of data being processed. In section A.2.3 the p dependence of S was considered, but the n dependence is also important in determining the performance of a parallel system. Complexity theory analyses this dependence in order to estimate how an algorithm varies with n and therefore provides an estimate of the resources required to solve the algorithm. It is therefore possible to define different classes of problems that can be solved by DTM and NDTM depending on the 'growth rate' of the problem with n.

A.2.4.1 Notation

For simplicity, we will look at the amount of resources, $f(n)$, which will scale linearly with the time for execution of the program on a serial processor, t_s. One can define asymptotic measures that specify the asymptotic order of the time complexities, which are the upper bound, O ("big oh"), the lower bound, Ω, and the exact bound, Θ. This notation is formally defined below.

1. O **notation**: $f(n) = O(g(n))$ if there exist positive constants, c and n_0, such that $0 \leq f(n) \leq cg(n)$ for all $n \geq n_0$.

2. Θ **notation** $f(n) = \Theta(g(n))$ if there exist positive constants, c_1, c_2 and n_0, such that $0 \leq c_1 g(n) \leq f(n) \leq c_2 g(n)$ for all $n \geq n_0$.

3. Ω **notation** $f(n) = \Omega(g(n))$ if there exist positive constants, c and n_0, such that $0 \leq cg(n) \leq cf(n)$ for all $n \geq n_0$.

For brevity, an example can be considered (Wilkinson & Allen, 2004, p. 65-67). If an algorithm varies with $f(n) = 4n^2 + 2n + 12$, $f(n) = O(n^2)$ is true since for $c = 6$, $0 < 4n^2 + 2n + 12 \leq 6n^2$ for $n \geq 3$. $f(n) = O(n^3)$ is also true, but it is customary to choose the lowest order term for which $f = O$, i.e. the term that grows the least. In any case, Θ captures the exact bound. There exists many ways to satisfy the condition with $g(n) = n^2$, such as $c_1 = 2$ and $c_2 = 6$ such that $2n^2 \leq f(n) \leq 6n^2$ for $n \geq 3$, yielding $f(n) = \Theta(n^2)$. Similarly for Ω notation, $f(n) = \Omega(n^2)$. Ω is useful if an algorithm behaves differently depending on the input parameters. For example, if a sorting algorithm has $f(n) = n\log(n)$ in one case and $f(n) = n^2$ in another, dependent on the initial order of the items of data, n, to be sorted, then $f(n) = \Omega(n\log(n)) = O(n^2)$. In general, O represents the worst case time complexity and Ω the best case time complexity.

A.2.4.2 Complexity classes

Different logic problems can be classed depending on their complexity. This complexity can exist in the time domain or the spatial domain, determined by the dependence of the input size, n, to the amount of computational resources units. The resource units

in space and time are defined by the particular choice of abstract model, which is the Turing Machine. Additional complexity classes arise when considering RAMs and PRAMs, as well as other abstract models not considered here. For additional and detailed information on complexity classes, Zomaya (see 1996, ch. 4).

The two fundamental complexity classes are P and NP. P is defined as the set of problems that can be computed by a Deterministic Turing Machine (DTM) in polynomial time, poly(n) (that is, the time $T(n)$ where n is a polynomial). This can be specified explicitly as:

$$\mathrm{P} = \mathrm{DTIME}(\mathrm{poly(n)}) \tag{A.10}$$

where DTIME denotes deterministic time. The set of problems that can be solved by a Non-Deterministic Turing Machine (NTDM) in polynomial time (and consequently, by a DTM in exponential time, which is denoted by exppoly(n)) is defined as

$$\mathrm{NP} = \mathrm{NTIME}(\mathrm{poly(n)}) \tag{A.11}$$

where NTIME denotes non-deterministic time. It is believed that P is a subset of NP, but a formal proof of this remains an open problem in complexity theory. However, due to the definitions of the DTM and NDTM, the following relationships apply:

$$\mathrm{DTIME}(\mathrm{poly(n)}) \subseteq \mathrm{NTIME}(\mathrm{poly(n)}) \tag{A.12}$$

$$\mathrm{NTIME}(\mathrm{poly(n)}) \subseteq \mathrm{DTIME}(\mathrm{exppoly(n)}) \tag{A.13}$$

There are also additional relative classes of NP, such as co-NP, NP-hard and NP-complete. Whereas NP is defined as the set of problems for which a NDTM can determine the solution "yes" in polynomial time, the set of 'complementary' problems,

which are problems that determine the solution "no" in polynomial time, is defined as co-NP. A problem, X, is NP-hard if every problem in NP can be reduced to X running in polynomial time. If X itself is NP, it is NP-complete. Task scheduling, discussed in section A.2.7, is known to be NP-complete.

Problems in NP or co-NP can be solved using a polynomial amount of space by a DTM. Therefore the class PSPACE is defined for which NP and co-NP are contained. Analogous to NP-hard and NP-complete problems, there also exist PSPACE-hard and PSPACE-complete problems. The existence of PSPACE-complete problems demonstrates that although there are problems that can be solved in a reasonable amount of space, these problems are not necessarily solvable in a reasonable amount of time. All polynomial time problems can be solved in a polynomial amount of space by a DTM, but not conversely.

It is typically difficult to find fast parallel algorithms for hard or complete problems, as opposed to NP or P problems. However, there exist complexity classes within P and NP (substructure) that are sublinear; they have growth rates that are slower than polynomials. Examples of sublinear classes are L (also known as DLOGSPACE), which is similar to PSPACE but bounded by $O(\log n)$, NL, co-NL and NC (Nick's Class) [1]. Such classes generally involve problems that allow for fast parallel algorithms.

MPPNP is a large program that solves a large variety of different problems. The majority of these problems can be solved directly using arithmetic and are therefore in P, but there exist some problems that belong to the NP class. Complexity classes factor into the decision of the choice of granularity for which to parallelise MPPNP (see section A.2.6).

[1] Nick's Class is defined as the class of decision problems solvable by a PRAM with a polynomial bound on the processors (space) and a polylogarithmic timebound; NC($n^{O(1)}$, $(\log n)^{O(1)}$)

A.2.5 Embarrassingly parallel computation

In some situations it is possible for a task to be split into a number of identical parts, which can be independently performed by separate processors simultaneously. Generally, no communications between processors or special techniques or algorithms are required in these situations, allowing for simple parallelisation schemes. This is known as embarrassingly parallel computing (Wilkinson & Allen, 2004, ch. 3). Splitting a sequential task into a series of smaller tasks to run in parallel is known as partitioning.

In embarrasingly parallel problems, the workload is normally predesignated. That is, a fixed amount of work is designated to processors only at the start of the program. Work is designated by the use of a conditional construct or constructs whose arguments feature the process rank or the total number of processes. Fig. A.5 shows an example of an embarrasingly parallel program. The program is executed and parallelism is initiated using `MPI_INIT`, `MPI_COMM_RANK` and `MPI_COMM_SIZE` where `iid` is the rank of each process (a positive integer starting from 0) and `inumprocs` is the total number of processes. `ierr` is a variable found in many MPI functions that returns an error should anything go wrong in the execution of the program and can be used for debugging and error checking. These three statements are typically the first three MPI calls of an MPI program. The statement `if (iid == 0)` is the condition forcing a single process to accept user input (in this case, the number of iterations of a loop). Once the user has entered a value, a message containing the input data is sent to every process, as each process operates on the following loop and therefore requires the variable to compute it. This message is sent using a broadcast command, `MPI_BCAST`. The arguments of `MPI_BCAST` specify the variable being sent, how many items are being sent, the data

type, the source of the message and the communicator[2].

Once the message is sent, every process has the required information to perform the calculation and the next step is to split the calculation over all processors. In Fig. A.5 this was achieved using an iterative loop where the total number of iterations is split evenly over all processors. The `iid` sets a different 'start' point for each processor and then the loop is incremented depending on the number of processors. Each processor therefore calculates its own iterations without any message passing involved between processors. This is an example of loop splitting. If, for example, the loop 'sums' some value, it is possible to collect all of the partial sums determined by each individual processor automatically using `MPI_REDUCE`. This function takes the variable specified in its argument and performs the sum. Once the sum is performed, the function then deposits the answer to the destination (in this case, process 0). `MPI_REDUCE` also allows other operations, such as subtraction.

If a program cannot be parallelised without requiring interactions between processing units, the program is no longer embarrassingly parallel and requires more sophisticated schemes. Such schemes can be determined using partitioning (with interactions between processors) or divide-and-conquer[3] stategies (see Wilkinson & Allen, 2004, ch. 4).

A.2.6 Granularity

If another iterative loop, an 'outer' loop, is placed surrounding the loop in Fig. A.5, the 'inner' loop, the set of calculations are repeated numerous times. This outer loop

[2]A communicator is the name given to the context, or group of processes.

[3]The divide-and-conquer strategy partitions a large task into smaller tasks that have the same form as the large task, often recursively.

```
program main

...

! Initiate parallelisation
call MPI_INIT(ierr)
call MPI_COMM_RANK(MPI_COMM_WORLD, iid, ierr)
call MPI_COMM_SIZE(MPI_COMM_WORLD, inumprocs, ierr)

! Get input data (number of iterations) from the user
if (iid == 0) then
     read *, iuseriter
end if

! Broadcast the input data to all users
call MPI_BCAST(iuseriter, 1, MPI_INTEGER, 0, MPI_COMM_WORLD, ierr)

! Perform the calculation
do I = iid+1, iuseriter, inumprocs

     <calculations>
     ...
end do

! Collect partial sums
call MPI_REDUCE(<result>, <answer>, 1, MPI_DOUBLE_PRECISION, // &
                & MPI_SUM, 0, MPI_COMM_WORLD, ierr)

call MPI_FINALIZE(ierr)
end program main
```

Figure A.5: An example of an embarrassingly parallel program.

could then be parallelised instead of the inner loop, whereby each processor performs the whole set of calculations rather than a part of the set. Applications like this are sometimes referred to as 'farming' applications due to the following analogy: each set of calculations is represented by a field of crops and each processor is represented by a farmer. One can parallelise the task of bringing in the harvest either by applying all the farmers to one field and then repeat the process for all fields or by assigning one farmer to each field. Therefore, depending on how parallelism is assigned, one can modify the 'scope' of the parallelisation (that is, the level at which the parallelism is implemented). Depending on whether the parallelism is applied to arithmetic at the bit level, or at the procedural level, the granularity can be described as *fine*, *medium* or *coarse* (Zomaya, 1996, p. 12). The farming method described above is also an embarrassingly parallel problem, but it has a coarser granularity than the parallel program in Fig. A.5.

An advantage of using a coarse-grain parallelisation is flexibility; the nature of the calculations can change within the same iterative loop using conditional constructs and/or subroutine calls. If a module is added to the program at a later date, the source code can simply be referenced, or 'pasted' into the main program to parallelise it, without making any major modifications to the code. It is even possible to modularise a program fully so that multiple processors can farm unrelated problems. Therefore, a coarser parallelisation is beneficial for programs that are constantly changing or contain NP problems and can therefore vary in execution time.

However, if the level of granularity is coarser it is more likely that at run-time there will be idle processors present due to load imbalances, which can represent a significant source of wastage (see section A.2.7.1). This problem can be ameliorated by using a finer granularity, but it must be noted that a finer grain parallelisation generates more communication overhead. In fact, this overhead has led to a quantitative

definition of granularity, which is the ratio of the time spent performing computations and the time spent communicating. When designing a parallel system, the granularity must be considered to ensure that at run-time the time spent performing computations is maximized and the time lost through load imbalancing and spent communicating is minimized.

A coarse grain parallelisation was chosen for MPPNP at the level of the calculation of the nuclear reaction network for each 1D spherical shell. Each shell involves a unique reaction network calculation dependent on the input parameters that vary as a function of radius, or mass coordinate, from the centre of the star to the surface. This calculation does not depend on the calculations performed on other shells, so parallelising at this level of granularity does not require communications between processors. The program is therefore embarrassingly parallel, which is desireable for a simple implementation of parallelism. However, some of the problems involved in calculating the reaction network are contained in NP (such as adaptive timestepping), or in P but are strongly dependent on the input parameters (such as the matrix inversion algorithm, which varies as $O(n^3)$ (Press et al., 1992, p. 39)). Therefore the workloads of each processor differ. It is advantageous, in this case, to use a scheduling routine to distribute work in order to avoid having significant time wastage due to idle processors.

A.2.7 Scheduling

In sec. A.2.5, the tasks were assigned to processors at the start of the program. This method requires that any distribution of work over the processors is specified precisely in the source code, which is reasonable for a stable platform, and whenever the program requires a change in workload, the programmer can change how it is assigned

before compiling the program again. However, even if a parallel system has identical processors, processors can be affected significantly by the physical environment, faults, competing resources, etc. Therefore, the possibility of a program adapting to its environment whenever there are any detrimental effects is aesthetic. The problem of allocating tasks to resources, such as processors, in the most optimal way is known as the task allocation problem. This problem is solved by load balancing, which is achieved using a static or dynamic task scheduler (Zomaya, 1996, ch. 9). A static scheduler aims to parameterise tasks and resources in order to estimate the sizes of tasks and determine the optimal allocation of those tasks to the available resources. A dynamic scheduler determines during run-time how tasks should be allocated, which can either use parameters like a static scheduler or employ a purely First-In-First-Out (FIFO) policy, whereby tasks are allocated the moment a processor becomes available for work. In addition, the scheduler may be deterministic or non-deterministic. In a deterministic scheduler, all of the tasks are known prior to operation and can be distributed accordingly. In a non-deterministic scheduler, the task size may vary whilst the program is running.

A.2.7.1 Load balancing

The best scheduler is one that aims to reduce the program execution time by distributing work such that the time spent by idle processors is minimal. Consider a system with two processors, A and B. If the clock speed of both processors is the same, then work should be distributed evenly across both processors for maximum efficiency. If A has twice the clock speed of B and the work is distributed evenly, A finishes its job before B and A is idle whilst B continues its calculations. The stage of the program

when A is idle but B is not is known as the maximal parallelization stage (Cirne et al., 2007). The aim of load balancing is to minimize the maximal parallelization time, which is the time spent during the maximal parallelization stage.

It is clear that assigning 2/3 of the work to A and 1/3 to B is a better solution in this case. However, in many cases the exact processor speed or amount of work is unknown, or deviates from parametric estimates. Any program must balance the load across processors 'like a jigsaw' where each 'piece' of work is fit into the available processors such that the final work of each processor is the same, or if there are processors with differing speeds, the work is distributed so that each processor operates for the same amount of time. A Gantt chart (Fig. A.6) shows this process diagrammatically and is often used to picture load balancing and assess the performance of load-balancing subroutines. In this particular case, tasks numbered 1 to 6 are assigned using a FIFO dynamic scheduler. Shaded regions correspond to idle processor time, which could arise due to the time required for communications, master processing, or because no more work is available for assignment.

Although the solution is easy to envisage in this way, the problem is NP-complete and cannot be calculated easily. Nevertheless, there are measures that can be taken to reduce the maximal parallelization time. One method is to sort the tasks so that the largest tasks are assigned first and the smallest tasks are assigned last. Another measure is to reduce the ratio of the size of the tasks to the number of tasks (that is, to have more small tasks rather than fewer large tasks). This last measure is known to be the main factor in obtaining an optimal solution for a variety of different schedulers (Cirne et al., 2007).

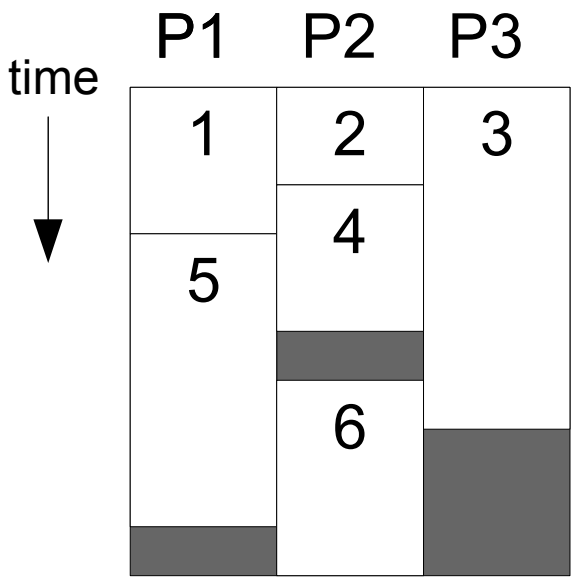

Figure A.6: An example Gantt chart with six tasks assigned in order using a FIFO scheduler. Pn denotes processor n. Shaded regions correspond to idle processor time.

A.2.7.2 The master-slave algorithm

A master-slave algorithm is an example of a FIFO dynamic task scheduler, also known as a master-worker algorithm or a work-pool algorithm, wherein 'master' processes allocate tasks to 'slave' processes, with all main computation carried out by the slaves. Fig. A.7 demonstrates this algorithm (Gropp et al., 1999, p. 35-42). In such a system,

there would be very few masters (typically a single master) with many slaves. In Fig. A.7 the program is split up into the master and slave parts using an 'if' condition. The code for the master constitutes the sending of information to slaves and organising the resulting answer, whereas the code for the slaves constitutes performing calculations and sending the answer back to the master. The master code may bias the distribution of work. This can be important in programs that read data from an external device or file; the input parameters for the program being random or unpredictable.

The algorithm reduces the impact of unexpected side-effects on processor operation. However, no other fault tolerance is applied and dynamic schedulers can suffer from significant communication overhead. Communication overhead can become a big problem in systems where the number of processors is very high resulting in a degradation in the overall performance.

A.3 Performance analysis of MPPNP

Ideally, one expects that the speed-up is linear with the number of processors, that is, if the number of processors is doubled, the duration of the execution time of the parallel program is halved. However, the speed-up attained is often affected by additional side-effects, such as communication overhead and load imbalances, which are often processor dependent. These effects can be shown by plotting a scaling graph, which is determined by plotting the inverse of the program duration (which is proportional to the speed-up) as a function of the number of processors. On logarithmic axes, the ideal scaling line is a straight line. Any deviations to the ideal scaling line are due to undesireable side-effects. Fig. A.8 shows a typical scaling plot of MPPNP. The plot

```
program main
     ...
     call MPI_INIT(ierr)
     call MPI_COMM_RANK(MPI_COMM_WORLD, iid, ierr)
     call MPI_COMM_SIZE(MPI_COMM_WORLD, numprocs, ierr)

     ! This is the master part of the program
     if (iid == master) then
          ...
          ! Send each process some work to start off
          ! (work is an array of integers)
          do i = 1, numprocs - 1
               buffer = work(i)
               call MPI_SEND(<buffer to ith slave>)
               numsent = numsent+1
          end do

          ! When master receives an answer, it assigns it to 'answer'
          ! and sends more work to the slave
10        call MPI_RECV(<answer from any slave>)

          final_answer = final_answer + received_answer
          if (<more work>) then
               buffer = work(numsent+1)
               call MPI_SEND(<buffer to the slave that sent the answer>)
               numsent = numsent+1
          else
               <stop sending work>
          end if
               goto 10
     else
          ! This is the slave part of the program
20        call MPI_RECV(<buffer from master>)

          <calculations>
          ...
          call MPI_SEND(<answer to master>)
          go to 20
     end if

     call MPI_FINALIZE(ierr)
end program main
```

Figure A.7: The master-slave algorithm.

was determined using test runs performed on the KHAOS cluster at Keele University, where the time to post-process the first 2000 cycles of a $15M_{\odot}$ massive star model was recorded for various numbers of slave processors. For comparison, a full post-processing run normally requires the calculation of $\sim 10^5$ cycles. Post-processing more cycles will increase the time spent by the program running parallel computations instead of serial ones, thereby reducing the impact of the serial start-up cost and improving the scaling relation. On the other hand, the calculations performed by each processor increase for later cycles due to the larger reaction networks required to calculate the burning for the advanced stages of the star. Therefore the scaling relation is time-dependent.

An analytical approach can be made to determine some useful properties of the parallel nature of the algorithm. This can be done by considering the time spent performing computations and the time spent communicating. Other side effects are not considered in this approach since they are difficult to predict and can usually be considered as negligible second-order effects.

A.3.1 Computations

The master-slave algorithm (see Fig. A.7) farms over a number of sets of calculations. Using the predefined measures from the PRAM model, it is possible to predict the execution time of the algorithm. It is assumed here that the system has enough space to store all relevant variables and that the processors are identical and maintain a constant clock speed.

The serial time is made up of computations made before and after the master slave algorithm and can be estimated as At_{flop}, where A is the number of floating point operations (flops) involved and t_{flop} is the execution time of one flop. Different types of

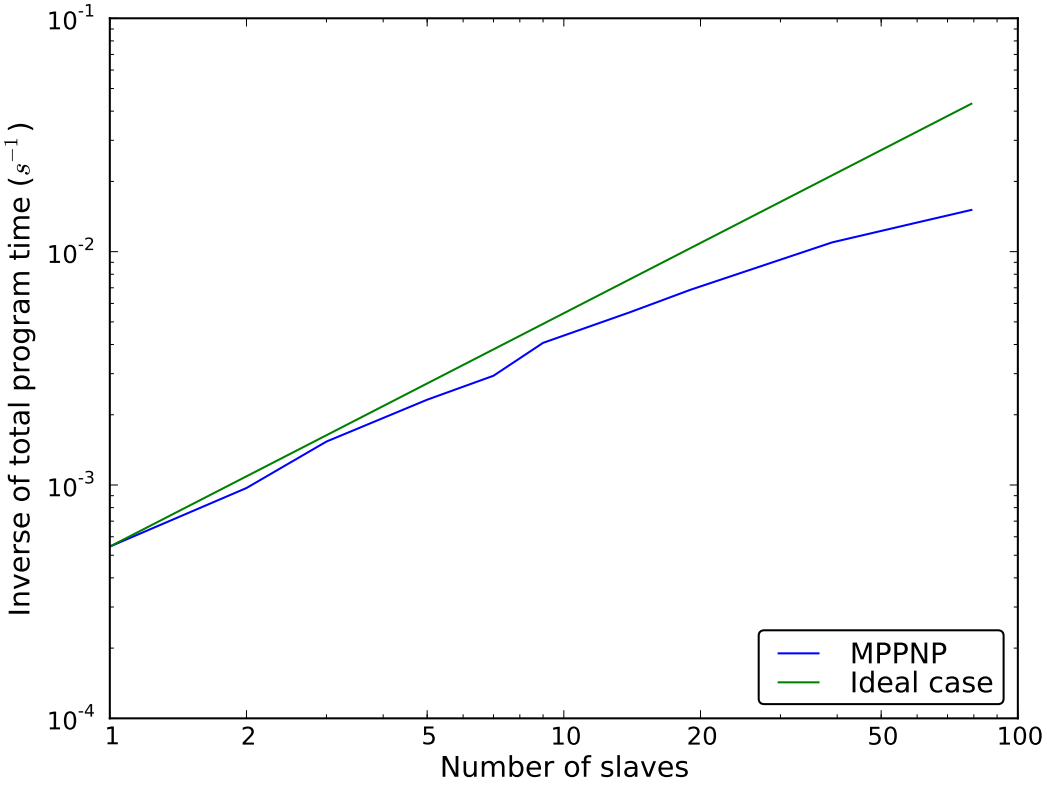

Figure A.8: Scaling of MPPNP from a test run. There is a deviation away from perfect scaling as the number of processors becomes large. The test takes $1835s$ to run using one slave (almost serial) and the ideal scaling line is normalised to this value.

floating point arithmetic operations are assumed to be take the same time to compute.

If each set of calculations performed by slaves involves B flops, then the total number of computations made in the parallel part of the program is $Bn + Cn$ where n is the number of sets of calculations shared over all slave processors, p, and C is the number of flops performed by the master in assigning work to send to a slave, receiving the answer and assigning and modifying the result. The work Bn is shared over all processors. Thus the total time spent performing parallel computations is $(Bn/p + Cn)t_{flop}$.

The total execution time, t_{comp}, is the sum of these contributions,

$$t_{comp} = At_{flop} + (Bn/p + Cn)t_{flop} = (A + Bn/p + Cn)t_{flop} \tag{A.14}$$

It is also possible to consider an unparallelised algorithm by setting $p = 1$ and $C = 0$. The computations C may, however, include modifications to the results, M, that need to remain in the serial program. These are generally performed for each set of calculations, so B can be redefined as $B' = B + M$ and

$$t_s = (A + B'n)t_{flop} \tag{A.15}$$

A.3.2 Communications

There are two main sources of communications in MPPNP: broadcasts and message-passing during the master-slave algorithm execution. In both cases, communications can be considered in the same way as in section A.3.1.

Concerning the master-slave algorithm, the total number of messages required in

the computation of one set of calculations is given by the sum of the messages sending work from the master to the slave, the messages from the slave to the master replying with an answer, and the termination messages. Messages have a startup cost, t_{start}, so the time to send a single message, t_m, can be estimated as

$$t_m = t_{start} + xt_{data}, \tag{A.16}$$

where t_{data} is the time to send one byte of data and x is the number of bytes of data in the message (or 'size'). If each message sent to a slave has size D, which replies with an answer of size E, then the total time spent sending messages, t_{comm1} is

$$\begin{aligned} t_{comm1} =& n(t_{start} + Dt_{data}) + n(t_{start} + Et_{data}) + p(t_{start} + t_{data}) \\ =& (2n + p)t_{start} + (nD + nE + p)t_{data}, \end{aligned} \tag{A.17}$$

assuming that termination messages take the same amount of time to send as data messages.

Broadcasts are a form of collective communications used to share information over all processors that are used primarily at the initiation of the program in order to communicate nuclear reaction rate information to all slaves[4]. Broadcasts are messages sent to all machines, following the node structure of the network, and the p-dependence of the broadcasts depends on this node structure and the architecture of the nodes. The theoretical p-dependence of the broadcast time for '1-to-N fan-out' broadcast and for a 'multi-level' is investigated in Wilkinson & Allen (2004, sec. 2.3.4), where the

[4]This mechanism exists as there is currently no implementation of parallel input/output (IO) and the time spent performing these operations is large. To reduce this cost, a single processor, the master, performs all IO and any variables required by the slaves are communicated via broadcasts.

former has a linear dependence on p and the latter has a logarithmic dependence. The node structure for the KHAOS cluster features a master node that splits off into 42 slave nodes using a switch, with each slave node operating two dual-core processors (providing a total of 4 slave processors per slave node). This cluster configuration results in broadcasts similar to a 1-to-N fan-out broadcast, but with each slave node having to perform additional communications between processors within the node. The mechanism of these additional communications is not clear. Therefore the p-dependence is likely to be a compromise between the linear dependence for a 1-to-N fan-out broadcast of single-level and the logarithmic dependence of multi-level broadcasts.

For simplicity and for theoretical study, the broadcasts will be estimated using a linear dependence,

$$t_{comm2} = Fpt_{data}, \tag{A.18}$$

which assumes that the start-up cost is negligible and corresponds to a situation where a master processor communicates broadcasts directly to all slave processors. The assumption is valid since the time spent performing start-up operations is of the order of a millisecond, whereas the the timescale for broadcasts (in MPPNP) is of the order of a few seconds. The total communication time is therefore

$$t_{comm} = t_{comm1} + t_{comm2} = (2n + p)t_{start} + (nD + nE + p(F + 1))t_{data}. \tag{A.19}$$

The ratio, R, of t_{comm} and t_{comp} is

$$R = \frac{t_{comm}}{t_{comp}} = \frac{(2n + p)t_{start} + (nD + nE + p(F + 1))t_{data}}{(A + \frac{Bn}{p} + Cn)t_{flop}}. \tag{A.20}$$

If $R << 1$, the communication overhead is minimal and the majority of the execution

time of the program is spent performing useful computations. If n is large,

$$R = \frac{2nt_{start} + n(D+E)t_{data}}{(\frac{B}{p} + C)nt_{flop}} = \left[\frac{2t_{start} + (D+E)t_{data}}{(B+Cp)t_{flop}}\right] \cdot p. \tag{A.21}$$

If C is negligibly small, R is linearly dependent on p. Therefore, communication overhead will become a problem when calculating the master-slave algorithm on systems with large numbers of processors. This problem can be reduced by increasing B with respect to D and E. If C is non-negligible, R asymptotically approaches the ratio

$$R = \frac{2t_{start} + (D+E)t_{data}}{Ct_{flop}}. \tag{A.22}$$

Communication overhead in this case will be less of a problem. One could reduce the need to worry about communication overhead by increasing C, but this adds more serial computation to the program and therefore one can expect the speed-up to decrease.

If p is large, then

$$R = \frac{p(t_{start} + (F+1)t_{data})}{(A+Cn)t_{flop}} \tag{A.23}$$

and the communication overhead is dominated by broadcasts and termination messages. In general, the number of processors used need never be larger than the number of sets of calculations, because in such a case there will be processors idle throughout the entire duration of the program. In any case, most problems can allow for a larger problem size n, minimizing the total communication overhead. Broadcasts could become significant source of overhead for large F, but since a typical instance of MPPNP usually operates over many timesteps (see sec. A.3.5), n is usually large enough such that the broadcasts become an allowable initialization cost rather than a significant problem.

A.3.3 Complexity

The total time of the execution of the parallel program is the sum of the computations and communications,

$$\begin{aligned} t_p =& t_{comp} + t_{comm} \\ =& (A + Bn/p + Cn)t_{flop} + (2n + p)t_{start} + (nD + nE + p(F + 1))t_{data} \end{aligned} \tag{A.24}$$

Therefore, provided B, C, D and E do not depend on n, the time complexity of the master-slave algorithm is $O(n)$. The growth rate is therefore, in the worst-case, linear. In MPPNP however, B entails a considerable amount of computations that involve, for example, recalculating the reaction rates for a specified temperature, setting up the reaction network, which is dynamic and varies with temperature, and solving the reaction network using a matrix inversion algorithm (with complexity $O(n^3)$). Therefore, B is a complicated function of n that varies between different applications of MPPNP and at different times during the execution of the program. Therefore, deviations from $O(n)$ and $O(p)$ for time and space complexities are expected.

A.3.4 Speed-up

Using Eq. A.1 for the master-slave algorithm,

$$\begin{aligned} S(n,p) =& \frac{t_s}{t_p} \\ =& \frac{(A + B'n)t_{flop}}{(A + Bn/p + Cn)t_{flop} + (2n + p)t_{start} + (nD + nE + p(F + 1))t_{data}}. \end{aligned} \tag{A.25}$$

If communications are minimal,

$$S(n,p) = \frac{t_s}{t_{comp}} = \frac{A + B'n}{A + Bn/p + Cn}. \tag{A.26}$$

Also, if n is large,

$$S(n,p) = \frac{B'}{\frac{B}{p} + C} = (\frac{B'}{B + Cp}) \cdot p. \tag{A.27}$$

The speed-up is linear with the number of processors if C is negligible, as expected from Amdahl's law. Also, if C is non-negligible, the speed-up asymptotically approaches the ratio given by

$$S = \frac{B'}{C} \tag{A.28}$$

as p increases. Comparing Eq. A.28 with Eq. A.5 yields an estimate for the serial fraction of the code,

$$f = \frac{C}{B'}. \tag{A.29}$$

Note that this estimate for the serial fraction is only true in the limit of large n and large p. A large n removes the effect of the serial computations A from the maximum speed-up and only the serial computations C, which scale linearly with n, affect the maximum speed-up. Therefore, to enhance performance, the calculations made by the slaves must be large compared to those of the master.

If the speed-up with large n is considered including communications,

$$S = \left[\frac{B' t_{flop}}{p\left(C t_{flop} + 2t_{start} + (D+E)t_{data}\right) + B t_{flop}}\right] \cdot p, \tag{A.30}$$

which is the same situation with regards to the speed-up without communications,

except that as $p \to \infty$, S asymptotically approaches a different ratio,

$$S = \frac{B' t_{flop}}{C t_{flop} + 2t_{start} + (D+E)t_{data}}. \tag{A.31}$$

In conclusion, communications reduce the maximum speed-up possible. In addition, the speed-up is no longer linear with p, even if C is neglibly small.

A.3.5 Scaling

The values of parameters A-F can be determined by counting the number of flops of computations in the algorithm and the number of bytes of data sent in messages. However, the program code is extensive and A and B are difficult to determine because the number of computations is large and varies in time. In addition, the time t_{flop} is difficult to determine theoretically as it varies between different types of processors and architectures (the relation between processor clock speed and the number of flops is not a trivial calculation). To avoid these difficulties, the parameters can be respecified in terms of a time rather than a number of computations.

The program repeats the master-slave algorithm for a number of timesteps. Rewriting Eq. A.24 including timesteps and with different parameters yields

$$t_p = A_{t1} + T\left(\frac{A_{t2}B_t n}{p} + C_t n + (2n+p)t_{start} + (nD + nE + p)t_{data}\right), \tag{A.32}$$

where $At_{flop} = A_{t1} + A_{t2}T$, $Bt_{flop} = B_t$ and $Ct_{flop} = C_t$. Some of the serial computations are only performed once, whereas some are performed at each timestep, which are A_{t1} and A_{t2} respectively. The introduction of timesteps to the equation for the total time does not change the theory of the parallel performance drastically, but describes

more specifically the operation of MPPNP, which uses timestepping. By inserting timing functions into MPPNP, A_{t1}, A_{t2} and B_t can be determined. C is small ($\sim 10^2$ flops) in MPPNP with respect to the other parameters and C_t can therefore be considered negligibly small. D and E are easily estimated as the size, in bytes, of the buffer variables used in the arguments of the `MPI_SEND` functions. The broadcasts in MPPNP were amalgamated into the measurement of A_{t1} and therefore F was omitted, a decision motivated also by the theoretical uncertainty of the unknown p-dependence of the broadcast communication time. Any variations in A_{t1} are therefore primarily due to varying broadcast times.

t_{data} was estimated using a separate program on the KHAOS cluster network. The program constitutes a two-processor algorithm where one processor sends a message of known size to a second processor, and the message, unmodified, is sent back. The process is timed, giving the duration of two message passes, for differing message sizes, with the message sizes large enough to make the duration calculable using the system clock. The total time for a single message pass is then half of this value. The main source of error originates from the precision of the system clock ($\sim 10ms$) and it is likely that the accuracy of the clock is affected by systematic errors. Therefore, the standard deviation of the data as an error estimate was preferred, raising the error from $\pm 0.005s$ to ± 0.01. The message-passing process above was repeated 100 times for each data point and the mode was taken (since variations in the time were minimal). The modes are plotted in Fig. A.9 along with a first order polynomial fit using least-squares regression. The parameter t_{data} is then given by the regression coefficient, which is $(6.62 \pm 0.11) \times 10^{-9} s\text{byte}^{-1}$. The regression constant, which is $0.007s$, provides an estimate of the parameter t_{start}, but the limited resolution of the system clock severly restricts an accurate determination of the parameter. Instead, t_{start} was chosen to be

the latency of the HP Procurve switch used by the KHAOS cluster network, which is $\sim 5.4\mu s$.

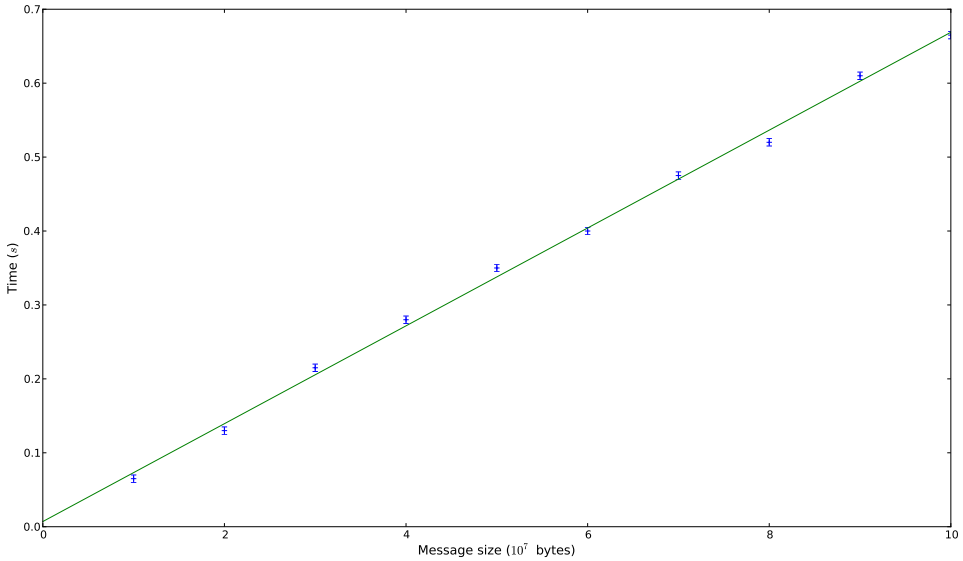

Figure A.9: The message time as a function of message size.

A $25M_{\odot}$ stellar model was repeatedly post-processed up to timestep 2000 with varying numbers of processors in order to determine the above parameters. The values for these parameters are summarised in table A.3.5. The variations of the parameters at each timestep were minimal, except for n, A_{t1}, B_t. The number of sets of calculations (per timestep), n, corresponds to the number of meshpoints used in the spatial domain which, in this case, is set by the stellar model and varies by $\sim 5\%$ around a value of 250 during the duration of the program. A_{t1} exhibits variations up to $\sim 1s$, which are likely due to the broadcasts. B_t is consistently $\sim 0.14s$ when calculating small networks, but can increase when calculating larger networks, which was by up to a factor of 2 in this test case.

Table A.1: Parameters used to determine the theoretical scaling of MPPNP.

Parameter	Value
A_{t1}	$28.37 \pm 0.01s$
A_{t2}	$0.04 \pm 0.01s$
B_t	$0.14 \pm 0.01s$
C_t	0
D	9240
E	9248
t_{start}	$5.4 \times 10^{-6}s$
t_{data}	$(6.62 \pm 0.11) \times 10^{-9}s$

In this particular test, B_t varied from between $0.13s$ and $0.28s$ throughout the duration of the program. Fig. A.10 shows the scaling of MPPNP compared to the ideal case and two theoretical scaling laws, with $B_t = 0.13s$ and $B_t = 0.28s$, using the parameters given in table A.3.5. The scaling for MPPNP deviates away from the ideal scaling line, showing that the there are indeed side effects affecting the performance of MPPNP. The theoretical curve with $B_t = 0.13s$ underestimates the total time required for MPPNP to make the calculations, which is unsurprising since the theoretical determination only includes communication overhead as a side effect. This difference could be accounted for by considering a larger average value for B_t, at approximately $0.15s$, but if additional computations were responsible for the difference in total computation time between the theoretical curve with $B_t = 0.13s$ and the experimentally determined one, one would expect this to be true for any choice of processor. Fig. A.11 shows the same scaling graph but with the theoretical curves normalised to the intercept by a constant multiplicative factor. The scaling of the theoretical curve with $B_t = 0.28s$ improves the scaling of MPPNP and the case with $B_t = 0.13s$ is not poor enough to account for the scaling of MPPNP. The increase in work cannot account for the

scaling behaviour of MPPNP and must come from another source, notably the choice of scheduler.

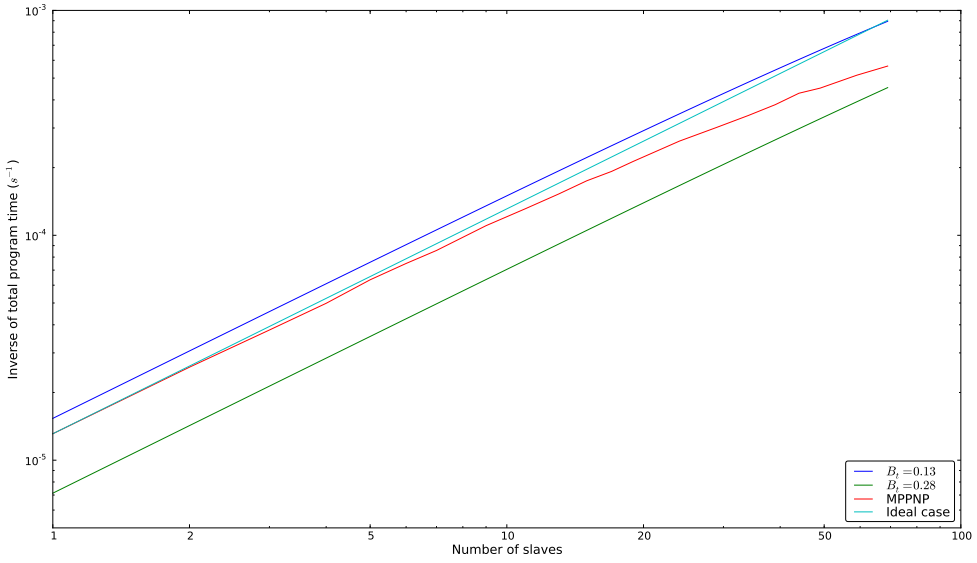

Figure A.10: MPPNP scaling plot.

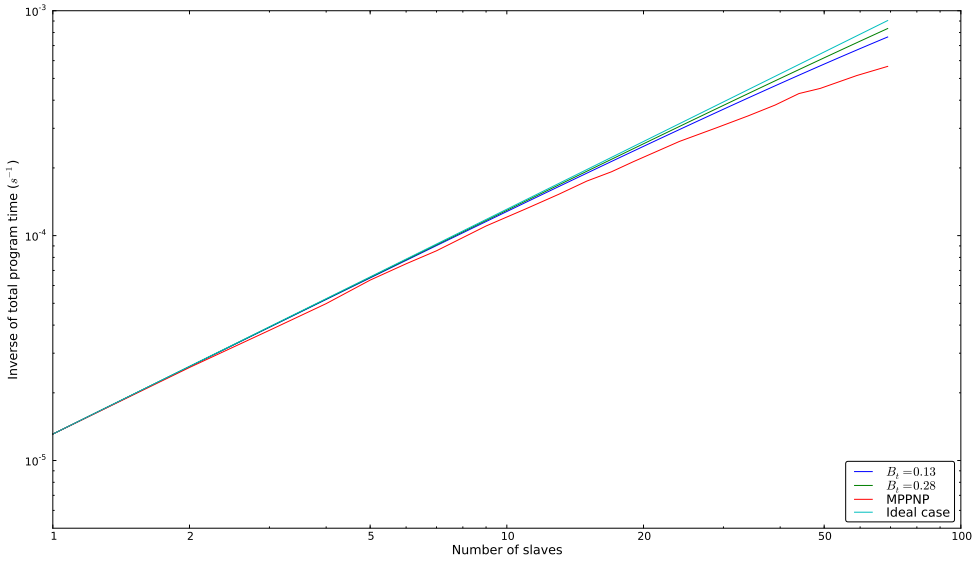

Figure A.11: MPPNP scaling plot with the theoretical curves normalised to the serial time by a constant multiplicative factor.

B Finite difference schemes for diffusion

This appendix outlines the equations and numerical methods used for the diffusion programs used in §5, together with numerical tests. Finite difference methods are formulated in order to solve Fick's second law (Eq. 5.3), which is

$$\frac{\partial X}{\partial t} = \frac{\partial}{\partial x}\left(D\frac{\partial X}{\partial x}\right), \tag{B.1}$$

where $X(x,t)$ is the mass fraction abundance of the diffusing substance as a function of space, x, and time, t, and D is the diffusion coefficient. Given some initial abundance profile, $X(x,0)$, and 'input' diffusion coefficients, Eq. B.1 gives the evolution of the abundance profile over time. The mixing described by diffusion is one that acts to smooth out any abundance gradients over time. Alternatively, Eq. B.1 can be used to solve for 'output' diffusion coefficients, D, when $X(x,t)$ is known.

Two diffusion programs were used: one that simulates implicitly the diffusion of an initial abundance profile over time with input diffusion coefficients and one that calculates output diffusion coefficients when provided with abundance profiles as a function of time. Diffusion simulations were generated in order to test the accuracy of the programs. The test case is the diffusion of an initial profile given by a step function with a constant diffusion coefficient, since analytical solution for this situation exist that can be compared with the output abundance profiles. The diffusion coefficient calculator was then invoked to see if the calculated diffusion coefficients compared well with the input coefficients.

Note that in this work, two methods for calculating diffusion coefficients are specified. The first is an 'instantaneous' calculation, which calculates $D = D(x,t)$, and

a 'constant D' calculation, where the diffusion coefficients are assumed to be constant in time. Both of these methods are used in §5.

B.1 Solving Fick's second law for $X(x,t)$

B.1.1 Explicit method and Von Neumann stability analysis

A finite differencing method can be applied to solve Eq. B.1 for $X(x,t)$ by replacing the infinitesimal derivatives with larger differences. This gives

$$\frac{\Delta X}{\Delta t} = \frac{\Delta}{\Delta x}\left(D\frac{\Delta X}{\Delta x}\right). \tag{B.2}$$

In a two-dimensional cartesian coordinate system with x as the asbcissa and t as the ordinate, one can define points in the parameter space defining a semi-infinite mesh with indices $k = 0, 1, 2, \ldots, M$ and $n = 0, 1, 2, \ldots$, corresponding to the spatial and temporal coordinates respectively. The value of a variable in this coordinate system is then specified as X_k^n, which is equivalent to $X(x,t) = X(k\Delta x, n\Delta t)$ where Δx and Δt are the distances between adjacent mesh points. If Δx and Δt are constant, the mesh is uniform and static. If $\Delta x = \Delta x(x,t)$ or $\Delta t = \Delta t(x,t)$, the mesh is variable and non-uniform. Rewriting the Δ quantities in Eqn. B.2 as mesh quantities on a temporally static mesh gives

$$\frac{X_k^{n+1} - X_k^n}{\Delta t} = \frac{1}{x_{k+1/2} - x_{k-1/2}}\left[\left(D_{k+1/2}\frac{X_{k+1}^n - X_k^n}{x_{k+1} - x_k}\right) - \left(D_{k-1/2}\frac{X_k^n - X_{k-1}^n}{x_k - x_{k-1}}\right)\right] \tag{B.3}$$

where the explicit formulation is used. This is the formulation where variables at coordinate n are used to evaluate X^{n+1}. This is also known as a Forward-Time Centred-Space (FTCS) scheme. The known quantities in a typical calculation are D_k^n and an initial abundance profile X_k^0, which therefore makes the calculation of quantities X_k^n for all n and k straightforward.

One can verify the stability of a numerical scheme by using the Von Neumann stability analysis (Press et al., 1992, Ch. 19.1). This asserts that solutions to X_k^n are of the form:

$$X_k^n = \xi^n e^{ijk\Delta x} \tag{B.4}$$

where j is a spatial wave number and $\xi = \xi(j)$ is the amplification factor. If $|\xi(j)| > 1$, then the errors associated with the evaluation of X_k^{n+1} increase with each calculation and the scheme can be described as unstable. By substituting Eq. B.4 into Eq. B.3, the amplification factor can be determined. For the case of a constant diffusion coefficient in time and a uniform mesh, this factor is

$$\xi = 1 - \frac{4D\Delta t}{(\Delta x)^2} \sin\left(\frac{j\Delta x}{2}\right). \tag{B.5}$$

For stability, $|\xi| \leq 1$, which gives the Courant condition

$$\frac{2D\Delta t}{(\Delta x)^2} \leq 1. \tag{B.6}$$

Therefore, the application of an explicit FTCS scheme is stable provided that the inequality B.6 is true. For the case of a diffusion coefficient that varies with x, the condition for stability is

$$\Delta t \leq \min_j \left[\frac{(\Delta x)^2}{2D_{k+1/2}}\right]. \tag{B.7}$$

That is, for a given $D = D(x)$ and Δx, Δt should be small enough so that the Courant condition holds over all space. Therefore, explicit computations can become limited to small choices of Δt in order for the numerical scheme to become stable. Such a problem is often found in stellar evolution models, where the timesteps required are large ($\sim 10^{12}$ s) compared to the mixing timescale (~ 1 s). The problem can be alleviated by using an implicit scheme.

B.1.2 Implicit method

In an implicit scheme, X^{n+1} is evaluated using quantities at $n+1$ instead of at n:

$$\frac{X_k^{n+1} - X_k^n}{\Delta t} = \frac{1}{x_{k+1/2} - x_{k-1/2}} \left[D_{k+1/2} \left(\frac{X_{k+1}^{n+1} - X_k^{n+1}}{x_{k+1} - x_k} \right) - D_{k-1/2} \left(\frac{X_k^{n+1} - X_{k-1}^{n+1}}{x_k - x_{k-1}} \right) \right]. \tag{B.8}$$

By setting $x_r = x_{k+1} - x_k$, $x_l = x_k - x_{k-1}$ and $x_m = x_{k+1/2} - x_{k-1/2} = \frac{x_{k+1} - x_{k-1}}{2}$, the following equation is obtained:

$$\begin{aligned} X_k^n = &- \frac{D_{k+1/2}\Delta t}{x_m x_r} \cdot X_{k+1}^{n+1} + \left(1 + \frac{D_{k+1/2}\Delta t}{x_m x_r} + \frac{D_{k-1/2}\Delta t}{x_m x_l} \right) \cdot X_k^{n+1} \\ &- \frac{D_{k-1/2}\Delta t}{x_m x_l} \cdot X_{k-1}^{n+1}. \end{aligned} \tag{B.9}$$

This can be solved using a tridiagonal solver (see for example Press et al., 1992, Ch. 2.4) with coefficients:

$$\begin{aligned} a &= -\frac{D_{k+1/2}\Delta t}{x_m x_r} \\ b &= \left(1 + \frac{D_{k+1/2}\Delta t}{x_m x_r} + \frac{D_{k-1/2}\Delta t}{x_m x_l}\right) \\ c &= -\frac{D_{k-1/2}\Delta t}{x_m x_l} \\ r &= X_k^n. \end{aligned} \tag{B.10}$$

At the boundaries, it is possible to approximate values of x_m, x_r or x_l that are undefined by using x_r or x_l. The tridiagonal coefficients become

$$\begin{aligned} a &= -\frac{D_{k+1/2}\Delta t}{x_r^2} \\ b &= \left(1 + \frac{D_{k+1/2}\Delta t}{x_r^2}\right) \\ c &= 0 \end{aligned} \tag{B.11}$$

at the left-hand boundary and

$$\begin{aligned} a &= 0 \\ b &= \left(1 + \frac{D_{k-1/2}\Delta t}{x_l^2}\right) \\ c &= -\frac{D_{k-1/2}\Delta t}{x_l^2} \end{aligned} \tag{B.12}$$

at the right-hand boundary (where $k = M$). r is unchanged. The final matrix equation has the form

$$\mathbf{G} = \begin{pmatrix} b_1^n & c_1^n & 0 & 0 & \dots & & \\ a_2^n & b_2^n & c_2^n & 0 & \dots & & \\ 0 & a_3^n & b_3^n & c_3^n & \dots & & \\ \vdots & \vdots & \vdots & \vdots & \ddots & & \\ & & & a_{m-1}^n & b_{m-1}^n & c_{m-1}^n & \\ & & & 0 & a_m^n & b_m^n \end{pmatrix} \begin{pmatrix} X_1^{n+1} \\ X_2^{n+1} \\ X_3^{n+1} \\ \vdots \\ X_{m-1}^{n+1} \\ X_m^{n+1} \end{pmatrix} - \begin{pmatrix} X_1^n \\ X_2^n \\ X_3^n \\ \vdots \\ X_{m-1}^n \\ X_m^n \end{pmatrix}. \quad \text{(B.13)}$$

Performing a Von Neumann stability analysis gives the amplification factor for the implicit method. For a constant diffusion coefficient in time and a uniform mesh,

$$\xi = \frac{1}{1 + 4\frac{D\Delta t}{(\Delta x)^2}\sin^2\left(\frac{j\Delta x}{2}\right)}. \quad \text{(B.14)}$$

Since Δx, Δt and D are positive quantities, the denominator of Eq. B.14 is always greater than 1. Consequently, $\xi(j) \leq 1$ for all j and the scheme is unconditionally stable.

B.2 Solving Fick's second law for D

There are typically two methods of evaluating diffusion coefficients. They can be evaluated either by matching concentration profiles as a function of time from an experiment (or computer simulation) with analytical or numerical concentration profiles evaluated using known diffusion coefficient, or by direct evaluation using known concentration-

distance profiles. Concerning the direct evaluation, there are two main methods of evaluation: an integrating method, such as the Boltzmann-Matano method, or a direct 'brute force' numerical technique, such as finite differencing.

In this section, finite differencing methods for solving Fick's second law are specified for the 1D case. Rearranging Eq. B.8 for $D_{k+1/2}$ gives

$$D_{k+1/2} = \left[\frac{x_{k+1} - x_k}{X^n_{k+1} - X^n_k}\right]\left(\frac{(x_{k+1/2} - x_{k-1/2})(X^{n+1}_k - X^n_k)}{\Delta t} + D_{k-1/2}\left[\frac{X^n_k - X^n_{k-1}}{x_k - x_{k-1}}\right]\right). \tag{B.15}$$

If $X(x,t)$ is known, $D_{k+1/2}$ can be calculated using a boundary condition for $D_{k-1/2}$. Repeated iterations over the k coordinate space provide D for all k. A more convenient description is to form a set of coupled equations for $D = D(x,t)$ and solve the system of equations inside a choice of domain where diffusion is occurring.

Eq. B.8 can be rewritten as

$$G_{k-1/2} = P_{k-1/2}D_{k-1/2} + Q_{k-1/2}D_{k+1/2} - R_{k-1/2} = 0, \tag{B.16}$$

where

$$\begin{aligned} P_{k-1/2} &= \left(\frac{X^{n+1}_k - X^{n+1}_{k-1}}{x_m x_l}\right) \\ Q_{k-1/2} &= -\left(\frac{X^{n+1}_{k+1} - X^{n+1}_k}{x_m x_r}\right) \\ R_{k-1/2} &= \frac{X^{n+1}_k - x^n_k}{\Delta t}. \end{aligned} \tag{B.17}$$

This equation can be written in the matrix form $\mathbf{Ax} = \mathbf{B}$, where the coefficients of the

matrix are formed from Q and P as follows:

$$\mathbf{G} = \begin{pmatrix} P_1 & Q_1 & 0 & 0 & \dots & \\ 0 & P_2 & Q_1 & 0 & \dots & \\ 0 & 0 & P_3 & Q_3 & \dots & \\ \vdots & \vdots & \vdots & \vdots & \ddots & \\ & & & P_{m-2} & Q_{m-2} & \\ & & & 0 & P_{m-1} & \end{pmatrix} \begin{pmatrix} D_1 \\ D_2 \\ D_3 \\ \vdots \\ D_{m-2} \\ D_{m-1} \end{pmatrix} - \begin{pmatrix} R_1 \\ R_2 \\ R_3 \\ \vdots \\ R_{m-2} \\ R_{m-1} \end{pmatrix}, \tag{B.18}$$

where m is the total number of meshpoints and $k - \frac{1}{2} \rightarrow k$ for convenience. The bidiagonal matrix of coefficients can be calculated using a tridiagonal solver with

$$a = 0, \quad b = Q, \quad c = P, \quad r = R. \tag{B.19}$$

It must be noted that the choice of boundary condition is a Dirichlet boundary condition, where the diffusion coefficient is zero outside the considered spatial domain.

B.2.1 Diffusion coefficients that are constant in time

So far, the calculation of D has assumed that $D = D(x,t)$. One can consider a diffusion coefficient that is constant in time ($D = D(x)$), which gives an alternative finite difference scheme for calculation of the diffusion coefficient. The 1D diffusion equation can be rearranged in the following way:

$$X_k^{n+1} = X_k^n + \frac{\Delta t}{x_m}\left(D_{k+1/2}\frac{X_{k+1}^n - X_k^n}{x_r} - D_{k-1/2}\frac{X_k^n - X_{k-1}^n}{x_l}\right). \tag{B.20}$$

Defining $X^n_{k+1/2} = X^n_{k+1} - X^n_k$ and $X^n_{k-1/2} = X^n_k - X^n_{k-1}$:

$$X^{n+1}_k = X^n_k + \frac{\Delta t}{x_m}\left(D_{k+1/2}\frac{X^n_{k+1/2}}{x_r} - D_{k-1/2}\frac{X^n_{k-1/2}}{x_l}\right). \tag{B.21}$$

Similarly:

$$X^{n+2}_k = X^{n+1}_k + \frac{\Delta t}{x_m}\left(D_{k+1/2}\frac{X^{n+1}_{k+1/2}}{x_r} - D_{k-1/2}\frac{X^{n+1}_{k-1/2}}{x_l}\right). \tag{B.22}$$

If one substitutes X^{n+1}_k into the first term of the RHS,

$$\begin{aligned} X^{n+2}_k =& X^n_k + \frac{\Delta t}{x_m}\left(D_{k+1/2}\frac{X^{n+1}_{k+1/2}}{x_r} - D_{k-1/2}\frac{X^{n+1}_{k-1/2}}{x_l}\right) + \\ =& \frac{\Delta t}{x_m}\left(D_{k+1/2}\frac{X^n_{k+1/2}}{x_r} - D_{k-1/2}\frac{X^n_{k-1/2}}{x_l}\right) \\ =& X^n_k + \frac{\Delta t}{x_m}\left(\frac{D_{k+1/2}}{x_r}\left(X^{n+1}_{k+1/2} + X^n_{k+1/2}\right) - \frac{D_{k-1/2}}{x_l}\left(X^{n+1}_{k-1/2} + X^n_{k-1/2}\right)\right) \end{aligned} \tag{B.23}$$

is obtained. With repeated substitutions up to some temporal meshpoint s, the equation becomes

$$X^s_k = X^0_k + \frac{\Delta t}{x_m}\left(\frac{D_{k+1/2}}{x_r}\sum_{n=0}^{s-1} X^n_{k+1/2} - \frac{D_{k-1/2}}{x_l}\sum_{n=0}^{s-1} X^n_{k-1/2}\right). \tag{B.24}$$

This can either be evaluated directly or by using a matrix interpretation similar to the previous case, which can also be solved using a tridiagonal solver. In this case $n = 0$ corresponds to $t = t_0$ and $n = s$ corresponds to $t = t_0 + s\Delta t$. The summation terms in Eq. B.24 could be replaced with $X^s_{k+1/2} - X^0_{k+1/2}$ and $X^s_{k-1/2} - X^0_{k-1/2}$. If the timesteps

are non-uniform,

$$X_k^s = X_k^0 + \frac{1}{x_m}\left(\frac{D_{k+1/2}}{x_r}\sum_{n=0}^{s-1}(t^{n+1}-t^n)X_{k+1/2}^n - \frac{D_{k-1/2}}{x_l}\sum_{n=0}^{s-1}(t^{n+1}-t^n)X_{k-1/2}^n\right). \tag{B.25}$$

B.3 Diffusion tests

B.3.1 Diffusion simulations

Firstly, tests are performed on the implicit diffusion simulator. A convenient test case for the implicit diffusion simulator is a comparison of the numerical concentration-distance profiles with analytical profiles for a simple case, such as the diffusion of an initial profile given by a step function. The analytical solution for the diffusion of a square wave (see for instance Crank, 1975, p. 15) with width $2h$ is

$$X = \frac{1}{2}X_0\left\{\mathrm{erf}\left(\frac{h-x}{2\sqrt{Dt}}\right) + \mathrm{erf}\left(\frac{h+x}{2\sqrt{Dt}}\right)\right\}, \tag{B.26}$$

where X_0 is the initial mass fraction abundance and the error function, $\mathrm{erf}(x)$, is defined by

$$\mathrm{erf}(x) = \frac{2}{\sqrt{\pi}}\int_0^x e^{-t^2}dt. \tag{B.27}$$

The other symbols have their usual meanings as outlined above. A plot of Eq. B.26 for four values of $(Dt/h^2)^{1/2}$ is displayed in Fig. B.1, along with the initial abundance distribution. Since the distribution is symmetrical about $x = 0$, the analytical solution can also be used for a step function, which is realised by considering the do-

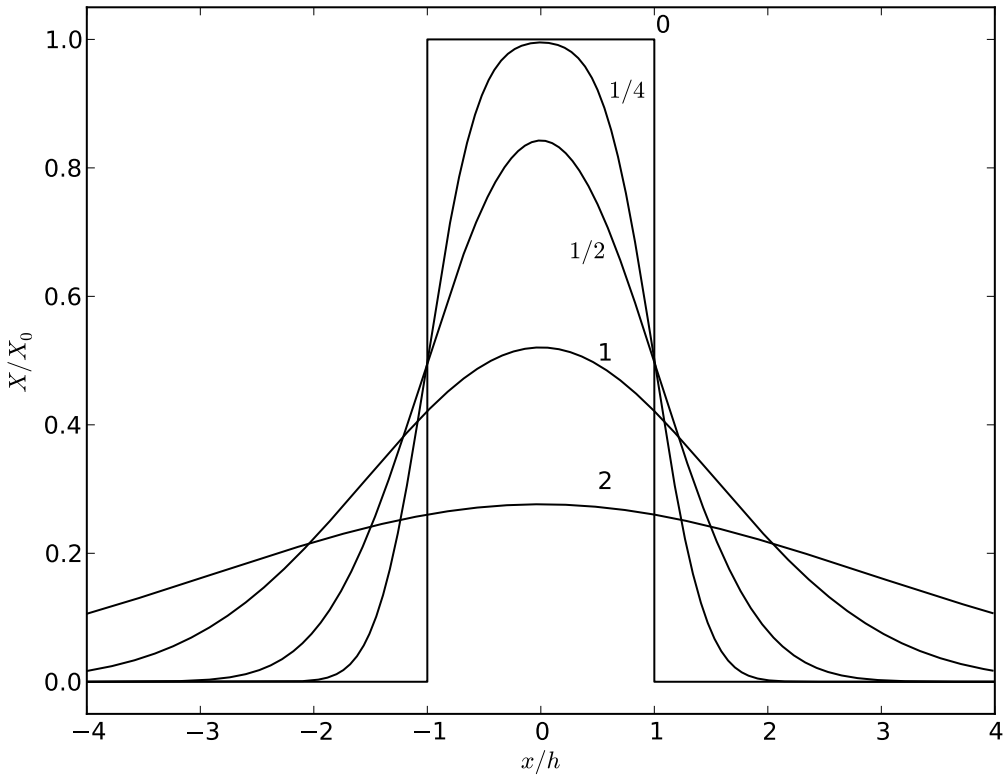

Figure B.1: Analytical solutions for the abundance profiles for diffusion of a square wave initial abundance. Numbers on the curve are values of $(Dt/h^2)^{1/2}$.

main $x/h > 0$. However, Eq. B.26 is only adequate for a semi-infinite domain. For a finite domain, $0 < x < l$, an analytical solution of the form

$$X_a = \frac{1}{2} X_0 \sum_{n=-\infty}^{\infty} \left\{ \text{erf}\left(\frac{h + 2nl - x}{2\sqrt{Dt}} \right) + \text{erf}\left(\frac{h - 2nl + x}{2\sqrt{Dt}} \right) \right\} \tag{B.28}$$

is used, where the series converges over index n rapidly (see for instance Crank, 1975, p. 16). Analytical solutions of this form (with n from -4 to $+4$) are compared with the numerical results obtained below.

Abundance curves were generated using the implicit diffusion simulator for $10,000$ timesteps with a step function for an initial profile:

$$X(x,0) = \begin{cases} 1 & 0 \leq x \leq 500\text{km} \\ 0 & 500 < x \leq 1000\text{km} \end{cases}, \tag{B.29}$$

where in this work, we refer to positions $x = 0$ and $x = l$ as the 'boundaries' (The total size of the 1D spatial domain, l, is 10^6 m) and $x = (l + \Delta x)/2$ as the 'interface', where Δx is the distance between two successive spatial mesh points, which is smaller for a higher spatial resolution. The reason that the interface is referred to in this way is to account for the fact that the step function is implemented using a finite mesh and the gradient of the profile at the step is not infinite between the mesh point at $x = 500$ km and the next one. Therefore, differences are expected to occur between the numerical and analytical results near to the boundary, which are dependent on the spatial resolution. The presence of the finite gradient also has the consequence of adding a small amount of abundance at the interface. Consequently, the comparative analytical solutions were centred at 500 km $+\Delta x/2$. Several different choices of spatial and temporal mesh points were made to investigate resolution effects. For each of these

tests, a constant diffusion coefficient of 10^6 m^2 s^{-1} was used.

Fig. B.2 shows typical abundance curves from the implicit diffusion simulator for five timesteps for $\Delta t = 1000$ s and $\Delta x = 10$ km. The choice of spatial resolution results in a total of 100 mesh points used over the whole spatial domain. Even at this relatively poor resolution, the abundance curves follow the analytical solution. This is because of the use of an implicit scheme and the fact that the evaluation of the abundance profiles improves over time as the profile becomes smoother over the spatial domain. This is verified in Fig. B.3, which shows the difference between the abundance profiles and the numerical solutions decreasing with time. The largest error is found at the points of the abundance curve which have the largest changes in gradient. Note that the abundance profile difference for the 50th timestep ($t = 50,000$ s) is non-symmetrical, which shows that at later times the effect of the finite gradient in the initial profile at the interface affects the diffusion.

The abundance ratio can also be plotted, which is shown in Fig. B.4. The figure demonstrates that when the abundance ratios are taken with values that are close to zero, the errors can be of orders of magnitude, especially for early timesteps where the abundances are still close to zero beyond the interface. Therefore, care must be taken when using abundance ratios to assess the validity of diffusion in this region.

B.3.2 Diffusion coefficient calculations

In this work, two diffusion calculators are used: an 'instantaneous' evaluation and a 'constant D' evaluation. The calculations for both cases can be compared. Diffusion coefficients for the diffusing step profile, with resolution parameters $\Delta t = 1000$ s and $\Delta x = 10$ km, are calculated using the diffusion coefficient calculator and are shown

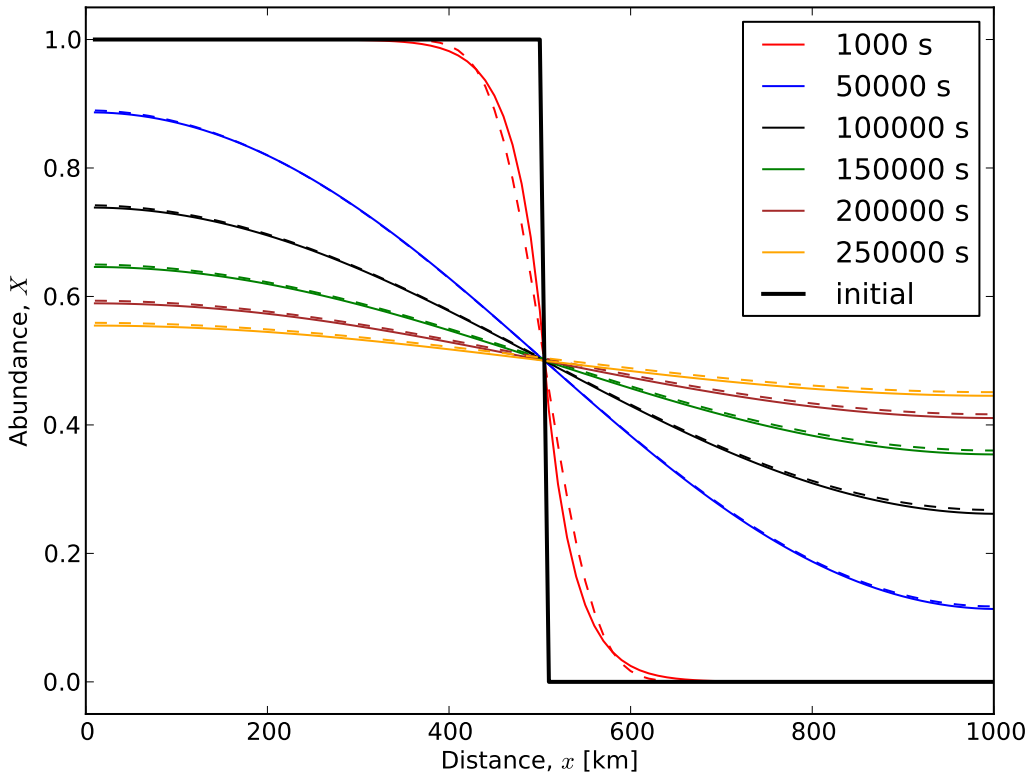

Figure B.2: Numerical (solid lines) and analytical (dashed lines) abundance profiles for the diffusion of the step function with $\Delta t = 1000$ s and $\Delta x = 10$ km. Despite the poor resolution, the scheme is stable and the numerical results compare well with the analytical solutions, especially at later times. The value of t, in seconds, is given in the legend.

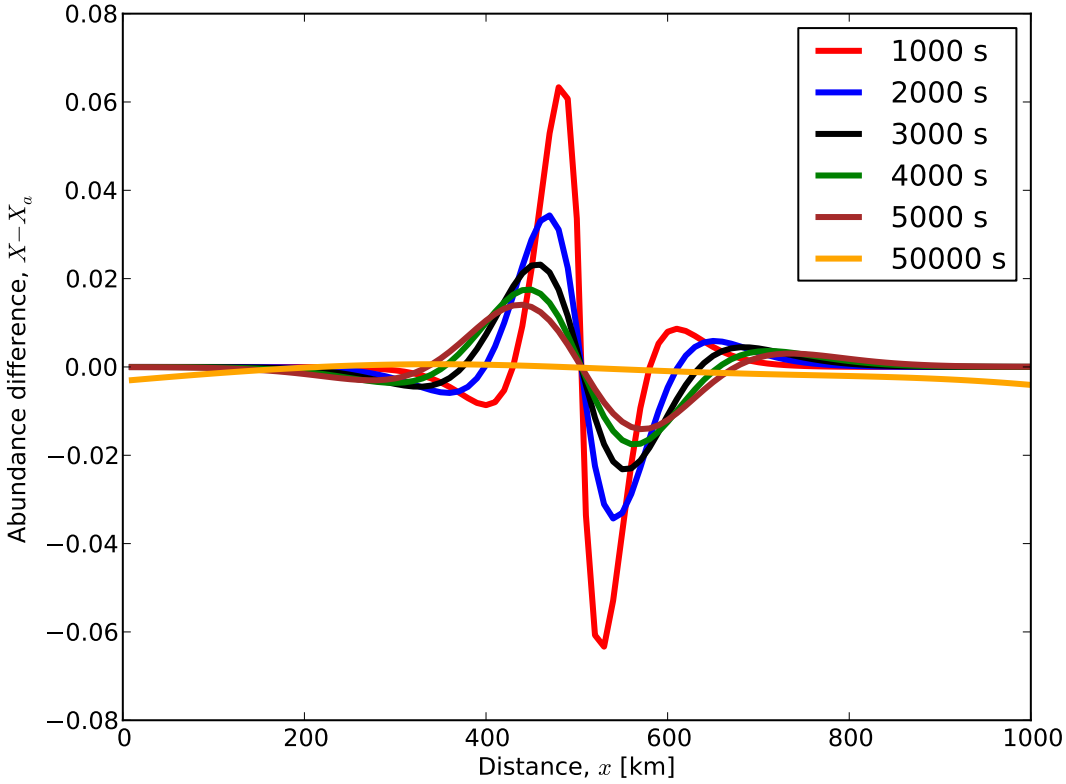

Figure B.3: The difference in abundance between the numerical result and the analytical solution as a function of radius for the first five timesteps and the 50th timestep. $\Delta t = 1000$ s and $\Delta x = 10$ km. The error decreases over time and is largest near to the interface. The value of t, in seconds, is given in the legend.

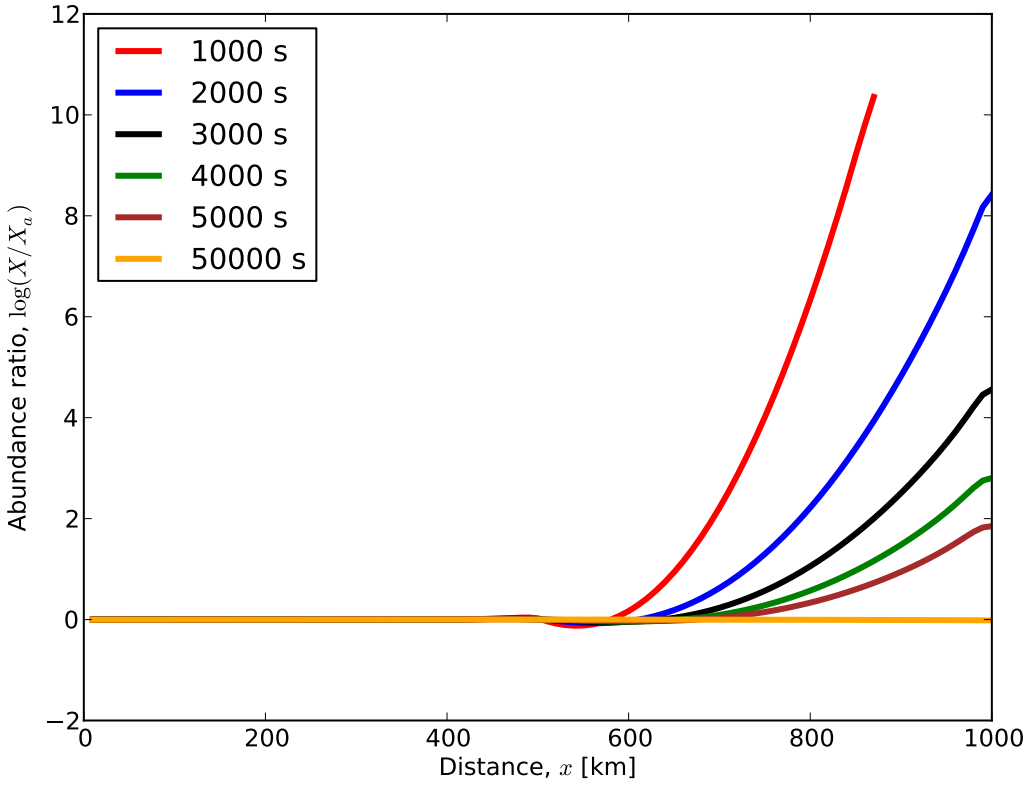

Figure B.4: Abundance ratio of the numerical result to the analytical solution for the first five timesteps and the 50th timestep. $\Delta t = 1000$ s and $\Delta x = 10$ km. The value of t, in seconds, is given in the legend.

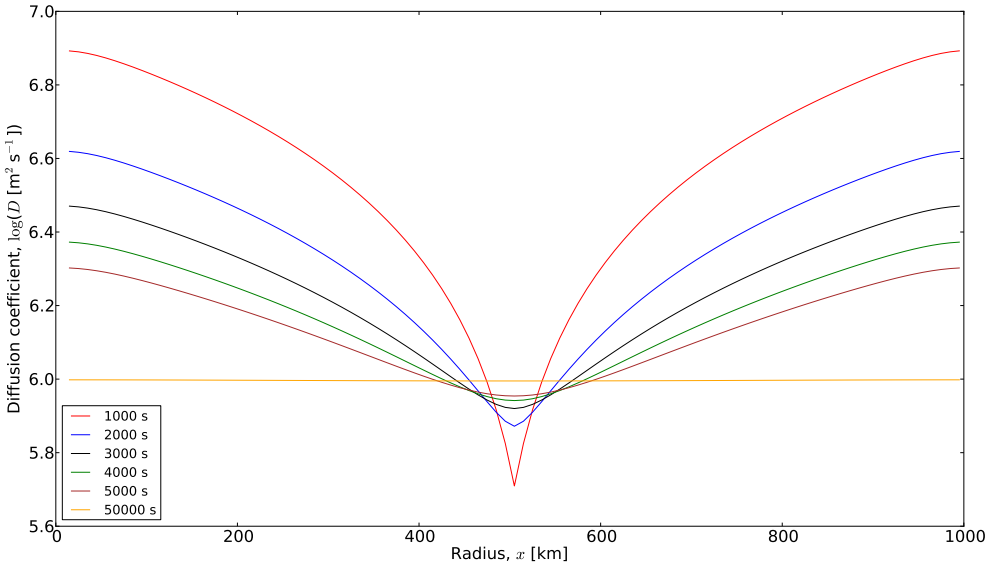

Figure B.5: Diffusion coefficient calculations for the diffusing step profile with resolution parameters $\Delta t = 1000$ s and $\Delta x = 10$ km. The input diffusion coefficient is a constant value of 10^6 m^2 s^{-1}. The value of t, in seconds, is given in the legend.

in Fig. B.5. We recall that the input diffusion coefficient is a constant value of 10^6 m^2 s^{-1}. The solutions are initially quite poor (by ≈ 1.0 dex near the boundaries), but converge on the correct answer as the profile becomes smoother. By the 50th timestep ($t = 50,000$ s), the correct solution is obtained over the whole space, with a consistent error of approximately 1% (lower) over the whole spatial domain. The diffusion coefficient evaluations are more accurate for smoother profiles, which is also true for the calculated abundance profiles for the implicit diffusion simulator.

Calculations assuming a constant diffusion coefficient over several choices of time domain are plotted in Fig. B.6 and B.7. In Fig. B.6, diffusion coefficients are calculated at different intervals using 100 timesteps (a total time domain of 9.9×10^4 s). All the domain choices show that the largest deviations are at the boundaries, whereas for the

earliest domain used, an additional error is found at the interface. The earliest domain (steps 1-100) is the only domain to show a difference from the others; all other curves lie at the same position (with differences between the curves at approximately $10^{-5}\%$). Ignoring the values at the boundaries (by considering the spatial domain between 200 and 800 km), the worst error for the earliest domain is 12%, which is at the interface, and 7% for the other curves, which were taken at 8 km.

One can conclude from Fig. B.5 and B.6 that the diffusion coefficient calculations at the early stages gives poorer results, akin to that of the implicit diffusion solver. The error in diffusing initial conditions that are approximately discontinuous is mitigated by using abundance profiles at later times. In addition, the assumed boundary conditions ($D = 0$ outside the spatial domain) affect the constant D evaluations more than in the instantaneous evaluations, which only use information from two timesteps, which is not enough temporal information to propagate boundary effects. Therefore, one can use either code to determine whether or not to probe boundary effects.

In Fig. B.7, constant D evaluations using different time domains are compared, which shows that the bigger the domain considered, the more accurate the solutions. Therefore, although one can see in Fig. B.6 that the instantaneous evaluations are often more accurate than the constant D evaluations, the accuracy can be increased by using a larger time domain. Therefore, in instances where the instantaneous evaluation cannot be used (for example, if boundary effects are interesting or when the data is noisy, see §5.3.1), the constant D evaluation can be used in its place.

Considering the errors in the profiles seen in Fig. B.3 and B.4 and the deviations from the correct answer in Fig. B.5, any calculations aiming to correctly determine the diffusion coefficient from abundance profiles should ignore the first few timesteps at least. However, it is possible to consider whether the diffusion coefficient evaluations

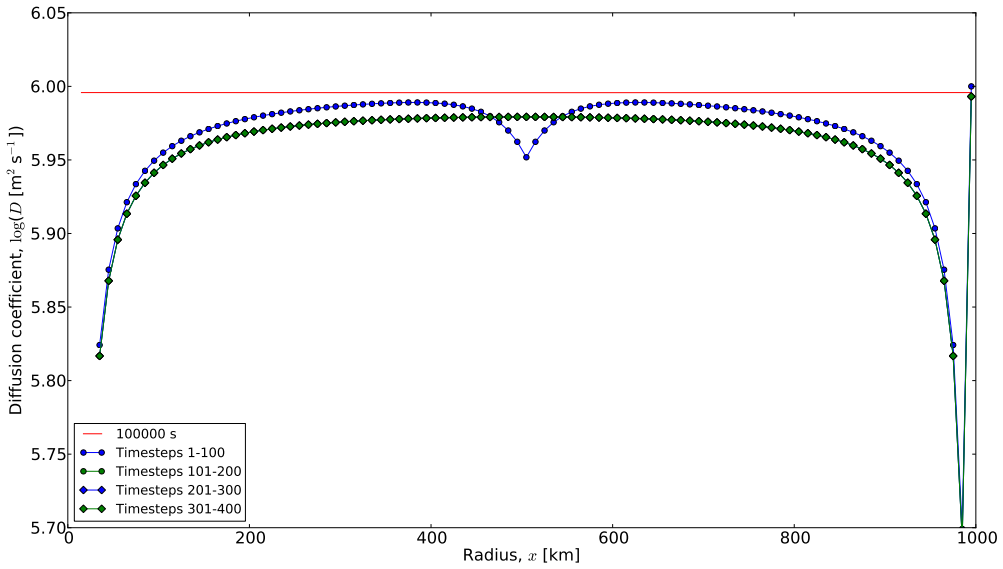

Figure B.6: Diffusion coefficient calculations assuming constant D for the diffusing step profile with resolution parameters $\Delta t = 1000$ s and $\Delta x = 10$ km. Similar time domains are considered, but at different intervals. The timesteps for the time domain considered in each case is given in the legend. Most plots take the same position in the diagram, except for the early domain (timesteps 1-100) and the instantaneous calculation at timestep 100 ($t = 10^5$ s), which is provided for comparison. The input diffusion coefficient is a constant value of 10^6 m^2 s^{-1}.

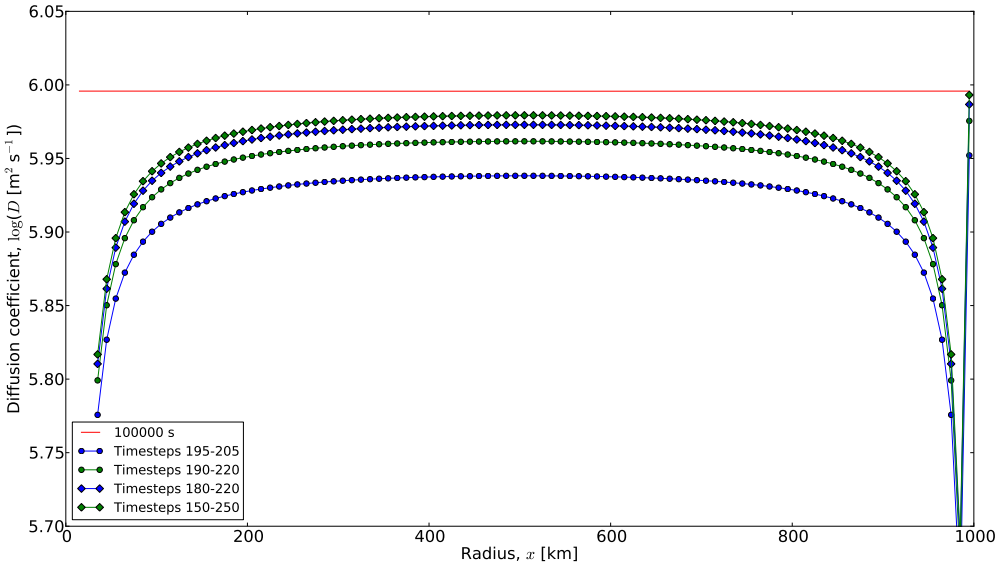

Figure B.7: Diffusion coefficient calculations assuming constant D for the diffusing step profile with resolution parameters $\Delta t = 1000$ s and $\Delta x = 10$ km. The timesteps for the time domain considered in each case is given in the legend. An instantaneous calculation at timestep 100 ($t = 10^5$ s) is provided for comparison. The input diffusion coefficient is a constant value of 10^6 m^2 s^{-1}.

are improved with changes to the temporal and spatial resolution.

B.3.2.1 The effect of an increased spatial resolution

Another set of abundance profiles was generated using the step function, but with 1000 spatial mesh points ($\Delta x = 1$ km) rather than the 100 used in the previous case ($\Delta x =$ 10 km). The abundance profiles are shown in Fig. B.8 and the abundance differences are shown in Fig. B.9. Using a higher spatial resolution causes the step function to have a larger gradient at the interface and consequently the numerical solutions follow more closely the analytical solutions. However, looking at the abundance differences in Fig. B.9, the errors in abundances have not changed, although the higher spatial resolution causes the curves shown to have a smoother shape. This demonstrates that the errors associated with the first few timesteps cannot be corrected by increasing the spatial resolution. However, comparison of Fig. B.8 with Fig. B.2 demonstrates that an improvement should occur at later times. Fig. B.10 shows the abundance differences for later times ($t = 100000$, 150000, 200000 and 250000 seconds, which correspond to timesteps 100, 150, 200 and 250). Indeed, an improvement in the differences between the numerical profile and the analytical one is seen. Therefore, the disparity seen in the early profiles is due to the inability of a digital computer to correctly account for a discontinuity. This fact is also responsible for the asymmetry seen in Fig. B.10.

Diffusion coefficient evaluations for the $\Delta x = 1$ km run is shown in Fig. B.11. For early timesteps, the calculations are similar to the case with $\Delta x = 10$ km and no benefit is gained with an increased spatial resolution. Later timesteps also exhibit similar values to the previous case, with values 1% lower than the initial input diffusion coefficient. However, changes in the evaluation of the diffusion coefficients calculated

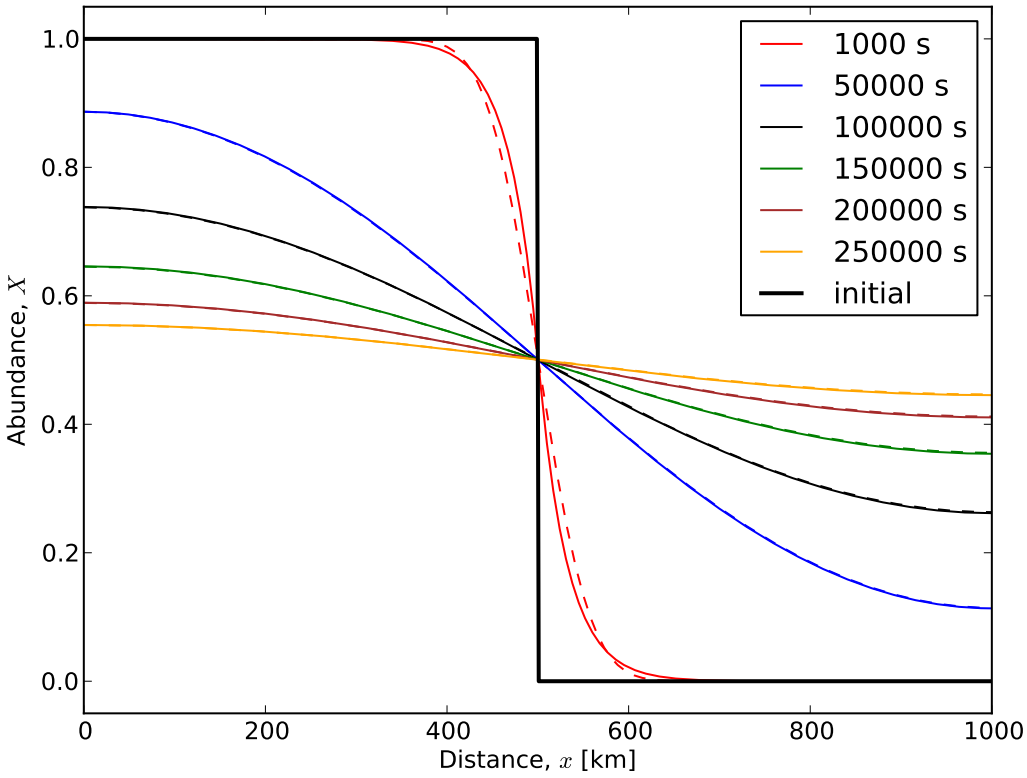

Figure B.8: Numerical (solid lines) and analytical (dashed lines) abundance profiles for the diffusion of the step function with $\Delta t = 1000$ s and $\Delta x = 1$ km. Values of t for the timesteps used are provided in the legend. The input diffusion coefficient is a constant value of 10^6 m^2 s^{-1}.

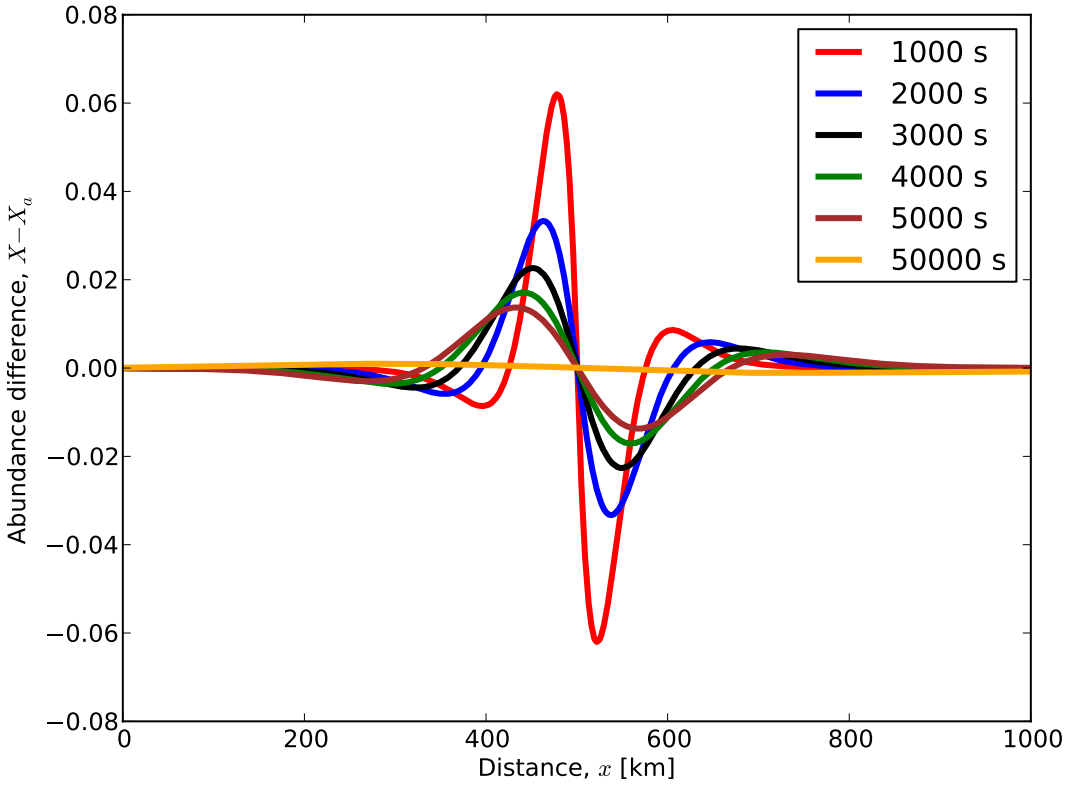

Figure B.9: The difference in abundance between the numerical result and the analytical solution as a function of radius for the first five timesteps and the 50th timestep. $\Delta t = 1000$ s and $\Delta x = 1$ km. The error decreases over time and is largest near to the interface.

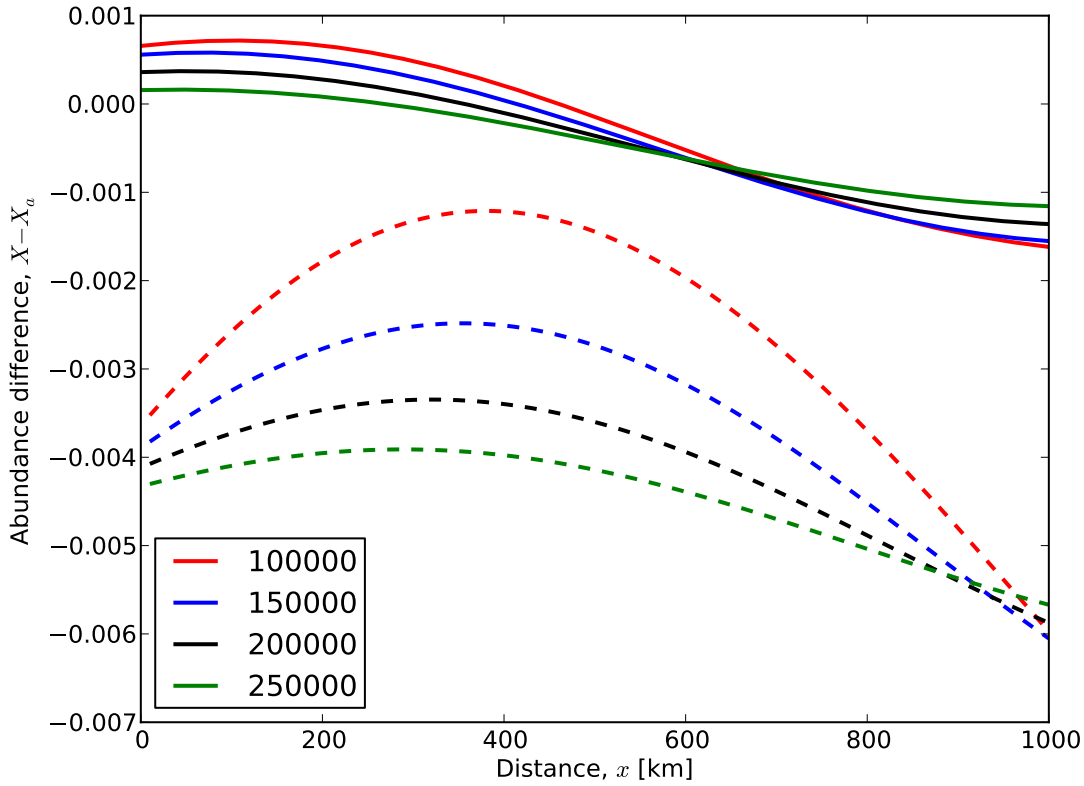

Figure B.10: The difference in abundance between the numerical result and the analytical solution as a function of radius for $\Delta x = 1$ km (solid lines) and $\Delta x = 10$ km (dashed lines) for timesteps 100, 150, 200 and 250. The time, t, is denoted by colour and is provided in the legend.

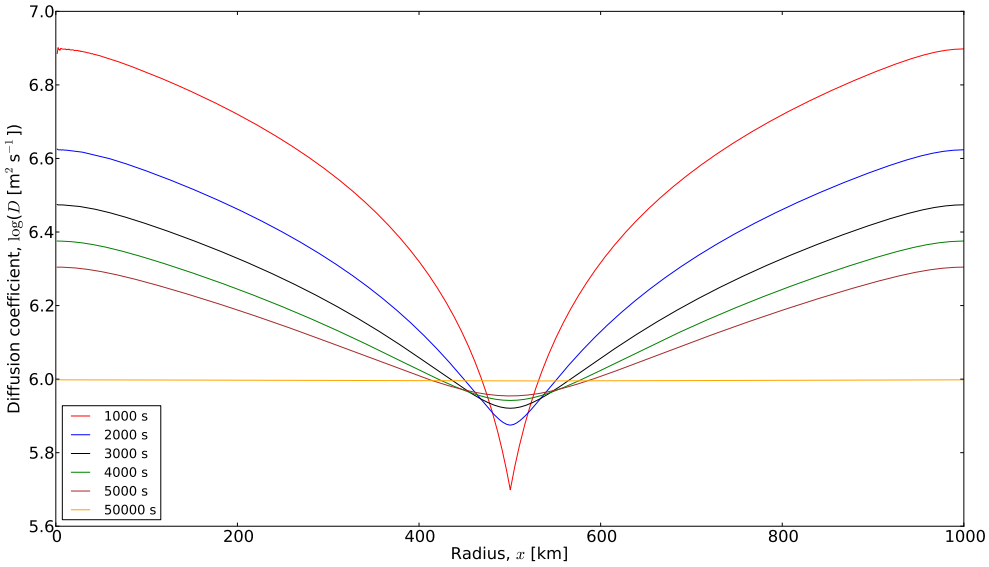

Figure B.11: Diffusion coefficient calculations for the diffusing step profile with resolution parameters $\Delta t = 1000$ s and $\Delta x = 1$ km. The input diffusion coefficient is a constant value of 10^6 m^2 s^{-1}. The value of t, in seconds, is given in the legend.

using the constant D assumption are affected by the change in resolution. This is seen also in Fig. B.12, where the diffusion coefficients for both resolutions are plotted. At 800 km, the deviation from the input coefficient is 7% for the $\Delta x = 10$ km case and 2% for the $\Delta x = 1$ km case.

B.3.2.2 The effect of an increased temporal resolution

In order to investigate the effect of an increased temporal resolution, another set of abundance profiles was generated for the step function with $\Delta t = 100$ seconds and $\Delta x = 10$ km. The diffusion profiles are shown in Fig. B.13, which are similar to those of the previous cases (Fig. B.2 and Fig. B.8). The differences in abundance

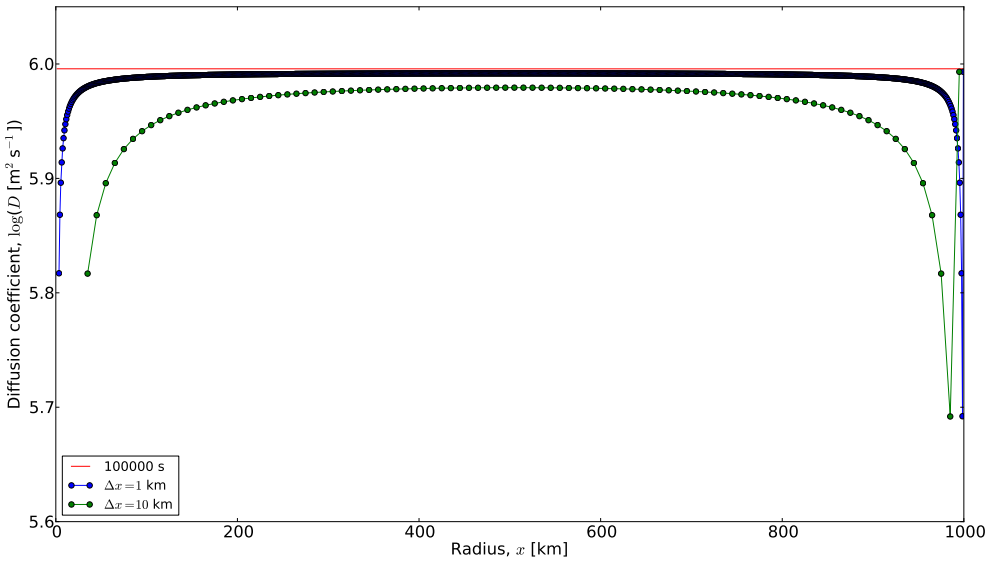

Figure B.12: Diffusion coefficient calculations for the diffusing step profile assuming a constant diffusion coefficient for both resolutions considered and $\Delta t = 1000$ s. Timesteps 15-250 are used for both plots.

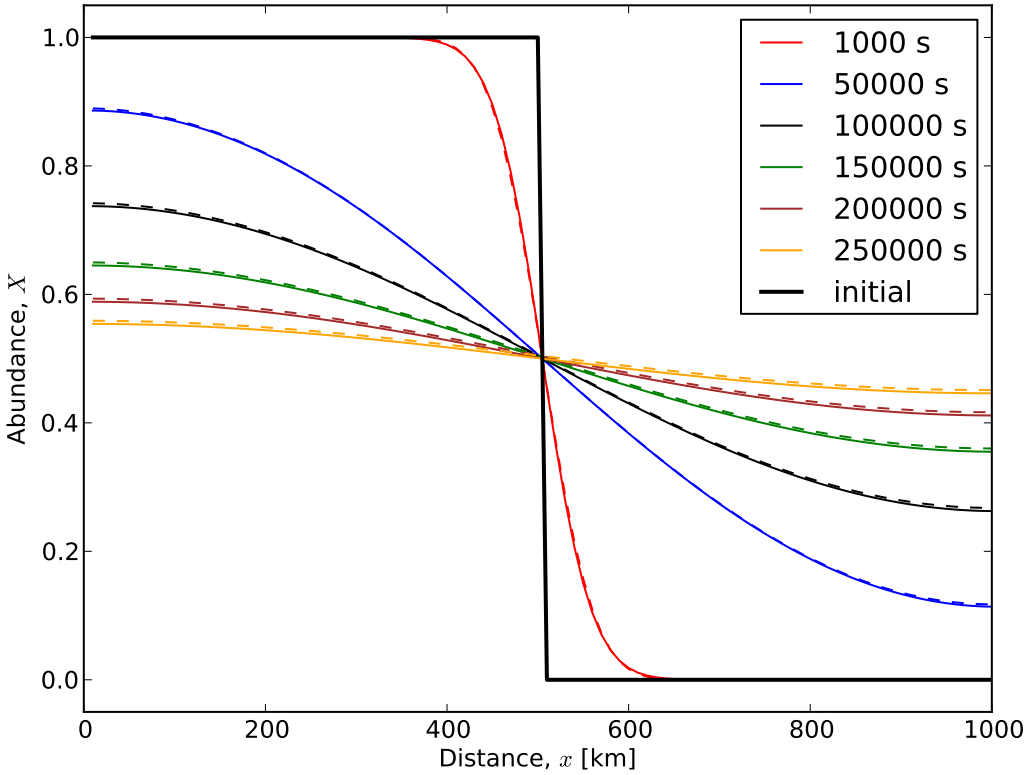

Figure B.13: Numerical (solid lines) and analytical (dashed lines) abundance profiles for the step function using $\Delta t = 100$ s and $\Delta x = 10$ km. The input diffusion coefficient is a constant value of 10^6 m^2 s^{-1}. The value of t, in seconds, is given in the legend.

between numerical and analytical solutions is much less for the $\Delta t = 100$ s case than the $\Delta t = 1000$ s case (see Fig. B.14). An increased temporal resolution mitigates the errors associated with diffusing a steep profile at the beginning of the model.

Diffusion coefficients for this run were calculated and are displayed in Fig. B.15. The instantaneous diffusion coefficient calculated has improved over the $\Delta t = 1000$ s case with an error of approximately 0.1%. Improvements are also seen for the evaluations using the constant D assumption. For the calculation over the first 50000 seconds,

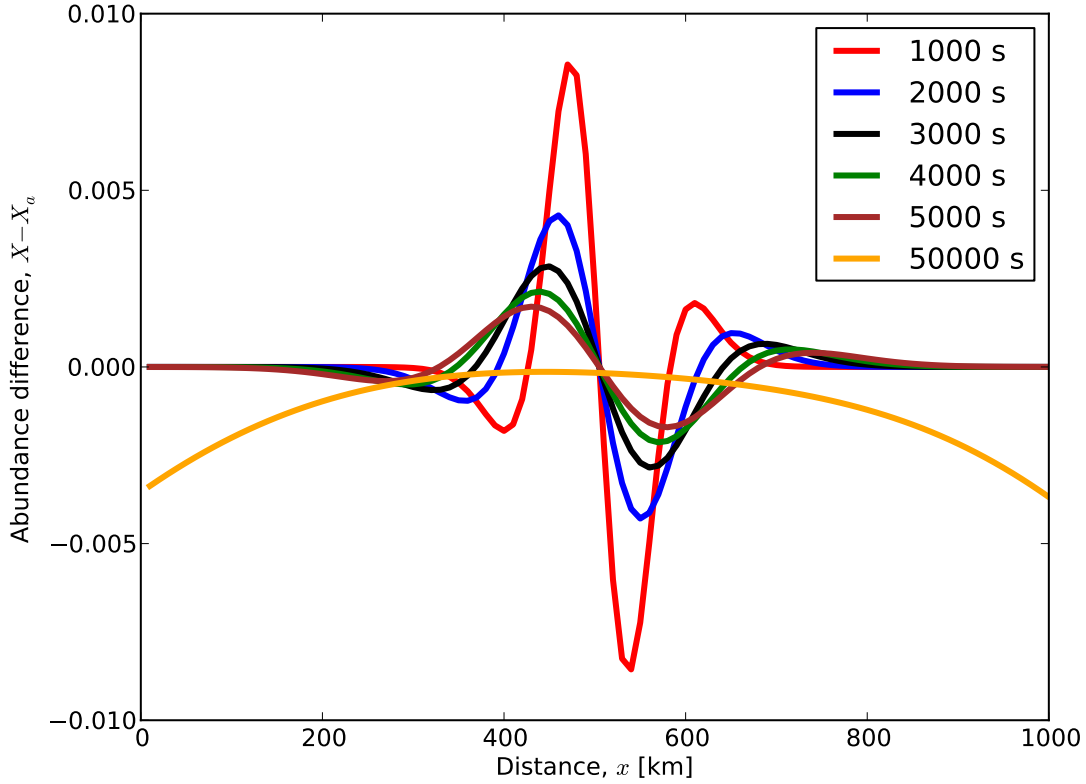

Figure B.14: The difference in abundance between the numerical result and the analytical solution as a function of radius for the the 10th, 20th, 30th, 40th, 50th and 500th timesteps. The times for these timesteps (see legend for t values, in seconds) correspond to those used for Fig. B.3 and B.9. $\Delta t = 100$ s and $\Delta x = 10$ km.

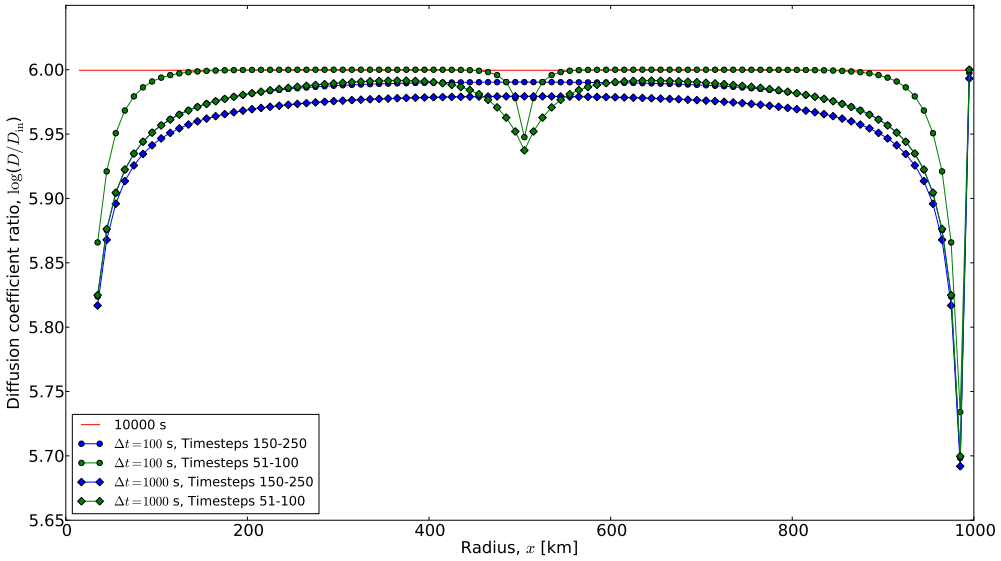

Figure B.15: Diffusion coefficients calculated assuming constant D for two time resolutions at $\Delta x = 10$ km. An instantaneous evaluation at $t = 100000$s with $\Delta t = 100$s is provided for comparison. The timesteps used for the constant D calculations are shown in the legend. The input diffusion coefficient is a constant value of 10^6 m^2 s^{-1}.

the improvements seen are mainly seen near to the interface, most likely because the errors associated with the early profiles determined using the implicit diffusion simulator have been reduced with the higher resolution. The coefficient calculation is otherwise similar. Over the next 50000 seconds however, an improvement is seen in the evaluation of the diffusion coefficient over the whole spatial domain, which is a constant 0.01 dex (or 2.3%).

To summarise, the tests indicate that both diffusion programs are capable of simulating diffusion and reproducing the input diffusion coefficients. However, sources of numerical error, which are namely the boundaries and the initial conditions, will affect both the simulated diffusion and the coefficients determined from those profiles.

Errors of this kind can be mitigated by ignoring the first 50-100 timesteps of a simulation. Diffusion coefficient evaluations can be determined either using an instantaneous calculation, which is accurate but does not probe boundary value effects, and the constant D evaluations, which can also be used as an alternative when the instantaneous evaluation is less useful.

C Yield tables

Full yield tables for all massive star models used in this work are listed here. For each stable isotope, i, included in the nuclear reaction network, the atomic mass (A), atomic number (Z), initial mass fraction abundance ($X^{\rm ini}$), wind yield ($mp^{\rm wind}$, in $M_{\odot}$), presupernova yield ($mp^{\rm preSN}$, in $M_{\odot}$), total yield ($mp^{\rm total}$, in $M_{\odot}$), total ejected mass (EM, in $M_{\odot}$) and average overproduction factor ($\langle OP \rangle$) are specified. The decays of unstable species to their stable isobars are taken into account.

Table C.1: Yields for model 15ST.

Isotope	A	Z	X^{ini}	mp^{wind}	mp^{preSN}	mp^{total}	EM	$\langle OP \rangle$
^{1}H	1	1	7.064E-01	-4.366E-02	-2.933E+00	-2.977E+00	6.485E+00	0.685
^{2}H	2	1	1.371E-05	-3.240E-05	-1.377E-04	-1.701E-04	1.346E-05	0.073
^{3}He	3	2	4.540E-05	-1.447E-05	-2.886E-04	-3.031E-04	3.050E-04	0.502
^{4}He	4	2	2.735E-01	4.345E-02	1.435E+00	1.479E+00	5.142E+00	1.404
^{7}Li	7	3	7.605E-11	-1.798E-10	-7.641E-10	-9.439E-10	7.468E-11	0.073
^{11}B	11	5	2.856E-09	-6.769E-14	9.734E-11	9.727E-11	3.835E-08	1.003
^{12}C	12	6	3.425E-03	-2.639E-03	3.101E-01	3.074E-01	3.533E-01	7.703
^{13}C	13	6	4.156E-05	2.302E-04	2.276E-04	4.577E-04	1.014E-03	1.822
^{14}N	14	7	1.059E-03	4.132E-03	3.401E-02	3.814E-02	5.232E-02	3.689
^{15}N	15	7	4.171E-06	-5.721E-06	-2.485E-05	-3.057E-05	2.529E-05	0.453
^{16}O	16	8	9.624E-03	-1.474E-03	7.579E-01	7.564E-01	8.853E-01	6.868
^{17}O	17	8	3.813E-06	3.859E-06	2.135E-05	2.520E-05	7.627E-05	1.494
^{18}O	18	8	2.171E-05	-1.173E-05	8.634E-03	8.623E-03	8.913E-03	30.654
^{19}F	19	9	5.611E-07	-9.796E-08	-2.190E-06	-2.288E-06	5.227E-06	0.696
^{20}Ne	20	10	1.818E-03	-2.514E-06	3.238E-01	3.238E-01	3.482E-01	14.302
^{21}Ne	21	10	4.575E-06	2.629E-06	9.420E-04	9.447E-04	1.006E-03	16.416
^{22}Ne	22	10	1.470E-04	-2.896E-05	2.587E-02	2.584E-02	2.781E-02	14.122
^{23}Na	23	11	4.000E-05	3.023E-05	1.337E-02	1.340E-02	1.394E-02	26.021
^{24}Mg	24	12	5.862E-04	-1.079E-08	2.747E-02	2.747E-02	3.532E-02	4.498
^{25}Mg	25	12	7.733E-05	-8.796E-06	1.259E-02	1.259E-02	1.362E-02	13.152
^{26}Mg	26	12	8.848E-05	9.098E-06	1.176E-02	1.177E-02	1.295E-02	10.931
^{27}Al	27	13	6.481E-05	4.579E-08	3.142E-03	3.142E-03	4.010E-03	4.620
^{28}Si	28	14	7.453E-04	-1.752E-08	1.844E-03	1.844E-03	1.183E-02	1.185
^{29}Si	29	14	3.919E-05	-9.322E-10	3.792E-04	3.792E-04	9.041E-04	1.722
^{30}Si	30	14	2.673E-05	-2.143E-09	2.734E-04	2.734E-04	6.314E-04	1.764
^{31}P	31	15	7.106E-06	1.394E-09	7.106E-05	7.106E-05	1.662E-04	1.747
^{32}S	32	16	4.011E-04	-9.512E-09	-1.897E-04	-1.897E-04	5.182E-03	0.965

TableC.1 – continued

Isotope	A	Z	$X^{\rm ini}$	$mp^{\rm wind}$	$mp^{\rm preSN}$	$mp^{\rm total}$	EM	$\langle OP \rangle$
^{33}S	33	16	3.265E-06	-7.194E-11	9.422E-06	9.422E-06	5.315E-05	1.215
^{34}S	34	16	1.890E-05	-4.481E-10	1.406E-05	1.406E-05	2.673E-04	1.056
^{36}S	36	16	8.073E-08	-1.914E-12	6.326E-06	6.326E-06	7.407E-06	6.850
^{35}Cl	35	17	6.821E-06	-1.617E-10	-4.188E-06	-4.188E-06	8.717E-05	0.954
^{37}Cl	37	17	2.306E-06	-5.465E-11	6.384E-05	6.384E-05	9.472E-05	3.067
^{36}Ar	36	18	8.202E-05	-1.944E-09	-7.472E-05	-7.472E-05	1.024E-03	0.932
^{38}Ar	38	18	1.574E-05	-3.731E-10	3.787E-05	3.787E-05	2.487E-04	1.180
^{40}Ar	40	18	2.650E-08	-6.255E-13	2.607E-06	2.607E-06	2.962E-06	8.346
^{39}K	39	19	3.900E-06	-9.244E-11	7.466E-06	7.466E-06	5.970E-05	1.143
^{40}K	40	19	5.005E-10	-6.366E-12	1.200E-06	1.200E-06	1.207E-06	180.075
^{41}K	41	19	2.959E-07	-7.013E-12	4.344E-06	4.344E-06	8.307E-06	2.096
^{40}Ca	40	20	7.225E-05	-1.706E-09	-5.212E-05	-5.212E-05	9.156E-04	0.946
^{42}Ca	42	20	5.063E-07	-1.200E-11	4.691E-06	4.691E-06	1.147E-05	1.692
^{43}Ca	43	20	1.082E-07	-2.564E-12	1.559E-06	1.559E-06	3.008E-06	2.076
^{44}Ca	44	20	1.710E-06	-4.054E-11	2.726E-06	2.726E-06	2.563E-05	1.119
^{46}Ca	46	20	3.428E-09	-8.126E-14	3.536E-08	3.536E-08	8.128E-08	1.770
^{48}Ca	48	20	1.672E-07	-3.964E-12	-2.082E-08	-2.083E-08	2.219E-06	0.991
^{45}Sc	45	21	5.414E-08	-1.283E-12	8.303E-07	8.303E-07	1.555E-06	2.145
^{46}Ti	46	22	3.232E-07	-7.660E-12	7.012E-07	7.012E-07	5.030E-06	1.162
^{47}Ti	47	22	2.977E-07	-7.056E-12	6.339E-08	6.338E-08	4.051E-06	1.016
^{48}Ti	48	22	3.014E-06	-7.144E-11	-3.460E-06	-3.460E-06	3.690E-05	0.914
^{49}Ti	49	22	2.257E-07	-5.351E-12	1.598E-06	1.598E-06	4.621E-06	1.529
^{50}Ti	50	22	2.208E-07	-5.234E-12	3.801E-06	3.801E-06	6.758E-06	2.285
^{50}V	50	23	1.015E-09	-2.407E-14	-3.554E-10	-3.554E-10	1.325E-08	0.974
^{51}V	51	23	4.138E-07	-9.808E-12	-6.535E-08	-6.536E-08	5.476E-06	0.988
^{50}Cr	50	24	8.265E-07	-1.959E-11	-1.327E-06	-1.327E-06	9.743E-06	0.880
^{52}Cr	52	24	1.658E-05	-3.929E-10	-1.282E-05	-1.282E-05	2.092E-04	0.942
^{53}Cr	53	24	1.916E-06	-4.541E-11	-7.646E-07	-7.647E-07	2.489E-05	0.970

TableC.1 – continued

Isotope	A	Z	$X^{\rm ini}$	$mp^{\rm wind}$	$mp^{\rm preSN}$	$mp^{\rm total}$	EM	$\langle OP \rangle$
^{54}Cr	54	24	4.858E-07	-1.151E-11	1.058E-05	1.058E-05	1.708E-05	2.625
^{55}Mn	55	25	1.098E-05	-2.603E-10	3.666E-06	3.666E-06	1.507E-04	1.025
^{54}Fe	54	26	8.118E-05	-1.924E-09	-1.208E-04	-1.208E-04	9.665E-04	0.889
^{56}Fe	56	26	1.322E-03	-3.133E-08	-1.213E-03	-1.213E-03	1.649E-02	0.931
^{57}Fe	57	26	3.107E-05	-7.364E-10	1.981E-04	1.981E-04	6.141E-04	1.476
^{58}Fe	58	26	4.207E-06	-9.972E-11	5.340E-04	5.340E-04	5.903E-04	10.477
^{59}Co	59	27	3.991E-06	-9.461E-11	2.580E-04	2.580E-04	3.114E-04	5.825
^{58}Ni	58	28	5.711E-05	-1.354E-09	-8.270E-05	-8.270E-05	6.822E-04	0.892
^{60}Ni	60	28	2.276E-05	-5.394E-10	1.437E-04	1.437E-04	4.485E-04	1.472
^{61}Ni	61	28	1.006E-06	-2.384E-11	6.465E-05	6.465E-05	7.811E-05	5.799
^{62}Ni	62	28	3.259E-06	-7.725E-11	1.402E-04	1.402E-04	1.838E-04	4.211
^{64}Ni	64	28	8.568E-07	-2.031E-11	5.627E-05	5.627E-05	6.775E-05	5.904
^{63}Cu	63	29	6.600E-07	-1.564E-11	5.493E-05	5.493E-05	6.376E-05	7.213
^{65}Cu	65	29	3.035E-07	-7.193E-12	3.249E-05	3.249E-05	3.655E-05	8.993
^{64}Zn	64	30	1.131E-06	-2.680E-11	1.792E-05	1.792E-05	3.306E-05	2.183
^{66}Zn	66	30	6.690E-07	-1.586E-11	1.856E-05	1.856E-05	2.752E-05	3.072
^{67}Zn	67	30	9.980E-08	-2.366E-12	5.495E-06	5.495E-06	6.831E-06	5.111
^{68}Zn	68	30	4.632E-07	-1.098E-11	1.835E-05	1.835E-05	2.456E-05	3.958
^{70}Zn	70	30	1.577E-08	-3.737E-13	-1.160E-08	-1.160E-08	1.996E-07	0.945
^{69}Ga	69	31	4.551E-08	-1.079E-12	2.367E-06	2.367E-06	2.977E-06	4.884
^{71}Ga	71	31	3.108E-08	-7.366E-13	2.012E-06	2.012E-06	2.428E-06	5.834
^{70}Ge	70	32	5.157E-08	-1.222E-12	3.185E-06	3.185E-06	3.876E-06	5.611
^{72}Ge	72	32	6.910E-08	-1.638E-12	2.614E-06	2.614E-06	3.539E-06	3.824
^{73}Ge	73	32	1.955E-08	-4.633E-13	1.090E-06	1.090E-06	1.352E-06	5.165
^{74}Ge	74	32	9.228E-08	-2.187E-12	3.365E-06	3.365E-06	4.601E-06	3.722
^{76}Ge	76	32	1.963E-08	-4.653E-13	-2.026E-08	-2.026E-08	2.426E-07	0.923
^{75}As	75	33	1.430E-08	-3.390E-13	4.113E-07	4.113E-07	6.028E-07	3.147
^{74}Se	74	34	1.198E-09	-2.839E-14	-2.382E-09	-2.382E-09	1.366E-08	0.852

TableC.1 – continued

Isotope	A	Z	$X^{\rm ini}$	$mp^{\rm wind}$	$mp^{\rm preSN}$	$mp^{\rm total}$	EM	$\langle OP \rangle$
^{76}Se	76	34	1.296E-08	-3.072E-13	6.260E-07	6.260E-07	7.995E-07	4.606
^{77}Se	77	34	1.070E-08	-2.537E-13	3.049E-07	3.049E-07	4.483E-07	3.127
^{78}Se	78	34	3.376E-08	-8.003E-13	1.441E-06	1.441E-06	1.894E-06	4.188
^{80}Se	80	34	7.226E-08	-1.713E-12	2.985E-07	2.985E-07	1.266E-06	1.308
^{82}Se	82	34	1.304E-08	-3.090E-13	-1.158E-08	-1.158E-08	1.630E-07	0.934
^{79}Br	79	35	1.389E-08	-3.293E-13	1.867E-07	1.867E-07	3.728E-07	2.003
^{81}Br	81	35	1.386E-08	-3.285E-13	2.041E-07	2.041E-07	3.897E-07	2.100
^{78}Kr	78	36	3.900E-10	-9.245E-15	-7.456E-10	-7.456E-10	4.478E-09	0.857
^{80}Kr	80	36	2.575E-09	-6.103E-14	2.610E-07	2.610E-07	2.955E-07	8.569
^{82}Kr	82	36	1.320E-08	-3.128E-13	7.028E-07	7.028E-07	8.795E-07	4.977
^{83}Kr	83	36	1.324E-08	-3.139E-13	3.113E-07	3.113E-07	4.886E-07	2.755
^{84}Kr	84	36	6.602E-08	-1.565E-12	1.031E-06	1.031E-06	1.915E-06	2.166
^{86}Kr	86	36	2.044E-08	-4.846E-13	1.289E-07	1.289E-07	4.027E-07	1.471
^{85}Rb	85	37	1.282E-08	-3.040E-13	1.721E-07	1.721E-07	3.438E-07	2.002
^{87}Rb	87	37	5.063E-09	-2.025E-12	6.776E-08	6.776E-08	1.356E-07	1.999
^{84}Sr	84	38	3.228E-10	-7.651E-15	-6.777E-10	-6.777E-10	3.646E-09	0.843
^{86}Sr	86	38	5.845E-09	-1.385E-13	3.642E-07	3.642E-07	4.424E-07	5.652
^{87}Sr	87	38	4.443E-09	1.800E-12	1.858E-07	1.858E-07	2.453E-07	4.123
^{88}Sr	88	38	5.011E-08	-1.188E-12	5.602E-07	5.602E-07	1.231E-06	1.835
^{89}Y	89	39	1.229E-08	-2.914E-13	9.875E-08	9.875E-08	2.634E-07	1.600
^{90}Zr	90	40	1.534E-08	-3.637E-13	4.445E-08	4.445E-08	2.500E-07	1.216
^{91}Zr	91	40	3.384E-09	-8.021E-14	1.514E-08	1.514E-08	6.046E-08	1.334
^{92}Zr	92	40	5.227E-09	-1.239E-13	1.871E-08	1.871E-08	8.872E-08	1.267
^{94}Zr	94	40	5.413E-09	-1.283E-13	6.178E-09	6.178E-09	7.868E-08	1.085
^{96}Zr	96	40	8.903E-10	-2.110E-14	2.698E-09	2.698E-09	1.462E-08	1.226
^{93}Nb	93	41	1.900E-09	-4.504E-14	7.083E-09	7.082E-09	3.253E-08	1.278
^{92}Mo	92	42	1.012E-09	-2.400E-14	-1.687E-09	-1.687E-09	1.187E-08	0.876
^{94}Mo	94	42	6.448E-10	-1.528E-14	2.073E-11	2.072E-11	8.656E-09	1.002

TableC.1 – continued

Isotope	A	Z	$X^{\rm ini}$	$mp^{\rm wind}$	$mp^{\rm preSN}$	$mp^{\rm total}$	EM	$\langle OP \rangle$
^{95}Mo	95	42	1.122E-09	-2.659E-14	1.094E-09	1.094E-09	1.612E-08	1.073
^{96}Mo	96	42	1.188E-09	-2.815E-14	3.811E-09	3.811E-09	1.972E-08	1.240
^{97}Mo	97	42	6.875E-10	-1.630E-14	8.287E-10	8.287E-10	1.004E-08	1.090
^{98}Mo	98	42	1.754E-09	-4.158E-14	3.213E-09	3.213E-09	2.671E-08	1.137
^{100}Mo	100	42	7.146E-10	-1.694E-14	-1.219E-09	-1.219E-09	8.352E-09	0.873
^{96}Ru	96	44	2.926E-10	-6.935E-15	-5.489E-10	-5.489E-10	3.369E-09	0.860
^{98}Ru	98	44	1.007E-10	-2.387E-15	-1.460E-10	-1.460E-10	1.203E-09	0.892
^{99}Ru	99	44	6.945E-10	-1.646E-14	-3.211E-10	-3.211E-10	8.981E-09	0.965
^{100}Ru	100	44	6.928E-10	-1.642E-14	1.898E-09	1.898E-09	1.118E-08	1.205
^{101}Ru	101	44	9.475E-10	-2.246E-14	-1.493E-09	-1.493E-09	1.120E-08	0.882
^{102}Ru	102	44	1.770E-09	-4.195E-14	1.499E-09	1.499E-09	2.520E-08	1.063
^{104}Ru	104	44	1.065E-09	-2.524E-14	-1.922E-09	-1.922E-09	1.234E-08	0.865
^{103}Rh	103	45	1.055E-09	-2.500E-14	-1.546E-09	-1.546E-09	1.258E-08	0.891
^{102}Pd	102	46	4.241E-11	-1.005E-15	-8.928E-11	-8.928E-11	4.787E-10	0.843
^{104}Pd	104	46	4.723E-10	-1.119E-14	1.827E-09	1.827E-09	8.153E-09	1.289
^{105}Pd	105	46	9.558E-10	-2.265E-14	-1.576E-09	-1.576E-09	1.123E-08	0.877
^{106}Pd	106	46	1.181E-09	-2.799E-14	9.412E-10	9.412E-10	1.676E-08	1.060
^{108}Pd	108	46	1.165E-09	-2.761E-14	5.511E-10	5.510E-10	1.615E-08	1.035
^{110}Pd	110	46	5.255E-10	-1.246E-14	-9.275E-10	-9.275E-10	6.111E-09	0.868
^{107}Ag	107	47	7.840E-10	-1.858E-14	-1.047E-09	-1.047E-09	9.453E-09	0.900
^{109}Ag	109	47	7.420E-10	-1.759E-14	-1.937E-10	-1.937E-10	9.744E-09	0.981
^{106}Cd	106	48	6.346E-11	-1.504E-15	-1.284E-10	-1.284E-10	7.215E-10	0.849
^{108}Cd	108	48	4.604E-11	-1.091E-15	7.351E-10	7.351E-10	1.352E-09	2.192
^{110}Cd	110	48	6.580E-10	-1.560E-14	1.547E-09	1.547E-09	1.036E-08	1.175
^{111}Cd	111	48	6.805E-10	-1.613E-14	-5.704E-10	-5.704E-10	8.543E-09	0.937
^{112}Cd	112	48	1.294E-09	-3.068E-14	8.301E-10	8.301E-10	1.817E-08	1.048
^{113}Cd	113	48	6.614E-10	-1.568E-14	-4.579E-10	-4.579E-10	8.400E-09	0.948
^{114}Cd	114	48	1.569E-09	-3.718E-14	1.565E-09	1.565E-09	2.257E-08	1.074

TableC.1 – continued

Isotope	A	Z	$X^{\rm ini}$	$mp^{\rm wind}$	$mp^{\rm preSN}$	$mp^{\rm total}$	EM	$\langle OP \rangle$
^{116}Cd	116	48	4.161E-10	-9.863E-15	-6.144E-10	-6.144E-10	4.959E-09	0.890
^{113}In	113	49	2.604E-11	-6.172E-16	-4.185E-11	-4.185E-11	3.069E-10	0.880
^{115}In	115	49	5.915E-10	-1.404E-14	-4.764E-10	-4.764E-10	7.445E-09	0.940
^{112}Sn	112	50	1.221E-10	-2.894E-15	-2.320E-10	-2.320E-10	1.403E-09	0.858
^{114}Sn	114	50	8.435E-11	-1.999E-15	-1.024E-10	-1.024E-10	1.027E-09	0.909
^{115}Sn	115	50	4.377E-11	-1.014E-15	3.826E-11	3.826E-11	6.245E-10	1.065
^{116}Sn	116	50	1.893E-09	-4.487E-14	2.190E-09	2.190E-09	2.755E-08	1.086
^{117}Sn	117	50	1.008E-09	-2.390E-14	-1.027E-10	-1.027E-10	1.340E-08	0.992
^{118}Sn	118	50	3.209E-09	-7.607E-14	2.859E-09	2.859E-09	4.584E-08	1.067
^{119}Sn	119	50	1.147E-09	-2.719E-14	5.697E-10	5.696E-10	1.593E-08	1.037
^{120}Sn	120	50	4.391E-09	-1.041E-13	5.806E-09	5.806E-09	6.462E-08	1.099
^{122}Sn	122	50	6.341E-10	-1.503E-14	-4.755E-10	-4.755E-10	8.017E-09	0.944
^{124}Sn	124	50	8.060E-10	-1.910E-14	-8.994E-10	-8.995E-10	9.895E-09	0.917
^{121}Sb	121	51	6.318E-10	-1.498E-14	-1.510E-10	-1.511E-10	8.310E-09	0.982
^{123}Sb	123	51	4.803E-10	-1.138E-14	-9.004E-10	-9.004E-10	5.532E-09	0.860
^{120}Te	120	52	1.628E-11	-3.860E-16	-3.636E-11	-3.636E-11	1.817E-10	0.833
^{122}Te	122	52	4.489E-10	-1.064E-14	1.113E-09	1.113E-09	7.124E-09	1.185
^{123}Te	123	52	1.579E-10	-3.742E-15	3.711E-10	3.711E-10	2.485E-09	1.176
^{124}Te	124	52	8.441E-10	-2.001E-14	2.060E-09	2.060E-09	1.337E-08	1.182
^{125}Te	125	52	1.261E-09	-2.990E-14	-1.484E-09	-1.485E-09	1.541E-08	0.912
^{126}Te	126	52	3.375E-09	-8.000E-14	1.260E-09	1.260E-09	4.647E-08	1.028
^{128}Te	128	52	5.733E-09	-1.359E-13	-8.401E-09	-8.401E-09	6.838E-08	0.891
^{130}Te	130	52	6.211E-09	-1.472E-13	-7.147E-09	-7.148E-09	7.603E-08	0.914
^{127}I	127	53	1.459E-09	-3.459E-14	-2.124E-09	-2.124E-09	1.742E-08	0.891
^{124}Xe	124	54	2.210E-11	-5.237E-16	-5.142E-11	-5.142E-11	2.445E-10	0.826
^{126}Xe	126	54	1.949E-11	-4.620E-16	-4.054E-11	-4.054E-11	2.205E-10	0.845
^{128}Xe	128	54	3.943E-10	-9.345E-15	2.166E-09	2.166E-09	7.447E-09	1.410
^{129}Xe	129	54	4.893E-09	-1.160E-13	-9.937E-09	-9.938E-09	5.559E-08	0.848

TableC.1 – continued

Isotope	A	Z	$X^{\rm ini}$	$mp^{\rm wind}$	$mp^{\rm preSN}$	$mp^{\rm total}$	EM	$\langle OP \rangle$
^{130}Xe	130	54	7.865E-10	-1.864E-14	6.434E-09	6.434E-09	1.697E-08	1.611
^{131}Xe	131	54	3.945E-09	-9.350E-14	-5.814E-09	-5.814E-09	4.702E-08	0.890
^{132}Xe	132	54	4.806E-09	-1.139E-13	3.726E-09	3.726E-09	6.810E-08	1.058
^{134}Xe	134	54	1.788E-09	-4.238E-14	-2.003E-09	-2.003E-09	2.194E-08	0.916
^{136}Xe	136	54	1.478E-09	-3.504E-14	-1.824E-10	-1.825E-10	1.962E-08	0.991
^{133}Cs	133	55	1.426E-09	-3.380E-14	-1.325E-09	-1.325E-09	1.777E-08	0.931
^{130}Ba	130	56	1.814E-11	-4.300E-16	-4.294E-11	-4.294E-11	2.000E-10	0.823
^{132}Ba	132	56	1.762E-11	-4.177E-16	-3.712E-11	-3.713E-11	1.989E-10	0.843
^{134}Ba	134	56	4.272E-10	-1.013E-14	3.770E-09	3.770E-09	9.492E-09	1.659
^{135}Ba	135	56	1.174E-09	-2.783E-14	-8.627E-10	-8.628E-10	1.486E-08	0.945
^{136}Ba	136	56	1.409E-09	-3.339E-14	8.630E-09	8.630E-09	2.750E-08	1.457
^{137}Ba	137	56	2.030E-09	-4.811E-14	5.218E-09	5.218E-09	3.240E-08	1.192
^{138}Ba	138	56	1.305E-08	-3.094E-13	4.693E-08	4.692E-08	2.217E-07	1.268
^{138}La	138	57	1.604E-12	-3.802E-17	-3.492E-12	-3.492E-12	1.799E-11	0.837
^{139}La	139	57	1.790E-09	-4.243E-14	4.805E-09	4.805E-09	2.878E-08	1.200
^{136}Ce	136	58	8.382E-12	-1.987E-16	-1.723E-11	-1.723E-11	9.502E-11	0.846
^{138}Ce	138	58	1.148E-11	-2.720E-16	-2.120E-11	-2.120E-11	1.325E-10	0.862
^{140}Ce	140	58	4.103E-09	-9.725E-14	6.214E-09	6.214E-09	6.117E-08	1.113
^{142}Ce	142	58	5.229E-10	-1.239E-14	-5.883E-10	-5.883E-10	6.415E-09	0.916
^{141}Pr	141	59	6.910E-10	-1.638E-14	2.649E-10	2.649E-10	9.520E-09	1.029
^{142}Nd	142	60	9.920E-10	-2.351E-14	1.634E-09	1.634E-09	1.492E-08	1.123
^{143}Nd	143	60	4.484E-10	-1.063E-14	-3.123E-10	-3.123E-10	5.693E-09	0.948
^{144}Nd	144	60	8.826E-10	-2.092E-14	9.305E-11	9.303E-11	1.191E-08	1.008
^{145}Nd	145	60	3.095E-10	-7.337E-15	-2.396E-10	-2.396E-10	3.906E-09	0.942
^{146}Nd	146	60	6.448E-10	-1.528E-14	3.146E-10	3.146E-10	8.950E-09	1.036
^{148}Nd	148	60	2.185E-10	-5.179E-15	-3.676E-10	-3.676E-10	2.559E-09	0.874
^{150}Nd	150	60	2.168E-10	-5.139E-15	-4.092E-10	-4.093E-10	2.495E-09	0.859
^{144}Sm	144	62	3.684E-11	-8.731E-16	-6.141E-11	-6.141E-11	4.319E-10	0.876

TableC.1 – continued

Isotope	A	Z	$X^{\rm ini}$	$mp^{\rm wind}$	$mp^{\rm preSN}$	$mp^{\rm total}$	EM	$\langle OP \rangle$
^{147}Sm	147	62	1.834E-10	-4.348E-15	-2.563E-10	-2.564E-10	2.201E-09	0.896
^{148}Sm	148	62	1.385E-10	-3.282E-15	3.028E-10	3.028E-10	2.157E-09	1.163
^{149}Sm	149	62	1.714E-10	-4.062E-15	-3.365E-10	-3.365E-10	1.959E-09	0.853
^{150}Sm	150	62	9.213E-11	-2.184E-15	2.493E-10	2.493E-10	1.483E-09	1.202
^{152}Sm	152	62	3.383E-10	-8.019E-15	-5.455E-10	-5.455E-10	3.986E-09	0.880
^{154}Sm	154	62	2.916E-10	-6.912E-15	-5.527E-10	-5.528E-10	3.353E-09	0.858
^{151}Eu	151	63	2.036E-10	-4.826E-15	-4.823E-10	-4.823E-10	2.245E-09	0.823
^{153}Eu	153	63	2.252E-10	-5.338E-15	-4.717E-10	-4.717E-10	2.544E-09	0.844
^{152}Gd	152	64	2.947E-12	-6.986E-17	1.369E-10	1.369E-10	1.763E-10	4.467
^{154}Gd	154	64	3.210E-11	-7.607E-16	2.712E-10	2.712E-10	7.011E-10	1.631
^{155}Gd	155	64	2.192E-10	-5.196E-15	-4.271E-10	-4.271E-10	2.509E-09	0.855
^{156}Gd	156	64	3.051E-10	-7.232E-15	-1.374E-10	-1.374E-10	3.949E-09	0.966
^{157}Gd	157	64	2.348E-10	-5.566E-15	-3.196E-10	-3.196E-10	2.825E-09	0.898
^{158}Gd	158	64	3.750E-10	-8.888E-15	-4.896E-12	-4.905E-12	5.017E-09	0.999
^{160}Gd	160	64	3.343E-10	-7.924E-15	-6.148E-10	-6.148E-10	3.862E-09	0.863
^{159}Tb	159	65	2.765E-10	-6.554E-15	-5.087E-10	-5.087E-10	3.194E-09	0.863
^{156}Dy	156	66	1.004E-12	-2.379E-17	-2.627E-12	-2.627E-12	1.082E-11	0.805
^{158}Dy	158	66	1.743E-12	-4.131E-17	3.703E-12	3.703E-12	2.704E-11	1.159
^{160}Dy	160	66	4.301E-11	-1.020E-15	2.581E-10	2.581E-10	8.342E-10	1.448
^{161}Dy	161	66	3.498E-10	-8.291E-15	-7.254E-10	-7.254E-10	3.959E-09	0.845
^{162}Dy	162	66	4.748E-10	-1.125E-14	-3.234E-10	-3.234E-10	6.036E-09	0.949
^{163}Dy	163	66	4.663E-10	-1.105E-14	-8.039E-10	-8.039E-10	5.441E-09	0.871
^{164}Dy	164	66	5.312E-10	-1.259E-14	2.047E-10	2.047E-10	7.319E-09	1.029
^{165}Ho	165	67	4.244E-10	-1.006E-14	-8.092E-10	-8.092E-10	4.875E-09	0.858
^{162}Er	162	68	1.609E-12	-3.813E-17	-4.209E-12	-4.209E-12	1.734E-11	0.805
^{164}Er	164	68	1.913E-11	-4.534E-16	-4.834E-11	-4.834E-11	2.078E-10	0.811
^{166}Er	166	68	4.044E-10	-9.587E-15	-3.134E-10	-3.134E-10	5.103E-09	0.942
^{167}Er	167	68	2.776E-10	-6.580E-15	-4.220E-10	-4.220E-10	3.296E-09	0.886

TableC.1 – continued

Isotope	A	Z	X^{ini}	mp^{wind}	mp^{preSN}	mp^{total}	EM	$\langle OP \rangle$
^{168}Er	168	68	3.263E-10	-7.733E-15	2.082E-10	2.082E-10	4.578E-09	1.048
^{170}Er	170	68	1.840E-10	-4.361E-15	-3.125E-10	-3.125E-10	2.152E-09	0.873
^{169}Tm	169	69	1.854E-10	-4.395E-15	-2.912E-10	-2.912E-10	2.192E-09	0.883
^{168}Yb	168	70	1.583E-12	-3.753E-17	-4.033E-12	-4.033E-12	1.717E-11	0.810
^{170}Yb	170	70	3.746E-11	-8.880E-16	2.735E-10	2.735E-10	7.752E-10	1.545
^{171}Yb	171	70	1.770E-10	-4.196E-15	-1.857E-10	-1.857E-10	2.185E-09	0.922
^{172}Yb	172	70	2.722E-10	-6.452E-15	9.480E-11	9.479E-11	3.740E-09	1.026
^{173}Yb	173	70	2.023E-10	-4.795E-15	-1.236E-10	-1.236E-10	2.586E-09	0.954
^{174}Yb	174	70	4.015E-10	-9.516E-15	4.259E-10	4.259E-10	5.803E-09	1.079
^{176}Yb	176	70	1.628E-10	-3.859E-15	-2.694E-10	-2.694E-10	1.911E-09	0.876
^{175}Lu	175	71	1.828E-10	-4.333E-15	-2.603E-10	-2.603E-10	2.188E-09	0.894
^{176}Lu	176	71	4.876E-12	-2.337E-15	2.734E-11	2.733E-11	9.264E-11	1.419
^{174}Hf	174	72	1.231E-12	-2.918E-17	-3.036E-12	-3.036E-12	1.345E-11	0.816
^{176}Hf	176	72	4.036E-11	1.265E-15	1.660E-10	1.660E-10	7.066E-10	1.307
^{177}Hf	177	72	1.438E-10	-3.408E-15	-1.951E-10	-1.951E-10	1.731E-09	0.899
^{178}Hf	178	72	2.121E-10	-5.028E-15	2.275E-10	2.275E-10	3.069E-09	1.080
^{179}Hf	179	72	1.065E-10	-2.525E-15	-7.143E-11	-7.143E-11	1.355E-09	0.950
^{180}Hf	180	72	2.758E-10	-6.538E-15	4.756E-10	4.755E-10	4.170E-09	1.129
^{180}Ta	180	73	2.429E-14	-5.765E-19	3.062E-12	3.062E-12	3.387E-12	10.411
^{181}Ta	181	73	1.986E-10	-4.707E-15	-2.238E-10	-2.238E-10	2.436E-09	0.916
^{180}W	180	74	8.395E-13	-1.990E-17	2.662E-11	2.662E-11	3.786E-11	3.367
^{182}W	182	74	1.877E-10	-4.450E-15	3.031E-10	3.031E-10	2.818E-09	1.121
^{183}W	183	74	1.020E-10	-2.417E-15	1.674E-10	1.674E-10	1.533E-09	1.123
^{184}W	184	74	2.195E-10	-5.203E-15	4.081E-10	4.081E-10	3.348E-09	1.139
^{186}W	186	74	2.058E-10	-4.879E-15	-3.143E-10	-3.143E-10	2.442E-09	0.886
^{185}Re	185	75	1.048E-10	-2.484E-15	-8.504E-11	-8.504E-11	1.318E-09	0.939
^{187}Re	187	75	1.773E-10	-4.203E-15	-3.941E-10	-3.941E-10	1.981E-09	0.834
^{184}Os	184	76	7.108E-13	-1.685E-17	-1.636E-12	-1.636E-12	7.884E-12	0.828

TableC.1 – continued

Isotope	A	Z	$X^{\rm ini}$	$mp^{\rm wind}$	$mp^{\rm preSN}$	$mp^{\rm total}$	EM	$\langle OP \rangle$
^{186}Os	186	76	5.778E-11	-1.370E-15	3.317E-10	3.317E-10	1.106E-09	1.429
^{187}Os	187	76	5.998E-11	-1.422E-15	2.273E-11	2.273E-11	8.261E-10	1.028
^{188}Os	188	76	4.874E-10	-1.155E-14	-1.364E-10	-1.364E-10	6.391E-09	0.979
^{189}Os	189	76	5.974E-10	-1.416E-14	-1.284E-09	-1.284E-09	6.717E-09	0.840
^{190}Os	190	76	9.766E-10	-2.315E-14	-6.278E-10	-6.278E-10	1.245E-08	0.952
^{192}Os	192	76	1.533E-09	-3.633E-14	-2.647E-09	-2.647E-09	1.788E-08	0.871
^{191}Ir	191	77	1.357E-09	-3.217E-14	-3.199E-09	-3.199E-09	1.498E-08	0.824
^{193}Ir	193	77	2.308E-09	-5.471E-14	-5.081E-09	-5.081E-09	2.583E-08	0.836
^{190}Pt	190	78	1.008E-12	-2.390E-17	-2.249E-12	-2.249E-12	1.126E-11	0.834
^{192}Pt	192	78	5.850E-11	-1.387E-15	1.100E-09	1.100E-09	1.883E-09	2.404
^{194}Pt	194	78	2.490E-09	-5.902E-14	-2.435E-09	-2.436E-09	3.091E-08	0.927
^{195}Pt	195	78	2.568E-09	-6.088E-14	-4.801E-09	-4.801E-09	2.960E-08	0.860
^{196}Pt	196	78	1.926E-09	-4.565E-14	8.435E-10	8.434E-10	2.664E-08	1.033
^{198}Pt	198	78	5.522E-10	-1.309E-14	-9.231E-10	-9.231E-10	6.472E-09	0.875
^{197}Au	197	79	1.083E-09	-2.568E-14	-1.279E-09	-1.279E-09	1.323E-08	0.912
^{196}Hg	196	80	3.009E-12	-7.133E-17	-5.732E-12	-5.732E-12	3.457E-11	0.858
^{198}Hg	198	80	1.975E-10	-4.681E-15	2.360E-09	2.360E-09	5.005E-09	1.892
^{199}Hg	199	80	3.360E-10	-7.964E-15	3.590E-10	3.589E-10	4.859E-09	1.080
^{200}Hg	200	80	4.622E-10	-1.096E-14	1.836E-09	1.836E-09	8.026E-09	1.297
^{201}Hg	201	80	2.651E-10	-6.284E-15	8.209E-10	8.209E-10	4.372E-09	1.231
^{202}Hg	202	80	6.036E-10	-1.431E-14	3.655E-09	3.655E-09	1.174E-08	1.452
^{204}Hg	204	80	1.401E-10	-3.322E-15	-1.670E-10	-1.670E-10	1.710E-09	0.911
^{203}Tl	203	81	3.221E-10	-7.634E-15	2.629E-09	2.629E-09	6.942E-09	1.609
^{205}Tl	205	81	7.764E-10	-1.840E-14	4.311E-09	4.311E-09	1.471E-08	1.415
^{204}Pb	204	82	2.931E-10	-6.947E-15	3.361E-09	3.361E-09	7.286E-09	1.856
^{206}Pb	206	82	2.798E-09	-6.631E-14	9.930E-09	9.930E-09	4.740E-08	1.265
^{207}Pb	207	82	3.090E-09	-7.323E-14	1.022E-08	1.022E-08	5.160E-08	1.247
^{208}Pb	208	82	8.850E-09	-2.098E-13	9.983E-09	9.983E-09	1.285E-07	1.084

TableC.1 – continued

Isotope	A	Z	X^{ini}	mp^{wind}	mp^{preSN}	mp^{total}	EM	$\langle OP \rangle$
^{209}Bi	209	83	8.718E-10	-2.066E-14	3.883E-10	3.882E-10	1.206E-08	1.033

Table C.2: Yields for model 15CI.

Isotope	A	Z	$X^{\rm ini}$	$mp^{\rm wind}$	$mp^{\rm preSN}$	$mp^{\rm total}$	EM	$\langle OP \rangle$
^{1}H	1	1	7.064E-01	-4.942E-02	-2.928E+00	-2.977E+00	6.484E+00	0.685
^{2}H	2	1	1.371E-05	-3.320E-05	-1.369E-04	-1.701E-04	1.345E-05	0.073
^{3}He	3	2	4.540E-05	-1.569E-05	-2.875E-04	-3.032E-04	3.049E-04	0.501
^{4}He	4	2	2.735E-01	4.921E-02	1.389E+00	1.438E+00	5.101E+00	1.393
^{7}Li	7	3	7.605E-11	-1.842E-10	-7.597E-10	-9.439E-10	7.466E-11	0.073
^{11}B	11	5	2.856E-09	-3.996E-14	9.784E-11	9.780E-11	3.835E-08	1.003
^{12}C	12	6	3.425E-03	-2.757E-03	1.623E-01	1.595E-01	2.054E-01	4.478
^{13}C	13	6	4.156E-05	2.331E-04	2.389E-04	4.720E-04	1.029E-03	1.848
^{14}N	14	7	1.059E-03	4.403E-03	4.147E-02	4.587E-02	6.005E-02	4.235
^{15}N	15	7	4.171E-06	-5.898E-06	-3.312E-05	-3.902E-05	1.684E-05	0.301
^{16}O	16	8	9.624E-03	-1.630E-03	7.288E-01	7.272E-01	8.561E-01	6.641
^{17}O	17	8	3.813E-06	4.024E-06	2.525E-05	2.927E-05	8.034E-05	1.573
^{18}O	18	8	2.171E-05	-1.239E-05	3.747E-03	3.735E-03	4.026E-03	13.845
^{19}F	19	9	5.611E-07	-1.083E-07	-2.856E-06	-2.965E-06	4.550E-06	0.605
^{20}Ne	20	10	1.818E-03	-2.824E-06	5.158E-01	5.158E-01	5.401E-01	22.186
^{21}Ne	21	10	4.575E-06	2.961E-06	2.236E-03	2.239E-03	2.301E-03	37.545
^{22}Ne	22	10	1.470E-04	-3.175E-05	1.371E-02	1.368E-02	1.565E-02	7.949
^{23}Na	23	11	4.000E-05	3.317E-05	2.794E-02	2.798E-02	2.851E-02	53.231
^{24}Mg	24	12	5.862E-04	-4.642E-09	3.993E-02	3.993E-02	4.778E-02	6.086
^{25}Mg	25	12	7.733E-05	-9.813E-06	1.831E-02	1.830E-02	1.933E-02	18.666
^{26}Mg	26	12	8.848E-05	1.015E-05	1.129E-02	1.130E-02	1.248E-02	10.532
^{27}Al	27	13	6.481E-05	5.349E-08	5.525E-03	5.525E-03	6.393E-03	7.365
^{28}Si	28	14	7.453E-04	-1.026E-08	1.839E-03	1.839E-03	1.182E-02	1.184
^{29}Si	29	14	3.919E-05	-5.520E-10	2.591E-04	2.591E-04	7.841E-04	1.494
^{30}Si	30	14	2.673E-05	-2.080E-09	3.126E-04	3.126E-04	6.706E-04	1.873
^{31}P	31	15	7.106E-06	1.667E-09	1.015E-04	1.015E-04	1.967E-04	2.067
^{32}S	32	16	4.011E-04	-5.617E-09	-2.536E-04	-2.536E-04	5.118E-03	0.953

TableC.2 – continued

Isotope	A	Z	$X^{\rm ini}$	$mp^{\rm wind}$	$mp^{\rm preSN}$	$mp^{\rm total}$	EM	$\langle OP \rangle$
^{33}S	33	16	3.265E-06	-3.947E-11	8.737E-06	8.737E-06	5.246E-05	1.200
^{34}S	34	16	1.890E-05	-2.645E-10	1.589E-05	1.589E-05	2.691E-04	1.063
^{36}S	36	16	8.073E-08	-1.129E-12	8.066E-06	8.066E-06	9.147E-06	8.460
^{35}Cl	35	17	6.821E-06	-9.543E-11	-4.806E-06	-4.807E-06	8.655E-05	0.947
^{37}Cl	37	17	2.306E-06	-3.226E-11	7.476E-05	7.476E-05	1.056E-04	3.421
^{36}Ar	36	18	8.202E-05	-1.148E-09	-8.852E-05	-8.852E-05	1.010E-03	0.919
^{38}Ar	38	18	1.574E-05	-2.202E-10	4.654E-05	4.654E-05	2.574E-04	1.221
^{40}Ar	40	18	2.650E-08	-3.680E-13	4.404E-06	4.404E-06	4.759E-06	13.407
^{39}K	39	19	3.900E-06	-5.456E-11	9.780E-06	9.780E-06	6.201E-05	1.187
^{40}K	40	19	5.005E-10	-6.525E-12	1.117E-06	1.117E-06	1.123E-06	167.592
^{41}K	41	19	2.959E-07	-4.139E-12	3.937E-06	3.937E-06	7.899E-06	1.993
^{40}Ca	40	20	7.225E-05	-1.004E-09	-6.395E-05	-6.395E-05	9.037E-04	0.934
^{42}Ca	42	20	5.063E-07	-7.084E-12	4.848E-06	4.848E-06	1.163E-05	1.715
^{43}Ca	43	20	1.082E-07	-1.513E-12	1.896E-06	1.896E-06	3.344E-06	2.309
^{44}Ca	44	20	1.710E-06	-2.393E-11	3.958E-06	3.958E-06	2.686E-05	1.173
^{46}Ca	46	20	3.428E-09	-4.797E-14	2.063E-08	2.063E-08	6.654E-08	1.449
^{48}Ca	48	20	1.672E-07	-2.340E-12	-2.754E-08	-2.754E-08	2.212E-06	0.988
^{45}Sc	45	21	5.414E-08	-7.574E-13	1.113E-06	1.113E-06	1.838E-06	2.535
^{46}Ti	46	22	3.232E-07	-4.521E-12	1.016E-06	1.016E-06	5.344E-06	1.235
^{47}Ti	47	22	2.977E-07	-4.165E-12	2.923E-07	2.923E-07	4.279E-06	1.073
^{48}Ti	48	22	3.014E-06	-4.216E-11	-3.263E-06	-3.263E-06	3.710E-05	0.919
^{49}Ti	49	22	2.257E-07	-3.158E-12	1.453E-06	1.453E-06	4.476E-06	1.481
^{50}Ti	50	22	2.208E-07	-3.089E-12	4.465E-06	4.465E-06	7.422E-06	2.510
^{50}V	50	23	1.015E-09	-1.421E-14	-8.613E-10	-8.613E-10	1.274E-08	0.937
^{51}V	51	23	4.138E-07	-5.789E-12	1.286E-08	1.285E-08	5.555E-06	1.002
^{50}Cr	50	24	8.265E-07	-1.156E-11	-1.341E-06	-1.341E-06	9.729E-06	0.879
^{52}Cr	52	24	1.658E-05	-2.319E-10	-1.621E-05	-1.621E-05	2.058E-04	0.927
^{53}Cr	53	24	1.916E-06	-2.680E-11	-9.011E-07	-9.011E-07	2.476E-05	0.965

TableC.2 – continued

Isotope	A	Z	$X^{\rm ini}$	$mp^{\rm wind}$	$mp^{\rm preSN}$	$mp^{\rm total}$	EM	$\langle OP \rangle$
^{54}Cr	54	24	4.858E-07	-6.797E-12	1.174E-05	1.174E-05	1.824E-05	2.804
^{55}Mn	55	25	1.098E-05	-1.536E-10	-3.171E-06	-3.171E-06	1.439E-04	0.978
^{54}Fe	54	26	8.118E-05	-1.136E-09	-1.255E-04	-1.255E-04	9.618E-04	0.885
^{56}Fe	56	26	1.322E-03	-1.849E-08	-1.506E-03	-1.506E-03	1.619E-02	0.915
^{57}Fe	57	26	3.107E-05	-4.346E-10	1.570E-04	1.570E-04	5.731E-04	1.377
^{58}Fe	58	26	4.207E-06	-5.886E-11	5.628E-04	5.628E-04	6.192E-04	10.989
^{59}Co	59	27	3.991E-06	-5.584E-11	2.874E-04	2.874E-04	3.408E-04	6.375
^{58}Ni	58	28	5.711E-05	-7.990E-10	-8.642E-05	-8.642E-05	6.785E-04	0.887
^{60}Ni	60	28	2.276E-05	-3.184E-10	2.001E-04	2.001E-04	5.049E-04	1.657
^{61}Ni	61	28	1.006E-06	-1.407E-11	9.253E-05	9.253E-05	1.060E-04	7.870
^{62}Ni	62	28	3.259E-06	-4.560E-11	2.246E-04	2.246E-04	2.683E-04	6.146
^{64}Ni	64	28	8.568E-07	-1.199E-11	8.666E-05	8.666E-05	9.813E-05	8.552
^{63}Cu	63	29	6.600E-07	-9.234E-12	7.077E-05	7.077E-05	7.961E-05	9.006
^{65}Cu	65	29	3.035E-07	-4.246E-12	6.603E-05	6.603E-05	7.010E-05	17.247
^{64}Zn	64	30	1.131E-06	-1.582E-11	3.396E-05	3.396E-05	4.910E-05	3.242
^{66}Zn	66	30	6.690E-07	-9.360E-12	3.913E-05	3.913E-05	4.809E-05	5.367
^{67}Zn	67	30	9.980E-08	-1.396E-12	1.150E-05	1.150E-05	1.284E-05	9.606
^{68}Zn	68	30	4.632E-07	-6.481E-12	4.004E-05	4.004E-05	4.625E-05	7.455
^{70}Zn	70	30	1.577E-08	-2.206E-13	-1.468E-08	-1.468E-08	1.965E-07	0.930
^{69}Ga	69	31	4.551E-08	-6.366E-13	5.061E-06	5.061E-06	5.671E-06	9.305
^{71}Ga	71	31	3.108E-08	-4.348E-13	4.668E-06	4.668E-06	5.084E-06	12.215
^{70}Ge	70	32	5.157E-08	-7.215E-13	6.768E-06	6.768E-06	7.459E-06	10.799
^{72}Ge	72	32	6.910E-08	-9.668E-13	5.779E-06	5.779E-06	6.705E-06	7.244
^{73}Ge	73	32	1.955E-08	-2.735E-13	2.352E-06	2.352E-06	2.613E-06	9.983
^{74}Ge	74	32	9.228E-08	-1.291E-12	7.351E-06	7.351E-06	8.587E-06	6.948
^{76}Ge	76	32	1.963E-08	-2.746E-13	-2.552E-08	-2.552E-08	2.374E-07	0.903
^{75}As	75	33	1.430E-08	-2.001E-13	8.518E-07	8.518E-07	1.043E-06	5.447
^{74}Se	74	34	1.198E-09	-1.676E-14	-2.265E-09	-2.265E-09	1.378E-08	0.859

TableC.2 – continued

Isotope	A	Z	$X^{\rm ini}$	$mp^{\rm wind}$	$mp^{\rm preSN}$	$mp^{\rm total}$	EM	$\langle OP \rangle$
^{76}Se	76	34	1.296E-08	-1.813E-13	1.342E-06	1.342E-06	1.515E-06	8.730
^{77}Se	77	34	1.070E-08	-1.498E-13	6.446E-07	6.446E-07	7.880E-07	5.496
^{78}Se	78	34	3.376E-08	-4.724E-13	3.049E-06	3.049E-06	3.501E-06	7.742
^{80}Se	80	34	7.226E-08	-1.011E-12	2.278E-07	2.278E-07	1.196E-06	1.235
^{82}Se	82	34	1.304E-08	-1.824E-13	-1.416E-08	-1.416E-08	1.604E-07	0.919
^{79}Br	79	35	1.389E-08	-1.944E-13	3.529E-07	3.529E-07	5.390E-07	2.897
^{81}Br	81	35	1.386E-08	-1.939E-13	3.802E-07	3.802E-07	5.658E-07	3.048
^{78}Kr	78	36	3.900E-10	-5.457E-15	-7.003E-10	-7.003E-10	4.523E-09	0.866
^{80}Kr	80	36	2.575E-09	-3.602E-14	5.845E-07	5.845E-07	6.190E-07	17.950
^{82}Kr	82	36	1.320E-08	-1.846E-13	1.481E-06	1.481E-06	1.658E-06	9.379
^{83}Kr	83	36	1.324E-08	-1.853E-13	6.697E-07	6.697E-07	8.471E-07	4.776
^{84}Kr	84	36	6.602E-08	-9.237E-13	2.476E-06	2.476E-06	3.360E-06	3.800
^{86}Kr	86	36	2.044E-08	-2.860E-13	2.469E-07	2.469E-07	5.207E-07	1.902
^{85}Rb	85	37	1.282E-08	-1.794E-13	3.738E-07	3.738E-07	5.455E-07	3.176
^{87}Rb	87	37	5.063E-09	-2.026E-12	1.044E-07	1.044E-07	1.722E-07	2.539
^{84}Sr	84	38	3.228E-10	-4.516E-15	-6.382E-10	-6.382E-10	3.685E-09	0.852
^{86}Sr	86	38	5.845E-09	-8.177E-14	9.605E-07	9.605E-07	1.039E-06	13.271
^{87}Sr	87	38	4.443E-09	1.893E-12	5.531E-07	5.531E-07	6.126E-07	10.295
^{88}Sr	88	38	5.011E-08	-7.010E-13	1.910E-06	1.910E-06	2.581E-06	3.845
^{89}Y	89	39	1.229E-08	-1.720E-13	3.505E-07	3.505E-07	5.151E-07	3.129
^{90}Zr	90	40	1.534E-08	-2.147E-13	1.891E-07	1.891E-07	3.946E-07	1.920
^{91}Zr	91	40	3.384E-09	-4.734E-14	6.241E-08	6.241E-08	1.077E-07	2.377
^{92}Zr	92	40	5.227E-09	-7.313E-14	7.959E-08	7.959E-08	1.496E-07	2.137
^{94}Zr	94	40	5.413E-09	-7.573E-14	3.770E-08	3.770E-08	1.102E-07	1.520
^{96}Zr	96	40	8.903E-10	-1.246E-14	2.961E-09	2.960E-09	1.489E-08	1.248
^{93}Nb	93	41	1.900E-09	-2.658E-14	3.188E-08	3.188E-08	5.732E-08	2.253
^{92}Mo	92	42	1.012E-09	-1.417E-14	-1.681E-09	-1.681E-09	1.188E-08	0.876
^{94}Mo	94	42	6.448E-10	-9.020E-15	-1.762E-10	-1.762E-10	8.459E-09	0.980

TableC.2 – continued

Isotope	A	Z	$X^{\rm ini}$	$mp^{\rm wind}$	$mp^{\rm preSN}$	$mp^{\rm total}$	EM	$\langle OP \rangle$
^{95}Mo	95	42	1.122E-09	-1.570E-14	6.574E-09	6.574E-09	2.160E-08	1.438
^{96}Mo	96	42	1.188E-09	-1.661E-14	1.509E-08	1.509E-08	3.099E-08	1.949
^{97}Mo	97	42	6.875E-10	-9.619E-15	5.083E-09	5.083E-09	1.429E-08	1.552
^{98}Mo	98	42	1.754E-09	-2.454E-14	1.478E-08	1.478E-08	3.827E-08	1.629
^{100}Mo	100	42	7.146E-10	-9.998E-15	-1.198E-09	-1.198E-09	8.373E-09	0.875
^{96}Ru	96	44	2.926E-10	-4.093E-15	-5.252E-10	-5.252E-10	3.393E-09	0.866
^{98}Ru	98	44	1.007E-10	-1.409E-15	-1.468E-10	-1.468E-10	1.202E-09	0.891
^{99}Ru	99	44	6.945E-10	-9.717E-15	1.978E-09	1.978E-09	1.128E-08	1.213
^{100}Ru	100	44	6.928E-10	-9.693E-15	7.006E-09	7.006E-09	1.628E-08	1.755
^{101}Ru	101	44	9.475E-10	-1.326E-14	-2.020E-10	-2.021E-10	1.249E-08	0.984
^{102}Ru	102	44	1.770E-09	-2.476E-14	8.738E-09	8.738E-09	3.244E-08	1.369
^{104}Ru	104	44	1.065E-09	-1.490E-14	-1.826E-09	-1.826E-09	1.244E-08	0.872
^{103}Rh	103	45	1.055E-09	-1.476E-14	-2.351E-10	-2.351E-10	1.389E-08	0.983
^{102}Pd	102	46	4.241E-11	-5.934E-16	-8.404E-11	-8.404E-11	4.840E-10	0.852
^{104}Pd	104	46	4.723E-10	-6.607E-15	4.914E-09	4.914E-09	1.124E-08	1.777
^{105}Pd	105	46	9.558E-10	-1.337E-14	-7.387E-10	-7.387E-10	1.206E-08	0.942
^{106}Pd	106	46	1.181E-09	-1.652E-14	4.674E-09	4.674E-09	2.049E-08	1.296
^{108}Pd	108	46	1.165E-09	-1.630E-14	3.538E-09	3.538E-09	1.914E-08	1.227
^{110}Pd	110	46	5.255E-10	-7.353E-15	-8.801E-10	-8.801E-10	6.159E-09	0.875
^{107}Ag	107	47	7.840E-10	-1.097E-14	-1.677E-10	-1.677E-10	1.033E-08	0.984
^{109}Ag	109	47	7.420E-10	-1.038E-14	2.113E-09	2.113E-09	1.205E-08	1.213
^{106}Cd	106	48	6.346E-11	-8.878E-16	-1.214E-10	-1.214E-10	7.285E-10	0.857
^{108}Cd	108	48	4.604E-11	-6.441E-16	1.895E-09	1.895E-09	2.512E-09	4.074
^{110}Cd	110	48	6.580E-10	-9.206E-15	4.812E-09	4.812E-09	1.362E-08	1.546
^{111}Cd	111	48	6.805E-10	-9.520E-15	4.783E-10	4.783E-10	9.592E-09	1.052
^{112}Cd	112	48	1.294E-09	-1.811E-14	4.638E-09	4.638E-09	2.197E-08	1.268
^{113}Cd	113	48	6.614E-10	-9.253E-15	5.878E-10	5.877E-10	9.445E-09	1.066
^{114}Cd	114	48	1.569E-09	-2.195E-14	6.560E-09	6.560E-09	2.757E-08	1.312

TableC.2 – continued

Isotope	A	Z	$X^{\rm ini}$	$mp^{\rm wind}$	$mp^{\rm preSN}$	$mp^{\rm total}$	EM	$\langle OP \rangle$
^{116}Cd	116	48	4.161E-10	-5.822E-15	-5.706E-10	-5.706E-10	5.003E-09	0.898
^{113}In	113	49	2.604E-11	-3.643E-16	-4.192E-11	-4.192E-11	3.068E-10	0.880
^{115}In	115	49	5.915E-10	-8.299E-15	3.367E-10	3.367E-10	8.259E-09	1.042
^{112}Sn	112	50	1.221E-10	-1.708E-15	-2.220E-10	-2.220E-10	1.413E-09	0.864
^{114}Sn	114	50	8.435E-11	-1.180E-15	-1.111E-10	-1.111E-10	1.019E-09	0.902
^{115}Sn	115	50	4.377E-11	-5.886E-16	2.550E-10	2.550E-10	8.412E-10	1.435
^{116}Sn	116	50	1.893E-09	-2.649E-14	7.756E-09	7.756E-09	3.311E-08	1.306
^{117}Sn	117	50	1.008E-09	-1.411E-14	1.688E-09	1.688E-09	1.519E-08	1.125
^{118}Sn	118	50	3.209E-09	-4.490E-14	9.545E-09	9.545E-09	5.253E-08	1.222
^{119}Sn	119	50	1.147E-09	-1.605E-14	2.505E-09	2.505E-09	1.787E-08	1.163
^{120}Sn	120	50	4.391E-09	-6.144E-14	1.361E-08	1.361E-08	7.242E-08	1.231
^{122}Sn	122	50	6.341E-10	-8.871E-15	-5.649E-10	-5.649E-10	7.927E-09	0.933
^{124}Sn	124	50	8.060E-10	-1.128E-14	-1.015E-09	-1.015E-09	9.779E-09	0.906
^{121}Sb	121	51	6.318E-10	-8.839E-15	4.940E-10	4.940E-10	8.955E-09	1.058
^{123}Sb	123	51	4.803E-10	-6.719E-15	-8.626E-10	-8.626E-10	5.570E-09	0.866
^{120}Te	120	52	1.628E-11	-2.278E-16	-3.401E-11	-3.401E-11	1.841E-10	0.844
^{122}Te	122	52	4.489E-10	-6.280E-15	1.964E-09	1.964E-09	7.976E-09	1.327
^{123}Te	123	52	1.579E-10	-2.209E-15	6.521E-10	6.521E-10	2.766E-09	1.308
^{124}Te	124	52	8.441E-10	-1.181E-14	3.630E-09	3.630E-09	1.494E-08	1.321
^{125}Te	125	52	1.261E-09	-1.765E-14	-8.646E-10	-8.646E-10	1.603E-08	0.949
^{126}Te	126	52	3.375E-09	-4.722E-14	4.063E-09	4.063E-09	4.927E-08	1.090
^{128}Te	128	52	5.733E-09	-8.021E-14	-8.695E-09	-8.695E-09	6.809E-08	0.887
^{130}Te	130	52	6.211E-09	-8.689E-14	-8.150E-09	-8.150E-09	7.503E-08	0.902
^{127}I	127	53	1.459E-09	-2.041E-14	-1.534E-09	-1.534E-09	1.801E-08	0.922
^{124}Xe	124	54	2.210E-11	-3.091E-16	-4.815E-11	-4.815E-11	2.478E-10	0.837
^{126}Xe	126	54	1.949E-11	-2.727E-16	-3.844E-11	-3.844E-11	2.226E-10	0.853
^{128}Xe	128	54	3.943E-10	-5.516E-15	2.754E-09	2.754E-09	8.035E-09	1.522
^{129}Xe	129	54	4.893E-09	-6.846E-14	-9.003E-09	-9.003E-09	5.653E-08	0.863

TableC.2 – continued

Isotope	A	Z	$X^{\rm ini}$	$mp^{\rm wind}$	$mp^{\rm preSN}$	$mp^{\rm total}$	EM	$\langle OP \rangle$
^{130}Xe	130	54	7.865E-10	-1.100E-14	6.875E-09	6.875E-09	1.741E-08	1.653
^{131}Xe	131	54	3.945E-09	-5.519E-14	-5.108E-09	-5.108E-09	4.772E-08	0.903
^{132}Xe	132	54	4.806E-09	-6.724E-14	5.174E-09	5.174E-09	6.954E-08	1.080
^{134}Xe	134	54	1.788E-09	-2.502E-14	-2.303E-09	-2.303E-09	2.164E-08	0.904
^{136}Xe	136	54	1.478E-09	-2.068E-14	-2.446E-10	-2.446E-10	1.956E-08	0.988
^{133}Cs	133	55	1.426E-09	-1.995E-14	-8.814E-10	-8.814E-10	1.822E-08	0.954
^{130}Ba	130	56	1.814E-11	-2.538E-16	-4.004E-11	-4.004E-11	2.030E-10	0.835
^{132}Ba	132	56	1.762E-11	-2.465E-16	-3.501E-11	-3.501E-11	2.010E-10	0.852
^{134}Ba	134	56	4.272E-10	-5.977E-15	3.985E-09	3.985E-09	9.707E-09	1.696
^{135}Ba	135	56	1.174E-09	-1.642E-14	-6.316E-10	-6.316E-10	1.509E-08	0.960
^{136}Ba	136	56	1.409E-09	-1.971E-14	9.479E-09	9.479E-09	2.835E-08	1.502
^{137}Ba	137	56	2.030E-09	-2.840E-14	5.966E-09	5.966E-09	3.315E-08	1.219
^{138}Ba	138	56	1.305E-08	-1.826E-13	6.349E-08	6.349E-08	2.383E-07	1.363
^{138}La	138	57	1.604E-12	-2.244E-17	-3.303E-12	-3.303E-12	1.818E-11	0.846
^{139}La	139	57	1.790E-09	-2.505E-14	6.985E-09	6.985E-09	3.096E-08	1.291
^{136}Ce	136	58	8.382E-12	-1.173E-16	-1.641E-11	-1.641E-11	9.585E-11	0.854
^{138}Ce	138	58	1.148E-11	-1.606E-16	-2.046E-11	-2.046E-11	1.333E-10	0.867
^{140}Ce	140	58	4.103E-09	-5.740E-14	1.004E-08	1.004E-08	6.499E-08	1.183
^{142}Ce	142	58	5.229E-10	-7.316E-15	-7.257E-10	-7.257E-10	6.278E-09	0.896
^{141}Pr	141	59	6.910E-10	-9.668E-15	7.702E-10	7.702E-10	1.003E-08	1.083
^{142}Nd	142	60	9.920E-10	-1.388E-14	2.622E-09	2.622E-09	1.591E-08	1.197
^{143}Nd	143	60	4.484E-10	-6.273E-15	-1.335E-10	-1.335E-10	5.871E-09	0.978
^{144}Nd	144	60	8.826E-10	-1.235E-14	3.696E-10	3.695E-10	1.219E-08	1.031
^{145}Nd	145	60	3.095E-10	-4.331E-15	-1.099E-10	-1.099E-10	4.036E-09	0.973
^{146}Nd	146	60	6.448E-10	-9.021E-15	4.467E-10	4.467E-10	9.082E-09	1.052
^{148}Nd	148	60	2.185E-10	-3.057E-15	-3.689E-10	-3.689E-10	2.558E-09	0.874
^{150}Nd	150	60	2.168E-10	-3.034E-15	-3.958E-10	-3.958E-10	2.508E-09	0.864
^{144}Sm	144	62	3.684E-11	-5.153E-16	-6.080E-11	-6.080E-11	4.325E-10	0.877

TableC.2 – continued

Isotope	A	Z	$X^{\rm ini}$	$mp^{\rm wind}$	$mp^{\rm preSN}$	$mp^{\rm total}$	EM	$\langle OP \rangle$
^{147}Sm	147	62	1.834E-10	-2.566E-15	-2.174E-10	-2.174E-10	2.239E-09	0.912
^{148}Sm	148	62	1.385E-10	-1.937E-15	3.643E-10	3.643E-10	2.219E-09	1.196
^{149}Sm	149	62	1.714E-10	-2.398E-15	-3.073E-10	-3.073E-10	1.988E-09	0.866
^{150}Sm	150	62	9.213E-11	-1.289E-15	2.661E-10	2.661E-10	1.500E-09	1.216
^{152}Sm	152	62	3.383E-10	-4.733E-15	-5.244E-10	-5.244E-10	4.007E-09	0.884
^{154}Sm	154	62	2.916E-10	-4.080E-15	-5.321E-10	-5.321E-10	3.374E-09	0.864
^{151}Eu	151	63	2.036E-10	-2.848E-15	-4.540E-10	-4.540E-10	2.273E-09	0.833
^{153}Eu	153	63	2.252E-10	-3.151E-15	-4.310E-10	-4.310E-10	2.585E-09	0.857
^{152}Gd	152	64	2.947E-12	-4.123E-17	1.601E-10	1.601E-10	1.995E-10	5.055
^{154}Gd	154	64	3.210E-11	-4.490E-16	2.674E-10	2.674E-10	6.972E-10	1.622
^{155}Gd	155	64	2.192E-10	-3.067E-15	-3.959E-10	-3.959E-10	2.540E-09	0.865
^{156}Gd	156	64	3.051E-10	-4.269E-15	-1.550E-10	-1.550E-10	3.931E-09	0.962
^{157}Gd	157	64	2.348E-10	-3.285E-15	-3.199E-10	-3.199E-10	2.825E-09	0.898
^{158}Gd	158	64	3.750E-10	-5.246E-15	-2.276E-11	-2.276E-11	4.999E-09	0.995
^{160}Gd	160	64	3.343E-10	-4.677E-15	-5.957E-10	-5.957E-10	3.881E-09	0.867
^{159}Tb	159	65	2.765E-10	-3.868E-15	-4.875E-10	-4.875E-10	3.216E-09	0.868
^{156}Dy	156	66	1.004E-12	-1.404E-17	-2.483E-12	-2.483E-12	1.096E-11	0.815
^{158}Dy	158	66	1.743E-12	-2.438E-17	3.924E-12	3.924E-12	2.726E-11	1.168
^{160}Dy	160	66	4.301E-11	-6.018E-16	2.387E-10	2.387E-10	8.149E-10	1.414
^{161}Dy	161	66	3.498E-10	-4.894E-15	-6.868E-10	-6.868E-10	3.998E-09	0.853
^{162}Dy	162	66	4.748E-10	-6.643E-15	-3.222E-10	-3.222E-10	6.037E-09	0.949
^{163}Dy	163	66	4.663E-10	-6.524E-15	-7.640E-10	-7.640E-10	5.481E-09	0.878
^{164}Dy	164	66	5.312E-10	-7.431E-15	1.233E-10	1.233E-10	7.237E-09	1.017
^{165}Ho	165	67	4.244E-10	-5.937E-15	-7.692E-10	-7.692E-10	4.915E-09	0.865
^{162}Er	162	68	1.609E-12	-2.251E-17	-3.983E-12	-3.983E-12	1.756E-11	0.815
^{164}Er	164	68	1.913E-11	-2.676E-16	-4.552E-11	-4.552E-11	2.107E-10	0.822
^{166}Er	166	68	4.044E-10	-5.658E-15	-3.149E-10	-3.149E-10	5.102E-09	0.942
^{167}Er	167	68	2.776E-10	-3.884E-15	-4.214E-10	-4.215E-10	3.296E-09	0.887

TableC.2 – continued

Isotope	A	Z	$X^{\rm ini}$	$mp^{\rm wind}$	$mp^{\rm preSN}$	$mp^{\rm total}$	EM	$\langle OP \rangle$
^{168}Er	168	68	3.263E-10	-4.565E-15	1.328E-10	1.328E-10	4.502E-09	1.030
^{170}Er	170	68	1.840E-10	-2.574E-15	-3.204E-10	-3.204E-10	2.144E-09	0.870
^{169}Tm	169	69	1.854E-10	-2.594E-15	-2.845E-10	-2.845E-10	2.199E-09	0.885
^{168}Yb	168	70	1.583E-12	-2.215E-17	-3.780E-12	-3.780E-12	1.742E-11	0.822
^{170}Yb	170	70	3.746E-11	-5.241E-16	2.527E-10	2.527E-10	7.544E-10	1.504
^{171}Yb	171	70	1.770E-10	-2.477E-15	-1.837E-10	-1.837E-10	2.187E-09	0.923
^{172}Yb	172	70	2.722E-10	-3.808E-15	3.764E-11	3.764E-11	3.683E-09	1.010
^{173}Yb	173	70	2.023E-10	-2.830E-15	-1.228E-10	-1.229E-10	2.586E-09	0.955
^{174}Yb	174	70	4.015E-10	-5.617E-15	3.217E-10	3.217E-10	5.699E-09	1.060
^{176}Yb	176	70	1.628E-10	-2.278E-15	-2.670E-10	-2.670E-10	1.913E-09	0.878
^{175}Lu	175	71	1.828E-10	-2.557E-15	-2.490E-10	-2.490E-10	2.199E-09	0.898
^{176}Lu	176	71	4.876E-12	-2.348E-15	8.497E-12	8.494E-12	7.380E-11	1.130
^{174}Hf	174	72	1.231E-12	-1.723E-17	-2.836E-12	-2.836E-12	1.365E-11	0.828
^{176}Hf	176	72	4.036E-11	1.715E-15	1.806E-10	1.806E-10	7.211E-10	1.334
^{177}Hf	177	72	1.438E-10	-2.012E-15	-1.905E-10	-1.905E-10	1.735E-09	0.901
^{178}Hf	178	72	2.121E-10	-2.968E-15	1.466E-10	1.466E-10	2.988E-09	1.052
^{179}Hf	179	72	1.065E-10	-1.490E-15	-9.397E-11	-9.397E-11	1.333E-09	0.934
^{180}Hf	180	72	2.758E-10	-3.859E-15	2.268E-10	2.268E-10	3.921E-09	1.061
^{180}Ta	180	73	2.429E-14	-3.406E-19	2.286E-13	2.286E-13	5.540E-13	1.703
^{181}Ta	181	73	1.986E-10	-2.778E-15	-2.318E-10	-2.318E-10	2.428E-09	0.913
^{180}W	180	74	8.395E-13	-1.174E-17	3.909E-11	3.909E-11	5.033E-11	4.476
^{182}W	182	74	1.877E-10	-2.627E-15	2.055E-10	2.054E-10	2.720E-09	1.082
^{183}W	183	74	1.020E-10	-1.427E-15	1.177E-10	1.177E-10	1.483E-09	1.086
^{184}W	184	74	2.195E-10	-3.071E-15	2.379E-10	2.379E-10	3.178E-09	1.081
^{186}W	186	74	2.058E-10	-2.880E-15	-3.436E-10	-3.436E-10	2.413E-09	0.875
^{185}Re	185	75	1.048E-10	-1.466E-15	-1.116E-10	-1.116E-10	1.292E-09	0.921
^{187}Re	187	75	1.773E-10	-2.481E-15	-3.863E-10	-3.863E-10	1.988E-09	0.837
^{184}Os	184	76	7.108E-13	-9.945E-18	-1.533E-12	-1.533E-12	7.987E-12	0.839

TableC.2 – continued

Isotope	A	Z	X^{ini}	mp^{wind}	mp^{preSN}	mp^{total}	EM	$\langle OP \rangle$
^{186}Os	186	76	5.778E-11	-8.084E-16	2.357E-10	2.357E-10	1.010E-09	1.305
^{187}Os	187	76	5.998E-11	-8.392E-16	1.115E-11	1.115E-11	8.145E-10	1.014
^{188}Os	188	76	4.874E-10	-6.818E-15	-3.056E-10	-3.056E-10	6.222E-09	0.953
^{189}Os	189	76	5.974E-10	-8.357E-15	-1.243E-09	-1.243E-09	6.757E-09	0.845
^{190}Os	190	76	9.766E-10	-1.366E-14	-7.909E-10	-7.909E-10	1.229E-08	0.940
^{192}Os	192	76	1.533E-09	-2.144E-14	-2.597E-09	-2.597E-09	1.793E-08	0.873
^{191}Ir	191	77	1.357E-09	-1.899E-14	-3.070E-09	-3.070E-09	1.511E-08	0.831
^{193}Ir	193	77	2.308E-09	-3.230E-14	-4.908E-09	-4.908E-09	2.601E-08	0.841
^{190}Pt	190	78	1.008E-12	-1.411E-17	-2.109E-12	-2.109E-12	1.140E-11	0.844
^{192}Pt	192	78	5.850E-11	-8.185E-16	9.929E-10	9.929E-10	1.776E-09	2.267
^{194}Pt	194	78	2.490E-09	-3.483E-14	-2.627E-09	-2.627E-09	3.072E-08	0.921
^{195}Pt	195	78	2.568E-09	-3.593E-14	-4.686E-09	-4.686E-09	2.971E-08	0.864
^{196}Pt	196	78	1.926E-09	-2.695E-14	-8.173E-11	-8.175E-11	2.571E-08	0.997
^{198}Pt	198	78	5.522E-10	-7.725E-15	-9.180E-10	-9.180E-10	6.477E-09	0.876
^{197}Au	197	79	1.083E-09	-1.516E-14	-1.444E-09	-1.444E-09	1.306E-08	0.900
^{196}Hg	196	80	3.009E-12	-4.210E-17	-5.507E-12	-5.507E-12	3.480E-11	0.863
^{198}Hg	198	80	1.975E-10	-2.763E-15	1.708E-09	1.708E-09	4.353E-09	1.646
^{199}Hg	199	80	3.360E-10	-4.701E-15	1.627E-10	1.626E-10	4.663E-09	1.036
^{200}Hg	200	80	4.622E-10	-6.467E-15	1.287E-09	1.287E-09	7.478E-09	1.208
^{201}Hg	201	80	2.651E-10	-3.709E-15	6.911E-10	6.911E-10	4.242E-09	1.195
^{202}Hg	202	80	6.036E-10	-8.445E-15	2.764E-09	2.764E-09	1.085E-08	1.342
^{204}Hg	204	80	1.401E-10	-1.961E-15	-1.939E-10	-1.939E-10	1.683E-09	0.897
^{203}Tl	203	81	3.221E-10	-4.506E-15	2.420E-09	2.420E-09	6.733E-09	1.561
^{205}Tl	205	81	7.764E-10	-1.086E-14	4.439E-09	4.439E-09	1.484E-08	1.427
^{204}Pb	204	82	2.931E-10	-4.101E-15	2.665E-09	2.665E-09	6.590E-09	1.679
^{206}Pb	206	82	2.798E-09	-3.914E-14	1.135E-08	1.135E-08	4.882E-08	1.303
^{207}Pb	207	82	3.090E-09	-4.323E-14	1.528E-08	1.528E-08	5.666E-08	1.369
^{208}Pb	208	82	8.850E-09	-1.238E-13	1.515E-08	1.515E-08	1.337E-07	1.128

TableC.2 – continued

Isotope	A	Z	X^{ini}	mp^{wind}	mp^{preSN}	mp^{total}	EM	$\langle OP \rangle$
^{209}Bi	209	83	8.718E-10	-1.220E-14	7.776E-10	7.775E-10	1.245E-08	1.067

Table C.3: Yields for model 15CU.

Isotope	A	Z	X^{ini}	mp^{wind}	mp^{preSN}	mp^{total}	EM	$\langle OP \rangle$
^{1}H	1	1	7.064E-01	-6.415E-02	-2.914E+00	-2.978E+00	6.483E+00	0.685
^{2}H	2	1	1.371E-05	-3.528E-05	-1.348E-04	-1.701E-04	1.345E-05	0.073
^{3}He	3	2	4.540E-05	-1.883E-05	-2.845E-04	-3.033E-04	3.047E-04	0.501
^{4}He	4	2	2.735E-01	6.398E-02	1.191E+00	1.255E+00	4.918E+00	1.343
^{7}Li	7	3	7.605E-11	-1.958E-10	-7.482E-10	-9.439E-10	7.464E-11	0.073
^{11}B	11	5	2.856E-09	2.994E-14	9.828E-11	9.831E-11	3.835E-08	1.003
^{12}C	12	6	3.425E-03	-3.060E-03	2.944E-01	2.914E-01	3.372E-01	7.353
^{13}C	13	6	4.156E-05	2.409E-04	2.305E-04	4.714E-04	1.028E-03	1.847
^{14}N	14	7	1.059E-03	5.103E-03	3.924E-02	4.434E-02	5.853E-02	4.127
^{15}N	15	7	4.171E-06	-6.357E-06	-3.252E-05	-3.888E-05	1.698E-05	0.304
^{16}O	16	8	9.624E-03	-2.033E-03	9.226E-01	9.205E-01	1.049E+00	8.141
^{17}O	17	8	3.813E-06	4.454E-06	4.655E-05	5.100E-05	1.021E-04	1.999
^{18}O	18	8	2.171E-05	-1.410E-05	3.648E-03	3.634E-03	3.925E-03	13.498
^{19}F	19	9	5.611E-07	-1.349E-07	-1.616E-06	-1.751E-06	5.764E-06	0.767
^{20}Ne	20	10	1.818E-03	-3.616E-06	3.532E-01	3.532E-01	3.776E-01	15.509
^{21}Ne	21	10	4.575E-06	3.815E-06	7.039E-03	7.043E-03	7.104E-03	115.935
^{22}Ne	22	10	1.470E-04	-3.893E-05	2.322E-02	2.319E-02	2.515E-02	12.774
^{23}Na	23	11	4.000E-05	4.070E-05	5.065E-02	5.069E-02	5.123E-02	95.638
^{24}Mg	24	12	5.862E-04	1.087E-08	2.769E-02	2.769E-02	3.555E-02	4.527
^{25}Mg	25	12	7.733E-05	-1.242E-05	1.528E-02	1.527E-02	1.630E-02	15.742
^{26}Mg	26	12	8.848E-05	1.285E-05	1.454E-02	1.455E-02	1.574E-02	13.279
^{27}Al	27	13	6.481E-05	7.315E-08	3.977E-03	3.977E-03	4.845E-03	5.582
^{28}Si	28	14	7.453E-04	8.027E-09	8.225E-04	8.225E-04	1.080E-02	1.082
^{29}Si	29	14	3.919E-05	4.059E-10	2.993E-04	2.993E-04	8.242E-04	1.570
^{30}Si	30	14	2.673E-05	-1.930E-09	5.839E-04	5.839E-04	9.419E-04	2.631
^{31}P	31	15	7.106E-06	2.364E-09	2.376E-04	2.376E-04	3.328E-04	3.496
^{32}S	32	16	4.011E-04	4.198E-09	-3.940E-04	-3.940E-04	4.978E-03	0.927

TableC.3 – continued

Isotope	A	Z	$X^{\rm ini}$	$mp^{\rm wind}$	$mp^{\rm preSN}$	$mp^{\rm total}$	EM	$\langle OP \rangle$
^{33}S	33	16	3.265E-06	4.240E-11	4.866E-06	4.866E-06	4.859E-05	1.111
^{34}S	34	16	1.890E-05	1.982E-10	2.594E-05	2.594E-05	2.791E-04	1.102
^{36}S	36	16	8.073E-08	8.465E-13	1.699E-05	1.699E-05	1.807E-05	16.717
^{35}Cl	35	17	6.821E-06	7.152E-11	-7.380E-06	-7.380E-06	8.398E-05	0.919
^{37}Cl	37	17	2.306E-06	2.418E-11	8.163E-05	8.163E-05	1.125E-04	3.643
^{36}Ar	36	18	8.202E-05	8.600E-10	-1.167E-04	-1.167E-04	9.818E-04	0.894
^{38}Ar	38	18	1.574E-05	1.651E-10	5.748E-05	5.748E-05	2.683E-04	1.273
^{40}Ar	40	18	2.650E-08	2.808E-13	1.668E-05	1.668E-05	1.704E-05	47.999
^{39}K	39	19	3.900E-06	4.089E-11	1.601E-05	1.601E-05	6.824E-05	1.307
^{40}K	40	19	5.005E-10	-6.939E-12	1.383E-06	1.383E-06	1.389E-06	207.267
^{41}K	41	19	2.959E-07	3.102E-12	4.812E-06	4.812E-06	8.774E-06	2.214
^{40}Ca	40	20	7.225E-05	7.645E-10	-9.242E-05	-9.241E-05	8.753E-04	0.904
^{42}Ca	42	20	5.063E-07	5.309E-12	5.327E-06	5.327E-06	1.211E-05	1.786
^{43}Ca	43	20	1.082E-07	1.134E-12	2.090E-06	2.090E-06	3.539E-06	2.443
^{44}Ca	44	20	1.710E-06	1.793E-11	6.134E-06	6.134E-06	2.904E-05	1.268
^{46}Ca	46	20	3.428E-09	3.595E-14	7.096E-08	7.096E-08	1.169E-07	2.545
^{48}Ca	48	20	1.672E-07	1.754E-12	-5.916E-08	-5.916E-08	2.181E-06	0.974
^{45}Sc	45	21	5.414E-08	5.676E-13	1.708E-06	1.708E-06	2.433E-06	3.355
^{46}Ti	46	22	3.232E-07	3.389E-12	2.025E-06	2.025E-06	6.353E-06	1.468
^{47}Ti	47	22	2.977E-07	3.121E-12	9.262E-07	9.262E-07	4.913E-06	1.232
^{48}Ti	48	22	3.014E-06	3.160E-11	-2.110E-06	-2.110E-06	3.825E-05	0.948
^{49}Ti	49	22	2.257E-07	2.367E-12	3.201E-06	3.201E-06	6.224E-06	2.059
^{50}Ti	50	22	2.208E-07	2.315E-12	9.168E-06	9.168E-06	1.213E-05	4.100
^{50}V	50	23	1.015E-09	1.065E-14	-1.578E-09	-1.578E-09	1.202E-08	0.884
^{51}V	51	23	4.138E-07	4.338E-12	5.652E-07	5.653E-07	6.107E-06	1.102
^{50}Cr	50	24	8.265E-07	8.666E-12	-1.458E-06	-1.458E-06	9.612E-06	0.868
^{52}Cr	52	24	1.658E-05	1.738E-10	-2.095E-05	-2.095E-05	2.011E-04	0.906
^{53}Cr	53	24	1.916E-06	2.009E-11	-1.829E-06	-1.829E-06	2.383E-05	0.929

TableC.3 – continued

Isotope	A	Z	X^{ini}	mp^{wind}	mp^{preSN}	mp^{total}	EM	$\langle OP \rangle$
^{54}Cr	54	24	4.858E-07	5.094E-12	9.707E-06	9.707E-06	1.621E-05	2.492
^{55}Mn	55	25	1.098E-05	1.151E-10	-7.283E-06	-7.283E-06	1.398E-04	0.950
^{54}Fe	54	26	8.118E-05	8.512E-10	-1.379E-04	-1.379E-04	9.494E-04	0.873
^{56}Fe	56	26	1.322E-03	1.386E-08	-1.942E-03	-1.942E-03	1.576E-02	0.890
^{57}Fe	57	26	3.107E-05	3.257E-10	5.155E-05	5.155E-05	4.676E-04	1.124
^{58}Fe	58	26	4.207E-06	4.411E-11	2.835E-04	2.835E-04	3.399E-04	6.032
^{59}Co	59	27	3.991E-06	4.185E-11	1.315E-04	1.315E-04	1.850E-04	3.460
^{58}Ni	58	28	5.711E-05	5.988E-10	-9.531E-05	-9.531E-05	6.696E-04	0.875
^{60}Ni	60	28	2.276E-05	2.386E-10	1.260E-04	1.260E-04	4.308E-04	1.413
^{61}Ni	61	28	1.006E-06	1.055E-11	7.072E-05	7.072E-05	8.419E-05	6.250
^{62}Ni	62	28	3.259E-06	3.417E-11	2.568E-04	2.568E-04	3.005E-04	6.884
^{64}Ni	64	28	8.568E-07	8.984E-12	2.485E-04	2.485E-04	2.600E-04	22.659
^{63}Cu	63	29	6.600E-07	6.921E-12	1.021E-04	1.021E-04	1.109E-04	12.548
^{65}Cu	65	29	3.035E-07	3.182E-12	1.589E-04	1.589E-04	1.630E-04	40.105
^{64}Zn	64	30	1.131E-06	1.186E-11	4.887E-05	4.887E-05	6.401E-05	4.227
^{66}Zn	66	30	6.690E-07	7.015E-12	1.441E-04	1.441E-04	1.531E-04	17.086
^{67}Zn	67	30	9.980E-08	1.046E-12	4.155E-05	4.155E-05	4.288E-05	32.082
^{68}Zn	68	30	4.632E-07	4.857E-12	2.519E-04	2.519E-04	2.581E-04	41.604
^{70}Zn	70	30	1.577E-08	1.653E-13	9.524E-08	9.524E-08	3.064E-07	1.451
^{69}Ga	69	31	4.551E-08	4.771E-13	3.275E-05	3.275E-05	3.336E-05	54.736
^{71}Ga	71	31	3.108E-08	3.258E-13	3.370E-05	3.370E-05	3.411E-05	81.962
^{70}Ge	70	32	5.157E-08	5.407E-13	5.057E-05	5.057E-05	5.126E-05	74.220
^{72}Ge	72	32	6.910E-08	7.246E-13	5.900E-05	5.900E-05	5.993E-05	64.749
^{73}Ge	73	32	1.955E-08	2.049E-13	2.239E-05	2.239E-05	2.265E-05	86.537
^{74}Ge	74	32	9.228E-08	9.676E-13	9.826E-05	9.826E-05	9.950E-05	80.503
^{76}Ge	76	32	1.963E-08	2.058E-13	8.092E-08	8.092E-08	3.438E-07	1.308
^{75}As	75	33	1.430E-08	1.499E-13	1.114E-05	1.114E-05	1.133E-05	59.155
^{74}Se	74	34	1.198E-09	1.256E-14	-2.401E-09	-2.401E-09	1.364E-08	0.850

TableC.3 – continued

Isotope	A	Z	$X^{\rm ini}$	$mp^{\rm wind}$	$mp^{\rm preSN}$	$mp^{\rm total}$	EM	$\langle OP \rangle$
^{76}Se	76	34	1.296E-08	1.359E-13	2.031E-05	2.031E-05	2.048E-05	117.997
^{77}Se	77	34	1.070E-08	1.122E-13	9.069E-06	9.069E-06	9.213E-06	64.257
^{78}Se	78	34	3.376E-08	3.540E-13	5.390E-05	5.390E-05	5.435E-05	120.188
^{80}Se	80	34	7.226E-08	7.577E-13	1.599E-05	1.599E-05	1.696E-05	17.522
^{82}Se	82	34	1.304E-08	1.367E-13	-1.338E-08	-1.338E-08	1.612E-07	0.923
^{79}Br	79	35	1.389E-08	1.457E-13	1.009E-05	1.009E-05	1.028E-05	55.233
^{81}Br	81	35	1.386E-08	1.453E-13	6.035E-06	6.035E-06	6.220E-06	33.512
^{78}Kr	78	36	3.900E-10	4.089E-15	-7.524E-10	-7.524E-10	4.471E-09	0.856
^{80}Kr	80	36	2.575E-09	2.700E-14	5.337E-06	5.337E-06	5.371E-06	155.768
^{82}Kr	82	36	1.320E-08	1.384E-13	2.848E-05	2.848E-05	2.866E-05	162.177
^{83}Kr	83	36	1.324E-08	1.388E-13	1.326E-05	1.326E-05	1.344E-05	75.794
^{84}Kr	84	36	6.602E-08	6.922E-13	7.104E-05	7.104E-05	7.192E-05	81.342
^{86}Kr	86	36	2.044E-08	2.144E-13	1.767E-05	1.767E-05	1.794E-05	65.531
^{85}Rb	85	37	1.282E-08	1.345E-13	1.681E-05	1.681E-05	1.698E-05	98.880
^{87}Rb	87	37	5.063E-09	-2.031E-12	5.507E-06	5.507E-06	5.575E-06	82.216
^{84}Sr	84	38	3.228E-10	3.385E-15	-6.706E-10	-6.706E-10	3.653E-09	0.845
^{86}Sr	86	38	5.845E-09	6.128E-14	2.517E-05	2.517E-05	2.525E-05	322.610
^{87}Sr	87	38	4.443E-09	2.130E-12	1.811E-05	1.811E-05	1.817E-05	305.331
^{88}Sr	88	38	5.011E-08	5.254E-13	9.181E-05	9.181E-05	9.248E-05	137.804
^{89}Y	89	39	1.229E-08	1.289E-13	1.711E-05	1.711E-05	1.728E-05	104.939
^{90}Zr	90	40	1.534E-08	1.609E-13	9.198E-06	9.198E-06	9.403E-06	45.757
^{91}Zr	91	40	3.384E-09	3.548E-14	2.842E-06	2.842E-06	2.887E-06	63.703
^{92}Zr	92	40	5.227E-09	5.480E-14	3.482E-06	3.482E-06	3.552E-06	50.739
^{94}Zr	94	40	5.413E-09	5.676E-14	1.677E-06	1.677E-06	1.749E-06	24.126
^{96}Zr	96	40	8.903E-10	9.335E-15	1.092E-07	1.092E-07	1.211E-07	10.158
^{93}Nb	93	41	1.900E-09	1.992E-14	1.213E-06	1.213E-06	1.238E-06	48.657
^{92}Mo	92	42	1.012E-09	1.062E-14	-1.822E-09	-1.822E-09	1.174E-08	0.866
^{94}Mo	94	42	6.448E-10	6.760E-15	3.256E-11	3.256E-11	8.668E-09	1.004

TableC.3 – continued

Isotope	A	Z	$X^{\rm ini}$	$mp^{\rm wind}$	$mp^{\rm preSN}$	$mp^{\rm total}$	EM	$\langle OP \rangle$
^{95}Mo	95	42	1.122E-09	1.176E-14	2.990E-07	2.990E-07	3.141E-07	20.901
^{96}Mo	96	42	1.188E-09	1.245E-14	5.006E-07	5.006E-07	5.165E-07	32.476
^{97}Mo	97	42	6.875E-10	7.209E-15	1.815E-07	1.815E-07	1.907E-07	20.710
^{98}Mo	98	42	1.754E-09	1.839E-14	5.249E-07	5.249E-07	5.484E-07	23.338
^{100}Mo	100	42	7.146E-10	7.493E-15	1.145E-09	1.145E-09	1.072E-08	1.120
^{96}Ru	96	44	2.926E-10	3.068E-15	-5.631E-10	-5.631E-10	3.355E-09	0.856
^{98}Ru	98	44	1.007E-10	1.056E-15	-1.616E-10	-1.616E-10	1.187E-09	0.880
^{99}Ru	99	44	6.945E-10	7.282E-15	7.824E-08	7.824E-08	8.754E-08	9.411
^{100}Ru	100	44	6.928E-10	7.264E-15	2.428E-07	2.428E-07	2.521E-07	27.168
^{101}Ru	101	44	9.475E-10	9.935E-15	5.069E-08	5.069E-08	6.338E-08	4.994
^{102}Ru	102	44	1.770E-09	1.856E-14	3.265E-07	3.265E-07	3.502E-07	14.774
^{104}Ru	104	44	1.065E-09	1.117E-14	8.293E-09	8.293E-09	2.256E-08	1.581
^{103}Rh	103	45	1.055E-09	1.106E-14	5.431E-08	5.431E-08	6.844E-08	4.845
^{102}Pd	102	46	4.241E-11	4.447E-16	-8.827E-11	-8.827E-11	4.798E-10	0.845
^{104}Pd	104	46	4.723E-10	4.952E-15	1.475E-07	1.475E-07	1.538E-07	24.311
^{105}Pd	105	46	9.558E-10	1.002E-14	3.264E-08	3.264E-08	4.544E-08	3.550
^{106}Pd	106	46	1.181E-09	1.238E-14	1.729E-07	1.729E-07	1.888E-07	11.934
^{108}Pd	108	46	1.165E-09	1.221E-14	1.965E-07	1.965E-07	2.121E-07	13.594
^{110}Pd	110	46	5.255E-10	5.510E-15	9.336E-09	9.336E-09	1.637E-08	2.326
^{107}Ag	107	47	7.840E-10	8.220E-15	3.099E-08	3.099E-08	4.149E-08	3.952
^{109}Ag	109	47	7.420E-10	7.780E-15	9.385E-08	9.385E-08	1.038E-07	10.444
^{106}Cd	106	48	6.346E-11	6.654E-16	-1.285E-10	-1.285E-10	7.214E-10	0.849
^{108}Cd	108	48	4.604E-11	4.827E-16	5.952E-09	5.952E-09	6.568E-09	10.653
^{110}Cd	110	48	6.580E-10	6.899E-15	1.561E-07	1.561E-07	1.649E-07	18.710
^{111}Cd	111	48	6.805E-10	7.135E-15	4.745E-08	4.745E-08	5.656E-08	6.206
^{112}Cd	112	48	1.294E-09	1.357E-14	1.896E-07	1.896E-07	2.070E-07	11.939
^{113}Cd	113	48	6.614E-10	6.934E-15	4.985E-08	4.985E-08	5.870E-08	6.628
^{114}Cd	114	48	1.569E-09	1.645E-14	2.539E-07	2.539E-07	2.749E-07	13.083

TableC.3 – continued

Isotope	A	Z	$X^{\rm ini}$	$mp^{\rm wind}$	$mp^{\rm preSN}$	$mp^{\rm total}$	EM	$\langle OP \rangle$
^{116}Cd	116	48	4.161E-10	4.363E-15	1.142E-08	1.142E-08	1.700E-08	3.049
^{113}In	113	49	2.604E-11	2.730E-16	-4.594E-11	-4.594E-11	3.028E-10	0.868
^{115}In	115	49	5.915E-10	6.176E-15	4.735E-08	4.735E-08	5.527E-08	6.977
^{112}Sn	112	50	1.221E-10	1.280E-15	-2.373E-10	-2.373E-10	1.398E-09	0.855
^{114}Sn	114	50	8.435E-11	8.844E-16	-1.265E-10	-1.265E-10	1.003E-09	0.888
^{115}Sn	115	50	4.377E-11	4.843E-16	2.328E-10	2.328E-10	8.190E-10	1.397
^{116}Sn	116	50	1.893E-09	1.985E-14	2.911E-07	2.911E-07	3.165E-07	12.481
^{117}Sn	117	50	1.008E-09	1.057E-14	9.192E-08	9.192E-08	1.054E-07	7.807
^{118}Sn	118	50	3.209E-09	3.365E-14	4.028E-07	4.028E-07	4.458E-07	10.372
^{119}Sn	119	50	1.147E-09	1.203E-14	1.156E-07	1.156E-07	1.310E-07	8.525
^{120}Sn	120	50	4.391E-09	4.604E-14	5.235E-07	5.235E-07	5.824E-07	9.902
^{122}Sn	122	50	6.341E-10	6.648E-15	1.247E-08	1.247E-08	2.096E-08	2.468
^{124}Sn	124	50	8.060E-10	8.450E-15	-1.218E-09	-1.218E-09	9.576E-09	0.887
^{121}Sb	121	51	6.318E-10	6.624E-15	4.136E-08	4.136E-08	4.982E-08	5.888
^{123}Sb	123	51	4.803E-10	5.036E-15	2.628E-09	2.628E-09	9.060E-09	1.409
^{120}Te	120	52	1.628E-11	1.707E-16	-3.534E-11	-3.534E-11	1.827E-10	0.838
^{122}Te	122	52	4.489E-10	4.706E-15	6.050E-08	6.050E-08	6.651E-08	11.064
^{123}Te	123	52	1.579E-10	1.655E-15	2.023E-08	2.023E-08	2.235E-08	10.569
^{124}Te	124	52	8.441E-10	8.850E-15	1.165E-07	1.165E-07	1.278E-07	11.306
^{125}Te	125	52	1.261E-09	1.323E-14	3.447E-08	3.447E-08	5.136E-08	3.041
^{126}Te	126	52	3.375E-09	3.539E-14	2.082E-07	2.082E-07	2.534E-07	5.605
^{128}Te	128	52	5.733E-09	6.011E-14	-3.044E-09	-3.044E-09	7.374E-08	0.960
^{130}Te	130	52	6.211E-09	6.512E-14	-9.659E-09	-9.658E-09	7.352E-08	0.884
^{127}I	127	53	1.459E-09	1.530E-14	2.776E-08	2.776E-08	4.730E-08	2.420
^{124}Xe	124	54	2.210E-11	2.317E-16	-4.956E-11	-4.956E-11	2.464E-10	0.833
^{126}Xe	126	54	1.949E-11	2.044E-16	-4.040E-11	-4.040E-11	2.207E-10	0.845
^{128}Xe	128	54	3.943E-10	4.134E-15	5.853E-08	5.853E-08	6.381E-08	12.085
^{129}Xe	129	54	4.893E-09	5.130E-14	1.445E-08	1.445E-08	7.998E-08	1.221

TableC.3 – continued

Isotope	A	Z	X^{ini}	mp^{wind}	mp^{preSN}	mp^{total}	EM	$\langle OP \rangle$
^{130}Xe	130	54	7.865E-10	8.247E-15	1.156E-07	1.156E-07	1.262E-07	11.978
^{131}Xe	131	54	3.945E-09	4.136E-14	3.930E-08	3.930E-08	9.213E-08	1.744
^{132}Xe	132	54	4.806E-09	5.039E-14	2.134E-07	2.134E-07	2.778E-07	4.316
^{134}Xe	134	54	1.788E-09	1.875E-14	3.903E-09	3.903E-09	2.785E-08	1.163
^{136}Xe	136	54	1.478E-09	1.550E-14	-4.968E-10	-4.968E-10	1.930E-08	0.975
^{133}Cs	133	55	1.426E-09	1.495E-14	3.061E-08	3.061E-08	4.971E-08	2.603
^{130}Ba	130	56	1.814E-11	1.902E-16	-4.114E-11	-4.114E-11	2.019E-10	0.831
^{132}Ba	132	56	1.762E-11	1.848E-16	-3.675E-11	-3.675E-11	1.993E-10	0.844
^{134}Ba	134	56	4.272E-10	4.480E-15	6.858E-08	6.858E-08	7.430E-08	12.985
^{135}Ba	135	56	1.174E-09	1.231E-14	2.970E-08	2.970E-08	4.542E-08	2.889
^{136}Ba	136	56	1.409E-09	1.477E-14	1.916E-07	1.916E-07	2.105E-07	11.156
^{137}Ba	137	56	2.030E-09	2.128E-14	1.412E-07	1.412E-07	1.684E-07	6.195
^{138}Ba	138	56	1.305E-08	1.369E-13	8.223E-07	8.223E-07	9.971E-07	5.704
^{138}La	138	57	1.604E-12	1.682E-17	-3.438E-12	-3.438E-12	1.805E-11	0.840
^{139}La	139	57	1.790E-09	1.877E-14	8.446E-08	8.446E-08	1.084E-07	4.523
^{136}Ce	136	58	8.382E-12	8.788E-17	-1.724E-11	-1.724E-11	9.502E-11	0.846
^{138}Ce	138	58	1.148E-11	1.203E-16	-2.194E-11	-2.194E-11	1.318E-10	0.857
^{140}Ce	140	58	4.103E-09	4.302E-14	1.196E-07	1.196E-07	1.746E-07	3.177
^{142}Ce	142	58	5.229E-10	5.483E-15	-8.031E-11	-8.031E-11	6.923E-09	0.989
^{141}Pr	141	59	6.910E-10	7.246E-15	1.306E-08	1.306E-08	2.231E-08	2.411
^{142}Nd	142	60	9.920E-10	1.040E-14	2.626E-08	2.626E-08	3.954E-08	2.976
^{143}Nd	143	60	4.484E-10	4.701E-15	3.859E-09	3.859E-09	9.864E-09	1.643
^{144}Nd	144	60	8.826E-10	9.254E-15	9.755E-09	9.755E-09	2.158E-08	1.825
^{145}Nd	145	60	3.095E-10	3.246E-15	2.249E-09	2.249E-09	6.395E-09	1.543
^{146}Nd	146	60	6.448E-10	6.760E-15	7.411E-09	7.411E-09	1.605E-08	1.858
^{148}Nd	148	60	2.185E-10	2.291E-15	6.439E-11	6.439E-11	2.991E-09	1.022
^{150}Nd	150	60	2.168E-10	2.273E-15	-4.180E-10	-4.180E-10	2.486E-09	0.856
^{144}Sm	144	62	3.684E-11	3.862E-16	-6.607E-11	-6.607E-11	4.273E-10	0.866

TableC.3 – continued

Isotope	A	Z	$X^{\rm ini}$	$mp^{\rm wind}$	$mp^{\rm preSN}$	$mp^{\rm total}$	EM	$\langle OP \rangle$
^{147}Sm	147	62	1.834E-10	1.923E-15	8.975E-10	8.975E-10	3.354E-09	1.365
^{148}Sm	148	62	1.385E-10	1.452E-15	1.888E-09	1.888E-09	3.743E-09	2.018
^{149}Sm	149	62	1.714E-10	1.797E-15	1.308E-10	1.308E-10	2.426E-09	1.057
^{150}Sm	150	62	9.213E-11	9.660E-16	1.699E-09	1.699E-09	2.933E-09	2.377
^{152}Sm	152	62	3.383E-10	3.547E-15	7.563E-10	7.563E-10	5.287E-09	1.167
^{154}Sm	154	62	2.916E-10	3.058E-15	-2.450E-10	-2.450E-10	3.661E-09	0.937
^{151}Eu	151	63	2.036E-10	2.135E-15	-1.451E-10	-1.451E-10	2.582E-09	0.947
^{153}Eu	153	63	2.252E-10	2.361E-15	-9.072E-11	-9.072E-11	2.925E-09	0.970
^{152}Gd	152	64	2.947E-12	3.090E-17	1.257E-10	1.257E-10	1.652E-10	4.184
^{154}Gd	154	64	3.210E-11	3.365E-16	6.236E-10	6.236E-10	1.053E-09	2.451
^{155}Gd	155	64	2.192E-10	2.298E-15	-1.696E-10	-1.696E-10	2.766E-09	0.942
^{156}Gd	156	64	3.051E-10	3.199E-15	5.560E-10	5.560E-10	4.642E-09	1.136
^{157}Gd	157	64	2.348E-10	2.462E-15	1.943E-10	1.943E-10	3.339E-09	1.062
^{158}Gd	158	64	3.750E-10	3.932E-15	1.424E-09	1.424E-09	6.446E-09	1.284
^{160}Gd	160	64	3.343E-10	3.505E-15	-4.440E-10	-4.440E-10	4.033E-09	0.901
^{159}Tb	159	65	2.765E-10	2.899E-15	-5.568E-11	-5.567E-11	3.647E-09	0.985
^{156}Dy	156	66	1.004E-12	1.052E-17	-2.498E-12	-2.498E-12	1.094E-11	0.814
^{158}Dy	158	66	1.743E-12	1.827E-17	6.554E-12	6.554E-12	2.989E-11	1.281
^{160}Dy	160	66	4.301E-11	4.510E-16	6.846E-10	6.846E-10	1.261E-09	2.188
^{161}Dy	161	66	3.498E-10	3.668E-15	-3.116E-10	-3.116E-10	4.373E-09	0.933
^{162}Dy	162	66	4.748E-10	4.978E-15	6.466E-10	6.466E-10	7.006E-09	1.102
^{163}Dy	163	66	4.663E-10	4.889E-15	-1.847E-10	-1.847E-10	6.061E-09	0.970
^{164}Dy	164	66	5.312E-10	5.569E-15	2.302E-09	2.302E-09	9.416E-09	1.324
^{165}Ho	165	67	4.244E-10	4.450E-15	-2.728E-10	-2.728E-10	5.411E-09	0.952
^{162}Er	162	68	1.609E-12	1.687E-17	-4.006E-12	-4.006E-12	1.754E-11	0.814
^{164}Er	164	68	1.913E-11	2.006E-16	-4.609E-11	-4.609E-11	2.101E-10	0.820
^{166}Er	166	68	4.044E-10	4.241E-15	2.474E-10	2.474E-10	5.664E-09	1.046
^{167}Er	167	68	2.776E-10	2.911E-15	-1.810E-12	-1.807E-12	3.716E-09	1.000

TableC.3 – continued

Isotope	A	Z	$X^{\rm ini}$	$mp^{\rm wind}$	$mp^{\rm preSN}$	$mp^{\rm total}$	EM	$\langle OP \rangle$
^{168}Er	168	68	3.263E-10	3.421E-15	1.476E-09	1.476E-09	5.846E-09	1.338
^{170}Er	170	68	1.840E-10	1.929E-15	9.427E-11	9.427E-11	2.558E-09	1.038
^{169}Tm	169	69	1.854E-10	1.944E-15	8.814E-11	8.814E-11	2.572E-09	1.035
^{168}Yb	168	70	1.583E-12	1.660E-17	-3.826E-12	-3.826E-12	1.738E-11	0.820
^{170}Yb	170	70	3.746E-11	3.928E-16	3.515E-10	3.515E-10	8.533E-10	1.701
^{171}Yb	171	70	1.770E-10	1.856E-15	7.028E-11	7.028E-11	2.441E-09	1.030
^{172}Yb	172	70	2.722E-10	2.854E-15	1.160E-09	1.160E-09	4.805E-09	1.318
^{173}Yb	173	70	2.023E-10	2.121E-15	6.836E-10	6.836E-10	3.393E-09	1.252
^{174}Yb	174	70	4.015E-10	4.210E-15	3.236E-09	3.236E-09	8.613E-09	1.602
^{176}Yb	176	70	1.628E-10	1.707E-15	-3.075E-11	-3.074E-11	2.150E-09	0.986
^{175}Lu	175	71	1.828E-10	1.917E-15	2.774E-10	2.774E-10	2.726E-09	1.113
^{176}Lu	176	71	4.876E-12	-2.377E-15	5.706E-11	5.706E-11	1.224E-10	1.874
^{174}Hf	174	72	1.231E-12	1.291E-17	-2.888E-12	-2.888E-12	1.360E-11	0.825
^{176}Hf	176	72	4.036E-11	2.852E-15	6.124E-10	6.125E-10	1.153E-09	2.133
^{177}Hf	177	72	1.438E-10	1.508E-15	1.683E-10	1.683E-10	2.094E-09	1.087
^{178}Hf	178	72	2.121E-10	2.224E-15	1.389E-09	1.389E-09	4.230E-09	1.489
^{179}Hf	179	72	1.065E-10	1.117E-15	5.345E-10	5.345E-10	1.961E-09	1.375
^{180}Hf	180	72	2.758E-10	2.892E-15	2.717E-09	2.717E-09	6.412E-09	1.735
^{180}Ta	180	73	2.429E-14	2.539E-19	5.639E-13	5.639E-13	8.893E-13	2.733
^{181}Ta	181	73	1.986E-10	2.082E-15	4.678E-10	4.678E-10	3.127E-09	1.176
^{180}W	180	74	8.395E-13	8.802E-18	2.157E-11	2.157E-11	3.282E-11	2.919
^{182}W	182	74	1.877E-10	1.969E-15	1.068E-09	1.068E-09	3.583E-09	1.425
^{183}W	183	74	1.020E-10	1.069E-15	9.773E-10	9.773E-10	2.343E-09	1.716
^{184}W	184	74	2.195E-10	2.301E-15	2.006E-09	2.006E-09	4.946E-09	1.682
^{186}W	186	74	2.058E-10	2.158E-15	2.003E-10	2.003E-10	2.957E-09	1.073
^{185}Re	185	75	1.048E-10	1.099E-15	4.853E-10	4.853E-10	1.889E-09	1.346
^{187}Re	187	75	1.773E-10	1.859E-15	-1.595E-10	-1.595E-10	2.215E-09	0.933
^{184}Os	184	76	7.108E-13	7.453E-18	-1.582E-12	-1.582E-12	7.938E-12	0.834

TableC.3 – continued

Isotope	A	Z	X^{ini}	mp^{wind}	mp^{preSN}	mp^{total}	EM	$\langle OP \rangle$
^{186}Os	186	76	5.778E-11	6.059E-16	5.914E-10	5.914E-10	1.365E-09	1.764
^{187}Os	187	76	5.998E-11	6.289E-16	1.597E-10	1.597E-10	9.630E-10	1.199
^{188}Os	188	76	4.874E-10	5.110E-15	6.045E-10	6.045E-10	7.132E-09	1.093
^{189}Os	189	76	5.974E-10	6.263E-15	-8.983E-10	-8.983E-10	7.102E-09	0.888
^{190}Os	190	76	9.766E-10	1.024E-14	3.720E-10	3.720E-10	1.345E-08	1.028
^{192}Os	192	76	1.533E-09	1.607E-14	-2.309E-09	-2.309E-09	1.822E-08	0.888
^{191}Ir	191	77	1.357E-09	1.423E-14	-2.796E-09	-2.796E-09	1.538E-08	0.846
^{193}Ir	193	77	2.308E-09	2.420E-14	-4.664E-09	-4.664E-09	2.625E-08	0.849
^{190}Pt	190	78	1.008E-12	1.057E-17	-2.190E-12	-2.190E-12	1.132E-11	0.838
^{192}Pt	192	78	5.850E-11	6.134E-16	1.026E-09	1.026E-09	1.809E-09	2.309
^{194}Pt	194	78	2.490E-09	2.611E-14	-2.198E-09	-2.198E-09	3.115E-08	0.934
^{195}Pt	195	78	2.568E-09	2.693E-14	-4.478E-09	-4.478E-09	2.992E-08	0.870
^{196}Pt	196	78	1.926E-09	2.019E-14	1.291E-09	1.291E-09	2.709E-08	1.050
^{198}Pt	198	78	5.522E-10	5.790E-15	-9.133E-10	-9.132E-10	6.482E-09	0.877
^{197}Au	197	79	1.083E-09	1.136E-14	-8.019E-10	-8.019E-10	1.371E-08	0.945
^{196}Hg	196	80	3.009E-12	3.155E-17	-5.872E-12	-5.872E-12	3.443E-11	0.854
^{198}Hg	198	80	1.975E-10	2.071E-15	3.272E-09	3.272E-09	5.917E-09	2.237
^{199}Hg	199	80	3.360E-10	3.523E-15	1.078E-09	1.078E-09	5.578E-09	1.239
^{200}Hg	200	80	4.622E-10	4.846E-15	3.725E-09	3.725E-09	9.916E-09	1.602
^{201}Hg	201	80	2.651E-10	2.780E-15	2.050E-09	2.050E-09	5.601E-09	1.577
^{202}Hg	202	80	6.036E-10	6.329E-15	6.308E-09	6.308E-09	1.439E-08	1.780
^{204}Hg	204	80	1.401E-10	1.469E-15	-1.888E-10	-1.888E-10	1.688E-09	0.899
^{203}Tl	203	81	3.221E-10	3.377E-15	4.593E-09	4.593E-09	8.907E-09	2.065
^{205}Tl	205	81	7.764E-10	8.140E-15	5.166E-09	5.166E-09	1.556E-08	1.497
^{204}Pb	204	82	2.931E-10	3.073E-15	4.401E-09	4.401E-09	8.327E-09	2.121
^{206}Pb	206	82	2.798E-09	2.933E-14	1.395E-08	1.395E-08	5.142E-08	1.372
^{207}Pb	207	82	3.090E-09	3.240E-14	2.188E-08	2.188E-08	6.326E-08	1.529
^{208}Pb	208	82	8.850E-09	9.279E-14	5.003E-08	5.003E-08	1.686E-07	1.422

TableC.3 – continued

Isotope	A	Z	X^{ini}	mp^{wind}	mp^{preSN}	mp^{total}	EM	$\langle OP \rangle$
^{209}Bi	209	83	8.718E-10	9.141E-15	4.046E-09	4.046E-09	1.572E-08	1.347

Table C.4: Yields for model 20ST.

Isotope	A	Z	X^{ini}	mp^{wind}	mp^{preSN}	mp^{total}	EM	$\langle OP \rangle$
^{1}H	1	1	7.064E-01	-1.711E-01	-4.874E+00	-5.045E+00	7.948E+00	0.651
^{2}H	2	1	1.371E-05	-6.969E-05	-1.683E-04	-2.380E-04	1.413E-05	0.060
^{3}He	3	2	4.540E-05	-1.253E-05	-4.628E-04	-4.753E-04	3.597E-04	0.459
^{4}He	4	2	2.735E-01	1.712E-01	1.526E+00	1.697E+00	6.728E+00	1.424
^{7}Li	7	3	7.605E-11	-3.867E-10	-9.337E-10	-1.320E-09	7.840E-11	0.060
^{11}B	11	5	2.856E-09	-1.498E-15	7.808E-11	7.808E-11	5.261E-08	1.066
^{12}C	12	6	3.425E-03	-4.002E-03	5.119E-01	5.079E-01	5.709E-01	9.650
^{13}C	13	6	4.156E-05	4.351E-04	1.499E-04	5.850E-04	1.349E-03	1.880
^{14}N	14	7	1.059E-03	8.660E-03	4.336E-02	5.202E-02	7.149E-02	3.909
^{15}N	15	7	4.171E-06	-1.047E-05	-4.022E-05	-5.069E-05	2.602E-05	0.361
^{16}O	16	8	9.624E-03	-5.070E-03	1.833E+00	1.828E+00	2.005E+00	12.062
^{17}O	17	8	3.813E-06	3.062E-06	1.113E-05	1.420E-05	8.433E-05	1.280
^{18}O	18	8	2.171E-05	-2.021E-05	1.502E-03	1.482E-03	1.881E-03	5.015
^{19}F	19	9	5.611E-07	-3.466E-07	-2.128E-06	-2.475E-06	7.845E-06	0.809
^{20}Ne	20	10	1.818E-03	-1.130E-05	7.452E-01	7.452E-01	7.786E-01	24.797
^{21}Ne	21	10	4.575E-06	9.739E-06	1.219E-03	1.228E-03	1.313E-03	16.607
^{22}Ne	22	10	1.470E-04	-8.878E-05	4.695E-02	4.686E-02	4.956E-02	19.515
^{23}Na	23	11	4.000E-05	9.512E-05	2.313E-02	2.322E-02	2.396E-02	34.677
^{24}Mg	24	12	5.862E-04	2.319E-08	8.654E-02	8.654E-02	9.732E-02	9.610
^{25}Mg	25	12	7.733E-05	-3.341E-05	3.025E-02	3.022E-02	3.164E-02	23.688
^{26}Mg	26	12	8.848E-05	3.441E-05	3.576E-02	3.580E-02	3.743E-02	24.486
^{27}Al	27	13	6.481E-05	3.421E-07	6.743E-03	6.743E-03	7.935E-03	7.088
^{28}Si	28	14	7.453E-04	4.397E-10	7.076E-03	7.076E-03	2.078E-02	1.614
^{29}Si	29	14	3.919E-05	-5.895E-11	2.037E-03	2.037E-03	2.758E-03	4.073
^{30}Si	30	14	2.673E-05	-6.209E-09	8.957E-04	8.957E-04	1.387E-03	3.005
^{31}P	31	15	7.106E-06	6.440E-09	2.211E-04	2.211E-04	3.518E-04	2.866
^{32}S	32	16	4.011E-04	-2.436E-10	-5.454E-04	-5.454E-04	6.832E-03	0.986

TableC.4 – continued

Isotope	A	Z	$X^{\rm ini}$	$mp^{\rm wind}$	$mp^{\rm preSN}$	$mp^{\rm total}$	EM	$\langle OP \rangle$
^{33}S	33	16	3.265E-06	3.250E-11	1.944E-05	1.944E-05	7.949E-05	1.409
^{34}S	34	16	1.890E-05	-9.917E-12	4.442E-05	4.442E-05	3.921E-04	1.201
^{36}S	36	16	8.073E-08	-4.235E-14	1.670E-05	1.670E-05	1.818E-05	13.038
^{35}Cl	35	17	6.821E-06	-3.580E-12	-1.132E-05	-1.132E-05	1.141E-04	0.969
^{37}Cl	37	17	2.306E-06	-1.210E-12	1.595E-04	1.595E-04	2.019E-04	5.069
^{36}Ar	36	18	8.202E-05	-4.303E-11	-2.071E-04	-2.071E-04	1.302E-03	0.919
^{38}Ar	38	18	1.574E-05	-8.258E-12	1.065E-04	1.065E-04	3.960E-04	1.456
^{40}Ar	40	18	2.650E-08	-1.000E-14	7.131E-06	7.131E-06	7.618E-06	16.640
^{39}K	39	19	3.900E-06	-2.046E-12	2.344E-05	2.344E-05	9.517E-05	1.413
^{40}K	40	19	5.005E-10	-9.224E-12	3.387E-06	3.387E-06	3.396E-06	392.822
^{41}K	41	19	2.959E-07	-1.552E-13	9.271E-06	9.271E-06	1.471E-05	2.879
^{40}Ca	40	20	7.225E-05	-2.868E-11	-1.484E-04	-1.484E-04	1.181E-03	0.946
^{42}Ca	42	20	5.063E-07	-2.656E-13	1.203E-05	1.203E-05	2.135E-05	2.440
^{43}Ca	43	20	1.082E-07	-5.674E-14	4.247E-06	4.247E-06	6.236E-06	3.337
^{44}Ca	44	20	1.710E-06	-8.972E-13	9.419E-06	9.419E-06	4.088E-05	1.384
^{46}Ca	46	20	3.428E-09	-1.799E-15	3.288E-07	3.288E-07	3.919E-07	6.617
^{48}Ca	48	20	1.672E-07	-8.774E-14	-7.577E-08	-7.577E-08	3.000E-06	1.039
^{45}Sc	45	21	5.414E-08	-2.840E-14	2.880E-06	2.880E-06	3.876E-06	4.144
^{46}Ti	46	22	3.232E-07	-1.695E-13	1.992E-06	1.992E-06	7.936E-06	1.421
^{47}Ti	47	22	2.977E-07	-1.562E-13	5.368E-07	5.368E-07	6.012E-06	1.169
^{48}Ti	48	22	3.014E-06	-1.581E-12	-7.702E-06	-7.702E-06	4.773E-05	0.917
^{49}Ti	49	22	2.257E-07	-1.184E-13	3.026E-06	3.026E-06	7.178E-06	1.841
^{50}Ti	50	22	2.208E-07	-1.158E-13	1.077E-05	1.077E-05	1.483E-05	3.888
^{50}V	50	23	1.015E-09	-5.327E-16	3.307E-09	3.307E-09	2.198E-08	1.253
^{51}V	51	23	4.138E-07	-2.171E-13	-1.635E-07	-1.635E-07	7.447E-06	1.042
^{50}Cr	50	24	8.265E-07	-4.336E-13	-2.994E-06	-2.994E-06	1.221E-05	0.855
^{52}Cr	52	24	1.658E-05	-8.696E-12	-3.597E-05	-3.597E-05	2.689E-04	0.939
^{53}Cr	53	24	1.916E-06	-1.005E-12	-2.203E-06	-2.203E-06	3.303E-05	0.998

TableC.4 – continued

Isotope	A	Z	$X^{\rm ini}$	$mp^{\rm wind}$	$mp^{\rm preSN}$	$mp^{\rm total}$	EM	$\langle OP \rangle$
^{54}Cr	54	24	4.858E-07	-2.548E-13	2.551E-05	2.551E-05	3.444E-05	4.104
^{55}Mn	55	25	1.098E-05	-5.760E-12	-1.341E-05	-1.341E-05	1.886E-04	0.994
^{54}Fe	54	26	8.118E-05	-4.259E-11	-2.836E-04	-2.836E-04	1.210E-03	0.863
^{56}Fe	56	26	1.322E-03	-6.933E-10	-3.353E-03	-3.353E-03	2.095E-02	0.918
^{57}Fe	57	26	3.107E-05	-1.630E-11	3.187E-04	3.187E-04	8.901E-04	1.659
^{58}Fe	58	26	4.207E-06	-2.207E-12	1.267E-03	1.267E-03	1.345E-03	18.501
^{59}Co	59	27	3.991E-06	-2.094E-12	6.661E-04	6.661E-04	7.395E-04	10.725
^{58}Ni	58	28	5.711E-05	-2.996E-11	-1.969E-04	-1.969E-04	8.536E-04	0.865
^{60}Ni	60	28	2.276E-05	-1.194E-11	3.611E-04	3.611E-04	7.797E-04	1.983
^{61}Ni	61	28	1.006E-06	-5.276E-13	1.808E-04	1.808E-04	1.993E-04	11.470
^{62}Ni	62	28	3.259E-06	-1.710E-12	4.642E-04	4.642E-04	5.241E-04	9.309
^{64}Ni	64	28	8.568E-07	-4.495E-13	2.049E-04	2.049E-04	2.207E-04	14.908
^{63}Cu	63	29	6.600E-07	-3.462E-13	2.094E-04	2.094E-04	2.216E-04	19.433
^{65}Cu	65	29	3.035E-07	-1.592E-13	1.208E-04	1.208E-04	1.264E-04	24.107
^{64}Zn	64	30	1.131E-06	-5.932E-13	4.768E-05	4.768E-05	6.848E-05	3.506
^{66}Zn	66	30	6.690E-07	-3.510E-13	9.221E-05	9.221E-05	1.045E-04	9.043
^{67}Zn	67	30	9.980E-08	-5.236E-14	2.974E-05	2.974E-05	3.158E-05	18.315
^{68}Zn	68	30	4.632E-07	-2.430E-13	9.866E-05	9.866E-05	1.072E-04	13.393
^{70}Zn	70	30	1.577E-08	-8.272E-15	1.040E-07	1.040E-07	3.941E-07	1.447
^{69}Ga	69	31	4.551E-08	-2.387E-14	1.268E-05	1.268E-05	1.351E-05	17.191
^{71}Ga	71	31	3.108E-08	-1.630E-14	7.594E-06	7.594E-06	8.166E-06	15.211
^{70}Ge	70	32	5.157E-08	-2.705E-14	1.701E-05	1.701E-05	1.796E-05	20.156
^{72}Ge	72	32	6.910E-08	-3.625E-14	1.539E-05	1.539E-05	1.666E-05	13.955
^{73}Ge	73	32	1.955E-08	-1.025E-14	6.668E-06	6.668E-06	7.028E-06	20.815
^{74}Ge	74	32	9.228E-08	-4.841E-14	1.832E-05	1.832E-05	2.002E-05	12.557
^{76}Ge	76	32	1.963E-08	-1.030E-14	2.268E-08	2.268E-08	3.837E-07	1.132
^{75}As	75	33	1.430E-08	-7.502E-15	2.417E-06	2.417E-06	2.680E-06	10.849
^{74}Se	74	34	1.198E-09	-6.284E-16	-4.983E-09	-4.983E-09	1.705E-08	0.824

TableC.4 – continued

Isotope	A	Z	$X^{\rm ini}$	$mp^{\rm wind}$	$mp^{\rm preSN}$	$mp^{\rm total}$	EM	$\langle OP \rangle$
^{76}Se	76	34	1.296E-08	-6.799E-15	3.228E-06	3.228E-06	3.466E-06	15.480
^{77}Se	77	34	1.070E-08	-5.616E-15	1.661E-06	1.661E-06	1.858E-06	10.047
^{78}Se	78	34	3.376E-08	-1.771E-14	7.113E-06	7.113E-06	7.734E-06	13.260
^{80}Se	80	34	7.226E-08	-3.791E-14	3.897E-06	3.897E-06	5.226E-06	4.186
^{82}Se	82	34	1.304E-08	-6.839E-15	-2.563E-08	-2.563E-08	2.142E-07	0.951
^{79}Br	79	35	1.389E-08	-7.288E-15	1.801E-06	1.801E-06	2.057E-06	8.571
^{81}Br	81	35	1.386E-08	-7.270E-15	8.589E-07	8.589E-07	1.114E-06	4.652
^{78}Kr	78	36	3.900E-10	-2.046E-16	-1.598E-09	-1.598E-09	5.576E-09	0.828
^{80}Kr	80	36	2.575E-09	-1.350E-15	3.900E-07	3.900E-07	4.374E-07	9.834
^{82}Kr	82	36	1.320E-08	-6.922E-15	1.965E-06	1.965E-06	2.208E-06	9.685
^{83}Kr	83	36	1.324E-08	-6.947E-15	9.693E-07	9.693E-07	1.213E-06	5.302
^{84}Kr	84	36	6.602E-08	-3.463E-14	4.078E-06	4.078E-06	5.292E-06	4.640
^{86}Kr	86	36	2.044E-08	-1.072E-14	9.187E-07	9.187E-07	1.295E-06	3.666
^{85}Rb	85	37	1.282E-08	-6.727E-15	1.321E-06	1.321E-06	1.557E-06	7.029
^{87}Rb	87	37	5.063E-09	-2.765E-12	4.860E-07	4.860E-07	5.791E-07	6.622
^{84}Sr	84	38	3.228E-10	-1.693E-16	-1.392E-09	-1.392E-09	4.546E-09	0.815
^{86}Sr	86	38	5.845E-09	-3.066E-15	7.698E-07	7.698E-07	8.773E-07	8.689
^{87}Sr	87	38	4.443E-09	2.760E-12	4.856E-07	4.856E-07	5.673E-07	7.392
^{88}Sr	88	38	5.011E-08	-2.629E-14	2.386E-06	2.386E-06	3.308E-06	3.821
^{89}Y	89	39	1.229E-08	-6.449E-15	4.553E-07	4.553E-07	6.815E-07	3.209
^{90}Zr	90	40	1.534E-08	-8.049E-15	1.921E-07	1.921E-07	4.744E-07	1.790
^{91}Zr	91	40	3.384E-09	-1.775E-15	6.414E-08	6.414E-08	1.264E-07	2.162
^{92}Zr	92	40	5.227E-09	-2.742E-15	8.569E-08	8.569E-08	1.818E-07	2.014
^{94}Zr	94	40	5.413E-09	-2.840E-15	3.113E-08	3.113E-08	1.307E-07	1.398
^{96}Zr	96	40	8.903E-10	-4.671E-16	1.824E-08	1.824E-08	3.462E-08	2.251
^{93}Nb	93	41	1.900E-09	-9.968E-16	3.469E-08	3.469E-08	6.964E-08	2.122
^{92}Mo	92	42	1.012E-09	-5.311E-16	-3.745E-09	-3.745E-09	1.488E-08	0.851
^{94}Mo	94	42	6.448E-10	-3.382E-16	-8.783E-10	-8.783E-10	1.098E-08	0.986

TableC.4 – continued

Isotope	A	Z	$X^{\rm ini}$	$mp^{\rm wind}$	$mp^{\rm preSN}$	$mp^{\rm total}$	EM	$\langle OP \rangle$
^{95}Mo	95	42	1.122E-09	-5.885E-16	1.531E-08	1.531E-08	3.595E-08	1.855
^{96}Mo	96	42	1.188E-09	-6.229E-16	4.935E-09	4.935E-09	2.678E-08	1.305
^{97}Mo	97	42	6.875E-10	-3.607E-16	9.113E-10	9.113E-10	1.356E-08	1.141
^{98}Mo	98	42	1.754E-09	-9.203E-16	6.079E-09	6.079E-09	3.835E-08	1.265
^{100}Mo	100	42	7.146E-10	-3.749E-16	-2.494E-09	-2.494E-09	1.065E-08	0.863
^{96}Ru	96	44	2.926E-10	-1.535E-16	-1.176E-09	-1.176E-09	4.205E-09	0.832
^{98}Ru	98	44	1.007E-10	-5.283E-17	-3.205E-10	-3.205E-10	1.532E-09	0.881
^{99}Ru	99	44	6.945E-10	-3.644E-16	-8.398E-10	-8.398E-10	1.193E-08	0.995
^{100}Ru	100	44	6.928E-10	-3.634E-16	3.862E-09	3.862E-09	1.660E-08	1.387
^{101}Ru	101	44	9.475E-10	-4.971E-16	-2.707E-09	-2.707E-09	1.472E-08	0.899
^{102}Ru	102	44	1.770E-09	-9.284E-16	4.303E-09	4.303E-09	3.685E-08	1.206
^{104}Ru	104	44	1.065E-09	-5.587E-16	-3.226E-09	-3.226E-09	1.636E-08	0.889
^{103}Rh	103	45	1.055E-09	-5.533E-16	-2.619E-09	-2.619E-09	1.678E-08	0.921
^{102}Pd	102	46	4.241E-11	-2.225E-17	-1.832E-10	-1.832E-10	5.969E-10	0.815
^{104}Pd	104	46	4.723E-10	-2.477E-16	3.637E-09	3.637E-09	1.232E-08	1.511
^{105}Pd	105	46	9.558E-10	-5.014E-16	-2.869E-09	-2.869E-09	1.471E-08	0.891
^{106}Pd	106	46	1.181E-09	-6.195E-16	2.662E-09	2.662E-09	2.438E-08	1.195
^{108}Pd	108	46	1.165E-09	-6.111E-16	2.923E-09	2.923E-09	2.435E-08	1.210
^{110}Pd	110	46	5.255E-10	-2.757E-16	-1.308E-09	-1.308E-09	8.358E-09	0.921
^{107}Ag	107	47	7.840E-10	-4.113E-16	-1.956E-09	-1.956E-09	1.246E-08	0.920
^{109}Ag	109	47	7.420E-10	-3.893E-16	6.975E-10	6.975E-10	1.435E-08	1.119
^{106}Cd	106	48	6.346E-11	-3.329E-17	-2.676E-10	-2.676E-10	8.996E-10	0.821
^{108}Cd	108	48	4.604E-11	-2.413E-17	7.256E-10	7.256E-10	1.572E-09	1.977
^{110}Cd	110	48	6.580E-10	-3.452E-16	3.206E-09	3.206E-09	1.531E-08	1.347
^{111}Cd	111	48	6.805E-10	-3.570E-16	-1.007E-09	-1.007E-09	1.151E-08	0.979
^{112}Cd	112	48	1.294E-09	-6.790E-16	2.149E-09	2.149E-09	2.596E-08	1.161
^{113}Cd	113	48	6.614E-10	-3.469E-16	-8.395E-10	-8.395E-10	1.132E-08	0.991
^{114}Cd	114	48	1.569E-09	-8.229E-16	3.975E-09	3.975E-09	3.283E-08	1.211

TableC.4 – continued

Isotope	A	Z	$X^{\rm ini}$	$mp^{\rm wind}$	$mp^{\rm preSN}$	$mp^{\rm total}$	EM	$\langle OP \rangle$
^{116}Cd	116	48	4.161E-10	-2.183E-16	4.284E-10	4.284E-10	8.082E-09	1.124
^{113}In	113	49	2.604E-11	-1.366E-17	-9.519E-11	-9.519E-11	3.837E-10	0.853
^{115}In	115	49	5.915E-10	-3.440E-16	-6.011E-10	-6.011E-10	1.028E-08	1.006
^{112}Sn	112	50	1.221E-10	-6.405E-17	-4.940E-10	-4.940E-10	1.752E-09	0.831
^{114}Sn	114	50	8.435E-11	-4.425E-17	-2.552E-10	-2.552E-10	1.296E-09	0.890
^{115}Sn	115	50	4.377E-11	1.069E-17	-6.516E-11	-6.516E-11	7.399E-10	0.979
^{116}Sn	116	50	1.893E-09	-9.931E-16	3.732E-09	3.732E-09	3.855E-08	1.179
^{117}Sn	117	50	1.008E-09	-5.290E-16	-5.069E-11	-5.069E-11	1.850E-08	1.062
^{118}Sn	118	50	3.209E-09	-1.684E-15	6.555E-09	6.555E-09	6.558E-08	1.183
^{119}Sn	119	50	1.147E-09	-6.017E-16	1.226E-09	1.226E-09	2.232E-08	1.127
^{120}Sn	120	50	4.391E-09	-2.304E-15	1.399E-08	1.399E-08	9.475E-08	1.249
^{122}Sn	122	50	6.341E-10	-3.326E-16	2.604E-09	2.604E-09	1.427E-08	1.303
^{124}Sn	124	50	8.060E-10	-4.228E-16	-2.338E-09	-2.338E-09	1.249E-08	0.897
^{121}Sb	121	51	6.318E-10	-3.314E-16	5.791E-10	5.791E-10	1.220E-08	1.118
^{123}Sb	123	51	4.803E-10	-2.520E-16	-1.457E-09	-1.457E-09	7.377E-09	0.889
^{120}Te	120	52	1.628E-11	-8.542E-18	-7.285E-11	-7.285E-11	2.266E-10	0.806
^{122}Te	122	52	4.489E-10	-2.355E-16	2.011E-09	2.011E-09	1.027E-08	1.324
^{123}Te	123	52	1.579E-10	-8.281E-17	6.524E-10	6.524E-10	3.556E-09	1.304
^{124}Te	124	52	8.441E-10	-4.428E-16	4.030E-09	4.030E-09	1.956E-08	1.341
^{125}Te	125	52	1.261E-09	-6.617E-16	-3.075E-09	-3.075E-09	2.013E-08	0.924
^{126}Te	126	52	3.375E-09	-1.771E-15	1.748E-09	1.748E-09	6.383E-08	1.095
^{128}Te	128	52	5.733E-09	-3.007E-15	-1.835E-08	-1.835E-08	8.710E-08	0.879
^{130}Te	130	52	6.211E-09	-3.258E-15	-1.864E-08	-1.864E-08	9.559E-08	0.891
^{127}I	127	53	1.459E-09	-7.655E-16	-4.122E-09	-4.122E-09	2.272E-08	0.901
^{124}Xe	124	54	2.210E-11	-1.159E-17	-1.009E-10	-1.009E-10	3.055E-10	0.800
^{126}Xe	126	54	1.949E-11	-1.023E-17	-8.298E-11	-8.298E-11	2.755E-10	0.818
^{128}Xe	128	54	3.943E-10	-2.068E-16	3.593E-09	3.593E-09	1.084E-08	1.592
^{129}Xe	129	54	4.893E-09	-2.567E-15	-1.965E-08	-1.965E-08	7.034E-08	0.832

TableC.4 – continued

Isotope	A	Z	$X^{\rm ini}$	$mp^{\rm wind}$	$mp^{\rm preSN}$	$mp^{\rm total}$	EM	$\langle OP \rangle$
^{130}Xe	130	54	7.865E-10	-4.125E-16	1.091E-08	1.091E-08	2.538E-08	1.868
^{131}Xe	131	54	3.945E-09	-2.069E-15	-1.197E-08	-1.197E-08	6.058E-08	0.889
^{132}Xe	132	54	4.806E-09	-2.521E-15	5.644E-09	5.644E-09	9.405E-08	1.133
^{134}Xe	134	54	1.788E-09	-9.380E-16	-1.570E-09	-1.570E-09	3.132E-08	1.014
^{136}Xe	136	54	1.478E-09	-7.756E-16	-6.267E-10	-6.267E-10	2.657E-08	1.040
^{133}Cs	133	55	1.426E-09	-7.481E-16	-2.567E-09	-2.567E-09	2.366E-08	0.961
^{130}Ba	130	56	1.814E-11	-9.518E-18	-8.387E-11	-8.387E-11	2.498E-10	0.797
^{132}Ba	132	56	1.762E-11	-9.244E-18	-7.579E-11	-7.579E-11	2.483E-10	0.816
^{134}Ba	134	56	4.272E-10	-2.241E-16	6.063E-09	6.063E-09	1.392E-08	1.886
^{135}Ba	135	56	1.174E-09	-6.158E-16	-1.080E-09	-1.080E-09	2.051E-08	1.011
^{136}Ba	136	56	1.409E-09	-7.390E-16	1.414E-08	1.414E-08	4.006E-08	1.646
^{137}Ba	137	56	2.030E-09	-1.065E-15	9.407E-09	9.407E-09	4.674E-08	1.333
^{138}Ba	138	56	1.305E-08	-6.847E-15	1.374E-07	1.374E-07	3.774E-07	1.674
^{138}La	138	57	1.604E-12	-8.415E-19	-7.002E-12	-7.002E-12	2.250E-11	0.812
^{139}La	139	57	1.790E-09	-9.391E-16	1.554E-08	1.554E-08	4.846E-08	1.567
^{136}Ce	136	58	8.382E-12	-4.397E-18	-3.541E-11	-3.541E-11	1.188E-10	0.820
^{138}Ce	138	58	1.148E-11	-6.021E-18	-4.542E-11	-4.542E-11	1.657E-10	0.836
^{140}Ce	140	58	4.103E-09	-2.152E-15	2.051E-08	2.051E-08	9.598E-08	1.354
^{142}Ce	142	58	5.229E-10	-2.743E-16	6.708E-10	6.708E-10	1.029E-08	1.139
^{141}Pr	141	59	6.910E-10	-3.625E-16	1.617E-09	1.617E-09	1.433E-08	1.200
^{142}Nd	142	60	9.920E-10	-5.204E-16	2.779E-09	2.779E-09	2.102E-08	1.227
^{143}Nd	143	60	4.484E-10	-2.352E-16	-5.991E-10	-5.991E-10	7.648E-09	0.987
^{144}Nd	144	60	8.826E-10	-4.630E-16	4.774E-10	4.774E-10	1.671E-08	1.096
^{145}Nd	145	60	3.095E-10	-1.624E-16	-4.424E-10	-4.424E-10	5.251E-09	0.982
^{146}Nd	146	60	6.448E-10	-3.382E-16	1.516E-09	1.516E-09	1.338E-08	1.201
^{148}Nd	148	60	2.185E-10	-1.146E-16	-7.056E-11	-7.056E-11	3.948E-09	1.046
^{150}Nd	150	60	2.168E-10	-1.137E-16	-8.511E-10	-8.511E-10	3.137E-09	0.838
^{144}Sm	144	62	3.684E-11	-1.932E-17	-1.366E-10	-1.366E-10	5.409E-10	0.850

TableC.4 – continued

Isotope	A	Z	$X^{\rm ini}$	$mp^{\rm wind}$	$mp^{\rm preSN}$	$mp^{\rm total}$	EM	$\langle OP \rangle$
^{147}Sm	147	62	1.834E-10	-9.624E-17	-4.668E-10	-4.668E-10	2.907E-09	0.917
^{148}Sm	148	62	1.385E-10	-7.263E-17	1.108E-10	1.108E-10	2.658E-09	1.111
^{149}Sm	149	62	1.714E-10	-8.991E-17	-6.515E-10	-6.515E-10	2.501E-09	0.845
^{150}Sm	150	62	9.213E-11	-4.832E-17	4.552E-10	4.552E-10	2.150E-09	1.351
^{152}Sm	152	62	3.383E-10	-1.775E-16	-1.050E-09	-1.050E-09	5.172E-09	0.885
^{154}Sm	154	62	2.916E-10	-1.530E-16	-1.003E-09	-1.003E-09	4.361E-09	0.866
^{151}Eu	151	63	2.036E-10	-1.068E-16	-8.891E-10	-8.891E-10	2.856E-09	0.812
^{153}Eu	153	63	2.252E-10	-1.181E-16	-8.882E-10	-8.882E-10	3.254E-09	0.836
^{152}Gd	152	64	2.947E-12	-1.541E-18	1.690E-10	1.690E-10	2.232E-10	4.385
^{154}Gd	154	64	3.210E-11	-1.682E-17	2.959E-10	2.959E-10	8.863E-10	1.598
^{155}Gd	155	64	2.192E-10	-1.150E-16	-8.386E-10	-8.386E-10	3.193E-09	0.843
^{156}Gd	156	64	3.051E-10	-1.600E-16	-4.491E-10	-4.491E-10	5.163E-09	0.980
^{157}Gd	157	64	2.348E-10	-1.232E-16	-6.556E-10	-6.556E-10	3.664E-09	0.903
^{158}Gd	158	64	3.750E-10	-1.967E-16	-1.650E-10	-1.650E-10	6.732E-09	1.039
^{160}Gd	160	64	3.343E-10	-1.754E-16	-1.157E-09	-1.157E-09	4.992E-09	0.864
^{159}Tb	159	65	2.765E-10	-1.451E-16	-9.609E-10	-9.609E-10	4.125E-09	0.864
^{156}Dy	156	66	1.004E-12	-5.266E-19	-4.871E-12	-4.871E-12	1.359E-11	0.784
^{158}Dy	158	66	1.743E-12	-9.143E-19	1.513E-11	1.513E-11	4.719E-11	1.567
^{160}Dy	160	66	4.301E-11	-2.255E-17	3.342E-10	3.342E-10	1.125E-09	1.515
^{161}Dy	161	66	3.498E-10	-1.835E-16	-1.385E-09	-1.385E-09	5.049E-09	0.836
^{162}Dy	162	66	4.748E-10	-2.491E-16	-8.640E-10	-8.640E-10	7.869E-09	0.959
^{163}Dy	163	66	4.663E-10	-2.446E-16	-1.645E-09	-1.645E-09	6.932E-09	0.861
^{164}Dy	164	66	5.312E-10	-2.786E-16	-6.600E-11	-6.600E-11	9.704E-09	1.058
^{165}Ho	165	67	4.244E-10	-2.226E-16	-1.582E-09	-1.582E-09	6.224E-09	0.849
^{162}Er	162	68	1.609E-12	-8.441E-19	-7.801E-12	-7.801E-12	2.179E-11	0.784
^{164}Er	164	68	1.913E-11	-1.004E-17	-9.119E-11	-9.119E-11	2.606E-10	0.789
^{166}Er	166	68	4.044E-10	-2.122E-16	-1.006E-09	-1.006E-09	6.433E-09	0.921
^{167}Er	167	68	2.776E-10	-1.456E-16	-9.169E-10	-9.169E-10	4.189E-09	0.874

TableC.4 – continued

Isotope	A	Z	$X^{\rm ini}$	$mp^{\rm wind}$	$mp^{\rm preSN}$	$mp^{\rm total}$	EM	$\langle OP \rangle$
^{168}Er	168	68	3.263E-10	-1.711E-16	1.372E-10	1.372E-10	6.138E-09	1.089
^{170}Er	170	68	1.840E-10	-9.652E-17	-1.357E-10	-1.357E-10	3.248E-09	1.022
^{169}Tm	169	69	1.854E-10	-9.728E-17	-5.097E-10	-5.097E-10	2.901E-09	0.906
^{168}Yb	168	70	1.583E-12	-8.306E-19	-7.591E-12	-7.591E-12	2.153E-11	0.787
^{170}Yb	170	70	3.746E-11	-1.964E-17	2.621E-10	2.621E-10	9.511E-10	1.470
^{171}Yb	171	70	1.770E-10	-9.286E-17	-5.292E-10	-5.292E-10	2.727E-09	0.892
^{172}Yb	172	70	2.722E-10	-1.428E-16	-1.295E-10	-1.295E-10	4.877E-09	1.037
^{173}Yb	173	70	2.023E-10	-1.061E-16	-3.655E-10	-3.655E-10	3.355E-09	0.960
^{174}Yb	174	70	4.015E-10	-2.106E-16	4.594E-10	4.594E-10	7.844E-09	1.131
^{176}Yb	176	70	1.628E-10	-8.540E-17	-3.436E-10	-3.436E-10	2.651E-09	0.943
^{175}Lu	175	71	1.828E-10	-9.589E-17	-5.134E-10	-5.134E-10	2.849E-09	0.902
^{176}Lu	176	71	4.876E-12	-3.225E-15	1.729E-11	1.729E-11	1.070E-10	1.270
^{174}Hf	174	72	1.231E-12	-6.460E-19	-5.805E-12	-5.805E-12	1.684E-11	0.792
^{176}Hf	176	72	4.036E-11	3.201E-15	2.055E-10	2.055E-10	9.478E-10	1.359
^{177}Hf	177	72	1.438E-10	-7.543E-17	-4.437E-10	-4.437E-10	2.201E-09	0.886
^{178}Hf	178	72	2.121E-10	-1.113E-16	2.373E-10	2.373E-10	4.139E-09	1.129
^{179}Hf	179	72	1.065E-10	-5.588E-17	-1.520E-10	-1.520E-10	1.807E-09	0.982
^{180}Hf	180	72	2.758E-10	-1.447E-16	6.462E-10	6.462E-10	5.720E-09	1.200
^{180}Ta	180	73	2.429E-14	-1.376E-20	3.110E-12	3.110E-12	3.557E-12	8.477
^{181}Ta	181	73	1.986E-10	-1.042E-16	-3.832E-10	-3.832E-10	3.269E-09	0.953
^{180}W	180	74	8.395E-13	-4.399E-19	9.541E-12	9.541E-12	2.498E-11	1.723
^{182}W	182	74	1.877E-10	-9.848E-17	5.037E-11	5.037E-11	3.504E-09	1.080
^{183}W	183	74	1.020E-10	-5.349E-17	5.170E-11	5.170E-11	1.927E-09	1.094
^{184}W	184	74	2.195E-10	-1.151E-16	4.801E-10	4.801E-10	4.517E-09	1.191
^{186}W	186	74	2.058E-10	-1.080E-16	-2.568E-10	-2.568E-10	3.529E-09	0.993
^{185}Re	185	75	1.048E-10	-5.497E-17	-1.334E-10	-1.334E-10	1.794E-09	0.991
^{187}Re	187	75	1.773E-10	-9.302E-17	-6.627E-10	-6.627E-10	2.598E-09	0.848
^{184}Os	184	76	7.108E-13	-3.729E-19	-3.230E-12	-3.230E-12	9.845E-12	0.802

TableC.4 – continued

Isotope	A	Z	X^{ini}	mp^{wind}	mp^{preSN}	mp^{total}	EM	$\langle OP \rangle$
^{186}Os	186	76	5.778E-11	-3.031E-17	1.378E-10	1.378E-10	1.201E-09	1.203
^{187}Os	187	76	5.998E-11	-3.147E-17	-1.587E-10	-1.587E-10	9.446E-10	0.912
^{188}Os	188	76	4.874E-10	-2.557E-16	-9.281E-10	-9.281E-10	8.036E-09	0.955
^{189}Os	189	76	5.974E-10	-3.134E-16	-2.554E-09	-2.554E-09	8.433E-09	0.817
^{190}Os	190	76	9.766E-10	-5.123E-16	-2.270E-09	-2.270E-09	1.569E-08	0.930
^{192}Os	192	76	1.533E-09	-8.040E-16	-5.211E-09	-5.211E-09	2.298E-08	0.868
^{191}Ir	191	77	1.357E-09	-7.121E-16	-6.099E-09	-6.099E-09	1.887E-08	0.805
^{193}Ir	193	77	2.308E-09	-1.211E-15	-1.000E-08	-1.000E-08	3.246E-08	0.814
^{190}Pt	190	78	1.008E-12	-5.291E-19	-4.501E-12	-4.501E-12	1.405E-11	0.806
^{192}Pt	192	78	5.850E-11	-3.062E-17	1.030E-09	1.030E-09	2.106E-09	2.084
^{194}Pt	194	78	2.490E-09	-1.306E-15	-7.005E-09	-7.005E-09	3.879E-08	0.902
^{195}Pt	195	78	2.568E-09	-1.347E-15	-1.011E-08	-1.011E-08	3.713E-08	0.837
^{196}Pt	196	78	1.926E-09	-1.010E-15	-1.241E-09	-1.241E-09	3.418E-08	1.027
^{198}Pt	198	78	5.522E-10	-2.897E-16	-1.892E-09	-1.892E-09	8.264E-09	0.866
^{197}Au	197	79	1.083E-09	-5.683E-16	-3.056E-09	-3.056E-09	1.687E-08	0.901
^{196}Hg	196	80	3.009E-12	-1.579E-18	-1.215E-11	-1.215E-11	4.320E-11	0.831
^{198}Hg	198	80	1.975E-10	-1.036E-16	3.032E-09	3.032E-09	6.665E-09	1.953
^{199}Hg	199	80	3.360E-10	-1.763E-16	1.724E-10	1.724E-10	6.352E-09	1.094
^{200}Hg	200	80	4.622E-10	-2.425E-16	2.436E-09	2.436E-09	1.094E-08	1.370
^{201}Hg	201	80	2.651E-10	-1.391E-16	1.015E-09	1.015E-09	5.891E-09	1.286
^{202}Hg	202	80	6.036E-10	-3.167E-16	5.815E-09	5.815E-09	1.692E-08	1.622
^{204}Hg	204	80	1.401E-10	-7.351E-17	-2.981E-10	-2.981E-10	2.279E-09	0.942
^{203}Tl	203	81	3.221E-10	-1.690E-16	4.737E-09	4.737E-09	1.066E-08	1.916
^{205}Tl	205	81	7.764E-10	-4.073E-16	8.905E-09	8.905E-09	2.319E-08	1.729
^{204}Pb	204	82	2.931E-10	-1.538E-16	5.610E-09	5.610E-09	1.100E-08	2.173
^{206}Pb	206	82	2.798E-09	-1.468E-15	2.912E-08	2.912E-08	8.058E-08	1.667
^{207}Pb	207	82	3.090E-09	-1.621E-15	3.297E-08	3.297E-08	8.980E-08	1.683
^{208}Pb	208	82	8.850E-09	-4.642E-15	3.334E-08	3.334E-08	1.961E-07	1.283

TableC.4 – continued

Isotope	A	Z	X^{ini}	mp^{wind}	mp^{preSN}	mp^{total}	EM	$\langle OP \rangle$
^{209}Bi	209	83	8.718E-10	-4.574E-16	7.472E-10	7.472E-10	1.678E-08	1.114

Table C.5: Yields for model 20CI.

Isotope	A	Z	X^{ini}	mp^{wind}	mp^{preSN}	mp^{total}	EM	$\langle OP \rangle$
^{1}H	1	1	7.064E-01	-1.806E-01	-4.867E+00	-5.047E+00	7.946E+00	0.651
^{2}H	2	1	1.371E-05	-7.048E-05	-1.675E-04	-2.380E-04	1.413E-05	0.060
^{3}He	3	2	4.540E-05	-1.434E-05	-4.612E-04	-4.755E-04	3.595E-04	0.458
^{4}He	4	2	2.735E-01	1.807E-01	1.510E+00	1.691E+00	6.721E+00	1.423
^{7}Li	7	3	7.605E-11	-3.911E-10	-9.294E-10	-1.320E-09	7.839E-11	0.060
^{11}B	11	5	2.856E-09	3.491E-15	8.273E-11	8.273E-11	5.261E-08	1.066
^{12}C	12	6	3.425E-03	-4.142E-03	3.507E-01	3.465E-01	4.095E-01	6.922
^{13}C	13	6	4.156E-05	4.381E-04	1.603E-04	5.984E-04	1.363E-03	1.898
^{14}N	14	7	1.059E-03	9.031E-03	4.755E-02	5.658E-02	7.606E-02	4.158
^{15}N	15	7	4.171E-06	-1.067E-05	-4.090E-05	-5.157E-05	2.515E-05	0.349
^{16}O	16	8	9.624E-03	-5.311E-03	1.784E+00	1.779E+00	1.956E+00	11.766
^{17}O	17	8	3.813E-06	3.177E-06	2.190E-05	2.508E-05	9.522E-05	1.446
^{18}O	18	8	2.171E-05	-2.106E-05	2.906E-03	2.885E-03	3.285E-03	8.758
^{19}F	19	9	5.611E-07	-3.643E-07	-3.131E-06	-3.495E-06	6.825E-06	0.704
^{20}Ne	20	10	1.818E-03	-1.193E-05	9.392E-01	9.392E-01	9.726E-01	30.975
^{21}Ne	21	10	4.575E-06	1.022E-05	3.637E-03	3.647E-03	3.731E-03	47.209
^{22}Ne	22	10	1.470E-04	-9.295E-05	3.521E-02	3.511E-02	3.782E-02	14.890
^{23}Na	23	11	4.000E-05	9.967E-05	4.736E-02	4.746E-02	4.820E-02	69.762
^{24}Mg	24	12	5.862E-04	2.567E-08	8.414E-02	8.414E-02	9.493E-02	9.374
^{25}Mg	25	12	7.733E-05	-3.507E-05	3.867E-02	3.863E-02	4.005E-02	29.983
^{26}Mg	26	12	8.848E-05	3.612E-05	3.406E-02	3.410E-02	3.572E-02	23.372
^{27}Al	27	13	6.481E-05	3.633E-07	1.147E-02	1.147E-02	1.266E-02	11.310
^{28}Si	28	14	7.453E-04	1.789E-09	5.066E-03	5.066E-03	1.877E-02	1.458
^{29}Si	29	14	3.919E-05	6.940E-12	9.652E-04	9.652E-04	1.686E-03	2.490
^{30}Si	30	14	2.673E-05	-6.503E-09	8.040E-04	8.040E-04	1.296E-03	2.806
^{31}P	31	15	7.106E-06	6.807E-09	2.525E-04	2.525E-04	3.832E-04	3.122
^{32}S	32	16	4.011E-04	4.551E-10	-5.751E-04	-5.751E-04	6.802E-03	0.982

TableC.5 – continued

Isotope	A	Z	$X^{\rm ini}$	$mp^{\rm wind}$	$mp^{\rm preSN}$	$mp^{\rm total}$	EM	$\langle OP \rangle$
^{33}S	33	16	3.265E-06	4.020E-11	1.726E-05	1.726E-05	7.731E-05	1.371
^{34}S	34	16	1.890E-05	2.311E-11	3.681E-05	3.681E-05	3.845E-04	1.177
^{36}S	36	16	8.073E-08	9.867E-14	1.779E-05	1.779E-05	1.927E-05	13.821
^{35}Cl	35	17	6.821E-06	8.335E-12	-1.297E-05	-1.297E-05	1.125E-04	0.955
^{37}Cl	37	17	2.306E-06	2.818E-12	1.713E-04	1.713E-04	2.137E-04	5.365
^{36}Ar	36	18	8.202E-05	1.003E-10	-2.080E-04	-2.080E-04	1.301E-03	0.918
^{38}Ar	38	18	1.574E-05	1.924E-11	1.055E-04	1.055E-04	3.951E-04	1.453
^{40}Ar	40	18	2.650E-08	3.634E-14	7.328E-06	7.328E-06	7.815E-06	17.071
^{39}K	39	19	3.900E-06	4.766E-12	2.229E-05	2.229E-05	9.402E-05	1.396
^{40}K	40	19	5.005E-10	-9.340E-12	3.950E-06	3.950E-06	3.960E-06	457.965
^{41}K	41	19	2.959E-07	3.616E-13	9.317E-06	9.317E-06	1.476E-05	2.888
^{40}Ca	40	20	7.225E-05	9.765E-11	-1.520E-04	-1.520E-04	1.177E-03	0.943
^{42}Ca	42	20	5.063E-07	6.189E-13	1.213E-05	1.213E-05	2.144E-05	2.451
^{43}Ca	43	20	1.082E-07	1.322E-13	4.433E-06	4.433E-06	6.422E-06	3.437
^{44}Ca	44	20	1.710E-06	2.090E-12	1.026E-05	1.026E-05	4.172E-05	1.412
^{46}Ca	46	20	3.428E-09	4.190E-15	5.049E-08	5.049E-08	1.135E-07	1.917
^{48}Ca	48	20	1.672E-07	2.044E-13	-7.911E-08	-7.911E-08	2.997E-06	1.037
^{45}Sc	45	21	5.414E-08	6.617E-14	2.746E-06	2.746E-06	3.742E-06	4.001
^{46}Ti	46	22	3.232E-07	3.950E-13	2.690E-06	2.690E-06	8.634E-06	1.547
^{47}Ti	47	22	2.977E-07	3.639E-13	9.378E-07	9.378E-07	6.413E-06	1.247
^{48}Ti	48	22	3.014E-06	3.684E-12	-6.732E-06	-6.732E-06	4.870E-05	0.935
^{49}Ti	49	22	2.257E-07	2.759E-13	3.564E-06	3.564E-06	7.716E-06	1.979
^{50}Ti	50	22	2.208E-07	2.699E-13	1.224E-05	1.224E-05	1.630E-05	4.274
^{50}V	50	23	1.015E-09	1.241E-15	-5.688E-10	-5.688E-10	1.811E-08	1.032
^{51}V	51	23	4.138E-07	5.057E-13	1.156E-07	1.156E-07	7.726E-06	1.081
^{50}Cr	50	24	8.265E-07	1.010E-12	-2.897E-06	-2.897E-06	1.231E-05	0.862
^{52}Cr	52	24	1.658E-05	2.026E-11	-3.614E-05	-3.614E-05	2.687E-04	0.939
^{53}Cr	53	24	1.916E-06	2.341E-12	-2.277E-06	-2.277E-06	3.296E-05	0.996

TableC.5 – continued

Isotope	A	Z	$X^{\rm ini}$	$mp^{\rm wind}$	$mp^{\rm preSN}$	$mp^{\rm total}$	EM	$\langle OP \rangle$
^{54}Cr	54	24	4.858E-07	5.938E-13	2.386E-05	2.386E-05	3.280E-05	3.908
^{55}Mn	55	25	1.098E-05	1.342E-11	-1.469E-05	-1.469E-05	1.873E-04	0.987
^{54}Fe	54	26	8.118E-05	9.922E-11	-2.753E-04	-2.753E-04	1.218E-03	0.868
^{56}Fe	56	26	1.322E-03	1.615E-09	-3.379E-03	-3.379E-03	2.093E-02	0.917
^{57}Fe	57	26	3.107E-05	3.797E-11	2.804E-04	2.804E-04	8.518E-04	1.587
^{58}Fe	58	26	4.207E-06	5.142E-12	1.123E-03	1.123E-03	1.200E-03	16.512
^{59}Co	59	27	3.991E-06	4.879E-12	5.542E-04	5.542E-04	6.276E-04	9.102
^{58}Ni	58	28	5.711E-05	6.980E-11	-1.911E-04	-1.911E-04	8.593E-04	0.871
^{60}Ni	60	28	2.276E-05	2.781E-11	3.560E-04	3.560E-04	7.745E-04	1.970
^{61}Ni	61	28	1.006E-06	1.229E-12	1.760E-04	1.760E-04	1.945E-04	11.195
^{62}Ni	62	28	3.259E-06	3.984E-12	4.673E-04	4.673E-04	5.272E-04	9.364
^{64}Ni	64	28	8.568E-07	1.047E-12	2.155E-04	2.155E-04	2.313E-04	15.626
^{63}Cu	63	29	6.600E-07	8.067E-13	1.788E-04	1.788E-04	1.909E-04	16.747
^{65}Cu	65	29	3.035E-07	3.709E-13	1.654E-04	1.654E-04	1.709E-04	32.607
^{64}Zn	64	30	1.131E-06	1.382E-12	6.205E-05	6.205E-05	8.284E-05	4.241
^{66}Zn	66	30	6.690E-07	8.177E-13	1.298E-04	1.298E-04	1.421E-04	12.295
^{67}Zn	67	30	9.980E-08	1.220E-13	4.295E-05	4.295E-05	4.479E-05	25.977
^{68}Zn	68	30	4.632E-07	5.662E-13	1.684E-04	1.684E-04	1.769E-04	22.105
^{70}Zn	70	30	1.577E-08	1.927E-14	7.019E-08	7.019E-08	3.602E-07	1.322
^{69}Ga	69	31	4.551E-08	5.562E-14	2.240E-05	2.240E-05	2.323E-05	29.555
^{71}Ga	71	31	3.108E-08	3.798E-14	1.865E-05	1.865E-05	1.922E-05	35.802
^{70}Ge	70	32	5.157E-08	6.303E-14	3.178E-05	3.178E-05	3.273E-05	36.736
^{72}Ge	72	32	6.910E-08	8.446E-14	3.257E-05	3.257E-05	3.384E-05	28.348
^{73}Ge	73	32	1.955E-08	2.389E-14	1.483E-05	1.483E-05	1.519E-05	44.996
^{74}Ge	74	32	9.228E-08	1.128E-13	4.999E-05	4.999E-05	5.169E-05	32.421
^{76}Ge	76	32	1.963E-08	2.399E-14	3.805E-08	3.805E-08	3.991E-07	1.177
^{75}As	75	33	1.430E-08	1.748E-14	6.829E-06	6.829E-06	7.092E-06	28.709
^{74}Se	74	34	1.198E-09	1.464E-15	-4.698E-09	-4.698E-09	1.733E-08	0.838

TableC.5 – continued

Isotope	A	Z	$X^{\rm ini}$	$mp^{\rm wind}$	$mp^{\rm preSN}$	$mp^{\rm total}$	EM	$\langle OP \rangle$
^{76}Se	76	34	1.296E-08	1.584E-14	9.340E-06	9.340E-06	9.579E-06	42.781
^{77}Se	77	34	1.070E-08	1.308E-14	5.108E-06	5.108E-06	5.305E-06	28.686
^{78}Se	78	34	3.376E-08	4.127E-14	2.606E-05	2.606E-05	2.668E-05	45.744
^{80}Se	80	34	7.226E-08	8.832E-14	9.532E-06	9.532E-06	1.086E-05	8.701
^{82}Se	82	34	1.304E-08	1.593E-14	-2.701E-08	-2.701E-08	2.128E-07	0.945
^{79}Br	79	35	1.389E-08	1.698E-14	5.605E-06	5.605E-06	5.861E-06	24.420
^{81}Br	81	35	1.386E-08	1.694E-14	3.408E-06	3.408E-06	3.663E-06	15.300
^{78}Kr	78	36	3.900E-10	4.767E-16	-1.497E-09	-1.497E-09	5.676E-09	0.843
^{80}Kr	80	36	2.575E-09	3.147E-15	3.053E-06	3.053E-06	3.100E-06	69.702
^{82}Kr	82	36	1.320E-08	1.613E-14	1.159E-05	1.159E-05	1.184E-05	51.921
^{83}Kr	83	36	1.324E-08	1.618E-14	6.328E-06	6.328E-06	6.571E-06	28.727
^{84}Kr	84	36	6.602E-08	8.069E-14	3.387E-05	3.387E-05	3.508E-05	30.760
^{86}Kr	86	36	2.044E-08	2.499E-14	4.048E-06	4.048E-06	4.424E-06	12.528
^{85}Rb	85	37	1.282E-08	1.567E-14	8.728E-06	8.728E-06	8.964E-06	40.463
^{87}Rb	87	37	5.063E-09	-2.792E-12	3.175E-06	3.175E-06	3.268E-06	37.372
^{84}Sr	84	38	3.228E-10	3.945E-16	-1.305E-09	-1.305E-09	4.633E-09	0.831
^{86}Sr	86	38	5.845E-09	7.144E-15	1.288E-05	1.288E-05	1.299E-05	128.665
^{87}Sr	87	38	4.443E-09	2.803E-12	9.619E-06	9.619E-06	9.701E-06	126.389
^{88}Sr	88	38	5.011E-08	6.124E-14	5.773E-05	5.773E-05	5.865E-05	67.754
^{89}Y	89	39	1.229E-08	1.503E-14	1.225E-05	1.225E-05	1.248E-05	58.753
^{90}Zr	90	40	1.534E-08	1.875E-14	6.813E-06	6.813E-06	7.095E-06	26.769
^{91}Zr	91	40	3.384E-09	4.136E-15	2.251E-06	2.251E-06	2.313E-06	39.571
^{92}Zr	92	40	5.227E-09	6.388E-15	2.570E-06	2.570E-06	2.666E-06	29.526
^{94}Zr	94	40	5.413E-09	6.616E-15	1.167E-06	1.167E-06	1.267E-06	13.545
^{96}Zr	96	40	8.903E-10	1.088E-15	1.476E-07	1.476E-07	1.640E-07	10.663
^{93}Nb	93	41	1.900E-09	2.322E-15	1.102E-06	1.102E-06	1.137E-06	34.626
^{92}Mo	92	42	1.012E-09	1.238E-15	-3.613E-09	-3.613E-09	1.501E-08	0.858
^{94}Mo	94	42	6.448E-10	7.881E-16	3.195E-09	3.195E-09	1.505E-08	1.352

TableC.5 – continued

Isotope	A	Z	$X^{\rm ini}$	$mp^{\rm wind}$	$mp^{\rm preSN}$	$mp^{\rm total}$	EM	$\langle OP \rangle$
^{95}Mo	95	42	1.122E-09	1.371E-15	3.307E-07	3.307E-07	3.513E-07	18.129
^{96}Mo	96	42	1.188E-09	1.451E-15	3.408E-07	3.408E-07	3.626E-07	17.678
^{97}Mo	97	42	6.875E-10	8.403E-16	1.278E-07	1.278E-07	1.404E-07	11.823
^{98}Mo	98	42	1.754E-09	2.144E-15	3.594E-07	3.594E-07	3.916E-07	12.923
^{100}Mo	100	42	7.146E-10	8.734E-16	-1.224E-09	-1.224E-09	1.192E-08	0.966
^{96}Ru	96	44	2.926E-10	3.576E-16	-1.112E-09	-1.112E-09	4.269E-09	0.845
^{98}Ru	98	44	1.007E-10	1.231E-16	-3.322E-10	-3.322E-10	1.520E-09	0.874
^{99}Ru	99	44	6.945E-10	8.489E-16	5.849E-08	5.849E-08	7.126E-08	5.940
^{100}Ru	100	44	6.928E-10	8.468E-16	1.589E-07	1.589E-07	1.716E-07	14.342
^{101}Ru	101	44	9.475E-10	1.158E-15	3.581E-08	3.581E-08	5.324E-08	3.253
^{102}Ru	102	44	1.770E-09	2.163E-15	2.457E-07	2.457E-07	2.782E-07	9.102
^{104}Ru	104	44	1.065E-09	1.302E-15	6.259E-09	6.259E-09	2.585E-08	1.405
^{103}Rh	103	45	1.055E-09	1.289E-15	4.149E-08	4.149E-08	6.089E-08	3.342
^{102}Pd	102	46	4.241E-11	5.184E-17	-1.717E-10	-1.717E-10	6.084E-10	0.830
^{104}Pd	104	46	4.723E-10	5.773E-16	9.975E-08	9.975E-08	1.084E-07	13.291
^{105}Pd	105	46	9.558E-10	1.168E-15	2.170E-08	2.170E-08	3.928E-08	2.379
^{106}Pd	106	46	1.181E-09	1.443E-15	1.282E-07	1.282E-07	1.499E-07	7.347
^{108}Pd	108	46	1.165E-09	1.424E-15	1.381E-07	1.381E-07	1.595E-07	7.928
^{110}Pd	110	46	5.255E-10	6.423E-16	5.710E-09	5.710E-09	1.538E-08	1.694
^{107}Ag	107	47	7.840E-10	9.582E-16	2.349E-08	2.349E-08	3.791E-08	2.799
^{109}Ag	109	47	7.420E-10	9.069E-16	8.247E-08	8.247E-08	9.611E-08	7.498
^{106}Cd	106	48	6.346E-11	7.756E-17	-2.514E-10	-2.514E-10	9.158E-10	0.835
^{108}Cd	108	48	4.604E-11	5.629E-17	8.647E-09	8.647E-09	9.494E-09	11.938
^{110}Cd	110	48	6.580E-10	8.043E-16	9.991E-08	9.991E-08	1.120E-07	9.854
^{111}Cd	111	48	6.805E-10	8.317E-16	2.993E-08	2.993E-08	4.244E-08	3.611
^{112}Cd	112	48	1.294E-09	1.582E-15	1.177E-07	1.177E-07	1.415E-07	6.330
^{113}Cd	113	48	6.614E-10	8.083E-16	2.962E-08	2.962E-08	4.179E-08	3.658
^{114}Cd	114	48	1.569E-09	1.917E-15	1.602E-07	1.602E-07	1.891E-07	6.977

TableC.5 – continued

Isotope	A	Z	$X^{\rm ini}$	$mp^{\rm wind}$	$mp^{\rm preSN}$	$mp^{\rm total}$	EM	$\langle OP \rangle$
^{116}Cd	116	48	4.161E-10	5.086E-16	9.656E-09	9.656E-09	1.731E-08	2.408
^{113}In	113	49	2.604E-11	3.183E-17	-9.155E-11	-9.155E-11	3.874E-10	0.861
^{115}In	115	49	5.915E-10	6.888E-16	2.727E-08	2.727E-08	3.815E-08	3.734
^{112}Sn	112	50	1.221E-10	1.492E-16	-4.673E-10	-4.673E-10	1.778E-09	0.843
^{114}Sn	114	50	8.435E-11	1.031E-16	-2.584E-10	-2.584E-10	1.293E-09	0.887
^{115}Sn	115	50	4.377E-11	8.758E-17	2.152E-09	2.152E-09	2.957E-09	3.911
^{116}Sn	116	50	1.893E-09	2.314E-15	1.682E-07	1.682E-07	2.031E-07	6.209
^{117}Sn	117	50	1.008E-09	1.232E-15	5.411E-08	5.411E-08	7.266E-08	4.171
^{118}Sn	118	50	3.209E-09	3.922E-15	2.117E-07	2.117E-07	2.707E-07	4.883
^{119}Sn	119	50	1.147E-09	1.402E-15	5.909E-08	5.909E-08	8.019E-08	4.047
^{120}Sn	120	50	4.391E-09	5.367E-15	2.265E-07	2.265E-07	3.073E-07	4.051
^{122}Sn	122	50	6.341E-10	7.750E-16	5.469E-09	5.469E-09	1.713E-08	1.564
^{124}Sn	124	50	8.060E-10	9.851E-16	-2.329E-09	-2.329E-09	1.249E-08	0.897
^{121}Sb	121	51	6.318E-10	7.722E-16	1.998E-08	1.998E-08	3.160E-08	2.896
^{123}Sb	123	51	4.803E-10	5.870E-16	-8.051E-11	-8.051E-11	8.753E-09	1.055
^{120}Te	120	52	1.628E-11	1.990E-17	-6.813E-11	-6.813E-11	2.314E-10	0.823
^{122}Te	122	52	4.489E-10	5.486E-16	2.347E-08	2.347E-08	3.173E-08	4.092
^{123}Te	123	52	1.579E-10	1.929E-16	7.785E-09	7.785E-09	1.069E-08	3.919
^{124}Te	124	52	8.441E-10	1.032E-15	4.391E-08	4.391E-08	5.943E-08	4.076
^{125}Te	125	52	1.261E-09	1.542E-15	1.024E-08	1.024E-08	3.344E-08	1.535
^{126}Te	126	52	3.375E-09	4.125E-15	6.669E-08	6.669E-08	1.288E-07	2.208
^{128}Te	128	52	5.733E-09	7.007E-15	-1.619E-08	-1.619E-08	8.926E-08	0.901
^{130}Te	130	52	6.211E-09	7.591E-15	-1.838E-08	-1.838E-08	9.585E-08	0.893
^{127}I	127	53	1.459E-09	1.783E-15	6.653E-09	6.653E-09	3.349E-08	1.329
^{124}Xe	124	54	2.210E-11	2.700E-17	-9.454E-11	-9.454E-11	3.119E-10	0.817
^{126}Xe	126	54	1.949E-11	2.382E-17	-7.833E-11	-7.833E-11	2.802E-10	0.832
^{128}Xe	128	54	3.943E-10	4.819E-16	1.893E-08	1.893E-08	2.618E-08	3.844
^{129}Xe	129	54	4.893E-09	5.980E-15	-1.146E-08	-1.146E-08	7.854E-08	0.929

TableC.5 – continued

Isotope	A	Z	$X^{\rm ini}$	$mp^{\rm wind}$	$mp^{\rm preSN}$	$mp^{\rm total}$	EM	$\langle OP \rangle$
^{130}Xe	130	54	7.865E-10	9.614E-16	3.879E-08	3.879E-08	5.325E-08	3.920
^{131}Xe	131	54	3.945E-09	4.821E-15	1.157E-09	1.157E-09	7.371E-08	1.082
^{132}Xe	132	54	4.806E-09	5.874E-15	5.258E-08	5.258E-08	1.410E-07	1.698
^{134}Xe	134	54	1.788E-09	2.185E-15	-3.089E-09	-3.089E-09	2.980E-08	0.965
^{136}Xe	136	54	1.478E-09	1.807E-15	-7.312E-10	-7.312E-10	2.646E-08	1.036
^{133}Cs	133	55	1.426E-09	1.743E-15	4.909E-09	4.909E-09	3.114E-08	1.264
^{130}Ba	130	56	1.814E-11	2.217E-17	-7.845E-11	-7.845E-11	2.553E-10	0.814
^{132}Ba	132	56	1.762E-11	2.154E-17	-7.134E-11	-7.134E-11	2.528E-10	0.830
^{134}Ba	134	56	4.272E-10	5.222E-16	1.877E-08	1.877E-08	2.663E-08	3.608
^{135}Ba	135	56	1.174E-09	1.435E-15	4.457E-09	4.457E-09	2.605E-08	1.285
^{136}Ba	136	56	1.409E-09	1.722E-15	4.677E-08	4.677E-08	7.269E-08	2.987
^{137}Ba	137	56	2.030E-09	2.481E-15	3.121E-08	3.121E-08	6.855E-08	1.955
^{138}Ba	138	56	1.305E-08	1.595E-14	2.042E-07	2.042E-07	4.443E-07	1.971
^{138}La	138	57	1.604E-12	1.961E-18	-6.610E-12	-6.610E-12	2.289E-11	0.826
^{139}La	139	57	1.790E-09	2.188E-15	2.141E-08	2.141E-08	5.434E-08	1.757
^{136}Ce	136	58	8.382E-12	1.024E-17	-3.343E-11	-3.343E-11	1.207E-10	0.834
^{138}Ce	138	58	1.148E-11	1.403E-17	-4.322E-11	-4.322E-11	1.679E-10	0.847
^{140}Ce	140	58	4.103E-09	5.015E-15	3.071E-08	3.071E-08	1.062E-07	1.498
^{142}Ce	142	58	5.229E-10	6.391E-16	-1.057E-09	-1.057E-09	8.562E-09	0.948
^{141}Pr	141	59	6.910E-10	8.446E-16	2.961E-09	2.961E-09	1.567E-08	1.313
^{142}Nd	142	60	9.920E-10	1.212E-15	6.892E-09	6.892E-09	2.514E-08	1.467
^{143}Nd	143	60	4.484E-10	5.480E-16	1.220E-10	1.220E-10	8.369E-09	1.080
^{144}Nd	144	60	8.826E-10	1.079E-15	1.551E-09	1.551E-09	1.779E-08	1.166
^{145}Nd	145	60	3.095E-10	3.783E-16	-7.240E-11	-7.240E-11	5.621E-09	1.051
^{146}Nd	146	60	6.448E-10	7.881E-16	1.600E-09	1.600E-09	1.346E-08	1.208
^{148}Nd	148	60	2.185E-10	2.671E-16	-4.658E-10	-4.658E-10	3.553E-09	0.941
^{150}Nd	150	60	2.168E-10	2.650E-16	-8.231E-10	-8.231E-10	3.165E-09	0.845
^{144}Sm	144	62	3.684E-11	4.502E-17	-1.315E-10	-1.315E-10	5.460E-10	0.858

TableC.5 – continued

Isotope	A	Z	$X^{\rm ini}$	$mp^{\rm wind}$	$mp^{\rm preSN}$	$mp^{\rm total}$	EM	$\langle OP \rangle$
^{147}Sm	147	62	1.834E-10	2.242E-16	-1.931E-10	-1.931E-10	3.181E-09	1.004
^{148}Sm	148	62	1.385E-10	1.692E-16	4.146E-10	4.146E-10	2.961E-09	1.238
^{149}Sm	149	62	1.714E-10	2.094E-16	-5.386E-10	-5.386E-10	2.613E-09	0.883
^{150}Sm	150	62	9.213E-11	1.126E-16	5.965E-10	5.965E-10	2.291E-09	1.440
^{152}Sm	152	62	3.383E-10	4.135E-16	-8.014E-10	-8.014E-10	5.421E-09	0.928
^{154}Sm	154	62	2.916E-10	3.564E-16	-1.001E-09	-1.001E-09	4.363E-09	0.866
^{151}Eu	151	63	2.036E-10	2.488E-16	-7.771E-10	-7.771E-10	2.968E-09	0.844
^{153}Eu	153	63	2.252E-10	2.752E-16	-7.841E-10	-7.841E-10	3.358E-09	0.863
^{152}Gd	152	64	2.947E-12	3.609E-18	1.402E-10	1.402E-10	1.944E-10	3.819
^{154}Gd	154	64	3.210E-11	3.925E-17	3.493E-10	3.493E-10	9.396E-10	1.695
^{155}Gd	155	64	2.192E-10	2.679E-16	-7.308E-10	-7.308E-10	3.301E-09	0.872
^{156}Gd	156	64	3.051E-10	3.729E-16	-4.148E-10	-4.148E-10	5.197E-09	0.986
^{157}Gd	157	64	2.348E-10	2.870E-16	-5.599E-10	-5.599E-10	3.759E-09	0.927
^{158}Gd	158	64	3.750E-10	4.583E-16	-4.815E-11	-4.814E-11	6.849E-09	1.057
^{160}Gd	160	64	3.343E-10	4.086E-16	-1.174E-09	-1.174E-09	4.975E-09	0.861
^{159}Tb	159	65	2.765E-10	3.379E-16	-8.677E-10	-8.677E-10	4.218E-09	0.883
^{156}Dy	156	66	1.004E-12	1.227E-18	-4.591E-12	-4.591E-12	1.387E-11	0.800
^{158}Dy	158	66	1.743E-12	2.130E-18	9.206E-12	9.206E-12	4.126E-11	1.371
^{160}Dy	160	66	4.301E-11	5.259E-17	3.553E-10	3.553E-10	1.146E-09	1.543
^{161}Dy	161	66	3.498E-10	4.275E-16	-1.241E-09	-1.241E-09	5.193E-09	0.859
^{162}Dy	162	66	4.748E-10	5.803E-16	-7.601E-10	-7.601E-10	7.973E-09	0.972
^{163}Dy	163	66	4.663E-10	5.699E-16	-1.449E-09	-1.449E-09	7.127E-09	0.885
^{164}Dy	164	66	5.312E-10	6.492E-16	1.673E-10	1.673E-10	9.937E-09	1.083
^{165}Ho	165	67	4.244E-10	5.187E-16	-1.425E-09	-1.425E-09	6.381E-09	0.870
^{162}Er	162	68	1.609E-12	1.966E-18	-7.357E-12	-7.357E-12	2.224E-11	0.800
^{164}Er	164	68	1.913E-11	2.338E-17	-8.587E-11	-8.587E-11	2.660E-10	0.805
^{166}Er	166	68	4.044E-10	4.943E-16	-8.765E-10	-8.765E-10	6.563E-09	0.939
^{167}Er	167	68	2.776E-10	3.393E-16	-8.084E-10	-8.084E-10	4.297E-09	0.896

TableC.5 – continued

Isotope	A	Z	X^{ini}	mp^{wind}	mp^{preSN}	mp^{total}	EM	$\langle OP \rangle$
^{168}Er	168	68	3.263E-10	3.988E-16	2.140E-10	2.140E-10	6.215E-09	1.103
^{170}Er	170	68	1.840E-10	2.249E-16	-2.799E-10	-2.799E-10	3.104E-09	0.977
^{169}Tm	169	69	1.854E-10	2.266E-16	-4.321E-10	-4.321E-10	2.978E-09	0.930
^{168}Yb	168	70	1.583E-12	1.935E-18	-7.134E-12	-7.134E-12	2.199E-11	0.804
^{170}Yb	170	70	3.746E-11	4.580E-17	2.643E-10	2.643E-10	9.534E-10	1.473
^{171}Yb	171	70	1.770E-10	2.163E-16	-3.972E-10	-3.972E-10	2.859E-09	0.935
^{172}Yb	172	70	2.722E-10	3.327E-16	4.130E-11	4.130E-11	5.048E-09	1.074
^{173}Yb	173	70	2.023E-10	2.472E-16	-1.594E-10	-1.594E-10	3.561E-09	1.019
^{174}Yb	174	70	4.015E-10	4.907E-16	9.964E-10	9.964E-10	8.381E-09	1.208
^{176}Yb	176	70	1.628E-10	1.990E-16	-4.651E-10	-4.651E-10	2.529E-09	0.899
^{175}Lu	175	71	1.828E-10	2.234E-16	-3.720E-10	-3.720E-10	2.990E-09	0.947
^{176}Lu	176	71	4.876E-12	-3.257E-15	3.624E-11	3.624E-11	1.259E-10	1.495
^{174}Hf	174	72	1.231E-12	1.505E-18	-5.444E-12	-5.444E-12	1.720E-11	0.809
^{176}Hf	176	72	4.036E-11	3.312E-15	2.815E-10	2.815E-10	1.024E-09	1.468
^{177}Hf	177	72	1.438E-10	1.757E-16	-3.422E-10	-3.422E-10	2.302E-09	0.927
^{178}Hf	178	72	2.121E-10	2.593E-16	3.826E-10	3.826E-10	4.284E-09	1.169
^{179}Hf	179	72	1.065E-10	1.302E-16	-1.187E-10	-1.187E-10	1.840E-09	1.000
^{180}Hf	180	72	2.758E-10	3.372E-16	9.251E-10	9.251E-10	5.999E-09	1.259
^{180}Ta	180	73	2.429E-14	2.866E-20	1.001E-11	1.001E-11	1.046E-11	24.923
^{181}Ta	181	73	1.986E-10	2.427E-16	-2.538E-10	-2.538E-10	3.399E-09	0.991
^{180}W	180	74	8.395E-13	1.027E-18	3.285E-11	3.285E-11	4.829E-11	3.330
^{182}W	182	74	1.877E-10	2.295E-16	2.968E-10	2.968E-10	3.750E-09	1.156
^{183}W	183	74	1.020E-10	1.246E-16	2.768E-10	2.768E-10	2.152E-09	1.222
^{184}W	184	74	2.195E-10	2.683E-16	7.290E-10	7.290E-10	4.766E-09	1.257
^{186}W	186	74	2.058E-10	2.516E-16	-3.283E-10	-3.283E-10	3.458E-09	0.972
^{185}Re	185	75	1.048E-10	1.281E-16	1.170E-11	1.170E-11	1.939E-09	1.071
^{187}Re	187	75	1.773E-10	2.167E-16	-5.861E-10	-5.861E-10	2.675E-09	0.873
^{184}Os	184	76	7.108E-13	8.688E-19	-3.025E-12	-3.025E-12	1.005E-11	0.818

TableC.5 – continued

Isotope	A	Z	$X^{\rm ini}$	$mp^{\rm wind}$	$mp^{\rm preSN}$	$mp^{\rm total}$	EM	$\langle OP \rangle$
^{186}Os	186	76	5.778E-11	7.063E-17	2.250E-10	2.250E-10	1.288E-09	1.290
^{187}Os	187	76	5.998E-11	7.331E-17	-9.239E-11	-9.239E-11	1.011E-09	0.976
^{188}Os	188	76	4.874E-10	5.957E-16	-6.715E-10	-6.715E-10	8.293E-09	0.985
^{189}Os	189	76	5.974E-10	7.301E-16	-2.312E-09	-2.312E-09	8.676E-09	0.841
^{190}Os	190	76	9.766E-10	1.194E-15	-1.920E-09	-1.920E-09	1.604E-08	0.951
^{192}Os	192	76	1.533E-09	1.873E-15	-5.268E-09	-5.268E-09	2.292E-08	0.866
^{191}Ir	191	77	1.357E-09	1.659E-15	-5.691E-09	-5.691E-09	1.928E-08	0.822
^{193}Ir	193	77	2.308E-09	2.821E-15	-9.379E-09	-9.379E-09	3.308E-08	0.830
^{190}Pt	190	78	1.008E-12	1.233E-18	-4.215E-12	-4.215E-12	1.433E-11	0.823
^{192}Pt	192	78	5.850E-11	7.159E-17	1.028E-09	1.028E-09	2.104E-09	2.082
^{194}Pt	194	78	2.490E-09	3.043E-15	-6.701E-09	-6.701E-09	3.909E-08	0.909
^{195}Pt	195	78	2.568E-09	3.139E-15	-9.546E-09	-9.546E-09	3.769E-08	0.850
^{196}Pt	196	78	1.926E-09	2.354E-15	-1.592E-09	-1.592E-09	3.383E-08	1.017
^{198}Pt	198	78	5.522E-10	6.749E-16	-1.922E-09	-1.922E-09	8.234E-09	0.863
^{197}Au	197	79	1.083E-09	1.324E-15	-2.922E-09	-2.922E-09	1.700E-08	0.909
^{196}Hg	196	80	3.009E-12	3.678E-18	-1.152E-11	-1.152E-11	4.383E-11	0.843
^{198}Hg	198	80	1.975E-10	2.414E-16	2.999E-09	2.999E-09	6.632E-09	1.944
^{199}Hg	199	80	3.360E-10	4.107E-16	4.099E-10	4.099E-10	6.590E-09	1.135
^{200}Hg	200	80	4.622E-10	5.649E-16	3.042E-09	3.042E-09	1.154E-08	1.446
^{201}Hg	201	80	2.651E-10	3.240E-16	1.625E-09	1.625E-09	6.501E-09	1.420
^{202}Hg	202	80	6.036E-10	7.378E-16	6.610E-09	6.610E-09	1.771E-08	1.699
^{204}Hg	204	80	1.401E-10	1.713E-16	-3.948E-10	-3.948E-10	2.183E-09	0.902
^{203}Tl	203	81	3.221E-10	3.936E-16	5.631E-09	5.631E-09	1.156E-08	2.077
^{205}Tl	205	81	7.764E-10	9.489E-16	9.717E-09	9.717E-09	2.400E-08	1.789
^{204}Pb	204	82	2.931E-10	3.582E-16	5.957E-09	5.957E-09	1.135E-08	2.241
^{206}Pb	206	82	2.798E-09	3.419E-15	2.826E-08	2.826E-08	7.972E-08	1.649
^{207}Pb	207	82	3.090E-09	3.776E-15	3.471E-08	3.471E-08	9.153E-08	1.715
^{208}Pb	208	82	8.850E-09	1.082E-14	4.380E-08	4.380E-08	2.066E-07	1.351

TableC.5 – continued

Isotope	A	Z	X^{ini}	mp^{wind}	mp^{preSN}	mp^{total}	EM	$\langle OP \rangle$
^{209}Bi	209	83	8.718E-10	1.066E-15	2.284E-09	2.284E-09	1.832E-08	1.216

Table C.6: Yields for model 20CU.

Isotope	A	Z	X^{ini}	mp^{wind}	mp^{preSN}	mp^{total}	EM	$\langle OP \rangle$
^{1}H	1	1	7.064E-01	-2.325E-01	-4.025E+00	-4.257E+00	7.946E+00	0.651
^{2}H	2	1	1.371E-05	-7.473E-05	-1.479E-04	-2.226E-04	1.412E-05	0.060
^{3}He	3	2	4.540E-05	-2.425E-05	-4.005E-04	-4.248E-04	3.595E-04	0.458
^{4}He	4	2	2.735E-01	2.327E-01	1.618E+00	1.851E+00	6.576E+00	1.392
^{7}Li	7	3	7.605E-11	-4.147E-10	-8.207E-10	-1.235E-09	7.838E-11	0.060
^{11}B	11	5	2.856E-09	3.086E-14	5.260E-11	5.263E-11	4.939E-08	1.001
^{12}C	12	6	3.425E-03	-4.905E-03	4.717E-01	4.668E-01	5.260E-01	8.891
^{13}C	13	6	4.156E-05	4.541E-04	1.798E-04	6.339E-04	1.352E-03	1.883
^{14}N	14	7	1.059E-03	1.106E-02	4.370E-02	5.476E-02	7.305E-02	3.994
^{15}N	15	7	4.171E-06	-1.174E-05	-3.357E-05	-4.531E-05	2.674E-05	0.371
^{16}O	16	8	9.624E-03	-6.629E-03	1.317E+00	1.311E+00	1.477E+00	8.882
^{17}O	17	8	3.813E-06	3.813E-06	5.624E-05	6.006E-05	1.259E-04	1.912
^{18}O	18	8	2.171E-05	-2.571E-05	4.480E-03	4.455E-03	4.830E-03	12.877
^{19}F	19	9	5.611E-07	-4.615E-07	-2.846E-06	-3.308E-06	6.385E-06	0.659
^{20}Ne	20	10	1.818E-03	-1.536E-05	4.466E-01	4.466E-01	4.780E-01	15.222
^{21}Ne	21	10	4.575E-06	1.288E-05	2.968E-03	2.981E-03	3.060E-03	38.711
^{22}Ne	22	10	1.470E-04	-1.158E-04	3.492E-02	3.481E-02	3.735E-02	14.705
^{23}Na	23	11	4.000E-05	1.246E-04	3.525E-02	3.537E-02	3.606E-02	52.194
^{24}Mg	24	12	5.862E-04	3.930E-08	2.362E-02	2.362E-02	3.374E-02	3.332
^{25}Mg	25	12	7.733E-05	-4.416E-05	1.806E-02	1.801E-02	1.935E-02	14.485
^{26}Mg	26	12	8.848E-05	4.546E-05	1.645E-02	1.649E-02	1.802E-02	11.789
^{27}Al	27	13	6.481E-05	4.793E-07	7.971E-03	7.972E-03	9.091E-03	8.120
^{28}Si	28	14	7.453E-04	9.194E-09	1.479E-03	1.479E-03	1.435E-02	1.115
^{29}Si	29	14	3.919E-05	3.685E-10	2.943E-04	2.943E-04	9.713E-04	1.435
^{30}Si	30	14	2.673E-05	-8.112E-09	5.106E-04	5.106E-04	9.723E-04	2.106
^{31}P	31	15	7.106E-06	8.817E-09	1.619E-04	1.619E-04	2.846E-04	2.319
^{32}S	32	16	4.011E-04	4.289E-09	-4.410E-04	-4.410E-04	6.488E-03	0.936

TableC.6 – continued

Isotope	A	Z	$X^{\rm ini}$	$mp^{\rm wind}$	$mp^{\rm preSN}$	$mp^{\rm total}$	EM	$\langle OP \rangle$
^{33}S	33	16	3.265E-06	8.248E-11	1.317E-05	1.317E-05	6.957E-05	1.234
^{34}S	34	16	1.890E-05	2.043E-10	3.441E-05	3.441E-05	3.610E-04	1.105
^{36}S	36	16	8.073E-08	8.725E-13	1.339E-05	1.339E-05	1.479E-05	10.604
^{35}Cl	35	17	6.821E-06	7.372E-11	-9.197E-06	-9.197E-06	1.086E-04	0.922
^{37}Cl	37	17	2.306E-06	2.492E-11	1.163E-04	1.163E-04	1.561E-04	3.920
^{36}Ar	36	18	8.202E-05	8.864E-10	-1.510E-04	-1.510E-04	1.266E-03	0.893
^{38}Ar	38	18	1.574E-05	1.701E-10	7.616E-05	7.616E-05	3.481E-04	1.280
^{40}Ar	40	18	2.650E-08	2.906E-13	7.153E-06	7.153E-06	7.611E-06	16.625
^{39}K	39	19	3.900E-06	4.215E-11	1.642E-05	1.642E-05	8.378E-05	1.244
^{40}K	40	19	5.005E-10	-9.968E-12	1.898E-06	1.898E-06	1.907E-06	220.565
^{41}K	41	19	2.959E-07	3.198E-12	6.413E-06	6.413E-06	1.152E-05	2.255
^{40}Ca	40	20	7.225E-05	7.908E-10	-1.107E-04	-1.107E-04	1.137E-03	0.911
^{42}Ca	42	20	5.063E-07	5.472E-12	7.945E-06	7.945E-06	1.669E-05	1.908
^{43}Ca	43	20	1.082E-07	1.169E-12	3.155E-06	3.155E-06	5.024E-06	2.689
^{44}Ca	44	20	1.710E-06	1.848E-11	7.530E-06	7.530E-06	3.707E-05	1.255
^{46}Ca	46	20	3.428E-09	3.705E-14	7.364E-07	7.364E-07	7.957E-07	13.435
^{48}Ca	48	20	1.672E-07	1.808E-12	-5.561E-08	-5.561E-08	2.834E-06	0.981
^{45}Sc	45	21	5.414E-08	5.851E-13	2.671E-06	2.671E-06	3.606E-06	3.856
^{46}Ti	46	22	3.232E-07	3.493E-12	1.325E-06	1.325E-06	6.908E-06	1.237
^{47}Ti	47	22	2.977E-07	3.217E-12	4.589E-07	4.589E-07	5.602E-06	1.089
^{48}Ti	48	22	3.014E-06	3.257E-11	-5.118E-06	-5.118E-06	4.694E-05	0.902
^{49}Ti	49	22	2.257E-07	2.440E-12	2.480E-06	2.480E-06	6.380E-06	1.636
^{50}Ti	50	22	2.208E-07	2.386E-12	7.996E-06	7.996E-06	1.181E-05	3.096
^{50}V	50	23	1.015E-09	1.097E-14	-1.618E-09	-1.618E-09	1.592E-08	0.908
^{51}V	51	23	4.138E-07	4.472E-12	1.347E-07	1.347E-07	7.283E-06	1.019
^{50}Cr	50	24	8.265E-07	8.933E-12	-2.136E-06	-2.136E-06	1.214E-05	0.850
^{52}Cr	52	24	1.658E-05	1.791E-10	-2.693E-05	-2.693E-05	2.594E-04	0.906
^{53}Cr	53	24	1.916E-06	2.070E-11	-1.802E-06	-1.802E-06	3.129E-05	0.946

TableC.6 – continued

Isotope	A	Z	$X^{\rm ini}$	$mp^{\rm wind}$	$mp^{\rm preSN}$	$mp^{\rm total}$	EM	$\langle OP \rangle$
^{54}Cr	54	24	4.858E-07	5.250E-12	1.779E-05	1.779E-05	2.618E-05	3.120
^{55}Mn	55	25	1.098E-05	1.187E-10	-7.073E-06	-7.073E-06	1.826E-04	0.963
^{54}Fe	54	26	8.118E-05	8.774E-10	-2.007E-04	-2.007E-04	1.202E-03	0.857
^{56}Fe	56	26	1.322E-03	1.428E-08	-2.502E-03	-2.502E-03	2.033E-02	0.890
^{57}Fe	57	26	3.107E-05	3.357E-10	2.042E-04	2.042E-04	7.409E-04	1.381
^{58}Fe	58	26	4.207E-06	4.547E-11	8.012E-04	8.012E-04	8.739E-04	12.025
^{59}Co	59	27	3.991E-06	4.314E-11	4.276E-04	4.276E-04	4.965E-04	7.201
^{58}Ni	58	28	5.711E-05	6.172E-10	-1.388E-04	-1.388E-04	8.477E-04	0.859
^{60}Ni	60	28	2.276E-05	2.459E-10	2.368E-04	2.368E-04	6.300E-04	1.602
^{61}Ni	61	28	1.006E-06	1.087E-11	1.317E-04	1.317E-04	1.490E-04	8.579
^{62}Ni	62	28	3.259E-06	3.522E-11	3.687E-04	3.687E-04	4.250E-04	7.548
^{64}Ni	64	28	8.568E-07	9.260E-12	2.416E-04	2.416E-04	2.564E-04	17.322
^{63}Cu	63	29	6.600E-07	7.133E-12	2.192E-04	2.192E-04	2.306E-04	20.222
^{65}Cu	65	29	3.035E-07	3.280E-12	6.908E-05	6.908E-05	7.432E-05	14.177
^{64}Zn	64	30	1.131E-06	1.222E-11	1.117E-05	1.117E-05	3.071E-05	1.572
^{66}Zn	66	30	6.690E-07	7.230E-12	6.098E-05	6.098E-05	7.254E-05	6.277
^{67}Zn	67	30	9.980E-08	1.079E-12	1.915E-05	1.915E-05	2.087E-05	12.108
^{68}Zn	68	30	4.632E-07	5.006E-12	9.442E-05	9.442E-05	1.024E-04	12.799
^{70}Zn	70	30	1.577E-08	1.704E-13	1.334E-07	1.334E-07	4.057E-07	1.490
^{69}Ga	69	31	4.551E-08	4.918E-13	1.242E-05	1.242E-05	1.320E-05	16.798
^{71}Ga	71	31	3.108E-08	3.359E-13	8.052E-06	8.052E-06	8.589E-06	15.999
^{70}Ge	70	32	5.157E-08	5.574E-13	1.781E-05	1.781E-05	1.870E-05	20.990
^{72}Ge	72	32	6.910E-08	7.468E-13	1.814E-05	1.814E-05	1.933E-05	16.193
^{73}Ge	73	32	1.955E-08	2.112E-13	7.329E-06	7.329E-06	7.667E-06	22.708
^{74}Ge	74	32	9.228E-08	9.973E-13	2.630E-05	2.630E-05	2.789E-05	17.498
^{76}Ge	76	32	1.963E-08	2.121E-13	5.738E-08	5.738E-08	3.965E-07	1.169
^{75}As	75	33	1.430E-08	1.545E-13	3.018E-06	3.018E-06	3.265E-06	13.218
^{74}Se	74	34	1.198E-09	1.295E-14	-3.679E-09	-3.679E-09	1.701E-08	0.822

TableC.6 – continued

Isotope	A	Z	$X^{\rm ini}$	$mp^{\rm wind}$	$mp^{\rm preSN}$	$mp^{\rm total}$	EM	$\langle OP \rangle$
^{76}Se	76	34	1.296E-08	1.401E-13	5.059E-06	5.059E-06	5.283E-06	23.595
^{77}Se	77	34	1.070E-08	1.157E-13	2.387E-06	2.387E-06	2.572E-06	13.910
^{78}Se	78	34	3.376E-08	3.649E-13	1.225E-05	1.225E-05	1.283E-05	22.006
^{80}Se	80	34	7.226E-08	7.810E-13	6.435E-06	6.435E-06	7.684E-06	6.155
^{82}Se	82	34	1.304E-08	1.409E-13	-7.015E-09	-7.015E-09	2.182E-07	0.969
^{79}Br	79	35	1.389E-08	1.501E-13	2.646E-06	2.646E-06	2.886E-06	12.026
^{81}Br	81	35	1.386E-08	1.498E-13	1.919E-06	1.919E-06	2.158E-06	9.014
^{78}Kr	78	36	3.900E-10	4.215E-15	-1.174E-09	-1.174E-09	5.563E-09	0.826
^{80}Kr	80	36	2.575E-09	2.783E-14	9.334E-07	9.334E-07	9.778E-07	21.985
^{82}Kr	82	36	1.320E-08	1.426E-13	5.152E-06	5.152E-06	5.380E-06	23.604
^{83}Kr	83	36	1.324E-08	1.431E-13	2.319E-06	2.319E-06	2.548E-06	11.139
^{84}Kr	84	36	6.602E-08	7.135E-13	1.083E-05	1.083E-05	1.197E-05	10.497
^{86}Kr	86	36	2.044E-08	2.209E-13	2.247E-06	2.247E-06	2.600E-06	7.363
^{85}Rb	85	37	1.282E-08	1.386E-13	2.725E-06	2.725E-06	2.947E-06	13.302
^{87}Rb	87	37	5.063E-09	-2.936E-12	1.112E-06	1.112E-06	1.199E-06	13.714
^{84}Sr	84	38	3.228E-10	3.489E-15	-1.034E-09	-1.034E-09	4.542E-09	0.815
^{86}Sr	86	38	5.845E-09	6.316E-14	3.610E-06	3.610E-06	3.711E-06	36.760
^{87}Sr	87	38	4.443E-09	3.038E-12	2.370E-06	2.370E-06	2.446E-06	31.873
^{88}Sr	88	38	5.011E-08	5.415E-13	1.507E-05	1.507E-05	1.593E-05	18.405
^{89}Y	89	39	1.229E-08	1.329E-13	3.099E-06	3.099E-06	3.311E-06	15.591
^{90}Zr	90	40	1.534E-08	1.658E-13	1.729E-06	1.729E-06	1.994E-06	7.521
^{91}Zr	91	40	3.384E-09	3.657E-14	5.247E-07	5.247E-07	5.832E-07	9.976
^{92}Zr	92	40	5.227E-09	5.649E-14	6.694E-07	6.694E-07	7.597E-07	8.414
^{94}Zr	94	40	5.413E-09	5.850E-14	2.776E-07	2.776E-07	3.711E-07	3.969
^{96}Zr	96	40	8.903E-10	9.622E-15	4.976E-08	4.976E-08	6.514E-08	4.235
^{93}Nb	93	41	1.900E-09	2.053E-14	2.242E-07	2.242E-07	2.570E-07	7.829
^{92}Mo	92	42	1.012E-09	1.094E-14	-2.688E-09	-2.688E-09	1.480E-08	0.846
^{94}Mo	94	42	6.448E-10	6.968E-15	1.440E-08	1.440E-08	2.554E-08	2.293

TableC.6 – continued

Isotope	A	Z	$X^{\rm ini}$	$mp^{\rm wind}$	$mp^{\rm preSN}$	$mp^{\rm total}$	EM	$\langle OP \rangle$
^{95}Mo	95	42	1.122E-09	1.212E-14	7.427E-08	7.427E-08	9.365E-08	4.832
^{96}Mo	96	42	1.188E-09	1.283E-14	8.431E-08	8.431E-08	1.048E-07	5.110
^{97}Mo	97	42	6.875E-10	7.430E-15	3.067E-08	3.067E-08	4.255E-08	3.583
^{98}Mo	98	42	1.754E-09	1.896E-14	8.290E-08	8.290E-08	1.132E-07	3.735
^{100}Mo	100	42	7.146E-10	7.723E-15	-1.827E-09	-1.827E-09	1.052E-08	0.852
^{96}Ru	96	44	2.926E-10	3.162E-15	-8.618E-10	-8.618E-10	4.192E-09	0.829
^{98}Ru	98	44	1.007E-10	1.088E-15	-2.191E-10	-2.191E-10	1.521E-09	0.874
^{99}Ru	99	44	6.945E-10	7.506E-15	1.220E-08	1.220E-08	2.420E-08	2.017
^{100}Ru	100	44	6.928E-10	7.487E-15	3.736E-08	3.736E-08	4.933E-08	4.122
^{101}Ru	101	44	9.475E-10	1.024E-14	5.541E-09	5.541E-09	2.191E-08	1.339
^{102}Ru	102	44	1.770E-09	1.913E-14	4.739E-08	4.739E-08	7.796E-08	2.550
^{104}Ru	104	44	1.065E-09	1.151E-14	-2.210E-09	-2.210E-09	1.619E-08	0.880
^{103}Rh	103	45	1.055E-09	1.140E-14	5.160E-09	5.160E-09	2.338E-08	1.283
^{102}Pd	102	46	4.241E-11	4.584E-16	-1.362E-10	-1.362E-10	5.965E-10	0.814
^{104}Pd	104	46	4.723E-10	5.104E-15	2.230E-08	2.230E-08	3.046E-08	3.733
^{105}Pd	105	46	9.558E-10	1.033E-14	2.254E-09	2.254E-09	1.876E-08	1.137
^{106}Pd	106	46	1.181E-09	1.276E-14	2.427E-08	2.427E-08	4.467E-08	2.190
^{108}Pd	108	46	1.165E-09	1.259E-14	1.924E-08	1.924E-08	3.936E-08	1.956
^{110}Pd	110	46	5.255E-10	5.680E-15	-8.860E-10	-8.860E-10	8.192E-09	0.902
^{107}Ag	107	47	7.840E-10	8.473E-15	2.828E-09	2.828E-09	1.637E-08	1.209
^{109}Ag	109	47	7.420E-10	8.019E-15	9.936E-09	9.936E-09	2.275E-08	1.775
^{106}Cd	106	48	6.346E-11	6.858E-16	-1.981E-10	-1.981E-10	8.982E-10	0.819
^{108}Cd	108	48	4.604E-11	4.976E-16	8.498E-09	8.498E-09	9.293E-09	11.686
^{110}Cd	110	48	6.580E-10	7.111E-15	2.248E-08	2.248E-08	3.385E-08	2.978
^{111}Cd	111	48	6.805E-10	7.354E-15	5.307E-09	5.307E-09	1.706E-08	1.451
^{112}Cd	112	48	1.294E-09	1.399E-14	2.421E-08	2.421E-08	4.657E-08	2.083
^{113}Cd	113	48	6.614E-10	7.147E-15	5.262E-09	5.262E-09	1.669E-08	1.461
^{114}Cd	114	48	1.569E-09	1.695E-14	3.048E-08	3.048E-08	5.758E-08	2.125

TableC.6 – continued

Isotope	A	Z	$X^{\rm ini}$	$mp^{\rm wind}$	$mp^{\rm preSN}$	$mp^{\rm total}$	EM	$\langle OP \rangle$
^{116}Cd	116	48	4.161E-10	4.497E-15	5.981E-10	5.981E-10	7.786E-09	1.083
^{113}In	113	49	2.604E-11	2.814E-16	-6.848E-11	-6.848E-11	3.813E-10	0.848
^{115}In	115	49	5.915E-10	6.356E-15	4.369E-09	4.369E-09	1.459E-08	1.428
^{112}Sn	112	50	1.221E-10	1.320E-15	-3.626E-10	-3.626E-10	1.747E-09	0.828
^{114}Sn	114	50	8.435E-11	9.116E-16	-1.727E-10	-1.727E-10	1.284E-09	0.881
^{115}Sn	115	50	4.377E-11	5.094E-16	7.984E-10	7.984E-10	1.555E-09	2.056
^{116}Sn	116	50	1.893E-09	2.046E-14	3.347E-08	3.347E-08	6.617E-08	2.023
^{117}Sn	117	50	1.008E-09	1.090E-14	9.133E-09	9.133E-09	2.655E-08	1.524
^{118}Sn	118	50	3.209E-09	3.468E-14	3.794E-08	3.794E-08	9.338E-08	1.684
^{119}Sn	119	50	1.147E-09	1.240E-14	1.006E-08	1.006E-08	2.987E-08	1.508
^{120}Sn	120	50	4.391E-09	4.746E-14	4.207E-08	4.207E-08	1.179E-07	1.555
^{122}Sn	122	50	6.341E-10	6.852E-15	2.942E-09	2.942E-09	1.390E-08	1.269
^{124}Sn	124	50	8.060E-10	8.710E-15	-1.662E-09	-1.662E-09	1.226E-08	0.881
^{121}Sb	121	51	6.318E-10	6.828E-15	2.717E-09	2.717E-09	1.363E-08	1.249
^{123}Sb	123	51	4.803E-10	5.191E-15	-9.983E-10	-9.983E-10	7.298E-09	0.880
^{120}Te	120	52	1.628E-11	1.760E-16	-5.451E-11	-5.451E-11	2.268E-10	0.806
^{122}Te	122	52	4.489E-10	4.851E-15	5.025E-09	5.025E-09	1.278E-08	1.648
^{123}Te	123	52	1.579E-10	1.706E-15	1.663E-09	1.663E-09	4.390E-09	1.610
^{124}Te	124	52	8.441E-10	9.122E-15	9.307E-09	9.307E-09	2.389E-08	1.638
^{125}Te	125	52	1.261E-09	1.363E-14	-4.197E-10	-4.196E-10	2.137E-08	0.981
^{126}Te	126	52	3.375E-09	3.648E-14	1.088E-08	1.088E-08	6.918E-08	1.187
^{128}Te	128	52	5.733E-09	6.196E-14	-1.304E-08	-1.304E-08	8.600E-08	0.868
^{130}Te	130	52	6.211E-09	6.712E-14	-1.335E-08	-1.335E-08	9.394E-08	0.876
^{127}I	127	53	1.459E-09	1.577E-14	-1.800E-09	-1.800E-09	2.341E-08	0.929
^{124}Xe	124	54	2.210E-11	2.388E-16	-7.576E-11	-7.576E-11	3.059E-10	0.802
^{126}Xe	126	54	1.949E-11	2.107E-16	-6.179E-11	-6.179E-11	2.749E-10	0.817
^{128}Xe	128	54	3.943E-10	4.261E-15	5.245E-09	5.245E-09	1.206E-08	1.770
^{129}Xe	129	54	4.893E-09	5.288E-14	-1.377E-08	-1.377E-08	7.076E-08	0.837

TableC.6 – continued

Isotope	A	Z	X^{ini}	mp^{wind}	mp^{preSN}	mp^{total}	EM	$\langle OP \rangle$
^{130}Xe	130	54	7.865E-10	8.500E-15	1.276E-08	1.276E-08	2.635E-08	1.939
^{131}Xe	131	54	3.945E-09	4.263E-14	-7.225E-09	-7.225E-09	6.092E-08	0.894
^{132}Xe	132	54	4.806E-09	5.194E-14	1.084E-08	1.084E-08	9.386E-08	1.131
^{134}Xe	134	54	1.788E-09	1.932E-14	-6.683E-10	-6.683E-10	3.022E-08	0.978
^{136}Xe	136	54	1.478E-09	1.598E-14	-5.007E-10	-5.007E-10	2.504E-08	0.980
^{133}Cs	133	55	1.426E-09	1.541E-14	-1.374E-09	-1.374E-09	2.326E-08	0.944
^{130}Ba	130	56	1.814E-11	1.961E-16	-6.308E-11	-6.308E-11	2.503E-10	0.799
^{132}Ba	132	56	1.762E-11	1.904E-16	-5.653E-11	-5.653E-11	2.479E-10	0.814
^{134}Ba	134	56	4.272E-10	4.617E-15	6.497E-09	6.497E-09	1.388E-08	1.880
^{135}Ba	135	56	1.174E-09	1.269E-14	9.327E-11	9.328E-11	2.037E-08	1.005
^{136}Ba	136	56	1.409E-09	1.523E-14	1.474E-08	1.474E-08	3.907E-08	1.606
^{137}Ba	137	56	2.030E-09	2.194E-14	9.192E-09	9.192E-09	4.426E-08	1.262
^{138}Ba	138	56	1.305E-08	1.411E-13	1.091E-07	1.091E-07	3.346E-07	1.484
^{138}La	138	57	1.604E-12	1.734E-17	-5.242E-12	-5.242E-12	2.247E-11	0.811
^{139}La	139	57	1.790E-09	1.935E-14	1.239E-08	1.239E-08	4.331E-08	1.401
^{136}Ce	136	58	8.382E-12	9.058E-17	-2.622E-11	-2.622E-11	1.186E-10	0.819
^{138}Ce	138	58	1.148E-11	1.240E-16	-3.319E-11	-3.319E-11	1.651E-10	0.833
^{140}Ce	140	58	4.103E-09	4.434E-14	1.861E-08	1.861E-08	8.949E-08	1.263
^{142}Ce	142	58	5.229E-10	5.651E-15	1.794E-09	1.794E-09	1.083E-08	1.199
^{141}Pr	141	59	6.910E-10	7.468E-15	2.198E-09	2.198E-09	1.414E-08	1.184
^{142}Nd	142	60	9.920E-10	1.072E-14	1.900E-09	1.900E-09	1.904E-08	1.111
^{143}Nd	143	60	4.484E-10	4.846E-15	-2.689E-10	-2.689E-10	7.476E-09	0.965
^{144}Nd	144	60	8.826E-10	9.539E-15	1.106E-09	1.106E-09	1.635E-08	1.073
^{145}Nd	145	60	3.095E-10	3.345E-15	-2.483E-11	-2.482E-11	5.323E-09	0.995
^{146}Nd	146	60	6.448E-10	6.968E-15	1.181E-09	1.181E-09	1.232E-08	1.106
^{148}Nd	148	60	2.185E-10	2.361E-15	4.231E-11	4.231E-11	3.817E-09	1.011
^{150}Nd	150	60	2.168E-10	2.343E-15	-6.226E-10	-6.226E-10	3.123E-09	0.834
^{144}Sm	144	62	3.684E-11	3.981E-16	-9.812E-11	-9.812E-11	5.382E-10	0.846

TableC.6 – continued

Isotope	A	Z	$X^{\rm ini}$	$mp^{\rm wind}$	$mp^{\rm preSN}$	$mp^{\rm total}$	EM	$\langle OP \rangle$
^{147}Sm	147	62	1.834E-10	1.983E-15	-9.573E-11	-9.573E-11	3.073E-09	0.970
^{148}Sm	148	62	1.385E-10	1.496E-15	7.058E-11	7.058E-11	2.462E-09	1.030
^{149}Sm	149	62	1.714E-10	1.852E-15	-4.684E-10	-4.684E-10	2.492E-09	0.842
^{150}Sm	150	62	9.213E-11	9.957E-16	4.651E-10	4.651E-10	2.057E-09	1.292
^{152}Sm	152	62	3.383E-10	3.656E-15	-5.620E-10	-5.620E-10	5.282E-09	0.904
^{154}Sm	154	62	2.916E-10	3.152E-15	-7.004E-10	-7.004E-10	4.337E-09	0.861
^{151}Eu	151	63	2.036E-10	2.200E-15	-6.028E-10	-6.028E-10	2.914E-09	0.829
^{153}Eu	153	63	2.252E-10	2.434E-15	-6.077E-10	-6.077E-10	3.282E-09	0.844
^{152}Gd	152	64	2.947E-12	3.186E-17	1.045E-10	1.045E-10	1.554E-10	3.052
^{154}Gd	154	64	3.210E-11	3.469E-16	2.703E-10	2.703E-10	8.247E-10	1.487
^{155}Gd	155	64	2.192E-10	2.369E-15	-6.282E-10	-6.282E-10	3.159E-09	0.834
^{156}Gd	156	64	3.051E-10	3.297E-15	-2.450E-10	-2.450E-10	5.026E-09	0.954
^{157}Gd	157	64	2.348E-10	2.538E-15	-3.988E-10	-3.988E-10	3.658E-09	0.902
^{158}Gd	158	64	3.750E-10	4.052E-15	8.000E-11	8.001E-11	6.557E-09	1.012
^{160}Gd	160	64	3.343E-10	3.613E-15	-8.465E-10	-8.465E-10	4.928E-09	0.853
^{159}Tb	159	65	2.765E-10	2.988E-15	-6.371E-10	-6.371E-10	4.139E-09	0.867
^{156}Dy	156	66	1.004E-12	1.085E-17	-3.689E-12	-3.689E-12	1.365E-11	0.787
^{158}Dy	158	66	1.743E-12	1.883E-17	3.234E-12	3.234E-12	3.334E-11	1.107
^{160}Dy	160	66	4.301E-11	4.649E-16	3.286E-10	3.286E-10	1.072E-09	1.442
^{161}Dy	161	66	3.498E-10	3.780E-15	-9.996E-10	-9.996E-10	5.043E-09	0.835
^{162}Dy	162	66	4.748E-10	5.131E-15	-5.268E-10	-5.268E-10	7.675E-09	0.936
^{163}Dy	163	66	4.663E-10	5.039E-15	-1.118E-09	-1.118E-09	6.937E-09	0.861
^{164}Dy	164	66	5.312E-10	5.740E-15	3.258E-10	3.258E-10	9.501E-09	1.036
^{165}Ho	165	67	4.244E-10	4.587E-15	-1.118E-09	-1.118E-09	6.213E-09	0.847
^{162}Er	162	68	1.609E-12	1.739E-17	-5.906E-12	-5.906E-12	2.189E-11	0.788
^{164}Er	164	68	1.913E-11	2.067E-16	-6.891E-11	-6.891E-11	2.615E-10	0.791
^{166}Er	166	68	4.044E-10	4.371E-15	-6.472E-10	-6.472E-10	6.339E-09	0.907
^{167}Er	167	68	2.776E-10	3.000E-15	-6.033E-10	-6.033E-10	4.192E-09	0.874

TableC.6 – continued

Isotope	A	Z	$X^{\rm ini}$	$mp^{\rm wind}$	$mp^{\rm preSN}$	$mp^{\rm total}$	EM	$\langle OP \rangle$
^{168}Er	168	68	3.263E-10	3.526E-15	2.545E-10	2.545E-10	5.891E-09	1.045
^{170}Er	170	68	1.840E-10	1.988E-15	3.917E-11	3.917E-11	3.218E-09	1.012
^{169}Tm	169	69	1.854E-10	2.004E-15	-2.602E-10	-2.602E-10	2.943E-09	0.919
^{168}Yb	168	70	1.583E-12	1.711E-17	-5.739E-12	-5.739E-12	2.161E-11	0.790
^{170}Yb	170	70	3.746E-11	4.049E-16	2.081E-10	2.081E-10	8.552E-10	1.322
^{171}Yb	171	70	1.770E-10	1.913E-15	-3.950E-10	-3.950E-10	2.663E-09	0.871
^{172}Yb	172	70	2.722E-10	2.942E-15	-2.212E-11	-2.212E-11	4.680E-09	0.995
^{173}Yb	173	70	2.023E-10	2.186E-15	-1.159E-10	-1.159E-10	3.378E-09	0.967
^{174}Yb	174	70	4.015E-10	4.339E-15	6.559E-10	6.559E-10	7.591E-09	1.095
^{176}Yb	176	70	1.628E-10	1.759E-15	-2.138E-10	-2.138E-10	2.598E-09	0.924
^{175}Lu	175	71	1.828E-10	1.975E-15	-3.128E-10	-3.128E-10	2.845E-09	0.901
^{176}Lu	176	71	4.876E-12	-3.432E-15	7.215E-11	7.215E-11	1.564E-10	1.857
^{174}Hf	174	72	1.231E-12	1.331E-17	-4.377E-12	-4.377E-12	1.689E-11	0.794
^{176}Hf	176	72	4.036E-11	3.921E-15	1.362E-10	1.362E-10	8.334E-10	1.195
^{177}Hf	177	72	1.438E-10	1.554E-15	-2.925E-10	-2.925E-10	2.191E-09	0.882
^{178}Hf	178	72	2.121E-10	2.293E-15	2.708E-10	2.708E-10	3.935E-09	1.074
^{179}Hf	179	72	1.065E-10	1.151E-15	3.152E-11	3.152E-11	1.871E-09	1.017
^{180}Hf	180	72	2.758E-10	2.981E-15	7.443E-10	7.443E-10	5.509E-09	1.156
^{180}Ta	180	73	2.429E-14	2.614E-19	2.895E-12	2.895E-12	3.314E-12	7.898
^{181}Ta	181	73	1.986E-10	2.146E-15	-2.598E-10	-2.598E-10	3.170E-09	0.924
^{180}W	180	74	8.395E-13	9.073E-18	6.379E-12	6.379E-12	2.088E-11	1.440
^{182}W	182	74	1.877E-10	2.029E-15	-9.095E-11	-9.095E-11	3.152E-09	0.972
^{183}W	183	74	1.020E-10	1.102E-15	1.088E-10	1.088E-10	1.870E-09	1.062
^{184}W	184	74	2.195E-10	2.372E-15	3.984E-10	3.984E-10	4.190E-09	1.105
^{186}W	186	74	2.058E-10	2.224E-15	-3.636E-11	-3.636E-11	3.519E-09	0.990
^{185}Re	185	75	1.048E-10	1.132E-15	8.004E-11	8.005E-11	1.890E-09	1.044
^{187}Re	187	75	1.773E-10	1.916E-15	-4.545E-10	-4.545E-10	2.608E-09	0.852
^{184}Os	184	76	7.108E-13	7.682E-18	-2.423E-12	-2.423E-12	9.856E-12	0.803

TableC.6 – continued

Isotope	A	Z	X^{ini}	mp^{wind}	mp^{preSN}	mp^{total}	EM	$\langle OP \rangle$
^{186}Os	186	76	5.778E-11	6.245E-16	6.861E-11	6.861E-11	1.067E-09	1.069
^{187}Os	187	76	5.998E-11	6.482E-16	-1.284E-10	-1.284E-10	9.078E-10	0.876
^{188}Os	188	76	4.874E-10	5.267E-15	-6.595E-10	-6.595E-10	7.759E-09	0.922
^{189}Os	189	76	5.974E-10	6.456E-15	-1.853E-09	-1.853E-09	8.466E-09	0.820
^{190}Os	190	76	9.766E-10	1.055E-14	-1.502E-09	-1.502E-09	1.537E-08	0.911
^{192}Os	192	76	1.533E-09	1.656E-14	-3.787E-09	-3.787E-09	2.269E-08	0.857
^{191}Ir	191	77	1.357E-09	1.467E-14	-4.566E-09	-4.566E-09	1.888E-08	0.805
^{193}Ir	193	77	2.308E-09	2.495E-14	-7.484E-09	-7.484E-09	3.239E-08	0.812
^{190}Pt	190	78	1.008E-12	1.090E-17	-3.366E-12	-3.366E-12	1.405E-11	0.807
^{192}Pt	192	78	5.850E-11	6.324E-16	8.932E-10	8.932E-10	1.904E-09	1.884
^{194}Pt	194	78	2.490E-09	2.691E-14	-4.795E-09	-4.795E-09	3.822E-08	0.889
^{195}Pt	195	78	2.568E-09	2.776E-14	-7.353E-09	-7.352E-09	3.701E-08	0.834
^{196}Pt	196	78	1.926E-09	2.082E-14	-6.009E-11	-6.007E-11	3.321E-08	0.998
^{198}Pt	198	78	5.522E-10	5.967E-15	-1.390E-09	-1.390E-09	8.149E-09	0.854
^{197}Au	197	79	1.083E-09	1.171E-14	-2.053E-09	-2.053E-09	1.666E-08	0.890
^{196}Hg	196	80	3.009E-12	3.252E-17	-8.910E-12	-8.910E-12	4.308E-11	0.829
^{198}Hg	198	80	1.975E-10	2.134E-15	2.690E-09	2.690E-09	6.102E-09	1.788
^{199}Hg	199	80	3.360E-10	3.631E-15	2.367E-10	2.367E-10	6.041E-09	1.041
^{200}Hg	200	80	4.622E-10	4.995E-15	1.659E-09	1.659E-09	9.644E-09	1.208
^{201}Hg	201	80	2.651E-10	2.865E-15	7.862E-10	7.862E-10	5.366E-09	1.172
^{202}Hg	202	80	6.036E-10	6.524E-15	3.507E-09	3.507E-09	1.393E-08	1.336
^{204}Hg	204	80	1.401E-10	1.515E-15	-2.482E-10	-2.482E-10	2.173E-09	0.897
^{203}Tl	203	81	3.221E-10	3.481E-15	2.991E-09	2.991E-09	8.554E-09	1.538
^{205}Tl	205	81	7.764E-10	8.391E-15	3.100E-09	3.100E-09	1.651E-08	1.231
^{204}Pb	204	82	2.931E-10	3.168E-15	3.377E-09	3.377E-09	8.440E-09	1.667
^{206}Pb	206	82	2.798E-09	3.024E-14	1.914E-08	1.914E-08	6.747E-08	1.396
^{207}Pb	207	82	3.090E-09	3.339E-14	2.747E-08	2.747E-08	8.084E-08	1.515
^{208}Pb	208	82	8.850E-09	9.564E-14	3.053E-08	3.053E-08	1.834E-07	1.200

TableC.6 – continued

Isotope	A	Z	X^{ini}	mp^{wind}	mp^{preSN}	mp^{total}	EM	$\langle OP \rangle$
^{209}Bi	209	83	8.718E-10	9.422E-15	1.456E-09	1.456E-09	1.652E-08	1.097

Table C.7: Yields for model 25ST.

Isotope	A	Z	X^{ini}	mp^{wind}	mp^{preSN}	mp^{total}	EM	$\langle OP \rangle$
^{1}H	1	1	7.064E-01	-7.612E-01	-5.623E+00	-6.384E+00	9.351E+00	0.686
^{2}H	2	1	1.371E-05	-1.385E-04	-1.509E-04	-2.894E-04	1.588E-05	0.060
^{3}He	3	2	4.540E-05	-7.844E-05	-4.875E-04	-5.660E-04	4.453E-04	0.509
^{4}He	4	2	2.735E-01	7.623E-01	1.336E+00	2.099E+00	8.191E+00	1.553
^{7}Li	7	3	7.605E-11	-7.686E-10	-8.373E-10	-1.606E-09	8.817E-11	0.060
^{11}B	11	5	2.856E-09	8.052E-13	4.504E-11	4.585E-11	6.366E-08	1.156
^{12}C	12	6	3.425E-03	-1.168E-02	5.551E-01	5.434E-01	6.197E-01	9.381
^{13}C	13	6	4.156E-05	5.133E-04	1.045E-02	1.096E-02	1.189E-02	14.832
^{14}N	14	7	1.059E-03	3.146E-02	4.060E-02	7.206E-02	9.564E-02	4.683
^{15}N	15	7	4.171E-06	-2.219E-05	-4.393E-05	-6.612E-05	2.678E-05	0.333
^{16}O	16	8	9.624E-03	-2.092E-02	2.392E+00	2.371E+00	2.586E+00	13.928
^{17}O	17	8	3.813E-06	4.480E-06	2.685E-05	3.133E-05	1.163E-04	1.581
^{18}O	18	8	2.171E-05	-6.999E-05	-2.178E-04	-2.878E-04	1.958E-04	0.468
^{19}F	19	9	5.611E-07	-1.505E-06	3.686E-06	2.181E-06	1.468E-05	1.356
^{20}Ne	20	10	1.818E-03	-5.567E-05	1.012E+00	1.012E+00	1.052E+00	30.016
^{21}Ne	21	10	4.575E-06	3.576E-05	1.454E-03	1.490E-03	1.592E-03	18.036
^{22}Ne	22	10	1.470E-04	-3.547E-04	5.268E-02	5.233E-02	5.560E-02	19.608
^{23}Na	23	11	4.000E-05	3.962E-04	3.535E-02	3.575E-02	3.664E-02	47.498
^{24}Mg	24	12	5.862E-04	3.358E-07	1.001E-01	1.001E-01	1.132E-01	10.012
^{25}Mg	25	12	7.733E-05	-1.437E-04	3.460E-02	3.445E-02	3.618E-02	24.254
^{26}Mg	26	12	8.848E-05	1.473E-04	4.582E-02	4.597E-02	4.794E-02	28.089
^{27}Al	27	13	6.481E-05	2.281E-06	1.078E-02	1.078E-02	1.222E-02	9.780
^{28}Si	28	14	7.453E-04	2.148E-07	8.191E-03	8.192E-03	2.479E-02	1.725
^{29}Si	29	14	3.919E-05	1.071E-08	2.995E-03	2.995E-03	3.868E-03	5.116
^{30}Si	30	14	2.673E-05	-2.084E-08	1.264E-03	1.264E-03	1.860E-03	3.607
^{31}P	31	15	7.106E-06	3.169E-08	3.505E-04	3.505E-04	5.088E-04	3.712
^{32}S	32	16	4.011E-04	1.129E-07	-7.450E-04	-7.449E-04	8.189E-03	1.059

TableC.7 – continued

Isotope	A	Z	X^{ini}	mp^{wind}	mp^{preSN}	mp^{total}	EM	$\langle OP \rangle$
^{33}S	33	16	3.265E-06	1.128E-09	2.408E-05	2.408E-05	9.680E-05	1.537
^{34}S	34	16	1.890E-05	5.330E-09	6.184E-05	6.184E-05	4.829E-04	1.324
^{36}S	36	16	8.073E-08	2.276E-11	2.052E-05	2.052E-05	2.232E-05	14.334
^{35}Cl	35	17	6.821E-06	1.923E-09	-1.249E-05	-1.249E-05	1.394E-04	1.060
^{37}Cl	37	17	2.306E-06	6.501E-10	1.965E-04	1.965E-04	2.479E-04	5.573
^{36}Ar	36	18	8.202E-05	2.313E-08	-2.731E-04	-2.731E-04	1.554E-03	0.982
^{38}Ar	38	18	1.574E-05	4.438E-09	1.440E-04	1.440E-04	4.947E-04	1.629
^{40}Ar	40	18	2.650E-08	7.479E-12	8.797E-06	8.797E-06	9.387E-06	18.365
^{39}K	39	19	3.900E-06	1.100E-09	3.563E-05	3.563E-05	1.225E-04	1.629
^{40}K	40	19	5.005E-10	-1.483E-11	5.171E-06	5.171E-06	5.182E-06	536.760
^{41}K	41	19	2.959E-07	8.342E-11	1.218E-05	1.218E-05	1.877E-05	3.288
^{40}Ca	40	20	7.225E-05	2.039E-08	-2.010E-04	-2.009E-04	1.408E-03	1.011
^{42}Ca	42	20	5.063E-07	1.428E-10	1.554E-05	1.554E-05	2.681E-05	2.746
^{43}Ca	43	20	1.082E-07	3.050E-11	5.682E-06	5.682E-06	8.091E-06	3.878
^{44}Ca	44	20	1.710E-06	4.822E-10	1.410E-05	1.410E-05	5.219E-05	1.582
^{46}Ca	46	20	3.428E-09	9.667E-13	4.268E-07	4.268E-07	5.032E-07	7.609
^{48}Ca	48	20	1.672E-07	4.716E-11	-1.143E-07	-1.143E-07	3.611E-06	1.119
^{45}Sc	45	21	5.414E-08	1.526E-11	4.125E-06	4.125E-06	5.331E-06	5.105
^{46}Ti	46	22	3.232E-07	9.112E-11	3.504E-06	3.504E-06	1.070E-05	1.717
^{47}Ti	47	22	2.977E-07	8.394E-11	1.163E-06	1.163E-06	7.794E-06	1.357
^{48}Ti	48	22	3.014E-06	8.497E-10	-8.869E-06	-8.868E-06	5.826E-05	1.002
^{49}Ti	49	22	2.257E-07	6.365E-11	4.191E-06	4.191E-06	9.219E-06	2.117
^{50}Ti	50	22	2.208E-07	6.226E-11	1.447E-05	1.447E-05	1.939E-05	4.552
^{50}V	50	23	1.015E-09	2.863E-13	9.651E-09	9.651E-09	3.227E-08	1.648
^{51}V	51	23	4.138E-07	1.167E-10	2.070E-08	2.082E-08	9.238E-06	1.157
^{50}Cr	50	24	8.265E-07	2.330E-10	-3.761E-06	-3.760E-06	1.465E-05	0.919
^{52}Cr	52	24	1.658E-05	4.674E-09	-4.795E-05	-4.794E-05	3.213E-04	1.005
^{53}Cr	53	24	1.916E-06	5.401E-10	-3.076E-06	-3.076E-06	3.959E-05	1.072

TableC.7 – continued

Isotope	A	Z	$X^{\rm ini}$	$mp^{\rm wind}$	$mp^{\rm preSN}$	$mp^{\rm total}$	EM	$\langle OP \rangle$
^{54}Cr	54	24	4.858E-07	1.370E-10	3.051E-05	3.051E-05	4.133E-05	4.411
^{55}Mn	55	25	1.098E-05	3.096E-09	-1.405E-05	-1.404E-05	2.306E-04	1.089
^{54}Fe	54	26	8.118E-05	2.289E-08	-3.550E-04	-3.549E-04	1.453E-03	0.928
^{56}Fe	56	26	1.322E-03	3.726E-07	-4.416E-03	-4.415E-03	2.502E-02	0.982
^{57}Fe	57	26	3.107E-05	8.759E-09	3.209E-04	3.209E-04	1.013E-03	1.690
^{58}Fe	58	26	4.207E-06	1.186E-09	1.363E-03	1.363E-03	1.457E-03	17.954
^{59}Co	59	27	3.991E-06	1.125E-09	8.291E-04	8.291E-04	9.180E-04	11.925
^{58}Ni	58	28	5.711E-05	1.610E-08	-2.461E-04	-2.461E-04	1.026E-03	0.931
^{60}Ni	60	28	2.276E-05	6.417E-09	4.630E-04	4.630E-04	9.699E-04	2.210
^{61}Ni	61	28	1.006E-06	2.836E-10	2.293E-04	2.293E-04	2.517E-04	12.975
^{62}Ni	62	28	3.259E-06	9.190E-10	6.591E-04	6.591E-04	7.317E-04	11.639
^{64}Ni	64	28	8.568E-07	2.416E-10	3.533E-04	3.533E-04	3.724E-04	22.535
^{63}Cu	63	29	6.600E-07	1.861E-10	3.550E-04	3.550E-04	3.697E-04	29.036
^{65}Cu	65	29	3.035E-07	8.556E-11	1.914E-04	1.914E-04	1.982E-04	33.862
^{64}Zn	64	30	1.131E-06	3.188E-10	6.506E-05	6.506E-05	9.024E-05	4.138
^{66}Zn	66	30	6.690E-07	1.886E-10	1.577E-04	1.577E-04	1.726E-04	13.375
^{67}Zn	67	30	9.980E-08	2.814E-11	5.576E-05	5.576E-05	5.799E-05	30.123
^{68}Zn	68	30	4.632E-07	1.306E-10	2.060E-04	2.060E-04	2.164E-04	24.215
^{70}Zn	70	30	1.577E-08	4.446E-12	4.389E-07	4.389E-07	7.901E-07	2.598
^{69}Ga	69	31	4.551E-08	1.283E-11	2.719E-05	2.719E-05	2.820E-05	32.132
^{71}Ga	71	31	3.108E-08	8.762E-12	1.763E-05	1.763E-05	1.832E-05	30.563
^{70}Ge	70	32	5.157E-08	1.454E-11	3.708E-05	3.708E-05	3.823E-05	38.432
^{72}Ge	72	32	6.910E-08	1.948E-11	3.283E-05	3.283E-05	3.437E-05	25.783
^{73}Ge	73	32	1.955E-08	5.511E-12	1.470E-05	1.470E-05	1.514E-05	40.156
^{74}Ge	74	32	9.228E-08	2.602E-11	4.086E-05	4.086E-05	4.292E-05	24.113
^{76}Ge	76	32	1.963E-08	5.535E-12	1.539E-07	1.539E-07	5.912E-07	1.561
^{75}As	75	33	1.430E-08	4.032E-12	5.620E-06	5.620E-06	5.938E-06	21.529
^{74}Se	74	34	1.198E-09	3.378E-13	-6.354E-09	-6.354E-09	2.033E-08	0.880

TableC.7 – continued

Isotope	A	Z	$X^{\rm ini}$	$mp^{\rm wind}$	$mp^{\rm preSN}$	$mp^{\rm total}$	EM	$\langle OP \rangle$
^{76}Se	76	34	1.296E-08	3.655E-12	7.239E-06	7.239E-06	7.527E-06	30.109
^{77}Se	77	34	1.070E-08	3.018E-12	3.863E-06	3.863E-06	4.101E-06	19.862
^{78}Se	78	34	3.376E-08	9.520E-12	1.631E-05	1.631E-05	1.707E-05	26.207
^{80}Se	80	34	7.226E-08	2.038E-11	1.030E-05	1.030E-05	1.191E-05	8.542
^{82}Se	82	34	1.304E-08	3.676E-12	8.083E-10	8.119E-10	2.912E-07	1.158
^{79}Br	79	35	1.389E-08	3.917E-12	4.153E-06	4.153E-06	4.462E-06	16.652
^{81}Br	81	35	1.386E-08	3.908E-12	2.457E-06	2.457E-06	2.765E-06	10.345
^{78}Kr	78	36	3.900E-10	1.100E-13	-2.049E-09	-2.049E-09	6.639E-09	0.883
^{80}Kr	80	36	2.575E-09	7.260E-13	1.020E-06	1.020E-06	1.078E-06	21.703
^{82}Kr	82	36	1.320E-08	3.721E-12	5.217E-06	5.217E-06	5.511E-06	21.652
^{83}Kr	83	36	1.324E-08	3.734E-12	2.515E-06	2.515E-06	2.810E-06	11.001
^{84}Kr	84	36	6.602E-08	1.861E-11	7.724E-06	7.724E-06	9.194E-06	7.220
^{86}Kr	86	36	2.044E-08	5.764E-12	2.482E-06	2.482E-06	2.937E-06	7.449
^{85}Rb	85	37	1.282E-08	3.616E-12	2.392E-06	2.392E-06	2.678E-06	10.827
^{87}Rb	87	37	5.063E-09	-3.074E-12	9.933E-07	9.932E-07	1.106E-06	11.326
^{84}Sr	84	38	3.228E-10	9.102E-14	-1.772E-09	-1.772E-09	5.418E-09	0.870
^{86}Sr	86	38	5.845E-09	1.648E-12	1.234E-06	1.234E-06	1.364E-06	12.098
^{87}Sr	87	38	4.443E-09	5.754E-12	6.349E-07	6.349E-07	7.339E-07	8.564
^{88}Sr	88	38	5.011E-08	1.413E-11	3.433E-06	3.433E-06	4.549E-06	4.707
^{89}Y	89	39	1.229E-08	3.466E-12	7.410E-07	7.410E-07	1.015E-06	4.280
^{90}Zr	90	40	1.534E-08	4.326E-12	3.671E-07	3.671E-07	7.089E-07	2.395
^{91}Zr	91	40	3.384E-09	9.541E-13	1.272E-07	1.272E-07	2.026E-07	3.104
^{92}Zr	92	40	5.227E-09	1.474E-12	1.471E-07	1.471E-07	2.635E-07	2.614
^{94}Zr	94	40	5.413E-09	1.526E-12	6.183E-08	6.183E-08	1.824E-07	1.747
^{96}Zr	96	40	8.903E-10	2.510E-13	5.031E-08	5.031E-08	7.014E-08	4.084
^{93}Nb	93	41	1.900E-09	5.357E-13	6.747E-08	6.747E-08	1.098E-07	2.996
^{92}Mo	92	42	1.012E-09	2.855E-13	-4.726E-09	-4.726E-09	1.783E-08	0.913
^{94}Mo	94	42	6.448E-10	1.818E-13	-9.504E-10	-9.502E-10	1.341E-08	1.078

TableC.7 – continued

Isotope	A	Z	$X^{\rm ini}$	$mp^{\rm wind}$	$mp^{\rm preSN}$	$mp^{\rm total}$	EM	$\langle OP \rangle$
^{95}Mo	95	42	1.122E-09	3.163E-13	2.602E-08	2.602E-08	5.101E-08	2.357
^{96}Mo	96	42	1.188E-09	3.348E-13	1.712E-08	1.712E-08	4.357E-08	1.902
^{97}Mo	97	42	6.875E-10	1.939E-13	5.608E-09	5.608E-09	2.092E-08	1.578
^{98}Mo	98	42	1.754E-09	4.947E-13	1.625E-08	1.625E-08	5.533E-08	1.635
^{100}Mo	100	42	7.146E-10	2.015E-13	-3.254E-09	-3.254E-09	1.266E-08	0.919
^{96}Ru	96	44	2.926E-10	8.249E-14	-1.502E-09	-1.502E-09	5.014E-09	0.889
^{98}Ru	98	44	1.007E-10	2.840E-14	-3.900E-10	-3.900E-10	1.853E-09	0.954
^{99}Ru	99	44	6.945E-10	1.958E-13	3.402E-10	3.404E-10	1.581E-08	1.180
^{100}Ru	100	44	6.928E-10	1.953E-13	7.506E-09	7.506E-09	2.294E-08	1.717
^{101}Ru	101	44	9.475E-10	2.672E-13	-2.828E-09	-2.828E-09	1.828E-08	1.000
^{102}Ru	102	44	1.770E-09	4.990E-13	6.921E-09	6.921E-09	4.634E-08	1.358
^{104}Ru	104	44	1.065E-09	3.003E-13	-4.740E-09	-4.740E-09	1.898E-08	0.924
^{103}Rh	103	45	1.055E-09	2.974E-13	-3.176E-09	-3.176E-09	2.032E-08	0.999
^{102}Pd	102	46	4.241E-11	1.196E-14	-2.332E-10	-2.332E-10	7.115E-10	0.870
^{104}Pd	104	46	4.723E-10	1.332E-13	5.093E-09	5.093E-09	1.561E-08	1.714
^{105}Pd	105	46	9.558E-10	2.695E-13	-3.569E-09	-3.568E-09	1.772E-08	0.961
^{106}Pd	106	46	1.181E-09	3.330E-13	3.340E-09	3.340E-09	2.965E-08	1.301
^{108}Pd	108	46	1.165E-09	3.285E-13	3.955E-09	3.955E-09	2.990E-08	1.331
^{110}Pd	110	46	5.255E-10	1.482E-13	-2.005E-09	-2.004E-09	9.702E-09	0.957
^{107}Ag	107	47	7.840E-10	2.211E-13	-2.493E-09	-2.493E-09	1.497E-08	0.990
^{109}Ag	109	47	7.420E-10	2.092E-13	1.524E-09	1.524E-09	1.805E-08	1.261
^{106}Cd	106	48	6.346E-11	1.789E-14	-3.413E-10	-3.413E-10	1.072E-09	0.876
^{108}Cd	108	48	4.604E-11	1.298E-14	8.199E-10	8.199E-10	1.845E-09	2.078
^{110}Cd	110	48	6.580E-10	1.855E-13	4.773E-09	4.773E-09	1.943E-08	1.531
^{111}Cd	111	48	6.805E-10	1.919E-13	-1.067E-09	-1.067E-09	1.409E-08	1.074
^{112}Cd	112	48	1.294E-09	3.650E-13	3.327E-09	3.327E-09	3.216E-08	1.288
^{113}Cd	113	48	6.614E-10	1.865E-13	-8.562E-10	-8.560E-10	1.388E-08	1.088
^{114}Cd	114	48	1.569E-09	4.423E-13	5.737E-09	5.738E-09	4.068E-08	1.344

TableC.7 – continued

Isotope	A	Z	$X^{\rm ini}$	$mp^{\rm wind}$	$mp^{\rm preSN}$	$mp^{\rm total}$	EM	$\langle OP \rangle$
^{116}Cd	116	48	4.161E-10	1.173E-13	-5.894E-10	-5.893E-10	8.680E-09	1.081
^{113}In	113	49	2.604E-11	7.342E-15	-1.221E-10	-1.221E-10	4.579E-10	0.912
^{115}In	115	49	5.915E-10	1.667E-13	-5.728E-10	-5.726E-10	1.260E-08	1.105
^{112}Sn	112	50	1.221E-10	3.443E-14	-6.307E-10	-6.307E-10	2.089E-09	0.887
^{114}Sn	114	50	8.435E-11	2.378E-14	-3.183E-10	-3.183E-10	1.561E-09	0.959
^{115}Sn	115	50	4.377E-11	1.240E-14	-1.389E-10	-1.389E-10	8.360E-10	0.990
^{116}Sn	116	50	1.893E-09	5.338E-13	6.735E-09	6.735E-09	4.890E-08	1.339
^{117}Sn	117	50	1.008E-09	2.843E-13	3.328E-10	3.331E-10	2.279E-08	1.172
^{118}Sn	118	50	3.209E-09	9.048E-13	9.417E-09	9.418E-09	8.090E-08	1.307
^{119}Sn	119	50	1.147E-09	3.234E-13	1.914E-09	1.914E-09	2.746E-08	1.241
^{120}Sn	120	50	4.391E-09	1.238E-12	1.721E-08	1.721E-08	1.150E-07	1.358
^{122}Sn	122	50	6.341E-10	1.788E-13	1.444E-09	1.444E-09	1.557E-08	1.273
^{124}Sn	124	50	8.060E-10	2.272E-13	-3.014E-09	-3.014E-09	1.494E-08	0.961
^{121}Sb	121	51	6.318E-10	1.781E-13	2.329E-10	2.331E-10	1.431E-08	1.174
^{123}Sb	123	51	4.803E-10	1.354E-13	-1.936E-09	-1.936E-09	8.762E-09	0.946
^{120}Te	120	52	1.628E-11	4.591E-15	-9.251E-11	-9.250E-11	2.702E-10	0.860
^{122}Te	122	52	4.489E-10	1.266E-13	2.761E-09	2.761E-09	1.276E-08	1.474
^{123}Te	123	52	1.579E-10	4.451E-14	8.904E-10	8.904E-10	4.407E-09	1.447
^{124}Te	124	52	8.441E-10	2.380E-13	5.607E-09	5.608E-09	2.441E-08	1.499
^{125}Te	125	52	1.261E-09	3.556E-13	-3.645E-09	-3.645E-09	2.445E-08	1.005
^{126}Te	126	52	3.375E-09	9.517E-13	3.237E-09	3.238E-09	7.842E-08	1.205
^{128}Te	128	52	5.733E-09	1.616E-12	-2.385E-08	-2.385E-08	1.039E-07	0.939
^{130}Te	130	52	6.211E-09	1.751E-12	-2.388E-08	-2.388E-08	1.145E-07	0.956
^{127}I	127	53	1.459E-09	4.114E-13	-5.025E-09	-5.024E-09	2.748E-08	0.976
^{124}Xe	124	54	2.210E-11	6.230E-15	-1.278E-10	-1.278E-10	3.644E-10	0.855
^{126}Xe	126	54	1.949E-11	5.496E-15	-1.058E-10	-1.058E-10	3.284E-10	0.874
^{128}Xe	128	54	3.943E-10	1.112E-13	4.790E-09	4.790E-09	1.357E-08	1.785
^{129}Xe	129	54	4.893E-09	1.380E-12	-2.485E-08	-2.485E-08	8.414E-08	0.892

TableC.7 – continued

Isotope	A	Z	$X^{\rm ini}$	$mp^{\rm wind}$	$mp^{\rm preSN}$	$mp^{\rm total}$	EM	$\langle OP \rangle$
^{130}Xe	130	54	7.865E-10	2.218E-13	1.396E-08	1.396E-08	3.147E-08	2.075
^{131}Xe	131	54	3.945E-09	1.112E-12	-1.487E-08	-1.487E-08	7.299E-08	0.959
^{132}Xe	132	54	4.806E-09	1.355E-12	7.627E-09	7.629E-09	1.147E-07	1.237
^{134}Xe	134	54	1.788E-09	5.041E-13	-3.882E-09	-3.881E-09	3.595E-08	1.042
^{136}Xe	136	54	1.478E-09	4.168E-13	-9.367E-10	-9.363E-10	3.199E-08	1.122
^{133}Cs	133	55	1.426E-09	4.021E-13	-2.681E-09	-2.681E-09	2.908E-08	1.057
^{130}Ba	130	56	1.814E-11	5.116E-15	-1.061E-10	-1.061E-10	2.980E-10	0.852
^{132}Ba	132	56	1.762E-11	4.968E-15	-9.662E-11	-9.661E-11	2.959E-10	0.871
^{134}Ba	134	56	4.272E-10	1.205E-13	8.600E-09	8.600E-09	1.812E-08	2.198
^{135}Ba	135	56	1.174E-09	3.310E-13	-1.466E-09	-1.466E-09	2.468E-08	1.090
^{136}Ba	136	56	1.409E-09	3.972E-13	2.078E-08	2.078E-08	5.216E-08	1.920
^{137}Ba	137	56	2.030E-09	5.723E-13	1.301E-08	1.301E-08	5.823E-08	1.487
^{138}Ba	138	56	1.305E-08	3.680E-12	1.861E-07	1.861E-07	4.768E-07	1.894
^{138}La	138	57	1.604E-12	4.523E-16	-8.906E-12	-8.906E-12	2.682E-11	0.867
^{139}La	139	57	1.790E-09	5.048E-13	2.189E-08	2.189E-08	6.177E-08	1.789
^{136}Ce	136	58	8.382E-12	2.363E-15	-4.504E-11	-4.504E-11	1.417E-10	0.876
^{138}Ce	138	58	1.148E-11	3.236E-15	-5.792E-11	-5.791E-11	1.977E-10	0.893
^{140}Ce	140	58	4.103E-09	1.157E-12	3.203E-08	3.203E-08	1.234E-07	1.560
^{142}Ce	142	58	5.229E-10	1.474E-13	8.410E-10	8.411E-10	1.249E-08	1.238
^{141}Pr	141	59	6.910E-10	1.948E-13	3.334E-09	3.334E-09	1.873E-08	1.405
^{142}Nd	142	60	9.920E-10	2.797E-13	5.603E-09	5.603E-09	2.770E-08	1.448
^{143}Nd	143	60	4.484E-10	1.264E-13	-2.071E-11	-2.058E-11	9.966E-09	1.152
^{144}Nd	144	60	8.826E-10	2.489E-13	1.727E-09	1.727E-09	2.139E-08	1.256
^{145}Nd	145	60	3.095E-10	8.728E-14	8.227E-12	8.314E-12	6.903E-09	1.156
^{146}Nd	146	60	6.448E-10	1.818E-13	2.210E-09	2.210E-09	1.657E-08	1.333
^{148}Nd	148	60	2.185E-10	6.161E-14	-3.266E-10	-3.265E-10	4.541E-09	1.077
^{150}Nd	150	60	2.168E-10	6.114E-14	-1.091E-09	-1.091E-09	3.739E-09	0.894
^{144}Sm	144	62	3.684E-11	1.039E-14	-1.730E-10	-1.730E-10	6.475E-10	0.911

TableC.7 – continued

Isotope	A	Z	$X^{\rm ini}$	$mp^{\rm wind}$	$mp^{\rm preSN}$	$mp^{\rm total}$	EM	$\langle OP \rangle$
^{147}Sm	147	62	1.834E-10	5.172E-14	-3.711E-10	-3.710E-10	3.715E-09	1.050
^{148}Sm	148	62	1.385E-10	3.904E-14	3.713E-10	3.713E-10	3.456E-09	1.294
^{149}Sm	149	62	1.714E-10	4.832E-14	-7.098E-10	-7.098E-10	3.108E-09	0.940
^{150}Sm	150	62	9.213E-11	2.598E-14	6.251E-10	6.252E-10	2.677E-09	1.507
^{152}Sm	152	62	3.383E-10	9.539E-14	-1.185E-09	-1.185E-09	6.351E-09	0.973
^{154}Sm	154	62	2.916E-10	8.223E-14	-1.322E-09	-1.322E-09	5.174E-09	0.920
^{151}Eu	151	63	2.036E-10	5.741E-14	-1.035E-09	-1.035E-09	3.500E-09	0.891
^{153}Eu	153	63	2.252E-10	6.350E-14	-1.066E-09	-1.066E-09	3.950E-09	0.909
^{152}Gd	152	64	2.947E-12	8.312E-16	1.838E-10	1.838E-10	2.495E-10	4.388
^{154}Gd	154	64	3.210E-11	9.050E-15	4.270E-10	4.270E-10	1.142E-09	1.845
^{155}Gd	155	64	2.192E-10	6.181E-14	-9.573E-10	-9.572E-10	3.926E-09	0.928
^{156}Gd	156	64	3.051E-10	8.603E-14	-5.704E-10	-5.703E-10	6.226E-09	1.058
^{157}Gd	157	64	2.348E-10	6.621E-14	-7.001E-10	-7.000E-10	4.531E-09	1.000
^{158}Gd	158	64	3.750E-10	1.057E-13	-7.619E-11	-7.609E-11	8.276E-09	1.144
^{160}Gd	160	64	3.343E-10	9.425E-14	-1.534E-09	-1.534E-09	5.912E-09	0.917
^{159}Tb	159	65	2.765E-10	7.796E-14	-1.113E-09	-1.113E-09	5.045E-09	0.946
^{156}Dy	156	66	1.004E-12	2.830E-16	-6.121E-12	-6.121E-12	1.624E-11	0.839
^{158}Dy	158	66	1.743E-12	4.913E-16	1.192E-11	1.192E-11	5.074E-11	1.510
^{160}Dy	160	66	4.301E-11	1.213E-14	5.591E-10	5.591E-10	1.517E-09	1.829
^{161}Dy	161	66	3.498E-10	9.862E-14	-1.607E-09	-1.607E-09	6.184E-09	0.917
^{162}Dy	162	66	4.748E-10	1.339E-13	-1.017E-09	-1.016E-09	9.559E-09	1.044
^{163}Dy	163	66	4.663E-10	1.315E-13	-1.861E-09	-1.861E-09	8.526E-09	0.948
^{164}Dy	164	66	5.312E-10	1.498E-13	3.933E-10	3.934E-10	1.222E-08	1.193
^{165}Ho	165	67	4.244E-10	1.197E-13	-1.847E-09	-1.847E-09	7.606E-09	0.929
^{162}Er	162	68	1.609E-12	4.536E-16	-9.806E-12	-9.806E-12	2.603E-11	0.839
^{164}Er	164	68	1.913E-11	5.393E-15	-1.149E-10	-1.149E-10	3.112E-10	0.844
^{166}Er	166	68	4.044E-10	1.140E-13	-1.050E-09	-1.050E-09	7.959E-09	1.020
^{167}Er	167	68	2.776E-10	7.827E-14	-1.038E-09	-1.038E-09	5.145E-09	0.961

TableC.7 – continued

Isotope	A	Z	$X^{\rm ini}$	$mp^{\rm wind}$	$mp^{\rm preSN}$	$mp^{\rm total}$	EM	$\langle OP \rangle$
^{168}Er	168	68	3.263E-10	9.199E-14	3.156E-10	3.157E-10	7.583E-09	1.205
^{170}Er	170	68	1.840E-10	5.188E-14	-2.331E-10	-2.330E-10	3.865E-09	1.089
^{169}Tm	169	69	1.854E-10	5.228E-14	-5.156E-10	-5.156E-10	3.615E-09	1.011
^{168}Yb	168	70	1.583E-12	4.464E-16	-9.561E-12	-9.560E-12	2.570E-11	0.842
^{170}Yb	170	70	3.746E-11	1.056E-14	5.275E-10	5.275E-10	1.362E-09	1.885
^{171}Yb	171	70	1.770E-10	4.991E-14	-3.894E-10	-3.893E-10	3.554E-09	1.041
^{172}Yb	172	70	2.722E-10	7.674E-14	2.106E-10	2.106E-10	6.273E-09	1.195
^{173}Yb	173	70	2.023E-10	5.704E-14	-1.292E-10	-1.292E-10	4.377E-09	1.122
^{174}Yb	174	70	4.015E-10	1.132E-13	1.147E-09	1.147E-09	1.009E-08	1.303
^{176}Yb	176	70	1.628E-10	4.590E-14	-5.415E-10	-5.414E-10	3.085E-09	0.982
^{175}Lu	175	71	1.828E-10	5.154E-14	-5.064E-10	-5.063E-10	3.565E-09	1.011
^{176}Lu	176	71	4.876E-12	-3.858E-15	5.094E-11	5.093E-11	1.596E-10	1.696
^{174}Hf	174	72	1.231E-12	3.472E-16	-7.329E-12	-7.329E-12	2.010E-11	0.846
^{176}Hf	176	72	4.036E-11	1.661E-14	3.626E-10	3.626E-10	1.262E-09	1.621
^{177}Hf	177	72	1.438E-10	4.054E-14	-4.272E-10	-4.271E-10	2.776E-09	1.001
^{178}Hf	178	72	2.121E-10	5.981E-14	4.194E-10	4.195E-10	5.145E-09	1.257
^{179}Hf	179	72	1.065E-10	3.003E-14	-6.322E-11	-6.319E-11	2.309E-09	1.124
^{180}Hf	180	72	2.758E-10	7.778E-14	1.270E-09	1.270E-09	7.415E-09	1.394
^{180}Ta	180	73	2.429E-14	6.848E-18	-5.871E-14	-5.871E-14	4.824E-13	1.030
^{181}Ta	181	73	1.986E-10	5.599E-14	-3.944E-10	-3.944E-10	4.029E-09	1.052
^{180}W	180	74	8.395E-13	2.367E-16	1.806E-11	1.806E-11	3.676E-11	2.270
^{182}W	182	74	1.877E-10	5.294E-14	2.824E-10	2.824E-10	4.464E-09	1.233
^{183}W	183	74	1.020E-10	2.875E-14	3.843E-10	3.843E-10	2.656E-09	1.350
^{184}W	184	74	2.195E-10	6.189E-14	7.290E-10	7.291E-10	5.618E-09	1.327
^{186}W	186	74	2.058E-10	5.804E-14	-3.883E-10	-3.883E-10	4.197E-09	1.057
^{185}Re	185	75	1.048E-10	2.955E-14	9.115E-12	9.145E-12	2.343E-09	1.159
^{187}Re	187	75	1.773E-10	4.999E-14	-7.789E-10	-7.788E-10	3.170E-09	0.927
^{184}Os	184	76	7.108E-13	2.004E-16	-4.093E-12	-4.092E-12	1.174E-11	0.856

TableC.7 – continued

Isotope	A	Z	$X^{\rm ini}$	$mp^{\rm wind}$	$mp^{\rm preSN}$	$mp^{\rm total}$	EM	$\langle OP \rangle$
^{186}Os	186	76	5.778E-11	1.629E-14	2.852E-10	2.853E-10	1.572E-09	1.411
^{187}Os	187	76	5.998E-11	1.691E-14	-1.443E-10	-1.442E-10	1.192E-09	1.030
^{188}Os	188	76	4.874E-10	1.374E-13	-1.117E-09	-1.117E-09	9.738E-09	1.036
^{189}Os	189	76	5.974E-10	1.684E-13	-3.093E-09	-3.093E-09	1.021E-08	0.886
^{190}Os	190	76	9.766E-10	2.754E-13	-2.898E-09	-2.898E-09	1.886E-08	1.001
^{192}Os	192	76	1.533E-09	4.322E-13	-6.996E-09	-6.995E-09	2.715E-08	0.918
^{191}Ir	191	77	1.357E-09	3.827E-13	-7.652E-09	-7.651E-09	2.258E-08	0.863
^{193}Ir	193	77	2.308E-09	6.509E-13	-1.262E-08	-1.262E-08	3.879E-08	0.871
^{190}Pt	190	78	1.008E-12	2.843E-16	-5.714E-12	-5.713E-12	1.675E-11	0.861
^{192}Pt	192	78	5.850E-11	1.650E-14	1.293E-09	1.293E-09	2.597E-09	2.301
^{194}Pt	194	78	2.490E-09	7.020E-13	-9.065E-09	-9.065E-09	4.639E-08	0.966
^{195}Pt	195	78	2.568E-09	7.241E-13	-1.274E-08	-1.274E-08	4.447E-08	0.898
^{196}Pt	196	78	1.926E-09	5.430E-13	-1.319E-09	-1.318E-09	4.158E-08	1.119
^{198}Pt	198	78	5.522E-10	1.557E-13	-2.506E-09	-2.506E-09	9.793E-09	0.920
^{197}Au	197	79	1.083E-09	3.054E-13	-3.624E-09	-3.624E-09	2.051E-08	0.981
^{196}Hg	196	80	3.009E-12	8.485E-16	-1.548E-11	-1.548E-11	5.155E-11	0.888
^{198}Hg	198	80	1.975E-10	5.569E-14	4.572E-09	4.572E-09	8.971E-09	2.355
^{199}Hg	199	80	3.360E-10	9.473E-14	5.064E-10	5.065E-10	7.991E-09	1.233
^{200}Hg	200	80	4.622E-10	1.303E-13	3.014E-09	3.014E-09	1.331E-08	1.493
^{201}Hg	201	80	2.651E-10	7.475E-14	1.318E-09	1.318E-09	7.223E-09	1.413
^{202}Hg	202	80	6.036E-10	1.702E-13	5.480E-09	5.480E-09	1.893E-08	1.626
^{204}Hg	204	80	1.401E-10	3.951E-14	-4.994E-10	-4.993E-10	2.622E-09	0.970
^{203}Tl	203	81	3.221E-10	9.081E-14	4.759E-09	4.759E-09	1.193E-08	1.921
^{205}Tl	205	81	7.764E-10	2.189E-13	7.999E-09	7.999E-09	2.529E-08	1.689
^{204}Pb	204	82	2.931E-10	8.264E-14	5.387E-09	5.387E-09	1.192E-08	2.108
^{206}Pb	206	82	2.798E-09	7.888E-13	3.165E-08	3.165E-08	9.397E-08	1.741
^{207}Pb	207	82	3.090E-09	8.711E-13	4.845E-08	4.845E-08	1.173E-07	1.968
^{208}Pb	208	82	8.850E-09	2.495E-12	5.437E-08	5.437E-08	2.515E-07	1.473

TableC.7 – continued

Isotope	A	Z	X^{ini}	mp^{wind}	mp^{preSN}	mp^{total}	EM	$\langle OP \rangle$
^{209}Bi	209	83	8.718E-10	2.458E-13	9.467E-10	9.470E-10	2.037E-08	1.211

Table C.8: Yields for model 25CI.

Isotope	A	Z	X^{ini}	mp^{wind}	mp^{preSN}	mp^{total}	EM	$\langle OP \rangle$
^{1}H	1	1	7.064E-01	-7.678E-01	-5.617E+00	-6.384E+00	9.351E+00	0.686
^{2}H	2	1	1.371E-05	-1.389E-04	-1.505E-04	-2.894E-04	1.588E-05	0.060
^{3}He	3	2	4.540E-05	-7.962E-05	-4.864E-04	-5.660E-04	4.452E-04	0.508
^{4}He	4	2	2.735E-01	7.690E-01	1.292E+00	2.061E+00	8.153E+00	1.546
^{7}Li	7	3	7.605E-11	-7.707E-10	-8.352E-10	-1.606E-09	8.814E-11	0.060
^{11}B	11	5	2.856E-09	8.120E-13	4.547E-11	4.628E-11	6.366E-08	1.156
^{12}C	12	6	3.425E-03	-1.177E-02	5.677E-01	5.559E-01	6.322E-01	9.571
^{13}C	13	6	4.156E-05	5.133E-04	-2.537E-04	2.596E-04	1.185E-03	1.479
^{14}N	14	7	1.059E-03	3.171E-02	3.806E-02	6.977E-02	9.335E-02	4.571
^{15}N	15	7	4.171E-06	-2.230E-05	-3.911E-05	-6.141E-05	3.149E-05	0.391
^{16}O	16	8	9.624E-03	-2.109E-02	2.401E+00	2.380E+00	2.594E+00	13.976
^{17}O	17	8	3.813E-06	4.557E-06	4.537E-05	4.992E-05	1.349E-04	1.834
^{18}O	18	8	2.171E-05	-7.054E-05	1.143E-03	1.072E-03	1.556E-03	3.715
^{19}F	19	9	5.611E-07	-1.518E-06	-7.799E-07	-2.298E-06	1.020E-05	0.943
^{20}Ne	20	10	1.818E-03	-5.616E-05	1.067E+00	1.067E+00	1.107E+00	31.582
^{21}Ne	21	10	4.575E-06	3.603E-05	2.861E-03	2.897E-03	2.999E-03	33.985
^{22}Ne	22	10	1.470E-04	-3.576E-04	4.772E-02	4.736E-02	5.064E-02	17.857
^{23}Na	23	11	4.000E-05	3.995E-04	5.169E-02	5.209E-02	5.298E-02	68.673
^{24}Mg	24	12	5.862E-04	3.388E-07	7.107E-02	7.107E-02	8.412E-02	7.440
^{25}Mg	25	12	7.733E-05	-1.449E-04	3.350E-02	3.336E-02	3.508E-02	23.518
^{26}Mg	26	12	8.848E-05	1.485E-04	3.746E-02	3.761E-02	3.958E-02	23.192
^{27}Al	27	13	6.481E-05	2.302E-06	1.518E-02	1.519E-02	1.663E-02	13.303
^{28}Si	28	14	7.453E-04	2.166E-07	4.758E-03	4.758E-03	2.136E-02	1.486
^{29}Si	29	14	3.919E-05	1.080E-08	1.025E-03	1.025E-03	1.898E-03	2.511
^{30}Si	30	14	2.673E-05	-2.102E-08	9.646E-04	9.646E-04	1.560E-03	3.026
^{31}P	31	15	7.106E-06	3.197E-08	3.159E-04	3.159E-04	4.742E-04	3.460
^{32}S	32	16	4.011E-04	1.138E-07	-7.822E-04	-7.821E-04	8.152E-03	1.054

TableC.8 – continued

Isotope	A	Z	$X^{\rm ini}$	$mp^{\rm wind}$	$mp^{\rm preSN}$	$mp^{\rm total}$	EM	$\langle OP \rangle$
^{33}S	33	16	3.265E-06	1.137E-09	2.317E-05	2.317E-05	9.589E-05	1.523
^{34}S	34	16	1.890E-05	5.375E-09	5.295E-05	5.296E-05	4.740E-04	1.300
^{36}S	36	16	8.073E-08	2.295E-11	2.200E-05	2.200E-05	2.379E-05	15.281
^{35}Cl	35	17	6.821E-06	1.939E-09	-1.569E-05	-1.569E-05	1.362E-04	1.036
^{37}Cl	37	17	2.306E-06	6.556E-10	2.204E-04	2.204E-04	2.718E-04	6.111
^{36}Ar	36	18	8.202E-05	2.332E-08	-2.801E-04	-2.800E-04	1.547E-03	0.978
^{38}Ar	38	18	1.574E-05	4.476E-09	1.452E-04	1.452E-04	4.958E-04	1.633
^{40}Ar	40	18	2.650E-08	7.541E-12	8.840E-06	8.840E-06	9.431E-06	18.449
^{39}K	39	19	3.900E-06	1.109E-09	3.245E-05	3.245E-05	1.193E-04	1.586
^{40}K	40	19	5.005E-10	-1.488E-11	4.932E-06	4.932E-06	4.943E-06	512.003
^{41}K	41	19	2.959E-07	8.412E-11	1.189E-05	1.189E-05	1.848E-05	3.239
^{40}Ca	40	20	7.225E-05	2.056E-08	-2.052E-04	-2.052E-04	1.404E-03	1.008
^{42}Ca	42	20	5.063E-07	1.440E-10	1.578E-05	1.578E-05	2.706E-05	2.771
^{43}Ca	43	20	1.082E-07	3.075E-11	5.932E-06	5.932E-06	8.341E-06	3.998
^{44}Ca	44	20	1.710E-06	4.863E-10	1.447E-05	1.447E-05	5.257E-05	1.594
^{46}Ca	46	20	3.428E-09	9.748E-13	1.222E-07	1.222E-07	1.986E-07	3.003
^{48}Ca	48	20	1.672E-07	4.755E-11	-1.075E-07	-1.074E-07	3.618E-06	1.122
^{45}Sc	45	21	5.414E-08	1.539E-11	3.900E-06	3.900E-06	5.106E-06	4.890
^{46}Ti	46	22	3.232E-07	9.189E-11	3.756E-06	3.757E-06	1.096E-05	1.758
^{47}Ti	47	22	2.977E-07	8.464E-11	1.356E-06	1.356E-06	7.988E-06	1.391
^{48}Ti	48	22	3.014E-06	8.569E-10	-8.857E-06	-8.856E-06	5.827E-05	1.002
^{49}Ti	49	22	2.257E-07	6.418E-11	4.139E-06	4.139E-06	9.167E-06	2.105
^{50}Ti	50	22	2.208E-07	6.278E-11	1.479E-05	1.479E-05	1.971E-05	4.628
^{50}V	50	23	1.015E-09	2.887E-13	9.415E-10	9.418E-10	2.356E-08	1.203
^{51}V	51	23	4.138E-07	1.176E-10	4.452E-08	4.464E-08	9.261E-06	1.160
^{50}Cr	50	24	8.265E-07	2.350E-10	-3.785E-06	-3.785E-06	1.463E-05	0.917
^{52}Cr	52	24	1.658E-05	4.713E-09	-4.910E-05	-4.909E-05	3.201E-04	1.001
^{53}Cr	53	24	1.916E-06	5.447E-10	-3.414E-06	-3.414E-06	3.926E-05	1.062

TableC.8 – continued

Isotope	A	Z	$X^{\rm ini}$	$mp^{\rm wind}$	$mp^{\rm preSN}$	$mp^{\rm total}$	EM	$\langle OP \rangle$
^{54}Cr	54	24	4.858E-07	1.381E-10	3.181E-05	3.181E-05	4.263E-05	4.550
^{55}Mn	55	25	1.098E-05	3.122E-09	-1.918E-05	-1.918E-05	2.254E-04	1.064
^{54}Fe	54	26	8.118E-05	2.308E-08	-3.596E-04	-3.596E-04	1.449E-03	0.925
^{56}Fe	56	26	1.322E-03	3.758E-07	-4.547E-03	-4.547E-03	2.489E-02	0.976
^{57}Fe	57	26	3.107E-05	8.833E-09	3.191E-04	3.191E-04	1.011E-03	1.687
^{58}Fe	58	26	4.207E-06	1.196E-09	1.434E-03	1.434E-03	1.527E-03	18.823
^{59}Co	59	27	3.991E-06	1.135E-09	7.859E-04	7.859E-04	8.748E-04	11.363
^{58}Ni	58	28	5.711E-05	1.624E-08	-2.496E-04	-2.496E-04	1.022E-03	0.928
^{60}Ni	60	28	2.276E-05	6.470E-09	5.139E-04	5.139E-04	1.021E-03	2.326
^{61}Ni	61	28	1.006E-06	2.860E-10	2.546E-04	2.546E-04	2.770E-04	14.281
^{62}Ni	62	28	3.259E-06	9.267E-10	7.148E-04	7.148E-04	7.874E-04	12.525
^{64}Ni	64	28	8.568E-07	2.436E-10	3.417E-04	3.417E-04	3.608E-04	21.833
^{63}Cu	63	29	6.600E-07	1.877E-10	3.173E-04	3.173E-04	3.320E-04	26.080
^{65}Cu	65	29	3.035E-07	8.628E-11	2.300E-04	2.300E-04	2.367E-04	40.445
^{64}Zn	64	30	1.131E-06	3.215E-10	8.412E-05	8.412E-05	1.093E-04	5.012
^{66}Zn	66	30	6.690E-07	1.902E-10	1.882E-04	1.882E-04	2.031E-04	15.737
^{67}Zn	67	30	9.980E-08	2.838E-11	6.206E-05	6.206E-05	6.429E-05	33.396
^{68}Zn	68	30	4.632E-07	1.317E-10	2.172E-04	2.172E-04	2.275E-04	25.467
^{70}Zn	70	30	1.577E-08	4.483E-12	9.637E-08	9.637E-08	4.476E-07	1.472
^{69}Ga	69	31	4.551E-08	1.294E-11	2.789E-05	2.789E-05	2.890E-05	32.927
^{71}Ga	71	31	3.108E-08	8.836E-12	1.949E-05	1.949E-05	2.018E-05	33.663
^{70}Ge	70	32	5.157E-08	1.466E-11	3.698E-05	3.698E-05	3.813E-05	38.331
^{72}Ge	72	32	6.910E-08	1.965E-11	3.159E-05	3.159E-05	3.313E-05	24.859
^{73}Ge	73	32	1.955E-08	5.557E-12	1.329E-05	1.329E-05	1.372E-05	36.398
^{74}Ge	74	32	9.228E-08	2.624E-11	3.642E-05	3.642E-05	3.848E-05	21.616
^{76}Ge	76	32	1.963E-08	5.581E-12	-9.844E-09	-9.839E-09	4.274E-07	1.129
^{75}As	75	33	1.430E-08	4.066E-12	4.566E-06	4.566E-06	4.884E-06	17.708
^{74}Se	74	34	1.198E-09	3.406E-13	-6.242E-09	-6.242E-09	2.044E-08	0.885

TableC.8 – continued

Isotope	A	Z	$X^{\rm ini}$	$mp^{\rm wind}$	$mp^{\rm preSN}$	$mp^{\rm total}$	EM	$\langle OP \rangle$
^{76}Se	76	34	1.296E-08	3.685E-12	6.278E-06	6.278E-06	6.567E-06	26.269
^{77}Se	77	34	1.070E-08	3.044E-12	3.176E-06	3.176E-06	3.414E-06	16.535
^{78}Se	78	34	3.376E-08	9.600E-12	1.352E-05	1.352E-05	1.427E-05	21.917
^{80}Se	80	34	7.226E-08	2.055E-11	5.258E-06	5.258E-06	6.868E-06	4.927
^{82}Se	82	34	1.304E-08	3.707E-12	-3.992E-08	-3.991E-08	2.505E-07	0.996
^{79}Br	79	35	1.389E-08	3.950E-12	2.812E-06	2.812E-06	3.121E-06	11.647
^{81}Br	81	35	1.386E-08	3.941E-12	1.549E-06	1.549E-06	1.858E-06	6.951
^{78}Kr	78	36	3.900E-10	1.109E-13	-2.006E-09	-2.006E-09	6.682E-09	0.888
^{80}Kr	80	36	2.575E-09	7.321E-13	1.306E-06	1.306E-06	1.363E-06	27.444
^{82}Kr	82	36	1.320E-08	3.752E-12	4.327E-06	4.327E-06	4.621E-06	18.155
^{83}Kr	83	36	1.324E-08	3.765E-12	2.051E-06	2.051E-06	2.346E-06	9.187
^{84}Kr	84	36	6.602E-08	1.877E-11	7.158E-06	7.158E-06	8.629E-06	6.776
^{86}Kr	86	36	2.044E-08	5.813E-12	1.342E-06	1.342E-06	1.797E-06	4.558
^{85}Rb	85	37	1.282E-08	3.646E-12	1.946E-06	1.946E-06	2.231E-06	9.021
^{87}Rb	87	37	5.063E-09	-3.077E-12	4.605E-07	4.605E-07	5.733E-07	5.871
^{84}Sr	84	38	3.228E-10	9.178E-14	-1.736E-09	-1.736E-09	5.455E-09	0.876
^{86}Sr	86	38	5.845E-09	1.662E-12	1.661E-06	1.661E-06	1.791E-06	15.886
^{87}Sr	87	38	4.443E-09	5.779E-12	1.030E-06	1.030E-06	1.129E-06	13.169
^{88}Sr	88	38	5.011E-08	1.425E-11	4.283E-06	4.283E-06	5.399E-06	5.586
^{89}Y	89	39	1.229E-08	3.495E-12	8.086E-07	8.086E-07	1.082E-06	4.565
^{90}Zr	90	40	1.534E-08	4.363E-12	4.012E-07	4.012E-07	7.430E-07	2.511
^{91}Zr	91	40	3.384E-09	9.622E-13	1.314E-07	1.314E-07	2.068E-07	3.168
^{92}Zr	92	40	5.227E-09	1.486E-12	1.500E-07	1.500E-07	2.665E-07	2.643
^{94}Zr	94	40	5.413E-09	1.539E-12	5.815E-08	5.815E-08	1.787E-07	1.712
^{96}Zr	96	40	8.903E-10	2.531E-13	1.122E-08	1.122E-08	3.105E-08	1.808
^{93}Nb	93	41	1.900E-09	5.402E-13	6.109E-08	6.109E-08	1.034E-07	2.822
^{92}Mo	92	42	1.012E-09	2.879E-13	-4.731E-09	-4.731E-09	1.782E-08	0.913
^{94}Mo	94	42	6.448E-10	1.833E-13	-1.244E-09	-1.244E-09	1.312E-08	1.055

TableC.8 – continued

Isotope	A	Z	$X^{\rm ini}$	$mp^{\rm wind}$	$mp^{\rm preSN}$	$mp^{\rm total}$	EM	$\langle OP \rangle$
^{95}Mo	95	42	1.122E-09	3.190E-13	1.671E-08	1.671E-08	4.170E-08	1.927
^{96}Mo	96	42	1.188E-09	3.376E-13	1.956E-08	1.956E-08	4.601E-08	2.009
^{97}Mo	97	42	6.875E-10	1.955E-13	5.846E-09	5.846E-09	2.116E-08	1.596
^{98}Mo	98	42	1.754E-09	4.988E-13	1.845E-08	1.845E-08	5.752E-08	1.700
^{100}Mo	100	42	7.146E-10	2.032E-13	-3.309E-09	-3.309E-09	1.261E-08	0.915
^{96}Ru	96	44	2.926E-10	8.318E-14	-1.479E-09	-1.479E-09	5.038E-09	0.893
^{98}Ru	98	44	1.007E-10	2.863E-14	-4.036E-10	-4.035E-10	1.840E-09	0.947
^{99}Ru	99	44	6.945E-10	1.975E-13	7.911E-10	7.913E-10	1.626E-08	1.214
^{100}Ru	100	44	6.928E-10	1.970E-13	9.081E-09	9.081E-09	2.451E-08	1.834
^{101}Ru	101	44	9.475E-10	2.694E-13	-2.366E-09	-2.365E-09	1.874E-08	1.025
^{102}Ru	102	44	1.770E-09	5.032E-13	9.825E-09	9.825E-09	4.925E-08	1.443
^{104}Ru	104	44	1.065E-09	3.028E-13	-4.869E-09	-4.869E-09	1.885E-08	0.918
^{103}Rh	103	45	1.055E-09	2.999E-13	-2.651E-09	-2.650E-09	2.084E-08	1.025
^{102}Pd	102	46	4.241E-11	1.206E-14	-2.284E-10	-2.284E-10	7.163E-10	0.876
^{104}Pd	104	46	4.723E-10	1.343E-13	6.559E-09	6.560E-09	1.708E-08	1.875
^{105}Pd	105	46	9.558E-10	2.718E-13	-3.157E-09	-3.157E-09	1.813E-08	0.984
^{106}Pd	106	46	1.181E-09	3.358E-13	4.962E-09	4.962E-09	3.127E-08	1.373
^{108}Pd	108	46	1.165E-09	3.312E-13	5.687E-09	5.687E-09	3.164E-08	1.408
^{110}Pd	110	46	5.255E-10	1.494E-13	-2.168E-09	-2.167E-09	9.539E-09	0.941
^{107}Ag	107	47	7.840E-10	2.229E-13	-2.109E-09	-2.109E-09	1.535E-08	1.015
^{109}Ag	109	47	7.420E-10	2.110E-13	2.560E-09	2.560E-09	1.909E-08	1.334
^{106}Cd	106	48	6.346E-11	1.804E-14	-3.348E-10	-3.348E-10	1.079E-09	0.881
^{108}Cd	108	48	4.604E-11	1.309E-14	8.070E-10	8.070E-10	1.832E-09	2.064
^{110}Cd	110	48	6.580E-10	1.871E-13	6.093E-09	6.093E-09	2.075E-08	1.635
^{111}Cd	111	48	6.805E-10	1.935E-13	-6.739E-10	-6.737E-10	1.448E-08	1.104
^{112}Cd	112	48	1.294E-09	3.680E-13	4.670E-09	4.670E-09	3.350E-08	1.342
^{113}Cd	113	48	6.614E-10	1.880E-13	-4.743E-10	-4.741E-10	1.426E-08	1.118
^{114}Cd	114	48	1.569E-09	4.460E-13	7.382E-09	7.382E-09	4.232E-08	1.399

TableC.8 – continued

Isotope	A	Z	$X^{\rm ini}$	$mp^{\rm wind}$	$mp^{\rm preSN}$	$mp^{\rm total}$	EM	$\langle OP \rangle$
^{116}Cd	116	48	4.161E-10	1.183E-13	-1.216E-09	-1.216E-09	8.053E-09	1.003
^{113}In	113	49	2.604E-11	7.403E-15	-1.213E-10	-1.213E-10	4.587E-10	0.913
^{115}In	115	49	5.915E-10	1.681E-13	-2.976E-10	-2.975E-10	1.288E-08	1.129
^{112}Sn	112	50	1.221E-10	3.472E-14	-6.209E-10	-6.209E-10	2.099E-09	0.891
^{114}Sn	114	50	8.435E-11	2.398E-14	-3.286E-10	-3.286E-10	1.550E-09	0.953
^{115}Sn	115	50	4.377E-11	1.250E-14	-1.532E-10	-1.532E-10	8.217E-10	0.973
^{116}Sn	116	50	1.893E-09	5.383E-13	8.772E-09	8.773E-09	5.094E-08	1.395
^{117}Sn	117	50	1.008E-09	2.867E-13	8.010E-10	8.013E-10	2.326E-08	1.196
^{118}Sn	118	50	3.209E-09	9.124E-13	1.066E-08	1.066E-08	8.215E-08	1.327
^{119}Sn	119	50	1.147E-09	3.261E-13	2.245E-09	2.245E-09	2.779E-08	1.256
^{120}Sn	120	50	4.391E-09	1.249E-12	1.834E-08	1.834E-08	1.162E-07	1.371
^{122}Sn	122	50	6.341E-10	1.803E-13	-1.447E-09	-1.447E-09	1.268E-08	1.037
^{124}Sn	124	50	8.060E-10	2.292E-13	-3.118E-09	-3.117E-09	1.483E-08	0.954
^{121}Sb	121	51	6.318E-10	1.796E-13	8.622E-11	8.640E-11	1.416E-08	1.162
^{123}Sb	123	51	4.803E-10	1.366E-13	-2.259E-09	-2.259E-09	8.439E-09	0.911
^{120}Te	120	52	1.628E-11	4.630E-15	-9.045E-11	-9.044E-11	2.723E-10	0.867
^{122}Te	122	52	4.489E-10	1.276E-13	2.953E-09	2.953E-09	1.295E-08	1.496
^{123}Te	123	52	1.579E-10	4.488E-14	9.686E-10	9.687E-10	4.485E-09	1.473
^{124}Te	124	52	8.441E-10	2.400E-13	5.581E-09	5.581E-09	2.438E-08	1.498
^{125}Te	125	52	1.261E-09	3.586E-13	-3.580E-09	-3.580E-09	2.452E-08	1.008
^{126}Te	126	52	3.375E-09	9.597E-13	3.407E-09	3.408E-09	7.859E-08	1.207
^{128}Te	128	52	5.733E-09	1.630E-12	-2.474E-08	-2.474E-08	1.030E-07	0.931
^{130}Te	130	52	6.211E-09	1.766E-12	-2.444E-08	-2.444E-08	1.139E-07	0.951
^{127}I	127	53	1.459E-09	4.149E-13	-4.939E-09	-4.939E-09	2.756E-08	0.979
^{124}Xe	124	54	2.210E-11	6.282E-15	-1.249E-10	-1.249E-10	3.673E-10	0.862
^{126}Xe	126	54	1.949E-11	5.542E-15	-1.038E-10	-1.038E-10	3.304E-10	0.879
^{128}Xe	128	54	3.943E-10	1.121E-13	4.840E-09	4.840E-09	1.362E-08	1.791
^{129}Xe	129	54	4.893E-09	1.391E-12	-2.444E-08	-2.444E-08	8.455E-08	0.896

TableC.8 – continued

Isotope	A	Z	$X^{\rm ini}$	$mp^{\rm wind}$	$mp^{\rm preSN}$	$mp^{\rm total}$	EM	$\langle OP \rangle$
^{130}Xe	130	54	7.865E-10	2.236E-13	1.332E-08	1.332E-08	3.084E-08	2.033
^{131}Xe	131	54	3.945E-09	1.122E-12	-1.475E-08	-1.475E-08	7.311E-08	0.961
^{132}Xe	132	54	4.806E-09	1.367E-12	7.471E-09	7.472E-09	1.145E-07	1.235
^{134}Xe	134	54	1.788E-09	5.084E-13	-6.447E-09	-6.446E-09	3.338E-08	0.968
^{136}Xe	136	54	1.478E-09	4.203E-13	-1.015E-09	-1.014E-09	3.192E-08	1.119
^{133}Cs	133	55	1.426E-09	4.055E-13	-3.129E-09	-3.128E-09	2.864E-08	1.041
^{130}Ba	130	56	1.814E-11	5.159E-15	-1.037E-10	-1.037E-10	3.005E-10	0.859
^{132}Ba	132	56	1.762E-11	5.010E-15	-9.473E-11	-9.473E-11	2.978E-10	0.876
^{134}Ba	134	56	4.272E-10	1.215E-13	8.711E-09	8.711E-09	1.823E-08	2.212
^{135}Ba	135	56	1.174E-09	3.338E-13	-1.854E-09	-1.854E-09	2.429E-08	1.073
^{136}Ba	136	56	1.409E-09	4.006E-13	2.210E-08	2.210E-08	5.348E-08	1.968
^{137}Ba	137	56	2.030E-09	5.771E-13	1.406E-08	1.406E-08	5.927E-08	1.514
^{138}Ba	138	56	1.305E-08	3.711E-12	1.912E-07	1.912E-07	4.820E-07	1.915
^{138}La	138	57	1.604E-12	4.561E-16	-8.743E-12	-8.742E-12	2.699E-11	0.872
^{139}La	139	57	1.790E-09	5.090E-13	2.238E-08	2.238E-08	6.226E-08	1.803
^{136}Ce	136	58	8.382E-12	2.383E-15	-4.425E-11	-4.424E-11	1.425E-10	0.881
^{138}Ce	138	58	1.148E-11	3.263E-15	-5.720E-11	-5.719E-11	1.985E-10	0.896
^{140}Ce	140	58	4.103E-09	1.167E-12	3.472E-08	3.472E-08	1.261E-07	1.594
^{142}Ce	142	58	5.229E-10	1.487E-13	-1.273E-09	-1.273E-09	1.037E-08	1.029
^{141}Pr	141	59	6.910E-10	1.965E-13	3.416E-09	3.416E-09	1.881E-08	1.411
^{142}Nd	142	60	9.920E-10	2.820E-13	7.911E-09	7.911E-09	3.001E-08	1.568
^{143}Nd	143	60	4.484E-10	1.275E-13	1.420E-11	1.433E-11	1.000E-08	1.157
^{144}Nd	144	60	8.826E-10	2.509E-13	1.719E-09	1.719E-09	2.138E-08	1.256
^{145}Nd	145	60	3.095E-10	8.801E-14	2.002E-11	2.010E-11	6.915E-09	1.158
^{146}Nd	146	60	6.448E-10	1.833E-13	1.676E-09	1.676E-09	1.604E-08	1.290
^{148}Nd	148	60	2.185E-10	6.213E-14	-7.152E-10	-7.152E-10	4.152E-09	0.985
^{150}Nd	150	60	2.168E-10	6.165E-14	-1.088E-09	-1.088E-09	3.742E-09	0.895
^{144}Sm	144	62	3.684E-11	1.047E-14	-1.727E-10	-1.727E-10	6.478E-10	0.912

TableC.8 – continued

Isotope	A	Z	$X^{\rm ini}$	$mp^{\rm wind}$	$mp^{\rm preSN}$	$mp^{\rm total}$	EM	$\langle OP \rangle$
^{147}Sm	147	62	1.834E-10	5.216E-14	-2.641E-10	-2.640E-10	3.822E-09	1.080
^{148}Sm	148	62	1.385E-10	3.937E-14	5.732E-10	5.732E-10	3.657E-09	1.369
^{149}Sm	149	62	1.714E-10	4.873E-14	-6.795E-10	-6.795E-10	3.138E-09	0.949
^{150}Sm	150	62	9.213E-11	2.620E-14	6.316E-10	6.317E-10	2.684E-09	1.510
^{152}Sm	152	62	3.383E-10	9.619E-14	-1.078E-09	-1.078E-09	6.458E-09	0.990
^{154}Sm	154	62	2.916E-10	8.292E-14	-1.377E-09	-1.377E-09	5.118E-09	0.910
^{151}Eu	151	63	2.036E-10	5.789E-14	-9.946E-10	-9.945E-10	3.541E-09	0.902
^{153}Eu	153	63	2.252E-10	6.403E-14	-1.039E-09	-1.039E-09	3.977E-09	0.916
^{152}Gd	152	64	2.947E-12	8.382E-16	1.459E-10	1.459E-10	2.115E-10	3.721
^{154}Gd	154	64	3.210E-11	9.126E-15	4.228E-10	4.228E-10	1.138E-09	1.838
^{155}Gd	155	64	2.192E-10	6.233E-14	-9.841E-10	-9.840E-10	3.899E-09	0.922
^{156}Gd	156	64	3.051E-10	8.675E-14	-5.597E-10	-5.596E-10	6.237E-09	1.060
^{157}Gd	157	64	2.348E-10	6.677E-14	-6.864E-10	-6.863E-10	4.544E-09	1.003
^{158}Gd	158	64	3.750E-10	1.066E-13	-1.698E-10	-1.697E-10	8.183E-09	1.131
^{160}Gd	160	64	3.343E-10	9.505E-14	-1.589E-09	-1.589E-09	5.857E-09	0.908
^{159}Tb	159	65	2.765E-10	7.861E-14	-1.118E-09	-1.118E-09	5.041E-09	0.945
^{156}Dy	156	66	1.004E-12	2.854E-16	-5.978E-12	-5.978E-12	1.638E-11	0.846
^{158}Dy	158	66	1.743E-12	4.955E-16	1.169E-11	1.169E-11	5.051E-11	1.503
^{160}Dy	160	66	4.301E-11	1.223E-14	4.919E-10	4.919E-10	1.450E-09	1.748
^{161}Dy	161	66	3.498E-10	9.945E-14	-1.610E-09	-1.610E-09	6.181E-09	0.916
^{162}Dy	162	66	4.748E-10	1.350E-13	-1.097E-09	-1.097E-09	9.479E-09	1.035
^{163}Dy	163	66	4.663E-10	1.326E-13	-1.882E-09	-1.882E-09	8.505E-09	0.946
^{164}Dy	164	66	5.312E-10	1.510E-13	1.268E-10	1.269E-10	1.196E-08	1.167
^{165}Ho	165	67	4.244E-10	1.207E-13	-1.865E-09	-1.865E-09	7.588E-09	0.927
^{162}Er	162	68	1.609E-12	4.574E-16	-9.576E-12	-9.575E-12	2.626E-11	0.846
^{164}Er	164	68	1.913E-11	5.439E-15	-1.122E-10	-1.122E-10	3.139E-10	0.851
^{166}Er	166	68	4.044E-10	1.150E-13	-1.125E-09	-1.125E-09	7.884E-09	1.011
^{167}Er	167	68	2.776E-10	7.893E-14	-1.042E-09	-1.042E-09	5.141E-09	0.960

TableC.8 – continued

Isotope	A	Z	$X^{\rm ini}$	$mp^{\rm wind}$	$mp^{\rm preSN}$	$mp^{\rm total}$	EM	$\langle OP \rangle$
^{168}Er	168	68	3.263E-10	9.276E-14	1.381E-10	1.381E-10	7.405E-09	1.177
^{170}Er	170	68	1.840E-10	5.231E-14	-5.383E-10	-5.382E-10	3.560E-09	1.003
^{169}Tm	169	69	1.854E-10	5.272E-14	-6.156E-10	-6.155E-10	3.515E-09	0.983
^{168}Yb	168	70	1.583E-12	4.501E-16	-9.334E-12	-9.334E-12	2.593E-11	0.849
^{170}Yb	170	70	3.746E-11	1.065E-14	3.771E-10	3.771E-10	1.212E-09	1.677
^{171}Yb	171	70	1.770E-10	5.033E-14	-5.498E-10	-5.498E-10	3.393E-09	0.994
^{172}Yb	172	70	2.722E-10	7.739E-14	8.331E-11	8.339E-11	6.146E-09	1.171
^{173}Yb	173	70	2.023E-10	5.751E-14	-2.235E-10	-2.234E-10	4.282E-09	1.098
^{174}Yb	174	70	4.015E-10	1.142E-13	8.538E-10	8.539E-10	9.797E-09	1.265
^{176}Yb	176	70	1.628E-10	4.629E-14	-6.533E-10	-6.532E-10	2.973E-09	0.947
^{175}Lu	175	71	1.828E-10	5.197E-14	-5.470E-10	-5.470E-10	3.525E-09	1.000
^{176}Lu	176	71	4.876E-12	-3.864E-15	6.504E-11	6.503E-11	1.737E-10	1.846
^{174}Hf	174	72	1.231E-12	3.501E-16	-7.154E-12	-7.154E-12	2.027E-11	0.854
^{176}Hf	176	72	4.036E-11	1.673E-14	3.311E-10	3.311E-10	1.230E-09	1.580
^{177}Hf	177	72	1.438E-10	4.088E-14	-4.490E-10	-4.490E-10	2.754E-09	0.993
^{178}Hf	178	72	2.121E-10	6.031E-14	3.047E-10	3.048E-10	5.030E-09	1.229
^{179}Hf	179	72	1.065E-10	3.028E-14	-1.356E-11	-1.353E-11	2.359E-09	1.148
^{180}Hf	180	72	2.758E-10	7.843E-14	1.050E-09	1.050E-09	7.194E-09	1.352
^{180}Ta	180	73	2.429E-14	6.905E-18	6.983E-12	6.983E-12	7.525E-12	16.060
^{181}Ta	181	73	1.986E-10	5.646E-14	-4.354E-10	-4.354E-10	3.988E-09	1.041
^{180}W	180	74	8.395E-13	2.387E-16	3.106E-11	3.106E-11	4.976E-11	3.073
^{182}W	182	74	1.877E-10	5.338E-14	1.280E-10	1.281E-10	4.310E-09	1.190
^{183}W	183	74	1.020E-10	2.899E-14	2.986E-10	2.986E-10	2.570E-09	1.307
^{184}W	184	74	2.195E-10	6.241E-14	6.753E-10	6.753E-10	5.564E-09	1.314
^{186}W	186	74	2.058E-10	5.852E-14	-5.314E-10	-5.313E-10	4.053E-09	1.021
^{185}Re	185	75	1.048E-10	2.979E-14	-6.955E-11	-6.952E-11	2.265E-09	1.120
^{187}Re	187	75	1.773E-10	5.041E-14	-8.056E-10	-8.056E-10	3.144E-09	0.919
^{184}Os	184	76	7.108E-13	2.021E-16	-4.001E-12	-4.001E-12	1.183E-11	0.863

TableC.8 – continued

Isotope	A	Z	$X^{\rm ini}$	$mp^{\rm wind}$	$mp^{\rm preSN}$	$mp^{\rm total}$	EM	$\langle OP \rangle$
^{186}Os	186	76	5.778E-11	1.643E-14	3.901E-10	3.902E-10	1.677E-09	1.505
^{187}Os	187	76	5.998E-11	1.705E-14	-6.950E-11	-6.949E-11	1.267E-09	1.095
^{188}Os	188	76	4.874E-10	1.386E-13	-1.068E-09	-1.068E-09	9.788E-09	1.041
^{189}Os	189	76	5.974E-10	1.698E-13	-3.015E-09	-3.015E-09	1.029E-08	0.893
^{190}Os	190	76	9.766E-10	2.777E-13	-2.876E-09	-2.876E-09	1.888E-08	1.002
^{192}Os	192	76	1.533E-09	4.358E-13	-7.140E-09	-7.140E-09	2.700E-08	0.913
^{191}Ir	191	77	1.357E-09	3.859E-13	-7.488E-09	-7.488E-09	2.275E-08	0.869
^{193}Ir	193	77	2.308E-09	6.563E-13	-1.238E-08	-1.238E-08	3.904E-08	0.877
^{190}Pt	190	78	1.008E-12	2.867E-16	-5.589E-12	-5.589E-12	1.687E-11	0.868
^{192}Pt	192	78	5.850E-11	1.663E-14	1.225E-09	1.225E-09	2.528E-09	2.240
^{194}Pt	194	78	2.490E-09	7.079E-13	-9.126E-09	-9.125E-09	4.633E-08	0.965
^{195}Pt	195	78	2.568E-09	7.302E-13	-1.257E-08	-1.257E-08	4.463E-08	0.901
^{196}Pt	196	78	1.926E-09	5.476E-13	-2.042E-09	-2.041E-09	4.086E-08	1.100
^{198}Pt	198	78	5.522E-10	1.570E-13	-2.550E-09	-2.549E-09	9.750E-09	0.915
^{197}Au	197	79	1.083E-09	3.080E-13	-3.777E-09	-3.776E-09	2.035E-08	0.974
^{196}Hg	196	80	3.009E-12	8.556E-16	-1.526E-11	-1.526E-11	5.177E-11	0.892
^{198}Hg	198	80	1.975E-10	5.615E-14	3.940E-09	3.941E-09	8.340E-09	2.189
^{199}Hg	199	80	3.360E-10	9.553E-14	2.773E-10	2.774E-10	7.761E-09	1.198
^{200}Hg	200	80	4.622E-10	1.314E-13	2.545E-09	2.545E-09	1.284E-08	1.440
^{201}Hg	201	80	2.651E-10	7.538E-14	1.238E-09	1.238E-09	7.143E-09	1.397
^{202}Hg	202	80	6.036E-10	1.716E-13	5.559E-09	5.559E-09	1.900E-08	1.632
^{204}Hg	204	80	1.401E-10	3.984E-14	-5.442E-10	-5.441E-10	2.577E-09	0.954
^{203}Tl	203	81	3.221E-10	9.157E-14	4.855E-09	4.855E-09	1.203E-08	1.936
^{205}Tl	205	81	7.764E-10	2.207E-13	7.192E-09	7.192E-09	2.449E-08	1.635
^{204}Pb	204	82	2.931E-10	8.334E-14	5.615E-09	5.615E-09	1.214E-08	2.148
^{206}Pb	206	82	2.798E-09	7.955E-13	3.512E-08	3.512E-08	9.744E-08	1.806
^{207}Pb	207	82	3.090E-09	8.785E-13	5.038E-08	5.038E-08	1.192E-07	2.000
^{208}Pb	208	82	8.850E-09	2.516E-12	5.316E-08	5.317E-08	2.503E-07	1.466

TableC.8 – continued

Isotope	A	Z	X^{ini}	mp^{wind}	mp^{preSN}	mp^{total}	EM	$\langle OP \rangle$
^{209}Bi	209	83	8.718E-10	2.479E-13	1.732E-09	1.732E-09	2.115E-08	1.258

Table C.9: Yields for model 25CU.

Isotope	A	Z	X^{ini}	mp^{wind}	mp^{preSN}	mp^{total}	EM	$\langle OP \rangle$
^{1}H	1	1	7.064E-01	-8.903E-01	-5.494E+00	-6.385E+00	9.351E+00	0.686
^{2}H	2	1	1.371E-05	-1.458E-04	-1.436E-04	-2.894E-04	1.588E-05	0.060
^{3}He	3	2	4.540E-05	-1.013E-04	-4.647E-04	-5.660E-04	4.452E-04	0.508
^{4}He	4	2	2.735E-01	8.917E-01	1.079E+00	1.971E+00	8.063E+00	1.528
^{7}Li	7	3	7.605E-11	-8.093E-10	-7.966E-10	-1.606E-09	8.813E-11	0.060
^{11}B	11	5	2.856E-09	9.361E-13	4.749E-11	4.842E-11	6.366E-08	1.156
^{12}C	12	6	3.425E-03	-1.336E-02	3.895E-01	3.761E-01	4.524E-01	6.849
^{13}C	13	6	4.156E-05	5.138E-04	-2.565E-04	2.573E-04	1.183E-03	1.476
^{14}N	14	7	1.059E-03	3.628E-02	3.308E-02	6.936E-02	9.294E-02	4.551
^{15}N	15	7	4.171E-06	-2.427E-05	-3.428E-05	-5.854E-05	3.436E-05	0.427
^{16}O	16	8	9.624E-03	-2.418E-02	2.577E+00	2.553E+00	2.767E+00	14.908
^{17}O	17	8	3.813E-06	6.003E-06	1.056E-04	1.116E-04	1.966E-04	2.673
^{18}O	18	8	2.171E-05	-8.078E-05	4.734E-03	4.654E-03	5.137E-03	12.268
^{19}F	19	9	5.611E-07	-1.766E-06	-3.322E-06	-5.087E-06	7.411E-06	0.685
^{20}Ne	20	10	1.818E-03	-6.517E-05	1.065E+00	1.065E+00	1.106E+00	31.535
^{21}Ne	21	10	4.575E-06	4.111E-05	8.723E-03	8.765E-03	8.866E-03	100.473
^{22}Ne	22	10	1.470E-04	-4.109E-04	5.158E-02	5.117E-02	5.444E-02	19.198
^{23}Na	23	11	4.000E-05	4.600E-04	1.045E-01	1.050E-01	1.059E-01	137.237
^{24}Mg	24	12	5.862E-04	3.943E-07	8.417E-02	8.417E-02	9.723E-02	8.598
^{25}Mg	25	12	7.733E-05	-1.666E-04	3.921E-02	3.904E-02	4.077E-02	27.332
^{26}Mg	26	12	8.848E-05	1.707E-04	4.721E-02	4.739E-02	4.936E-02	28.921
^{27}Al	27	13	6.481E-05	2.692E-06	1.991E-02	1.991E-02	2.135E-02	17.081
^{28}Si	28	14	7.453E-04	2.498E-07	4.610E-03	4.610E-03	2.121E-02	1.476
^{29}Si	29	14	3.919E-05	1.244E-08	9.182E-04	9.182E-04	1.791E-03	2.369
^{30}Si	30	14	2.673E-05	-2.440E-08	1.484E-03	1.484E-03	2.079E-03	4.034
^{31}P	31	15	7.106E-06	3.703E-08	5.570E-04	5.570E-04	7.153E-04	5.219
^{32}S	32	16	4.011E-04	1.312E-07	-9.463E-04	-9.462E-04	7.988E-03	1.033

TableC.9 – continued

Isotope	A	Z	$X^{\rm ini}$	$mp^{\rm wind}$	$mp^{\rm preSN}$	$mp^{\rm total}$	EM	$\langle OP \rangle$
^{33}S	33	16	3.265E-06	1.314E-09	1.653E-05	1.654E-05	8.926E-05	1.417
^{34}S	34	16	1.890E-05	6.196E-09	5.801E-05	5.802E-05	4.791E-04	1.314
^{36}S	36	16	8.073E-08	2.646E-11	2.889E-05	2.889E-05	3.069E-05	19.711
^{35}Cl	35	17	6.821E-06	2.236E-09	-2.047E-05	-2.046E-05	1.315E-04	0.999
^{37}Cl	37	17	2.306E-06	7.558E-10	2.388E-04	2.388E-04	2.901E-04	6.524
^{36}Ar	36	18	8.202E-05	2.689E-08	-3.057E-04	-3.057E-04	1.521E-03	0.962
^{38}Ar	38	18	1.574E-05	5.160E-09	1.491E-04	1.491E-04	4.998E-04	1.646
^{40}Ar	40	18	2.650E-08	8.693E-12	1.448E-05	1.448E-05	1.507E-05	29.478
^{39}K	39	19	3.900E-06	1.278E-09	3.491E-05	3.491E-05	1.218E-04	1.619
^{40}K	40	19	5.005E-10	-1.575E-11	7.149E-06	7.149E-06	7.161E-06	741.740
^{41}K	41	19	2.959E-07	9.698E-11	1.408E-05	1.408E-05	2.067E-05	3.623
^{40}Ca	40	20	7.225E-05	2.370E-08	-2.370E-04	-2.370E-04	1.372E-03	0.985
^{42}Ca	42	20	5.063E-07	1.660E-10	1.755E-05	1.755E-05	2.882E-05	2.952
^{43}Ca	43	20	1.082E-07	3.545E-11	6.424E-06	6.424E-06	8.833E-06	4.234
^{44}Ca	44	20	1.710E-06	5.606E-10	1.892E-05	1.892E-05	5.702E-05	1.729
^{46}Ca	46	20	3.428E-09	1.124E-12	3.466E-08	3.466E-08	1.110E-07	1.679
^{48}Ca	48	20	1.672E-07	5.482E-11	-1.570E-07	-1.569E-07	3.568E-06	1.106
^{45}Sc	45	21	5.414E-08	1.775E-11	4.776E-06	4.776E-06	5.982E-06	5.729
^{46}Ti	46	22	3.232E-07	1.059E-10	5.953E-06	5.953E-06	1.315E-05	2.110
^{47}Ti	47	22	2.977E-07	9.758E-11	2.607E-06	2.607E-06	9.238E-06	1.609
^{48}Ti	48	22	3.014E-06	9.879E-10	-6.027E-06	-6.026E-06	6.110E-05	1.051
^{49}Ti	49	22	2.257E-07	7.399E-11	8.310E-06	8.310E-06	1.334E-05	3.063
^{50}Ti	50	22	2.208E-07	7.237E-11	2.615E-05	2.615E-05	3.107E-05	7.295
^{50}V	50	23	1.015E-09	3.329E-13	-3.135E-09	-3.134E-09	1.949E-08	0.995
^{51}V	51	23	4.138E-07	1.356E-10	1.434E-06	1.434E-06	1.065E-05	1.335
^{50}Cr	50	24	8.265E-07	2.709E-10	-3.853E-06	-3.853E-06	1.456E-05	0.913
^{52}Cr	52	24	1.658E-05	5.433E-09	-5.155E-05	-5.155E-05	3.177E-04	0.994
^{53}Cr	53	24	1.916E-06	6.279E-10	-4.562E-06	-4.561E-06	3.811E-05	1.031

TableC.9 – continued

Isotope	A	Z	$X^{\rm ini}$	$mp^{\rm wind}$	$mp^{\rm preSN}$	$mp^{\rm total}$	EM	$\langle OP \rangle$
^{54}Cr	54	24	4.858E-07	1.592E-10	2.700E-05	2.700E-05	3.783E-05	4.037
^{55}Mn	55	25	1.098E-05	3.599E-09	-2.267E-05	-2.267E-05	2.219E-04	1.048
^{54}Fe	54	26	8.118E-05	2.661E-08	-3.668E-04	-3.668E-04	1.442E-03	0.921
^{56}Fe	56	26	1.322E-03	4.332E-07	-4.909E-03	-4.908E-03	2.453E-02	0.962
^{57}Fe	57	26	3.107E-05	1.018E-08	1.865E-04	1.865E-04	8.785E-04	1.466
^{58}Fe	58	26	4.207E-06	1.379E-09	9.698E-04	9.698E-04	1.064E-03	13.107
^{59}Co	59	27	3.991E-06	1.308E-09	3.857E-04	3.857E-04	4.746E-04	6.165
^{58}Ni	58	28	5.711E-05	1.872E-08	-2.549E-04	-2.548E-04	1.017E-03	0.923
^{60}Ni	60	28	2.276E-05	7.459E-09	3.326E-04	3.326E-04	8.395E-04	1.913
^{61}Ni	61	28	1.006E-06	3.297E-10	1.777E-04	1.777E-04	2.001E-04	10.317
^{62}Ni	62	28	3.259E-06	1.068E-09	5.318E-04	5.318E-04	6.044E-04	9.614
^{64}Ni	64	28	8.568E-07	2.808E-10	4.607E-04	4.607E-04	4.798E-04	29.031
^{63}Cu	63	29	6.600E-07	2.163E-10	2.041E-04	2.041E-04	2.188E-04	17.189
^{65}Cu	65	29	3.035E-07	9.947E-11	3.471E-04	3.471E-04	3.539E-04	60.454
^{64}Zn	64	30	1.131E-06	3.706E-10	1.156E-04	1.156E-04	1.408E-04	6.454
^{66}Zn	66	30	6.690E-07	2.193E-10	2.882E-04	2.882E-04	3.031E-04	23.489
^{67}Zn	67	30	9.980E-08	3.271E-11	8.849E-05	8.849E-05	9.071E-05	47.124
^{68}Zn	68	30	4.632E-07	1.518E-10	5.219E-04	5.219E-04	5.322E-04	59.571
^{70}Zn	70	30	1.577E-08	5.168E-12	8.578E-08	8.579E-08	4.370E-07	1.437
^{69}Ga	69	31	4.551E-08	1.492E-11	7.013E-05	7.013E-05	7.114E-05	81.052
^{71}Ga	71	31	3.108E-08	1.019E-11	8.033E-05	8.033E-05	8.102E-05	135.175
^{70}Ge	70	32	5.157E-08	1.690E-11	1.082E-04	1.082E-04	1.093E-04	109.899
^{72}Ge	72	32	6.910E-08	2.265E-11	1.252E-04	1.252E-04	1.267E-04	95.096
^{73}Ge	73	32	1.955E-08	6.407E-12	5.265E-05	5.265E-05	5.309E-05	140.817
^{74}Ge	74	32	9.228E-08	3.025E-11	2.309E-04	2.309E-04	2.330E-04	130.891
^{76}Ge	76	32	1.963E-08	6.434E-12	-1.539E-08	-1.538E-08	4.219E-07	1.114
^{75}As	75	33	1.430E-08	4.687E-12	2.754E-05	2.754E-05	2.786E-05	101.009
^{74}Se	74	34	1.198E-09	3.926E-13	-6.322E-09	-6.322E-09	2.036E-08	0.881

TableC.9 – continued

Isotope	A	Z	$X^{\rm ini}$	$mp^{\rm wind}$	$mp^{\rm preSN}$	$mp^{\rm total}$	EM	$\langle OP \rangle$
^{76}Se	76	34	1.296E-08	4.248E-12	4.747E-05	4.747E-05	4.776E-05	191.050
^{77}Se	77	34	1.070E-08	3.509E-12	2.349E-05	2.349E-05	2.373E-05	114.913
^{78}Se	78	34	3.376E-08	1.107E-11	1.373E-04	1.373E-04	1.381E-04	212.021
^{80}Se	80	34	7.226E-08	2.369E-11	1.875E-05	1.875E-05	2.036E-05	14.606
^{82}Se	82	34	1.304E-08	4.273E-12	-4.702E-08	-4.701E-08	2.434E-07	0.968
^{79}Br	79	35	1.389E-08	4.554E-12	1.931E-05	1.931E-05	1.962E-05	73.214
^{81}Br	81	35	1.386E-08	4.543E-12	1.931E-05	1.931E-05	1.962E-05	73.382
^{78}Kr	78	36	3.900E-10	1.278E-13	-2.033E-09	-2.033E-09	6.654E-09	0.885
^{80}Kr	80	36	2.575E-09	8.440E-13	2.465E-05	2.465E-05	2.471E-05	497.492
^{82}Kr	82	36	1.320E-08	4.325E-12	8.521E-05	8.521E-05	8.551E-05	335.959
^{83}Kr	83	36	1.324E-08	4.340E-12	4.112E-05	4.112E-05	4.142E-05	162.173
^{84}Kr	84	36	6.602E-08	2.164E-11	2.141E-04	2.141E-04	2.156E-04	169.306
^{86}Kr	86	36	2.044E-08	6.701E-12	9.817E-06	9.817E-06	1.027E-05	26.052
^{85}Rb	85	37	1.282E-08	4.204E-12	3.680E-05	3.680E-05	3.709E-05	149.935
^{87}Rb	87	37	5.063E-09	-3.129E-12	1.350E-05	1.350E-05	1.362E-05	139.440
^{84}Sr	84	38	3.228E-10	1.058E-13	-1.757E-09	-1.756E-09	5.434E-09	0.873
^{86}Sr	86	38	5.845E-09	1.916E-12	9.996E-05	9.996E-05	1.001E-04	887.922
^{87}Sr	87	38	4.443E-09	6.245E-12	6.710E-05	6.710E-05	6.720E-05	784.095
^{88}Sr	88	38	5.011E-08	1.642E-11	3.656E-04	3.656E-04	3.667E-04	379.406
^{89}Y	89	39	1.229E-08	4.030E-12	7.280E-05	7.280E-05	7.308E-05	308.197
^{90}Zr	90	40	1.534E-08	5.029E-12	4.014E-05	4.014E-05	4.048E-05	136.796
^{91}Zr	91	40	3.384E-09	1.109E-12	1.218E-05	1.218E-05	1.225E-05	187.734
^{92}Zr	92	40	5.227E-09	1.713E-12	1.422E-05	1.422E-05	1.434E-05	142.249
^{94}Zr	94	40	5.413E-09	1.774E-12	5.893E-06	5.893E-06	6.013E-06	57.593
^{96}Zr	96	40	8.903E-10	2.918E-13	1.248E-07	1.248E-07	1.446E-07	8.423
^{93}Nb	93	41	1.900E-09	6.228E-13	5.072E-06	5.072E-06	5.114E-06	139.540
^{92}Mo	92	42	1.012E-09	3.319E-13	-4.813E-09	-4.812E-09	1.774E-08	0.908
^{94}Mo	94	42	6.448E-10	2.113E-13	9.106E-08	9.106E-08	1.054E-07	8.477

TableC.9 – continued

Isotope	A	Z	$X^{\rm ini}$	$mp^{\rm wind}$	$mp^{\rm preSN}$	$mp^{\rm total}$	EM	$\langle OP \rangle$
^{95}Mo	95	42	1.122E-09	3.677E-13	1.096E-06	1.096E-06	1.121E-06	51.823
^{96}Mo	96	42	1.188E-09	3.892E-13	2.023E-06	2.023E-06	2.050E-06	89.497
^{97}Mo	97	42	6.875E-10	2.254E-13	7.433E-07	7.433E-07	7.586E-07	57.209
^{98}Mo	98	42	1.754E-09	5.750E-13	1.939E-06	1.939E-06	1.978E-06	58.455
^{100}Mo	100	42	7.146E-10	2.342E-13	-2.380E-09	-2.379E-09	1.354E-08	0.982
^{96}Ru	96	44	2.926E-10	9.590E-14	-1.500E-09	-1.500E-09	5.017E-09	0.889
^{98}Ru	98	44	1.007E-10	3.301E-14	-4.104E-10	-4.104E-10	1.833E-09	0.944
^{99}Ru	99	44	6.945E-10	2.277E-13	3.357E-07	3.357E-07	3.511E-07	26.212
^{100}Ru	100	44	6.928E-10	2.271E-13	8.357E-07	8.357E-07	8.511E-07	63.696
^{101}Ru	101	44	9.475E-10	3.106E-13	1.829E-07	1.829E-07	2.040E-07	11.163
^{102}Ru	102	44	1.770E-09	5.801E-13	1.083E-06	1.083E-06	1.123E-06	32.897
^{104}Ru	104	44	1.065E-09	3.491E-13	2.492E-09	2.493E-09	2.621E-08	1.276
^{103}Rh	103	45	1.055E-09	3.457E-13	1.715E-07	1.715E-07	1.950E-07	9.584
^{102}Pd	102	46	4.241E-11	1.390E-14	-2.311E-10	-2.311E-10	7.136E-10	0.872
^{104}Pd	104	46	4.723E-10	1.548E-13	4.734E-07	4.734E-07	4.839E-07	53.121
^{105}Pd	105	46	9.558E-10	3.133E-13	1.049E-07	1.049E-07	1.262E-07	6.845
^{106}Pd	106	46	1.181E-09	3.871E-13	5.401E-07	5.401E-07	5.664E-07	24.867
^{108}Pd	108	46	1.165E-09	3.818E-13	4.727E-07	4.727E-07	4.986E-07	22.192
^{110}Pd	110	46	5.255E-10	1.723E-13	2.272E-09	2.272E-09	1.398E-08	1.379
^{107}Ag	107	47	7.840E-10	2.570E-13	1.033E-07	1.033E-07	1.208E-07	7.986
^{109}Ag	109	47	7.420E-10	2.432E-13	2.735E-07	2.735E-07	2.900E-07	20.265
^{106}Cd	106	48	6.346E-11	2.080E-14	-3.390E-10	-3.390E-10	1.075E-09	0.878
^{108}Cd	108	48	4.604E-11	1.509E-14	1.160E-07	1.160E-07	1.171E-07	131.827
^{110}Cd	110	48	6.580E-10	2.157E-13	4.309E-07	4.309E-07	4.456E-07	35.109
^{111}Cd	111	48	6.805E-10	2.230E-13	1.269E-07	1.269E-07	1.420E-07	10.820
^{112}Cd	112	48	1.294E-09	4.243E-13	4.844E-07	4.844E-07	5.133E-07	20.559
^{113}Cd	113	48	6.614E-10	2.168E-13	1.255E-07	1.255E-07	1.402E-07	10.994
^{114}Cd	114	48	1.569E-09	5.142E-13	6.170E-07	6.170E-07	6.519E-07	21.547

TableC.9 – continued

Isotope	A	Z	$X^{\rm ini}$	$mp^{\rm wind}$	$mp^{\rm preSN}$	$mp^{\rm total}$	EM	$\langle OP \rangle$
^{116}Cd	116	48	4.161E-10	1.364E-13	5.577E-09	5.577E-09	1.485E-08	1.850
^{113}In	113	49	2.604E-11	8.535E-15	-1.234E-10	-1.234E-10	4.566E-10	0.909
^{115}In	115	49	5.915E-10	1.938E-13	1.048E-07	1.048E-07	1.180E-07	10.343
^{112}Sn	112	50	1.221E-10	4.002E-14	-6.295E-10	-6.295E-10	2.090E-09	0.888
^{114}Sn	114	50	8.435E-11	2.765E-14	-3.372E-10	-3.372E-10	1.542E-09	0.948
^{115}Sn	115	50	4.377E-11	1.441E-14	1.056E-08	1.056E-08	1.154E-08	13.665
^{116}Sn	116	50	1.893E-09	6.205E-13	6.667E-07	6.667E-07	7.088E-07	19.412
^{117}Sn	117	50	1.008E-09	3.305E-13	2.022E-07	2.022E-07	2.246E-07	11.551
^{118}Sn	118	50	3.209E-09	1.052E-12	7.434E-07	7.434E-07	8.149E-07	13.165
^{119}Sn	119	50	1.147E-09	3.760E-13	2.039E-07	2.039E-07	2.295E-07	10.373
^{120}Sn	120	50	4.391E-09	1.439E-12	7.140E-07	7.140E-07	8.118E-07	9.585
^{122}Sn	122	50	6.341E-10	2.078E-13	3.283E-09	3.283E-09	1.741E-08	1.423
^{124}Sn	124	50	8.060E-10	2.642E-13	-3.278E-09	-3.278E-09	1.467E-08	0.944
^{121}Sb	121	51	6.318E-10	2.071E-13	5.294E-08	5.294E-08	6.701E-08	5.499
^{123}Sb	123	51	4.803E-10	1.574E-13	-1.437E-09	-1.437E-09	9.261E-09	1.000
^{120}Te	120	52	1.628E-11	5.337E-15	-9.144E-11	-9.143E-11	2.713E-10	0.864
^{122}Te	122	52	4.489E-10	1.471E-13	7.997E-08	7.997E-08	8.996E-08	10.391
^{123}Te	123	52	1.579E-10	5.174E-14	2.665E-08	2.665E-08	3.017E-08	9.908
^{124}Te	124	52	8.441E-10	2.767E-13	1.383E-07	1.383E-07	1.571E-07	9.648
^{125}Te	125	52	1.261E-09	4.134E-13	3.721E-08	3.721E-08	6.531E-08	2.684
^{126}Te	126	52	3.375E-09	1.106E-12	2.055E-07	2.055E-07	2.807E-07	4.311
^{128}Te	128	52	5.733E-09	1.879E-12	-2.355E-08	-2.355E-08	1.041E-07	0.942
^{130}Te	130	52	6.211E-09	2.036E-12	-2.544E-08	-2.543E-08	1.129E-07	0.943
^{127}I	127	53	1.459E-09	4.783E-13	2.406E-08	2.406E-08	5.656E-08	2.010
^{124}Xe	124	54	2.210E-11	7.242E-15	-1.262E-10	-1.262E-10	3.660E-10	0.859
^{126}Xe	126	54	1.949E-11	6.389E-15	-1.051E-10	-1.051E-10	3.291E-10	0.875
^{128}Xe	128	54	3.943E-10	1.292E-13	5.729E-08	5.729E-08	6.607E-08	8.688
^{129}Xe	129	54	4.893E-09	1.604E-12	-3.386E-09	-3.384E-09	1.056E-07	1.119

TableC.9 – continued

Isotope	A	Z	$X^{\rm ini}$	$mp^{\rm wind}$	$mp^{\rm preSN}$	$mp^{\rm total}$	EM	$\langle OP \rangle$
^{130}Xe	130	54	7.865E-10	2.578E-13	1.044E-07	1.044E-07	1.219E-07	8.035
^{131}Xe	131	54	3.945E-09	1.293E-12	2.174E-08	2.174E-08	1.096E-07	1.441
^{132}Xe	132	54	4.806E-09	1.575E-12	1.500E-07	1.500E-07	2.571E-07	2.773
^{134}Xe	134	54	1.788E-09	5.861E-13	-6.060E-09	-6.059E-09	3.377E-08	0.979
^{136}Xe	136	54	1.478E-09	4.846E-13	-1.456E-09	-1.455E-09	3.148E-08	1.104
^{133}Cs	133	55	1.426E-09	4.674E-13	1.816E-08	1.816E-08	4.993E-08	1.815
^{130}Ba	130	56	1.814E-11	5.947E-15	-1.047E-10	-1.047E-10	2.994E-10	0.856
^{132}Ba	132	56	1.762E-11	5.776E-15	-9.590E-11	-9.590E-11	2.966E-10	0.873
^{134}Ba	134	56	4.272E-10	1.400E-13	5.093E-08	5.094E-08	6.045E-08	7.336
^{135}Ba	135	56	1.174E-09	3.848E-13	1.509E-08	1.509E-08	4.124E-08	1.821
^{136}Ba	136	56	1.409E-09	4.618E-13	1.175E-07	1.175E-07	1.489E-07	5.480
^{137}Ba	137	56	2.030E-09	6.653E-13	7.640E-08	7.640E-08	1.216E-07	3.106
^{138}Ba	138	56	1.305E-08	4.278E-12	4.252E-07	4.252E-07	7.160E-07	2.844
^{138}La	138	57	1.604E-12	5.258E-16	-8.847E-12	-8.846E-12	2.688E-11	0.869
^{139}La	139	57	1.790E-09	5.868E-13	4.371E-08	4.372E-08	8.359E-08	2.421
^{136}Ce	136	58	8.382E-12	2.747E-15	-4.476E-11	-4.476E-11	1.419E-10	0.878
^{138}Ce	138	58	1.148E-11	3.762E-15	-5.803E-11	-5.802E-11	1.976E-10	0.893
^{140}Ce	140	58	4.103E-09	1.345E-12	7.360E-08	7.360E-08	1.650E-07	2.085
^{142}Ce	142	58	5.229E-10	1.714E-13	-2.030E-09	-2.029E-09	9.619E-09	0.954
^{141}Pr	141	59	6.910E-10	2.265E-13	7.420E-09	7.420E-09	2.281E-08	1.712
^{142}Nd	142	60	9.920E-10	3.252E-13	1.949E-08	1.949E-08	4.159E-08	2.174
^{143}Nd	143	60	4.484E-10	1.470E-13	1.713E-09	1.713E-09	1.170E-08	1.353
^{144}Nd	144	60	8.826E-10	2.893E-13	6.019E-09	6.019E-09	2.568E-08	1.508
^{145}Nd	145	60	3.095E-10	1.015E-13	1.160E-09	1.160E-09	8.055E-09	1.349
^{146}Nd	146	60	6.448E-10	2.113E-13	5.271E-09	5.271E-09	1.963E-08	1.579
^{148}Nd	148	60	2.185E-10	7.162E-14	-9.179E-10	-9.178E-10	3.949E-09	0.937
^{150}Nd	150	60	2.168E-10	7.107E-14	-1.107E-09	-1.107E-09	3.723E-09	0.890
^{144}Sm	144	62	3.684E-11	1.207E-14	-1.757E-10	-1.757E-10	6.448E-10	0.908

TableC.9 – continued

Isotope	A	Z	$X^{\rm ini}$	$mp^{\rm wind}$	$mp^{\rm preSN}$	$mp^{\rm total}$	EM	$\langle OP \rangle$
^{147}Sm	147	62	1.834E-10	6.013E-14	1.977E-10	1.977E-10	4.284E-09	1.211
^{148}Sm	148	62	1.385E-10	4.539E-14	2.114E-09	2.114E-09	5.199E-09	1.947
^{149}Sm	149	62	1.714E-10	5.617E-14	-4.033E-10	-4.032E-10	3.414E-09	1.033
^{150}Sm	150	62	9.213E-11	3.020E-14	1.487E-09	1.487E-09	3.540E-09	1.992
^{152}Sm	152	62	3.383E-10	1.109E-13	-6.389E-10	-6.388E-10	6.897E-09	1.057
^{154}Sm	154	62	2.916E-10	9.559E-14	-1.457E-09	-1.457E-09	5.039E-09	0.896
^{151}Eu	151	63	2.036E-10	6.674E-14	-8.458E-10	-8.457E-10	3.689E-09	0.939
^{153}Eu	153	63	2.252E-10	7.381E-14	-9.146E-10	-9.145E-10	4.102E-09	0.944
^{152}Gd	152	64	2.947E-12	9.663E-16	2.496E-10	2.496E-10	3.153E-10	5.546
^{154}Gd	154	64	3.210E-11	1.052E-14	6.876E-10	6.876E-10	1.403E-09	2.266
^{155}Gd	155	64	2.192E-10	7.185E-14	-8.465E-10	-8.464E-10	4.036E-09	0.955
^{156}Gd	156	64	3.051E-10	1.000E-13	-2.003E-10	-2.002E-10	6.596E-09	1.121
^{157}Gd	157	64	2.348E-10	7.697E-14	-4.050E-10	-4.049E-10	4.826E-09	1.065
^{158}Gd	158	64	3.750E-10	1.229E-13	7.622E-10	7.624E-10	9.115E-09	1.260
^{160}Gd	160	64	3.343E-10	1.096E-13	-1.644E-09	-1.644E-09	5.803E-09	0.900
^{159}Tb	159	65	2.765E-10	9.063E-14	-8.942E-10	-8.941E-10	5.265E-09	0.987
^{156}Dy	156	66	1.004E-12	3.290E-16	-6.031E-12	-6.031E-12	1.633E-11	0.843
^{158}Dy	158	66	1.743E-12	5.712E-16	7.884E-12	7.884E-12	4.670E-11	1.389
^{160}Dy	160	66	4.301E-11	1.410E-14	8.367E-10	8.367E-10	1.795E-09	2.163
^{161}Dy	161	66	3.498E-10	1.147E-13	-1.369E-09	-1.369E-09	6.422E-09	0.952
^{162}Dy	162	66	4.748E-10	1.556E-13	-4.480E-10	-4.478E-10	1.013E-08	1.106
^{163}Dy	163	66	4.663E-10	1.528E-13	-1.482E-09	-1.482E-09	8.905E-09	0.990
^{164}Dy	164	66	5.312E-10	1.741E-13	1.545E-09	1.545E-09	1.338E-08	1.306
^{165}Ho	165	67	4.244E-10	1.391E-13	-1.565E-09	-1.565E-09	7.888E-09	0.964
^{162}Er	162	68	1.609E-12	5.274E-16	-9.659E-12	-9.658E-12	2.618E-11	0.844
^{164}Er	164	68	1.913E-11	6.270E-15	-1.133E-10	-1.132E-10	3.128E-10	0.848
^{166}Er	166	68	4.044E-10	1.326E-13	-6.532E-10	-6.531E-10	8.356E-09	1.071
^{167}Er	167	68	2.776E-10	9.099E-14	-7.967E-10	-7.966E-10	5.387E-09	1.006

TableC.9 – continued

Isotope	A	Z	$X^{\rm ini}$	$mp^{\rm wind}$	$mp^{\rm preSN}$	$mp^{\rm total}$	EM	$\langle OP \rangle$
^{168}Er	168	68	3.263E-10	1.069E-13	1.005E-09	1.005E-09	8.273E-09	1.315
^{170}Er	170	68	1.840E-10	6.031E-14	-7.282E-10	-7.282E-10	3.370E-09	0.950
^{169}Tm	169	69	1.854E-10	6.078E-14	-4.586E-10	-4.585E-10	3.672E-09	1.027
^{168}Yb	168	70	1.583E-12	5.189E-16	-9.419E-12	-9.418E-12	2.585E-11	0.846
^{170}Yb	170	70	3.746E-11	1.228E-14	7.872E-10	7.872E-10	1.622E-09	2.244
^{171}Yb	171	70	1.770E-10	5.802E-14	-1.066E-10	-1.065E-10	3.836E-09	1.124
^{172}Yb	172	70	2.722E-10	8.922E-14	9.196E-10	9.197E-10	6.983E-09	1.330
^{173}Yb	173	70	2.023E-10	6.631E-14	3.803E-10	3.803E-10	4.886E-09	1.252
^{174}Yb	174	70	4.015E-10	1.316E-13	3.193E-09	3.193E-09	1.214E-08	1.567
^{176}Yb	176	70	1.628E-10	5.336E-14	-7.143E-10	-7.142E-10	2.912E-09	0.927
^{175}Lu	175	71	1.828E-10	5.991E-14	-1.462E-10	-1.462E-10	3.925E-09	1.113
^{176}Lu	176	71	4.876E-12	-3.965E-15	2.468E-11	2.468E-11	1.333E-10	1.417
^{174}Hf	174	72	1.231E-12	4.036E-16	-7.220E-12	-7.220E-12	2.021E-11	0.851
^{176}Hf	176	72	4.036E-11	1.879E-14	8.826E-10	8.826E-10	1.782E-09	2.289
^{177}Hf	177	72	1.438E-10	4.713E-14	-1.693E-10	-1.693E-10	3.033E-09	1.094
^{178}Hf	178	72	2.121E-10	6.953E-14	1.360E-09	1.360E-09	6.085E-09	1.487
^{179}Hf	179	72	1.065E-10	3.491E-14	-4.087E-12	-4.052E-12	2.368E-09	1.153
^{180}Hf	180	72	2.758E-10	9.042E-14	2.059E-09	2.059E-09	8.203E-09	1.542
^{180}Ta	180	73	2.429E-14	7.961E-18	8.774E-12	8.774E-12	9.315E-12	19.881
^{181}Ta	181	73	1.986E-10	6.509E-14	-2.916E-11	-2.910E-11	4.394E-09	1.147
^{180}W	180	74	8.395E-13	2.752E-16	2.246E-10	2.246E-10	2.433E-10	15.024
^{182}W	182	74	1.877E-10	6.154E-14	1.513E-09	1.513E-09	5.695E-09	1.573
^{183}W	183	74	1.020E-10	3.342E-14	1.246E-09	1.246E-09	3.517E-09	1.788
^{184}W	184	74	2.195E-10	7.195E-14	2.439E-09	2.439E-09	7.328E-09	1.731
^{186}W	186	74	2.058E-10	6.747E-14	-6.594E-10	-6.593E-10	3.925E-09	0.989
^{185}Re	185	75	1.048E-10	3.435E-14	2.418E-10	2.419E-10	2.576E-09	1.275
^{187}Re	187	75	1.773E-10	5.812E-14	-8.546E-10	-8.545E-10	3.095E-09	0.905
^{184}Os	184	76	7.108E-13	2.330E-16	-4.043E-12	-4.043E-12	1.179E-11	0.860

TableC.9 – continued

Isotope	A	Z	X^{ini}	mp^{wind}	mp^{preSN}	mp^{total}	EM	$\langle OP \rangle$
^{186}Os	186	76	5.778E-11	1.894E-14	1.088E-09	1.088E-09	2.375E-09	2.131
^{187}Os	187	76	5.998E-11	1.966E-14	3.382E-10	3.382E-10	1.674E-09	1.447
^{188}Os	188	76	4.874E-10	1.597E-13	2.809E-12	2.969E-12	1.086E-08	1.155
^{189}Os	189	76	5.974E-10	1.958E-13	-2.621E-09	-2.621E-09	1.068E-08	0.927
^{190}Os	190	76	9.766E-10	3.201E-13	-1.449E-09	-1.448E-09	2.030E-08	1.078
^{192}Os	192	76	1.533E-09	5.024E-13	-7.291E-09	-7.291E-09	2.685E-08	0.908
^{191}Ir	191	77	1.357E-09	4.449E-13	-7.205E-09	-7.204E-09	2.303E-08	0.880
^{193}Ir	193	77	2.308E-09	7.566E-13	-1.216E-08	-1.216E-08	3.926E-08	0.882
^{190}Pt	190	78	1.008E-12	3.306E-16	-5.650E-12	-5.649E-12	1.681E-11	0.864
^{192}Pt	192	78	5.850E-11	1.918E-14	1.753E-09	1.753E-09	3.056E-09	2.708
^{194}Pt	194	78	2.490E-09	8.161E-13	-8.104E-09	-8.103E-09	4.736E-08	0.986
^{195}Pt	195	78	2.568E-09	8.418E-13	-1.211E-08	-1.211E-08	4.510E-08	0.910
^{196}Pt	196	78	1.926E-09	6.313E-13	9.080E-11	9.143E-11	4.299E-08	1.157
^{198}Pt	198	78	5.522E-10	1.810E-13	-2.615E-09	-2.614E-09	9.685E-09	0.909
^{197}Au	197	79	1.083E-09	3.551E-13	-2.914E-09	-2.914E-09	2.122E-08	1.015
^{196}Hg	196	80	3.009E-12	9.864E-16	-1.547E-11	-1.547E-11	5.156E-11	0.888
^{198}Hg	198	80	1.975E-10	6.474E-14	6.174E-09	6.174E-09	1.057E-08	2.776
^{199}Hg	199	80	3.360E-10	1.101E-13	1.602E-09	1.602E-09	9.086E-09	1.402
^{200}Hg	200	80	4.622E-10	1.515E-13	6.290E-09	6.290E-09	1.659E-08	1.860
^{201}Hg	201	80	2.651E-10	8.690E-14	3.546E-09	3.546E-09	9.451E-09	1.848
^{202}Hg	202	80	6.036E-10	1.979E-13	1.189E-08	1.189E-08	2.534E-08	2.176
^{204}Hg	204	80	1.401E-10	4.593E-14	-5.593E-10	-5.593E-10	2.562E-09	0.948
^{203}Tl	203	81	3.221E-10	1.056E-13	9.160E-09	9.160E-09	1.633E-08	2.629
^{205}Tl	205	81	7.764E-10	2.545E-13	1.400E-08	1.400E-08	3.129E-08	2.090
^{204}Pb	204	82	2.931E-10	9.607E-14	9.459E-09	9.459E-09	1.599E-08	2.828
^{206}Pb	206	82	2.798E-09	9.170E-13	4.135E-08	4.136E-08	1.037E-07	1.921
^{207}Pb	207	82	3.090E-09	1.013E-12	5.254E-08	5.254E-08	1.214E-07	2.036
^{208}Pb	208	82	8.850E-09	2.901E-12	1.154E-07	1.154E-07	3.125E-07	1.831

TableC.9 – continued

Isotope	A	Z	X^{ini}	mp^{wind}	mp^{preSN}	mp^{total}	EM	$\langle OP \rangle$
^{209}Bi	209	83	8.718E-10	2.858E-13	8.479E-09	8.480E-09	2.790E-08	1.659

Table C.10: Yields for model 32ST.

Isotope	A	Z	$X^{\rm ini}$	$mp^{\rm wind}$	$mp^{\rm preSN}$	$mp^{\rm total}$	EM	$\langle OP \rangle$
^{1}H	1	1	7.064E-01	-2.562E+00	-6.902E+00	-9.464E+00	1.122E+01	0.683
^{2}H	2	1	1.371E-05	-2.519E-04	-1.339E-04	-3.858E-04	1.547E-05	0.049
^{3}He	3	2	4.540E-05	-3.283E-04	-4.436E-04	-7.719E-04	5.572E-04	0.528
^{4}He	4	2	2.735E-01	2.567E+00	-5.425E-01	2.025E+00	1.003E+01	1.578
^{7}Li	7	3	7.605E-11	-1.398E-09	-7.430E-10	-2.141E-09	8.583E-11	0.049
^{11}B	11	5	2.856E-09	3.125E-12	1.746E-11	2.059E-11	8.363E-08	1.259
^{12}C	12	6	3.425E-03	-3.177E-02	8.231E-01	7.913E-01	8.916E-01	11.197
^{13}C	13	6	4.156E-05	6.291E-04	-3.837E-04	2.454E-04	1.462E-03	1.513
^{14}N	14	7	1.059E-03	9.745E-02	-5.958E-03	9.149E-02	1.225E-01	4.976
^{15}N	15	7	4.171E-06	-4.912E-05	-2.977E-05	-7.889E-05	4.321E-05	0.446
^{16}O	16	8	9.624E-03	-6.953E-02	4.597E+00	4.527E+00	4.809E+00	21.491
^{17}O	17	8	3.813E-06	-9.329E-07	-1.261E-05	-1.354E-05	9.809E-05	1.106
^{18}O	18	8	2.171E-05	-2.005E-04	1.363E-04	-6.421E-05	5.714E-04	1.132
^{19}F	19	9	5.611E-07	-4.826E-06	3.482E-05	3.000E-05	4.642E-05	3.558
^{20}Ne	20	10	1.818E-03	-2.258E-04	1.592E+00	1.592E+00	1.645E+00	38.932
^{21}Ne	21	10	4.575E-06	8.602E-05	1.649E-03	1.735E-03	1.869E-03	17.572
^{22}Ne	22	10	1.470E-04	-1.147E-03	5.429E-02	5.314E-02	5.744E-02	16.805
^{23}Na	23	11	4.000E-05	1.366E-03	5.415E-02	5.552E-02	5.669E-02	60.963
^{24}Mg	24	12	5.862E-04	2.088E-06	1.550E-01	1.550E-01	1.722E-01	12.631
^{25}Mg	25	12	7.733E-05	-4.925E-04	4.952E-02	4.903E-02	5.129E-02	28.530
^{26}Mg	26	12	8.848E-05	5.005E-04	8.915E-02	8.965E-02	9.224E-02	44.837
^{27}Al	27	13	6.481E-05	1.233E-05	1.903E-02	1.904E-02	2.094E-02	13.896
^{28}Si	28	14	7.453E-04	8.364E-07	1.250E-02	1.251E-02	3.432E-02	1.981
^{29}Si	29	14	3.919E-05	4.032E-08	6.958E-03	6.958E-03	8.106E-03	8.895
^{30}Si	30	14	2.673E-05	-7.543E-08	2.498E-03	2.498E-03	3.280E-03	5.279
^{31}P	31	15	7.106E-06	1.187E-07	6.893E-04	6.894E-04	8.974E-04	5.432
^{32}S	32	16	4.011E-04	4.379E-07	-1.445E-03	-1.445E-03	1.030E-02	1.104

TableC.10 – continued

Isotope	A	Z	X^{ini}	mp^{wind}	mp^{preSN}	mp^{total}	EM	$\langle OP \rangle$
^{33}S	33	16	3.265E-06	4.585E-09	4.659E-05	4.660E-05	1.422E-04	1.873
^{34}S	34	16	1.890E-05	2.068E-08	1.289E-04	1.289E-04	6.823E-04	1.552
^{36}S	36	16	8.073E-08	8.833E-11	3.689E-05	3.689E-05	3.925E-05	20.914
^{35}Cl	35	17	6.821E-06	7.463E-09	-2.306E-05	-2.305E-05	1.766E-04	1.114
^{37}Cl	37	17	2.306E-06	2.523E-09	3.510E-04	3.510E-04	4.185E-04	7.806
^{36}Ar	36	18	8.202E-05	8.974E-08	-5.157E-04	-5.156E-04	1.886E-03	0.989
^{38}Ar	38	18	1.574E-05	1.722E-08	2.744E-04	2.744E-04	7.353E-04	2.009
^{40}Ar	40	18	2.650E-08	2.901E-11	1.536E-05	1.536E-05	1.614E-05	26.186
^{39}K	39	19	3.900E-06	4.267E-09	7.054E-05	7.054E-05	1.847E-04	2.037
^{40}K	40	19	5.005E-10	-2.212E-11	1.075E-05	1.075E-05	1.077E-05	925.231
^{41}K	41	19	2.959E-07	3.237E-10	2.211E-05	2.211E-05	3.077E-05	4.473
^{40}Ca	40	20	7.225E-05	7.908E-08	-3.837E-04	-3.836E-04	1.732E-03	1.031
^{42}Ca	42	20	5.063E-07	5.540E-10	2.920E-05	2.920E-05	4.402E-05	3.740
^{43}Ca	43	20	1.082E-07	1.184E-10	1.067E-05	1.067E-05	1.384E-05	5.504
^{44}Ca	44	20	1.710E-06	1.871E-09	2.835E-05	2.835E-05	7.841E-05	1.972
^{46}Ca	46	20	3.428E-09	3.751E-12	1.131E-06	1.131E-06	1.232E-06	15.450
^{48}Ca	48	20	1.672E-07	1.830E-10	-2.338E-07	-2.336E-07	4.663E-06	1.199
^{45}Sc	45	21	5.414E-08	5.923E-11	9.044E-06	9.044E-06	1.063E-05	8.444
^{46}Ti	46	22	3.232E-07	3.536E-10	6.592E-06	6.592E-06	1.605E-05	2.136
^{47}Ti	47	22	2.977E-07	3.257E-10	2.695E-06	2.695E-06	1.141E-05	1.648
^{48}Ti	48	22	3.014E-06	3.298E-09	-1.515E-05	-1.514E-05	7.308E-05	1.043
^{49}Ti	49	22	2.257E-07	2.470E-10	8.559E-06	8.559E-06	1.517E-05	2.890
^{50}Ti	50	22	2.208E-07	2.416E-10	2.866E-05	2.866E-05	3.513E-05	6.842
^{50}V	50	23	1.015E-09	1.111E-12	3.305E-08	3.305E-08	6.278E-08	2.659
^{51}V	51	23	4.138E-07	4.527E-10	2.123E-07	2.127E-07	1.233E-05	1.281
^{50}Cr	50	24	8.265E-07	9.044E-10	-6.795E-06	-6.794E-06	1.740E-05	0.906
^{52}Cr	52	24	1.658E-05	1.814E-08	-9.052E-05	-9.050E-05	3.948E-04	1.024
^{53}Cr	53	24	1.916E-06	2.096E-09	-5.720E-06	-5.718E-06	5.036E-05	1.131

TableC.10 – continued

Isotope	A	Z	$X^{\rm ini}$	$mp^{\rm wind}$	$mp^{\rm preSN}$	$mp^{\rm total}$	EM	$\langle OP \rangle$
^{54}Cr	54	24	4.858E-07	5.315E-10	5.341E-05	5.341E-05	6.763E-05	5.988
^{55}Mn	55	25	1.098E-05	1.202E-08	-3.229E-05	-3.228E-05	2.892E-04	1.133
^{54}Fe	54	26	8.118E-05	8.883E-08	-6.425E-04	-6.424E-04	1.734E-03	0.919
^{56}Fe	56	26	1.322E-03	1.446E-06	-8.349E-03	-8.347E-03	3.034E-02	0.987
^{57}Fe	57	26	3.107E-05	3.399E-08	5.307E-04	5.307E-04	1.440E-03	1.994
^{58}Fe	58	26	4.207E-06	4.603E-09	2.251E-03	2.251E-03	2.374E-03	24.275
^{59}Co	59	27	3.991E-06	4.367E-09	1.326E-03	1.326E-03	1.443E-03	15.545
^{58}Ni	58	28	5.711E-05	6.249E-08	-4.521E-04	-4.520E-04	1.220E-03	0.919
^{60}Ni	60	28	2.276E-05	2.490E-08	7.321E-04	7.321E-04	1.398E-03	2.643
^{61}Ni	61	28	1.006E-06	1.100E-09	4.086E-04	4.086E-04	4.380E-04	18.731
^{62}Ni	62	28	3.259E-06	3.566E-09	1.298E-03	1.298E-03	1.393E-03	18.387
^{64}Ni	64	28	8.568E-07	9.375E-10	7.348E-04	7.348E-04	7.599E-04	38.146
^{63}Cu	63	29	6.600E-07	7.222E-10	6.876E-04	6.876E-04	7.069E-04	46.063
^{65}Cu	65	29	3.035E-07	3.320E-10	4.716E-04	4.716E-04	4.804E-04	68.094
^{64}Zn	64	30	1.131E-06	1.237E-09	1.435E-04	1.435E-04	1.766E-04	6.717
^{66}Zn	66	30	6.690E-07	7.320E-10	4.391E-04	4.391E-04	4.587E-04	29.492
^{67}Zn	67	30	9.980E-08	1.092E-10	1.556E-04	1.556E-04	1.585E-04	68.308
^{68}Zn	68	30	4.632E-07	5.068E-10	5.527E-04	5.527E-04	5.662E-04	52.575
^{70}Zn	70	30	1.577E-08	1.725E-11	1.726E-06	1.726E-06	2.187E-06	5.967
^{69}Ga	69	31	4.551E-08	4.979E-11	7.217E-05	7.217E-05	7.350E-05	69.472
^{71}Ga	71	31	3.108E-08	3.400E-11	4.164E-05	4.164E-05	4.255E-05	58.894
^{70}Ge	70	32	5.157E-08	5.643E-11	9.690E-05	9.690E-05	9.841E-05	82.074
^{72}Ge	72	32	6.910E-08	7.561E-11	8.774E-05	8.774E-05	8.976E-05	55.870
^{73}Ge	73	32	1.955E-08	2.139E-11	3.921E-05	3.921E-05	3.978E-05	87.538
^{74}Ge	74	32	9.228E-08	1.010E-10	1.065E-04	1.065E-04	1.092E-04	50.891
^{76}Ge	76	32	1.963E-08	2.148E-11	7.173E-07	7.173E-07	1.292E-06	2.831
^{75}As	75	33	1.430E-08	1.565E-11	1.461E-05	1.461E-05	1.502E-05	45.187
^{74}Se	74	34	1.198E-09	1.311E-12	-1.101E-08	-1.101E-08	2.406E-08	0.864

TableC.10 – continued

Isotope	A	Z	$X^{\rm ini}$	$mp^{\rm wind}$	$mp^{\rm preSN}$	$mp^{\rm total}$	EM	$\langle OP \rangle$
^{76}Se	76	34	1.296E-08	1.418E-11	1.856E-05	1.856E-05	1.894E-05	62.846
^{77}Se	77	34	1.070E-08	1.171E-11	9.912E-06	9.912E-06	1.023E-05	41.085
^{78}Se	78	34	3.376E-08	3.694E-11	4.101E-05	4.101E-05	4.200E-05	53.505
^{80}Se	80	34	7.226E-08	7.907E-11	2.745E-05	2.745E-05	2.957E-05	17.598
^{82}Se	82	34	1.304E-08	1.426E-11	5.689E-08	5.690E-08	4.385E-07	1.447
^{79}Br	79	35	1.389E-08	1.520E-11	1.154E-05	1.154E-05	1.195E-05	36.985
^{81}Br	81	35	1.386E-08	1.516E-11	5.563E-06	5.563E-06	5.968E-06	18.523
^{78}Kr	78	36	3.900E-10	4.267E-13	-3.598E-09	-3.598E-09	7.820E-09	0.862
^{80}Kr	80	36	2.575E-09	2.817E-12	1.238E-06	1.238E-06	1.314E-06	21.945
^{82}Kr	82	36	1.320E-08	1.444E-11	1.017E-05	1.017E-05	1.055E-05	34.404
^{83}Kr	83	36	1.324E-08	1.449E-11	4.906E-06	4.906E-06	5.293E-06	17.193
^{84}Kr	84	36	6.602E-08	7.224E-11	1.790E-05	1.790E-05	1.984E-05	12.923
^{86}Kr	86	36	2.044E-08	2.237E-11	6.416E-06	6.416E-06	7.014E-06	14.756
^{85}Rb	85	37	1.282E-08	1.403E-11	6.950E-06	6.950E-06	7.325E-06	24.568
^{87}Rb	87	37	5.063E-09	-1.321E-12	2.225E-06	2.225E-06	2.373E-06	20.161
^{84}Sr	84	38	3.228E-10	3.532E-13	-2.999E-09	-2.998E-09	6.452E-09	0.860
^{86}Sr	86	38	5.845E-09	6.395E-12	2.110E-06	2.110E-06	2.281E-06	16.787
^{87}Sr	87	38	4.443E-09	1.172E-11	1.418E-06	1.418E-06	1.548E-06	14.985
^{88}Sr	88	38	5.011E-08	5.483E-11	9.818E-06	9.819E-06	1.129E-05	9.687
^{89}Y	89	39	1.229E-08	1.345E-11	2.095E-06	2.095E-06	2.455E-06	8.589
^{90}Zr	90	40	1.534E-08	1.679E-11	9.278E-07	9.278E-07	1.377E-06	3.860
^{91}Zr	91	40	3.384E-09	3.703E-12	2.706E-07	2.706E-07	3.697E-07	4.699
^{92}Zr	92	40	5.227E-09	5.719E-12	3.987E-07	3.987E-07	5.517E-07	4.540
^{94}Zr	94	40	5.413E-09	5.923E-12	1.634E-07	1.635E-07	3.219E-07	2.558
^{96}Zr	96	40	8.903E-10	9.742E-13	1.254E-07	1.254E-07	1.515E-07	7.319
^{93}Nb	93	41	1.900E-09	2.079E-12	1.791E-07	1.792E-07	2.348E-07	5.315
^{92}Mo	92	42	1.012E-09	1.108E-12	-8.540E-09	-8.539E-09	2.110E-08	0.896
^{94}Mo	94	42	6.448E-10	7.055E-13	-3.315E-09	-3.314E-09	1.556E-08	1.038

TableC.10 – continued

Isotope	A	Z	$X^{\rm ini}$	$mp^{\rm wind}$	$mp^{\rm preSN}$	$mp^{\rm total}$	EM	$\langle OP \rangle$
^{95}Mo	95	42	1.122E-09	1.228E-12	8.958E-08	8.958E-08	1.224E-07	4.694
^{96}Mo	96	42	1.188E-09	1.299E-12	1.847E-08	1.847E-08	5.323E-08	1.928
^{97}Mo	97	42	6.875E-10	7.523E-13	6.277E-09	6.278E-09	2.640E-08	1.652
^{98}Mo	98	42	1.754E-09	1.920E-12	2.132E-08	2.132E-08	7.268E-08	1.782
^{100}Mo	100	42	7.146E-10	7.819E-13	-5.681E-09	-5.680E-09	1.524E-08	0.917
^{96}Ru	96	44	2.926E-10	3.201E-13	-2.656E-09	-2.656E-09	5.909E-09	0.869
^{98}Ru	98	44	1.007E-10	1.102E-13	-8.118E-10	-8.116E-10	2.137E-09	0.912
^{99}Ru	99	44	6.945E-10	7.599E-13	-3.720E-10	-3.712E-10	1.996E-08	1.236
^{100}Ru	100	44	6.928E-10	7.580E-13	1.137E-08	1.138E-08	3.166E-08	1.965
^{101}Ru	101	44	9.475E-10	1.037E-12	-4.478E-09	-4.477E-09	2.326E-08	1.056
^{102}Ru	102	44	1.770E-09	1.936E-12	1.366E-08	1.366E-08	6.547E-08	1.591
^{104}Ru	104	44	1.065E-09	1.165E-12	-6.472E-09	-6.470E-09	2.470E-08	0.998
^{103}Rh	103	45	1.055E-09	1.154E-12	-3.814E-09	-3.813E-09	2.706E-08	1.104
^{102}Pd	102	46	4.241E-11	4.640E-14	-3.941E-10	-3.941E-10	8.475E-10	0.859
^{104}Pd	104	46	4.723E-10	5.168E-13	8.496E-09	8.496E-09	2.232E-08	2.033
^{105}Pd	105	46	9.558E-10	1.046E-12	-5.411E-09	-5.410E-09	2.257E-08	1.016
^{106}Pd	106	46	1.181E-09	1.292E-12	8.445E-09	8.447E-09	4.302E-08	1.567
^{108}Pd	108	46	1.165E-09	1.275E-12	1.248E-08	1.248E-08	4.658E-08	1.720
^{110}Pd	110	46	5.255E-10	5.750E-13	-1.831E-09	-1.831E-09	1.355E-08	1.109
^{107}Ag	107	47	7.840E-10	8.578E-13	-3.410E-09	-3.409E-09	1.954E-08	1.072
^{109}Ag	109	47	7.420E-10	8.119E-13	6.242E-09	6.243E-09	2.796E-08	1.621
^{106}Cd	106	48	6.346E-11	6.944E-14	-5.861E-10	-5.860E-10	1.272E-09	0.862
^{108}Cd	108	48	4.604E-11	5.037E-14	1.796E-10	1.796E-10	1.527E-09	1.427
^{110}Cd	110	48	6.580E-10	7.200E-13	1.103E-08	1.103E-08	3.029E-08	1.980
^{111}Cd	111	48	6.805E-10	7.446E-13	-5.085E-10	-5.077E-10	1.941E-08	1.227
^{112}Cd	112	48	1.294E-09	1.416E-12	1.017E-08	1.017E-08	4.807E-08	1.597
^{113}Cd	113	48	6.614E-10	7.236E-13	-1.526E-10	-1.519E-10	1.921E-08	1.249
^{114}Cd	114	48	1.569E-09	1.716E-12	1.593E-08	1.593E-08	6.185E-08	1.696

TableC.10 – continued

Isotope	A	Z	$X^{\rm ini}$	$mp^{\rm wind}$	$mp^{\rm preSN}$	$mp^{\rm total}$	EM	$\langle OP \rangle$
^{116}Cd	116	48	4.161E-10	4.553E-13	3.686E-09	3.686E-09	1.587E-08	1.640
^{113}In	113	49	2.604E-11	2.849E-14	-2.328E-10	-2.328E-10	5.295E-10	0.875
^{115}In	115	49	5.915E-10	6.471E-13	1.112E-09	1.113E-09	1.843E-08	1.340
^{112}Sn	112	50	1.221E-10	1.336E-13	-1.109E-09	-1.109E-09	2.465E-09	0.868
^{114}Sn	114	50	8.435E-11	9.229E-14	-6.389E-10	-6.388E-10	1.830E-09	0.933
^{115}Sn	115	50	4.377E-11	4.797E-14	-3.210E-10	-3.210E-10	9.604E-10	0.944
^{116}Sn	116	50	1.893E-09	2.071E-12	1.462E-08	1.462E-08	7.004E-08	1.591
^{117}Sn	117	50	1.008E-09	1.103E-12	2.785E-09	2.786E-09	3.230E-08	1.378
^{118}Sn	118	50	3.209E-09	3.511E-12	2.427E-08	2.428E-08	1.182E-07	1.584
^{119}Sn	119	50	1.147E-09	1.255E-12	5.409E-09	5.410E-09	3.899E-08	1.462
^{120}Sn	120	50	4.391E-09	4.805E-12	3.646E-08	3.647E-08	1.650E-07	1.616
^{122}Sn	122	50	6.341E-10	6.938E-13	1.138E-08	1.138E-08	2.994E-08	2.031
^{124}Sn	124	50	8.060E-10	8.818E-13	-5.485E-09	-5.484E-09	1.811E-08	0.966
^{121}Sb	121	51	6.318E-10	6.913E-13	2.663E-09	2.663E-09	2.116E-08	1.440
^{123}Sb	123	51	4.803E-10	5.255E-13	-2.392E-09	-2.392E-09	1.167E-08	1.045
^{120}Te	120	52	1.628E-11	1.782E-14	-1.522E-10	-1.522E-10	3.245E-10	0.857
^{122}Te	122	52	4.489E-10	4.911E-13	3.971E-09	3.971E-09	1.711E-08	1.640
^{123}Te	123	52	1.579E-10	1.727E-13	1.334E-09	1.334E-09	5.956E-09	1.623
^{124}Te	124	52	8.441E-10	9.236E-13	9.686E-09	9.687E-09	3.440E-08	1.753
^{125}Te	125	52	1.261E-09	1.380E-12	-6.054E-09	-6.053E-09	3.087E-08	1.053
^{126}Te	126	52	3.375E-09	3.693E-12	1.842E-09	1.845E-09	1.007E-07	1.283
^{128}Te	128	52	5.733E-09	6.273E-12	-4.171E-08	-4.171E-08	1.261E-07	0.946
^{130}Te	130	52	6.211E-09	6.795E-12	-4.410E-08	-4.409E-08	1.377E-07	0.954
^{127}I	127	53	1.459E-09	1.596E-12	-8.327E-09	-8.326E-09	3.439E-08	1.014
^{124}Xe	124	54	2.210E-11	2.418E-14	-2.070E-10	-2.070E-10	4.398E-10	0.856
^{126}Xe	126	54	1.949E-11	2.133E-14	-1.789E-10	-1.789E-10	3.918E-10	0.864
^{128}Xe	128	54	3.943E-10	4.314E-13	5.624E-09	5.625E-09	1.717E-08	1.873
^{129}Xe	129	54	4.893E-09	5.354E-12	-4.022E-08	-4.021E-08	1.030E-07	0.906

TableC.10 – continued

Isotope	A	Z	$X^{\rm ini}$	$mp^{\rm wind}$	$mp^{\rm preSN}$	$mp^{\rm total}$	EM	$\langle OP \rangle$
^{130}Xe	130	54	7.865E-10	8.606E-13	1.749E-08	1.749E-08	4.052E-08	2.216
^{131}Xe	131	54	3.945E-09	4.316E-12	-2.555E-08	-2.555E-08	8.993E-08	0.981
^{132}Xe	132	54	4.806E-09	5.259E-12	9.934E-09	9.940E-09	1.506E-07	1.348
^{134}Xe	134	54	1.788E-09	1.956E-12	-6.756E-10	-6.736E-10	5.167E-08	1.243
^{136}Xe	136	54	1.478E-09	1.618E-12	-1.832E-09	-1.830E-09	4.145E-08	1.206
^{133}Cs	133	55	1.426E-09	1.560E-12	-6.285E-09	-6.283E-09	3.546E-08	1.070
^{130}Ba	130	56	1.814E-11	1.985E-14	-1.701E-10	-1.701E-10	3.610E-10	0.856
^{132}Ba	132	56	1.762E-11	1.928E-14	-1.627E-10	-1.627E-10	3.532E-10	0.862
^{134}Ba	134	56	4.272E-10	4.675E-13	1.171E-08	1.171E-08	2.422E-08	2.438
^{135}Ba	135	56	1.174E-09	1.284E-12	2.439E-12	3.719E-12	3.437E-08	1.259
^{136}Ba	136	56	1.409E-09	1.541E-12	3.126E-08	3.126E-08	7.251E-08	2.214
^{137}Ba	137	56	2.030E-09	2.221E-12	2.023E-08	2.023E-08	7.965E-08	1.688
^{138}Ba	138	56	1.305E-08	1.428E-11	3.585E-07	3.586E-07	7.406E-07	2.441
^{138}La	138	57	1.604E-12	1.755E-15	-1.428E-11	-1.428E-11	3.268E-11	0.876
^{139}La	139	57	1.790E-09	1.959E-12	4.337E-08	4.337E-08	9.578E-08	2.301
^{136}Ce	136	58	8.382E-12	9.171E-15	-7.735E-11	-7.734E-11	1.680E-10	0.862
^{138}Ce	138	58	1.148E-11	1.256E-14	-1.029E-10	-1.029E-10	2.331E-10	0.874
^{140}Ce	140	58	4.103E-09	4.489E-12	6.654E-08	6.655E-08	1.867E-07	1.957
^{142}Ce	142	58	5.229E-10	5.722E-13	7.171E-09	7.172E-09	2.248E-08	1.849
^{141}Pr	141	59	6.910E-10	7.561E-13	5.219E-09	5.220E-09	2.545E-08	1.584
^{142}Nd	142	60	9.920E-10	1.085E-12	6.853E-09	6.854E-09	3.589E-08	1.556
^{143}Nd	143	60	4.484E-10	4.906E-13	-4.992E-10	-4.987E-10	1.263E-08	1.211
^{144}Nd	144	60	8.826E-10	9.657E-13	4.411E-09	4.412E-09	3.025E-08	1.474
^{145}Nd	145	60	3.095E-10	3.387E-13	1.200E-10	1.203E-10	9.182E-09	1.276
^{146}Nd	146	60	6.448E-10	7.055E-13	7.425E-09	7.426E-09	2.630E-08	1.754
^{148}Nd	148	60	2.185E-10	2.391E-13	1.209E-09	1.210E-09	7.606E-09	1.497
^{150}Nd	150	60	2.168E-10	2.372E-13	-1.888E-09	-1.887E-09	4.460E-09	0.885
^{144}Sm	144	62	3.684E-11	4.030E-14	-3.152E-10	-3.152E-10	7.631E-10	0.891

TableC.10 – continued

Isotope	A	Z	$X^{\rm ini}$	$mp^{\rm wind}$	$mp^{\rm preSN}$	$mp^{\rm total}$	EM	$\langle OP \rangle$
^{147}Sm	147	62	1.834E-10	2.007E-13	-9.822E-10	-9.820E-10	4.388E-09	1.029
^{148}Sm	148	62	1.385E-10	1.515E-13	-3.812E-10	-3.811E-10	3.672E-09	1.141
^{149}Sm	149	62	1.714E-10	1.875E-13	-1.317E-09	-1.317E-09	3.700E-09	0.929
^{150}Sm	150	62	9.213E-11	1.008E-13	9.554E-10	9.556E-10	3.653E-09	1.705
^{152}Sm	152	62	3.383E-10	3.702E-13	-1.572E-09	-1.571E-09	8.333E-09	1.059
^{154}Sm	154	62	2.916E-10	3.191E-13	-1.912E-09	-1.912E-09	6.625E-09	0.977
^{151}Eu	151	63	2.036E-10	2.228E-13	-1.628E-09	-1.628E-09	4.332E-09	0.915
^{153}Eu	153	63	2.252E-10	2.464E-13	-1.614E-09	-1.614E-09	4.978E-09	0.951
^{152}Gd	152	64	2.947E-12	3.226E-15	-6.817E-12	-6.814E-12	7.946E-11	1.160
^{154}Gd	154	64	3.210E-11	3.512E-14	1.109E-10	1.109E-10	1.050E-09	1.408
^{155}Gd	155	64	2.192E-10	2.399E-13	-1.825E-09	-1.825E-09	4.593E-09	0.901
^{156}Gd	156	64	3.051E-10	3.338E-13	-1.542E-09	-1.542E-09	7.390E-09	1.042
^{157}Gd	157	64	2.348E-10	2.569E-13	-1.227E-09	-1.227E-09	5.648E-09	1.034
^{158}Gd	158	64	3.750E-10	4.103E-13	-3.560E-10	-3.556E-10	1.062E-08	1.218
^{160}Gd	160	64	3.343E-10	3.658E-13	-2.317E-09	-2.316E-09	7.470E-09	0.961
^{159}Tb	159	65	2.765E-10	3.025E-13	-1.594E-09	-1.593E-09	6.501E-09	1.011
^{156}Dy	156	66	1.004E-12	1.098E-15	-9.436E-12	-9.435E-12	1.995E-11	0.855
^{158}Dy	158	66	1.743E-12	1.907E-15	-1.285E-11	-1.285E-11	3.816E-11	0.942
^{160}Dy	160	66	4.301E-11	4.707E-14	3.787E-10	3.788E-10	1.638E-09	1.638
^{161}Dy	161	66	3.498E-10	3.827E-13	-2.613E-09	-2.612E-09	7.628E-09	0.938
^{162}Dy	162	66	4.748E-10	5.195E-13	-2.050E-09	-2.049E-09	1.185E-08	1.073
^{163}Dy	163	66	4.663E-10	5.102E-13	-2.965E-09	-2.964E-09	1.069E-08	0.986
^{164}Dy	164	66	5.312E-10	5.812E-13	4.254E-10	4.260E-10	1.598E-08	1.294
^{165}Ho	165	67	4.244E-10	4.644E-13	-2.915E-09	-2.915E-09	9.509E-09	0.964
^{162}Er	162	68	1.609E-12	1.760E-15	-1.513E-11	-1.513E-11	3.197E-11	0.855
^{164}Er	164	68	1.913E-11	2.093E-14	-1.796E-10	-1.796E-10	3.804E-10	0.855
^{166}Er	166	68	4.044E-10	4.425E-13	-2.656E-09	-2.655E-09	9.185E-09	0.977
^{167}Er	167	68	2.776E-10	3.037E-13	-1.716E-09	-1.716E-09	6.411E-09	0.993

TableC.10 – continued

Isotope	A	Z	$X^{\rm ini}$	$mp^{\rm wind}$	$mp^{\rm preSN}$	$mp^{\rm total}$	EM	$\langle OP \rangle$
^{168}Er	168	68	3.263E-10	3.570E-13	4.588E-10	4.592E-10	1.001E-08	1.320
^{170}Er	170	68	1.840E-10	2.013E-13	1.053E-09	1.053E-09	6.439E-09	1.505
^{169}Tm	169	69	1.854E-10	2.029E-13	-4.745E-10	-4.743E-10	4.954E-09	1.149
^{168}Yb	168	70	1.583E-12	1.732E-15	-1.488E-11	-1.487E-11	3.147E-11	0.855
^{170}Yb	170	70	3.746E-11	4.099E-14	-2.203E-10	-2.203E-10	8.764E-10	1.006
^{171}Yb	171	70	1.770E-10	1.937E-13	-1.433E-09	-1.433E-09	3.749E-09	0.911
^{172}Yb	172	70	2.722E-10	2.978E-13	-4.815E-10	-4.812E-10	7.487E-09	1.183
^{173}Yb	173	70	2.023E-10	2.213E-13	-1.205E-10	-1.202E-10	5.802E-09	1.234
^{174}Yb	174	70	4.015E-10	4.393E-13	2.721E-09	2.722E-09	1.447E-08	1.551
^{176}Yb	176	70	1.628E-10	1.781E-13	-4.350E-10	-4.348E-10	4.331E-09	1.144
^{175}Lu	175	71	1.828E-10	2.000E-13	-6.454E-10	-6.452E-10	4.706E-09	1.107
^{176}Lu	176	71	4.876E-12	-2.598E-15	3.343E-10	3.343E-10	4.771E-10	4.208
^{174}Hf	174	72	1.231E-12	1.347E-15	-1.156E-11	-1.156E-11	2.448E-11	0.855
^{176}Hf	176	72	4.036E-11	5.210E-14	-1.056E-11	-1.051E-11	1.171E-09	1.248
^{177}Hf	177	72	1.438E-10	1.573E-13	-7.107E-10	-7.105E-10	3.499E-09	1.047
^{178}Hf	178	72	2.121E-10	2.321E-13	7.972E-10	7.974E-10	7.008E-09	1.421
^{179}Hf	179	72	1.065E-10	1.165E-13	2.108E-10	2.109E-10	3.329E-09	1.344
^{180}Hf	180	72	2.758E-10	3.018E-13	2.924E-09	2.924E-09	1.100E-08	1.715
^{180}Ta	180	73	2.429E-14	2.658E-17	8.801E-12	8.801E-12	9.512E-12	16.841
^{181}Ta	181	73	1.986E-10	2.173E-13	-3.273E-10	-3.271E-10	5.486E-09	1.188
^{180}W	180	74	8.395E-13	9.185E-16	1.112E-12	1.113E-12	2.569E-11	1.316
^{182}W	182	74	1.877E-10	2.054E-13	-5.736E-10	-5.734E-10	4.923E-09	1.128
^{183}W	183	74	1.020E-10	1.116E-13	3.591E-10	3.592E-10	3.344E-09	1.411
^{184}W	184	74	2.195E-10	2.402E-13	2.044E-09	2.044E-09	8.470E-09	1.660
^{186}W	186	74	2.058E-10	2.252E-13	5.710E-10	5.712E-10	6.597E-09	1.378
^{185}Re	185	75	1.048E-10	1.147E-13	2.429E-11	2.440E-11	3.092E-09	1.269
^{187}Re	187	75	1.773E-10	1.940E-13	-1.191E-09	-1.191E-09	4.000E-09	0.970
^{184}Os	184	76	7.108E-13	7.778E-16	-6.656E-12	-6.655E-12	1.415E-11	0.856

TableC.10 – continued

Isotope	A	Z	X^{ini}	mp^{wind}	mp^{preSN}	mp^{total}	EM	$\langle OP \rangle$
^{186}Os	186	76	5.778E-11	6.322E-14	-1.746E-10	-1.746E-10	1.517E-09	1.129
^{187}Os	187	76	5.998E-11	6.563E-14	-4.326E-10	-4.326E-10	1.323E-09	0.949
^{188}Os	188	76	4.874E-10	5.333E-13	-2.775E-09	-2.775E-09	1.149E-08	1.014
^{189}Os	189	76	5.974E-10	6.536E-13	-5.001E-09	-5.001E-09	1.249E-08	0.899
^{190}Os	190	76	9.766E-10	1.069E-12	-5.917E-09	-5.916E-09	2.267E-08	0.999
^{192}Os	192	76	1.533E-09	1.677E-12	-1.112E-08	-1.112E-08	3.375E-08	0.947
^{191}Ir	191	77	1.357E-09	1.485E-12	-1.207E-08	-1.206E-08	2.767E-08	0.877
^{193}Ir	193	77	2.308E-09	2.526E-12	-2.066E-08	-2.066E-08	4.692E-08	0.874
^{190}Pt	190	78	1.008E-12	1.103E-15	-9.424E-12	-9.423E-12	2.010E-11	0.857
^{192}Pt	192	78	5.850E-11	6.402E-14	-7.618E-11	-7.612E-11	1.636E-09	1.203
^{194}Pt	194	78	2.490E-09	2.724E-12	-1.958E-08	-1.957E-08	5.331E-08	0.921
^{195}Pt	195	78	2.568E-09	2.810E-12	-2.206E-08	-2.205E-08	5.313E-08	0.890
^{196}Pt	196	78	1.926E-09	2.107E-12	-6.747E-09	-6.745E-09	4.964E-08	1.109
^{198}Pt	198	78	5.522E-10	6.042E-13	-4.251E-09	-4.250E-09	1.191E-08	0.928
^{197}Au	197	79	1.083E-09	1.185E-12	-6.148E-09	-6.147E-09	2.557E-08	1.015
^{196}Hg	196	80	3.009E-12	3.293E-15	-2.729E-11	-2.729E-11	6.081E-11	0.869
^{198}Hg	198	80	1.975E-10	2.161E-13	7.413E-09	7.413E-09	1.319E-08	2.874
^{199}Hg	199	80	3.360E-10	3.676E-13	1.535E-09	1.535E-09	1.137E-08	1.456
^{200}Hg	200	80	4.622E-10	5.057E-13	6.397E-09	6.398E-09	1.993E-08	1.854
^{201}Hg	201	80	2.651E-10	2.901E-13	2.787E-09	2.788E-09	1.055E-08	1.711
^{202}Hg	202	80	6.036E-10	6.605E-13	9.266E-09	9.267E-09	2.694E-08	1.919
^{204}Hg	204	80	1.401E-10	1.533E-13	-8.305E-10	-8.304E-10	3.272E-09	1.004
^{203}Tl	203	81	3.221E-10	3.524E-13	7.512E-09	7.512E-09	1.694E-08	2.262
^{205}Tl	205	81	7.764E-10	8.495E-13	1.053E-08	1.053E-08	3.326E-08	1.842
^{204}Pb	204	82	2.931E-10	3.207E-13	7.262E-09	7.262E-09	1.584E-08	2.325
^{206}Pb	206	82	2.798E-09	3.061E-12	5.288E-08	5.289E-08	1.348E-07	2.072
^{207}Pb	207	82	3.090E-09	3.381E-12	9.222E-08	9.222E-08	1.827E-07	2.543
^{208}Pb	208	82	8.850E-09	9.683E-12	1.173E-07	1.174E-07	3.764E-07	1.829

TableC.10 – continued

Isotope	A	Z	X^{ini}	mp^{wind}	mp^{preSN}	mp^{total}	EM	$\langle OP \rangle$
^{209}Bi	209	83	8.718E-10	9.539E-13	1.339E-09	1.340E-09	2.686E-08	1.325

Table C.11: Yields for model 32CI.

Isotope	A	Z	X^{ini}	mp^{wind}	mp^{preSN}	mp^{total}	EM	$\langle OP \rangle$
^{1}H	1	1	7.064E-01	-2.562E+00	-4.792E+00	-7.354E+00	1.122E+01	0.683
^{2}H	2	1	1.371E-05	-2.519E-04	-9.297E-05	-3.448E-04	1.547E-05	0.049
^{3}He	3	2	4.540E-05	-3.283E-04	-3.080E-04	-6.363E-04	5.572E-04	0.528
^{4}He	4	2	2.735E-01	2.567E+00	2.794E-01	2.847E+00	1.004E+01	1.578
^{7}Li	7	3	7.605E-11	-1.398E-09	-5.159E-10	-1.913E-09	8.583E-11	0.049
^{11}B	11	5	2.856E-09	3.125E-12	1.051E-11	1.364E-11	7.509E-08	1.131
^{12}C	12	6	3.425E-03	-3.177E-02	6.875E-01	6.557E-01	7.457E-01	9.365
^{13}C	13	6	4.156E-05	6.291E-04	-2.617E-04	3.675E-04	1.460E-03	1.511
^{14}N	14	7	1.059E-03	9.745E-02	-3.098E-03	9.435E-02	1.222E-01	4.963
^{15}N	15	7	4.171E-06	-4.912E-05	-2.693E-05	-7.604E-05	3.359E-05	0.346
^{16}O	16	8	9.624E-03	-6.953E-02	2.738E+00	2.669E+00	2.922E+00	13.057
^{17}O	17	8	3.813E-06	-9.326E-07	2.503E-05	2.410E-05	1.243E-04	1.403
^{18}O	18	8	2.171E-05	-2.005E-04	-1.330E-04	-3.336E-04	2.372E-04	0.470
^{19}F	19	9	5.611E-07	-4.826E-06	1.121E-05	6.384E-06	2.113E-05	1.620
^{20}Ne	20	10	1.818E-03	-2.258E-04	8.503E-01	8.501E-01	8.979E-01	21.246
^{21}Ne	21	10	4.575E-06	8.602E-05	1.912E-03	1.998E-03	2.119E-03	19.916
^{22}Ne	22	10	1.470E-04	-1.147E-03	5.598E-02	5.483E-02	5.869E-02	17.171
^{23}Na	23	11	4.000E-05	1.366E-03	4.621E-02	4.757E-02	4.862E-02	52.288
^{24}Mg	24	12	5.862E-04	2.090E-06	5.013E-02	5.013E-02	6.554E-02	4.809
^{25}Mg	25	12	7.733E-05	-4.925E-04	2.639E-02	2.590E-02	2.793E-02	15.534
^{26}Mg	26	12	8.848E-05	5.005E-04	4.193E-02	4.243E-02	4.476E-02	21.756
^{27}Al	27	13	6.481E-05	1.233E-05	1.685E-02	1.686E-02	1.856E-02	12.319
^{28}Si	28	14	7.453E-04	8.364E-07	2.949E-03	2.950E-03	2.254E-02	1.301
^{29}Si	29	14	3.919E-05	4.032E-08	7.250E-04	7.250E-04	1.755E-03	1.926
^{30}Si	30	14	2.673E-05	-7.543E-08	9.709E-04	9.709E-04	1.673E-03	2.693
^{31}P	31	15	7.106E-06	1.187E-07	3.189E-04	3.191E-04	5.059E-04	3.062
^{32}S	32	16	4.011E-04	4.379E-07	-8.184E-04	-8.180E-04	9.726E-03	1.043

TableC.11 – continued

Isotope	A	Z	$X^{\rm ini}$	$mp^{\rm wind}$	$mp^{\rm preSN}$	$mp^{\rm total}$	EM	$\langle OP \rangle$
^{33}S	33	16	3.265E-06	4.584E-09	2.567E-05	2.567E-05	1.115E-04	1.469
^{34}S	34	16	1.890E-05	2.068E-08	5.230E-05	5.232E-05	5.493E-04	1.250
^{36}S	36	16	8.073E-08	8.833E-11	2.311E-05	2.311E-05	2.523E-05	13.441
^{35}Cl	35	17	6.821E-06	7.463E-09	-1.897E-05	-1.896E-05	1.603E-04	1.011
^{37}Cl	37	17	2.306E-06	2.523E-09	2.423E-04	2.423E-04	3.029E-04	5.650
^{36}Ar	36	18	8.202E-05	8.974E-08	-2.988E-04	-2.987E-04	1.857E-03	0.974
^{38}Ar	38	18	1.574E-05	1.722E-08	1.509E-04	1.509E-04	5.647E-04	1.543
^{40}Ar	40	18	2.650E-08	2.901E-11	8.004E-06	8.004E-06	8.701E-06	14.121
^{39}K	39	19	3.900E-06	4.267E-09	3.243E-05	3.244E-05	1.350E-04	1.488
^{40}K	40	19	5.005E-10	-2.212E-11	6.211E-06	6.211E-06	6.225E-06	534.897
^{41}K	41	19	2.959E-07	3.237E-10	1.381E-05	1.381E-05	2.159E-05	3.138
^{40}Ca	40	20	7.225E-05	7.908E-08	-2.185E-04	-2.184E-04	1.681E-03	1.001
^{42}Ca	42	20	5.063E-07	5.540E-10	1.728E-05	1.728E-05	3.059E-05	2.599
^{43}Ca	43	20	1.082E-07	1.183E-10	5.880E-06	5.880E-06	8.724E-06	3.469
^{44}Ca	44	20	1.710E-06	1.871E-09	1.560E-05	1.560E-05	6.056E-05	1.523
^{46}Ca	46	20	3.428E-09	3.751E-12	9.997E-09	1.000E-08	1.001E-07	1.256
^{48}Ca	48	20	1.672E-07	1.830E-10	-1.160E-07	-1.158E-07	4.281E-06	1.101
^{45}Sc	45	21	5.414E-08	5.923E-11	3.917E-06	3.917E-06	5.340E-06	4.243
^{46}Ti	46	22	3.232E-07	3.536E-10	4.704E-06	4.704E-06	1.320E-05	1.757
^{47}Ti	47	22	2.977E-07	3.257E-10	1.499E-06	1.499E-06	9.325E-06	1.347
^{48}Ti	48	22	3.014E-06	3.298E-09	-9.616E-06	-9.612E-06	6.961E-05	0.993
^{49}Ti	49	22	2.257E-07	2.470E-10	5.237E-06	5.237E-06	1.117E-05	2.128
^{50}Ti	50	22	2.208E-07	2.416E-10	1.650E-05	1.650E-05	2.231E-05	4.346
^{50}V	50	23	1.015E-09	1.111E-12	-5.777E-10	-5.766E-10	2.612E-08	1.106
^{51}V	51	23	4.138E-07	4.527E-10	-3.146E-08	-3.101E-08	1.085E-05	1.127
^{50}Cr	50	24	8.265E-07	9.044E-10	-4.105E-06	-4.104E-06	1.762E-05	0.917
^{52}Cr	52	24	1.658E-05	1.814E-08	-5.097E-05	-5.095E-05	3.848E-04	0.998
^{53}Cr	53	24	1.916E-06	2.096E-09	-4.337E-06	-4.335E-06	4.602E-05	1.033

TableC.11 – continued

Isotope	A	Z	$X^{\rm ini}$	$mp^{\rm wind}$	$mp^{\rm preSN}$	$mp^{\rm total}$	EM	$\langle OP \rangle$
^{54}Cr	54	24	4.858E-07	5.315E-10	3.302E-05	3.302E-05	4.580E-05	4.055
^{55}Mn	55	25	1.098E-05	1.202E-08	-1.510E-05	-1.509E-05	2.736E-04	1.072
^{54}Fe	54	26	8.118E-05	8.883E-08	-3.864E-04	-3.863E-04	1.748E-03	0.926
^{56}Fe	56	26	1.322E-03	1.446E-06	-4.766E-03	-4.764E-03	2.998E-02	0.976
^{57}Fe	57	26	3.107E-05	3.399E-08	3.402E-04	3.402E-04	1.157E-03	1.602
^{58}Fe	58	26	4.207E-06	4.603E-09	1.458E-03	1.458E-03	1.569E-03	16.037
^{59}Co	59	27	3.991E-06	4.367E-09	6.375E-04	6.375E-04	7.424E-04	8.000
^{58}Ni	58	28	5.711E-05	6.249E-08	-2.695E-04	-2.695E-04	1.232E-03	0.928
^{60}Ni	60	28	2.276E-05	2.490E-08	5.400E-04	5.400E-04	1.138E-03	2.151
^{61}Ni	61	28	1.006E-06	1.100E-09	2.658E-04	2.658E-04	2.922E-04	12.497
^{62}Ni	62	28	3.259E-06	3.566E-09	7.223E-04	7.223E-04	8.080E-04	10.663
^{64}Ni	64	28	8.568E-07	9.375E-10	3.651E-04	3.651E-04	3.876E-04	19.457
^{63}Cu	63	29	6.600E-07	7.222E-10	2.837E-04	2.837E-04	3.011E-04	19.619
^{65}Cu	65	29	3.035E-07	3.320E-10	3.607E-04	3.607E-04	3.687E-04	52.259
^{64}Zn	64	30	1.131E-06	1.237E-09	1.542E-04	1.542E-04	1.839E-04	6.996
^{66}Zn	66	30	6.690E-07	7.320E-10	2.475E-04	2.475E-04	2.651E-04	17.043
^{67}Zn	67	30	9.980E-08	1.092E-10	7.421E-05	7.421E-05	7.684E-05	33.113
^{68}Zn	68	30	4.632E-07	5.068E-10	2.587E-04	2.587E-04	2.709E-04	25.156
^{70}Zn	70	30	1.577E-08	1.725E-11	-1.610E-08	-1.609E-08	3.984E-07	1.087
^{69}Ga	69	31	4.551E-08	4.979E-11	3.312E-05	3.312E-05	3.432E-05	32.440
^{71}Ga	71	31	3.108E-08	3.400E-11	2.929E-05	2.929E-05	3.011E-05	41.669
^{70}Ge	70	32	5.157E-08	5.643E-11	4.470E-05	4.470E-05	4.605E-05	38.408
^{72}Ge	72	32	6.910E-08	7.561E-11	3.849E-05	3.849E-05	4.031E-05	25.088
^{73}Ge	73	32	1.955E-08	2.139E-11	1.548E-05	1.548E-05	1.600E-05	35.198
^{74}Ge	74	32	9.228E-08	1.010E-10	4.579E-05	4.579E-05	4.822E-05	22.472
^{76}Ge	76	32	1.963E-08	2.148E-11	-6.735E-08	-6.733E-08	4.487E-07	0.983
^{75}As	75	33	1.430E-08	1.565E-11	5.563E-06	5.563E-06	5.939E-06	17.864
^{74}Se	74	34	1.198E-09	1.311E-12	-6.928E-09	-6.927E-09	2.456E-08	0.882

TableC.11 – continued

Isotope	A	Z	$X^{\rm ini}$	$mp^{\rm wind}$	$mp^{\rm preSN}$	$mp^{\rm total}$	EM	$\langle OP \rangle$
^{76}Se	76	34	1.296E-08	1.418E-11	8.070E-06	8.070E-06	8.411E-06	27.911
^{77}Se	77	34	1.070E-08	1.171E-11	4.037E-06	4.037E-06	4.318E-06	17.350
^{78}Se	78	34	3.376E-08	3.694E-11	1.796E-05	1.796E-05	1.885E-05	24.012
^{80}Se	80	34	7.226E-08	7.907E-11	1.794E-06	1.794E-06	3.693E-06	2.198
^{82}Se	82	34	1.304E-08	1.426E-11	-4.755E-08	-4.753E-08	2.952E-07	0.974
^{79}Br	79	35	1.389E-08	1.520E-11	2.630E-06	2.630E-06	2.996E-06	9.274
^{81}Br	81	35	1.386E-08	1.516E-11	1.897E-06	1.897E-06	2.262E-06	7.019
^{78}Kr	78	36	3.900E-10	4.267E-13	-2.256E-09	-2.255E-09	7.997E-09	0.882
^{80}Kr	80	36	2.575E-09	2.817E-12	2.803E-06	2.803E-06	2.871E-06	47.957
^{82}Kr	82	36	1.320E-08	1.444E-11	7.649E-06	7.649E-06	7.996E-06	26.062
^{83}Kr	83	36	1.324E-08	1.449E-11	3.475E-06	3.475E-06	3.823E-06	12.419
^{84}Kr	84	36	6.602E-08	7.224E-11	1.181E-05	1.181E-05	1.355E-05	8.825
^{86}Kr	86	36	2.044E-08	2.237E-11	3.984E-07	3.984E-07	9.358E-07	1.969
^{85}Rb	85	37	1.282E-08	1.403E-11	2.014E-06	2.014E-06	2.351E-06	7.886
^{87}Rb	87	37	5.063E-09	-1.321E-12	1.770E-07	1.770E-07	3.101E-07	2.635
^{84}Sr	84	38	3.228E-10	3.532E-13	-1.926E-09	-1.926E-09	6.560E-09	0.874
^{86}Sr	86	38	5.845E-09	6.395E-12	3.960E-06	3.960E-06	4.114E-06	30.273
^{87}Sr	87	38	4.443E-09	1.172E-11	2.298E-06	2.298E-06	2.415E-06	23.378
^{88}Sr	88	38	5.011E-08	5.483E-11	6.798E-06	6.798E-06	8.115E-06	6.966
^{89}Y	89	39	1.229E-08	1.345E-11	1.127E-06	1.127E-06	1.450E-06	5.074
^{90}Zr	90	40	1.534E-08	1.679E-11	5.517E-07	5.517E-07	9.550E-07	2.677
^{91}Zr	91	40	3.384E-09	3.703E-12	1.624E-07	1.624E-07	2.513E-07	3.195
^{92}Zr	92	40	5.227E-09	5.719E-12	1.885E-07	1.885E-07	3.259E-07	2.682
^{94}Zr	94	40	5.413E-09	5.923E-12	7.508E-08	7.508E-08	2.174E-07	1.727
^{96}Zr	96	40	8.903E-10	9.742E-13	-9.282E-10	-9.272E-10	2.248E-08	1.086
^{93}Nb	93	41	1.900E-09	2.079E-12	6.860E-08	6.861E-08	1.186E-07	2.684
^{92}Mo	92	42	1.012E-09	1.108E-12	-5.167E-09	-5.166E-09	2.145E-08	0.911
^{94}Mo	94	42	6.448E-10	7.055E-13	-9.310E-10	-9.303E-10	1.602E-08	1.069

TableC.11 – continued

Isotope	A	Z	$X^{\rm ini}$	$mp^{\rm wind}$	$mp^{\rm preSN}$	$mp^{\rm total}$	EM	$\langle OP \rangle$
^{95}Mo	95	42	1.122E-09	1.228E-12	1.428E-08	1.428E-08	4.378E-08	1.678
^{96}Mo	96	42	1.188E-09	1.299E-12	2.928E-08	2.928E-08	6.049E-08	2.191
^{97}Mo	97	42	6.875E-10	7.523E-13	9.090E-09	9.091E-09	2.716E-08	1.699
^{98}Mo	98	42	1.754E-09	1.920E-12	2.653E-08	2.653E-08	7.265E-08	1.781
^{100}Mo	100	42	7.146E-10	7.819E-13	-3.715E-09	-3.714E-09	1.507E-08	0.907
^{96}Ru	96	44	2.926E-10	3.201E-13	-1.644E-09	-1.644E-09	6.047E-09	0.889
^{98}Ru	98	44	1.007E-10	1.102E-13	-4.396E-10	-4.395E-10	2.208E-09	0.943
^{99}Ru	99	44	6.945E-10	7.599E-13	2.155E-09	2.155E-09	2.041E-08	1.264
^{100}Ru	100	44	6.928E-10	7.580E-13	1.259E-08	1.259E-08	3.080E-08	1.912
^{101}Ru	101	44	9.475E-10	1.037E-12	-2.031E-09	-2.030E-09	2.288E-08	1.039
^{102}Ru	102	44	1.770E-09	1.936E-12	1.338E-08	1.338E-08	5.990E-08	1.456
^{104}Ru	104	44	1.065E-09	1.165E-12	-5.664E-09	-5.663E-09	2.233E-08	0.902
^{103}Rh	103	45	1.055E-09	1.154E-12	-2.560E-09	-2.559E-09	2.517E-08	1.026
^{102}Pd	102	46	4.241E-11	4.640E-14	-2.535E-10	-2.535E-10	8.614E-10	0.874
^{104}Pd	104	46	4.723E-10	5.168E-13	8.471E-09	8.472E-09	2.089E-08	1.902
^{105}Pd	105	46	9.558E-10	1.046E-12	-3.163E-09	-3.162E-09	2.196E-08	0.988
^{106}Pd	106	46	1.181E-09	1.292E-12	6.795E-09	6.796E-09	3.784E-08	1.378
^{108}Pd	108	46	1.165E-09	1.275E-12	6.885E-09	6.886E-09	3.751E-08	1.385
^{110}Pd	110	46	5.255E-10	5.750E-13	-2.705E-09	-2.704E-09	1.111E-08	0.909
^{107}Ag	107	47	7.840E-10	8.578E-13	-2.076E-09	-2.075E-09	1.854E-08	1.017
^{109}Ag	109	47	7.420E-10	8.119E-13	2.611E-09	2.611E-09	2.212E-08	1.282
^{106}Cd	106	48	6.346E-11	6.943E-14	-3.719E-10	-3.718E-10	1.296E-09	0.879
^{108}Cd	108	48	4.604E-11	5.037E-14	1.794E-09	1.794E-09	3.004E-09	2.806
^{110}Cd	110	48	6.580E-10	7.200E-13	8.000E-09	8.001E-09	2.530E-08	1.654
^{111}Cd	111	48	6.805E-10	7.445E-13	-3.962E-10	-3.955E-10	1.749E-08	1.106
^{112}Cd	112	48	1.294E-09	1.416E-12	6.578E-09	6.579E-09	4.061E-08	1.349
^{113}Cd	113	48	6.614E-10	7.236E-13	-1.233E-10	-1.226E-10	1.726E-08	1.123
^{114}Cd	114	48	1.569E-09	1.716E-12	1.022E-08	1.022E-08	5.145E-08	1.411

TableC.11 – continued

Isotope	A	Z	$X^{\rm ini}$	$mp^{\rm wind}$	$mp^{\rm preSN}$	$mp^{\rm total}$	EM	$\langle OP \rangle$
^{116}Cd	116	48	4.161E-10	4.553E-13	-1.894E-09	-1.894E-09	9.045E-09	0.935
^{113}In	113	49	2.604E-11	2.849E-14	-1.352E-10	-1.352E-10	5.493E-10	0.907
^{115}In	115	49	5.915E-10	6.471E-13	-2.641E-11	-2.576E-11	1.552E-08	1.129
^{112}Sn	112	50	1.221E-10	1.336E-13	-6.888E-10	-6.887E-10	2.521E-09	0.888
^{114}Sn	114	50	8.435E-11	9.229E-14	-3.531E-10	-3.530E-10	1.864E-09	0.951
^{115}Sn	115	50	4.377E-11	4.797E-14	-7.064E-11	-7.060E-11	1.080E-09	1.061
^{116}Sn	116	50	1.893E-09	2.071E-12	1.267E-08	1.267E-08	6.244E-08	1.419
^{117}Sn	117	50	1.008E-09	1.103E-12	1.620E-09	1.621E-09	2.813E-08	1.200
^{118}Sn	118	50	3.209E-09	3.511E-12	1.455E-08	1.455E-08	9.891E-08	1.326
^{119}Sn	119	50	1.147E-09	1.255E-12	3.181E-09	3.182E-09	3.333E-08	1.250
^{120}Sn	120	50	4.391E-09	4.805E-12	2.162E-08	2.163E-08	1.371E-07	1.342
^{122}Sn	122	50	6.341E-10	6.938E-13	-2.484E-09	-2.483E-09	1.418E-08	0.962
^{124}Sn	124	50	8.060E-10	8.818E-13	-3.324E-09	-3.324E-09	1.786E-08	0.953
^{121}Sb	121	51	6.318E-10	6.913E-13	-3.352E-11	-3.283E-11	1.658E-08	1.128
^{123}Sb	123	51	4.803E-10	5.255E-13	-2.650E-09	-2.650E-09	9.976E-09	0.893
^{120}Te	120	52	1.628E-11	1.782E-14	-1.001E-10	-1.001E-10	3.280E-10	0.866
^{122}Te	122	52	4.489E-10	4.911E-13	3.413E-09	3.414E-09	1.521E-08	1.458
^{123}Te	123	52	1.579E-10	1.727E-13	1.152E-09	1.152E-09	5.302E-09	1.445
^{124}Te	124	52	8.441E-10	9.236E-13	6.537E-09	6.538E-09	2.873E-08	1.464
^{125}Te	125	52	1.261E-09	1.380E-12	-3.861E-09	-3.859E-09	2.930E-08	0.999
^{126}Te	126	52	3.375E-09	3.693E-12	3.871E-09	3.875E-09	9.260E-08	1.180
^{128}Te	128	52	5.733E-09	6.273E-12	-2.722E-08	-2.721E-08	1.235E-07	0.926
^{130}Te	130	52	6.211E-09	6.795E-12	-2.590E-08	-2.589E-08	1.374E-07	0.951
^{127}I	127	53	1.459E-09	1.596E-12	-5.505E-09	-5.503E-09	3.285E-08	0.968
^{124}Xe	124	54	2.210E-11	2.418E-14	-1.377E-10	-1.377E-10	4.431E-10	0.863
^{126}Xe	126	54	1.949E-11	2.133E-14	-1.142E-10	-1.142E-10	3.983E-10	0.879
^{128}Xe	128	54	3.943E-10	4.314E-13	5.391E-09	5.391E-09	1.576E-08	1.719
^{129}Xe	129	54	4.893E-09	5.354E-12	-2.688E-08	-2.688E-08	1.017E-07	0.894

TableC.11 – continued

Isotope	A	Z	$X^{\rm ini}$	$mp^{\rm wind}$	$mp^{\rm preSN}$	$mp^{\rm total}$	EM	$\langle OP \rangle$
^{130}Xe	130	54	7.865E-10	8.606E-13	1.505E-08	1.505E-08	3.572E-08	1.954
^{131}Xe	131	54	3.945E-09	4.316E-12	-1.599E-08	-1.599E-08	8.771E-08	0.956
^{132}Xe	132	54	4.806E-09	5.259E-12	9.103E-09	9.109E-09	1.355E-07	1.212
^{134}Xe	134	54	1.788E-09	1.956E-12	-7.693E-09	-7.691E-09	3.931E-08	0.946
^{136}Xe	136	54	1.478E-09	1.618E-12	-1.148E-09	-1.146E-09	3.772E-08	1.097
^{133}Cs	133	55	1.426E-09	1.560E-12	-3.260E-09	-3.259E-09	3.423E-08	1.032
^{130}Ba	130	56	1.814E-11	1.985E-14	-1.141E-10	-1.140E-10	3.629E-10	0.860
^{132}Ba	132	56	1.762E-11	1.928E-14	-1.050E-10	-1.050E-10	3.583E-10	0.874
^{134}Ba	134	56	4.272E-10	4.675E-13	1.029E-08	1.029E-08	2.152E-08	2.167
^{135}Ba	135	56	1.174E-09	1.284E-12	-2.023E-09	-2.022E-09	2.884E-08	1.057
^{136}Ba	136	56	1.409E-09	1.541E-12	2.531E-08	2.531E-08	6.235E-08	1.903
^{137}Ba	137	56	2.030E-09	2.221E-12	1.513E-08	1.514E-08	6.850E-08	1.451
^{138}Ba	138	56	1.305E-08	1.428E-11	2.019E-07	2.019E-07	5.450E-07	1.796
^{138}La	138	57	1.604E-12	1.755E-15	-9.642E-12	-9.640E-12	3.253E-11	0.872
^{139}La	139	57	1.790E-09	1.959E-12	2.260E-08	2.261E-08	6.967E-08	1.674
^{136}Ce	136	58	8.382E-12	9.171E-15	-4.898E-11	-4.897E-11	1.714E-10	0.879
^{138}Ce	138	58	1.148E-11	1.256E-14	-6.333E-11	-6.332E-11	2.384E-10	0.893
^{140}Ce	140	58	4.103E-09	4.489E-12	3.951E-08	3.952E-08	1.474E-07	1.545
^{142}Ce	142	58	5.229E-10	5.722E-13	-2.271E-09	-2.270E-09	1.148E-08	0.944
^{141}Pr	141	59	6.910E-10	7.561E-13	3.280E-09	3.281E-09	2.145E-08	1.335
^{142}Nd	142	60	9.920E-10	1.085E-12	1.037E-08	1.038E-08	3.645E-08	1.581
^{143}Nd	143	60	4.484E-10	4.906E-13	4.589E-11	4.638E-11	1.183E-08	1.135
^{144}Nd	144	60	8.826E-10	9.657E-13	2.039E-09	2.040E-09	2.524E-08	1.230
^{145}Nd	145	60	3.095E-10	3.387E-13	-1.426E-11	-1.392E-11	8.123E-09	1.129
^{146}Nd	146	60	6.448E-10	7.055E-13	2.093E-09	2.094E-09	1.904E-08	1.270
^{148}Nd	148	60	2.185E-10	2.391E-13	-1.088E-09	-1.087E-09	4.657E-09	0.917
^{150}Nd	150	60	2.168E-10	2.372E-13	-1.202E-09	-1.202E-09	4.498E-09	0.892
^{144}Sm	144	62	3.684E-11	4.030E-14	-1.900E-10	-1.900E-10	7.783E-10	0.909

TableC.11 – continued

Isotope	A	Z	$X^{\rm ini}$	$mp^{\rm wind}$	$mp^{\rm preSN}$	$mp^{\rm total}$	EM	$\langle OP \rangle$
^{147}Sm	147	62	1.834E-10	2.007E-13	-3.420E-10	-3.418E-10	4.480E-09	1.051
^{148}Sm	148	62	1.385E-10	1.515E-13	1.144E-09	1.144E-09	4.784E-09	1.486
^{149}Sm	149	62	1.714E-10	1.875E-13	-6.955E-10	-6.953E-10	3.810E-09	0.956
^{150}Sm	150	62	9.213E-11	1.008E-13	8.066E-10	8.067E-10	3.229E-09	1.507
^{152}Sm	152	62	3.383E-10	3.702E-13	-1.139E-09	-1.139E-09	7.755E-09	0.986
^{154}Sm	154	62	2.916E-10	3.191E-13	-1.607E-09	-1.607E-09	6.059E-09	0.894
^{151}Eu	151	63	2.036E-10	2.228E-13	-1.052E-09	-1.052E-09	4.300E-09	0.908
^{153}Eu	153	63	2.252E-10	2.464E-13	-1.144E-09	-1.143E-09	4.777E-09	0.912
^{152}Gd	152	64	2.947E-12	3.226E-15	1.397E-10	1.397E-10	2.172E-10	3.170
^{154}Gd	154	64	3.210E-11	3.512E-14	4.310E-10	4.311E-10	1.275E-09	1.708
^{155}Gd	155	64	2.192E-10	2.399E-13	-1.065E-09	-1.064E-09	4.698E-09	0.922
^{156}Gd	156	64	3.051E-10	3.338E-13	-6.761E-10	-6.757E-10	7.345E-09	1.035
^{157}Gd	157	64	2.348E-10	2.569E-13	-7.526E-10	-7.524E-10	5.421E-09	0.993
^{158}Gd	158	64	3.750E-10	4.103E-13	-4.489E-11	-4.448E-11	9.813E-09	1.126
^{160}Gd	160	64	3.343E-10	3.658E-13	-1.810E-09	-1.810E-09	6.978E-09	0.898
^{159}Tb	159	65	2.765E-10	3.025E-13	-1.208E-09	-1.208E-09	6.060E-09	0.943
^{156}Dy	156	66	1.004E-12	1.098E-15	-6.462E-12	-6.460E-12	1.992E-11	0.854
^{158}Dy	158	66	1.743E-12	1.907E-15	-4.446E-12	-4.444E-12	4.137E-11	1.021
^{160}Dy	160	66	4.301E-11	4.707E-14	5.775E-10	5.776E-10	1.708E-09	1.708
^{161}Dy	161	66	3.498E-10	3.827E-13	-1.717E-09	-1.717E-09	7.478E-09	0.920
^{162}Dy	162	66	4.748E-10	5.195E-13	-1.202E-09	-1.201E-09	1.128E-08	1.022
^{163}Dy	163	66	4.663E-10	5.102E-13	-2.029E-09	-2.028E-09	1.023E-08	0.944
^{164}Dy	164	66	5.312E-10	5.812E-13	2.957E-10	2.963E-10	1.426E-08	1.155
^{165}Ho	165	67	4.244E-10	4.643E-13	-1.981E-09	-1.981E-09	9.175E-09	0.930
^{162}Er	162	68	1.609E-12	1.760E-15	-1.036E-11	-1.036E-11	3.194E-11	0.854
^{164}Er	164	68	1.913E-11	2.093E-14	-1.221E-10	-1.221E-10	3.808E-10	0.856
^{166}Er	166	68	4.044E-10	4.425E-13	-1.172E-09	-1.171E-09	9.461E-09	1.006
^{167}Er	167	68	2.776E-10	3.037E-13	-1.120E-09	-1.120E-09	6.178E-09	0.957

TableC.11 – continued

Isotope	A	Z	$X^{\rm ini}$	$mp^{\rm wind}$	$mp^{\rm preSN}$	$mp^{\rm total}$	EM	$\langle OP \rangle$
^{168}Er	168	68	3.263E-10	3.570E-13	2.984E-10	2.987E-10	8.875E-09	1.170
^{170}Er	170	68	1.840E-10	2.013E-13	-9.031E-10	-9.029E-10	3.934E-09	0.920
^{169}Tm	169	69	1.854E-10	2.029E-13	-7.110E-10	-7.108E-10	4.164E-09	0.966
^{168}Yb	168	70	1.583E-12	1.732E-15	-1.015E-11	-1.015E-11	3.147E-11	0.855
^{170}Yb	170	70	3.746E-11	4.099E-14	6.563E-10	6.564E-10	1.641E-09	1.884
^{171}Yb	171	70	1.770E-10	1.937E-13	-3.864E-10	-3.862E-10	4.267E-09	1.037
^{172}Yb	172	70	2.722E-10	2.978E-13	3.058E-10	3.061E-10	7.461E-09	1.179
^{173}Yb	173	70	2.023E-10	2.213E-13	-1.315E-10	-1.313E-10	5.186E-09	1.103
^{174}Yb	174	70	4.015E-10	4.393E-13	1.532E-09	1.532E-09	1.209E-08	1.295
^{176}Yb	176	70	1.628E-10	1.781E-13	-8.161E-10	-8.159E-10	3.464E-09	0.915
^{175}Lu	175	71	1.828E-10	2.000E-13	-5.164E-10	-5.162E-10	4.289E-09	1.009
^{176}Lu	176	71	4.876E-12	-2.598E-15	1.038E-10	1.038E-10	2.320E-10	2.047
^{174}Hf	174	72	1.231E-12	1.347E-15	-7.835E-12	-7.834E-12	2.453E-11	0.857
^{176}Hf	176	72	4.036E-11	5.210E-14	3.740E-10	3.741E-10	1.435E-09	1.529
^{177}Hf	177	72	1.438E-10	1.573E-13	-4.213E-10	-4.212E-10	3.359E-09	1.005
^{178}Hf	178	72	2.121E-10	2.321E-13	6.423E-10	6.425E-10	6.219E-09	1.261
^{179}Hf	179	72	1.065E-10	1.165E-13	-2.642E-11	-2.631E-11	2.774E-09	1.120
^{180}Hf	180	72	2.758E-10	3.018E-13	1.440E-09	1.440E-09	8.691E-09	1.355
^{180}Ta	180	73	2.429E-14	2.658E-17	-1.566E-13	-1.566E-13	4.820E-13	0.853
^{181}Ta	181	73	1.986E-10	2.173E-13	-4.430E-10	-4.428E-10	4.777E-09	1.035
^{180}W	180	74	8.395E-13	9.185E-16	8.796E-11	8.796E-11	1.100E-10	5.637
^{182}W	182	74	1.877E-10	2.054E-13	7.545E-10	7.547E-10	5.690E-09	1.304
^{183}W	183	74	1.020E-10	1.116E-13	5.503E-10	5.504E-10	3.231E-09	1.363
^{184}W	184	74	2.195E-10	2.402E-13	1.167E-09	1.167E-09	6.937E-09	1.359
^{186}W	186	74	2.058E-10	2.252E-13	-9.377E-10	-9.375E-10	4.473E-09	0.935
^{185}Re	185	75	1.048E-10	1.147E-13	-1.349E-10	-1.348E-10	2.620E-09	1.075
^{187}Re	187	75	1.773E-10	1.940E-13	-1.005E-09	-1.005E-09	3.656E-09	0.887
^{184}Os	184	76	7.108E-13	7.778E-16	-4.414E-12	-4.413E-12	1.427E-11	0.864

TableC.11 – continued

Isotope	A	Z	$X^{\rm ini}$	$mp^{\rm wind}$	$mp^{\rm preSN}$	$mp^{\rm total}$	EM	$\langle OP \rangle$
^{186}Os	186	76	5.778E-11	6.322E-14	7.519E-10	7.519E-10	2.271E-09	1.690
^{187}Os	187	76	5.998E-11	6.563E-14	7.601E-11	7.607E-11	1.653E-09	1.185
^{188}Os	188	76	4.874E-10	5.332E-13	-9.369E-10	-9.363E-10	1.188E-08	1.048
^{189}Os	189	76	5.974E-10	6.536E-13	-3.206E-09	-3.205E-09	1.250E-08	0.900
^{190}Os	190	76	9.766E-10	1.069E-12	-2.988E-09	-2.987E-09	2.269E-08	0.999
^{192}Os	192	76	1.533E-09	1.677E-12	-8.106E-09	-8.104E-09	3.219E-08	0.903
^{191}Ir	191	77	1.357E-09	1.485E-12	-8.061E-09	-8.060E-09	2.762E-08	0.875
^{193}Ir	193	77	2.308E-09	2.526E-12	-1.357E-08	-1.357E-08	4.712E-08	0.878
^{190}Pt	190	78	1.008E-12	1.103E-15	-6.183E-12	-6.182E-12	2.033E-11	0.867
^{192}Pt	192	78	5.850E-11	6.402E-14	1.307E-09	1.307E-09	2.845E-09	2.092
^{194}Pt	194	78	2.490E-09	2.724E-12	-1.011E-08	-1.011E-08	5.534E-08	0.956
^{195}Pt	195	78	2.568E-09	2.810E-12	-1.369E-08	-1.368E-08	5.383E-08	0.902
^{196}Pt	196	78	1.926E-09	2.107E-12	-1.518E-09	-1.516E-09	4.911E-08	1.097
^{198}Pt	198	78	5.522E-10	6.042E-13	-2.839E-09	-2.838E-09	1.168E-08	0.910
^{197}Au	197	79	1.083E-09	1.185E-12	-3.796E-09	-3.795E-09	2.468E-08	0.980
^{196}Hg	196	80	3.009E-12	3.293E-15	-1.690E-11	-1.690E-11	6.221E-11	0.889
^{198}Hg	198	80	1.975E-10	2.161E-13	4.991E-09	4.991E-09	1.018E-08	2.218
^{199}Hg	199	80	3.360E-10	3.676E-13	5.557E-10	5.560E-10	9.389E-09	1.202
^{200}Hg	200	80	4.622E-10	5.057E-13	3.841E-09	3.842E-09	1.599E-08	1.488
^{201}Hg	201	80	2.651E-10	2.901E-13	1.743E-09	1.743E-09	8.712E-09	1.413
^{202}Hg	202	80	6.036E-10	6.605E-13	7.240E-09	7.241E-09	2.311E-08	1.647
^{204}Hg	204	80	1.401E-10	1.533E-13	-6.125E-10	-6.124E-10	3.072E-09	0.943
^{203}Tl	203	81	3.221E-10	3.524E-13	4.572E-09	4.573E-09	1.304E-08	1.741
^{205}Tl	205	81	7.764E-10	8.495E-13	7.598E-09	7.599E-09	2.801E-08	1.552
^{204}Pb	204	82	2.931E-10	3.207E-13	5.679E-09	5.679E-09	1.338E-08	1.964
^{206}Pb	206	82	2.798E-09	3.061E-12	3.637E-08	3.637E-08	1.099E-07	1.690
^{207}Pb	207	82	3.090E-09	3.381E-12	4.907E-08	4.908E-08	1.303E-07	1.814
^{208}Pb	208	82	8.850E-09	9.683E-12	5.983E-08	5.984E-08	2.925E-07	1.422

TableC.11 – continued

Isotope	A	Z	X^{ini}	mp^{wind}	mp^{preSN}	mp^{total}	EM	$\langle OP \rangle$
^{209}Bi	209	83	8.718E-10	9.539E-13	1.492E-09	1.493E-09	2.441E-08	1.204

Table C.12: Yields for model 32CU.

Isotope	A	Z	X^{ini}	mp^{wind}	mp^{preSN}	mp^{total}	EM	$\langle OP \rangle$
^{1}H	1	1	7.064E-01	-2.564E+00	-4.791E+00	-7.354E+00	1.122E+01	0.683
^{2}H	2	1	1.371E-05	-2.519E-04	-9.294E-05	-3.448E-04	1.547E-05	0.049
^{3}He	3	2	4.540E-05	-3.284E-04	-3.079E-04	-6.363E-04	5.572E-04	0.528
^{4}He	4	2	2.735E-01	2.569E+00	2.273E-01	2.796E+00	9.986E+00	1.570
^{7}Li	7	3	7.605E-11	-1.398E-09	-5.157E-10	-1.913E-09	8.583E-11	0.049
^{11}B	11	5	2.856E-09	3.125E-12	1.085E-11	1.398E-11	7.509E-08	1.131
^{12}C	12	6	3.425E-03	-3.178E-02	5.029E-01	4.711E-01	5.611E-01	7.047
^{13}C	13	6	4.156E-05	6.292E-04	-2.456E-04	3.836E-04	1.476E-03	1.528
^{14}N	14	7	1.059E-03	9.747E-02	1.596E-03	9.907E-02	1.269E-01	5.155
^{15}N	15	7	4.171E-06	-4.912E-05	-2.302E-05	-7.214E-05	3.750E-05	0.387
^{16}O	16	8	9.624E-03	-6.955E-02	2.890E+00	2.821E+00	3.074E+00	13.736
^{17}O	17	8	3.813E-06	-9.402E-07	8.868E-05	8.774E-05	1.880E-04	2.120
^{18}O	18	8	2.171E-05	-2.006E-04	6.959E-04	4.953E-04	1.066E-03	2.112
^{19}F	19	9	5.611E-07	-4.827E-06	-3.659E-07	-5.193E-06	9.557E-06	0.733
^{20}Ne	20	10	1.818E-03	-2.260E-04	8.634E-01	8.631E-01	9.109E-01	21.554
^{21}Ne	21	10	4.575E-06	8.601E-05	6.442E-03	6.528E-03	6.648E-03	62.498
^{22}Ne	22	10	1.470E-04	-1.147E-03	4.443E-02	4.328E-02	4.715E-02	13.793
^{23}Na	23	11	4.000E-05	1.366E-03	8.208E-02	8.345E-02	8.450E-02	90.870
^{24}Mg	24	12	5.862E-04	2.413E-06	5.882E-02	5.882E-02	7.423E-02	5.446
^{25}Mg	25	12	7.733E-05	-4.926E-04	3.090E-02	3.041E-02	3.244E-02	18.042
^{26}Mg	26	12	8.848E-05	5.005E-04	6.111E-02	6.162E-02	6.394E-02	31.082
^{27}Al	27	13	6.481E-05	1.243E-05	1.730E-02	1.731E-02	1.902E-02	12.619
^{28}Si	28	14	7.453E-04	8.367E-07	4.442E-03	4.442E-03	2.403E-02	1.387
^{29}Si	29	14	3.919E-05	4.021E-08	1.126E-03	1.126E-03	2.156E-03	2.366
^{30}Si	30	14	2.673E-05	-7.534E-08	1.538E-03	1.538E-03	2.241E-03	3.606
^{31}P	31	15	7.106E-06	1.188E-07	5.399E-04	5.401E-04	7.269E-04	4.399
^{32}S	32	16	4.011E-04	4.380E-07	-1.074E-03	-1.074E-03	9.470E-03	1.016

TableC.12 – continued

Isotope	A	Z	$X^{\rm ini}$	$mp^{\rm wind}$	$mp^{\rm preSN}$	$mp^{\rm total}$	EM	$\langle OP \rangle$
^{33}S	33	16	3.265E-06	4.587E-09	1.438E-05	1.439E-05	1.002E-04	1.320
^{34}S	34	16	1.890E-05	2.069E-08	7.486E-05	7.488E-05	5.718E-04	1.301
^{36}S	36	16	8.073E-08	8.835E-11	3.167E-05	3.167E-05	3.379E-05	18.004
^{35}Cl	35	17	6.821E-06	7.465E-09	-2.275E-05	-2.275E-05	1.566E-04	0.987
^{37}Cl	37	17	2.306E-06	2.523E-09	2.518E-04	2.518E-04	3.124E-04	5.828
^{36}Ar	36	18	8.202E-05	8.976E-08	-3.388E-04	-3.387E-04	1.817E-03	0.953
^{38}Ar	38	18	1.574E-05	1.723E-08	1.673E-04	1.673E-04	5.811E-04	1.588
^{40}Ar	40	18	2.650E-08	2.901E-11	1.771E-05	1.771E-05	1.841E-05	29.879
^{39}K	39	19	3.900E-06	4.268E-09	4.036E-05	4.037E-05	1.429E-04	1.576
^{40}K	40	19	5.005E-10	-2.212E-11	7.174E-06	7.174E-06	7.188E-06	617.660
^{41}K	41	19	2.959E-07	3.238E-10	1.376E-05	1.376E-05	2.154E-05	3.131
^{40}Ca	40	20	7.225E-05	7.910E-08	-2.634E-04	-2.633E-04	1.636E-03	0.974
^{42}Ca	42	20	5.063E-07	5.541E-10	1.828E-05	1.828E-05	3.159E-05	2.683
^{43}Ca	43	20	1.082E-07	1.184E-10	6.793E-06	6.793E-06	9.636E-06	3.832
^{44}Ca	44	20	1.710E-06	1.872E-09	2.145E-05	2.145E-05	6.641E-05	1.670
^{46}Ca	46	20	3.428E-09	3.752E-12	4.726E-07	4.726E-07	5.627E-07	7.059
^{48}Ca	48	20	1.672E-07	1.830E-10	-1.713E-07	-1.711E-07	4.226E-06	1.087
^{45}Sc	45	21	5.414E-08	5.925E-11	5.750E-06	5.750E-06	7.173E-06	5.699
^{46}Ti	46	22	3.232E-07	3.537E-10	6.204E-06	6.204E-06	1.470E-05	1.956
^{47}Ti	47	22	2.977E-07	3.258E-10	2.988E-06	2.988E-06	1.081E-05	1.562
^{48}Ti	48	22	3.014E-06	3.298E-09	-6.134E-06	-6.131E-06	7.309E-05	1.043
^{49}Ti	49	22	2.257E-07	2.470E-10	8.421E-06	8.421E-06	1.436E-05	2.735
^{50}Ti	50	22	2.208E-07	2.416E-10	2.692E-05	2.692E-05	3.272E-05	6.374
^{50}V	50	23	1.015E-09	1.111E-12	-1.879E-09	-1.878E-09	2.482E-08	1.051
^{51}V	51	23	4.138E-07	4.528E-10	1.251E-06	1.251E-06	1.213E-05	1.261
^{50}Cr	50	24	8.265E-07	9.046E-10	-4.028E-06	-4.027E-06	1.770E-05	0.921
^{52}Cr	52	24	1.658E-05	1.814E-08	-5.849E-05	-5.847E-05	3.773E-04	0.979
^{53}Cr	53	24	1.916E-06	2.096E-09	-5.224E-06	-5.222E-06	4.514E-05	1.013

TableC.12 – continued

Isotope	A	Z	$X^{\rm ini}$	$mp^{\rm wind}$	$mp^{\rm preSN}$	$mp^{\rm total}$	EM	$\langle OP \rangle$
^{54}Cr	54	24	4.858E-07	5.317E-10	2.933E-05	2.933E-05	4.210E-05	3.727
^{55}Mn	55	25	1.098E-05	1.202E-08	-3.338E-05	-3.337E-05	2.553E-04	1.000
^{54}Fe	54	26	8.118E-05	8.885E-08	-3.882E-04	-3.881E-04	1.746E-03	0.925
^{56}Fe	56	26	1.322E-03	1.446E-06	-5.494E-03	-5.493E-03	2.925E-02	0.952
^{57}Fe	57	26	3.107E-05	3.400E-08	1.217E-04	1.218E-04	9.384E-04	1.299
^{58}Fe	58	26	4.207E-06	4.604E-09	1.026E-03	1.026E-03	1.136E-03	11.619
^{59}Co	59	27	3.991E-06	4.368E-09	4.598E-04	4.599E-04	5.648E-04	6.086
^{58}Ni	58	28	5.711E-05	6.250E-08	-2.710E-04	-2.710E-04	1.230E-03	0.927
^{60}Ni	60	28	2.276E-05	2.491E-08	3.398E-04	3.398E-04	9.381E-04	1.773
^{61}Ni	61	28	1.006E-06	1.101E-09	2.126E-04	2.126E-04	2.391E-04	10.224
^{62}Ni	62	28	3.259E-06	3.567E-09	7.030E-04	7.030E-04	7.886E-04	10.407
^{64}Ni	64	28	8.568E-07	9.377E-10	6.154E-04	6.154E-04	6.379E-04	32.020
^{63}Cu	63	29	6.600E-07	7.223E-10	3.241E-04	3.241E-04	3.415E-04	22.253
^{65}Cu	65	29	3.035E-07	3.321E-10	4.062E-04	4.062E-04	4.142E-04	58.708
^{64}Zn	64	30	1.131E-06	1.238E-09	1.189E-04	1.189E-04	1.486E-04	5.652
^{66}Zn	66	30	6.690E-07	7.322E-10	3.511E-04	3.511E-04	3.687E-04	23.703
^{67}Zn	67	30	9.980E-08	1.092E-10	1.123E-04	1.123E-04	1.149E-04	49.532
^{68}Zn	68	30	4.632E-07	5.070E-10	5.869E-04	5.869E-04	5.991E-04	55.623
^{70}Zn	70	30	1.577E-08	1.726E-11	3.412E-07	3.412E-07	7.557E-07	2.061
^{69}Ga	69	31	4.551E-08	4.980E-11	8.045E-05	8.045E-05	8.165E-05	77.170
^{71}Ga	71	31	3.108E-08	3.401E-11	7.383E-05	7.383E-05	7.465E-05	103.320
^{70}Ge	70	32	5.157E-08	5.644E-11	1.202E-04	1.202E-04	1.215E-04	101.353
^{72}Ge	72	32	6.910E-08	7.563E-11	1.415E-04	1.415E-04	1.433E-04	89.192
^{73}Ge	73	32	1.955E-08	2.139E-11	6.169E-05	6.169E-05	6.221E-05	136.883
^{74}Ge	74	32	9.228E-08	1.010E-10	2.353E-04	2.353E-04	2.377E-04	110.805
^{76}Ge	76	32	1.963E-08	2.148E-11	2.739E-07	2.739E-07	7.899E-07	1.731
^{75}As	75	33	1.430E-08	1.565E-11	3.109E-05	3.109E-05	3.147E-05	94.645
^{74}Se	74	34	1.198E-09	1.311E-12	-6.369E-09	-6.367E-09	2.512E-08	0.902

TableC.12 – continued

Isotope	A	Z	$X^{\rm ini}$	$mp^{\rm wind}$	$mp^{\rm preSN}$	$mp^{\rm total}$	EM	$\langle OP \rangle$
^{76}Se	76	34	1.296E-08	1.419E-11	4.553E-05	4.553E-05	4.587E-05	152.224
^{77}Se	77	34	1.070E-08	1.172E-11	2.469E-05	2.469E-05	2.497E-05	100.343
^{78}Se	78	34	3.376E-08	3.695E-11	1.347E-04	1.347E-04	1.356E-04	172.777
^{80}Se	80	34	7.226E-08	7.909E-11	4.104E-05	4.105E-05	4.294E-05	25.561
^{82}Se	82	34	1.304E-08	1.427E-11	-2.847E-08	-2.846E-08	3.142E-07	1.037
^{79}Br	79	35	1.389E-08	1.520E-11	3.114E-05	3.114E-05	3.150E-05	97.522
^{81}Br	81	35	1.386E-08	1.517E-11	1.462E-05	1.462E-05	1.499E-05	46.505
^{78}Kr	78	36	3.900E-10	4.268E-13	-2.044E-09	-2.044E-09	8.209E-09	0.905
^{80}Kr	80	36	2.575E-09	2.818E-12	1.154E-05	1.154E-05	1.161E-05	193.964
^{82}Kr	82	36	1.320E-08	1.444E-11	6.821E-05	6.821E-05	6.856E-05	223.462
^{83}Kr	83	36	1.324E-08	1.449E-11	3.757E-05	3.757E-05	3.791E-05	123.148
^{84}Kr	84	36	6.602E-08	7.225E-11	1.895E-04	1.895E-04	1.912E-04	124.581
^{86}Kr	86	36	2.044E-08	2.237E-11	1.669E-05	1.669E-05	1.722E-05	36.235
^{85}Rb	85	37	1.282E-08	1.403E-11	4.876E-05	4.876E-05	4.910E-05	164.675
^{87}Rb	87	37	5.063E-09	-1.321E-12	1.242E-05	1.242E-05	1.256E-05	106.667
^{84}Sr	84	38	3.228E-10	3.533E-13	-1.761E-09	-1.760E-09	6.725E-09	0.896
^{86}Sr	86	38	5.845E-09	6.396E-12	6.583E-05	6.583E-05	6.599E-05	485.604
^{87}Sr	87	38	4.443E-09	1.172E-11	5.204E-05	5.204E-05	5.216E-05	504.941
^{88}Sr	88	38	5.011E-08	5.484E-11	2.639E-04	2.639E-04	2.652E-04	227.628
^{89}Y	89	39	1.229E-08	1.345E-11	4.913E-05	4.913E-05	4.946E-05	173.028
^{90}Zr	90	40	1.534E-08	1.679E-11	2.428E-05	2.428E-05	2.468E-05	69.195
^{91}Zr	91	40	3.384E-09	3.703E-12	7.225E-06	7.225E-06	7.314E-06	92.955
^{92}Zr	92	40	5.227E-09	5.720E-12	7.782E-06	7.782E-06	7.919E-06	65.168
^{94}Zr	94	40	5.413E-09	5.924E-12	2.980E-06	2.980E-06	3.122E-06	24.809
^{96}Zr	96	40	8.903E-10	9.744E-13	2.272E-07	2.272E-07	2.506E-07	12.108
^{93}Nb	93	41	1.900E-09	2.079E-12	2.896E-06	2.896E-06	2.946E-06	66.697
^{92}Mo	92	42	1.012E-09	1.108E-12	-4.993E-09	-4.991E-09	2.162E-08	0.919
^{94}Mo	94	42	6.448E-10	7.056E-13	3.424E-08	3.424E-08	5.119E-08	3.415

TableC.12 – continued

Isotope	A	Z	$X^{\rm ini}$	$mp^{\rm wind}$	$mp^{\rm preSN}$	$mp^{\rm total}$	EM	$\langle OP \rangle$
^{95}Mo	95	42	1.122E-09	1.228E-12	8.258E-07	8.258E-07	8.553E-07	32.791
^{96}Mo	96	42	1.188E-09	1.300E-12	7.673E-07	7.673E-07	7.985E-07	28.923
^{97}Mo	97	42	6.875E-10	7.524E-13	3.129E-07	3.129E-07	3.310E-07	20.705
^{98}Mo	98	42	1.754E-09	1.920E-12	8.636E-07	8.636E-07	9.098E-07	22.304
^{100}Mo	100	42	7.146E-10	7.821E-13	2.400E-10	2.408E-10	1.903E-08	1.145
^{96}Ru	96	44	2.926E-10	3.202E-13	-1.518E-09	-1.518E-09	6.173E-09	0.907
^{98}Ru	98	44	1.007E-10	1.102E-13	-4.662E-10	-4.661E-10	2.181E-09	0.932
^{99}Ru	99	44	6.945E-10	7.601E-13	1.407E-07	1.407E-07	1.589E-07	9.843
^{100}Ru	100	44	6.928E-10	7.582E-13	3.705E-07	3.705E-07	3.887E-07	24.134
^{101}Ru	101	44	9.475E-10	1.037E-12	8.482E-08	8.482E-08	1.097E-07	4.981
^{102}Ru	102	44	1.770E-09	1.937E-12	5.053E-07	5.053E-07	5.518E-07	13.411
^{104}Ru	104	44	1.065E-09	1.165E-12	1.312E-08	1.312E-08	4.112E-08	1.661
^{103}Rh	103	45	1.055E-09	1.154E-12	8.957E-08	8.957E-08	1.173E-07	4.784
^{102}Pd	102	46	4.241E-11	4.642E-14	-2.317E-10	-2.317E-10	8.832E-10	0.896
^{104}Pd	104	46	4.723E-10	5.169E-13	1.942E-07	1.942E-07	2.066E-07	18.815
^{105}Pd	105	46	9.558E-10	1.046E-12	4.490E-08	4.490E-08	7.002E-08	3.151
^{106}Pd	106	46	1.181E-09	1.292E-12	2.399E-07	2.399E-07	2.710E-07	9.869
^{108}Pd	108	46	1.165E-09	1.275E-12	2.474E-07	2.474E-07	2.780E-07	10.264
^{110}Pd	110	46	5.255E-10	5.751E-13	1.066E-08	1.066E-08	2.447E-08	2.003
^{107}Ag	107	47	7.840E-10	8.580E-13	4.434E-08	4.434E-08	6.495E-08	3.563
^{109}Ag	109	47	7.420E-10	8.120E-13	1.404E-07	1.404E-07	1.599E-07	9.269
^{106}Cd	106	48	6.346E-11	6.945E-14	-3.406E-10	-3.405E-10	1.328E-09	0.900
^{108}Cd	108	48	4.604E-11	5.039E-14	1.406E-08	1.406E-08	1.527E-08	14.269
^{110}Cd	110	48	6.580E-10	7.201E-13	1.709E-07	1.709E-07	1.882E-07	12.303
^{111}Cd	111	48	6.805E-10	7.447E-13	5.207E-08	5.208E-08	6.996E-08	4.422
^{112}Cd	112	48	1.294E-09	1.417E-12	2.041E-07	2.041E-07	2.382E-07	7.914
^{113}Cd	113	48	6.614E-10	7.238E-13	5.264E-08	5.264E-08	7.002E-08	4.554
^{114}Cd	114	48	1.569E-09	1.717E-12	2.681E-07	2.681E-07	3.093E-07	8.481

TableC.12 – continued

Isotope	A	Z	$X^{\rm ini}$	$mp^{\rm wind}$	$mp^{\rm preSN}$	$mp^{\rm total}$	EM	$\langle OP \rangle$
^{116}Cd	116	48	4.161E-10	4.554E-13	1.571E-08	1.571E-08	2.665E-08	2.755
^{113}In	113	49	2.604E-11	2.850E-14	-1.262E-10	-1.262E-10	5.583E-10	0.922
^{115}In	115	49	5.915E-10	6.472E-13	5.353E-08	5.353E-08	6.908E-08	5.023
^{112}Sn	112	50	1.221E-10	1.336E-13	-6.368E-10	-6.366E-10	2.573E-09	0.906
^{114}Sn	114	50	8.435E-11	9.231E-14	-3.686E-10	-3.685E-10	1.849E-09	0.943
^{115}Sn	115	50	4.377E-11	4.799E-14	5.334E-10	5.335E-10	1.684E-09	1.655
^{116}Sn	116	50	1.893E-09	2.072E-12	2.743E-07	2.743E-07	3.240E-07	7.362
^{117}Sn	117	50	1.008E-09	1.104E-12	8.726E-08	8.726E-08	1.138E-07	4.853
^{118}Sn	118	50	3.209E-09	3.512E-12	3.226E-07	3.226E-07	4.070E-07	5.455
^{119}Sn	119	50	1.147E-09	1.255E-12	8.877E-08	8.877E-08	1.189E-07	4.459
^{120}Sn	120	50	4.391E-09	4.806E-12	3.228E-07	3.228E-07	4.382E-07	4.292
^{122}Sn	122	50	6.341E-10	6.939E-13	8.958E-09	8.959E-09	2.563E-08	1.738
^{124}Sn	124	50	8.060E-10	8.820E-13	-3.420E-09	-3.420E-09	1.777E-08	0.948
^{121}Sb	121	51	6.318E-10	6.914E-13	3.035E-08	3.035E-08	4.696E-08	3.197
^{123}Sb	123	51	4.803E-10	5.256E-13	9.951E-11	1.000E-10	1.273E-08	1.140
^{120}Te	120	52	1.628E-11	1.782E-14	-9.151E-11	-9.150E-11	3.365E-10	0.889
^{122}Te	122	52	4.489E-10	4.912E-13	2.995E-08	2.995E-08	4.175E-08	4.000
^{123}Te	123	52	1.579E-10	1.728E-13	1.012E-08	1.012E-08	1.427E-08	3.888
^{124}Te	124	52	8.441E-10	9.238E-13	5.996E-08	5.997E-08	8.215E-08	4.186
^{125}Te	125	52	1.261E-09	1.380E-12	1.411E-08	1.411E-08	4.727E-08	1.612
^{126}Te	126	52	3.375E-09	3.694E-12	9.262E-08	9.262E-08	1.814E-07	2.311
^{128}Te	128	52	5.733E-09	6.274E-12	-2.270E-08	-2.270E-08	1.280E-07	0.960
^{130}Te	130	52	6.211E-09	6.797E-12	-2.778E-08	-2.777E-08	1.355E-07	0.938
^{127}I	127	53	1.459E-09	1.597E-12	9.547E-09	9.549E-09	4.791E-08	1.412
^{124}Xe	124	54	2.210E-11	2.418E-14	-1.263E-10	-1.263E-10	4.545E-10	0.885
^{126}Xe	126	54	1.949E-11	2.133E-14	-1.057E-10	-1.057E-10	4.068E-10	0.897
^{128}Xe	128	54	3.943E-10	4.315E-13	2.555E-08	2.555E-08	3.591E-08	3.917
^{129}Xe	129	54	4.893E-09	5.355E-12	-1.506E-08	-1.505E-08	1.136E-07	0.998

TableC.12 – continued

Isotope	A	Z	$X^{\rm ini}$	$mp^{\rm wind}$	$mp^{\rm preSN}$	$mp^{\rm total}$	EM	$\langle OP \rangle$
^{130}Xe	130	54	7.865E-10	8.608E-13	5.249E-08	5.249E-08	7.317E-08	4.001
^{131}Xe	131	54	3.945E-09	4.317E-12	1.659E-09	1.663E-09	1.054E-07	1.149
^{132}Xe	132	54	4.806E-09	5.260E-12	7.239E-08	7.239E-08	1.987E-07	1.778
^{134}Xe	134	54	1.788E-09	1.957E-12	-1.927E-09	-1.925E-09	4.508E-08	1.084
^{136}Xe	136	54	1.478E-09	1.618E-12	-1.525E-09	-1.523E-09	3.734E-08	1.086
^{133}Cs	133	55	1.426E-09	1.561E-12	8.542E-09	8.544E-09	4.603E-08	1.388
^{130}Ba	130	56	1.814E-11	1.986E-14	-1.049E-10	-1.049E-10	3.720E-10	0.882
^{132}Ba	132	56	1.762E-11	1.928E-14	-9.621E-11	-9.619E-11	3.670E-10	0.896
^{134}Ba	134	56	4.272E-10	4.676E-13	2.363E-08	2.363E-08	3.486E-08	3.510
^{135}Ba	135	56	1.174E-09	1.285E-12	6.487E-09	6.488E-09	3.735E-08	1.368
^{136}Ba	136	56	1.409E-09	1.542E-12	6.403E-08	6.404E-08	1.011E-07	3.086
^{137}Ba	137	56	2.030E-09	2.221E-12	4.336E-08	4.336E-08	9.672E-08	2.049
^{138}Ba	138	56	1.305E-08	1.428E-11	3.437E-07	3.437E-07	6.869E-07	2.263
^{138}La	138	57	1.604E-12	1.756E-15	-8.857E-12	-8.855E-12	3.331E-11	0.893
^{139}La	139	57	1.790E-09	1.959E-12	3.821E-08	3.821E-08	8.527E-08	2.049
^{136}Ce	136	58	8.382E-12	9.173E-15	-4.502E-11	-4.502E-11	1.753E-10	0.900
^{138}Ce	138	58	1.148E-11	1.256E-14	-5.897E-11	-5.896E-11	2.428E-10	0.910
^{140}Ce	140	58	4.103E-09	4.490E-12	6.919E-08	6.920E-08	1.771E-07	1.856
^{142}Ce	142	58	5.229E-10	5.723E-13	4.583E-10	4.589E-10	1.421E-08	1.168
^{141}Pr	141	59	6.910E-10	7.563E-13	8.552E-09	8.553E-09	2.672E-08	1.663
^{142}Nd	142	60	9.920E-10	1.086E-12	1.671E-08	1.671E-08	4.279E-08	1.855
^{143}Nd	143	60	4.484E-10	4.907E-13	1.701E-09	1.702E-09	1.349E-08	1.294
^{144}Nd	144	60	8.826E-10	9.659E-13	6.030E-09	6.031E-09	2.923E-08	1.425
^{145}Nd	145	60	3.095E-10	3.388E-13	1.299E-09	1.299E-09	9.437E-09	1.311
^{146}Nd	146	60	6.448E-10	7.056E-13	5.275E-09	5.275E-09	2.222E-08	1.483
^{148}Nd	148	60	2.185E-10	2.391E-13	2.898E-10	2.900E-10	6.034E-09	1.188
^{150}Nd	150	60	2.168E-10	2.373E-13	-1.030E-09	-1.030E-09	4.670E-09	0.926
^{144}Sm	144	62	3.684E-11	4.031E-14	-1.819E-10	-1.818E-10	7.865E-10	0.918

TableC.12 – continued

Isotope	A	Z	$X^{\rm ini}$	$mp^{\rm wind}$	$mp^{\rm preSN}$	$mp^{\rm total}$	EM	$\langle OP \rangle$
^{147}Sm	147	62	1.834E-10	2.008E-13	6.002E-10	6.004E-10	5.423E-09	1.271
^{148}Sm	148	62	1.385E-10	1.515E-13	6.207E-10	6.209E-10	4.261E-09	1.324
^{149}Sm	149	62	1.714E-10	1.875E-13	-4.467E-10	-4.465E-10	4.058E-09	1.019
^{150}Sm	150	62	9.213E-11	1.008E-13	1.221E-09	1.221E-09	3.643E-09	1.701
^{152}Sm	152	62	3.383E-10	3.703E-13	-3.395E-10	-3.391E-10	8.554E-09	1.088
^{154}Sm	154	62	2.916E-10	3.192E-13	-8.733E-10	-8.730E-10	6.793E-09	1.002
^{151}Eu	151	63	2.036E-10	2.228E-13	-8.154E-10	-8.152E-10	4.537E-09	0.958
^{153}Eu	153	63	2.252E-10	2.465E-13	-7.369E-10	-7.367E-10	5.183E-09	0.990
^{152}Gd	152	64	2.947E-12	3.231E-15	1.339E-10	1.339E-10	2.114E-10	3.085
^{154}Gd	154	64	3.210E-11	3.513E-14	5.175E-10	5.175E-10	1.361E-09	1.824
^{155}Gd	155	64	2.192E-10	2.399E-13	-8.494E-10	-8.492E-10	4.913E-09	0.964
^{156}Gd	156	64	3.051E-10	3.339E-13	-3.195E-10	-3.192E-10	7.701E-09	1.086
^{157}Gd	157	64	2.348E-10	2.570E-13	-4.459E-10	-4.457E-10	5.727E-09	1.049
^{158}Gd	158	64	3.750E-10	4.104E-13	5.162E-10	5.166E-10	1.037E-08	1.190
^{160}Gd	160	64	3.343E-10	3.658E-13	-1.215E-09	-1.214E-09	7.573E-09	0.974
^{159}Tb	159	65	2.765E-10	3.026E-13	-7.492E-10	-7.489E-10	6.519E-09	1.014
^{156}Dy	156	66	1.004E-12	1.098E-15	-6.097E-12	-6.096E-12	2.029E-11	0.869
^{158}Dy	158	66	1.743E-12	1.907E-15	1.695E-12	1.697E-12	4.751E-11	1.173
^{160}Dy	160	66	4.301E-11	4.708E-14	5.325E-10	5.325E-10	1.663E-09	1.663
^{161}Dy	161	66	3.498E-10	3.828E-13	-1.470E-09	-1.470E-09	7.725E-09	0.950
^{162}Dy	162	66	4.748E-10	5.196E-13	-7.672E-10	-7.667E-10	1.171E-08	1.061
^{163}Dy	163	66	4.663E-10	5.103E-13	-1.600E-09	-1.600E-09	1.066E-08	0.983
^{164}Dy	164	66	5.312E-10	5.813E-13	1.012E-09	1.012E-09	1.498E-08	1.213
^{165}Ho	165	67	4.244E-10	4.645E-13	-1.642E-09	-1.642E-09	9.515E-09	0.964
^{162}Er	162	68	1.609E-12	1.761E-15	-9.764E-12	-9.762E-12	3.253E-11	0.870
^{164}Er	164	68	1.913E-11	2.093E-14	-1.143E-10	-1.143E-10	3.886E-10	0.874
^{166}Er	166	68	4.044E-10	4.426E-13	-1.111E-09	-1.111E-09	9.521E-09	1.013
^{167}Er	167	68	2.776E-10	3.038E-13	-8.586E-10	-8.583E-10	6.439E-09	0.998

TableC.12 – continued

Isotope	A	Z	$X^{\rm ini}$	$mp^{\rm wind}$	$mp^{\rm preSN}$	$mp^{\rm total}$	EM	$\langle OP \rangle$
^{168}Er	168	68	3.263E-10	3.571E-13	7.124E-10	7.128E-10	9.290E-09	1.225
^{170}Er	170	68	1.840E-10	2.014E-13	5.066E-10	5.068E-10	5.344E-09	1.249
^{169}Tm	169	69	1.854E-10	2.029E-13	5.576E-11	5.596E-11	4.930E-09	1.144
^{168}Yb	168	70	1.583E-12	1.733E-15	-9.492E-12	-9.490E-12	3.213E-11	0.873
^{170}Yb	170	70	3.746E-11	4.100E-14	1.720E-10	1.720E-10	1.157E-09	1.328
^{171}Yb	171	70	1.770E-10	1.937E-13	-6.928E-10	-6.926E-10	3.961E-09	0.962
^{172}Yb	172	70	2.722E-10	2.979E-13	9.942E-11	9.972E-11	7.255E-09	1.146
^{173}Yb	173	70	2.023E-10	2.214E-13	1.928E-10	1.931E-10	5.511E-09	1.172
^{174}Yb	174	70	4.015E-10	4.394E-13	2.600E-09	2.600E-09	1.315E-08	1.409
^{176}Yb	176	70	1.628E-10	1.782E-13	-1.073E-10	-1.072E-10	4.172E-09	1.102
^{175}Lu	175	71	1.828E-10	2.000E-13	-2.733E-11	-2.713E-11	4.778E-09	1.124
^{176}Lu	176	71	4.876E-12	-2.597E-15	1.707E-11	1.707E-11	1.453E-10	1.281
^{174}Hf	174	72	1.231E-12	1.347E-15	-7.249E-12	-7.248E-12	2.512E-11	0.877
^{176}Hf	176	72	4.036E-11	5.211E-14	5.380E-10	5.381E-10	1.599E-09	1.704
^{177}Hf	177	72	1.438E-10	1.574E-13	-2.553E-10	-2.552E-10	3.525E-09	1.054
^{178}Hf	178	72	2.121E-10	2.322E-13	9.790E-10	9.792E-10	6.556E-09	1.329
^{179}Hf	179	72	1.065E-10	1.166E-13	3.564E-10	3.565E-10	3.156E-09	1.275
^{180}Hf	180	72	2.758E-10	3.019E-13	2.542E-09	2.542E-09	9.794E-09	1.527
^{180}Ta	180	73	2.429E-14	2.658E-17	8.781E-14	8.784E-14	7.264E-13	1.286
^{181}Ta	181	73	1.986E-10	2.173E-13	2.585E-10	2.587E-10	5.479E-09	1.187
^{180}W	180	74	8.395E-13	9.187E-16	3.350E-11	3.350E-11	5.557E-11	2.847
^{182}W	182	74	1.877E-10	2.055E-13	4.274E-10	4.276E-10	5.363E-09	1.229
^{183}W	183	74	1.020E-10	1.116E-13	9.180E-10	9.182E-10	3.599E-09	1.518
^{184}W	184	74	2.195E-10	2.402E-13	1.737E-09	1.737E-09	7.507E-09	1.471
^{186}W	186	74	2.058E-10	2.253E-13	4.958E-10	4.960E-10	5.907E-09	1.234
^{185}Re	185	75	1.048E-10	1.147E-13	8.736E-10	8.737E-10	3.628E-09	1.489
^{187}Re	187	75	1.773E-10	1.940E-13	-4.907E-10	-4.905E-10	4.170E-09	1.012
^{184}Os	184	76	7.108E-13	7.779E-16	-4.052E-12	-4.051E-12	1.464E-11	0.886

TableC.12 – continued

Isotope	A	Z	$X^{\rm ini}$	$mp^{\rm wind}$	$mp^{\rm preSN}$	$mp^{\rm total}$	EM	$\langle OP \rangle$
^{186}Os	186	76	5.778E-11	6.324E-14	9.761E-11	9.767E-11	1.617E-09	1.203
^{187}Os	187	76	5.998E-11	6.564E-14	-1.545E-10	-1.545E-10	1.422E-09	1.020
^{188}Os	188	76	4.874E-10	5.334E-13	-8.654E-10	-8.649E-10	1.195E-08	1.054
^{189}Os	189	76	5.974E-10	6.537E-13	-2.767E-09	-2.766E-09	1.294E-08	0.931
^{190}Os	190	76	9.766E-10	1.069E-12	-2.011E-09	-2.010E-09	2.366E-08	1.042
^{192}Os	192	76	1.533E-09	1.677E-12	-6.369E-09	-6.367E-09	3.392E-08	0.952
^{191}Ir	191	77	1.357E-09	1.485E-12	-7.279E-09	-7.277E-09	2.841E-08	0.900
^{193}Ir	193	77	2.308E-09	2.526E-12	-1.240E-08	-1.239E-08	4.829E-08	0.900
^{190}Pt	190	78	1.008E-12	1.104E-15	-5.658E-12	-5.657E-12	2.085E-11	0.889
^{192}Pt	192	78	5.850E-11	6.405E-14	1.131E-09	1.131E-09	2.669E-09	1.962
^{194}Pt	194	78	2.490E-09	2.725E-12	-9.255E-09	-9.252E-09	5.620E-08	0.971
^{195}Pt	195	78	2.568E-09	2.811E-12	-1.261E-08	-1.261E-08	5.491E-08	0.920
^{196}Pt	196	78	1.926E-09	2.108E-12	-1.948E-09	-1.946E-09	4.868E-08	1.087
^{198}Pt	198	78	5.522E-10	6.043E-13	-2.303E-09	-2.302E-09	1.221E-08	0.951
^{197}Au	197	79	1.083E-09	1.186E-12	-3.311E-09	-3.310E-09	2.517E-08	0.999
^{196}Hg	196	80	3.009E-12	3.293E-15	-1.567E-11	-1.567E-11	6.344E-11	0.907
^{198}Hg	198	80	1.975E-10	2.162E-13	4.178E-09	4.178E-09	9.370E-09	2.041
^{199}Hg	199	80	3.360E-10	3.677E-13	1.167E-09	1.168E-09	1.000E-08	1.280
^{200}Hg	200	80	4.622E-10	5.059E-13	4.737E-09	4.737E-09	1.689E-08	1.571
^{201}Hg	201	80	2.651E-10	2.901E-13	3.078E-09	3.078E-09	1.005E-08	1.630
^{202}Hg	202	80	6.036E-10	6.606E-13	9.990E-09	9.990E-09	2.586E-08	1.843
^{204}Hg	204	80	1.401E-10	1.534E-13	-2.218E-10	-2.216E-10	3.462E-09	1.063
^{203}Tl	203	81	3.221E-10	3.525E-13	8.300E-09	8.300E-09	1.677E-08	2.239
^{205}Tl	205	81	7.764E-10	8.497E-13	1.104E-08	1.104E-08	3.145E-08	1.742
^{204}Pb	204	82	2.931E-10	3.208E-13	7.248E-09	7.248E-09	1.495E-08	2.194
^{206}Pb	206	82	2.798E-09	3.062E-12	4.022E-08	4.023E-08	1.138E-07	1.749
^{207}Pb	207	82	3.090E-09	3.381E-12	5.770E-08	5.770E-08	1.389E-07	1.934
^{208}Pb	208	82	8.850E-09	9.685E-12	1.218E-07	1.218E-07	3.545E-07	1.723

TableC.12 – continued

Isotope	A	Z	X^{ini}	mp^{wind}	mp^{preSN}	mp^{total}	EM	$\langle OP \rangle$
^{209}Bi	209	83	8.718E-10	9.541E-13	7.706E-09	7.707E-09	3.063E-08	1.511

Table C.13: Yields for model 60ST.

Isotope	A	Z	X^{ini}	mp^{wind}	mp^{preSN}	mp^{total}	EM	$\langle OP \rangle$
^{1}H	1	1	7.064E-01	-1.464E+01	-5.451E+00	-2.009E+01	1.826E+01	0.519
^{2}H	2	1	1.371E-05	-6.158E-04	-1.057E-04	-7.215E-04	2.248E-05	0.033
^{3}He	3	2	4.540E-05	-1.187E-03	-3.503E-04	-1.538E-03	9.269E-04	0.410
^{4}He	4	2	2.735E-01	1.122E+01	-1.775E+00	9.448E+00	2.430E+01	1.785
^{7}Li	7	3	7.605E-11	-3.417E-09	-5.868E-10	-4.004E-09	1.250E-10	0.033
^{11}B	11	5	2.856E-09	-1.792E-14	6.053E-14	4.261E-14	1.550E-07	1.091
^{12}C	12	6	3.425E-03	2.761E+00	1.550E+00	4.312E+00	4.497E+00	26.390
^{13}C	13	6	4.156E-05	2.163E-04	-3.206E-04	-1.044E-04	2.152E-03	1.040
^{14}N	14	7	1.059E-03	2.505E-01	-8.124E-03	2.424E-01	2.998E-01	5.691
^{15}N	15	7	4.171E-06	-1.355E-04	-3.205E-05	-1.676E-04	5.886E-05	0.284
^{16}O	16	8	9.624E-03	2.265E-01	4.169E+00	4.395E+00	4.918E+00	10.268
^{17}O	17	8	3.813E-06	-7.860E-05	-1.251E-05	-9.110E-05	1.159E-04	0.611
^{18}O	18	8	2.171E-05	-6.843E-04	-1.665E-04	-8.508E-04	3.278E-04	0.303
^{19}F	19	9	5.611E-07	2.740E-05	-4.145E-06	2.325E-05	5.372E-05	1.924
^{20}Ne	20	10	1.818E-03	-1.494E-03	1.172E+00	1.170E+00	1.269E+00	14.031
^{21}Ne	21	10	4.575E-06	3.233E-05	1.723E-03	1.756E-03	2.004E-03	8.802
^{22}Ne	22	10	1.470E-04	1.731E-01	1.492E-02	1.880E-01	1.960E-01	26.785
^{23}Na	23	11	4.000E-05	6.217E-03	3.923E-02	4.544E-02	4.761E-02	23.923
^{24}Mg	24	12	5.862E-04	4.738E-05	1.089E-01	1.090E-01	1.408E-01	4.827
^{25}Mg	25	12	7.733E-05	-1.576E-03	5.018E-02	4.861E-02	5.281E-02	13.722
^{26}Mg	26	12	8.848E-05	4.810E-03	9.917E-02	1.040E-01	1.088E-01	24.706
^{27}Al	27	13	6.481E-05	1.586E-04	1.418E-02	1.434E-02	1.786E-02	5.536
^{28}Si	28	14	7.453E-04	-1.002E-05	7.991E-03	7.980E-03	4.844E-02	1.306
^{29}Si	29	14	3.919E-05	1.049E-05	4.936E-03	4.947E-03	7.075E-03	3.627
^{30}Si	30	14	2.673E-05	4.685E-05	2.401E-03	2.448E-03	3.899E-03	2.932
^{31}P	31	15	7.106E-06	5.285E-06	6.510E-04	6.563E-04	1.042E-03	2.947
^{32}S	32	16	4.011E-04	-5.933E-05	-1.551E-03	-1.610E-03	2.016E-02	1.010

TableC.13 – continued

Isotope	A	Z	$X^{\rm ini}$	$mp^{\rm wind}$	$mp^{\rm preSN}$	$mp^{\rm total}$	EM	$\langle OP \rangle$
^{33}S	33	16	3.265E-06	2.239E-05	3.211E-05	5.450E-05	2.317E-04	1.426
^{34}S	34	16	1.890E-05	2.315E-06	1.594E-04	1.617E-04	1.188E-03	1.263
^{36}S	36	16	8.073E-08	1.419E-06	4.553E-05	4.695E-05	5.134E-05	12.779
^{35}Cl	35	17	6.821E-06	-4.238E-06	-2.758E-05	-3.181E-05	3.385E-04	0.997
^{37}Cl	37	17	2.306E-06	4.497E-05	3.322E-04	3.772E-04	5.024E-04	4.378
^{36}Ar	36	18	8.202E-05	-4.158E-05	-5.240E-04	-5.656E-04	3.887E-03	0.952
^{38}Ar	38	18	1.574E-05	7.972E-06	2.685E-04	2.765E-04	1.131E-03	1.444
^{40}Ar	40	18	2.650E-08	7.570E-08	3.240E-05	3.248E-05	3.391E-05	25.716
^{39}K	39	19	3.900E-06	5.572E-07	6.898E-05	6.954E-05	2.812E-04	1.449
^{40}K	40	19	5.005E-10	2.033E-06	7.551E-06	9.584E-06	9.611E-06	385.878
^{41}K	41	19	2.959E-07	1.338E-05	1.721E-05	3.058E-05	4.665E-05	3.168
^{40}Ca	40	20	7.225E-05	-2.627E-05	-3.926E-04	-4.189E-04	3.504E-03	0.974
^{42}Ca	42	20	5.063E-07	2.141E-06	2.643E-05	2.857E-05	5.606E-05	2.225
^{43}Ca	43	20	1.082E-07	1.430E-07	9.765E-06	9.908E-06	1.578E-05	2.932
^{44}Ca	44	20	1.710E-06	-3.919E-07	2.878E-05	2.838E-05	1.212E-04	1.424
^{46}Ca	46	20	3.428E-09	-1.021E-09	4.180E-06	4.179E-06	4.365E-06	25.584
^{48}Ca	48	20	1.672E-07	-8.361E-09	-2.318E-07	-2.401E-07	8.839E-06	1.062
^{45}Sc	45	21	5.414E-08	5.028E-07	1.053E-05	1.104E-05	1.398E-05	5.188
^{46}Ti	46	22	3.232E-07	-3.809E-08	5.082E-06	5.044E-06	2.259E-05	1.405
^{47}Ti	47	22	2.977E-07	-6.896E-07	2.407E-06	1.717E-06	1.788E-05	1.207
^{48}Ti	48	22	3.014E-06	-4.669E-06	-1.461E-05	-1.928E-05	1.443E-04	0.962
^{49}Ti	49	22	2.257E-07	5.115E-06	7.349E-06	1.246E-05	2.472E-05	2.201
^{50}Ti	50	22	2.208E-07	7.961E-07	2.980E-05	3.060E-05	4.259E-05	3.876
^{50}V	50	23	1.015E-09	-2.727E-09	2.162E-08	1.889E-08	7.402E-08	1.465
^{51}V	51	23	4.138E-07	8.208E-07	8.240E-08	9.032E-07	2.337E-05	1.135
^{50}Cr	50	24	8.265E-07	-2.340E-06	-6.268E-06	-8.609E-06	3.626E-05	0.882
^{52}Cr	52	24	1.658E-05	-4.383E-06	-9.297E-05	-9.735E-05	8.025E-04	0.973
^{53}Cr	53	24	1.916E-06	-2.418E-06	-6.938E-06	-9.355E-06	9.464E-05	0.993

TableC.13 – continued

Isotope	A	Z	$X^{\rm ini}$	$mp^{\rm wind}$	$mp^{\rm preSN}$	$mp^{\rm total}$	EM	$\langle OP \rangle$
^{54}Cr	54	24	4.858E-07	8.239E-06	5.259E-05	6.083E-05	8.721E-05	3.607
^{55}Mn	55	25	1.098E-05	1.053E-04	-5.970E-05	4.555E-05	6.417E-04	1.174
^{54}Fe	54	26	8.118E-05	-1.633E-04	-6.097E-04	-7.730E-04	3.634E-03	0.900
^{56}Fe	56	26	1.322E-03	-5.035E-04	-8.575E-03	-9.078E-03	6.267E-02	0.953
^{57}Fe	57	26	3.107E-05	4.086E-04	2.837E-04	6.923E-04	2.379E-03	1.539
^{58}Fe	58	26	4.207E-06	1.601E-04	2.165E-03	2.325E-03	2.553E-03	12.197
^{59}Co	59	27	3.991E-06	4.553E-05	1.241E-03	1.287E-03	1.504E-03	7.570
^{58}Ni	58	28	5.711E-05	-9.613E-05	-4.288E-04	-5.250E-04	2.575E-03	0.906
^{60}Ni	60	28	2.276E-05	-7.639E-06	6.210E-04	6.133E-04	1.849E-03	1.633
^{61}Ni	61	28	1.006E-06	2.661E-05	4.026E-04	4.292E-04	4.838E-04	9.667
^{62}Ni	62	28	3.259E-06	8.273E-06	1.344E-03	1.352E-03	1.529E-03	9.428
^{64}Ni	64	28	8.568E-07	6.791E-07	1.203E-03	1.204E-03	1.251E-03	29.329
^{63}Cu	63	29	6.600E-07	5.481E-06	8.191E-04	8.245E-04	8.604E-04	26.195
^{65}Cu	65	29	3.035E-07	3.208E-06	5.025E-04	5.057E-04	5.222E-04	34.578
^{64}Zn	64	30	1.131E-06	-1.176E-06	1.119E-04	1.107E-04	1.721E-04	3.058
^{66}Zn	66	30	6.690E-07	-4.248E-07	4.313E-04	4.309E-04	4.672E-04	14.035
^{67}Zn	67	30	9.980E-08	2.373E-07	1.379E-04	1.381E-04	1.435E-04	28.901
^{68}Zn	68	30	4.632E-07	5.201E-07	5.212E-04	5.217E-04	5.469E-04	23.725
^{70}Zn	70	30	1.577E-08	-1.783E-08	1.736E-06	1.719E-06	2.575E-06	3.281
^{69}Ga	69	31	4.551E-08	1.956E-07	6.768E-05	6.787E-05	7.034E-05	31.065
^{71}Ga	71	31	3.108E-08	6.618E-08	3.741E-05	3.747E-05	3.916E-05	25.324
^{70}Ge	70	32	5.157E-08	1.854E-07	9.155E-05	9.174E-05	9.454E-05	36.839
^{72}Ge	72	32	6.910E-08	-1.343E-08	8.546E-05	8.545E-05	8.920E-05	25.940
^{73}Ge	73	32	1.955E-08	-4.482E-09	3.470E-05	3.469E-05	3.575E-05	36.758
^{74}Ge	74	32	9.228E-08	8.323E-08	1.078E-04	1.078E-04	1.129E-04	24.575
^{76}Ge	76	32	1.963E-08	-2.296E-08	9.435E-07	9.206E-07	1.986E-06	2.033
^{75}As	75	33	1.430E-08	-2.999E-08	1.361E-05	1.358E-05	1.435E-05	20.169
^{74}Se	74	34	1.198E-09	-7.972E-09	-9.237E-09	-1.721E-08	4.782E-08	0.802

TableC.13 – continued

Isotope	A	Z	$X^{\rm ini}$	$mp^{\rm wind}$	$mp^{\rm preSN}$	$mp^{\rm total}$	EM	$\langle OP \rangle$
^{76}Se	76	34	1.296E-08	7.793E-08	1.999E-05	2.006E-05	2.077E-05	32.199
^{77}Se	77	34	1.070E-08	-1.004E-08	9.628E-06	9.618E-06	1.020E-05	19.146
^{78}Se	78	34	3.376E-08	8.526E-08	4.422E-05	4.430E-05	4.613E-05	27.459
^{80}Se	80	34	7.226E-08	-1.441E-07	3.448E-05	3.434E-05	3.826E-05	10.640
^{82}Se	82	34	1.304E-08	-7.190E-09	1.170E-07	1.098E-07	8.175E-07	1.260
^{79}Br	79	35	1.389E-08	-7.885E-08	1.147E-05	1.139E-05	1.214E-05	17.562
^{81}Br	81	35	1.386E-08	1.881E-08	6.533E-06	6.552E-06	7.304E-06	10.591
^{78}Kr	78	36	3.900E-10	-2.548E-09	-3.008E-09	-5.556E-09	1.562E-08	0.805
^{80}Kr	80	36	2.575E-09	6.001E-08	9.719E-07	1.032E-06	1.172E-06	9.145
^{82}Kr	82	36	1.320E-08	1.598E-07	1.286E-05	1.302E-05	1.373E-05	20.915
^{83}Kr	83	36	1.324E-08	-2.203E-08	5.548E-06	5.526E-06	6.245E-06	9.477
^{84}Kr	84	36	6.602E-08	2.602E-08	2.407E-05	2.410E-05	2.768E-05	8.426
^{86}Kr	86	36	2.044E-08	-3.909E-09	1.118E-05	1.118E-05	1.229E-05	12.079
^{85}Rb	85	37	1.282E-08	6.612E-10	8.702E-06	8.703E-06	9.399E-06	14.728
^{87}Rb	87	37	5.063E-09	2.524E-10	5.084E-06	5.084E-06	5.359E-06	21.272
^{84}Sr	84	38	3.228E-10	-2.371E-09	-2.490E-09	-4.861E-09	1.266E-08	0.788
^{86}Sr	86	38	5.845E-09	9.890E-08	2.551E-06	2.650E-06	2.967E-06	10.202
^{87}Sr	87	38	4.443E-09	1.995E-08	1.380E-06	1.400E-06	1.642E-06	7.425
^{88}Sr	88	38	5.011E-08	1.942E-08	1.076E-05	1.078E-05	1.350E-05	5.413
^{89}Y	89	39	1.229E-08	5.184E-09	2.160E-06	2.165E-06	2.833E-06	4.630
^{90}Zr	90	40	1.534E-08	-3.376E-10	9.584E-07	9.580E-07	1.791E-06	2.346
^{91}Zr	91	40	3.384E-09	1.257E-09	2.506E-07	2.519E-07	4.356E-07	2.587
^{92}Zr	92	40	5.227E-09	4.211E-09	4.543E-07	4.585E-07	7.423E-07	2.854
^{94}Zr	94	40	5.413E-09	-6.980E-09	2.111E-07	2.041E-07	4.980E-07	1.849
^{96}Zr	96	40	8.903E-10	-4.657E-10	1.896E-07	1.891E-07	2.374E-07	5.359
^{93}Nb	93	41	1.900E-09	-4.815E-09	1.756E-07	1.708E-07	2.739E-07	2.897
^{92}Mo	92	42	1.012E-09	-3.509E-09	-7.719E-09	-1.123E-08	4.374E-08	0.868
^{94}Mo	94	42	6.448E-10	7.394E-09	-4.545E-09	2.850E-09	3.785E-08	1.180

TableC.13 – continued

Isotope	A	Z	$X^{\rm ini}$	$mp^{\rm wind}$	$mp^{\rm preSN}$	$mp^{\rm total}$	EM	$\langle OP \rangle$
^{95}Mo	95	42	1.122E-09	-2.998E-10	9.617E-08	9.587E-08	1.568E-07	2.808
^{96}Mo	96	42	1.188E-09	6.964E-09	1.523E-08	2.220E-08	8.667E-08	1.467
^{97}Mo	97	42	6.875E-10	-1.711E-10	6.887E-09	6.716E-09	4.404E-08	1.287
^{98}Mo	98	42	1.754E-09	2.418E-09	2.288E-08	2.529E-08	1.205E-07	1.381
^{100}Mo	100	42	7.146E-10	-2.967E-09	-3.425E-09	-6.392E-09	3.240E-08	0.911
^{96}Ru	96	44	2.926E-10	-1.746E-09	-2.254E-09	-4.000E-09	1.188E-08	0.816
^{98}Ru	98	44	1.007E-10	2.138E-10	-7.601E-10	-5.464E-10	4.921E-09	0.982
^{99}Ru	99	44	6.945E-10	-2.714E-09	4.038E-10	-2.311E-09	3.539E-08	1.024
^{100}Ru	100	44	6.928E-10	3.284E-09	1.121E-08	1.450E-08	5.211E-08	1.511
^{101}Ru	101	44	9.475E-10	-5.740E-09	-3.218E-09	-8.958E-09	4.248E-08	0.901
^{102}Ru	102	44	1.770E-09	2.167E-09	1.331E-08	1.548E-08	1.116E-07	1.267
^{104}Ru	104	44	1.065E-09	-5.741E-09	-4.406E-09	-1.015E-08	4.767E-08	0.899
^{103}Rh	103	45	1.055E-09	-5.687E-09	-2.866E-09	-8.553E-09	4.870E-08	0.928
^{102}Pd	102	46	4.241E-11	-3.128E-10	-3.272E-10	-6.400E-10	1.662E-09	0.788
^{104}Pd	104	46	4.723E-10	6.412E-09	7.853E-09	1.427E-08	3.990E-08	1.698
^{105}Pd	105	46	9.558E-10	-4.925E-09	-4.179E-09	-9.104E-09	4.278E-08	0.900
^{106}Pd	106	46	1.181E-09	4.908E-09	7.666E-09	1.257E-08	7.668E-08	1.305
^{108}Pd	108	46	1.165E-09	3.789E-09	1.093E-08	1.472E-08	7.796E-08	1.345
^{110}Pd	110	46	5.255E-10	-2.763E-09	-6.063E-10	-3.369E-09	2.516E-08	0.962
^{107}Ag	107	47	7.840E-10	-3.204E-09	-2.719E-09	-5.923E-09	3.664E-08	0.939
^{109}Ag	109	47	7.420E-10	-1.485E-09	4.714E-09	3.229E-09	4.351E-08	1.178
^{106}Cd	106	48	6.346E-11	-4.419E-10	-4.895E-10	-9.313E-10	2.514E-09	0.796
^{108}Cd	108	48	4.604E-11	3.545E-09	-1.554E-10	3.390E-09	5.889E-09	2.571
^{110}Cd	110	48	6.580E-10	6.684E-09	9.130E-09	1.581E-08	5.154E-08	1.574
^{111}Cd	111	48	6.805E-10	-1.358E-09	-2.551E-10	-1.613E-09	3.533E-08	1.043
^{112}Cd	112	48	1.294E-09	3.701E-09	9.266E-09	1.297E-08	8.323E-08	1.292
^{113}Cd	113	48	6.614E-10	-1.265E-09	1.517E-10	-1.113E-09	3.479E-08	1.057
^{114}Cd	114	48	1.569E-09	4.686E-09	1.470E-08	1.938E-08	1.045E-07	1.339

TableC.13 – continued

Isotope	A	Z	$X^{\rm ini}$	$mp^{\rm wind}$	$mp^{\rm preSN}$	$mp^{\rm total}$	EM	$\langle OP \rangle$
^{116}Cd	116	48	4.161E-10	-1.401E-09	6.480E-09	5.080E-09	2.767E-08	1.336
^{113}In	113	49	2.604E-11	-1.193E-10	-2.005E-10	-3.198E-10	1.094E-09	0.844
^{115}In	115	49	5.915E-10	-1.536E-09	1.258E-09	-2.779E-10	3.183E-08	1.082
^{112}Sn	112	50	1.221E-10	-7.432E-10	-9.409E-10	-1.684E-09	4.945E-09	0.814
^{114}Sn	114	50	8.435E-11	8.976E-11	-6.376E-10	-5.479E-10	4.031E-09	0.960
^{115}Sn	115	50	4.377E-11	-1.664E-11	-3.159E-10	-3.325E-10	2.044E-09	0.938
^{116}Sn	116	50	1.893E-09	4.900E-09	1.254E-08	1.744E-08	1.202E-07	1.276
^{117}Sn	117	50	1.008E-09	-1.375E-09	3.067E-09	1.692E-09	5.643E-08	1.125
^{118}Sn	118	50	3.209E-09	2.950E-09	2.404E-08	2.699E-08	2.012E-07	1.260
^{119}Sn	119	50	1.147E-09	-4.278E-10	5.557E-09	5.130E-09	6.740E-08	1.181
^{120}Sn	120	50	4.391E-09	3.150E-09	3.704E-08	4.019E-08	2.786E-07	1.275
^{122}Sn	122	50	6.341E-10	-7.769E-10	1.851E-08	1.773E-08	5.215E-08	1.653
^{124}Sn	124	50	8.060E-10	-7.214E-10	-5.149E-09	-5.870E-09	3.788E-08	0.945
^{121}Sb	121	51	6.318E-10	-2.073E-09	2.922E-09	8.492E-10	3.515E-08	1.118
^{123}Sb	123	51	4.803E-10	-3.056E-09	-1.031E-09	-4.086E-09	2.199E-08	0.920
^{120}Te	120	52	1.628E-11	-1.289E-10	-1.256E-10	-2.545E-10	6.295E-10	0.777
^{122}Te	122	52	4.489E-10	2.010E-09	4.050E-09	6.060E-09	3.043E-08	1.362
^{123}Te	123	52	1.579E-10	7.355E-10	1.232E-09	1.968E-09	1.054E-08	1.341
^{124}Te	124	52	8.441E-10	3.836E-09	8.921E-09	1.276E-08	5.858E-08	1.395
^{125}Te	125	52	1.261E-09	-6.380E-09	-4.826E-09	-1.121E-08	5.727E-08	0.912
^{126}Te	126	52	3.375E-09	9.541E-10	1.027E-09	1.981E-09	1.852E-07	1.103
^{128}Te	128	52	5.733E-09	-1.139E-08	-3.776E-08	-4.915E-08	2.621E-07	0.919
^{130}Te	130	52	6.211E-09	-4.981E-09	-4.385E-08	-4.883E-08	2.883E-07	0.933
^{127}I	127	53	1.459E-09	-8.197E-09	-7.061E-09	-1.526E-08	6.395E-08	0.881
^{124}Xe	124	54	2.210E-11	-1.801E-10	-1.705E-10	-3.506E-10	8.489E-10	0.772
^{126}Xe	126	54	1.949E-11	-1.410E-10	-1.504E-10	-2.914E-10	7.668E-10	0.791
^{128}Xe	128	54	3.943E-10	7.609E-09	4.320E-09	1.193E-08	3.333E-08	1.699
^{129}Xe	129	54	4.893E-09	-3.386E-08	-3.363E-08	-6.749E-08	1.981E-07	0.814

TableC.13 – continued

Isotope	A	Z	$X^{\rm ini}$	$mp^{\rm wind}$	$mp^{\rm preSN}$	$mp^{\rm total}$	EM	$\langle OP \rangle$
^{130}Xe	130	54	7.865E-10	3.331E-08	1.105E-08	4.436E-08	8.706E-08	2.224
^{131}Xe	131	54	3.945E-09	-1.548E-08	-2.289E-08	-3.837E-08	1.758E-07	0.895
^{132}Xe	132	54	4.806E-09	2.535E-08	2.414E-09	2.776E-08	2.887E-07	1.207
^{134}Xe	134	54	1.788E-09	-1.910E-09	5.097E-09	3.187E-09	1.003E-07	1.127
^{136}Xe	136	54	1.478E-09	-9.899E-11	-1.783E-09	-1.882E-09	7.838E-08	1.065
^{133}Cs	133	55	1.426E-09	-3.778E-09	-5.493E-09	-9.271E-09	6.815E-08	0.960
^{130}Ba	130	56	1.814E-11	-1.507E-10	-1.400E-10	-2.907E-10	6.942E-10	0.769
^{132}Ba	132	56	1.762E-11	-1.303E-10	-1.359E-10	-2.662E-10	6.904E-10	0.787
^{134}Ba	134	56	4.272E-10	1.508E-08	7.702E-09	2.278E-08	4.597E-08	2.162
^{135}Ba	135	56	1.174E-09	-2.904E-09	1.000E-09	-1.904E-09	6.182E-08	1.058
^{136}Ba	136	56	1.409E-09	1.263E-08	2.070E-08	3.333E-08	1.098E-07	1.566
^{137}Ba	137	56	2.030E-09	1.136E-11	1.292E-08	1.293E-08	1.231E-07	1.219
^{138}Ba	138	56	1.305E-08	5.798E-09	3.569E-07	3.626E-07	1.071E-06	1.649
^{138}La	138	57	1.604E-12	-1.221E-11	-1.237E-11	-2.459E-11	6.249E-11	0.783
^{139}La	139	57	1.790E-09	-1.333E-10	4.341E-08	4.328E-08	1.405E-07	1.577
^{136}Ce	136	58	8.382E-12	-5.752E-11	-6.464E-11	-1.222E-10	3.329E-10	0.798
^{138}Ce	138	58	1.148E-11	-6.308E-11	-8.833E-11	-1.514E-10	4.717E-10	0.826
^{140}Ce	140	58	4.103E-09	8.475E-10	6.842E-08	6.927E-08	2.920E-07	1.430
^{142}Ce	142	58	5.229E-10	-7.436E-10	1.244E-08	1.170E-08	4.009E-08	1.541
^{141}Pr	141	59	6.910E-10	-1.523E-09	8.807E-09	7.284E-09	4.480E-08	1.303
^{142}Nd	142	60	9.920E-10	1.867E-09	5.264E-09	7.130E-09	6.098E-08	1.235
^{143}Nd	143	60	4.484E-10	-1.682E-09	-9.150E-12	-1.691E-09	2.265E-08	1.015
^{144}Nd	144	60	8.826E-10	4.488E-10	5.151E-09	5.600E-09	5.351E-08	1.218
^{145}Nd	145	60	3.095E-10	-1.099E-09	6.987E-10	-4.005E-10	1.640E-08	1.065
^{146}Nd	146	60	6.448E-10	1.742E-09	6.775E-09	8.517E-09	4.352E-08	1.356
^{148}Nd	148	60	2.185E-10	-1.103E-09	2.079E-09	9.761E-10	1.284E-08	1.181
^{150}Nd	150	60	2.168E-10	-1.235E-09	-1.555E-09	-2.790E-09	8.981E-09	0.832
^{144}Sm	144	62	3.684E-11	-1.350E-10	-2.814E-10	-4.164E-10	1.583E-09	0.864

TableC.13 – continued

Isotope	A	Z	$X^{\rm ini}$	$mp^{\rm wind}$	$mp^{\rm preSN}$	$mp^{\rm total}$	EM	$\langle OP \rangle$
^{147}Sm	147	62	1.834E-10	-9.759E-10	-2.708E-10	-1.247E-09	8.712E-09	0.954
^{148}Sm	148	62	1.385E-10	1.362E-09	-4.091E-10	9.534E-10	8.470E-09	1.229
^{149}Sm	149	62	1.714E-10	-1.116E-09	-9.788E-10	-2.094E-09	7.209E-09	0.845
^{150}Sm	150	62	9.213E-11	1.009E-09	1.049E-09	2.058E-09	7.060E-09	1.540
^{152}Sm	152	62	3.383E-10	-2.518E-09	-1.016E-09	-3.535E-09	1.483E-08	0.881
^{154}Sm	154	62	2.916E-10	-1.817E-09	-1.224E-09	-3.040E-09	1.279E-08	0.881
^{151}Eu	151	63	2.036E-10	-1.615E-09	-1.215E-09	-2.831E-09	8.222E-09	0.812
^{153}Eu	153	63	2.252E-10	-1.551E-09	-1.231E-09	-2.783E-09	9.443E-09	0.843
^{152}Gd	152	64	2.947E-12	8.178E-10	1.547E-11	8.332E-10	9.932E-10	6.773
^{154}Gd	154	64	3.210E-11	9.651E-10	1.440E-10	1.109E-09	2.851E-09	1.785
^{155}Gd	155	64	2.192E-10	-1.369E-09	-1.470E-09	-2.839E-09	9.061E-09	0.831
^{156}Gd	156	64	3.051E-10	1.117E-10	-1.060E-09	-9.481E-10	1.562E-08	1.028
^{157}Gd	157	64	2.348E-10	-8.738E-10	-9.189E-10	-1.793E-09	1.096E-08	0.938
^{158}Gd	158	64	3.750E-10	1.496E-09	-3.399E-10	1.156E-09	2.151E-08	1.153
^{160}Gd	160	64	3.343E-10	-1.848E-09	-1.711E-09	-3.559E-09	1.459E-08	0.877
^{159}Tb	159	65	2.765E-10	-1.186E-09	-1.296E-09	-2.482E-09	1.253E-08	0.911
^{156}Dy	156	66	1.004E-12	-8.729E-12	-7.744E-12	-1.647E-11	3.801E-11	0.761
^{158}Dy	158	66	1.743E-12	3.442E-10	-6.226E-12	3.380E-10	4.326E-10	4.989
^{160}Dy	160	66	4.301E-11	1.856E-09	2.805E-10	2.136E-09	4.471E-09	2.089
^{161}Dy	161	66	3.498E-10	-2.004E-09	-2.151E-09	-4.155E-09	1.483E-08	0.852
^{162}Dy	162	66	4.748E-10	7.643E-10	-1.775E-09	-1.011E-09	2.477E-08	1.048
^{163}Dy	163	66	4.663E-10	-2.047E-09	-2.483E-09	-4.529E-09	2.079E-08	0.896
^{164}Dy	164	66	5.312E-10	4.701E-09	-1.527E-10	4.548E-09	3.338E-08	1.263
^{165}Ho	165	67	4.244E-10	-2.043E-09	-2.450E-09	-4.494E-09	1.855E-08	0.878
^{162}Er	162	68	1.609E-12	-1.398E-11	-1.241E-11	-2.639E-11	6.095E-11	0.761
^{164}Er	164	68	1.913E-11	-1.643E-10	-1.476E-10	-3.118E-10	7.266E-10	0.763
^{166}Er	166	68	4.044E-10	3.969E-10	-2.321E-09	-1.924E-09	2.003E-08	0.995
^{167}Er	167	68	2.776E-10	-9.283E-10	-1.469E-09	-2.397E-09	1.267E-08	0.917

TableC.13 – continued

Isotope	A	Z	$X^{\rm ini}$	$mp^{\rm wind}$	$mp^{\rm preSN}$	$mp^{\rm total}$	EM	$\langle OP \rangle$
^{168}Er	168	68	3.263E-10	3.267E-09	-2.088E-10	3.058E-09	2.077E-08	1.279
^{170}Er	170	68	1.840E-10	-1.085E-09	1.209E-09	1.232E-10	1.011E-08	1.104
^{169}Tm	169	69	1.854E-10	-5.623E-10	-3.916E-10	-9.539E-10	9.112E-09	0.988
^{168}Yb	168	70	1.583E-12	-1.365E-11	-1.222E-11	-2.587E-11	6.008E-11	0.763
^{170}Yb	170	70	3.746E-11	2.303E-09	-1.356E-10	2.167E-09	4.201E-09	2.253
^{171}Yb	171	70	1.770E-10	1.411E-10	-1.206E-09	-1.065E-09	8.545E-09	0.970
^{172}Yb	172	70	2.722E-10	2.621E-09	-6.743E-10	1.946E-09	1.672E-08	1.235
^{173}Yb	173	70	2.023E-10	3.353E-10	-2.195E-10	1.158E-10	1.110E-08	1.102
^{174}Yb	174	70	4.015E-10	3.557E-09	1.797E-09	5.354E-09	2.715E-08	1.359
^{176}Yb	176	70	1.628E-10	-7.370E-10	1.461E-10	-5.910E-10	8.247E-09	1.018
^{175}Lu	175	71	1.828E-10	-7.372E-10	-4.966E-10	-1.234E-09	8.689E-09	0.955
^{176}Lu	176	71	4.876E-12	5.429E-11	2.689E-10	3.232E-10	5.879E-10	2.423
^{174}Hf	174	72	1.231E-12	-1.045E-11	-9.500E-12	-1.995E-11	4.689E-11	0.765
^{176}Hf	176	72	4.036E-11	9.867E-10	1.266E-11	9.993E-10	3.190E-09	1.588
^{177}Hf	177	72	1.438E-10	-5.679E-10	-5.821E-10	-1.150E-09	6.656E-09	0.930
^{178}Hf	178	72	2.121E-10	1.239E-09	7.318E-10	1.971E-09	1.349E-08	1.278
^{179}Hf	179	72	1.065E-10	8.269E-11	2.208E-10	3.035E-10	6.086E-09	1.148
^{180}Hf	180	72	2.758E-10	2.050E-09	2.293E-09	4.342E-09	1.932E-08	1.407
^{180}Ta	180	73	2.429E-14	-2.133E-13	6.950E-12	6.737E-12	8.055E-12	6.664
^{181}Ta	181	73	1.986E-10	-9.334E-10	-2.527E-10	-1.186E-09	9.594E-09	0.971
^{180}W	180	74	8.395E-13	-4.290E-12	4.212E-12	-7.841E-14	4.550E-11	1.089
^{182}W	182	74	1.877E-10	7.873E-10	-4.818E-10	3.054E-10	1.050E-08	1.124
^{183}W	183	74	1.020E-10	2.187E-10	2.857E-10	5.044E-10	6.040E-09	1.190
^{184}W	184	74	2.195E-10	5.634E-10	1.332E-09	1.896E-09	1.381E-08	1.265
^{186}W	186	74	2.058E-10	-1.196E-09	6.822E-10	-5.134E-10	1.066E-08	1.041
^{185}Re	185	75	1.048E-10	-5.189E-10	3.833E-10	-1.356E-10	5.553E-09	1.065
^{187}Re	187	75	1.773E-10	-1.395E-09	-8.717E-10	-2.267E-09	7.358E-09	0.834
^{184}Os	184	76	7.108E-13	-5.756E-12	-5.484E-12	-1.124E-11	2.735E-11	0.773

TableC.13 – continued

Isotope	A	Z	$X^{\rm ini}$	$mp^{\rm wind}$	$mp^{\rm preSN}$	$mp^{\rm total}$	EM	$\langle OP \rangle$
^{186}Os	186	76	5.778E-11	8.075E-10	-1.782E-10	6.292E-10	3.766E-09	1.310
^{187}Os	187	76	5.998E-11	-1.207E-10	-3.744E-10	-4.951E-10	2.761E-09	0.925
^{188}Os	188	76	4.874E-10	-8.849E-10	-2.201E-09	-3.086E-09	2.337E-08	0.964
^{189}Os	189	76	5.974E-10	-4.502E-09	-3.992E-09	-8.495E-09	2.393E-08	0.805
^{190}Os	190	76	9.766E-10	-2.158E-09	-5.069E-09	-7.227E-09	4.579E-08	0.942
^{192}Os	192	76	1.533E-09	-7.512E-09	-9.375E-09	-1.689E-08	6.632E-08	0.870
^{191}Ir	191	77	1.357E-09	-1.068E-08	-9.886E-09	-2.056E-08	5.313E-08	0.787
^{193}Ir	193	77	2.308E-09	-1.652E-08	-1.711E-08	-3.363E-08	9.169E-08	0.798
^{190}Pt	190	78	1.008E-12	-7.929E-12	-7.781E-12	-1.571E-11	3.904E-11	0.778
^{192}Pt	192	78	5.850E-11	3.893E-09	-1.523E-10	3.741E-09	6.917E-09	2.376
^{194}Pt	194	78	2.490E-09	-4.451E-09	-1.738E-08	-2.183E-08	1.133E-07	0.915
^{195}Pt	195	78	2.568E-09	-1.416E-08	-1.878E-08	-3.295E-08	1.065E-07	0.833
^{196}Pt	196	78	1.926E-09	2.186E-08	-1.050E-08	1.136E-08	1.159E-07	1.209
^{198}Pt	198	78	5.522E-10	-2.110E-09	-3.651E-09	-5.762E-09	2.421E-08	0.881
^{197}Au	197	79	1.083E-09	1.219E-09	-6.684E-09	-5.465E-09	5.335E-08	0.990
^{196}Hg	196	80	3.009E-12	-1.789E-11	-2.318E-11	-4.107E-11	1.223E-10	0.817
^{198}Hg	198	80	1.975E-10	2.226E-08	2.373E-09	2.463E-08	3.535E-08	3.597
^{199}Hg	199	80	3.360E-10	5.589E-09	-2.544E-10	5.334E-09	2.357E-08	1.410
^{200}Hg	200	80	4.622E-10	9.220E-09	2.823E-09	1.204E-08	3.714E-08	1.615
^{201}Hg	201	80	2.651E-10	1.497E-09	1.422E-09	2.919E-09	1.731E-08	1.312
^{202}Hg	202	80	6.036E-10	2.580E-09	6.213E-09	8.793E-09	4.156E-08	1.384
^{204}Hg	204	80	1.401E-10	-2.595E-10	-5.746E-10	-8.341E-10	6.774E-09	0.971
^{203}Tl	203	81	3.221E-10	1.364E-11	5.561E-09	5.575E-09	2.306E-08	1.439
^{205}Tl	205	81	7.764E-10	-2.055E-10	8.280E-09	8.074E-09	5.022E-08	1.300
^{204}Pb	204	82	2.931E-10	9.182E-10	5.428E-09	6.346E-09	2.226E-08	1.526
^{206}Pb	206	82	2.798E-09	4.625E-10	5.355E-08	5.401E-08	2.059E-07	1.479
^{207}Pb	207	82	3.090E-09	4.070E-10	9.386E-08	9.427E-08	2.620E-07	1.704
^{208}Pb	208	82	8.850E-09	1.536E-09	1.324E-07	1.340E-07	6.144E-07	1.395

TableC.13 – continued

Isotope	A	Z	X^{ini}	mp^{wind}	mp^{preSN}	mp^{total}	EM	$\langle OP \rangle$
^{209}Bi	209	83	8.718E-10	-9.303E-11	2.588E-09	2.495E-09	4.982E-08	1.148

Table C.14: Yields for model 60CI.

Isotope	A	Z	X^{ini}	mp^{wind}	mp^{preSN}	mp^{total}	EM	$\langle OP \rangle$
^{1}H	1	1	7.064E-01	-1.464E+01	-5.448E+00	-2.009E+01	1.826E+01	0.519
^{2}H	2	1	1.371E-05	-6.159E-04	-1.057E-04	-7.215E-04	2.248E-05	0.033
^{3}He	3	2	4.540E-05	-1.188E-03	-3.501E-04	-1.538E-03	9.269E-04	0.410
^{4}He	4	2	2.735E-01	1.122E+01	-1.745E+00	9.477E+00	2.432E+01	1.787
^{7}Li	7	3	7.605E-11	-3.417E-09	-5.864E-10	-4.004E-09	1.250E-10	0.033
^{11}B	11	5	2.856E-09	-1.792E-14	6.036E-13	5.857E-13	1.550E-07	1.091
^{12}C	12	6	3.425E-03	2.764E+00	1.493E+00	4.257E+00	4.443E+00	26.069
^{13}C	13	6	4.156E-05	2.161E-04	-3.205E-04	-1.044E-04	2.152E-03	1.040
^{14}N	14	7	1.059E-03	2.505E-01	-8.002E-03	2.425E-01	3.000E-01	5.693
^{15}N	15	7	4.171E-06	-1.355E-04	-3.171E-05	-1.672E-04	5.918E-05	0.285
^{16}O	16	8	9.624E-03	2.274E-01	4.164E+00	4.391E+00	4.913E+00	10.259
^{17}O	17	8	3.813E-06	-7.861E-05	3.296E-05	-4.566E-05	1.613E-04	0.850
^{18}O	18	8	2.171E-05	-6.844E-04	-1.647E-04	-8.491E-04	3.295E-04	0.305
^{19}F	19	9	5.611E-07	2.740E-05	-4.088E-06	2.331E-05	5.377E-05	1.926
^{20}Ne	20	10	1.818E-03	-1.494E-03	1.226E+00	1.225E+00	1.323E+00	14.630
^{21}Ne	21	10	4.575E-06	3.231E-05	2.247E-03	2.279E-03	2.528E-03	11.102
^{22}Ne	22	10	1.470E-04	1.731E-01	3.987E-02	2.130E-01	2.210E-01	30.206
^{23}Na	23	11	4.000E-05	6.218E-03	6.146E-02	6.768E-02	6.985E-02	35.097
^{24}Mg	24	12	5.862E-04	4.737E-05	7.700E-02	7.705E-02	1.089E-01	3.732
^{25}Mg	25	12	7.733E-05	-1.575E-03	3.946E-02	3.789E-02	4.209E-02	10.937
^{26}Mg	26	12	8.848E-05	4.815E-03	6.888E-02	7.370E-02	7.850E-02	17.829
^{27}Al	27	13	6.481E-05	1.586E-04	2.252E-02	2.268E-02	2.620E-02	8.123
^{28}Si	28	14	7.453E-04	-1.004E-05	4.554E-03	4.544E-03	4.500E-02	1.213
^{29}Si	29	14	3.919E-05	1.051E-05	1.325E-03	1.336E-03	3.464E-03	1.776
^{30}Si	30	14	2.673E-05	4.691E-05	1.570E-03	1.617E-03	3.068E-03	2.307
^{31}P	31	15	7.106E-06	5.291E-06	4.851E-04	4.904E-04	8.762E-04	2.478
^{32}S	32	16	4.011E-04	-5.940E-05	-1.295E-03	-1.354E-03	2.042E-02	1.023

TableC.14 – continued

Isotope	A	Z	$X^{\rm ini}$	$mp^{\rm wind}$	$mp^{\rm preSN}$	$mp^{\rm total}$	EM	$\langle OP \rangle$
^{33}S	33	16	3.265E-06	2.242E-05	3.557E-05	5.799E-05	2.352E-04	1.448
^{34}S	34	16	1.890E-05	2.319E-06	9.671E-05	9.903E-05	1.125E-03	1.196
^{36}S	36	16	8.073E-08	1.421E-06	3.730E-05	3.872E-05	4.310E-05	10.729
^{35}Cl	35	17	6.821E-06	-4.243E-06	-2.996E-05	-3.420E-05	3.361E-04	0.990
^{37}Cl	37	17	2.306E-06	4.502E-05	3.666E-04	4.116E-04	5.368E-04	4.678
^{36}Ar	36	18	8.202E-05	-4.162E-05	-4.711E-04	-5.127E-04	3.940E-03	0.965
^{38}Ar	38	18	1.574E-05	7.986E-06	2.385E-04	2.465E-04	1.101E-03	1.406
^{40}Ar	40	18	2.650E-08	7.584E-08	1.468E-05	1.475E-05	1.619E-05	12.278
^{39}K	39	19	3.900E-06	5.579E-07	5.092E-05	5.147E-05	2.632E-04	1.356
^{40}K	40	19	5.005E-10	2.035E-06	8.404E-06	1.044E-05	1.047E-05	420.197
^{41}K	41	19	2.959E-07	1.339E-05	1.854E-05	3.193E-05	4.799E-05	3.259
^{40}Ca	40	20	7.225E-05	-2.630E-05	-3.430E-04	-3.694E-04	3.553E-03	0.988
^{42}Ca	42	20	5.063E-07	2.144E-06	2.723E-05	2.938E-05	5.686E-05	2.257
^{43}Ca	43	20	1.082E-07	1.433E-07	9.270E-06	9.414E-06	1.529E-05	2.840
^{44}Ca	44	20	1.710E-06	-3.924E-07	2.423E-05	2.383E-05	1.167E-04	1.371
^{46}Ca	46	20	3.428E-09	-1.023E-09	1.055E-07	1.045E-07	2.906E-07	1.703
^{48}Ca	48	20	1.672E-07	-8.370E-09	-1.828E-07	-1.911E-07	8.888E-06	1.068
^{45}Sc	45	21	5.414E-08	5.033E-07	6.109E-06	6.612E-06	9.551E-06	3.545
^{46}Ti	46	22	3.232E-07	-3.804E-08	7.171E-06	7.133E-06	2.468E-05	1.534
^{47}Ti	47	22	2.977E-07	-6.902E-07	2.309E-06	1.619E-06	1.778E-05	1.200
^{48}Ti	48	22	3.014E-06	-4.674E-06	-1.507E-05	-1.975E-05	1.439E-04	0.959
^{49}Ti	49	22	2.257E-07	5.120E-06	7.349E-06	1.247E-05	2.472E-05	2.201
^{50}Ti	50	22	2.208E-07	7.974E-07	2.620E-05	2.700E-05	3.899E-05	3.548
^{50}V	50	23	1.015E-09	-2.729E-09	6.090E-10	-2.120E-09	5.301E-08	1.049
^{51}V	51	23	4.138E-07	8.212E-07	-3.333E-07	4.880E-07	2.295E-05	1.115
^{50}Cr	50	24	8.265E-07	-2.343E-06	-6.193E-06	-8.536E-06	3.633E-05	0.883
^{52}Cr	52	24	1.658E-05	-4.389E-06	-8.072E-05	-8.511E-05	8.148E-04	0.988
^{53}Cr	53	24	1.916E-06	-2.419E-06	-6.449E-06	-8.868E-06	9.513E-05	0.998

TableC.14 – continued

Isotope	A	Z	$X^{\rm ini}$	$mp^{\rm wind}$	$mp^{\rm preSN}$	$mp^{\rm total}$	EM	$\langle OP \rangle$
^{54}Cr	54	24	4.858E-07	8.248E-06	5.247E-05	6.072E-05	8.709E-05	3.603
^{55}Mn	55	25	1.098E-05	1.053E-04	-4.752E-05	5.782E-05	6.540E-04	1.197
^{54}Fe	54	26	8.118E-05	-1.635E-04	-5.956E-04	-7.590E-04	3.648E-03	0.903
^{56}Fe	56	26	1.322E-03	-5.041E-04	-7.559E-03	-8.063E-03	6.368E-02	0.968
^{57}Fe	57	26	3.107E-05	4.091E-04	4.976E-04	9.066E-04	2.593E-03	1.677
^{58}Fe	58	26	4.207E-06	1.604E-04	2.445E-03	2.606E-03	2.834E-03	13.537
^{59}Co	59	27	3.991E-06	4.559E-05	1.033E-03	1.079E-03	1.296E-03	6.522
^{58}Ni	58	28	5.711E-05	-9.623E-05	-4.187E-04	-5.149E-04	2.585E-03	0.910
^{60}Ni	60	28	2.276E-05	-7.634E-06	8.587E-04	8.511E-04	2.087E-03	1.842
^{61}Ni	61	28	1.006E-06	2.663E-05	4.154E-04	4.420E-04	4.966E-04	9.924
^{62}Ni	62	28	3.259E-06	8.289E-06	1.135E-03	1.143E-03	1.320E-03	8.140
^{64}Ni	64	28	8.568E-07	6.802E-07	6.008E-04	6.014E-04	6.479E-04	15.197
^{63}Cu	63	29	6.600E-07	5.488E-06	4.885E-04	4.940E-04	5.298E-04	16.130
^{65}Cu	65	29	3.035E-07	3.212E-06	5.059E-04	5.091E-04	5.255E-04	34.802
^{64}Zn	64	30	1.131E-06	-1.177E-06	2.010E-04	1.998E-04	2.612E-04	4.642
^{66}Zn	66	30	6.690E-07	-4.249E-07	3.750E-04	3.745E-04	4.108E-04	12.341
^{67}Zn	67	30	9.980E-08	2.375E-07	1.126E-04	1.129E-04	1.183E-04	23.815
^{68}Zn	68	30	4.632E-07	5.207E-07	3.921E-04	3.927E-04	4.178E-04	18.126
^{70}Zn	70	30	1.577E-08	-1.785E-08	-1.008E-08	-2.793E-08	8.281E-07	1.055
^{69}Ga	69	31	4.551E-08	1.958E-07	5.022E-05	5.041E-05	5.288E-05	23.353
^{71}Ga	71	31	3.108E-08	6.628E-08	4.093E-05	4.100E-05	4.269E-05	27.603
^{70}Ge	70	32	5.157E-08	1.856E-07	6.760E-05	6.779E-05	7.059E-05	27.505
^{72}Ge	72	32	6.910E-08	-1.341E-08	5.915E-05	5.914E-05	6.289E-05	18.288
^{73}Ge	73	32	1.955E-08	-4.478E-09	2.350E-05	2.349E-05	2.455E-05	25.244
^{74}Ge	74	32	9.228E-08	8.331E-08	6.906E-05	6.914E-05	7.415E-05	16.146
^{76}Ge	76	32	1.963E-08	-2.298E-08	-9.867E-08	-1.217E-07	9.440E-07	0.966
^{75}As	75	33	1.430E-08	-3.000E-08	8.448E-06	8.418E-06	9.194E-06	12.920
^{74}Se	74	34	1.198E-09	-7.977E-09	-9.229E-09	-1.721E-08	4.782E-08	0.802

TableC.14 – continued

Isotope	A	Z	$X^{\rm ini}$	$mp^{\rm wind}$	$mp^{\rm preSN}$	$mp^{\rm total}$	EM	$\langle OP \rangle$
^{76}Se	76	34	1.296E-08	7.798E-08	1.214E-05	1.222E-05	1.292E-05	20.031
^{77}Se	77	34	1.070E-08	-1.004E-08	6.029E-06	6.019E-06	6.600E-06	12.389
^{78}Se	78	34	3.376E-08	8.535E-08	2.663E-05	2.672E-05	2.855E-05	16.994
^{80}Se	80	34	7.226E-08	-1.443E-07	5.033E-06	4.889E-06	8.812E-06	2.451
^{82}Se	82	34	1.304E-08	-7.198E-09	-7.422E-08	-8.142E-08	6.263E-07	0.965
^{79}Br	79	35	1.389E-08	-7.889E-08	4.573E-06	4.495E-06	5.249E-06	7.592
^{81}Br	81	35	1.386E-08	1.881E-08	2.655E-06	2.674E-06	3.426E-06	4.968
^{78}Kr	78	36	3.900E-10	-2.550E-09	-3.005E-09	-5.555E-09	1.562E-08	0.805
^{80}Kr	80	36	2.575E-09	6.004E-08	3.335E-06	3.395E-06	3.534E-06	27.586
^{82}Kr	82	36	1.320E-08	1.599E-07	1.026E-05	1.042E-05	1.114E-05	16.962
^{83}Kr	83	36	1.324E-08	-2.203E-08	4.731E-06	4.709E-06	5.428E-06	8.238
^{84}Kr	84	36	6.602E-08	2.607E-08	1.641E-05	1.643E-05	2.002E-05	6.093
^{86}Kr	86	36	2.044E-08	-3.913E-09	1.107E-06	1.103E-06	2.212E-06	2.175
^{85}Rb	85	37	1.282E-08	6.605E-10	3.288E-06	3.289E-06	3.985E-06	6.245
^{87}Rb	87	37	5.063E-09	2.528E-10	3.720E-07	3.722E-07	6.471E-07	2.569
^{84}Sr	84	38	3.228E-10	-2.372E-09	-2.489E-09	-4.861E-09	1.266E-08	0.788
^{86}Sr	86	38	5.845E-09	9.900E-08	4.934E-06	5.033E-06	5.350E-06	18.396
^{87}Sr	87	38	4.443E-09	1.998E-08	2.967E-06	2.987E-06	3.228E-06	14.601
^{88}Sr	88	38	5.011E-08	1.945E-08	9.481E-06	9.500E-06	1.222E-05	4.901
^{89}Y	89	39	1.229E-08	5.191E-09	1.625E-06	1.630E-06	2.298E-06	3.756
^{90}Zr	90	40	1.534E-08	-3.378E-10	8.044E-07	8.041E-07	1.637E-06	2.144
^{91}Zr	91	40	3.384E-09	1.258E-09	2.376E-07	2.389E-07	4.226E-07	2.509
^{92}Zr	92	40	5.227E-09	4.216E-09	2.807E-07	2.849E-07	5.686E-07	2.186
^{94}Zr	94	40	5.413E-09	-6.985E-09	1.142E-07	1.072E-07	4.011E-07	1.489
^{96}Zr	96	40	8.903E-10	-4.662E-10	2.272E-09	1.806E-09	5.014E-08	1.132
^{93}Nb	93	41	1.900E-09	-4.817E-09	1.029E-07	9.809E-08	2.012E-07	2.128
^{92}Mo	92	42	1.012E-09	-3.512E-09	-7.660E-09	-1.117E-08	4.379E-08	0.869
^{94}Mo	94	42	6.448E-10	7.396E-09	-4.055E-09	3.341E-09	3.834E-08	1.195

TableC.14 – continued

Isotope	A	Z	$X^{\rm ini}$	$mp^{\rm wind}$	$mp^{\rm preSN}$	$mp^{\rm total}$	EM	$\langle OP \rangle$
^{95}Mo	95	42	1.122E-09	-3.005E-10	2.334E-08	2.304E-08	8.395E-08	1.504
^{96}Mo	96	42	1.188E-09	6.969E-09	3.995E-08	4.692E-08	1.114E-07	1.885
^{97}Mo	97	42	6.875E-10	-1.705E-10	1.282E-08	1.265E-08	4.997E-08	1.461
^{98}Mo	98	42	1.754E-09	2.421E-09	3.754E-08	3.996E-08	1.352E-07	1.549
^{100}Mo	100	42	7.146E-10	-2.970E-09	-5.324E-09	-8.294E-09	3.050E-08	0.858
^{96}Ru	96	44	2.926E-10	-1.747E-09	-2.251E-09	-3.999E-09	1.188E-08	0.816
^{98}Ru	98	44	1.007E-10	2.136E-10	-7.502E-10	-5.366E-10	4.931E-09	0.984
^{99}Ru	99	44	6.945E-10	-2.716E-09	3.096E-09	3.801E-10	3.809E-08	1.102
^{100}Ru	100	44	6.928E-10	3.286E-09	1.717E-08	2.045E-08	5.806E-08	1.684
^{101}Ru	101	44	9.475E-10	-5.743E-09	-2.031E-09	-7.774E-09	4.366E-08	0.926
^{102}Ru	102	44	1.770E-09	2.167E-09	1.795E-08	2.011E-08	1.162E-07	1.319
^{104}Ru	104	44	1.065E-09	-5.746E-09	-7.843E-09	-1.359E-08	4.422E-08	0.835
^{103}Rh	103	45	1.055E-09	-5.691E-09	-2.870E-09	-8.561E-09	4.870E-08	0.928
^{102}Pd	102	46	4.241E-11	-3.130E-10	-3.270E-10	-6.400E-10	1.662E-09	0.788
^{104}Pd	104	46	4.723E-10	6.415E-09	1.052E-08	1.694E-08	4.258E-08	1.812
^{105}Pd	105	46	9.558E-10	-4.928E-09	-3.875E-09	-8.803E-09	4.308E-08	0.906
^{106}Pd	106	46	1.181E-09	4.910E-09	8.089E-09	1.300E-08	7.711E-08	1.312
^{108}Pd	108	46	1.165E-09	3.792E-09	1.019E-08	1.398E-08	7.722E-08	1.332
^{110}Pd	110	46	5.255E-10	-2.765E-09	-3.714E-09	-6.479E-09	2.205E-08	0.843
^{107}Ag	107	47	7.840E-10	-3.206E-09	-2.615E-09	-5.822E-09	3.674E-08	0.942
^{109}Ag	109	47	7.420E-10	-1.485E-09	4.344E-09	2.859E-09	4.314E-08	1.168
^{106}Cd	106	48	6.346E-11	-4.421E-10	-4.891E-10	-9.312E-10	2.514E-09	0.796
^{108}Cd	108	48	4.604E-11	3.546E-09	6.799E-10	4.226E-09	6.725E-09	2.936
^{110}Cd	110	48	6.580E-10	6.689E-09	1.047E-08	1.716E-08	5.288E-08	1.615
^{111}Cd	111	48	6.805E-10	-1.358E-09	-3.127E-10	-1.671E-09	3.527E-08	1.042
^{112}Cd	112	48	1.294E-09	3.705E-09	8.783E-09	1.249E-08	8.276E-08	1.285
^{113}Cd	113	48	6.614E-10	-1.265E-09	3.789E-11	-1.227E-09	3.468E-08	1.054
^{114}Cd	114	48	1.569E-09	4.690E-09	1.398E-08	1.867E-08	1.038E-07	1.330

TableC.14 – continued

Isotope	A	Z	$X^{\rm ini}$	$mp^{\rm wind}$	$mp^{\rm preSN}$	$mp^{\rm total}$	EM	$\langle OP \rangle$
^{116}Cd	116	48	4.161E-10	-1.402E-09	-2.628E-09	-4.030E-09	1.856E-08	0.896
^{113}In	113	49	2.604E-11	-1.194E-10	-2.001E-10	-3.195E-10	1.094E-09	0.844
^{115}In	115	49	5.915E-10	-1.537E-09	2.839E-10	-1.253E-09	3.086E-08	1.048
^{112}Sn	112	50	1.221E-10	-7.437E-10	-9.397E-10	-1.683E-09	4.945E-09	0.814
^{114}Sn	114	50	8.435E-11	8.959E-11	-6.298E-10	-5.402E-10	4.039E-09	0.962
^{115}Sn	115	50	4.377E-11	-1.672E-11	-2.224E-10	-2.391E-10	2.137E-09	0.981
^{116}Sn	116	50	1.893E-09	4.904E-09	1.779E-08	2.269E-08	1.255E-07	1.332
^{117}Sn	117	50	1.008E-09	-1.375E-09	2.555E-09	1.180E-09	5.592E-08	1.114
^{118}Sn	118	50	3.209E-09	2.953E-09	2.191E-08	2.486E-08	1.991E-07	1.247
^{119}Sn	119	50	1.147E-09	-4.278E-10	5.047E-09	4.619E-09	6.689E-08	1.172
^{120}Sn	120	50	4.391E-09	3.153E-09	3.448E-08	3.763E-08	2.760E-07	1.263
^{122}Sn	122	50	6.341E-10	-7.777E-10	-3.517E-09	-4.295E-09	3.013E-08	0.955
^{124}Sn	124	50	8.060E-10	-7.221E-10	-5.210E-09	-5.932E-09	3.782E-08	0.943
^{121}Sb	121	51	6.318E-10	-2.074E-09	5.917E-10	-1.483E-09	3.282E-08	1.044
^{123}Sb	123	51	4.803E-10	-3.058E-09	-3.467E-09	-6.525E-09	1.955E-08	0.818
^{120}Te	120	52	1.628E-11	-1.289E-10	-1.256E-10	-2.545E-10	6.295E-10	0.777
^{122}Te	122	52	4.489E-10	2.011E-09	4.925E-09	6.936E-09	3.130E-08	1.401
^{123}Te	123	52	1.579E-10	7.359E-10	1.680E-09	2.416E-09	1.099E-08	1.399
^{124}Te	124	52	8.441E-10	3.838E-09	9.668E-09	1.351E-08	5.933E-08	1.413
^{125}Te	125	52	1.261E-09	-6.384E-09	-4.340E-09	-1.072E-08	5.775E-08	0.920
^{126}Te	126	52	3.375E-09	9.530E-10	5.413E-09	6.366E-09	1.896E-07	1.129
^{128}Te	128	52	5.733E-09	-1.140E-08	-4.189E-08	-5.329E-08	2.579E-07	0.904
^{130}Te	130	52	6.211E-09	-4.987E-09	-4.082E-08	-4.580E-08	2.914E-07	0.943
^{127}I	127	53	1.459E-09	-8.201E-09	-6.646E-09	-1.485E-08	6.436E-08	0.886
^{124}Xe	124	54	2.210E-11	-1.802E-10	-1.704E-10	-3.506E-10	8.489E-10	0.772
^{126}Xe	126	54	1.949E-11	-1.411E-10	-1.503E-10	-2.914E-10	7.668E-10	0.791
^{128}Xe	128	54	3.943E-10	7.612E-09	6.225E-09	1.384E-08	3.524E-08	1.796
^{129}Xe	129	54	4.893E-09	-3.388E-08	-3.369E-08	-6.757E-08	1.981E-07	0.813

TableC.14 – continued

Isotope	A	Z	$X^{\rm ini}$	$mp^{\rm wind}$	$mp^{\rm preSN}$	$mp^{\rm total}$	EM	$\langle OP \rangle$
^{130}Xe	130	54	7.865E-10	3.333E-08	1.384E-08	4.717E-08	8.987E-08	2.296
^{131}Xe	131	54	3.945E-09	-1.549E-08	-2.167E-08	-3.716E-08	1.770E-07	0.902
^{132}Xe	132	54	4.806E-09	2.537E-08	7.949E-09	3.332E-08	2.942E-07	1.230
^{134}Xe	134	54	1.788E-09	-1.912E-09	-1.180E-08	-1.371E-08	8.336E-08	0.937
^{136}Xe	136	54	1.478E-09	-9.910E-11	-1.797E-09	-1.896E-09	7.836E-08	1.065
^{133}Cs	133	55	1.426E-09	-3.779E-09	-4.185E-09	-7.965E-09	6.945E-08	0.979
^{130}Ba	130	56	1.814E-11	-1.508E-10	-1.399E-10	-2.907E-10	6.942E-10	0.769
^{132}Ba	132	56	1.762E-11	-1.303E-10	-1.359E-10	-2.662E-10	6.904E-10	0.787
^{134}Ba	134	56	4.272E-10	1.509E-08	1.263E-08	2.772E-08	5.091E-08	2.395
^{135}Ba	135	56	1.174E-09	-2.904E-09	-2.150E-09	-5.054E-09	5.867E-08	1.004
^{136}Ba	136	56	1.409E-09	1.265E-08	3.717E-08	4.982E-08	1.263E-07	1.802
^{137}Ba	137	56	2.030E-09	1.371E-11	2.441E-08	2.442E-08	1.346E-07	1.333
^{138}Ba	138	56	1.305E-08	5.805E-09	3.205E-07	3.263E-07	1.035E-06	1.593
^{138}La	138	57	1.604E-12	-1.222E-11	-1.237E-11	-2.459E-11	6.249E-11	0.783
^{139}La	139	57	1.790E-09	-1.334E-10	3.535E-08	3.522E-08	1.324E-07	1.486
^{136}Ce	136	58	8.382E-12	-5.755E-11	-6.459E-11	-1.221E-10	3.329E-10	0.798
^{138}Ce	138	58	1.148E-11	-6.313E-11	-8.816E-11	-1.513E-10	4.718E-10	0.826
^{140}Ce	140	58	4.103E-09	8.484E-10	6.072E-08	6.157E-08	2.843E-07	1.393
^{142}Ce	142	58	5.229E-10	-7.444E-10	-3.242E-09	-3.986E-09	2.440E-08	0.938
^{141}Pr	141	59	6.910E-10	-1.524E-09	5.227E-09	3.703E-09	4.122E-08	1.199
^{142}Nd	142	60	9.920E-10	1.868E-09	1.524E-08	1.711E-08	7.096E-08	1.438
^{143}Nd	143	60	4.484E-10	-1.683E-09	3.314E-10	-1.351E-09	2.299E-08	1.030
^{144}Nd	144	60	8.826E-10	4.486E-10	2.845E-09	3.293E-09	5.121E-08	1.166
^{145}Nd	145	60	3.095E-10	-1.100E-09	1.426E-10	-9.573E-10	1.585E-08	1.029
^{146}Nd	146	60	6.448E-10	1.743E-09	2.795E-09	4.538E-09	3.954E-08	1.232
^{148}Nd	148	60	2.185E-10	-1.104E-09	-1.399E-09	-2.503E-09	9.359E-09	0.861
^{150}Nd	150	60	2.168E-10	-1.236E-09	-1.665E-09	-2.901E-09	8.870E-09	0.822
^{144}Sm	144	62	3.684E-11	-1.351E-10	-2.796E-10	-4.147E-10	1.585E-09	0.865

TableC.14 – continued

Isotope	A	Z	$X^{\rm ini}$	$mp^{\rm wind}$	$mp^{\rm preSN}$	$mp^{\rm total}$	EM	$\langle OP \rangle$
^{147}Sm	147	62	1.834E-10	-9.764E-10	-2.598E-10	-1.236E-09	8.722E-09	0.956
^{148}Sm	148	62	1.385E-10	1.363E-09	1.251E-09	2.614E-09	1.013E-08	1.470
^{149}Sm	149	62	1.714E-10	-1.116E-09	-8.178E-10	-1.934E-09	7.369E-09	0.864
^{150}Sm	150	62	9.213E-11	1.010E-09	9.143E-10	1.924E-09	6.926E-09	1.511
^{152}Sm	152	62	3.383E-10	-2.520E-09	-1.378E-09	-3.898E-09	1.447E-08	0.859
^{154}Sm	154	62	2.916E-10	-1.818E-09	-2.146E-09	-3.964E-09	1.187E-08	0.818
^{151}Eu	151	63	2.036E-10	-1.616E-09	-1.239E-09	-2.855E-09	8.198E-09	0.809
^{153}Eu	153	63	2.252E-10	-1.552E-09	-1.364E-09	-2.917E-09	9.309E-09	0.831
^{152}Gd	152	64	2.947E-12	8.181E-10	8.767E-11	9.058E-10	1.066E-09	7.267
^{154}Gd	154	64	3.210E-11	9.653E-10	3.564E-10	1.322E-09	3.064E-09	1.918
^{155}Gd	155	64	2.192E-10	-1.370E-09	-1.347E-09	-2.717E-09	9.184E-09	0.842
^{156}Gd	156	64	3.051E-10	1.111E-10	-1.337E-09	-1.226E-09	1.534E-08	1.010
^{157}Gd	157	64	2.348E-10	-8.746E-10	-1.117E-09	-1.991E-09	1.076E-08	0.921
^{158}Gd	158	64	3.750E-10	1.496E-09	-9.353E-10	5.607E-10	2.092E-08	1.121
^{160}Gd	160	64	3.343E-10	-1.850E-09	-2.501E-09	-4.351E-09	1.380E-08	0.829
^{159}Tb	159	65	2.765E-10	-1.187E-09	-1.606E-09	-2.792E-09	1.222E-08	0.888
^{156}Dy	156	66	1.004E-12	-8.734E-12	-7.740E-12	-1.647E-11	3.801E-11	0.761
^{158}Dy	158	66	1.743E-12	3.443E-10	9.780E-13	3.453E-10	4.399E-10	5.073
^{160}Dy	160	66	4.301E-11	1.856E-09	3.760E-10	2.232E-09	4.567E-09	2.134
^{161}Dy	161	66	3.498E-10	-2.005E-09	-2.186E-09	-4.191E-09	1.480E-08	0.850
^{162}Dy	162	66	4.748E-10	7.640E-10	-2.195E-09	-1.431E-09	2.435E-08	1.030
^{163}Dy	163	66	4.663E-10	-2.048E-09	-2.722E-09	-4.770E-09	2.054E-08	0.885
^{164}Dy	164	66	5.312E-10	4.703E-09	-8.204E-10	3.883E-09	3.272E-08	1.238
^{165}Ho	165	67	4.244E-10	-2.044E-09	-2.565E-09	-4.609E-09	1.843E-08	0.873
^{162}Er	162	68	1.609E-12	-1.399E-11	-1.241E-11	-2.639E-11	6.095E-11	0.761
^{164}Er	164	68	1.913E-11	-1.643E-10	-1.475E-10	-3.118E-10	7.266E-10	0.763
^{166}Er	166	68	4.044E-10	3.971E-10	-1.941E-09	-1.544E-09	2.041E-08	1.014
^{167}Er	167	68	2.776E-10	-9.287E-10	-1.547E-09	-2.476E-09	1.259E-08	0.912

TableC.14 – continued

Isotope	A	Z	$X^{\rm ini}$	$mp^{\rm wind}$	$mp^{\rm preSN}$	$mp^{\rm total}$	EM	$\langle OP \rangle$
^{168}Er	168	68	3.263E-10	3.268E-09	-4.486E-10	2.820E-09	2.053E-08	1.265
^{170}Er	170	68	1.840E-10	-1.086E-09	-1.095E-09	-2.181E-09	7.807E-09	0.853
^{169}Tm	169	69	1.854E-10	-5.626E-10	-9.307E-10	-1.493E-09	8.573E-09	0.929
^{168}Yb	168	70	1.583E-12	-1.366E-11	-1.221E-11	-2.587E-11	6.008E-11	0.763
^{170}Yb	170	70	3.746E-11	2.304E-09	3.220E-10	2.626E-09	4.660E-09	2.500
^{171}Yb	171	70	1.770E-10	1.412E-10	-7.808E-10	-6.396E-10	8.970E-09	1.018
^{172}Yb	172	70	2.722E-10	2.623E-09	-1.043E-10	2.518E-09	1.729E-08	1.277
^{173}Yb	173	70	2.023E-10	3.359E-10	-2.910E-10	4.497E-11	1.103E-08	1.095
^{174}Yb	174	70	4.015E-10	3.561E-09	1.609E-09	5.170E-09	2.697E-08	1.350
^{176}Yb	176	70	1.628E-10	-7.376E-10	-1.135E-09	-1.872E-09	6.966E-09	0.860
^{175}Lu	175	71	1.828E-10	-7.373E-10	-6.157E-10	-1.353E-09	8.570E-09	0.942
^{176}Lu	176	71	4.876E-12	5.445E-11	6.831E-11	1.228E-10	3.875E-10	1.597
^{174}Hf	174	72	1.231E-12	-1.046E-11	-9.494E-12	-1.995E-11	4.689E-11	0.765
^{176}Hf	176	72	4.036E-11	9.874E-10	4.859E-10	1.473E-09	3.664E-09	1.824
^{177}Hf	177	72	1.438E-10	-5.680E-10	-5.439E-10	-1.112E-09	6.694E-09	0.936
^{178}Hf	178	72	2.121E-10	1.240E-09	5.002E-10	1.740E-09	1.326E-08	1.256
^{179}Hf	179	72	1.065E-10	8.299E-11	-2.205E-11	6.094E-11	5.843E-09	1.102
^{180}Hf	180	72	2.758E-10	2.052E-09	1.710E-09	3.762E-09	1.874E-08	1.365
^{180}Ta	180	73	2.429E-14	-2.134E-13	1.112E-14	-2.023E-13	1.116E-12	0.924
^{181}Ta	181	73	1.986E-10	-9.336E-10	-4.926E-10	-1.426E-09	9.353E-09	0.947
^{180}W	180	74	8.395E-13	-4.289E-12	8.778E-11	8.349E-11	1.291E-10	3.090
^{182}W	182	74	1.877E-10	7.881E-10	5.380E-10	1.326E-09	1.152E-08	1.233
^{183}W	183	74	1.020E-10	2.190E-10	6.165E-10	8.355E-10	6.371E-09	1.256
^{184}W	184	74	2.195E-10	5.641E-10	1.416E-09	1.980E-09	1.390E-08	1.272
^{186}W	186	74	2.058E-10	-1.196E-09	-9.423E-10	-2.139E-09	9.035E-09	0.882
^{185}Re	185	75	1.048E-10	-5.191E-10	-2.657E-11	-5.456E-10	5.143E-09	0.986
^{187}Re	187	75	1.773E-10	-1.396E-09	-1.138E-09	-2.534E-09	7.091E-09	0.804
^{184}Os	184	76	7.108E-13	-5.759E-12	-5.481E-12	-1.124E-11	2.735E-11	0.773

TableC.14 – continued

Isotope	A	Z	X^{ini}	mp^{wind}	mp^{preSN}	mp^{total}	EM	$\langle OP \rangle$
^{186}Os	186	76	5.778E-11	8.080E-10	7.816E-10	1.590E-09	4.727E-09	1.644
^{187}Os	187	76	5.998E-11	-1.207E-10	3.842E-11	-8.229E-11	3.174E-09	1.063
^{188}Os	188	76	4.874E-10	-8.857E-10	-1.491E-09	-2.377E-09	2.408E-08	0.993
^{189}Os	189	76	5.974E-10	-4.505E-09	-3.898E-09	-8.402E-09	2.403E-08	0.808
^{190}Os	190	76	9.766E-10	-2.161E-09	-4.751E-09	-6.912E-09	4.611E-08	0.949
^{192}Os	192	76	1.533E-09	-7.517E-09	-1.140E-08	-1.891E-08	6.429E-08	0.843
^{191}Ir	191	77	1.357E-09	-1.068E-08	-9.859E-09	-2.054E-08	5.315E-08	0.787
^{193}Ir	193	77	2.308E-09	-1.653E-08	-1.708E-08	-3.360E-08	9.171E-08	0.798
^{190}Pt	190	78	1.008E-12	-7.933E-12	-7.776E-12	-1.571E-11	3.904E-11	0.778
^{192}Pt	192	78	5.850E-11	3.894E-09	4.136E-10	4.308E-09	7.483E-09	2.571
^{194}Pt	194	78	2.490E-09	-4.460E-09	-1.691E-08	-2.137E-08	1.138E-07	0.918
^{195}Pt	195	78	2.568E-09	-1.417E-08	-1.867E-08	-3.284E-08	1.066E-07	0.834
^{196}Pt	196	78	1.926E-09	2.186E-08	-9.332E-09	1.253E-08	1.171E-07	1.222
^{198}Pt	198	78	5.522E-10	-2.112E-09	-4.138E-09	-6.250E-09	2.373E-08	0.863
^{197}Au	197	79	1.083E-09	1.218E-09	-6.329E-09	-5.111E-09	5.370E-08	0.996
^{196}Hg	196	80	3.009E-12	-1.790E-11	-2.315E-11	-4.105E-11	1.223E-10	0.817
^{198}Hg	198	80	1.975E-10	2.227E-08	4.668E-09	2.694E-08	3.766E-08	3.832
^{199}Hg	199	80	3.360E-10	5.595E-09	6.382E-10	6.233E-09	2.447E-08	1.464
^{200}Hg	200	80	4.622E-10	9.235E-09	5.716E-09	1.495E-08	4.004E-08	1.741
^{201}Hg	201	80	2.651E-10	1.501E-09	2.675E-09	4.177E-09	1.857E-08	1.408
^{202}Hg	202	80	6.036E-10	2.586E-09	1.066E-08	1.325E-08	4.602E-08	1.532
^{204}Hg	204	80	1.401E-10	-2.598E-10	-9.242E-10	-1.184E-09	6.424E-09	0.921
^{203}Tl	203	81	3.221E-10	1.450E-11	7.110E-09	7.125E-09	2.461E-08	1.536
^{205}Tl	205	81	7.764E-10	-2.056E-10	1.042E-08	1.022E-08	5.237E-08	1.355
^{204}Pb	204	82	2.931E-10	9.193E-10	9.663E-09	1.058E-08	2.649E-08	1.817
^{206}Pb	206	82	2.798E-09	4.630E-10	6.240E-08	6.286E-08	2.147E-07	1.542
^{207}Pb	207	82	3.090E-09	4.075E-10	7.692E-08	7.733E-08	2.451E-07	1.594
^{208}Pb	208	82	8.850E-09	1.538E-09	9.239E-08	9.392E-08	5.744E-07	1.304

TableC.14 – continued

Isotope	A	Z	X^{ini}	mp^{wind}	mp^{preSN}	mp^{total}	EM	$\langle OP \rangle$
^{209}Bi	209	83	8.718E-10	-9.311E-11	2.196E-09	2.103E-09	4.943E-08	1.139

Table C.15: Yields for model 60CU.

Isotope	A	Z	X^{ini}	mp^{wind}	mp^{preSN}	mp^{total}	EM	$\langle OP \rangle$
^{1}H	1	1	7.064E-01	-1.475E+01	-5.345E+00	-2.009E+01	1.826E+01	0.519
^{2}H	2	1	1.371E-05	-6.179E-04	-1.037E-04	-7.215E-04	2.248E-05	0.033
^{3}He	3	2	4.540E-05	-1.194E-03	-3.435E-04	-1.538E-03	9.269E-04	0.410
^{4}He	4	2	2.735E-01	1.122E+01	-1.773E+00	9.448E+00	2.430E+01	1.785
^{7}Li	7	3	7.605E-11	-3.428E-09	-5.754E-10	-4.004E-09	1.250E-10	0.033
^{11}B	11	5	2.856E-09	-1.794E-14	2.732E-12	2.714E-12	1.550E-07	1.091
^{12}C	12	6	3.425E-03	2.837E+00	1.198E+00	4.035E+00	4.221E+00	24.768
^{13}C	13	6	4.156E-05	2.100E-04	-3.144E-04	-1.044E-04	2.152E-03	1.040
^{14}N	14	7	1.059E-03	2.503E-01	-7.746E-03	2.426E-01	3.001E-01	5.695
^{15}N	15	7	4.171E-06	-1.361E-04	-3.053E-05	-1.667E-04	5.976E-05	0.288
^{16}O	16	8	9.624E-03	2.563E-01	4.202E+00	4.458E+00	4.980E+00	10.399
^{17}O	17	8	3.813E-06	-7.909E-05	1.301E-04	5.102E-05	2.580E-04	1.360
^{18}O	18	8	2.171E-05	-6.876E-04	-1.578E-04	-8.454E-04	3.333E-04	0.308
^{19}F	19	9	5.611E-07	2.735E-05	-3.157E-06	2.419E-05	5.465E-05	1.957
^{20}Ne	20	10	1.818E-03	-1.499E-03	1.287E+00	1.286E+00	1.385E+00	15.306
^{21}Ne	21	10	4.575E-06	3.184E-05	1.062E-02	1.065E-02	1.090E-02	47.874
^{22}Ne	22	10	1.470E-04	1.760E-01	2.403E-02	2.000E-01	2.080E-01	28.425
^{23}Na	23	11	4.000E-05	6.253E-03	1.231E-01	1.293E-01	1.315E-01	66.064
^{24}Mg	24	12	5.862E-04	4.711E-05	9.261E-02	9.265E-02	1.245E-01	4.267
^{25}Mg	25	12	7.733E-05	-1.553E-03	5.020E-02	4.865E-02	5.285E-02	13.733
^{26}Mg	26	12	8.848E-05	4.981E-03	1.026E-01	1.076E-01	1.124E-01	25.532
^{27}Al	27	13	6.481E-05	1.595E-04	2.481E-02	2.497E-02	2.849E-02	8.835
^{28}Si	28	14	7.453E-04	-1.064E-05	6.441E-03	6.431E-03	4.689E-02	1.264
^{29}Si	29	14	3.919E-05	1.108E-05	1.705E-03	1.717E-03	3.844E-03	1.971
^{30}Si	30	14	2.673E-05	4.919E-05	2.490E-03	2.539E-03	3.990E-03	3.000
^{31}P	31	15	7.106E-06	5.484E-06	8.653E-04	8.707E-04	1.257E-03	3.553
^{32}S	32	16	4.011E-04	-6.197E-05	-1.743E-03	-1.805E-03	1.997E-02	1.001

TableC.15 – continued

Isotope	A	Z	$X^{\rm ini}$	$mp^{\rm wind}$	$mp^{\rm preSN}$	$mp^{\rm total}$	EM	$\langle OP \rangle$
^{33}S	33	16	3.265E-06	2.310E-05	1.916E-05	4.226E-05	2.195E-04	1.351
^{34}S	34	16	1.890E-05	2.428E-06	1.381E-04	1.405E-04	1.167E-03	1.240
^{36}S	36	16	8.073E-08	1.507E-06	5.333E-05	5.484E-05	5.922E-05	14.742
^{35}Cl	35	17	6.821E-06	-4.401E-06	-3.490E-05	-3.930E-05	3.310E-04	0.975
^{37}Cl	37	17	2.306E-06	4.674E-05	3.681E-04	4.149E-04	5.400E-04	4.707
^{36}Ar	36	18	8.202E-05	-4.325E-05	-5.296E-04	-5.729E-04	3.880E-03	0.951
^{38}Ar	38	18	1.574E-05	8.464E-06	2.575E-04	2.660E-04	1.121E-03	1.430
^{40}Ar	40	18	2.650E-08	8.074E-08	3.732E-05	3.740E-05	3.884E-05	29.453
^{39}K	39	19	3.900E-06	5.817E-07	6.461E-05	6.519E-05	2.769E-04	1.427
^{40}K	40	19	5.005E-10	2.097E-06	9.922E-06	1.202E-05	1.205E-05	483.658
^{41}K	41	19	2.959E-07	1.370E-05	1.934E-05	3.304E-05	4.910E-05	3.335
^{40}Ca	40	20	7.225E-05	-2.731E-05	-4.150E-04	-4.423E-04	3.480E-03	0.968
^{42}Ca	42	20	5.063E-07	2.255E-06	2.639E-05	2.865E-05	5.614E-05	2.228
^{43}Ca	43	20	1.082E-07	1.543E-07	1.011E-05	1.026E-05	1.614E-05	2.998
^{44}Ca	44	20	1.710E-06	-4.063E-07	3.328E-05	3.287E-05	1.257E-04	1.477
^{46}Ca	46	20	3.428E-09	-1.064E-09	3.753E-06	3.752E-06	3.938E-06	23.082
^{48}Ca	48	20	1.672E-07	-8.703E-09	-2.431E-07	-2.518E-07	8.828E-06	1.061
^{45}Sc	45	21	5.414E-08	5.197E-07	1.063E-05	1.115E-05	1.409E-05	5.230
^{46}Ti	46	22	3.232E-07	-3.614E-08	8.332E-06	8.296E-06	2.584E-05	1.607
^{47}Ti	47	22	2.977E-07	-7.103E-07	4.573E-06	3.863E-06	2.002E-05	1.352
^{48}Ti	48	22	3.014E-06	-4.843E-06	-9.828E-06	-1.467E-05	1.489E-04	0.993
^{49}Ti	49	22	2.257E-07	5.284E-06	1.286E-05	1.814E-05	3.040E-05	2.706
^{50}Ti	50	22	2.208E-07	8.438E-07	4.192E-05	4.276E-05	5.475E-05	4.983
^{50}V	50	23	1.015E-09	-2.816E-09	-3.616E-09	-6.432E-09	4.870E-08	0.964
^{51}V	51	23	4.138E-07	8.355E-07	2.034E-06	2.869E-06	2.533E-05	1.230
^{50}Cr	50	24	8.265E-07	-2.416E-06	-6.113E-06	-8.529E-06	3.634E-05	0.884
^{52}Cr	52	24	1.658E-05	-4.574E-06	-9.246E-05	-9.703E-05	8.028E-04	0.973
^{53}Cr	53	24	1.916E-06	-2.472E-06	-8.139E-06	-1.061E-05	9.338E-05	0.980

TableC.15 – continued

Isotope	A	Z	$X^{\rm ini}$	$mp^{\rm wind}$	$mp^{\rm preSN}$	$mp^{\rm total}$	EM	$\langle OP \rangle$
^{54}Cr	54	24	4.858E-07	8.535E-06	4.373E-05	5.227E-05	7.864E-05	3.253
^{55}Mn	55	25	1.098E-05	1.081E-04	-5.557E-05	5.251E-05	6.486E-04	1.187
^{54}Fe	54	26	8.118E-05	-1.689E-04	-5.926E-04	-7.615E-04	3.646E-03	0.902
^{56}Fe	56	26	1.322E-03	-5.250E-04	-8.658E-03	-9.183E-03	6.256E-02	0.951
^{57}Fe	57	26	3.107E-05	4.238E-04	1.273E-04	5.510E-04	2.238E-03	1.447
^{58}Fe	58	26	4.207E-06	1.691E-04	1.400E-03	1.569E-03	1.797E-03	8.585
^{59}Co	59	27	3.991E-06	4.761E-05	7.242E-04	7.719E-04	9.885E-04	4.977
^{58}Ni	58	28	5.711E-05	-9.972E-05	-4.167E-04	-5.164E-04	2.584E-03	0.909
^{60}Ni	60	28	2.276E-05	-7.458E-06	3.688E-04	3.614E-04	1.597E-03	1.410
^{61}Ni	61	28	1.006E-06	2.743E-05	2.742E-04	3.016E-04	3.562E-04	7.118
^{62}Ni	62	28	3.259E-06	8.833E-06	1.030E-03	1.039E-03	1.216E-03	7.496
^{64}Ni	64	28	8.568E-07	7.189E-07	1.222E-03	1.222E-03	1.269E-03	29.757
^{63}Cu	63	29	6.600E-07	5.717E-06	5.494E-04	5.551E-04	5.909E-04	17.992
^{65}Cu	65	29	3.035E-07	3.325E-06	6.372E-04	6.405E-04	6.570E-04	43.505
^{64}Zn	64	30	1.131E-06	-1.189E-06	1.566E-04	1.554E-04	2.168E-04	3.852
^{66}Zn	66	30	6.690E-07	-4.285E-07	5.471E-04	5.467E-04	5.830E-04	17.512
^{67}Zn	67	30	9.980E-08	2.433E-07	1.710E-04	1.712E-04	1.766E-04	35.565
^{68}Zn	68	30	4.632E-07	5.430E-07	9.241E-04	9.247E-04	9.498E-04	41.205
^{70}Zn	70	30	1.577E-08	-1.850E-08	1.950E-06	1.932E-06	2.788E-06	3.553
^{69}Ga	69	31	4.551E-08	2.016E-07	1.266E-04	1.268E-04	1.292E-04	57.067
^{71}Ga	71	31	3.108E-08	6.985E-08	1.148E-04	1.149E-04	1.166E-04	75.391
^{70}Ge	70	32	5.157E-08	1.932E-07	1.878E-04	1.880E-04	1.908E-04	74.363
^{72}Ge	72	32	6.910E-08	-1.239E-08	2.232E-04	2.232E-04	2.270E-04	66.000
^{73}Ge	73	32	1.955E-08	-4.353E-09	9.581E-05	9.581E-05	9.687E-05	99.593
^{74}Ge	74	32	9.228E-08	8.619E-08	3.733E-04	3.733E-04	3.783E-04	82.388
^{76}Ge	76	32	1.963E-08	-2.382E-08	1.664E-06	1.640E-06	2.705E-06	2.770
^{75}As	75	33	1.430E-08	-3.047E-08	4.896E-05	4.893E-05	4.971E-05	69.852
^{74}Se	74	34	1.198E-09	-8.148E-09	-9.057E-09	-1.721E-08	4.783E-08	0.802

TableC.15 – continued

Isotope	A	Z	$X^{\rm ini}$	$mp^{\rm wind}$	$mp^{\rm preSN}$	$mp^{\rm total}$	EM	$\langle OP \rangle$
^{76}Se	76	34	1.296E-08	7.971E-08	7.263E-05	7.271E-05	7.341E-05	113.818
^{77}Se	77	34	1.070E-08	-1.006E-08	3.885E-05	3.884E-05	3.942E-05	74.001
^{78}Se	78	34	3.376E-08	8.845E-08	2.148E-04	2.149E-04	2.167E-04	128.989
^{80}Se	80	34	7.226E-08	-1.493E-07	6.735E-05	6.720E-05	7.113E-05	19.780
^{82}Se	82	34	1.304E-08	-7.473E-09	2.703E-07	2.628E-07	9.705E-07	1.496
^{79}Br	79	35	1.389E-08	-8.014E-08	4.914E-05	4.906E-05	4.982E-05	72.060
^{81}Br	81	35	1.386E-08	1.872E-08	2.398E-05	2.400E-05	2.475E-05	35.886
^{78}Kr	78	36	3.900E-10	-2.606E-09	-2.949E-09	-5.555E-09	1.562E-08	0.805
^{80}Kr	80	36	2.575E-09	6.110E-08	1.818E-05	1.825E-05	1.839E-05	143.497
^{82}Kr	82	36	1.320E-08	1.646E-07	1.099E-04	1.101E-04	1.108E-04	168.747
^{83}Kr	83	36	1.324E-08	-2.173E-08	6.037E-05	6.035E-05	6.107E-05	92.679
^{84}Kr	84	36	6.602E-08	2.777E-08	3.031E-04	3.031E-04	3.067E-04	93.354
^{86}Kr	86	36	2.044E-08	-4.080E-09	2.785E-05	2.785E-05	2.896E-05	28.466
^{85}Rb	85	37	1.282E-08	6.457E-10	7.620E-05	7.620E-05	7.690E-05	120.504
^{87}Rb	87	37	5.063E-09	2.677E-10	2.088E-05	2.088E-05	2.116E-05	83.975
^{84}Sr	84	38	3.228E-10	-2.419E-09	-2.442E-09	-4.861E-09	1.266E-08	0.788
^{86}Sr	86	38	5.845E-09	1.021E-07	1.063E-04	1.064E-04	1.067E-04	366.874
^{87}Sr	87	38	4.443E-09	2.114E-08	8.370E-05	8.372E-05	8.396E-05	379.746
^{88}Sr	88	38	5.011E-08	2.069E-08	4.222E-04	4.222E-04	4.249E-04	170.411
^{89}Y	89	39	1.229E-08	5.418E-09	7.845E-05	7.845E-05	7.912E-05	129.336
^{90}Zr	90	40	1.534E-08	-3.468E-10	3.888E-05	3.888E-05	3.972E-05	52.015
^{91}Zr	91	40	3.384E-09	1.310E-09	1.148E-05	1.148E-05	1.166E-05	69.262
^{92}Zr	92	40	5.227E-09	4.379E-09	1.248E-05	1.249E-05	1.277E-05	49.093
^{94}Zr	94	40	5.413E-09	-7.154E-09	4.829E-06	4.822E-06	5.116E-06	18.991
^{96}Zr	96	40	8.903E-10	-4.832E-10	4.222E-07	4.217E-07	4.700E-07	10.608
^{93}Nb	93	41	1.900E-09	-4.870E-09	4.613E-06	4.609E-06	4.712E-06	49.833
^{92}Mo	92	42	1.012E-09	-3.616E-09	-7.544E-09	-1.116E-08	4.381E-08	0.869
^{94}Mo	94	42	6.448E-10	7.453E-09	5.858E-08	6.603E-08	1.010E-07	3.149

TableC.15 – continued

Isotope	A	Z	$X^{\rm ini}$	$mp^{\rm wind}$	$mp^{\rm preSN}$	$mp^{\rm total}$	EM	$\langle OP \rangle$
^{95}Mo	95	42	1.122E-09	-3.263E-10	1.334E-06	1.334E-06	1.395E-06	24.984
^{96}Mo	96	42	1.188E-09	7.144E-09	1.229E-06	1.236E-06	1.301E-06	22.014
^{97}Mo	97	42	6.875E-10	-1.505E-10	5.004E-07	5.003E-07	5.376E-07	15.713
^{98}Mo	98	42	1.754E-09	2.528E-09	1.384E-06	1.387E-06	1.482E-06	16.978
^{100}Mo	100	42	7.146E-10	-3.054E-09	2.127E-09	-9.265E-10	3.787E-08	1.065
^{96}Ru	96	44	2.926E-10	-1.788E-09	-2.210E-09	-3.998E-09	1.188E-08	0.816
^{98}Ru	98	44	1.007E-10	2.077E-10	-7.420E-10	-5.343E-10	4.933E-09	0.984
^{99}Ru	99	44	6.945E-10	-2.757E-09	2.258E-07	2.231E-07	2.608E-07	7.545
^{100}Ru	100	44	6.928E-10	3.354E-09	5.947E-07	5.980E-07	6.356E-07	18.438
^{101}Ru	101	44	9.475E-10	-5.842E-09	1.371E-07	1.313E-07	1.827E-07	3.876
^{102}Ru	102	44	1.770E-09	2.165E-09	8.050E-07	8.072E-07	9.033E-07	10.257
^{104}Ru	104	44	1.065E-09	-5.889E-09	1.974E-08	1.385E-08	7.167E-08	1.352
^{103}Rh	103	45	1.055E-09	-5.798E-09	1.419E-07	1.361E-07	1.934E-07	3.685
^{102}Pd	102	46	4.241E-11	-3.192E-10	-3.208E-10	-6.400E-10	1.662E-09	0.788
^{104}Pd	104	46	4.723E-10	6.495E-09	3.103E-07	3.168E-07	3.424E-07	14.570
^{105}Pd	105	46	9.558E-10	-5.026E-09	7.236E-08	6.733E-08	1.192E-07	2.507
^{106}Pd	106	46	1.181E-09	4.945E-09	3.802E-07	3.851E-07	4.492E-07	7.644
^{108}Pd	108	46	1.165E-09	3.886E-09	3.868E-07	3.907E-07	4.539E-07	7.830
^{110}Pd	110	46	5.255E-10	-2.835E-09	1.536E-08	1.253E-08	4.106E-08	1.570
^{107}Ag	107	47	7.840E-10	-3.276E-09	7.086E-08	6.758E-08	1.101E-07	2.823
^{109}Ag	109	47	7.420E-10	-1.507E-09	2.171E-07	2.156E-07	2.559E-07	6.931
^{106}Cd	106	48	6.346E-11	-4.513E-10	-4.799E-10	-9.312E-10	2.514E-09	0.796
^{108}Cd	108	48	4.604E-11	3.574E-09	2.752E-08	3.110E-08	3.360E-08	14.665
^{110}Cd	110	48	6.580E-10	6.853E-09	2.737E-07	2.806E-07	3.163E-07	9.659
^{111}Cd	111	48	6.805E-10	-1.368E-09	8.365E-08	8.228E-08	1.192E-07	3.521
^{112}Cd	112	48	1.294E-09	3.828E-09	3.299E-07	3.338E-07	4.040E-07	6.273
^{113}Cd	113	48	6.614E-10	-1.271E-09	8.566E-08	8.439E-08	1.203E-07	3.655
^{114}Cd	114	48	1.569E-09	4.846E-09	4.300E-07	4.348E-07	5.200E-07	6.661

TableC.15 – continued

Isotope	A	Z	$X^{\rm ini}$	$mp^{\rm wind}$	$mp^{\rm preSN}$	$mp^{\rm total}$	EM	$\langle OP \rangle$
^{116}Cd	116	48	4.161E-10	-1.445E-09	2.610E-08	2.465E-08	4.724E-08	2.281
^{113}In	113	49	2.604E-11	-1.229E-10	-1.965E-10	-3.195E-10	1.094E-09	0.844
^{115}In	115	49	5.915E-10	-1.550E-09	8.525E-08	8.370E-08	1.158E-07	3.935
^{112}Sn	112	50	1.221E-10	-7.608E-10	-9.224E-10	-1.683E-09	4.945E-09	0.814
^{114}Sn	114	50	8.435E-11	8.389E-11	-6.223E-10	-5.384E-10	4.041E-09	0.963
^{115}Sn	115	50	4.377E-11	-1.934E-11	1.220E-09	1.201E-09	3.577E-09	1.642
^{116}Sn	116	50	1.893E-09	5.063E-09	4.381E-07	4.431E-07	5.459E-07	5.795
^{117}Sn	117	50	1.008E-09	-1.389E-09	1.390E-07	1.376E-07	1.924E-07	3.834
^{118}Sn	118	50	3.209E-09	3.053E-09	5.112E-07	5.143E-07	6.885E-07	4.311
^{119}Sn	119	50	1.147E-09	-4.266E-10	1.406E-07	1.402E-07	2.025E-07	3.548
^{120}Sn	120	50	4.391E-09	3.265E-09	5.101E-07	5.133E-07	7.517E-07	3.440
^{122}Sn	122	50	6.341E-10	-8.058E-10	2.357E-08	2.277E-08	5.719E-08	1.813
^{124}Sn	124	50	8.060E-10	-7.477E-10	-3.130E-09	-3.877E-09	3.988E-08	0.994
^{121}Sb	121	51	6.318E-10	-2.110E-09	4.813E-08	4.602E-08	8.032E-08	2.555
^{123}Sb	123	51	4.803E-10	-3.122E-09	1.089E-09	-2.032E-09	2.404E-08	1.006
^{120}Te	120	52	1.628E-11	-1.313E-10	-1.232E-10	-2.545E-10	6.295E-10	0.777
^{122}Te	122	52	4.489E-10	2.044E-09	4.730E-08	4.935E-08	7.372E-08	3.300
^{123}Te	123	52	1.579E-10	7.486E-10	1.601E-08	1.676E-08	2.533E-08	3.225
^{124}Te	124	52	8.441E-10	3.916E-09	9.447E-08	9.839E-08	1.442E-07	3.433
^{125}Te	125	52	1.261E-09	-6.497E-09	2.334E-08	1.684E-08	8.532E-08	1.359
^{126}Te	126	52	3.375E-09	9.131E-10	1.449E-07	1.458E-07	3.291E-07	1.959
^{128}Te	128	52	5.733E-09	-1.180E-08	-3.304E-08	-4.483E-08	2.664E-07	0.934
^{130}Te	130	52	6.211E-09	-5.174E-09	-4.250E-08	-4.767E-08	2.895E-07	0.937
^{127}I	127	53	1.459E-09	-8.354E-09	1.624E-08	7.886E-09	8.710E-08	1.200
^{124}Xe	124	54	2.210E-11	-1.834E-10	-1.672E-10	-3.506E-10	8.489E-10	0.772
^{126}Xe	126	54	1.949E-11	-1.439E-10	-1.474E-10	-2.914E-10	7.668E-10	0.791
^{128}Xe	128	54	3.943E-10	7.710E-09	3.853E-08	4.624E-08	6.764E-08	3.448
^{129}Xe	129	54	4.893E-09	-3.450E-08	-1.752E-08	-5.202E-08	2.136E-07	0.877

TableC.15 – continued

Isotope	A	Z	$X^{\rm ini}$	$mp^{\rm wind}$	$mp^{\rm preSN}$	$mp^{\rm total}$	EM	$\langle OP \rangle$
^{130}Xe	130	54	7.865E-10	3.379E-08	7.471E-08	1.085E-07	1.512E-07	3.863
^{131}Xe	131	54	3.945E-09	-1.580E-08	4.788E-09	-1.102E-08	2.031E-07	1.035
^{132}Xe	132	54	4.806E-09	2.598E-08	1.086E-07	1.346E-07	3.955E-07	1.654
^{134}Xe	134	54	1.788E-09	-1.983E-09	5.851E-09	3.869E-09	1.009E-07	1.134
^{136}Xe	136	54	1.478E-09	-1.029E-10	-7.820E-10	-8.849E-10	7.937E-08	1.079
^{133}Cs	133	55	1.426E-09	-3.819E-09	1.368E-08	9.860E-09	8.728E-08	1.230
^{130}Ba	130	56	1.814E-11	-1.535E-10	-1.373E-10	-2.907E-10	6.942E-10	0.769
^{132}Ba	132	56	1.762E-11	-1.329E-10	-1.333E-10	-2.662E-10	6.904E-10	0.787
^{134}Ba	134	56	4.272E-10	1.549E-08	3.540E-08	5.089E-08	7.408E-08	3.484
^{135}Ba	135	56	1.174E-09	-2.899E-09	1.231E-08	9.406E-09	7.314E-08	1.252
^{136}Ba	136	56	1.409E-09	1.314E-08	9.491E-08	1.081E-07	1.845E-07	2.632
^{137}Ba	137	56	2.030E-09	9.940E-11	6.246E-08	6.256E-08	1.728E-07	1.710
^{138}Ba	138	56	1.305E-08	6.058E-09	5.211E-07	5.272E-07	1.236E-06	1.903
^{138}La	138	57	1.604E-12	-1.245E-11	-1.213E-11	-2.459E-11	6.249E-11	0.783
^{139}La	139	57	1.790E-09	-1.357E-10	5.889E-08	5.875E-08	1.559E-07	1.750
^{136}Ce	136	58	8.382E-12	-5.876E-11	-6.338E-11	-1.221E-10	3.329E-10	0.798
^{138}Ce	138	58	1.148E-11	-6.468E-11	-8.658E-11	-1.513E-10	4.718E-10	0.826
^{140}Ce	140	58	4.103E-09	8.787E-10	1.019E-07	1.028E-07	3.255E-07	1.594
^{142}Ce	142	58	5.229E-10	-7.711E-10	8.885E-09	8.114E-09	3.650E-08	1.403
^{141}Pr	141	59	6.910E-10	-1.562E-09	1.456E-08	1.300E-08	5.052E-08	1.469
^{142}Nd	142	60	9.920E-10	1.916E-09	2.335E-08	2.527E-08	7.912E-08	1.603
^{143}Nd	143	60	4.484E-10	-1.716E-09	2.376E-09	6.592E-10	2.500E-08	1.120
^{144}Nd	144	60	8.826E-10	4.418E-10	8.612E-09	9.054E-09	5.697E-08	1.297
^{145}Nd	145	60	3.095E-10	-1.122E-09	2.171E-09	1.049E-09	1.785E-08	1.159
^{146}Nd	146	60	6.448E-10	1.775E-09	8.642E-09	1.042E-08	4.542E-08	1.416
^{148}Nd	148	60	2.185E-10	-1.132E-09	1.245E-09	1.125E-10	1.197E-08	1.101
^{150}Nd	150	60	2.168E-10	-1.265E-09	-1.181E-09	-2.447E-09	9.324E-09	0.864
^{144}Sm	144	62	3.684E-11	-1.391E-10	-2.752E-10	-4.143E-10	1.585E-09	0.865

TableC.15 – continued

Isotope	A	Z	X^{ini}	mp^{wind}	mp^{preSN}	mp^{total}	EM	$\langle OP \rangle$
^{147}Sm	147	62	1.834E-10	-9.923E-10	1.296E-09	3.039E-10	1.026E-08	1.124
^{148}Sm	148	62	1.385E-10	1.390E-09	6.978E-10	2.088E-09	9.605E-09	1.394
^{149}Sm	149	62	1.714E-10	-1.135E-09	-3.908E-10	-1.526E-09	7.778E-09	0.912
^{150}Sm	150	62	9.213E-11	1.025E-09	1.571E-09	2.596E-09	7.598E-09	1.657
^{152}Sm	152	62	3.383E-10	-2.567E-09	-1.778E-10	-2.745E-09	1.562E-08	0.928
^{154}Sm	154	62	2.916E-10	-1.859E-09	-7.856E-10	-2.645E-09	1.319E-08	0.909
^{151}Eu	151	63	2.036E-10	-1.643E-09	-9.383E-10	-2.581E-09	8.472E-09	0.836
^{153}Eu	153	63	2.252E-10	-1.581E-09	-8.076E-10	-2.388E-09	9.837E-09	0.878
^{152}Gd	152	64	2.947E-12	8.288E-10	2.520E-11	8.540E-10	1.014E-09	6.914
^{154}Gd	154	64	3.210E-11	9.730E-10	3.933E-10	1.366E-09	3.109E-09	1.946
^{155}Gd	155	64	2.192E-10	-1.397E-09	-1.123E-09	-2.520E-09	9.380E-09	0.860
^{156}Gd	156	64	3.051E-10	8.860E-11	-7.652E-10	-6.766E-10	1.589E-08	1.046
^{157}Gd	157	64	2.348E-10	-8.997E-10	-5.689E-10	-1.469E-09	1.128E-08	0.965
^{158}Gd	158	64	3.750E-10	1.480E-09	4.016E-10	1.882E-09	2.224E-08	1.192
^{160}Gd	160	64	3.343E-10	-1.895E-09	-1.155E-09	-3.050E-09	1.510E-08	0.908
^{159}Tb	159	65	2.765E-10	-1.216E-09	-7.780E-10	-1.994E-09	1.302E-08	0.946
^{156}Dy	156	66	1.004E-12	-8.880E-12	-7.593E-12	-1.647E-11	3.801E-11	0.761
^{158}Dy	158	66	1.743E-12	3.478E-10	-3.854E-12	3.439E-10	4.385E-10	5.057
^{160}Dy	160	66	4.301E-11	1.872E-09	4.565E-10	2.328E-09	4.663E-09	2.179
^{161}Dy	161	66	3.498E-10	-2.046E-09	-1.885E-09	-3.931E-09	1.506E-08	0.865
^{162}Dy	162	66	4.748E-10	7.498E-10	-1.400E-09	-6.503E-10	2.513E-08	1.063
^{163}Dy	163	66	4.663E-10	-2.092E-09	-2.085E-09	-4.176E-09	2.114E-08	0.911
^{164}Dy	164	66	5.312E-10	4.773E-09	1.077E-09	5.850E-09	3.469E-08	1.312
^{165}Ho	165	67	4.244E-10	-2.079E-09	-2.049E-09	-4.128E-09	1.891E-08	0.895
^{162}Er	162	68	1.609E-12	-1.422E-11	-1.217E-11	-2.639E-11	6.095E-11	0.761
^{164}Er	164	68	1.913E-11	-1.671E-10	-1.447E-10	-3.118E-10	7.266E-10	0.763
^{166}Er	166	68	4.044E-10	4.037E-10	-1.841E-09	-1.438E-09	2.052E-08	1.020
^{167}Er	167	68	2.776E-10	-9.437E-10	-1.149E-09	-2.093E-09	1.298E-08	0.939

TableC.15 – continued

Isotope	A	Z	$X^{\rm ini}$	$mp^{\rm wind}$	$mp^{\rm preSN}$	$mp^{\rm total}$	EM	$\langle OP \rangle$
^{168}Er	168	68	3.263E-10	3.330E-09	7.874E-10	4.117E-09	2.183E-08	1.345
^{170}Er	170	68	1.840E-10	-1.112E-09	1.418E-09	3.064E-10	1.029E-08	1.124
^{169}Tm	169	69	1.854E-10	-5.708E-10	3.552E-10	-2.156E-10	9.851E-09	1.068
^{168}Yb	168	70	1.583E-12	-1.389E-11	-1.198E-11	-2.587E-11	6.008E-11	0.763
^{170}Yb	170	70	3.746E-11	2.348E-09	4.436E-11	2.392E-09	4.426E-09	2.374
^{171}Yb	171	70	1.770E-10	1.470E-10	-9.892E-10	-8.422E-10	8.767E-09	0.995
^{172}Yb	172	70	2.722E-10	2.690E-09	2.521E-11	2.715E-09	1.749E-08	1.291
^{173}Yb	173	70	2.023E-10	3.554E-10	4.182E-10	7.736E-10	1.176E-08	1.168
^{174}Yb	174	70	4.015E-10	3.703E-09	4.407E-09	8.111E-09	2.991E-08	1.497
^{176}Yb	176	70	1.628E-10	-7.578E-10	5.558E-10	-2.021E-10	8.636E-09	1.066
^{175}Lu	175	71	1.828E-10	-7.386E-10	3.258E-10	-4.129E-10	9.510E-09	1.046
^{176}Lu	176	71	4.876E-12	6.012E-11	1.838E-11	7.850E-11	3.432E-10	1.414
^{174}Hf	174	72	1.231E-12	-1.064E-11	-9.315E-12	-1.995E-11	4.689E-11	0.765
^{176}Hf	176	72	4.036E-11	1.013E-09	7.216E-10	1.734E-09	3.926E-09	1.955
^{177}Hf	177	72	1.438E-10	-5.693E-10	-2.553E-10	-8.246E-10	6.981E-09	0.976
^{178}Hf	178	72	2.121E-10	1.291E-09	1.540E-09	2.831E-09	1.435E-08	1.359
^{179}Hf	179	72	1.065E-10	9.379E-11	6.197E-10	7.135E-10	6.496E-09	1.226
^{180}Hf	180	72	2.758E-10	2.128E-09	4.140E-09	6.268E-09	2.124E-08	1.548
^{180}Ta	180	73	2.429E-14	-2.170E-13	5.011E-12	4.794E-12	6.113E-12	5.057
^{181}Ta	181	73	1.986E-10	-9.418E-10	9.165E-10	-2.529E-11	1.075E-08	1.088
^{180}W	180	74	8.395E-13	-4.240E-12	5.408E-11	4.984E-11	9.542E-11	2.284
^{182}W	182	74	1.877E-10	8.162E-10	9.138E-10	1.730E-09	1.192E-08	1.276
^{183}W	183	74	1.020E-10	2.289E-10	1.308E-09	1.537E-09	7.073E-09	1.394
^{184}W	184	74	2.195E-10	5.864E-10	2.551E-09	3.138E-09	1.505E-08	1.378
^{186}W	186	74	2.058E-10	-1.224E-09	1.011E-09	-2.135E-10	1.096E-08	1.070
^{185}Re	185	75	1.048E-10	-5.259E-10	1.487E-09	9.607E-10	6.649E-09	1.275
^{187}Re	187	75	1.773E-10	-1.422E-09	-5.507E-10	-1.972E-09	7.653E-09	0.867
^{184}Os	184	76	7.108E-13	-5.862E-12	-5.378E-12	-1.124E-11	2.735E-11	0.773

TableC.15 – continued

Isotope	A	Z	$X^{\rm ini}$	$mp^{\rm wind}$	$mp^{\rm preSN}$	$mp^{\rm total}$	EM	$\langle OP \rangle$
^{186}Os	186	76	5.778E-11	8.274E-10	5.582E-11	8.832E-10	4.020E-09	1.398
^{187}Os	187	76	5.998E-11	-1.207E-10	-1.904E-10	-3.111E-10	2.945E-09	0.987
^{188}Os	188	76	4.874E-10	-9.153E-10	-1.472E-09	-2.387E-09	2.407E-08	0.993
^{189}Os	189	76	5.974E-10	-4.584E-09	-3.428E-09	-8.012E-09	2.442E-08	0.821
^{190}Os	190	76	9.766E-10	-2.253E-09	-3.661E-09	-5.914E-09	4.710E-08	0.969
^{192}Os	192	76	1.533E-09	-7.716E-09	-9.254E-09	-1.697E-08	6.624E-08	0.868
^{191}Ir	191	77	1.357E-09	-1.087E-08	-9.158E-09	-2.003E-08	5.366E-08	0.794
^{193}Ir	193	77	2.308E-09	-1.684E-08	-1.641E-08	-3.326E-08	9.206E-08	0.801
^{190}Pt	190	78	1.008E-12	-8.080E-12	-7.629E-12	-1.571E-11	3.904E-11	0.778
^{192}Pt	192	78	5.850E-11	3.913E-09	4.629E-11	3.959E-09	7.135E-09	2.451
^{194}Pt	194	78	2.490E-09	-4.735E-09	-1.630E-08	-2.104E-08	1.141E-07	0.921
^{195}Pt	195	78	2.568E-09	-1.450E-08	-1.785E-08	-3.235E-08	1.071E-07	0.838
^{196}Pt	196	78	1.926E-09	2.197E-08	-7.548E-09	1.442E-08	1.190E-07	1.241
^{198}Pt	198	78	5.522E-10	-2.174E-09	-3.031E-09	-5.205E-09	2.477E-08	0.902
^{197}Au	197	79	1.083E-09	1.191E-09	-4.895E-09	-3.704E-09	5.511E-08	1.022
^{196}Hg	196	80	3.009E-12	-1.832E-11	-2.273E-11	-4.104E-11	1.223E-10	0.817
^{198}Hg	198	80	1.975E-10	2.280E-08	5.141E-09	2.794E-08	3.867E-08	3.934
^{199}Hg	199	80	3.360E-10	5.796E-09	2.160E-09	7.956E-09	2.620E-08	1.567
^{200}Hg	200	80	4.622E-10	9.742E-09	7.771E-09	1.751E-08	4.261E-08	1.852
^{201}Hg	201	80	2.651E-10	1.644E-09	5.018E-09	6.663E-09	2.105E-08	1.596
^{202}Hg	202	80	6.036E-10	2.791E-09	1.474E-08	1.753E-08	5.030E-08	1.675
^{204}Hg	204	80	1.401E-10	-2.688E-10	1.571E-10	-1.117E-10	7.496E-09	1.075
^{203}Tl	203	81	3.221E-10	4.652E-11	1.213E-08	1.218E-08	2.966E-08	1.851
^{205}Tl	205	81	7.764E-10	-2.066E-10	1.578E-08	1.557E-08	5.772E-08	1.494
^{204}Pb	204	82	2.931E-10	9.585E-10	9.772E-09	1.073E-08	2.664E-08	1.827
^{206}Pb	206	82	2.798E-09	4.784E-10	5.440E-08	5.488E-08	2.068E-07	1.485
^{207}Pb	207	82	3.090E-09	4.235E-10	8.971E-08	9.013E-08	2.579E-07	1.677
^{208}Pb	208	82	8.850E-09	1.602E-09	2.023E-07	2.039E-07	6.844E-07	1.554

TableC.15 – continued

Isotope	A	Z	X^{ini}	mp^{wind}	mp^{preSN}	mp^{total}	EM	$\langle OP \rangle$
^{209}Bi	209	83	8.718E-10	-9.580E-11	1.283E-08	1.273E-08	6.006E-08	1.384

D Other works

This appendix contains publications and associated works relevant for this thesis.

First-author refereed publications

Bennett M. E., Hirschi R., Pignatari M., Diehl S., Fryer C., Herwig F., Hungerford A., Magkotsios G., Rockefeller G., Timmes F. X., Wiescher M., Young P., 2010, Journal of Physics: Conference Series, 202, 012023, *"The effect of ^{12}C + ^{12}C rate uncertainties on s-process yields"*.

Bennett M. E., Hirschi R., Pignatari M., Diehl S., Fryer C., Herwig F., Hillary W., Hungerford A., Richman D., Rockefeller G., Timmes F. X., Wiescher M., 2010, in Nuclei in the Cosmos XI, Proceedings of Science, *"The effect of ^{12}C + ^{12}C rate uncertainties on the weak s-process component"*.

Bennett M. E., Hirschi R., Pignatari M., Diehl S., Fryer C., Herwig F., Hungerford A., Nomoto K., Rockefeller G., Timmes F. X., Wiescher M., 2012, MNRAS, *"The effect of ^{12}C + ^{12}C rate uncertainties on the evolution and nucleosynthesis of massive stars"*.

Other relevant refereed publications

Hirschi R., Frischknecht U., Pignatari M., Thielemann F. K., Bennet M. E., Diehl S., Fryer C. L., Herwig F., Hungerford A., Magkotsios G., Rockefeller G., Timmes F. X., Young, P., 2008, in Nuclei in the Cosmos X, Proceedings of Science, *"NuGrid: s process in massive stars".*

Herwig F., Diehl S., Fryer C. L., Hirschi R., Hungerford A., Magkotsios G., Pignatari M., Rockefeller G., Timmes F. X., Young P., Bennet M. E., 2008, in Nuclei in the Cosmos X, Proceedings of Science, *"Nucleosynthesis simulations for a wide range of nuclear production sites from NuGrid".*

Pignatari M., Herwig F., Bennet M. E., Diehl S., Fryer C. L., Hirschi R., Hungerford A., Magkotsios G., Rockefeller G., Timmes F. X., Young, P. in Nuclei in the Cosmos X, Proceedings of Science, *"Complete nucleosynthesis calculations for lowmass stars from NuGrid".*

Herwig F., Pignatari M., Woodward P., Porter D., Rockefeller G., Fryer C. L., Bennett M. E., Hirschi R., 2010, ApJ, 727, 89, *"Convective–reactive proton–^{12}C combustion in Sakurai's object (V4334 Sagittarii) and implications for the evolution and yields from the first generations of stars".*

The effect of ^{12}C + ^{12}C rate uncertainties on s-process yields

M E Bennett[1], R Hirschi[1,2], M Pignatari[7,3,4], S Diehl[5], C Fryer[6], F Herwig[7], A Hungerford[6], G Magkotsios[3,8], G Rockefeller[6], F Timmes[8], M Wiescher[3] and P Young[8].

[1] Astrophysics Group, Keele University, ST5 5BG, UK
[2] IPMU, University of Tokyo, Kashiwa, Chiba 277-8582, Japan
[3] Joint Institute for Nuclear Astrophysics, University of Notre Dame, IN, 46556, USA
[4] TRIUMF, 4004 Wesbrook Mall, Vancouver, BC, Canada, V6T 2A3
[5] Theoretical Astrophysics Group (T-6), LANL, Los Alamos, NM, 87544, USA
[6] Computation, Physics and Methods (CCS2), LANL, Los Alamos, NM, 87544, USA
[7] Dept. of Physics & Astronomy, Victoria, BC, V8W 3P6,Canada
[8] School of Earth and Space Exploration, University of Arizona, Tempe, AZ 85287, USA

E-mail: meb@astro.keele.ac.uk

Abstract. The slow neutron capture process in massive stars (the weak s-process) produces most of the s-only isotopes in the mass region $60 < A < 90$. The nuclear reaction rates used in simulations of this process have a profound effect on the final s-process yields. We generated 1D stellar models of a $25M_{\odot}$ star varying the ^{12}C + ^{12}C rate by a factor of 10 and calculated full nucleosynthesis using the post-processing code PPN. Increasing or decreasing the rate by a factor of 10 affects the convective history and nucleosynthesis, and consequently the final yields.

1. Introduction

Elements in the solar system are formed from a variety of nucleosynthesis processes in stars, such as the slow and rapid neutron-capture processes (the s-process and r-process respectively). The s-process signature of the solar system abundances can be split into three components; the weak-component, which involves nuclei with $60 < A < 90$, the main-component, which involves nuclei having atomic mass between $90 < A < 208$, and the strong component, which accounts for the production of the solar ^{208}Pb [1]. The s-process site is attributed to massive stars for the weak component, and to AGB stars having initial mass between 1 and $3M_{\odot}$ at solar-like metallicity for the main component and at low metallicity for the strong component [2]. Stellar evolution models of massive stars can be used to determine information on the conditions within stellar interiors and calculate the s-process yields relevant for the weak-component. Any changes to the input physics, such as improved laboratory nuclear reaction rates, can affect the evolution of the simulated star and consequently affect the s-process yields. Therefore, different nuclear reaction rates can be tested for their astrophysical impact. In this work, we will show how variations in the rate of the ^{12}C + ^{12}C reaction affect the evolution of a $25M_{\odot}$ star and the consequential s-process yields of the star. The motivation for this work originates from nuclear physics experiments and theory (see for instance Spillane et al. 2007 [3] and Gasques et al.

2007 [4]), which are probing low enough energies to investigate the reaction within the Gamow window for ^{12}C+^{12}C fusion.

2. Carbon burning in massive stars and the s-process

Carbon-core burning occurs at $T = 0.6 - 0.8$ GK. The dominating reactions are ^{12}C(^{12}C,α)^{20}Ne and ^{12}C(^{12}C,p)^{23}Na which, combined with the efficient ^{23}Na(p,α)^{20}Ne reaction, leaves ^{16}O and ^{20}Ne as the dominant isotopes in the core (the ^{16}O being a remnant from the previous helium burning stage). In addition to core burning, there are typically multiple stages of shell burning later in the evolution of the star, where the number of shells differs depending on the initial mass of the star. The main neutron source for the s-process in massive stars is ^{22}Ne by the reaction ^{22}Ne(α,n)^{25}Mg. ^{22}Ne is produced in helium burning from the ^{14}N$(\alpha,\gamma)^{18}$F$(\beta^+)^{18}$O$(\alpha,\gamma)^{22}$Ne reaction chain during the supergiant phase. ^{22}Ne is partially burnt at the end of helium burning with a neutron density, $n_n \sim 10^6$ cm^{-3} (see, for example, Raiteri et al. 1991 [5]). The ^{22}Ne left in the CO-core is then burnt during carbon-shell burning with higher neutron densities ($n_n \sim 10^{11} - 10^{12}$cm^{-3}), with the ^{12}C(^{12}C,α)^{20}Ne reaction providing the α particles [6]. The carbon-shell burning is sensitive to the profile of ^{12}C after core-carbon burning, which is in turn sensitive to the still uncertain ^{12}C$(\alpha,\gamma)^{16}$O rate and the choice of convection physics in the models [6][7][8]. In addition, the yields are sensitive to changes in reactions involving ^{22}Ne or its formation [6][9]. Most of the s-process-rich material ejected by the supernova event of a $25M_\odot$ star is formed by carbon-shell burning, affecting the weak s-component [10][11].

Stellar models of a $25M_\odot$ star with metallicity $Z = 0.01$ were generated using the Geneva Stellar Evolution Code [12], with the nuclear network post-processed using the NuGrid PPN tool [13]. The post-processing was computed using the KHAOS cluster at Keele University. Variations in the carbon burning rate were chosen in relation to the 'standard' Caughlan and Fowler rate (CF88 from now on). Models were generated with the CF88 rate (referred to as model C12s in this work), the CF88 rate multiplied by 10 (C12t10) and divided by 10 (C12d10). The ratio of the p- and α-channels was chosen to be 35%:65% [14]. The additional uncertainty associated with this choice of ratio will be investigated in a forth-coming paper.

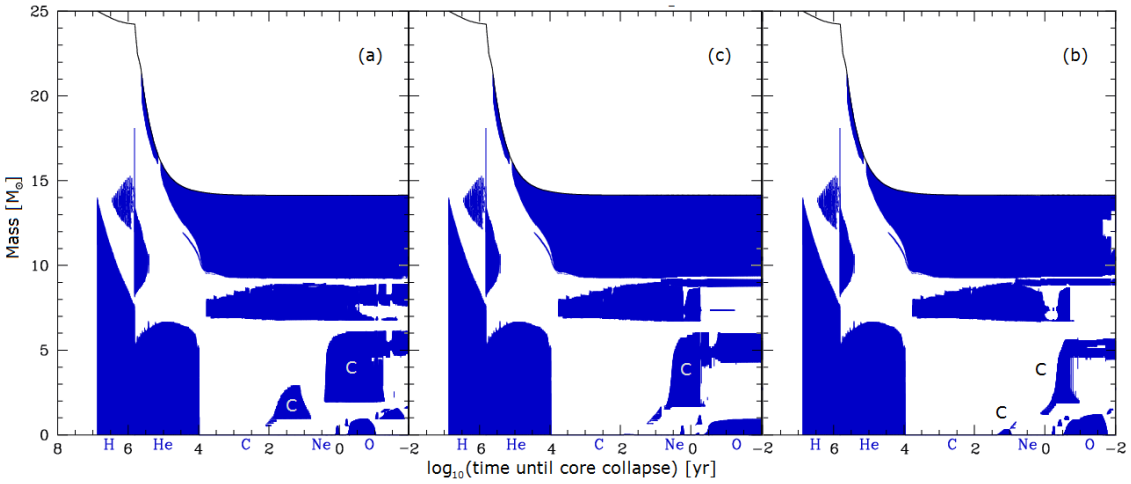

Figure 1. Structure evolution diagrams of $25M_\odot$ models at solar metallicity using different ^{12}C burning rates. Here, (a) is model C12t10, (b) is model C12s and (c) is model C12d10. The shaded regions correspond to convection zones present in the star, with the type of burning indicated by labels.

Differences in the convective history can be seen in each of the different models. Fig. 1 shows structure evolution diagrams for the models C12t10, C12s and C12d10. In each case the convection zones for carbon shell burning at $\log_{10}$(time in years until core collapse) $\sim$ 1 to -2 differ in size and duration. For model C12t10, the duration of the second carbon-shell burning process is much longer and the size of the convection zones is larger. A large fraction of overlap between the first shell and the second shell is observed and isotopes produced in the first shell by the s-process will be mixed into the second. The presence of overlapping carbon shells was previously noted by Chieffi et. al. [15]. For model C12d10, the second carbon-shell burning episode occurs later in time than for the other two models, which is due to the star contracting further before it can reach a temperature high enough so that carbon burning is activated in the shell.

Fig. 2 shows the relative abundances of stable isotopes in the second carbon shell of the C12d10 model with respect to the C12s model. Fig. 3 shows the equivalent plot for the C12t10 model with respect to the C12s model. In fig. 2, a clear signature of a higher neutron density is shown, e.g. higher production of r-only species ^{70}Zn, ^{76}Ge and lower production of ^{80}Sr due to the ^{79}Se branching. The reason is that the star in model C12d10 contracts further, resulting in carbon shells that burn at a higher temperature than the C12s model. Therefore the ^{22}Ne neutron source is burned at a higher temperature, increasing the neutron density. The s-process efficiency is quite similar in model C12s and C12d10 (see, for example, the similar production of neutron magic isotope ^{88}Sr). Concerning model C12t10, in fig. 3, a general increase in the s-process efficiency for isotopes with $60 < A < 90$ is shown, compared to model C12s. The overlap between the first and second convective shells causes the initial distribution of isotopes at the start of the second carbon-shell burning to be affected by the products of the first shell. In the first shell, neutrons are also efficiently produced by an additional neutron source, ^{17}O(α,n)^{21}Ne, where ^{17}O is mostly produced by ^{16}O(p,γ)^{17}F(β^+)^{17}O.

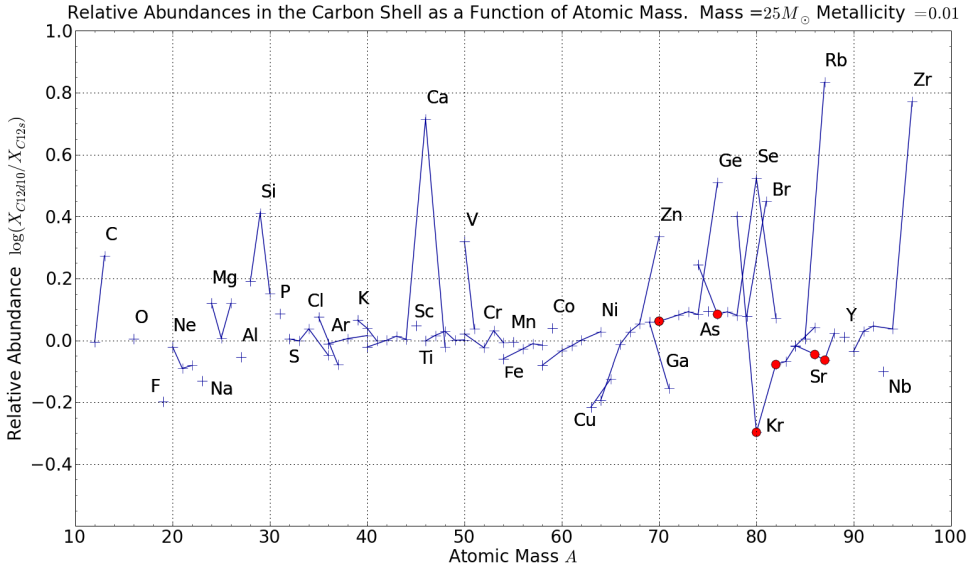

Figure 2. The relative abundances of stable isotopes up to Niobium between models C12d10 and C12s. S-only isotopes are indicated with a red circle.

In this paper, it has been shown that changes to the carbon burning rate by a factor of 10 in

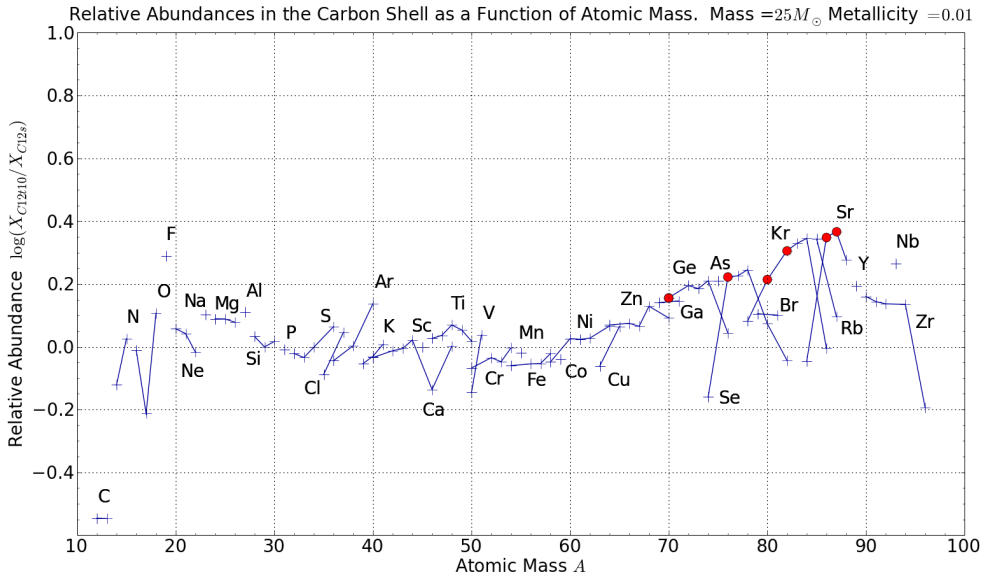

Figure 3. The relative abundances of stable isotopes up to Niobium between models C12t10 and C12s. S-only isotopes are indicated with a red circle.

stellar models of a $25M_\odot$ star significantly affect the s-process yields. The overlap of convective carbon shells active at different burning temperatures also has important implications for the s-process yields. Further analysis will be conducted in a forth-coming paper.

References

[1] Kappeler F, Beer H and Wisshak K 1989 *Reports on Progress in Physics* **52** 945–1013

[2] Gallino R, Arlandini C, Busso M, Lugaro M, Travaglio C, Straniero O, Chieffi A and Limongi M 1998 *Astrophysical Journal* **497** 388

[3] Spillane T, Raiola F, Rolfs C, Schürmann D, Strieder F, Zeng S, Becker H W, Bordeanu C, Gialanella L, Romano M and Schweitzer J 2007 *Physical Review Letters* **98** 122501

[4] Gasques L R, Brown E F, Chieffi A, Jiang C L, Limongi M, Rolfs C, Wiescher M and Yakovlev D G 2007 *Physical Review C* **76** 035802

[5] Raiteri C M, Busso M, Picchio G, Gallino R and Pulone L 1991 *Astrophysical Journal* **367** 228–238

[6] The L S, El Eid M F and Meyer B S 2007 *Astrophysical Journal* **655** 1058–1078

[7] Imbriani G, Limongi M, Gialanella L, Terrasi F, Straniero O and Chieffi A 2001 *Astrophysical Journal* **558** 903–915

[8] El Eid M F, Meyer B S and The L S 2004 *Astrophysical Journal* **611** 452–465

[9] Kaeppeler F, Wiescher M, Giesen U, Goerres J, Baraffe I, El Eid M, Raiteri C M, Busso M, Gallino R, Limongi M and Chieffi A 1994 *Astrophysical Journal* **437** 396–409

[10] Raiteri C M, Busso M, Picchio G and Gallino R 1991 *Astrophysical Journal* **371** 665–672

[11] Hoffman R D, Woosley S E and Weaver T A 2001 *Astrophysical Journal* **549** 1085–1092

[12] Eggenberger P, Meynet G, Maeder A, Hirschi R, Charbonnel C, Talon S and Ekström S 2008 *Astrophysics and Space Science* **316** 43–54

[13] Herwig F, Diehl S, Fryer C L, Hirschi R, Hungerford A, Magkotsios G, Pignatari M, Rockefeller G, Timmes F X, Young P and Bennett M E 2008 *Proceedings of the 10th Symposium on Nuclei in the Cosmos (NIC X). July 27 - August 1, 2008 Mackinac Island, Michigan, USA. Available online at http://pos.sissa.it/cgi-bin/reader/conf.cgi?confid=53*

[14] Aguilera E F, Rosales P, Martinez-Quiroz E, Murillo G, Fernández M, Berdejo H, Lizcano D, Gómez-Camacho A, Policroniades R, Varela A, Moreno E, Chávez E, Ortíz M E, Huerta A, Belyaeva T and Wiescher M 2006 *Physical Review C* **73** 064601

[15] Chieffi A, Limongi M and Straniero O 1998 *Astrophysical Journal* **502** 737

PROCEEDINGS OF SCIENCE

The effect of ^{12}C + ^{12}C rate uncertainties on the weak s-process component

Michael E. Bennett[*a], **Raphael Hirschi**[ab], **Marco Pignatari**[gcd], **Steven Diehl**[e], **Chris Fryer**[f], **Falk Herwig**[g], **William Hillary**[g], **Aimee Hungerford**[f], **Debra Richman**[g], **Gabriel Rockefeller**[f], **Frank X. Timmes**[h], **Michael Wiescher**[c].

[a] *Astrophysics Group, Keele University, ST5 5BG, UK*
[b] *IPMU, University of Tokyo, Kashiwa, Chiba 277-8582, Japan*
[c] *Joint Institute for Nuclear Astrophysics, University of Notre Dame, IN, 46556, USA*
[d] *TRIUMF, 4004 Wesbrook Mall, Vancouver, BC, Canada, V6T 2A3*
[e] *Theoretical Astrophysics (T-6), LANL, Los Alamos, NM, 87545, USA*
[f] *Computational Physics and Methods (CCS-2), LANL, Los Alamos, NM, 87545, USA*
[g] *Dept. of Physics & Astronomy, Victoria, BC, V8W 3P6,Canada*
[h] *School of Earth and Space Exploration, University of Arizona, Tempe, AZ 85287, USA*
Email: meb@astro.keele.ac.uk

The contribution by massive stars ($M > 9M_{\odot}$) to the weak s-process component of the solar system abundances is primarily due to the ^{22}Ne neutron source, which is activated near the end of helium-core burning. The residual ^{22}Ne left over from helium-core burning is then reignited during carbon burning, initiating further s-processing that modifies the isotopic distribution. This modification is sensitive to the stellar structure and the carbon burning reaction rate. Recent work on the ^{12}C + ^{12}C reaction suggests that resonances located within the Gamow peak may exist, causing a strong increase in the astrophysical S-factor and consequently the reaction rate. To investigate the effect of an increased rate, $25M_{\odot}$ stellar models with three different carbon burning rates, at solar metallicity, were generated using the Geneva Stellar Evolution Code (GENEC) with nucleosynthesis post-processing calculated using the NuGrid Multi-zone Post-Processing Network code (MPPNP). The strongest rate caused carbon burning to occur in a large convective core rather than a radiative one. The presence of this large convective core leads to an overlap with the subsequent convective carbon-shell, significantly altering the initial composition of the carbon-shell. In addition, an enhanced rate causes carbon-shell burning episodes to ignite earlier in the evolution of the star, igniting the ^{22}Ne source at lower temperatures and reducing the neutron density.

11th Symposium on Nuclei in the Cosmos, NIC XI
July 19-23, 2010
Heidelberg, Germany

[*]Speaker.

1. Introduction

The s-process components identified to contribute to the solar abundance distribution are the weak component, that is produced in massive stars (M > $9M_{\odot}$), and the main and strong components, that are produced in AGB stars. In particular, the weak s-process component is responsible for most of the isotopes in the mass range $60 < A < 90$. During helium-core burning in massive stars, ^{22}Ne is formed from ^{14}N synthesized by the CNO cycle, via the reaction chain $^{14}\mathrm{N}(\alpha,\gamma)^{18}\mathrm{F}(\beta^{+})^{18}\mathrm{O}(\alpha,\gamma)^{22}\mathrm{Ne}$. At the end of helium burning, when the temperature reaches 0.25 GK (1 GK = 10^9 K), the $^{22}\mathrm{Ne}(\alpha,\mathrm{n})^{25}\mathrm{Mg}$ reaction becomes efficient, resulting in an s process characterised by an average neutron density $n_n \sim 10^6$ n cm^{-3} and a neutron exposure (for a $25M_{\odot}$ star) $\tau_n \sim 0.2$ mbarn^{-1}. During the advanced stages, convective carbon-shell burning reignites the remaining ^{22}Ne with a much higher neutron density but lower neutron exposure ($n_n \simeq 10^{11}$ n cm^{-3} and $\tau_n \simeq 0.06$ mbarn^{-1} [10]). The s process also occurs during (radiative) carbon-core burning via the $^{13}\mathrm{C}(\alpha,\mathrm{n})^{16}\mathrm{O}$ neutron source [4]. However, in standard $25M_{\odot}$ stars heavy elements synthesized in the core are further processed and are not ejected during the supernova explosion. Thus they do not contribute to the final yields. Changes to the ^{12}C + ^{12}C reaction have an effect on the s process in massive stars [1], but a detailed analysis has so far been limited to the effect of a reduced rate due to fusion hindrance [7], although the consequences of an increased rate have been considered in superbursts on accreting neutron stars in X-ray binaries [5].

2. The ^{12}C + ^{12}C reaction

The ^{12}C + ^{12}C rate used in most stellar models is that of Caughlan & Fowler (1988) [3]. The recommended average S-factor, $S(E)^{*}$, at low energies is 3×10^{16} MeV barn, which corresponds to an approximate average over resonance structures from $E = 2.5$ to 6.5 MeV. Unfortunately, information on the resonance structures of ^{12}C + ^{12}C near the Gamow peak energy $E_0 = 1.5$ MeV is lacking; due to the very low cross-section at these energies ($\ll 1$ nbarn), experiments at these energies are strongly affected by hydrogen and deuterium contamination of the target [11][12] (see also contribution by F. Strieder et al. in this volume) and resonance structures at low energies are known to be quasimolecular states, which represents a difficult problem in nuclear physics [2]. Nevertheless, the presence of resonances at low energies has been predicted [9] and a resonance within the Gamow window could dominate the S-factor.

The three carbon burning rates considered here are the Caughlan & Fowler (1988) rate (ST), an upper-limit rate (CU) that corresponds to a strong resonance at $E = 1.5$ MeV and an intermediate rate (CI), which is the geometric mean of the standard and upper limit rates (see Fig. 1). The enhancement corresponds to a factor $\sim 50,000$ for the upper limit rate and a factor ~ 250 for the intermediate rate at a temperature of 0.5 GK.

3. Stellar structure and nucleosynthesis

Non-rotating stellar models of a $25M_{\odot}$ star were generated for each of three rates in Fig. 1 using the Geneva Stellar Evolution Code (GENEC) [6]. The models were post-processed with the parallel variant of the NuGrid Multi-zone Post-Processing Network code (MPPNP) [8] with a network of $\simeq 1000$ isotopes, up to bismuth.

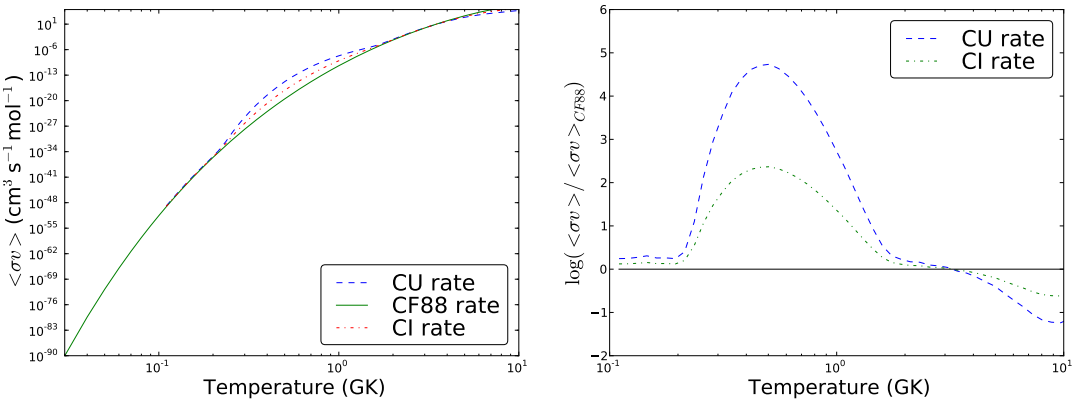

Figure 1: *Left panel*: the cross section of the Caughlan & Fowler (1988) rate (CF88), upper limit rate (CU) and intermediate rate (CI) as a function of temperature. *Right panel*: the cross section of the CU and CI rates relative to the CF88 rate.

Figure 2 shows the Kippenhahn diagrams for the three models. The CU model features a convective core during carbon-core burning. Here, the ^{13}C(α,n)^{16}O reaction is efficient and provides a neutron exposure comparable to the one in the previous helium-core, increasing significantly the s-process yields due to the previous helium-burning phase. The convective carbon-core is about $4M_{\odot}$ and overlaps with the subsequent carbon-shell. In Fig. 3 we provide the abundances at the end of the convective carbon-shell compared to the ST case. The s process powered by the ^{13}C(α, n)^{16}O activation in the carbon-core is strongly efficient and through convective mixing changes the initial composition of the carbon-shell and of the final yields. Such an effect is particularly evident in the mass range $80 < A < 120$. Figure 4 shows the CI model abundances relative to the ST case at the end of the second carbon-shell. Since the carbon-core is radiative and there is no overlap between the final convective carbon-shell and previous carbon burning events (see Fig. 2), the changes in the relative abundances of isotopes are mostly due only to a lower neutron density in the carbon shell, which in turn is caused by the ^{22}Ne neutron source activating at a lower temperature. Both the CU and CI models show lowered ignition temperatures (ST: 0.95GK, CI: 0.74GK, CU: 0.73GK) and thus lower neutron densities (ST: 2.02×10^{11} n cm^{-3}, CI: 2.07×10^{10} n cm^{-3},CU: 4.97×10^{8} n cm^{-3}). Notice also that the shells have increased lifetimes in the CU and CI models (ST: 3.4yr, CI: 10.7yr, CU: 34.0yr) and that the neutron exposure in the last convective carbon-shell is similar in each case with a value of $\simeq 0.035$ mbarn^{-1}.

To summarise, the presence of a strong resonance in the Gamow window may change the structure and nucleosynthesis of a $25M_{\odot}$ star, with the main effects being the presence of a convective carbon-core, longer shell-burning lifetimes and decreased ignition temperatures. Overlap between the convective core and the ensuing shell and lower neutron densities caused by these structural changes will strongly affect the final yields of the star, but firm conclusions should await yields calculations of massive star models at different initial masses, which will be presented in a forthcoming paper (Bennett et al., in prep.).

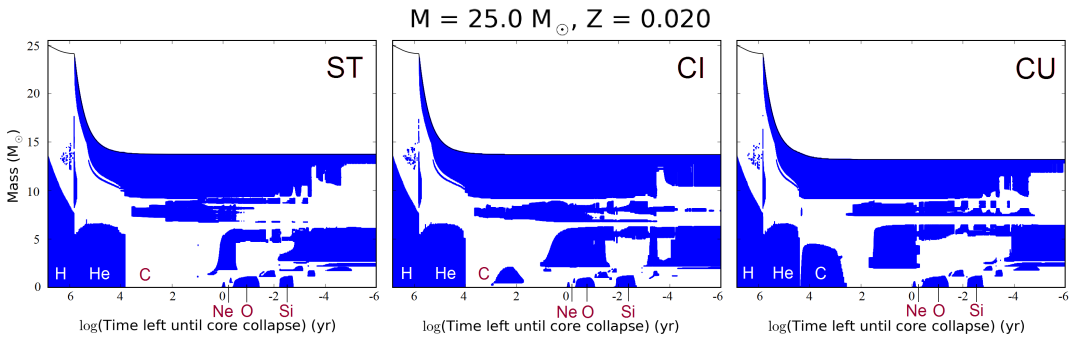

Figure 2: Kippenhahn diagrams for non-rotating stellar models using the CF88 (ST), CI and CU rates (left, centre and right panels respectively). Shaded regions correspond to convection zones with the main burning stages indicated.

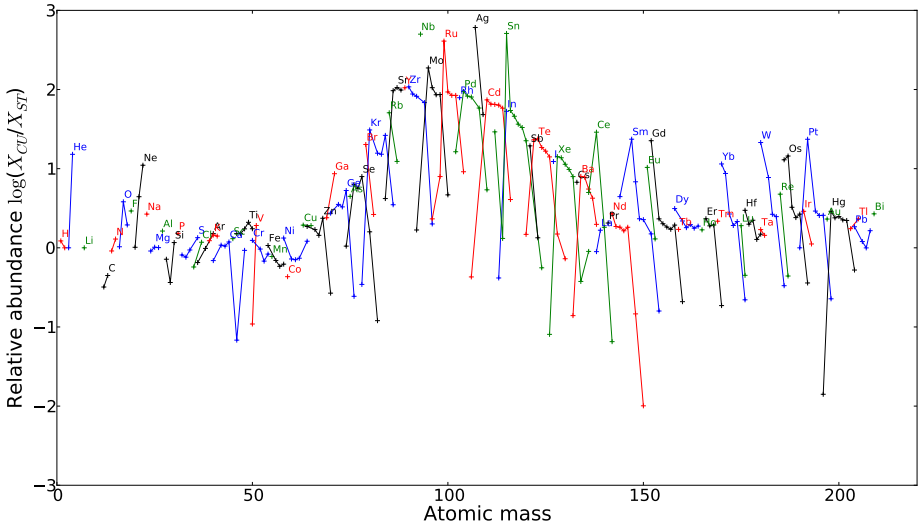

Figure 3: CU model abundances relative to the ST case in the carbon-burning shell. Lines connect isotopes belonging to the same element.

Acknowledgments

The simulations were generated using the KHAOS cluster at Keele University.

References

[1] M. E. Bennett, R. Hirschi, M. Pignatari, S. Diehl, C. Fryer, F. Herwig, A. Hungerford, G. Magkotsios, G. Rockefeller, F. Timmes, M. Wiescher, and P. Young. *The effect of $^{12}C + {}^{12}C$ rate uncertainties on s-process yields*. *JPhCS*, **202(1)**, 012023 (2010).

[2] R. R. Betts and A. H. Wuosmaa. *Nuclear molecules*. *RPPh*, **60**, 819–861 (1997).

[3] G. R. Caughlan and W. A. Fowler. *Thermonuclear Reaction Rates V*. *ADNDT*, **40**, 283 (1988).

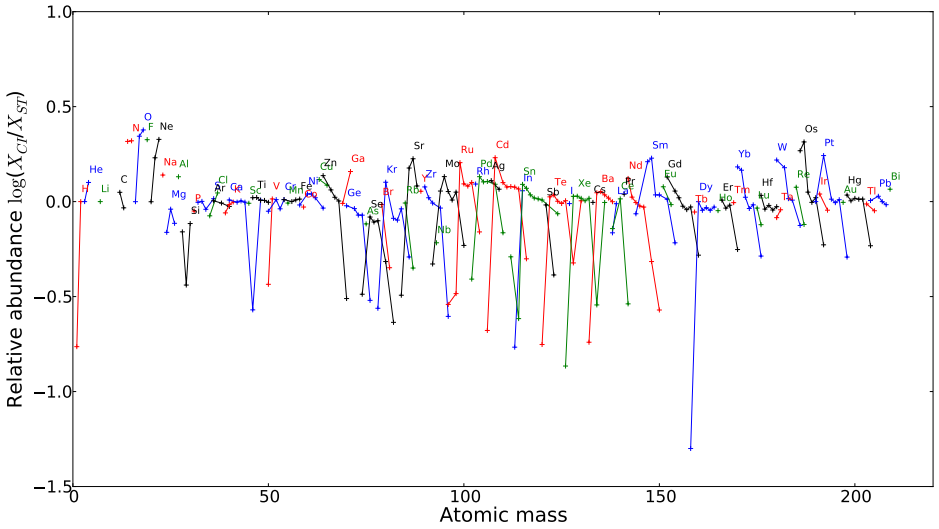

Figure 4: CI model abundances in the second carbon-burning shell relative to ST abundances. Lines connect isotopes with equal atomic number. The lower neutron density modifies the isotopic chain, but it should be noted however that some isotopes which appear strongly produced or depleted have very low abundances.

[4] A. Chieffi, M. Limongi, and O. Straniero. *The Evolution of a 25 $M_\odot$ Star from the Main Sequence Up to the Onset of the Iron Core Collapse*. *ApJ*, **502**, 737 (1998).

[5] R. L. Cooper, A. W. Steiner, and E. F. Brown. *Possible Resonances in the $^{12}C + {}^{12}C$ Fusion Rate and Superburst Ignition*. *ApJ*, **702**, 660–671 (2009).

[6] P. Eggenberger, G. Meynet, A. Maeder, R. Hirschi, C. Charbonnel, S. Talon, and S. Ekström. *The Geneva stellar evolution code*. *ApSS*, **316**, 43–54 (2008).

[7] L. R. Gasques, E. F. Brown, A. Chieffi, C. L. Jiang, M. Limongi, C. Rolfs, M. Wiescher, and D. G. Yakovlev. *Implications of low-energy fusion hindrance on stellar burning and nucleosynthesis*. *PhRvC*, **76**(3), 035802 (2007).

[8] F. Herwig, S. Diehl, C. L. Fryer, R. Hirschi, A. Hungerford, G. Magkotsios, M. Pignatari, G. Rockefeller, F. X. Timmes, P. Young, and M. E. Bennett. *Nucleosynthesis simulations for a wide range of nuclear production sites from NuGrid*. in proceedings of *The 10th Symposium on Nuclei in the Cosmos (NIC X)* PoS(NIC X)023 (2008).

[9] R. Perez-Torres, T. L. Belyaeva, and E. F. Aguilera. *Fusion and elastic-scattering cross-section analysis of the $^{12}C + {}^{12}C$ system at low energies*. *PAN*, **69**, 1372–1382 (2006).

[10] C. M. Raiteri, M. Busso, G. Picchio, and R. Gallino. *S-process nucleosynthesis in massive stars and the weak component. II - Carbon burning and galactic enrichment*. *ApJ*, **371**, 665–672 (1991).

[11] T. Spillane, F. Raiola, C. Rolfs, D. Schürmann, F. Strieder, S. Zeng, H.-W. Becker, C. Bordeanu, L. Gialanella, M. Romano, and J. Schweitzer. $^{12}C + {}^{12}C$ *Fusion Reactions near the Gamow Energy*. *PhRvL*, **98**(12), 122501 (2007).

[12] F. Strieder. *Carbon burning in stars - Prospects for underground measurements of the ^{12}C+^{12}C fusion reactions*. *JPhCS*, **202**(1), 012025 (2010).

Monthly Notices
of the
ROYAL ASTRONOMICAL SOCIETY

Mon. Not. R. Astron. Soc. (2012) doi:10.1111/j.1365-2966.2012.20193.x

The effect of $^{12}C + {}^{12}C$ rate uncertainties on the evolution and nucleosynthesis of massive stars

M. E. Bennett,[1⋆]† R. Hirschi,[1,2]† M. Pignatari,[3]† S. Diehl,[4]† C. Fryer,[5]† F. Herwig,[6]† A. Hungerford,[5]† K. Nomoto,[7] G. Rockefeller,[5]† F. X. Timmes[8,9]† and M. Wiescher[8]

[1]*Astrophysics Group, Keele University, Staffordshire ST5 5BG*
[2]*IPMU, University of Tokyo, Kashiwa, Chiba 277-8582, Japan*
[3]*Department of Physics, Basel University, Klingelbergstrasse 82, 4056 Basel, Switzerland*
[4]*Theoretical Astrophysics (T-6), LANL, Los Alamos, NM 87545, USA*
[5]*Computational Physics and Methods (CCS-2), LANL, Los Alamos, NM 87545, USA*
[6]*Department of Physics and Astronomy, Victoria, BC V8W 3P6, Canada*
[7]*Institute for Physics and Mathematics of the Universe, University of Tokyo, Kashiwa, Chiba 277-8583, Japan*
[8]*Joint Institute for Nuclear Astrophysics, University of Notre Dame, IN 46556, USA*
[9]*School of Earth and Space Exploration, University of Arizona, Tempe, AZ 85287, USA*

Accepted 2011 November 13. Received 2011 November 11; in original form 2011 August 19

ABSTRACT

Over the last 40 years, the $^{12}C + {}^{12}C$ fusion reaction has been the subject of considerable experimental efforts to constrain uncertainties at temperatures relevant for stellar nucleosynthesis. Recent studies have indicated that the reaction rate may be higher than that currently used in stellar models. In order to investigate the effect of an enhanced carbon-burning rate on massive star structure and nucleosynthesis, new stellar evolution models and their yields are presented exploring the impact of three different $^{12}C + {}^{12}C$ reaction rates. Non-rotating stellar models considering five different initial masses, 15, 20, 25, 32 and 60 $M_{\odot}$, at solar metallicity, were generated using the Geneva Stellar Evolution Code (GENEC) and were later post-processed with the NuGrid Multi-zone Post-Processing Network tool (MPPNP). A dynamic nuclear reaction network of ∼1100 isotopes was used to track the *s*-process nucleosynthesis. An enhanced $^{12}C + {}^{12}C$ reaction rate causes core carbon burning to be ignited more promptly and at lower temperature. This reduces the neutrino losses, which increases the core carbon-burning lifetime. An increased carbon-burning rate also increases the upper initial mass limit for which a star exhibits a convective carbon core (rather than a radiative one). Carbon-shell burning is also affected, with fewer convective-shell episodes and convection zones that tend to be larger in mass. Consequently, the chance of an overlap between the ashes of carbon-core burning and the following carbon shell convection zones is increased, which can cause a portion of the ashes of carbon-core burning to be included in the carbon shell. Therefore, during the supernova explosion, the ejecta will be enriched by *s*-process nuclides synthesized from the carbon-core *s*-process. The yields were used to estimate the weak *s*-process component in order to compare with the Solar system abundance distribution. The enhanced rate models were found to produce a significant proportion of Kr, Sr, Y, Zr, Mo, Ru, Pd and Cd in the weak component, which is primarily the signature of the carbon-core *s*-process. Consequently, it is shown that the production of isotopes in the Kr–Sr region can be used to constrain the $^{12}C + {}^{12}C$ rate using the current branching ratio for α- and p-exit channels.

Key words: nuclear reactions, nucleosynthesis, abundances – stars: abundances – stars: evolution.

1 INTRODUCTION

Despite the limitations of one-dimensional (1D) stellar models, their capability to reproduce several observables makes them a fundamental tool to understand stellar nucleosynthesis sites in the Galaxy.

⋆E-mail: meb@astro.keele.ac.uk
†The NuGrid collaboration.

Calculated stellar abundances can be compared with observed abundances from meteoritic data or stellar spectra. In massive stars ($M > 8\,M_{\odot}$) the presence of advanced burning stages during their evolution and their final fate as a supernova explosion provides a useful test-bed for many sensitivity studies, which are important to constrain uncertainties in input physics. In particular, nuclear reaction rates are often found to be sources of uncertainty as the task of experimentally determining precise cross-sections at astrophysically relevant energies is often difficult. The $^{12}C + {}^{12}C$ reaction is a good example where, despite over four decades of research, the reaction rate still carries substantial uncertainties because of the nuclear structure and reaction dynamics governing the low-energy cross-section of the fusion process (Strieder 2010). The extrapolation of the laboratory data into the stellar energy range – Gamow peak energies ($E_0 \simeq 1.5$ MeV or $T \simeq 0.5$ GK) – depends critically on a reliable theoretical treatment of the reaction mechanism. Present model extrapolations differ by orders of magnitude; this affects directly the reaction rate with significant impact on a number of stellar burning scenarios (Gasques et al. 2007).

The $^{12}C + {}^{12}C$ reaction cross-section is characterized by a complex resonance structure, associated either with scattering states in the nucleon–nucleon potential or with quasi-molecular states of the compound nucleus ^{24}Mg (Imanishi 1968), which at low energies can be described by a resonant-part superimposed on a non-resonant part, where the latter is also rather uncertain (Yakovlev et al. 2010). A theory that predicts the location and strength of the resonant-part has not yet been proposed (Strieder 2008), but resonance characteristics can be determined either by coupled-channel calculations or by optical model potentials based on, for example, α-particle condensates or cluster structures (Betts & Wuosmaa 1997; Xu et al. 2010, and references therein). Resonances have consequently been predicted by both approaches at energies $\sim$2 MeV (Michaud & Vogt 1972; Perez-Torres, Belyaeva & Aguilera 2006) and it was shown that the experimentally observed data could be reasonably well reproduced in the framework of these models (Kondo, Matsuse & Abe 1978). Yet, none of these models provides the quantitative accuracy in resonance parameter predictions required for a reliable extrapolation of the data into the stellar energy range. Complementary to the classical potential model approach, dynamic reaction theories are being developed. They have been tested successfully for fusion of spherical nuclei like $^{16}O + {}^{16}O$ (Diaz-Torres, Gasques & Wiescher 2007), but the theoretical treatment of fusion reactions of two deformed ^{12}C nuclei requires a non-axial symmetric formalism for a fully reliable treatment (Diaz-Torres 2008).

Taking a phenomenological approach, a resonance with strength $(\omega\gamma) \simeq 3.4 \times 10^{-7}$ eV has been invoked to correct the ignition depth of neutron star superbursts (Cooper, Steiner & Brown 2009), which are believed to be caused by ignition of carbon-burning reactions, triggering a thermonuclear runaway in the crust of a neutron star. Type Ia supernovae should also exhibit changes to the ignition characteristics, but these conditions (other than central density) are less sensitive to an enhancement in the carbon-burning rate (Cooper et al. 2009; Iapichino & Lesaffre 2010). The possible existence of such a resonance, associated with a pronounced $^{12}C + {}^{12}C$ cluster structure of the compound nucleus ^{24}Mg, represents a source of uncertainty.

Alternatively, the reaction rate may not be dominated by resonances at lower energies because of predictions that the cross-section drops much steeper than usually anticipated due to a fusion hindrance reported in heavy-ion reactions (see for example Jiang et al. 2004, 2007). The consequences of the hindrance phenomenon for the $^{12}C+ {}^{12}C$ reaction in astrophysical scenarios were examined by Gasques et al. (2007), where it was demonstrated that hindrance is much more significant in the pycnonuclear regime than the thermonuclear regime, but does exhibit a noticeable effect on the yields of massive stars. The reduced rate, by approximately a factor of 10–100 at carbon-burning temperatures (see their fig. 1), increases the temperature with which carbon burning occurs and therefore affects the nucleosynthesis. Changes in the yields were generally rather small, but some specific isotopes, such as ^{26}Al, ^{40}Ca, ^{46}Ca, ^{46}Ti, ^{50}Cr, ^{60}Fe, ^{74}Se, ^{78}Kr and ^{84}Sr, exhibited larger changes most likely due to the increased neutron density exhibited by the burning of neutron sources at higher temperatures.

The wide range of presently discussed model predictions requires new experimental effort to reduce the uncertainty range. However, the measurements towards low energies are extremely difficult, because the low cross-section ($\sigma \ll 1$ nbarn) limits the experimental yield to an event rate below the natural and beam-induced background events in the detectors. Particle measurements are difficult because of the limited energy resolution of the particle detectors which makes a separation of the particle groups extremely difficult at the low count rate conditions. Beam-induced background from reactions on target impurities is therefore difficult to distinguish from the actual reaction products (Zickefoose et al. 2010). The measurement of secondary gamma radiation associated with the particle decay is also handicapped by natural and cosmic ray-induced background radiation (Strieder 2010). While recent experiments suggest an increase in the low-energy S-factor indicating the possibility of narrow resonances at lower energies (Aguilera et al. 2006; Barrón-Palos et al. 2006; Spillane et al. 2007), the confirmation of the results and the experimental pursuit towards lower energies is stalled due to the present inability to differentiate the reaction data from the different background components (Zickefoose et al. 2010). Improved experimental conditions require the preparation of ultra-pure target materials for experiments in a cosmic ray shielded underground environment (Strieder 2010).

The three dominant carbon-burning reactions, with Q-values, are

$$^{12}C(^{12}C, \alpha)^{20}Ne, \qquad Q = +4.617, \tag{1.1}$$

$$^{12}C(^{12}C, p)^{23}Na, \qquad Q = +2.240, \tag{1.2}$$

$$^{12}C(^{12}C, n)^{23}Mg, \qquad Q = -2.599. \tag{1.3}$$

During carbon burning, the α- and p-channels dominate with the n-channel, making up less than 1 per cent of all $^{12}C + {}^{12}C$ reactions (Dayras, Switkowski & Woosley 1977). At this stage, the composition of the star is largely ^{12}C and ^{16}O, with the initial ratio of ^{12}C to ^{16}O at this stage largely governed by the $^{12}C(\alpha, \gamma)^{16}O$ reactions occurring during helium-core burning. Carbon-core burning occurs at a central temperature of $\sim$0.7 GK and produces mainly ^{20}Ne and ^{24}Mg, since $\sim$99 per cent of ^{23}Na synthesized through the p-channel is destroyed via efficient $^{23}Na(p, \alpha)^{20}Ne$ and $^{23}Na(p, \gamma)^{24}Mg$ reactions (Arnett & Thielemann 1985). Carbon-core burning, which is convective for stars with initial mass $M \lesssim 20\,M_{\odot}$ and radiative for $M \gtrsim 20\,M_{\odot}$ (see for example Hirschi, Meynet & Maeder 2005), is followed by convective carbon-shell burning episodes at temperatures of $\sim$0.8–1.4 GK. The number of episodes and the spatial extent of each shell differs between massive stars of different initial mass as the development of the carbon shells is sensitive to the spatial ^{12}C profile at the end of helium-core burning; the formation of a convective carbon shell often lies at the same spatial coordinate as the top of the previous convective shell (Arnett 1972; El Eid, Meyer & The 2004). The presence of a convective carbon core depends on the CO core mass

as both the neutrino losses and energy generation rate depend on the density, which decreases with increasing CO core mass (Arnett 1972; Woosley & Weaver 1986; Limongi, Straniero & Chieffi 2000). Consequently, mechanisms that affect the CO core mass or the carbon-burning energy budget, such as rotation (Hirschi, Meynet & Maeder 2004) and the ^{12}C abundance following helium burning (Imbriani et al. 2001; El Eid, The & Meyer 2009), will affect the limiting mass for the presence of a convective core.

Massive stars are a site for the *s*-process, which starts during helium-core burning and also occurs during the following carbon-burning stages. The *s*-process nucleosynthesis also occurs in the helium shell via the ^{22}Ne neutron source, but this process is marginal compared to the *s*-process operating in the helium core or the carbon shells (see for example The, El Eid & Meyer 2007). Beyond carbon burning, the temperature becomes high enough in the interior ($\sim$2 GK) for photodisintegration reactions to destroy heavy nuclides. Because the *s*-process can probably occur during both central and shell carbon burning, one can expect that changes in the $^{12}C + ^{12}C$ rate affect the stellar structure and nucleosynthesis and therefore also the *s*-process.

The ^{22}Ne neutron source, which is formed during helium burning via the $^{14}N(\alpha, \gamma)^{18}F(\beta^+)^{18}O(\alpha, \gamma)^{22}Ne$ reaction chain is the main neutron source (Peters 1968; Couch, Schmiedekamp & Arnett 1974; Lamb et al. 1977). As the temperature approaches 0.25 GK near the end of helium burning, $^{22}Ne(\alpha, n)^{25}Mg$ reactions become efficient (Busso & Gallino 1985; Raiteri et al. 1991a). During this phase, a 25–M$_\odot$ star, for example, has a neutron density $n_n \sim 10^6$ cm^{-3} and a neutron exposure $\tau_n \sim 0.2$ mb^{-1} (see for instance Pignatari et al. 2010, and references therein). The ^{22}Ne source becomes efficient in a convective environment and heavy elements formed through neutron captures are mixed out from the centre of the star. Some of these abundances will be modified by further explosive nucleosynthesis later in the evolution, but will otherwise survive long enough to be present in the supernova ejecta and contribute to the total yields of the star. Consequently, ^{22}Ne in massive stars is the dominant neutron source responsible for the classical weak *s*-process component (Truran & Iben 1977; Prantzos, Arnould & Arcoragi 1987; Käppeler, Beer & Wisshak 1989; Raiteri et al. 1991b).

Any remaining ^{22}Ne present at the end of helium-core burning is later reignited during carbon-shell burning, resulting in an *s*-process with a higher neutron density and a lower neutron exposure ($n_n \sim 10^{11-12}$ cm^{-3} and $\tau_n \sim 0.06$ mb^{-1}; Raiteri et al. 1991b). The increased neutron density is responsible for changing the branching ratios of unstable isotopes, which is particularly important for branching isotopes, such as ^{69}Zn, ^{79}Se and ^{85}Kr, since they inhabit positions in the isotope chart of nuclides where different *s*-process paths across the valley of stability are available (Käppeler et al. 1989). The increase in neutron density is responsible for opening the *s*-process path so that the carbon-shell burning contribution to specific isotopes, such as ^{70}Zn, ^{86}Kr and ^{80}Se, may be relevant (see for example Raiteri et al. 1991b; The et al. 2007).

Another potential neutron source is ^{13}C, which is formed through the $^{12}C(p,\gamma)^{13}N(\beta^+)^{13}C$ reaction chain (Arnett & Truran 1969). During carbon-core burning, this neutron source, via the $^{13}C(\alpha, n)^{16}O$ reaction, becomes efficient, which results in an *s*-process in the carbon core with a typical neutron density of $n_n = 10^7$ cm^{-3} (Arnett & Thielemann 1985; Chieffi, Limongi & Straniero 1998). The abundance of ^{13}C is dependent on the $^{13}N(\gamma, p)^{12}C$ reaction, which dominates the depletion of ^{13}N at temperatures above 0.8 GK. The ^{22}Ne neutron source is the dominant neutron source when the temperature rises above such a temperature, although the ^{13}C neutron source may also provide an important contribution to the total neutron exposure (Clayton 1968; Arcoragi, Langer & Arnould 1991). In any case, the carbon-core *s*-process occurs primarily in radiative conditions with a relatively small neutron exposure and any heavy elements synthesized via the ensuing neutron captures usually remain in the core (see however the discussion on overlapping convection zones in Section 4); photodisintegration and the supernova explosion process will ensure that these elements are not present in the final ejecta and do not contribute to the final yields of the star (see for example Chieffi et al. 1998).

A preliminary study (Bennett et al. 2010a) found that changes to the total $^{12}C + ^{12}C$ rates within a factor of 10 affect the convection zone structure and nucleosynthesis of a 25-M$_\odot$ star at solar metallicity. The main conclusions were an increase in the carbon-burning shell contribution to the *s*-process abundances by two different scenarios. The first, applicable to the case where the rate was increased by a factor of 10, was due to the presence of large carbon-burning shells that 'overlapped'. In this situation, the second carbon-burning shell was polluted with ashes from the first carbon-burning shell, modifying the overall composition. The second scenario, applicable to the case where the rate was reduced by a factor of 10, was an increase in neutron density associated with the neutron source, ^{22}Ne, burning at a higher temperature in the convective shell. The overall increase in the abundances of most isotopes with $60 < A < 90$ was approximately 0.1–0.4 dex. Strongly enhanced rates were also investigated (Bennett et al. 2010b), which show that the presence of a larger convective core has a significant impact on the total yields, since the convective core adds an additional neutron exposure towards the total contribution of *s*-process yields; abundances of many heavy nuclides increased by up to $\sim$2 dex. However, no comparison could be made with observations as a 25-M$_\odot$ stellar model (at solar metallicity) was the only one considered.

In this paper, a sensitivity study is made over a set of massive star models, at solar metallicity, to determine whether a comparison between the yields and the Solar system abundances can constrain the $^{12}C + ^{12}C$ rate. Section 2 explains the models and the choice of input physics in the simulations. In Section 3, the changes in stellar structure are analysed. Section 4 describes the nucleosynthesis, focusing on the *s*-process during carbon-core and carbon-shell burning. Section 5 presents the yields. The discussion and conclusions can be found in Sections 6 and 7, respectively.

2 COMPUTATIONAL APPROACH

2.1 The $^{12}C + ^{12}C$ reaction rates

We build on the previous work (Bennett et al. 2010b) where three carbon-burning rates in a 25–M$_\odot$ star were considered. These are the Caughlan & Fowler (1988) 'standard' rate (ST) and two enhanced rates: an 'upper limit' rate (CU) and an intermediate rate (CI), the latter of which is a geometric mean of the ST and CU rates. The CU rate is the ST rate including a resonance of strength $(\omega\gamma) = 6.8 \times 10^{-5}$ eV at a centre-of-mass energy $E_{com} = 1.5$ MeV. This choice of resonance originates from a preliminary particle spectroscopy experiment on $^{12}C + ^{12}C$ obtained at the CIRCE radioactive beam facility in Caserta/Napoli, Italy (Terrasi et al. 2007). Although the CI rate was determined via a geometric mean, a resonance that would replicate the peak at 1.5 MeV for this rate would have a magnitude of $(\omega\gamma) \simeq 3.4 \times 10^{-7}$ eV. The top panel of Fig. 1 shows the Maxwellian-averaged cross-sections of the reaction rates as a function of temperature. The bottom panel shows the reaction rates relative to the ST rate. As indicated by Fig. 1, the peak of the CU and CI rates is at $\sim$0.5 GK and is a factor of approximately 50 000 and

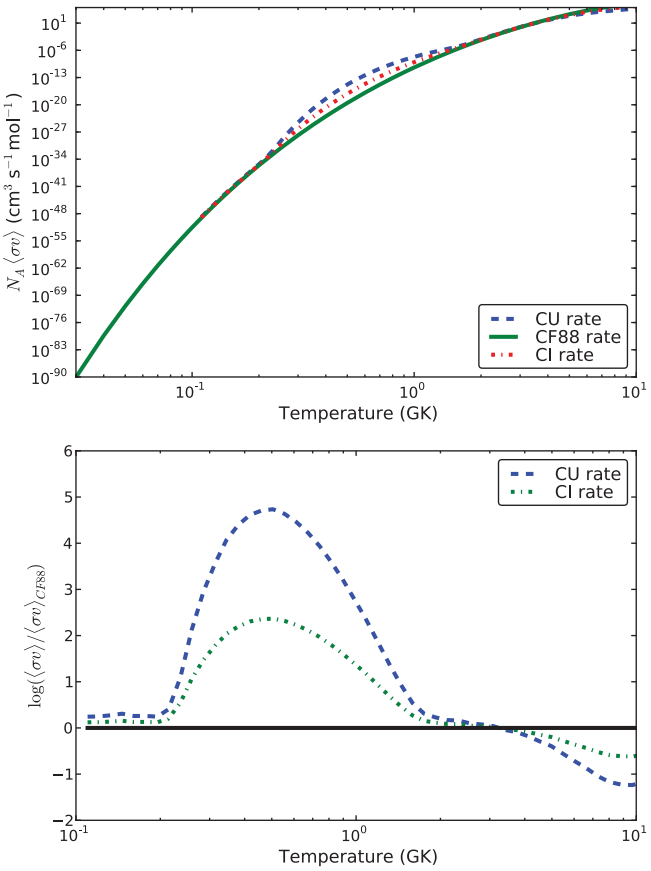

Figure 1. Top panel: Maxwellian-averaged cross-sections for $^{12}C + {}^{12}C$ rates used in Bennett et al. (2010b) and also in this study. The three rates are the Caughlan & Fowler (1988) 'standard' rate (ST), an upper limit rate (CU) and an intermediate rate (CI). The CI rate is a geometric mean of the ST and CU rates. Bottom panel: the Maxwellian-averaged cross-sections relative to the ST rate.

250 times the ST rate at that temperature, respectively. The choice of branching ratio for the α- and p-exit channels is 13:7, which is valid within the energy range $4.42 < E_{\rm com} < 6.48$ MeV (Aguilera et al. 2006). It is assumed in this work that the branching ratio is preserved to lower centre-of-mass energies. For the n-exit channel, we use the branching ratio from Dayras et al. (1977).

2.2 Stellar models

Non-rotating stellar models at solar metallicity ($Z = 0.02$) were generated using the Geneva Stellar Evolution Code (GENEC), with a small nuclear reaction network that takes into account the reactions important for energy generation. Five masses were considered for each carbon-burning rate, which are 15, 20, 25, 32 and 60 $M_\odot$, for a total of 15 stellar models. These will be referred to as XXYY, where XX is the initial mass of the star in solar masses and YY denotes the rate and is 'ST', 'CI' or 'CU' for the standard, intermediate and upper limit rates, respectively. The reason for this choice of initial masses is to provide yields data over a range of masses with approximately even spacing in log space.

GENEC is described in detail in Eggenberger et al. (2008), but some important features are recalled here for convenience. The Schwarzschild criterion for convection is used and convective mixing is treated as a diffusive process from oxygen burning onwards. No overshooting is included except for hydrogen- and helium-burning cores, where an overshooting parameter of $\alpha = 0.2H_P$ is used. Neutrino loss rates are calculated using fitting formulae from Itoh et al. (1989), which are the same as those of the more recent evaluation from Itoh et al. (1996) for pair and photoneutrino processes. The initial abundances used were those of Grevesse & Noels (1993), which correspond directly to the OPAL opacity tables used (Rogers, Swenson & Iglesias 1996). For lower temperatures, opacities from Ferguson et al. (2005) are used.

Several mass-loss rates are used depending on the effective temperature, $T_{\rm eff}$, and the evolutionary stage of the star. For main-sequence massive stars, where $\log T_{\rm eff} > 3.9$, mass-loss rates are taken from Vink, de Koter & Lamers (2001). Otherwise the rates are taken from de Jager, Nieuwenhuijzen & van der Hucht (1988). However, for lower temperatures ($\log T_{\rm eff} < 3.7$), a scaling law of the form

$$\dot{M} = -1.479 \times 10^{-14} \times \left(\frac{L}{L_\odot}\right)^{1.7} \quad (2.1)$$

is used, where $\dot{M}$ is the mass-loss rate in solar masses per year, L is the total luminosity and $L_\odot$ is the solar luminosity. For a recent discussion on mass-loss rates in the red-supergiant phase, see Mauron & Josselin (2011). During the Wolf–Rayet (WR) phase, mass-loss rates by Nugis & Lamers (2000) are used.

In GENEC, the reaction rates are chosen to be those of the NACRE compilation; Angulo et al. (1999) for the experimental rates and from their website[1] for theoretical rates. However, there are a few exceptions. The rate of Mukhamedzhanov et al. (2003) was used for $^{14}N(p, \gamma)^{15}O$ below 0.1 GK and the lower limit NACRE rate was used for temperatures above 0.1 GK. This combined rate is very similar to the more recent LUNA rate (Imbriani et al. 2005) at relevant temperatures. The Fynbo (2005) rate was used for the 3α reaction and the Kunz et al. (2002) rate was used for $^{12}C(\alpha, \gamma)^{16}O$. The $^{22}Ne(\alpha,n)^{25}Mg$ rate was taken from Jaeger et al. (2001) and used for the available temperature range ($T \leq 1$ GK). Above this range, the NACRE rate was used. The $^{22}Ne(\alpha,n)^{25}Mg$ rate competes with $^{22}Ne(\alpha, \gamma)^{26}Mg$ for α–particles. For this rate, the NACRE rate was used. The ^{16}O neutron poison is effective at capturing neutrons, forming ^{17}O, which can either resupply the 'recycled' neutrons via the $^{17}O(\alpha,n)^{20}Ne$ reaction or undergo the competing reaction $^{17}O(\alpha, \gamma)^{21}Ne$. For $^{17}O(\alpha, n)^{20}Ne$ the NACRE reaction is used and for the $^{17}O(\alpha, \gamma)^{21}Ne$ reaction the correction of the Caughlan & Fowler (1988) rate by Descouvemont (1993) is applied.

The models were calculated for as far into the evolution as possible, which for most models is after or during the silicon-burning stage. The models that ceased before silicon burning were the 15CI, 15CU, 60CI and 60CU models, which proceeded to oxygen-shell burning, and the 20CI and 20CU models, which proceeded to just after the oxygen-shell burning stage. The *s*-process yields are not significantly affected by hydrostatic burning stages following oxygen burning because most of the isotopes produced via the *s*-process will be destroyed by photodisintegration and the choice of remnant mass for the supernova explosion, which defines the boundary between matter that falls back on to the remnant and matter that forms supernova ejecta, reduces the impact of nucleosynthesis that neon-, oxygen- and silicon-burning stages would have on the total yields (see also Section 5.1). However, it must be noted that there will be explosive burning processes during the supernova explosion and photodisintegration occurring at the bottom of the convective carbon, neon and oxygen shells during the advanced stages, which will

[1] http://pntpm3.ulb.ac.be/Nacre/nacre.htm

affect the abundances (see for example Rauscher et al. 2002; Tur, Heger & Austin 2009). In this work, the contribution of explosive burning and photodisintegration to the total yields is not considered.

Since the $^{12}C + {}^{12}C$ reactions do not become efficient until after helium-core burning, the CU and CI models for a particular choice of initial mass were started just before the end of helium-core burning using the ST model data as initial conditions, reducing some of the computational expense.

2.3 Post-processing

The NuGrid[2] Multi-Zone Post-Processing tool (the parallel variant; MPPNP) is described in Herwig et al. (2008) and Pignatari et al. (in preparation). See also Appendix A for details of the parallel implementation. The system of equations for the rate of change of abundances of isotopes is solved using an implicit finite differencing method combined with the Newton–Raphson scheme, with the output temperature, density and the distribution of convection (and radiation) zones from GENEC as input. Additional features have been included to enhance the calculations or save on unnecessary computations. Sub-timesteps are inserted where appropriate to improve convergence in the case where the time-scale of reactions is smaller than the stellar evolution timestep. Also, the nuclear network is dynamic, adding or removing isotopes from the network depending on the stellar conditions (up to the maximal network defined in Table 1). This is useful in reducing the number of computations associated with nuclear reactions where the change in abundance is zero or negligible. The same (adaptive) mesh as used in GENEC was used for the post-processing calculations.

The nuclear networks used are shown in Fig. 2. The isotopes used in each network are discriminated depending on whether they are involved in reactions important for energy generation (featured in both the stellar model and the post-processing tool) or not (featured only in the post-processing tool). GENEC uses a skeleton network of 31 isotopes, which is the same network as used in previous GENEC models (see for example Hirschi et al. 2004, 2005). This network is a combination of fundamental isotopes relevant for pp-chain reactions, the CNO tricycle and helium burning and a network similar to the $\alpha 7$ network of Hix et al. (1998), enacted during the advanced burning stages, which reduces the computational expense associated with a larger network without causing significant errors in energy generation rates. The isotopes included in the network for MPPNP are specified in Table 1 and are shown in Fig. 2. Five isomeric states are also included, which are treated as separate nuclei from their ground state equivalents. These are $^{26}Al^m$, $^{85}Kr^m$, $^{115}Cd^m$, $^{176}Lu^m$ and $^{180}Ta^m$.

The reaction rates in MPPNP were set to those used in the skeleton network of GENEC, as specified in Section 2.2, for the same reactions. Additional reactions are taken from the default set-up of MPPNP and are specified as follows. Charged particle reactions are from Angulo et al. (1999) and Iliadis et al. (2001). β-decays and electron captures are from Oda et al. (1994), Fuller, Fowler & Newman (1985) and Aikawa et al. (2005). Neutron captures are from the Karlsruhe astrophysical data base of nucleosynthesis in stars (KADoNiS) (Dillmann et al. 2006). For reactions not found in these references, reaction rates from the REACLIB data base[3] were used, which incorporates a compilation of experimental rates and theoretical rates from NON-SMOKER (Rauscher & Thielemann 2000, 2001).

[2] http://forum.astro.keele.ac.uk:8080/nugrid
[3] http://nucastro.org/reaclib.html

Table 1. Nuclides included in the nuclear reaction network used for the post-processing calculations.

Element	A_{min}	A_{max}	Element	A_{min}	A_{max}
n	1	1	Tc	93	105
H	1	2	Ru	94	106
He	3	4	Rh	98	108
Li	7	7	Pd	99	112
Be	7	8	Ag	101	113
B[a]	8	11	Cd	102	118
C	11	14	In	106	119
N	13	15	Sn	108	130
O	14	18	Sb	112	133
F	17	20	Te	114	134
Ne	19	22	I	117	135
Na	21	24	Xe	118	138
Mg	23	28	Cs	123	139
Al	25	29	Ba	124	142
Si	27	32	La	127	143
P	29	35	Ce	130	146
S	31	38	Pr	133	149
Cl	34	40	Nd	134	152
Ar	35	44	Pm	137	154
K	38	46	Sm	140	158
Ca	39	49	Eu	143	159
Sc	43	50	Gd	144	162
Ti	44	52	Tb	147	165
V	47	53	Dy	148	168
Cr	48	56	Ho	153	169
Mn	51	57	Er	154	175
Fe	52	61	Tm	159	176
Co	55	63	Yb	160	180
Ni	56	68	Lu	165	182
Cu	60	71	Hf	166	185
Zn	62	74	Ta	169	186
Ga	65	75	W	172	190
Ge	66	78	Re	175	191
As	69	81	Os	179	196
Se	72	84	Ir	181	197
Br	74	87	Pt	184	202
Kr	76	90	Au	185	203
Rb	79	91	Hg	189	208
Sr	80	94	Tl	192	210
Y	85	96	Pb	193	211
Zr	86	98	Bi	202	211
Nb	89	99	Po	204	210
Mo	90	102			

[a] ^{9}B is not included.

3 STELLAR STRUCTURE AND EVOLUTION

3.1 Hydrogen and helium burning

The evolution of each stellar model during hydrogen and helium burning is given entirely by the ST models, as the CI and CU models were started using the profile just before the end of helium burning. Fig. 3 shows the Hertzsprung–Russell (HR) diagram for all models, which shows that the evolutionary tracks for all models follow their course in the HR diagram primarily during the hydrogen- and helium-burning phases and are not modified by enhanced rates. The reason for this is that the surface evolution of the stellar models is unaffected by changes in the carbon-burning rate, which is a consequence of the small time-scale for burning associated with advanced burning stages in massive stars; the envelope has insufficient time to react significantly to changes in core properties.

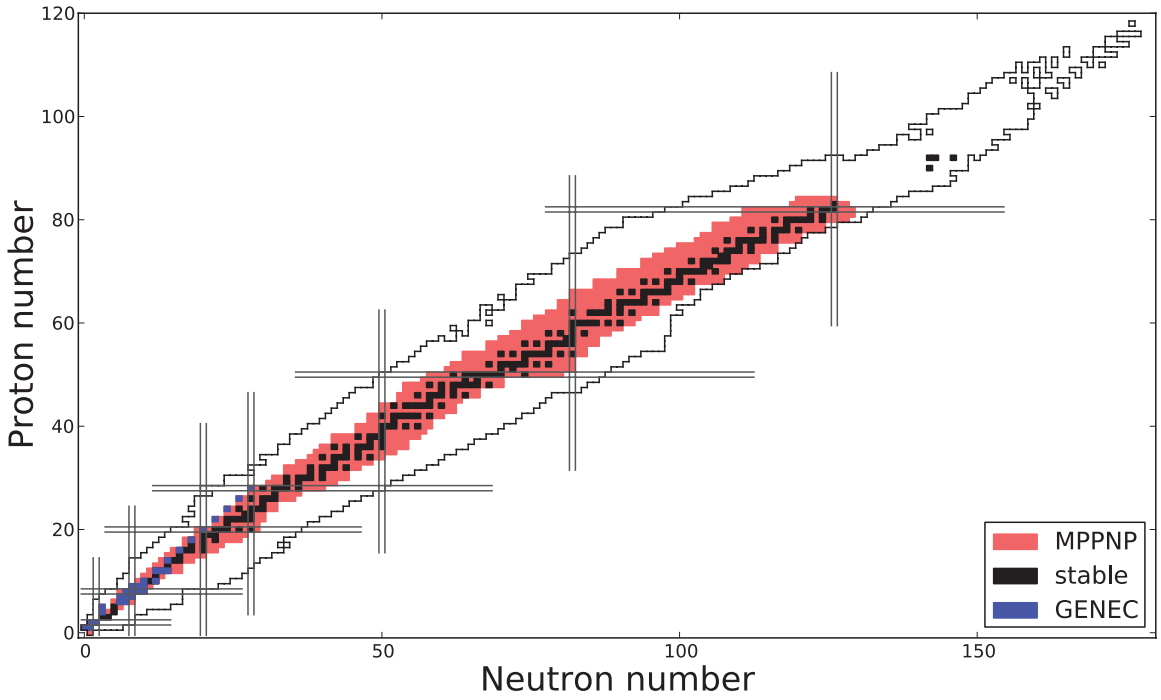

Figure 2. Chart of isotopes indicating the nuclear reaction networks used in this work: GENEC (blue squares) and MPPNP (pale red squares). The network used by MPPNP includes all stable isotopes, which are indicated by black squares. The outer boundary to each side of the valley of stability indicates the position of all currently known isotopes, including heavy transuranic isotopes. Parallel grid lines indicate values of Z or N that are magic as specified in the nuclear shell model (2, 8, 20, 28, 50, 82, 126).

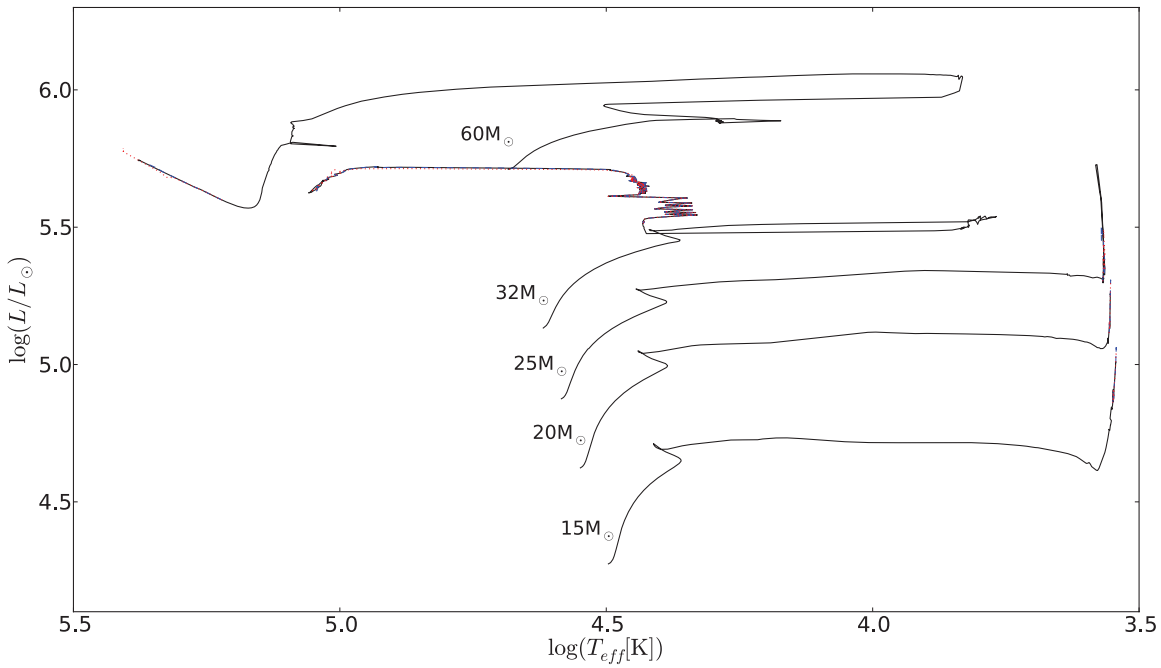

Figure 3. The HR diagram for all models. Solid black lines refer to ST model tracks, dashed blue lines refer to CI model tracks and the dotted red lines refer to the CU model tracks. The tracks indicate that the enhanced rates do not affect the surface evolution, since changes in the carbon-burning rate do not affect the surface properties. The tracks exhibited by the 32-$M_\odot$ and 60-$M_\odot$ models show evolution into the WR phase, which is explained by mass-loss.

Overall, the ST models are very similar to those previously published by the Geneva group, such as the non-rotating stars of Meynet & Maeder (2003) and Hirschi et al. (2004). The 15-, 20- and 25-$M_\odot$ model stars evolve towards the red and remain as red supergiants (RSGs) during the advanced stages of evolution. The 32- and 60-$M_\odot$ model stars evolve towards the Humphreys–Davidson limit at $\log T_{\rm eff} \sim 3.8$ before becoming WR stars.

The 32-$M_\odot$ model star proceeds to the WR phase during helium burning. This is because the mass-loss is strong enough for the star to expel the entire hydrogen envelope during helium burning,

with the composition of the remaining envelope rich in helium. The lower opacity of the helium-rich envelope lowers the radius and favours evolution towards the blue (Maeder 2009, section 27.3.2). The deviations from the ST track for the CI or CU tracks for this mass are slightly larger than those for other masses. These deviations are generally of the order of 0.1 per cent with a maximum deviation of 0.01 in $\log T_{\rm eff}$ ($\simeq$2 per cent), which occurs during the rapid transit to the blue after helium burning.

The 60-$M_\odot$ star becomes a WR star just after hydrogen burning. At the end of the hydrogen-burning phase, the star enters the first 'loop' towards the blue (at $\log T_{\rm eff} \simeq 4.4$), which occurs because of mass-loss being high enough to expose the helium-rich outer layer. Following the first loop to the blue, helium burning is ignited. During this phase the core shrinks, lowering the core fraction, q, favouring evolution to the red (Maeder 2009, section 27.3.2). However, the star approaches the Humphreys–Davidson limit in the HR diagram during the evolution and the mass-loss becomes high enough to, eventually, peel away the envelope, exposing the helium-burning core ($q \simeq 75$ per cent during helium burning). The star consequently evolves towards the blue (at $\log T_{\rm eff} \simeq 5.0$).

3.2 Carbon burning

Unlike the surface evolution, the interior evolution of the star is modified significantly by the enhanced carbon-burning rates and changes to the central evolution of the star are important in order to assess changes to the main burning regimes.

Fig. 4 shows T_c–ρ_c diagrams for the 15-, 20- and 25-$M_\odot$ models, separated into panels by initial mass. The enhanced rate models in all cases (including the 32- and 60-$M_\odot$ models) ignite carbon burning at lower temperatures and densities, which consequently affects the evolution of the central properties of the star. This is seen, for example, in the top and middle panels of Fig. 4, where the curves for the CI and CU cases deviate away from that of the ST case towards the higher temperature (at a given density) side of the curve (see also column 7 in Table 2). The tendency to deviate in this direction is caused by the presence of a convective core. This is verified in the bottom panel for the case of the 25CU model whereby the 'kink' at carbon ignition is larger than that of the 25ST and 25CI models, since the CU model is the only 25-$M_\odot$ model to have a convective core (see also Fig. 7).

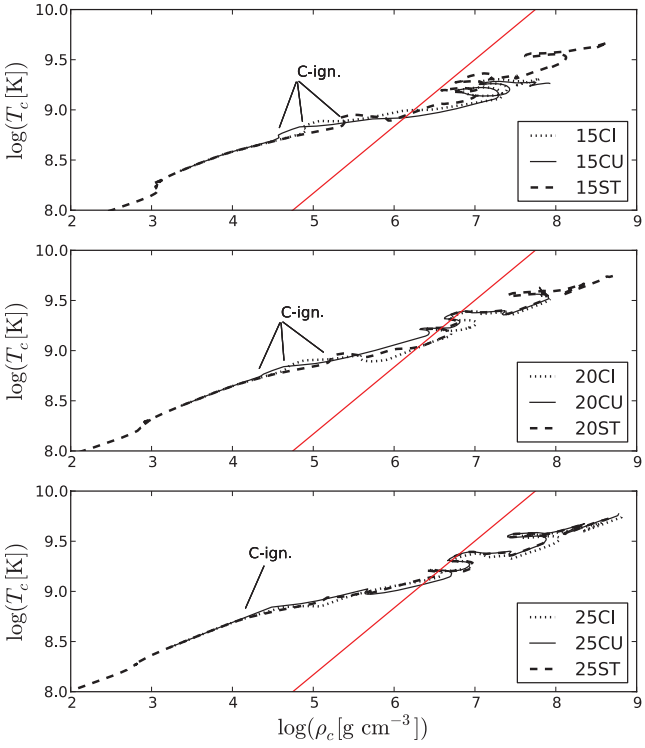

Figure 4. The T_c–ρ_c diagram for all 15 (top panel), 20 (middle panel) and 25 $M_\odot$ (bottom panel) models. The straight line in each panel indicates the location in the diagram where the ideal gas pressure is equal to the electron degeneracy pressure; $P_{\rm gas} = P_{\rm e,deg}$. Ignition points for convective core carbon burning are indicated by the annotation.

Fig. 4 shows the impact that the enhanced carbon-burning rates have on the central evolution during carbon burning. However, despite the deviations, many of the models at a particular mass are similar, especially the 25-$M_\odot$ models. Fig. 5 shows T_c–ρ_c diagrams for the 32- and 60-$M_\odot$ models, which are also quite similar. In the case of Fig. 5, the 32- and 60-$M_\odot$ models exhibit significant mass-loss during the hydrogen- and helium-burning stages such that the total mass during the advanced burning stages is very similar ($\sim$13 $M_\odot$). Combined with the fact that the helium cores at this stage are qualitatively similar, the models from this point onwards evolve similarly, with the 32CI and 60CI models entering the more degenerate region of the diagram. Consequently, the tracks follow similar paths dependent on the choice of $^{12}C + {}^{12}C$ reaction rate.

Kippenhahn diagrams for all models are presented in Figs 6–8, with the shaded regions corresponding to convection zones and the intermediate regions corresponding to radiative zones. The total mass is given by the thin black line at the top of each diagram. Overall, Figs 6–8 show that the convection zone structure of the carbon-burning stage is heavily modified by the increased rates, particularly for the CU cases where a convective carbon core is present over the entire mass range considered. The presence of a convective carbon core is important for nucleosynthesis as the convective mixing provides more fuel for carbon burning and the carbon-core *s*-process. The mass-loss increases significantly with initial mass, but does not change much with the $^{12}C + {}^{12}C$ rate. Small deviations in the mass-loss, which are less than 1 per cent, are due to the increased lifetime of the core carbon-burning stage in the CI and CU models (see Table 4).

Model data complementary to Figs 6–8 are presented in Table 2, which specify properties pertaining to convection zones during carbon burning. Column 2 ('core/shell') identifies the presence, or not, of a convective core or shell and labels the shells in chronological order during the evolution. The other columns specify the lifetime of the convection zone[4] ($\tau_{\rm C}$) in years, the lower and upper limits in mass coordinate of the convection zone ($M_{\rm low}$ and $M_{\rm upp}$, respectively, in $M_\odot$), the size of the convection zone in mass (ΔM, in $M_\odot$) and the temperature (T, in GK), density (ρ, in g cm^{-3}) and the mass-fraction abundances of ^{12}C and ^{16}O ($X_{^{12}\rm C}$ and $X_{^{16}\rm O}$, respectively) at the onset of convection at position $M_{\rm low}$.

The ST models indicate an upper mass limit for the presence of a convective carbon core with a value between 20 and 25 $M_\odot$, which is consistent with previous models (Heger, Langer & Woosley 2000;

[4] Many of the convective shells persist until the pre-supernova stage. In models 15CI, 20CI, 25ST, 25CI, 25CU, 32CI, 32CU and 60CU, however, the carbon shell shrinks because of the influence of another burning stage (such as neon or oxygen burning). The convective carbon shell can therefore feature a rather complicated structure through the following advanced stages. In these cases, the lifetime is calculated from the onset of convection to the point where the convective shell shrinks significantly in size.

Table 2. Stellar structure properties for carbon-burning cores and shells at the onset of convection. Shells are labelled in chronological order. $\tau_{\rm conv}$ is the lifetime of the convection zone, $M_{\rm low}$ and $M_{\rm upp}$ are lower and upper mass coordinates for the location of the zone. ΔM is the size of the zone in mass, T and ρ are the temperature and density of the zone at $M_{\rm low}$, and $X_{^{12}{\rm C}}$ and $X_{^{16}{\rm O}}$ are the ^{12}C and ^{16}O mass-fraction abundances within the convection zone, respectively.

Model	Core/shell	$\tau_{\rm conv}$ (yr)	$M_{\rm low}$ ($M_\odot$)	$M_{\rm upp}$ ($M_\odot$)	ΔM ($M_\odot$)	T (GK)	ρ (g cm^{-3})	$X_{^{12}{\rm C}}$	$X_{^{16}{\rm O}}$
15ST	Core	1458	0	0.588	0.588	0.717	2.367×10^5	0.2947	0.6296
	1	187.2	0.604	1.293	0.689	0.773	1.816×10^5	0.3002	0.6332
	2	17.92	1.302	2.435	1.134	0.904	1.936×10^5	0.0862	0.5041
15CI	Core	15 720	0	1.381	1.381	0.589	7.409×10^4	0.3104	0.6400
	1	150.1	1.396	2.907	1.511	0.758	1.139×10^5	0.0472	0.4883
15CU	Core	51 890	0	1.517	1.517	0.486	3.011×10^4	0.3192	0.6458
	1	594.2	1.536	3.270	1.734	0.531	3.557×10^4	0.3185	0.6453
20ST	Core	219	0	0.466	0.466	0.783	1.587×10^5	0.2320	0.6441
	1	41.55	0.507	1.157	0.650	0.843	1.390×10^5	0.2150	0.6332
	2	13.40	1.024	3.088	1.884	0.873	1.109×10^5	0.2438	0.6516
	3	0.228	2.021	3.319	1.298	1.132	1.447×10^5	0.0469	0.5350
20CI	Core	5418	0	1.921	1.921	0.626	4.155×10^4	0.2636	0.6647
	1	290.9	1.047	3.631	2.584	0.781	7.203×10^4	0.0675	0.5481
	2	1.985	1.784	4.137	2.354	0.872	6.615×10^4	0.0488	0.5380
20CU	Core	32 280	0	2.771	2.771	0.498	1.553×10^4	0.2861	0.6794
	1	10.05	2.158	2.609	0.450	0.712	4.792×10^4	0.0147	0.5275
	2	3.714	2.815	4.696	1.880	0.592	2.706×10^4	0.2861	0.6794
25ST	1	3.734	1.819	5.928	4.109	0.946	1.017×10^5	0.1449	0.6306
25CI	1	925.4	0.436	2.075	1.640	0.718	3.656×10^4	0.1830	0.6554
	2	12.69	2.111	6.208	4.097	0.516	3.893×10^4	0.2492	0.6975
25CU	Core	22 520	0	4.452	4.452	0.510	1.191×10^4	0.2586	0.7038
	1	34.77	1.954	6.429	4.475	0.735	3.622×10^4	0.0191	0.5656
32ST	1	0.373	2.586	8.948	6.361	1.059	7.925×10^4	0.1346	0.6869
32CI	1	33.06	1.869	8.789	6.920	0.773	3.290×10^4	0.1507	0.6973
32CU	Core	13 780	0	6.897	6.897	0.539	1.001×10^4	0.2164	0.7399
	1	5.679	2.774	9.077	6.303	0.710	2.390×10^4	0.0269	0.6265
60ST	1	0.260	2.900	10.12	7.221	1.073	7.159×10^4	0.1360	0.6794
60CI	1	15.04	2.171	10.04	7.866	0.793	3.080×10^4	0.1541	0.6911
60CU	Core	12 900	0	8.326	8.326	0.542	9.210×10^3	0.2205	0.7341
	1	4.276	2.975	10.39	7.412	0.721	2.207×10^4	0.0309	0.6207

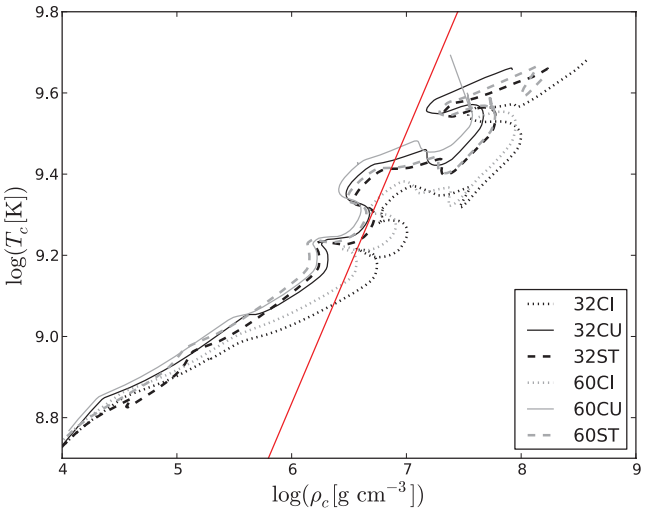

Figure 5. The T_c–ρ_c diagram for all 32- and 60-$M_\odot$ models. The straight line indicates the location in the diagram where the ideal gas pressure is equal to the electron degeneracy pressure; $P_{\rm gas} = P_{\rm e,deg}$.

Hirschi et al. 2004). For model 25CI, a strong convective shell is ignited slightly off-centre (at a mass coordinate of 0.436 $M_\odot$), and model 25CU exhibits a large convective carbon core. In all CU models, the carbon-core burning stage is convective, which, in models 25CU, 32CU and 60CU, replaces the radiative cores. In model 25CI the first carbon shell ignites close to the centre and models 20CI and 15CI have larger convective cores. Considering these facts and the presence of a convective core in every CU model, one can hypothesize that the limiting mass for the presence of a convective carbon core increases with the carbon-burning rate, which will consequently represent a source of uncertainty for the presence of a convective core near to the limiting mass of $\sim$22 $M_\odot$. A firm verification of the limiting mass for the CI case would however require a finer grid of stellar models between 20 and 25 $M_\odot$.

The sizes, in mass, of the carbon-burning zones (column 6 in Table 2) are generally larger in the CI and CU models. This affects the ^{12}C abundance profile within the star and consequently the number of carbon-burning shells during the evolution. The Kippenhahn diagrams for the 15- and 20-$M_\odot$ models (Fig. 6) demonstrate this effect fairly well; the 15ST and 20ST models have many carbon-burning shells where the ignition of a successive shell lies at a

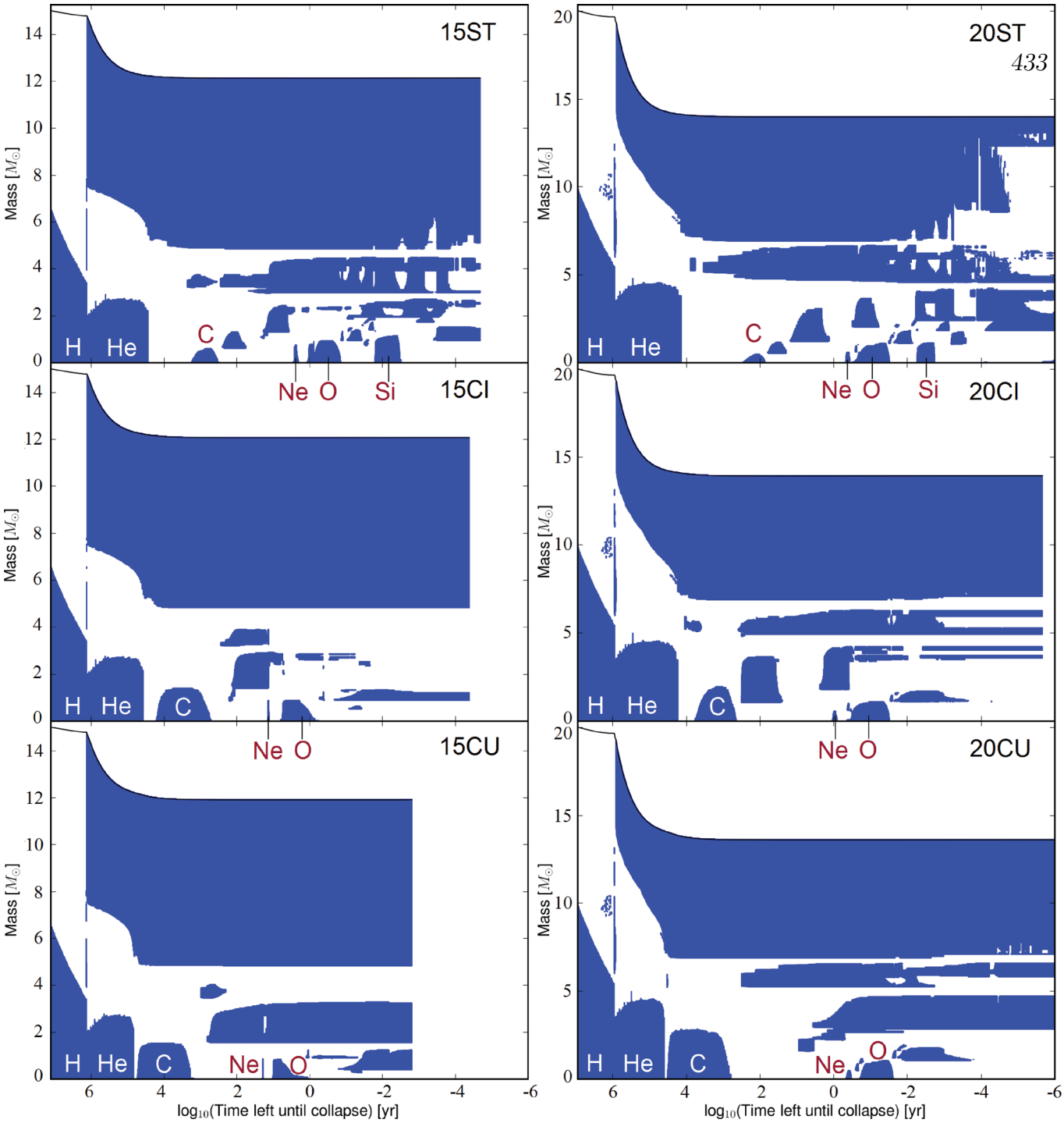

Figure 6. Kippenhahn diagrams for the ST, CI and CU models for initial masses of 15 and 20 $M_\odot$. Shaded regions correspond to convection zones. The major central burning regimes are indicated by the text.

position that corresponds to the maximum coordinate reached by the previous convection zone.

As the rate is increased, the tendency for convective shells to 'overlap' (where the lower bound in mass of the convective region extends below the upper bound of the previous convection zone) is increased. All CU models, except the 15CU model, show this overlap, which occurs between a convective carbon core and the first convective carbon shell. The amount of overlap between the carbon core and the first carbon shell, and the first and second carbon shells, in the 20CI model (in Fig. 6) is also much larger than that in the 20ST model. This overlap effect occurs because successive carbon-shell burning episodes, caused by ignition of residual ^{12}C fuel left over from previous burning stages, can occur at a lower temperature and density or with a lower abundance of ^{12}C fuel (see

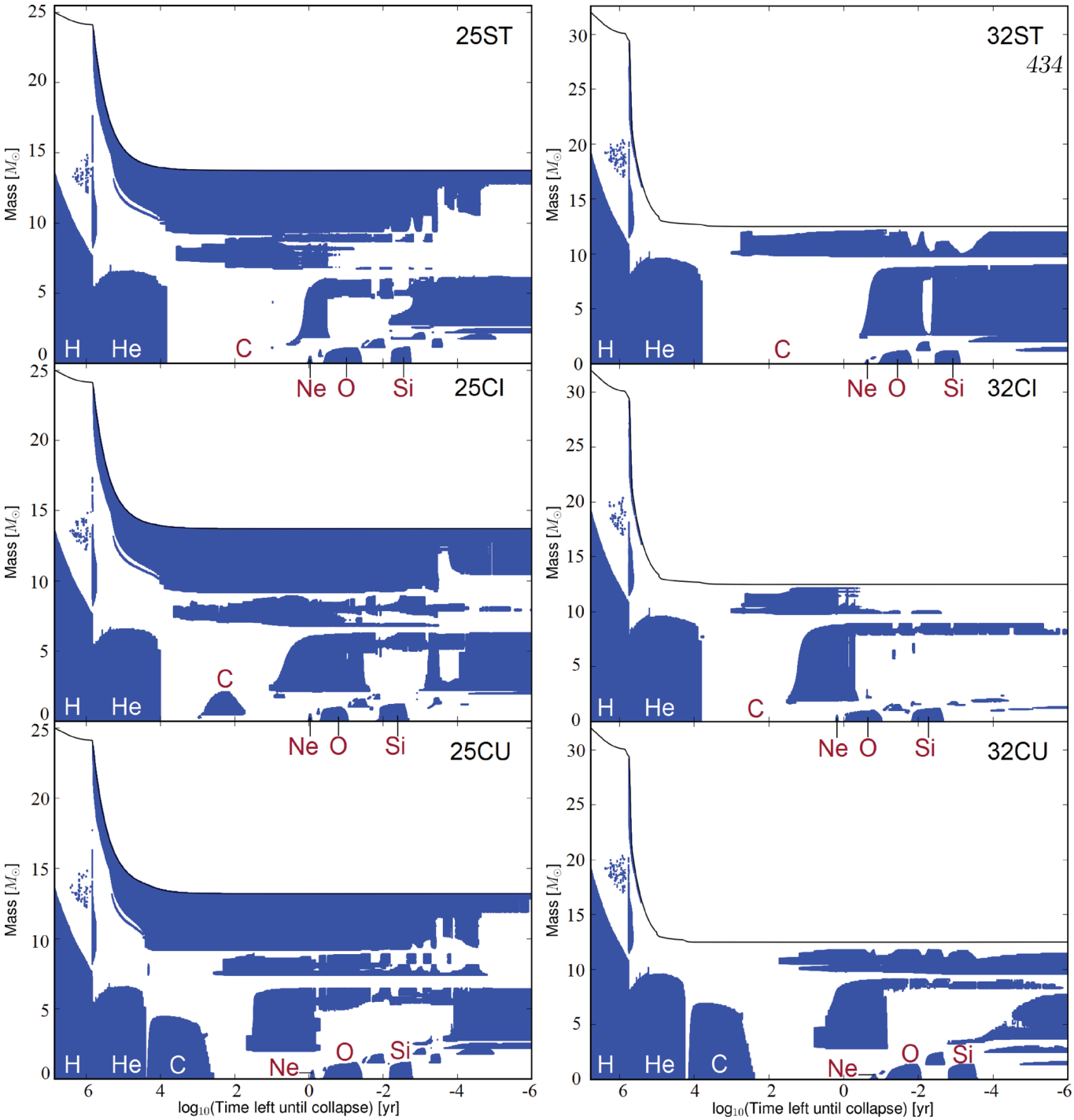

Figure 7. Kippenhahn diagrams for the ST, CI and CU models for initial masses of 25 and 32 $M_\odot$. Shaded regions correspond to convection zones. The major central burning regimes are indicated by the text.

column 9 of Table 2). This effect has been noted previously by Chieffi et al. (1998) and in the preliminary studies (Bennett et al. 2010a,b).

The total energy generation of the $^{12}C + {}^{12}C$ reaction is given by (Woosley, Heger & Weaver 2002)

$$\epsilon_{\rm nuc}(^{12}{\rm C}) \approx 4.8 \times 10^{18} Y^2(^{12}{\rm C}) \rho \lambda_{12,12}\ {\rm erg\ g^{-1}\ s^{-1}}, \quad (3.1)$$

where $Y^2(^{12}C)$ is the number abundance of ^{12}C ($Y = X/A$), ρ is the density and $\lambda_{12,12}$ is the nuclear reaction rate, which is dependent on temperature. For a given density and abundance, an increased $^{12}C + {}^{12}C$ rate increases the energy generation rate from nuclear reactions. The effect this has on the ignition conditions (temperature and density) for core carbon burning is displayed in Figs 9 and 10 (the ignition point is defined as the point in time when the central mass-fraction abundance of ^{12}C is 0.3 per cent lower than its maximum value). An increased rate allows a star to reach the required energy output to support the star against gravitational contraction at a lower temperature (and also lower density). Note also the dependence on initial mass, with ignition conditions favouring higher temperatures and lower densities with increasing initial

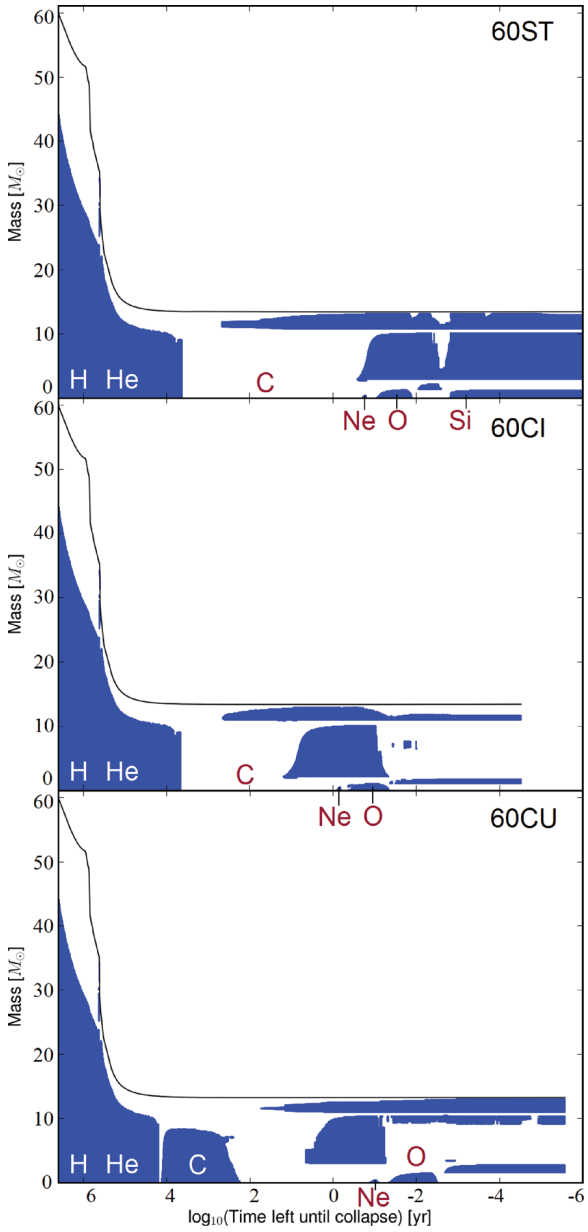

Figure 8. Kippenhahn diagrams for the ST, CI and CU models for initial masses of 15 and 20 $M_\odot$. Shaded regions correspond to convection zones. The major central burning regimes are indicated by the text.

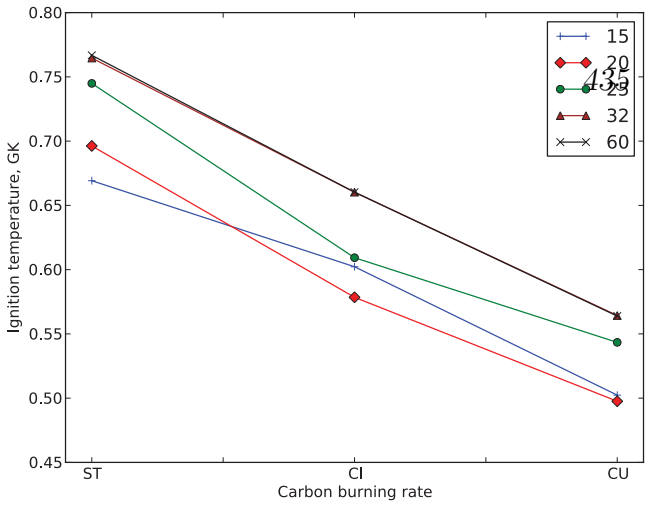

Figure 9. Ignition temperatures for core carbon burning for all models.

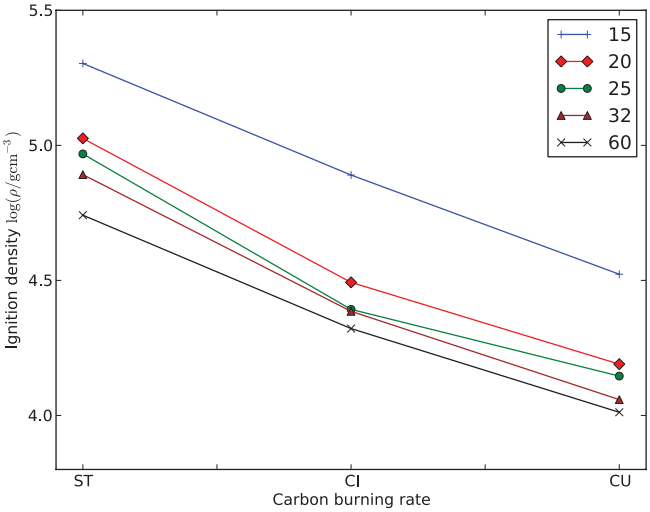

Figure 10. Ignition densities for core carbon burning for all models.

mass. In the case of lower ignition temperatures and densities, the convective core ignites more promptly in the CI and CU models. Changes to the ignition conditions and the ^{12}C abundance at the start of core carbon burning are responsible for the increased likelihood of having overlapping convection zones.

The lifetime of convection zones is generally longer in the CI and CU models. This could be perceived as counterintuitive, since with an enhanced rate one would expect that the ^{12}C fuel would be expended more rapidly. However, the burning takes place in lower temperature and density conditions, which affect the neutrino losses. Table 3 shows the energy generation terms for nuclear reactions ($\epsilon_{\rm nuc}$) and neutrino losses (ϵ_ν) at the centre of the star when the mass fraction of ^{12}C is half the amount available just prior to carbon-core burning. The proportion of neutrinos formed by various neutrino processes is also specified in Table 3, which are given as fractions, f, of the total neutrino losses (in per cent). These processes are pair production ($f_{\rm pair}$), photoneutrino interactions ($f_{\rm phot}$) and the rest ($f_{\rm rest}$), which are bremsstrahlung, recombination and plasmon decay processes (Itoh et al. 1996). Neutrino formation through these last three processes is negligibly small at carbon-burning temperatures.

As shown in Table 3, the energy generation rate from nuclear reactions and the neutrino losses is reduced in the CI and CU models, although an increase in energy generation rate is seen in models 25CU, 32CU and 60CU from their CI counterparts. This increase is due to the presence of the convective carbon core, where there is an increased availability of the ^{12}C fuel from mixing. During carbon burning, the time-scale for burning is governed primarily by the neutrino losses (as is true for all advanced burning stages) and these losses generally increase monotonically with increasing temperature. In fact, massive star evolution during the advanced stages of evolution can be described as a neutrino-mediated Kelvin–Helmholtz contraction of a carbon–oxygen core (Woosley et al. 2002; El Eid et al. 2009). Therefore, a reduction in the neutrino losses has the consequence of increasing the lifetime of carbon-burning stages. Only the carbon shells in models 32CU and 60CU do

Table 3. Energy generation and neutrino parameters during core carbon burning. For each model, the central values of temperature, T, density, ρ, energy generation rates for nuclear burning, $\epsilon_{\rm nuc}$, and neutrino losses, ϵ_ν, and percentage fractions of the total neutrinos formed by pair production ($f_{\rm pair}$), photoneutrino interactions ($f_{\rm phot}$) and other processes ($f_{\rm rest}$) are specified. These parameters are determined at the time when the mass fraction of ^{12}C is half of the value just prior to carbon burning.

Model	T (GK)	ρ (g cm^{-3})	$\epsilon_{\rm nuc}$ (erg g^{-1} s^{-1})	ϵ_ν (erg g^{-1} s^{-1})	$f_{\rm pair}$	$f_{\rm phot}$	$f_{\rm rest}$
15ST	0.830	2.141×10^5	4.762×10^7	-1.542×10^7	89.665	10.253	0.082
15CI	0.686	7.659×10^4	6.822×10^6	-1.454×10^6	70.007	29.861	0.132
15CU	0.566	3.772×10^4	2.277×10^6	-1.448×10^5	19.800	79.902	0.298
20ST	0.883	1.679×10^5	1.663×10^8	-5.910×10^7	95.651	4.327	0.022
20CI	0.723	5.356×10^4	1.529×10^7	-5.260×10^6	87.461	12.508	0.031
20CU	0.588	2.477×10^4	3.727×10^6	-2.643×10^5	41.935	57.943	0.122
25ST	0.859	1.439×10^5	5.176×10^7	-4.435×10^7	95.061	4.917	0.022
25CI	0.690	3.942×10^4	2.603×10^6	-2.975×10^6	83.475	16.490	0.035
25CU	0.603	1.889×10^4	4.975×10^6	-4.533×10^5	58.913	41.026	0.061
32ST	0.904	1.313×10^5	1.360×10^8	-1.234×10^8	97.310	2.680	0.010
32CI	0.711	3.532×10^4	3.682×10^6	-5.995×10^6	89.439	10.543	0.018
32CU	0.621	1.510×10^4	5.725×10^6	-9.148×10^5	74.347	25.625	0.028
60ST	0.919	1.106×10^5	1.900×10^8	-1.954×10^8	98.053	1.941	0.006
60CI	0.725	3.260×10^4	5.863×10^6	-9.442×10^6	92.247	7.741	0.012
60CU	0.625	1.375×10^4	6.244×10^6	-1.096×10^6	77.670	22.309	0.021

not show this behaviour (see Figs 7 and 8). This can be explained by the presence of a previous convective carbon core in those models, which reduces the abundance of carbon fuel available for burning in these shells. Systematic trends during shell burning are less clear because of the rather complicated evolution of the shell structure, but convective shells often form at lower temperatures in CI and CU models (see column 7 in Table 2), similar to the situation in the core. For carbon-core burning, on the other hand, there is a clear increase in the lifetime with increasing rate, which is shown in Fig. 11.

The main neutrino processes during carbon burning are those caused by pair production and photoneutrino interactions (Itoh et al. 1996; Woosley et al. 2002). It is worth noting that the decrease in temperature in the CI and CU models is responsible for a larger proportion of neutrinos formed by the photoneutrino process rather than pair production. This trend at larger carbon-burning rates is opposite to the trend with initial mass, which favours higher temperatures and production of neutrinos by pair production with increasing initial mass.

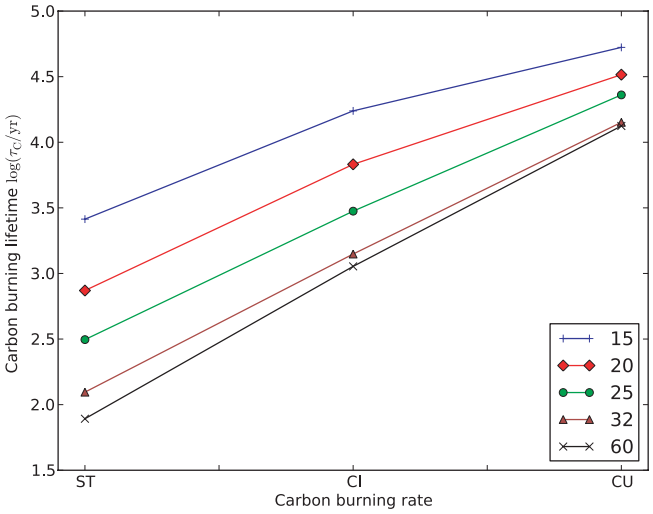

Figure 11. Carbon-core burning lifetimes for all models. Note that for some models, the core carbon burning is radiative rather than convective. The carbon-burning lifetime is defined as the time for the mass-fraction abundance of ^{12}C to reduce from 0.3 per cent of its maximum value to a value of 10^{-3}.

These effects on the central evolution are responsible for the different tracks exhibited by the CI and CU models with respect to the ST models in Figs 4 and 5. For the 15- and 20-M$_\odot$ models, the larger cores cause the CI and CU tracks to tend towards the higher temperature, lower density side of the ST track, but only for the duration the convective core is present. When the star moves on to carbon-shell burning, the core cools and the track returns to the standard curve.

As explained above, the overlap exhibited by convective shells over the ashes of convective carbon cores is due to the ignition of carbon that represents the unburnt remainder from carbon-core burning. The presence of this remainder is caused by the gradual shrinking of the carbon core near the end of the burning stage. This occurs in the 20CI model and all CU models, except model 15CU where the shell is located at the top of the previous convective carbon core. The convective carbon shell in the 20CU model (see Fig. 6), however, shows an interesting structure. In this case a carbon shell is ignited at a position that overlaps with the core and then shortly after an additional shell is ignited at the point corresponding to the top of the previous core. Because of the unusual structure, the lifetime given in Table 2 for the 20CU model, shell 1, is defined from the onset of convection to the time it shrinks back up into the second shell.

The presence of overlap with a carbon core has a significant impact on the composition of the shell at the onset of convection. Indeed, carbon-core burning ashes, including *s*-process nuclides, will mix out to a position above the remnant mass and be present in the supernova ejecta. As mentioned above, overlapping shells have previously been noted in the literature, but the

consequences of overlapping shells of this nature are not well studied. The nucleosynthetic consequences of overlap will be discussed in Section 4.

3.3 Advanced stages beyond carbon burning

Despite the changes to the stellar structure during carbon burning, the evolution of the advanced burning stages in the core following carbon burning seems only slightly affected in terms of the convection zone structure, as seen in Figs 6–8, but exhibit burning stages with different lifetimes. The burning lifetimes for the hydrostatic burning stages are presented in Table 4, which are defined for each stage as the difference in age from the point where the principal fuel for that stage (^{1}H for hydrogen burning, ^{4}He for helium burning, etc.) is depleted by 0.3 per cent from its maximum value to the age where the mass fraction of that fuel depletes below a value of 10^{-5}, except for carbon burning and neon burning, where this value is 10^{-3}, and oxygen burning, where this value is 10^{-2}. These criteria are necessary to ensure that a lifetime is calculated in those cases where residual fuel is unburnt (such as during oxygen burning in the 15CU model, where the ^{16}O mass-fraction abundance that remains unburnt following the end of core oxygen burning is $\sim 3.177 \times 10^{-3}$) and to ensure that the burning stages are correctly separated. The lifetime of the advanced stages is relatively sensitive to the mass fractions of isotopes defining the lifetime.

Carbon-burning lifetimes are longer for the CI and CU rates, as explained in Section 3.2, but lifetimes for the other advanced stages do not show a general trend with the carbon-burning rate. This lack of trend also applies to the central properties, as seen in Fig. 4, where the tracks are modified by the enhanced rate models but the modifications do not follow a general pattern. In fact, there are examples of T_c–ρ_c tracks, e.g. the 25CI and 25CU models in Fig. 4, where following the deviation caused by carbon ignition the track returns to that of the ST rate (especially for the 15-, 20- and 25-M$_\odot$ models). The main property determining the variations in the lifetime is the central temperature, which is linked with the neutrino loss rates.

The last column of Table 4 shows that the total lifetime of the star increases slightly with an enhanced carbon-burning rate, because of the longer carbon-burning lifetime. Since the total lifetime increases by $\approx$1–5 $\times$ 10^4 yr, the strong mass-loss (characteristic of massive stars), which can increase by up to $\sim 10^{-5}$ M$_\odot$ yr^{-1}, increases the mass lost by up to 0.5 M$_\odot$. This is demonstrated in column 2 of Table 5, which shows the core masses at the end of oxygen burning for all models. In column 3 of Table 5, we see that the carbon-burning rate does not affect the helium core mass (the helium core mass is defined as the mass coordinate where the mass-fraction abundance of ^{4}He is 0.75 at the interface between the hydrogen and helium-rich layers). There is only a tiny difference for the 25-M$_\odot$ case because of the small structure re-arrangement of the hydrogen-burning shell. In column 4, we see that with an increasing carbon-burning rate, the CO core mass is larger (the CO core mass is defined as the mass coordinate where the ^{4}He mass-fraction abundance is 10^{-3}). The reason is the following. With an increased rate, carbon burning occurs at lower temperatures where the energy production dominates over neutrino cooling and this leads to a stronger carbon-core burning in a larger convective zone. Thus,

Table 5. Core masses at the end of oxygen burning, in solar masses. For each model, the final total mass ($M_{\rm Final}$), helium core mass ($M_\alpha^{75\,\rm per\,cent}$), CO core mass ($M_{\rm CO}$) and the oxygen-free core mass ($M_{\rm O-free}$) are specified. Note that the 32- and 60-M$_\odot$ models expel most of their helium-rich envelopes, consequently becoming WR stars.

Model	$M_{\rm Final}$	$M_\alpha^{75\,\rm per\,cent}$	$M_{\rm CO}$	$M_{\rm O-free}$
15ST	12.132	4.791	2.805	0.921
15CI	12.069	4.791	2.923	0.867
15CU	11.907	4.791	3.239	0.849
20ST	13.974	6.826	4.494	1.083
20CI	13.916	6.826	4.491	1.099
20CU	13.602	6.826	4.696	1.040
25ST	13.738	9.199	6.301	1.081
25CI	13.710	9.092	6.384	0.980
25CU	13.202	9.092	6.544	1.124
32ST	12.495	12.495	9.146	1.187
32CI	12.495	12.495	9.146	0.984
32CU	12.493	12.493	9.425	1.334
60ST	13.428	13.428	10.701	1.242
60CI	13.423	13.423	10.446	0.990
60CU	13.278	13.278	10.929	1.519

Table 4. Lifetimes for all core burning stages in all models (in yr). Lifetimes are provided for hydrogen burning ($\tau_{\rm H}$), helium burning ($\tau_{\rm He}$), carbon burning ($\tau_{\rm C}$), neon burning ($\tau_{\rm Ne}$), oxygen burning ($\tau_{\rm O}$) and silicon burning ($\tau_{\rm Si}$). The total lifetime is given by ($\tau_{\rm Total}$).

Model	$\tau_{\rm H}$	$\tau_{\rm He}$	$\tau_{\rm C}$	$\tau_{\rm Ne}$	$\tau_{\rm O}$	$\tau_{\rm Si}$	$\tau_{\rm Total}$
15ST	1.137×10^7	1.255×10^6	2.595×10^3	1.253	1.233	1.685×10^{-2}	1.268×10^7
15CI	1.137×10^7	1.255×10^6	1.735×10^4	14.296	4.745	–	1.269×10^7
15CU	1.137×10^7	1.255×10^6	5.288×10^4	12.918	8.815	–	1.272×10^7
20ST	7.926×10^6	8.396×10^5	7.409×10^2	0.193	0.293	1.302×10^{-2}	8.799×10^6
20CI	7.926×10^6	8.396×10^5	6.786×10^3	0.655	0.542	–	8.803×10^6
20CU	7.926×10^6	8.396×10^5	3.275×10^4	0.265	0.253	–	8.825×10^6
25ST	6.492×10^6	6.519×10^5	3.131×10^2	0.634	0.603	4.322×10^{-3}	7.168×10^6
25CI	6.492×10^6	6.519×10^5	2.984×10^3	0.539	0.597	1.097×10^{-2}	7.169×10^6
25CU	6.492×10^6	6.519×10^5	2.296×10^4	0.505	0.515	1.746×10^{-2}	7.186×10^6
32ST	5.287×10^6	5.346×10^5	1.245×10^2	0.111	0.167	8.997×10^{-3}	5.840×10^6
32CI	5.287×10^6	5.346×10^5	1.406×10^3	0.726	1.123	1.173×10^{-2}	5.840×10^6
32CU	5.287×10^6	5.346×10^5	1.419×10^4	0.148	0.111	5.458×10^{-3}	5.852×10^6
60ST	3.549×10^6	3.935×10^5	7.808×10^1	0.090	0.119	8.624×10^{-3}	3.955×10^6
60CI	3.549×10^6	3.935×10^5	1.132×10^3	0.425	0.505	–	3.955×10^6
60CU	3.549×10^6	3.935×10^5	1.331×10^4	0.112	0.071	–	3.966×10^6

the carbon-burning core produces more energy and this leads to a less energetic helium-burning shell that is radiative rather than convective, which is the case for the ST models. When the He shell is radiative, the burning front depletes completely the helium available at one mass coordinate and then moves upwards leading to a more massive CO core, whereas with a convective He shell, the bottom of the shell stays at the same mass coordinate since the helium in the convective shell is never completely exhausted due to mixing. Note also that the 32- and 60-$M_\odot$ models do not exhibit a value for $M_\alpha^{75\,\mathrm{per\,cent}}$. This is because the mass-loss is strong enough in these WR stars to expel the majority of their helium-rich envelopes and the ^{4}He abundance is not high enough to satisfy the criterion for $M_\alpha^{75\,\mathrm{per\,cent}}$. In these cases, the helium core mass is taken as the final mass, M_{Final} (see column 2 of Table 5).

As mentioned above, the size of the convective cores during neon, oxygen and silicon burnings is only slightly affected by changes in the carbon-burning rate, as can be seen in the last column of Table 5 for the oxygen-free core, $M_{\mathrm{O-free}}$, calculated at the end of core oxygen burning. The changes in $M_{\mathrm{O-free}}$ with the carbon-burning rate are because of changes in the position of the lower boundary of the last convective carbon shell. Generally, the magnitude of the changes in $M_{\mathrm{O-free}}$ is small and does not present a clear pattern.

4 NUCLEOSYNTHESIS

4.1 Neutron sources

The main effects on the nucleosynthesis in the stellar models are due to the lower central temperature of the star and the increased lifetime. In particular, the lower central temperature will affect the efficiency of neutron source reactions. We recall that the main neutron sources for the *s*-process are ^{13}C, which is important during carbon-core burning, and ^{22}Ne, which is important during helium-core burning and carbon-shell burning. The ^{13}C neutron source is mainly produced during carbon-core burning by the ^{12}C(p,γ)^{13}N(β^+)^{13}C reaction chain. Neutrons are then produced by ^{13}C(α,n)^{16}O reactions. The protons and α-particles originate directly from the ^{12}C + ^{12}C fusion reactions. There is competition between the ^{13}N(β^+)^{13}C and ^{13}N(γ,p)^{12}C reactions, where at temperatures above 0.8 GK, the (γ,p) reaction dominates over the β-decay. The ^{13}C neutron source is thus an efficient neutron producer only at lower temperatures. During carbon-shell burning, where the temperatures are higher, the ^{22}Ne source is the dominant neutron source. One can therefore expect that as the carbon-burning rate is increased and the interior temperature is lowered, the efficiency of the ^{13}C neutron source will increase. This efficiency will also be higher given the increased lifetimes.

A non-negligible fraction of neutrons are also present from the ^{17}O and ^{21}Ne neutron sources, but these nuclei are mainly produced by neutron captures on ^{16}O and ^{20}Ne [and ^{17}O(α, γ)^{21}Ne] and therefore only act as mediators of the neutron irradiance. The ^{25}Mg(α,n)^{28}Si and ^{12}C(^{12}C,n)^{23}Mg neutron sources are marginal for all models considered here, despite the increases to the carbon-burning rate. We refer to Pignatari et al. (in preparation) for a more detailed discussion about the ^{12}C(^{12}C,n)^{23}Mg reaction.

4.2 *s*-process parameters

Several indicators for the neutron-capture nucleosynthesis are considered. The *s*-process is typically characterized by the neutron density, n_{n}, the neutron captures per iron seed, n_{c}, and the neutron exposure, τ_{n}. Here, n_{c} is defined as follows:

$$n_{\mathrm{c}} = \frac{\sum_i^n (A_i - 56)\left(X_i - X_i^0\right)}{X_{^{56}\mathrm{Fe}}}, \tag{4.1}$$

where X_i^0 is the initial mass-fraction abundance of isotope X_i with atomic mass A_i and $X_{^{56}\mathrm{Fe}}$ is the initial mass-fraction abundance of ^{56}Fe, which is the dominant seed isotope for the *s*-process nucleosynthesis. τ_{n} is defined as $\tau_{\mathrm{n}} = \int v_T n_{\mathrm{n}} \mathrm{d}t$ (Clayton 1968). However, these definitions are of limited use in the multi-zone calculations used here. The reason for this is that in the multi-zone stellar models, convective mixing affects the neutron irradiance experienced by a given mass element (The et al. 2007). Stellar matter, including the neutron sources, seeds and poisons, is mixed into and out of the bottom of the convection zone, where the temperature is highest and where the majority of the *s*-process occurs. Consequently, an evaluation of n_{c} or τ_{n} at a particular mass coordinate will be different from that experienced by a given mass element.

Therefore, in order to evaluate relevant parameters to describe the neutron irradiance, convective mixing needs to be taken into account in the evaluation of the parameter. This can be achieved for the neutron exposure by considering the initial and final abundances of ^{54}Fe, an isotope that is slowly destroyed by neutron captures in the *s*-process sites considered here. It cannot be used during or after oxygen burning where temperatures are high enough to photodisintegrate heavy elements (Woosley & Weaver 1995). An estimate of the neutron exposure using ^{54}Fe can be made using the following formula (Woosley & Weaver 1995; The, El Eid & Meyer 2000):

$$\tau_{54} = -\frac{1}{\sigma}[\ln X_{\mathrm{i}}(^{54}\mathrm{Fe}) - \ln X_{\mathrm{f}}(^{54}\mathrm{Fe})], \tag{4.2}$$

where σ is the ^{54}Fe(n,γ)^{55}Fe reaction rate ($\sigma = 29.6 \pm 1.3$ mb; Dillmann et al. 2006) and $X_{\mathrm{i}}(^{54}\mathrm{Fe})$ and $X_{\mathrm{f}}(^{54}\mathrm{Fe})$ are the mass-fraction abundances of ^{54}Fe before and after the neutron exposure, respectively. A better estimate of n_{c} can be obtained by using mass-averaged abundances for X_i, X_i^0 and $X_{^{56}\mathrm{Fe}}$ over the maximum size of the convective region,

$$n_{\mathrm{c,av}} = \frac{\sum_i^n (A_i - 56)(\langle X_i\rangle - \langle X_i^0\rangle)}{\langle X_{^{56}\mathrm{Fe}}\rangle}. \tag{4.3}$$

This takes into account any changes to the size of the convective region during the burning stage where the *s*-process nucleosynthesis occurs.

Table 6 lists, for all models, the neutron exposure, τ_{54}, the neutron captures per iron seed, $n_{\mathrm{c,av}}$, the mass-fraction abundances of the isotopes ^{54}Fe and ^{88}Sr and the isobaric ratios ^{70}Ge/^{70}Zn, ^{80}Kr/^{80}Se and ^{86}Sr/^{86}Kr. ^{88}Sr, like ^{54}Fe, is also a useful *s*-process indicator as it has a neutron-magic nucleus ($N = 50$) and is slowly built up over the course of the *s*-process. The isobaric ratios are also specified, because changes to the ratios demonstrate deviations to the *s*-process path at branching point nuclides (^{69}Zn, ^{79}Se and ^{85}Kr for ^{70}Ge/^{70}Zn, ^{80}Kr/^{80}Se and ^{86}Sr/^{86}Kr, respectively). Indeed, if the neutron density increases, the *s*-process path opens to allow the production of more neutron-rich isotopes, lowering these ratios.

4.3 Core carbon burning

According to Table 6, all CI and CU models show a depletion of ^{54}Fe and production of ^{88}Sr relative to the ST case, indicating that a higher neutron exposure is present in the convective carbon core. For all CI and CU models, irrespective of mass, the neutron exposure is

Table 6. *s*-process tracers, neutron-capture parameters and isotopic ratios at the end of helium-core burning, carbon-core burning and convective carbon-shell burning. $n_{c,av}$ is the neutron capture per iron seed averaged over the convective region and τ_{54} is the neutron exposure calculated using equation (4.2). The ^{88}Sr and ^{54}Fe abundances are specified as average mass-fraction abundances, $X_{^{88}\mathrm{Sr}}$ and $X_{^{54}\mathrm{Fe}}$, respectively, at the end of the burning stage over the convective region, except for radiative burning where the central values are taken. The *s*-process parameters for a shell that persists to the pre-supernova stage use final abundances that are evaluated at start of oxygen burning, which removes the effects of photodisintegration occurring during the late evolutionary stages from the evaluation of the *s*-process parameters.

Model	Shell	^{88}Sr	^{54}Fe	$n_{c,av}$	τ_{54} (mb^{-1})	^{70}Ge/^{70}Zn	^{80}Kr/^{80}Se	^{86}Sr/^{86}Kr
15ST	He-core	2.005×10^{-7}	5.750×10^{-6}	1.641	0.088	115.913	2.690	4.247
15ST	C-core	1.556×10^{-6}	7.721×10^{-7}	6.601	0.062	1165.633	5.107	46.001
15ST	1	1.000×10^{-6}	1.089×10^{-6}	4.740	0.048	1036.915	3.668	20.178
15ST	2	6.629×10^{-7}	1.266×10^{-6}	3.903	0.042	335.818	0.701	2.708
15CI	C-core	1.009×10^{-4}	9.137×10^{-8}	29.270	0.134	901.882	4.284	45.048
15CI	1	2.803×10^{-5}	6.958×10^{-7}	6.005	0.059	862.687	3.172	23.268
15CU	C-core	2.182×10^{-4}	3.716×10^{-8}	46.293	0.165	743.822	4.080	44.065
15CU	1	5.046×10^{-5}	2.163×10^{-6}	19.423	0.055	638.189	0.765	1.726
20ST	He-core	3.817×10^{-7}	1.070×10^{-6}	3.069	0.143	928.859	3.588	7.503
20ST	C-core	1.286×10^{-6}	1.615×10^{-7}	8.080	0.062	1315.250	4.012	30.741
20ST	1	1.064×10^{-6}	2.303×10^{-7}	6.605	0.043	1245.114	2.605	17.583
20ST	2	9.403×10^{-7}	3.382×10^{-7}	4.934	0.033	518.314	0.774	4.205
20ST	3	8.762×10^{-7}	4.292×10^{-7}	0.119	0.001	487.403	0.696	3.802
20CI	C-core	5.197×10^{-5}	8.818×10^{-8}	27.796	0.084	970.039	4.200	41.853
20CI	1	2.424×10^{-5}	3.828×10^{-7}	5.920	0.023	975.182	2.873	20.450
20CI	2	2.160×10^{-5}	3.869×10^{-7}	2.737	0.012	347.183	0.366	3.352
20CU	C-core	1.727×10^{-4}	4.802×10^{-9}	60.722	0.182	779.749	4.104	36.648
20CU	1	7.074×10^{-5}	5.484×10^{-7}	4.073	0.019	494.139	2.019	22.567
20CU	2	1.194×10^{-5}	6.573×10^{-7}	4.651	0.027	151.579	0.348	4.048
25ST	He-core	6.153×10^{-7}	3.539×10^{-7}	4.280	0.180	2220.036	3.755	11.329
25ST	C-core	1.472×10^{-6}	7.918×10^{-8}	8.271	0.045	1432.597	4.385	35.554
25ST	1	9.499×10^{-7}	1.482×10^{-7}	5.632	0.028	87.609	0.109	0.515
25CI	C-core	4.092×10^{-5}	1.411×10^{-9}	48.421	0.179	970.416	4.576	59.426
25CI	1	1.772×10^{-5}	6.313×10^{-8}	23.538	0.045	1063.729	4.066	38.990
25CI	2	1.111×10^{-6}	1.564×10^{-7}	5.543	0.028	315.357	0.280	1.401
25CU	C-core	1.475×10^{-4}	1.509×10^{-9}	73.339	0.184	804.018	4.072	36.419
25CU	1	9.824×10^{-5}	1.347×10^{-7}	15.755	0.015	698.157	1.283	10.094
32ST	He-core	1.097×10^{-6}	1.192×10^{-7}	5.623	0.217	3380.614	3.900	16.340
32ST	C-core	1.788×10^{-6}	5.333×10^{-8}	6.239	0.024	1640.445	3.640	28.449
32ST	1	1.315×10^{-6}	8.625×10^{-8}	3.016	0.010	75.996	0.130	1.014
32CI	C-core	1.825×10^{-5}	3.955×10^{-9}	38.296	0.110	1042.993	4.740	60.126
32CI	1	2.045×10^{-6}	6.562×10^{-8}	5.220	0.017	1021.836	1.646	9.944
32CU	C-core	1.007×10^{-4}	8.498×10^{-10}	77.718	0.167	837.791	3.949	39.032
32CU	1	7.633×10^{-5}	3.346×10^{-8}	16.738	0.011	509.651	0.428	4.911
60ST	He-core	1.524×10^{-6}	6.404×10^{-8}	6.489	0.238	1741.270	1.125	12.267
60ST	C-core	1.701×10^{-6}	5.297×10^{-8}	5.862	0.023	1743.568	3.246	25.865
60ST	1	1.335×10^{-6}	7.814×10^{-8}	2.779	0.009	69.670	0.146	1.136
60CI	C-core	1.491×10^{-5}	4.808×10^{-9}	33.897	0.104	1072.384	4.619	52.637
60CI	1	1.622×10^{-6}	5.837×10^{-7}	3.800	0.029	871.777	0.921	5.676
60CU	C-core	1.076×10^{-4}	6.551×10^{-10}	81.743	0.172	837.512	3.877	36.865
60CU	1	8.908×10^{-5}	2.512×10^{-8}	17.940	0.010	455.999	0.370	4.862

high enough to allow an increasing production of isotopes beyond the Sr–Y–Zr peak, which is quantified in a higher neutron capture per iron seed. An example of this nucleosynthesis for the 15-$M_\odot$ model is seen in Fig. 12, which shows the central overproduction factors for heavy, stable isotopes in the star at the end of carbon burning. The distribution of synthesized isotopes is extended, with increasing rate, beyond the Sr–Y–Zr peak to include isotopes up to the Ba–La peak at $A \approx 140$. This is an anomalous distribution compared to the weak *s*-process component.

The neutron density in the carbon core decreases from a typical value of $\sim 10^8$ cm^{-3}, which is maintained throughout the burning, to $\sim 10^7$ cm^{-3} in the models with an increasing carbon-burning rate. In the 25CU, 32CU and 60CU models, the neutron density is enhanced over the CI cases because of the presence of the convective core; the mixing into and out of the centre acts to maintain a supply of neutron sources at the centre. Concerning the ST case, the neutron exposures for the cores are similar in magnitude to that of the helium-burning core (~ 0.06 mb^{-1}), but are lower for the most massive stars considered here (~ 0.02 mb^{-1} for the 32ST and 60ST models). For the CI and CU rates, the neutron exposures are significantly enhanced, typically exceeding 0.1 mb^{-1}. This is mainly due to the rising efficiency of the ^{13}C neutron source at lower temperatures, coupled with the increased lifetime of the core carbon-burning stage.

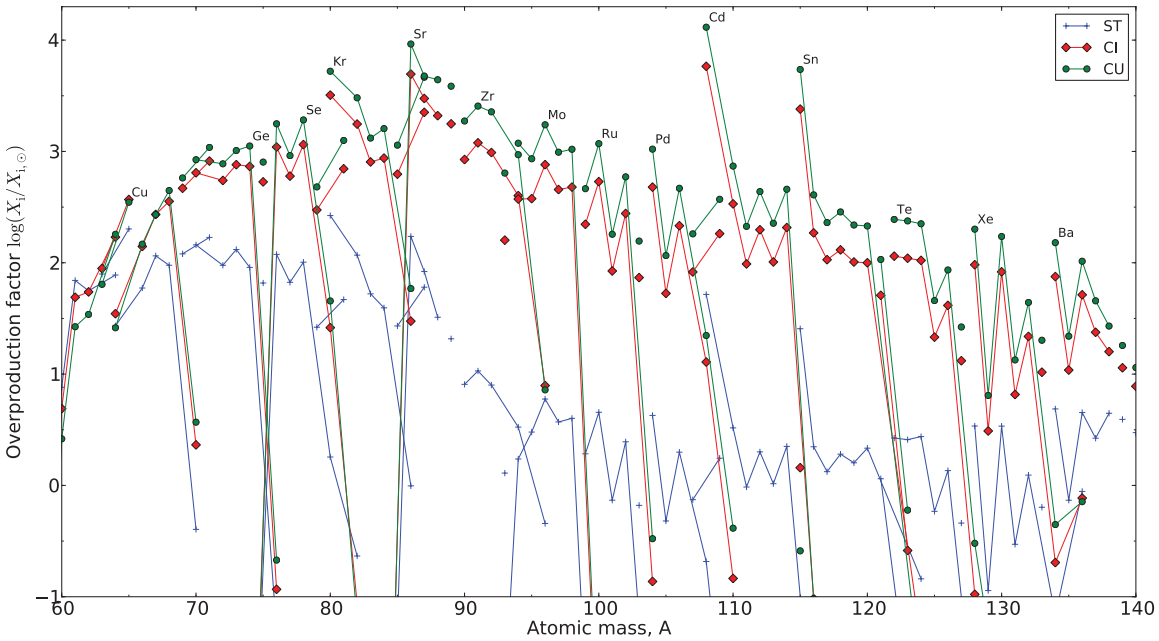

Figure 12. Central overproduction factors for most stable isotopes at the end of central carbon burning for the 15-$M_\odot$ models. The plot shows a significant increase in nucleosynthesis of isotopes for $60 < A < 140$ in the CI and CU models, which is beyond the Sr–Y–Zr peak at an atomic mass of ≈90.

4.4 Carbon-shell burning

Nucleosynthesis in the carbon shells is characterized by the *s*-process with a high neutron density but lower neutron exposure compared to carbon core, with ^{22}Ne being the dominant neutron source. In the ST models, the neutron densities vary from $\sim 10^8$ cm^{-3} for early convective shells (models 15ST and 20ST), and increase to a typical value of $\sim 10^{10}$ cm^{-3} in the final carbon-burning shell. In the CI and CU models, the neutron density is $\sim 10^7$ cm^{-3} in early shells, similar to the values obtained during core carbon burning, and then rises to $\sim 10^{8-9}$ cm^{-3}. The lifetimes for the carbon-shell burning stages vary quite differently from model to model, but are generally increasing with increasing rate. For example, in the 15CU case, the lifetimes of the last carbon shell in Table 2 for the 15ST, CI and CU models are 17.92, 150.1 and 594.2 years, respectively. The carbon shell in model 15CU consequently exhibits a strong neutron exposure of similar magnitude as to the carbon core (see Table 6). It should be noted however that in almost every instance of a carbon-burning shell, the neutron exposure is smaller than that of the carbon core in the same model. This asserts the fact that carbon shells are characterized by a lower neutron exposure and higher neutron density (with ^{22}Ne as the main neutron source), although the degree with which this is true is reduced with an increasing carbon-burning rate. That is, the general trend with increasing rate is a decrease in the neutron density and an increase in the neutron exposure in the carbon shells.

The above can be verified by considering the ratios of isotopes involved at branching points, since the lower neutron density will close the *s*-process path to the synthesis of more neutron-rich isotopes at branching points. The last three columns of Table 6 show the isobaric ratios at the end of the core and shell carbon-burning stages for ^{70}Ge/^{70}Zn, ^{80}Kr/^{80}Se and ^{86}Sr/^{86}Kr, with values for the end of helium-core burning specified for reference. For most models, the ratios increase in the last carbon shell with increasing carbon-burning rate, favouring production of the *s*-only isotopes ^{70}Ge, ^{80}Kr and ^{86}Sr, due to the lower neutron density in the carbon shells in the CI and CU models. However, the ratios are sensitive to convection, since shell overlap causes the shells to be polluted with carbon-core *s*-process ashes. Consequently, the 25CU, 32CU and 60CU models instead show a decrease in the ratios. Considering that the ratios in the initial composition are 3.271, 6.124 and 0.036 for ^{70}Ge/^{70}Zn, ^{80}Kr/^{80}Se and ^{86}Sr/^{86}Kr, respectively, the presence of lower isobaric ratios than those in the shells indicates that the branching is indeed affected during the carbon shell *s*-process and that the decrease is not associated purely with the mixing of carbon-core matter with helium-burning ashes.

5 YIELDS

5.1 Calculations

The yields calculations were made in the same manner as that of Hirschi et al. (2005), which considers two contributions to the yields: the stellar wind and the supernova explosion. The wind yield for nuclide i for a star with initial mass m (in $M_\odot$) is calculated using

$$mp_{\rm im}^{\rm wind} = \int_0^{\tau(m)} \dot{M}(m,t)\left[X_i^{\rm S}(m,t) - X_i^0\right] {\rm d}t, \qquad (5.1)$$

where $\tau(m)$ is the final age of the star, $\dot{M}(m,t)$ is the mass-loss rate, $X_i^{\rm S}$ is the surface mass-fraction abundance and X_i^0 is the initial mass-fraction abundance. The majority of the matter lost through the stellar wind occurs during hydrogen and helium burning. The composition of the wind is similar to that of the initial composition, except for the 32-$M_\odot$ and 60-$M_\odot$ models where the mass-loss is significant enough to include some of the hydrogen-burning ashes. Table 5 shows that the total mass lost over the stellar evolution due to the stellar wind increases significantly with initial mass (≈20 per cent lost for the 15-$M_\odot$ models to ≈80 per cent lost for the 60-$M_\odot$ models).

The pre-supernova yields are calculated using

$$mp_{\rm im}^{\rm preSN} = \int_{M_{{\rm rem},m}}^{m_\tau} \left[X_i(m_r) - X_i^0\right] {\rm d}m_r, \qquad (5.2)$$

where m_τ is the total mass of the star at $\tau(m)$, $M_{\mathrm{rem},m}$ is the remnant mass, X_i^0 is the initial mass-fraction abundance of element i and $X_i(m_r)$ is the mass fraction abundance at mass coordinate m_r. The total yields are then just the sum of the wind and the pre-supernova yields. The calculated yields of selected isotopes for model 15ST are shown in Table 7 (full yield tables for all models are provided with the electronic version of this paper, see Supporting Information).

The point in the evolution in which the yields are taken in this work is at the end of central oxygen burning, as explained in Section 2.2. This choice was made since not all the models were post-processed until the end of silicon burning. Note that, as mentioned in Section 2.2, after central oxygen burning, the material outside the remnant mass is not affected much by the pre-explosive evolution. The only potential contributions that may affect the *s*-process abundances are during the early collapse, when the neutron density may increase significantly (e.g. in the carbon shell; see Pignatari et al. 2010), or partial or complete photodisintegration at the bottom of the carbon, neon and oxygen shells. The effects of photodisintegration will be discussed in a forthcoming paper (Pignatari et al., in preparation).

With regard to explosive burning, the supernova explosion is responsible for destroying and recreating a portion of the ejecta, which includes p-process-rich and, to a smaller extent, *s*-process-rich layers, possibly having a relevant impact on the total yields of *s*-process nuclides (see for instance Rauscher et al. 2002; Tur et al. 2009). However, the explosive burning process is sensitive to uncertainties in the supernova explosion mechanism for the range of initial masses considered here (Fryer 2009). The uncertainties associated with the supernova explosion, namely the explosion energy, the ignition mechanism and the amount of fallback, are important especially for the 15-, 20- and 25-$M_\odot$ models. These uncertainties would also affect the amount of matter locked up in the remnants. In this work, the remnant mass takes into account the additional matter that falls back on to the remnant following the initial explosion. The choice of remnant masses for the models is taken from the analytical fits of Fryer et al. (in preparation) for solar metallicity stars, which derive from energy-driven explosions (see for instance Fryer 2009). The remnant masses, $M_{\mathrm{rem},m}$, are given by

$$M_{\mathrm{rem},m} = \begin{cases} 1.1 + 0.2\mathrm{e}^{(m-11)/4} - 3\mathrm{e}^{0.4(m-26)}, & 11 < m \leq 30, \\ 18.35 - 0.3m, & 30 < m < 50, \end{cases} \tag{5.3}$$

which gives remnant masses of 1.61, 2.73, 5.71 and 8.75 $M_\odot$ for initial masses, m, of 15, 20, 25 and 32 $M_\odot$, respectively. For the 60-$M_\odot$ models, a remnant mass was calculated by scaling with the CO core mass ratio for the ST models,

$$M_{\mathrm{rem},60\,\mathrm{M}_\odot} = M_{\mathrm{rem},32\,\mathrm{M}_\odot} \left(\frac{M_{\mathrm{CO},60\,\mathrm{M}_\odot}}{M_{\mathrm{CO},32\,\mathrm{M}_\odot}} \right), \tag{5.4}$$

giving a remnant mass of 10.24 $M_\odot$. The resultant remnant masses are such that for the 15-$M_\odot$ models, the oxygen shell is partially included in the supernova ejecta. For the other models however, the remnants are large and the ejecta include the upper portion of the carbon shell and the overlying layers only. The remnant masses here are larger in comparison with those used in previous studies of explosive nucleosynthesis (Limongi et al. 2000; Rauscher et al. 2002). This is due to the use, in those studies, of piston-driven models that are known to underestimate the amount of fallback on to the supernova remnant (Young & Fryer 2007). The large remnant masses may cause the explosive nucleosynthesis to occur predominantly in the layers that fall back on to the remnant.

In addition to the yields, the ejected masses, E_{im}, can be calculated, which are the exact analogues of equations (5.1) and (5.2), but without the inclusion of the X_i^0 term. If the total mass of matter ejected is $M_{\mathrm{ej},m} = m_\tau - M_{\mathrm{rem},m}$, the overproduction factors averaged over the ejecta are calculated using

$$\langle \mathrm{OP} \rangle_{\mathrm{im}} = \frac{E_{\mathrm{im}}}{M_{\mathrm{ej},m} X_i^0}. \tag{5.5}$$

The overproduction factors averaged over the ejecta for the *s*-only isotopes are shown in Fig. 13, which represents well the general abundance distribution for stable isotopes created by the models. A considerable amount of the *s*-process nucleosynthesis occurs for all CU models by up to 3 dex, which is either because of an overlap between the carbon shells and the carbon core (for models 20CI, 25CU, 32CU and 60CU) or because of strong neutron exposures in the carbon shells (models 15CU and 20CU). The 20CI model features a strong overlap between the convective carbon core and the successive carbon shells, which is not seen in model 20CU and therefore has more significant production than model 20CU. In fact, for the CI rate, only the 20-$M_\odot$ model shows a significantly enhanced production over the ST rate. The 15CI model also shows some production, but the distribution of isotopes is very similar to that of model 15ST. This is in contrast to the 20CI model, which shows an extended distribution of production featuring heavier nuclides.

A first-order approximation of the weak *s*-process component can be made by taking the sum of the yields for each stellar model, taking into account the number of stars with that initial mass formed,

$$y_{\mathrm{weak},i} = \frac{\sum_m r_m E_{\mathrm{im}}}{\sum_m M_{\mathrm{ej},m} r_m}, \tag{5.6}$$

where r_m is a weighting factor determined by the integration of the Salpeter initial mass function (IMF), $\mathrm{d}N/\mathrm{d}m = \xi_0 m^{-2.35}$, over a certain range. Yields from the 15-, 20-, 25-, 32- and 60-$M_\odot$ models were applied to stars within the initial mass ranges of 12.5–17.5, 17.5–22.5, 22.5–28.5, 28.5–46 and 46–80 $M_\odot$, respectively, giving values of r_m equal to 39.75, 19.89, 13.45, 14.59, 12.32 per cent, respectively (with $\xi_0 = 0.304$). Consequently, the 15- and 20-$M_\odot$ models dominate as the main contributors to the evaluation of the weak component (≈60 per cent of all stars in the total massive star mass range considered here). Stars with initial masses less than 12.5 $M_\odot$ or greater than 80 $M_\odot$ are assumed to have a zero contribution to the weak *s*-process component.

The ^{13}C neutron source during carbon-core burning is mainly primary whereas the ^{22}Ne source is secondary,[5] since it depends on the initial ^{14}N abundance from the CNO cycle. If a solar metallicity star of a given mass is the dominant site for the production of particular primary and secondary nuclides, A and B, respectively, the overproduction factor for B is expected to be approximately twice that of A (Truran & Cameron 1971). Although this is a rather crude approximation regarding the detailed nature of chemical evolution within galaxies and/or star clusters and the nucleosynthesis processes themselves (Tinsley 1979), the weak *s*-process in massive stars is expected to hold reasonably to this approximation because

[5] The products of nucleosynthesis processes in stars, to first order, can be described as being primary or secondary depending on whether the processes responsible for the production depend on the initial metallicity. The production of primary nuclides does not vary with metallicity whereas secondary nuclides will be produced in proportion to their initial seed nuclei.

Table 7. Yields for model 15ST. For each isotope, i, the atomic mass (A), atomic number (Z), initial mass-fraction abundance (X_i^0), wind yield ($mp^{\rm wind}$, in $M_\odot$), pre-supernova yield ($mp^{\rm preSN}$, in $M_\odot$), total yield ($mp^{\rm total}$, in $M_\odot$), total ejected mass ($E_{\rm im}$, in $M_\odot$) and average overproduction factor ($\langle OP\rangle$) are specified. The decays of unstable species to their stable isobars are taken into account. Full yield tables for all models are provided with the electronic version of this paper, see Supporting Information.

Isotope	A	Z	X_i^0	$mp^{\rm wind}$	$mp^{\rm preSN}$	$mp^{\rm total}$	$E_{\rm im}$	$\langle OP\rangle$
^{1}H	1	1	7.064E−01	−4.366E−02	−2.933E+00	−2.977E+00	6.485E+00	0.685
^{4}He	4	2	2.735E−01	4.345E−02	1.435E+00	1.479E+00	5.142E+00	1.404
^{12}C	12	6	3.425E−03	−2.639E−03	3.101E−01	3.074E−01	3.533E−01	7.703
^{13}C	13	6	4.156E−05	2.302E−04	2.276E−04	4.577E−04	1.014E−03	1.822
^{14}N	14	7	1.059E−03	4.132E−03	3.401E−02	3.814E−02	5.232E−02	3.689
^{16}O	16	8	9.624E−03	−1.474E−03	7.579E−01	7.564E−01	8.853E−01	6.868
^{19}F	19	9	5.611E−07	−9.796E−08	−2.190E−06	−2.288E−06	5.227E−06	0.696
^{20}Ne	20	10	1.818E−03	−2.514E−06	3.238E−01	3.238E−01	3.482E−01	14.302
^{23}Na	23	11	4.000E−05	3.023E−05	1.337E−02	1.340E−02	1.394E−02	26.021
^{24}Mg	24	12	5.862E−04	−1.079E−08	2.747E−02	2.747E−02	3.532E−02	4.498
^{27}Al	27	13	6.481E−05	4.579E−08	3.142E−03	3.142E−03	4.010E−03	4.620
^{28}Si	28	14	7.453E−04	−1.752E−08	1.844E−03	1.844E−03	1.183E−02	1.185
^{31}P	31	15	7.106E−06	1.394E−09	7.106E−05	7.106E−05	1.662E−04	1.747
^{32}S	32	16	4.011E−04	−9.512E−09	−1.897E−04	−1.897E−04	5.182E−03	0.965
^{36}Ar	36	18	8.202E−05	−1.944E−09	−7.472E−05	−7.472E−05	1.024E−03	0.932
^{39}K	39	19	3.900E−06	−9.244E−11	7.466E−06	7.466E−06	5.970E−05	1.143
^{40}Ca	40	20	7.225E−05	−1.706E−09	−5.212E−05	−5.212E−05	9.156E−04	0.946
^{45}Sc	45	21	5.414E−08	−1.283E−12	8.303E−07	8.303E−07	1.555E−06	2.145
^{50}Ti	50	22	2.208E−07	−5.234E−12	3.801E−06	3.801E−06	6.758E−06	2.285
^{51}V	51	23	4.138E−07	−9.808E−12	−6.535E−08	−6.536E−08	5.476E−06	0.988
^{52}Cr	52	24	1.658E−05	−3.929E−10	−1.282E−05	−1.282E−05	2.092E−04	0.942
^{55}Mn	55	25	1.098E−05	−2.603E−10	3.666E−06	3.666E−06	1.507E−04	1.025
^{54}Fe	54	26	8.118E−05	−1.924E−09	−1.208E−04	−1.208E−04	9.665E−04	0.889
^{56}Fe	56	26	1.322E−03	−3.133E−08	−1.213E−03	−1.213E−03	1.649E−02	0.931
^{59}Co	59	27	3.991E−06	−9.461E−11	2.580E−04	2.580E−04	3.114E−04	5.825
^{60}Ni	60	28	2.276E−05	−5.394E−10	1.437E−04	1.437E−04	4.485E−04	1.472
^{63}Cu	63	29	6.600E−07	−1.564E−11	5.493E−05	5.493E−05	6.376E−05	7.213
^{65}Cu	65	29	3.035E−07	−7.193E−12	3.249E−05	3.249E−05	3.655E−05	8.993
^{64}Zn	64	30	1.131E−06	−2.680E−11	1.792E−05	1.792E−05	3.306E−05	2.183
^{66}Zn	66	30	6.690E−07	−1.586E−11	1.856E−05	1.856E−05	2.752E−05	3.072
^{70}Zn	70	30	1.577E−08	−3.737E−13	−1.160E−08	−1.160E−08	1.996E−07	0.945
^{69}Ga	69	31	4.551E−08	−1.079E−12	2.367E−06	2.367E−06	2.977E−06	4.884
^{71}Ga	71	31	3.108E−08	−7.366E−13	2.012E−06	2.012E−06	2.428E−06	5.834
^{70}Ge	70	32	5.157E−08	−1.222E−12	3.185E−06	3.185E−06	3.876E−06	5.611
^{72}Ge	72	32	6.910E−08	−1.638E−12	2.614E−06	2.614E−06	3.539E−06	3.824
^{75}As	75	33	1.430E−08	−3.390E−13	4.113E−07	4.113E−07	6.028E−07	3.147
^{76}Se	76	34	1.296E−08	−3.072E−13	6.260E−07	6.260E−07	7.995E−07	4.606
^{78}Se	78	34	3.376E−08	−8.003E−13	1.441E−06	1.441E−06	1.894E−06	4.188
^{80}Se	80	34	7.226E−08	−1.713E−12	2.985E−07	2.985E−07	1.266E−06	1.308
^{79}Br	79	35	1.389E−08	−3.293E−13	1.867E−07	1.867E−07	3.728E−07	2.003
^{81}Br	81	35	1.386E−08	−3.285E−13	2.041E−07	2.041E−07	3.897E−07	2.100
^{80}Kr	80	36	2.575E−09	−6.103E−14	2.610E−07	2.610E−07	2.955E−07	8.569
^{82}Kr	82	36	1.320E−08	−3.128E−13	7.028E−07	7.028E−07	8.795E−07	4.977
^{84}Kr	84	36	6.602E−08	−1.565E−12	1.031E−06	1.031E−06	1.915E−06	2.166
^{86}Kr	86	36	2.044E−08	−4.846E−13	1.289E−07	1.289E−07	4.027E−07	1.471
^{85}Rb	85	37	1.282E−08	−3.040E−13	1.721E−07	1.721E−07	3.438E−07	2.002
^{87}Rb	87	37	5.063E−09	−2.025E−12	6.776E−08	6.776E−08	1.356E−07	1.999
^{84}Sr	84	38	3.228E−10	−7.651E−15	−6.777E−10	−6.777E−10	3.646E−09	0.843
^{86}Sr	86	38	5.845E−09	−1.385E−13	3.642E−07	3.642E−07	4.424E−07	5.652
^{87}Sr	87	38	4.443E−09	1.800E−12	1.858E−07	1.858E−07	2.453E−07	4.123
^{88}Sr	88	38	5.011E−08	−1.188E−12	5.602E−07	5.602E−07	1.231E−06	1.835
^{89}Y	89	39	1.229E−08	−2.914E−13	9.875E−08	9.875E−08	2.634E−07	1.600
^{90}Zr	90	40	1.534E−08	−3.637E−13	4.445E−08	4.445E−08	2.500E−07	1.216
^{92}Zr	92	40	5.227E−09	−1.239E−13	1.871E−08	1.871E−08	8.872E−08	1.267
^{94}Zr	94	40	5.413E−09	−1.283E−13	6.178E−09	6.178E−09	7.868E−08	1.085
^{93}Nb	93	41	1.900E−09	−4.504E−14	7.083E−09	7.082E−09	3.253E−08	1.278
^{92}Mo	92	42	1.012E−09	−2.400E−14	−1.687E−09	−1.687E−09	1.187E−08	0.876
^{94}Mo	94	42	6.448E−10	−1.528E−14	2.073E−11	2.072E−11	8.656E−09	1.002
^{96}Mo	96	42	1.188E−09	−2.815E−14	3.811E−09	3.811E−09	1.972E−08	1.240
^{98}Mo	98	42	1.754E−09	−4.158E−14	3.213E−09	3.213E−09	2.671E−08	1.137
^{100}Mo	100	42	7.146E−10	−1.694E−14	−1.219E−09	−1.219E−09	8.352E−09	0.873

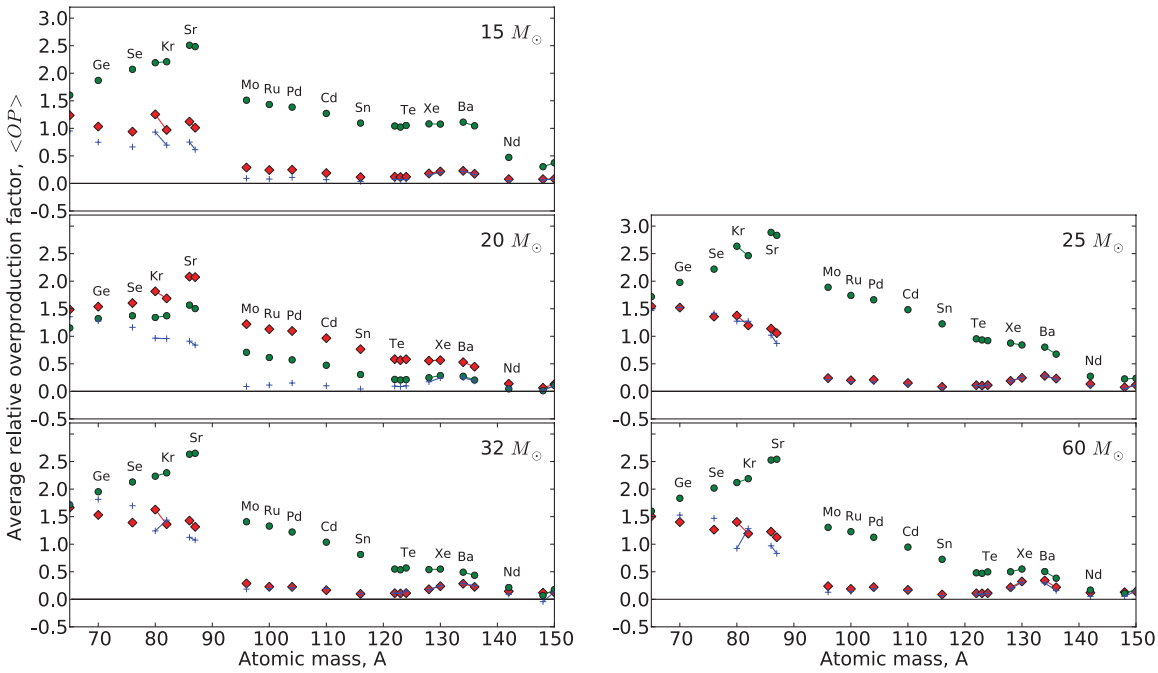

Figure 13. The overproduction factors averaged over the total ejected mass for *s*-only nuclides as a function of atomic mass. The ST, CI and CU rates are indicated by the blue crosses, red diamonds and green circles, respectively. Isotopes of the same element are connected by adjoining lines.

the dominant neutron sources, seeds and poisons of the weak *s*-process are secondary. It can be expected therefore that the overproduction factors for the weak *s*-process nuclides reproduce the Solar system abundances when the overproduction factor is approximately twice that of ^{16}O (Tur et al. 2009). In any case, this rule of thumb can be used as a rough guide to indicate the typical solar production of *s*-process nuclides (Rauscher et al. 2002; Pignatari et al. 2010).

The overproduction factors of the weak component, $y_{\mathrm{weak},i}/X_i^0$, for nuclides with atomic masses $50 < A < 150$, are displayed in Fig. 14. Concerning the CU rate, the overproduction factors are very large (up to 2.56 dex for ^{86}Sr) with respect to the ST model,

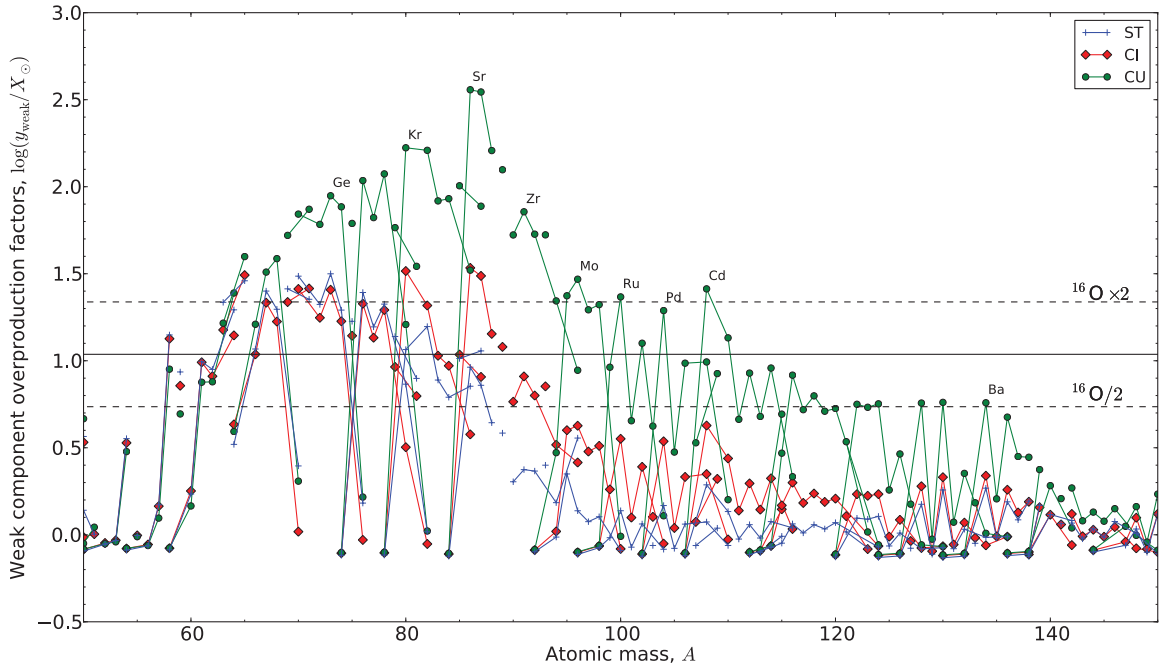

Figure 14. The overproduction factors of the predicted weak component for each rate, focusing on isotopes with atomic mass $50 < A < 150$. Isotopes of the same element are connected by adjoining lines. The solid black line indicates the overproduction factor ^{16}O and the two dashed lines correspond to the overproduction factors of ^{16}O multiplied and divided by two. Changes to the overproduction factor of ^{16}O are negligibly small between the ST, CI and CU models. The isotopic chains for Ge, Kr, Sr, Zr, Mo, Ru, Pd, Cd and Ba in the CU model are labelled for darity.

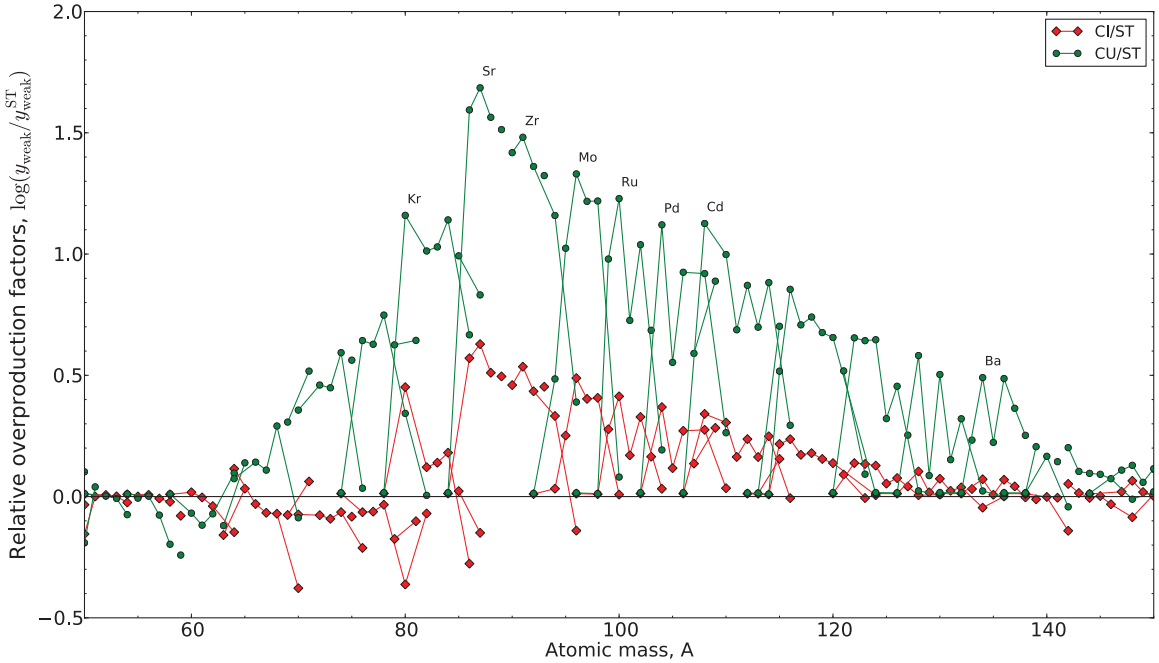

Figure 15. The overproduction factors of the predicted weak component for the CI and CU rates relative to the ST rate. Isotopes are connected by adjoining lines. The isotopic chains for Kr, Sr, Zr, Mo, Ru, Pd, Cd and Ba in the CU model are labelled for clarity.

with a significant *s*-process production of nuclides up to the Ba–La peak at $A \approx 140$. The resulting *s*-process distribution, peaked at the Sr–Y–Zr, is not characteristic of the weak *s*-process component, stopping at $A \approx 90$. The *s*-process nuclides with $90 < A < 110$ have overproduction factors that are comparable to ^{16}O multiplied by two. Such differences for the CU case compared to the classical weak *s*-process component occur because of the ^{13}C neutron source.

For the CI case, the overabundances of many nuclides are similar to the ST case, except for nuclides that are close to the Sr–Y–Zr peak or with higher atomic mass (Mo, Ru, Cd and Pd for example). Note that *s*-process isotopes of Kr and Sr have overproduction factors that are higher than ^{16}O multiplied by two. The abundances of the heavier nuclides Y, Zr, Mo, Ru, Cd and Pd show an enhanced production, which is 0.5–1.0 dex lower than the Kr–Sr peak. Overall, the resulting *s*-process distribution is approximately flat from Ni to Sr.

Fig. 15 shows the overproduction factors for the weak components of the CI and CU cases plotted relative to the ST case. The peak of the relative production of *s*-process nuclides lies at ^{87}Sr in both cases and declines smoothly with increasing mass number, although the overproduction factor for ^{86}Sr is slightly larger than the ^{87}Sr for all cases (see Fig. 14). For the CU case, the overabundance of ^{87}Sr is 1.7 dex larger than that for the ST case. The enhancement stops at Ba, with 0.5 dex more production and declines steeply, with a production of heavier nuclides similar to that of the ST case. For the CI case however, the peak production at ^{87}Sr is 0.6 dex larger than the ST case and tends to 0.0 at Ba.

The overproduction factors of Sr, Y, Zr, Mo, Ru, Pd and Cd are enhanced in the carbon-core *s*-process (for example see Fig. 12). In the CU case, this occurs for all models other than model 15CU. In the CI case, the overlap between the convective carbon core and the carbon shell only occurs for model 20CI. Removing the 20-$M_\odot$ models from the evaluation of the weak component allows for a comparison between the predicted weak component with and without the occurrence of an overlap. Fig. 16 shows the predicted weak component (CI-no20) using the 15-, 25-, 32- and 60-$M_\odot$ models using initial mass ranges of 12.5–20.0, 20.0–28.5, 28.5–46 and 46–80 $M_\odot$ in the IMF calculation. The overproduction factors for the CI-no20 case show a reduction in Sr isotopes to values just less than the ^{16}O×2 line and a significant reduction in Y, Zr, Mo, Ru, Pd and Cd isotopes to values similar to the ST case and a reduction in Br and Rb isotopes to values close to the ^{16}O/2 line. The branching at ^{95}Zr is also affected, which mainly affects the relative overproduction factors of ^{96}Zr and ^{95}Mo.

6 DISCUSSION

The results in the previous section show that with an increased carbon-burning rate, the contribution of the neutron-capture processes during hydrostatic burning stages to the yields of massive stars is modified significantly.

The CU case exhibits a strong production of isotopes between the iron-group nuclides and the Ba-peak nuclides with regard to current massive star models (see Fig. 14). This production originates from the *s*-process production in a convective carbon core in which mixing has caused the ashes of carbon burning to be transported out from the centre of the star where it will be present in the supernova ejecta. This overlap was found in all but one of the CU models (15CU). Fig. 14 shows that the yields of the CU case are inconsistent with the weak *s*-process contribution to the Solar system abundances (see for example the anomalously high abundance of Sr–Y–Zr peak and Ba–La peak nuclides compared to those with $60 < A < 90$). Therefore, a strong resonance with $(\omega\gamma) \simeq 6.8 \times 10^{-5}$ eV at a centre-of-mass energy $E_{\rm com} = 1.5$ MeV in the ^{12}C + ^{12}C reaction rate is unlikely to be present in the reaction rate, according to the models used in the present analysis.

For the CI case, an extended distribution is found but the overproduction factors are not as high as the CU case (see Fig. 15). The main nucleosynthesis differences occur at the Sr–Y–Zr peak and beyond, which is a signature dominated by the presence of an overlap

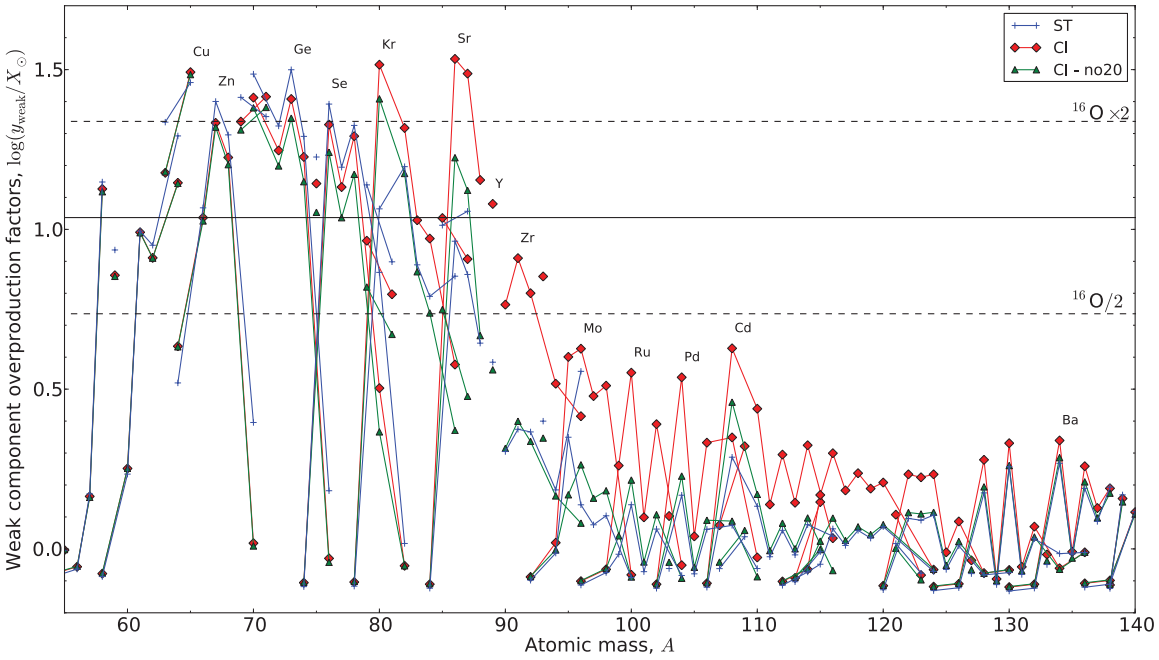

Figure 16. The overproduction factors of the predicted weak component relative to the Solar system abundances with the 20–$M_\odot$ models removed from the calculation (CI-no20). The weak components for the ST and CI cases including the 20-$M_\odot$ models are included for comparison. Isotopes of a given element are connected by adjoining lines. The isotopic chains for Cu, Zn, Ge, Se, Kr, Sr, Y, Zr, Mo, Ru, Pd, Cd and Ba in the CU model are labelled for clarity.

of a carbon shell with the convective carbon core. The large overproduction of Kr and Sr could suggest that the CI carbon-burning rate is too high. In any case, it is unlikely that a solar metallicity model should demonstrate a strong overlap between the convective carbon core and the carbon shell of the kind experienced in model 20CI. However, considering the present uncertainties in the stellar models such as the reaction rates [for example, the critical reactions ^{12}C(α, γ)^{16}O and ^{22}Ne(α,n)^{25}Mg], the initial composition and the treatment of convective–radiative boundaries, the abundance of Sr is not a significant enough constraint to assert that the CI rate would be inconsistent with the Solar system abundance distribution.

The production of Sr, Y, Zr and other heavier nuclides has been studied extensively as galactic chemical evolution models and observations have suggested the existence of an additional primary nucleosynthesis process, the lighter element primary process (LEPP) (Travaglio et al. 2004; Montes et al. 2007). The carbon-core *s*-process and the mixing of heavy nuclei out from the centre could provide an alternative nucleosynthesis scenario for the LEPP. It is tempting to underline the similarity between the LEPP signature and the anomalous carbon-burning *s*-process component present in the CU models and partly in the CI models. However, we recall that the LEPP process should be primary if the solar LEPP and (low metallicity) stellar LEPP are indeed the same process (see for example Montes et al. 2007). Although the carbon-core *s*-process features a primary neutron source, ^{13}C, the seed nuclei, ^{56}Fe, are secondary. Consequently, an *s*-process component using iron seeds in these conditions cannot reproduce the stellar LEPP abundances at low metallicity. Therefore, the carbon-core *s*-process component is unlikely to represent the site for the stellar LEPP component at low metallicity. In addition, when the number of seeds is lowered, the neutron capture per iron seed increases (see equation 4.1) and the distribution of *s*-process nuclides extends to higher atomic mass. However, if the solar and stellar LEPPs differ in origin, the carbon-core *s*-process may provide a solution to the solar LEPP.

7 SUMMARY AND CONCLUSIONS

In order to investigate the sensitivity of massive star evolution to the potentially large uncertainties in the carbon-burning rate, 15 stellar models with five initial masses of 15, 20, 25, 32 and 60 $M_\odot$ and three different carbon-burning rates were generated with GENEC and post-processed with the parallel post-processing code MPPNP. The yields for each model were then calculated and the consequences of the different rates on stellar evolution and nucleosynthesis were examined. The main results are summarized as follows.

An enhanced carbon-burning rate directly affects the ignition conditions for carbon burning, which move to lower temperatures and densities. The reduced temperature lowers the neutrino losses, causing the carbon-burning stage to occur for a longer lifetime. An increasing dominance of neutrinos formed through photoneutrino interactions is seen, rather than formation by pair production. The change in temperature and the neutrino losses affects the convection zone structure. In the models using the CI rate, the maximum initial mass for the formation of a convective carbon core increases by a few solar masses from its current value of $\approx$22 $M_\odot$. In models using the CU rate, carbon-core burning occurs in a convective core in the entire mass range. The increased carbon-burning rates generally reduce the number of carbon-burning shells (because they have a larger mass extent) and increase the probability of overlap between different convective zones. Although the increased carbon-burning rates used in this study strongly affect carbon burning, the impact on further burning stages (neon, oxygen and silicon) is small and does not present any clear trend. Therefore, no constraint can be applied to the $^{12}C + {}^{12}C$ rate directly from stellar evolution considerations.

The presence of a significant overlap between the convective carbon core and the convective carbon shell, as seen in most of the CU models and in model 20CI, may present a further nucleosynthesis site worthy of investigation. This is especially true considering the present uncertainties in stellar models with regard to

convective–radiative boundaries and the abundance distribution exhibited by the carbon-core *s*-process. In particular, the carbon-core *s*-process bears similarities to the solar LEPP. However, because of the secondary nature of the iron seeds, it cannot provide a solution to the stellar LEPP at low metallicity. Further studies into the uncertainties relevant for low-metallicity massive stars are required to confirm this statement.

According to the present models, a strongly enhanced rate (the CU rate) due to the presence of a low-energy resonance (near to the Gamow peak) causes a large convective carbon core to exist in every stellar model. The large convective core will mix isotopes a considerable distance away from the centre of the star, causing the ejecta to be polluted with matter rich in *s*-process isotopes. The overabundance distribution obtained with the CU rate is too high and has a vastly different shape. The yields are therefore incompatible with the weak *s*-process contribution to the Solar system and the CU rate is therefore ruled out.

A moderately enhanced rate (the CI rate), like the strongly enhanced rate, also affects the interior convection zones and consequently the structure of the star. With the CI rate, an overlap is only present in the 20–$M_\odot$ case, which enriches the ejecta with products of the carbon-core *s*-process. This enrichment predominantly involves nuclides at the Sr–Y–Zr peak and the heavier elements Mo, Ru, Pd and Cd. With this additional nucleosynthesis component, the overproduction factor for Kr and Sr seems to be too high to be consistent with the Solar system abundances since it would imply that the majority, if not all, of the solar Kr and Sr comes from massive stars, with only a smaller contribution from asymptotic giant branch (AGB) stars at the Sr peak. For all the other masses, the changes in nucleosynthesis occur only from changes to carbon-shell burning, which are more subtle and involve isotopes primarily at branching points. If the contribution from the 20-$M_\odot$ model is not included (CI-no20), the yields obtained are very similar to the standard yields. Consequently, the CI rate is probably very close to the 'upper limit' for the carbon-burning rate to lead to a weak *s*-process production compatible with the Solar system composition.

Given that an overlap between the convective carbon core and shells has such a strong impact on the yields and that 1D stellar models use the mixing-length theory (MLT), which might not exactly represent the complex 3D nature of convective–radiative interfaces, it will be crucial to study such potential shell overlaps as well as overlap between burning shells of different burning stages (Arnett & Meakin 2011) in 3D hydrodynamic simulations. It should also be acknowledged that the present conclusions are built on the assumption that the ratio of the α- and p-exit channels of the $^{12}C + {}^{12}C$ (13:7) reaction is preserved to lower energies. Further studies of this uncertainty, including also an analysis of the p-process in massive stars, will be discussed in a forthcoming paper (Pignatari et al., in preparation).

The effects of the carbon-burning rate on the stellar evolution and nucleosynthesis of massive stars demonstrates that nuclear physics experiments investigating $^{12}C + {}^{12}C$ continue to remain relevant for the understanding of stars and further nuclear physics experiments, particularly at energies close to the Gamow peak for hydrostatic carbon fusion, are highly desirable in order to improve stellar models.

ACKNOWLEDGMENTS

NuGrid acknowledges significant support from NSF grant PHY0922648 (Joint Institute for Nuclear Astrophysics, JINA) and EU MIRG-CT-2006-046520. KN and RH acknowledge support from the World Premier International Research Center Initiative (WPI Initiative), MEXT, Japan. RH acknowledges support from the STFC (UK). MP acknowledges support from the Ambizione grant of the SNSF (Switzerland). RH and MP also acknowledge support from the EUROCORE Eurogenesis programme. FH acknowledges NSERC Discovery Grant funding. The work of CF and GR was funded in part under the auspices of the National Nuclear Security Administration of the U.S. Department of Energy at Los Alamos National Laboratory and supported by Contract No. DE-AC52-06NA25396. Computations were performed at the Arizona State University's Fulton High-performance Computing Center (USA), the high-performance computer KHAOS at EPSAM Institute at Keele University (UK) and the CFI (Canada) funded computing resources at the Department of Physics and Astronomy at the University of Victoria. This work used the SE library (LA-CC-08-057) developed at Los Alamos National Laboratory as part of the NuGrid collaboration; the SE library makes use of the HDF5 library, which was developed by The HDF Group and by the National Center for Supercomputing Applications at the University of Illinois at Urbana-Champaign.

REFERENCES

Aguilera E. F. et al., 2006, Phys. Rev. C, 73, 064601
Aikawa M., Arnould M., Goriely S., Jorissen A., Takahashi K., 2005, A&A, 441, 1195
Angulo C. et al., 1999, Nuclear Phys. A, 656, 3
Arcoragi J., Langer N., Arnould M., 1991, A&A, 249, 134
Arnett W. D., 1972, ApJ, 176, 699
Arnett W. D., Meakin C., 2011, ApJ, 733, 78
Arnett W. D., Thielemann F., 1985, ApJ, 295, 589
Arnett W. D., Truran J. W., 1969, ApJ, 157, 339
Barrón-Palos et al., 2006, Nuclear Phys. A, 779, 318
Bennett M. E. et al., 2010a, J. Phys. Conf. Ser., 202, 012023
Bennett M. E. et al., 2010b, Proc. 11th Symp. on Nuclei in the Cosmos, Heidelberg, Germany
Betts R. R., Wuosmaa A. H., 1997, Rep. Prog. Phys., 60, 819
Busso M., Gallino R., 1985, A&A, 151, 205
Caughlan G. R., Fowler W. A., 1988, At. Data Nucl. Data Tables, 40, 283
Chieffi A., Limongi M., Straniero O., 1998, ApJ, 502, 737
Clayton D. D., 1968, Principles of Stellar Evolution and Nucleosynthesis: Univ. Chicago Press, Chicago
Cooper R. L., Steiner A. W., Brown E. F., 2009, ApJ, 702, 660
Couch R. G., Schmiedekamp A. B., Arnett W. D., 1974, ApJ, 190, 95
Dayras R., Switkowski Z. E., Woosley S. E., 1977, Nuclear Phys. A, 279, 70
de Jager C., Nieuwenhuijzen H., van der Hucht K. A., 1988, A&AS, 72, 259
Descouvemont P., 1993, Phys. Rev. C, 48, 2746
Diaz-Torres A., 2008, Phys. Rev. Lett., 101, 122501
Diaz-Torres A., Gasques L. R., Wiescher M., 2007, Phys. Lett. B, 652, 255
Dillmann I., Heil M., Käppeler F., Plag R., Rauscher T., Thielemann F., 2006, in Woehr A., Aprahamian A., eds, AIP Conf. Ser. Vol. 819, Capture Gamma-Ray Spectroscopy and Related Topics. Am. Inst. Phys., New York, p. 123
Eggenberger P., Meynet G., Maeder A., Hirschi R., Charbonnel C., Talon S., Ekström S., 2008, Ap&SS, 316, 43
El Eid M. F., Meyer B. S., The L., 2004, ApJ, 611, 452
El Eid M. F., The L.-S., Meyer B. S., 2009, Space Sci. Rev., 147, 1
Ferguson J. W., Alexander D. R., Allard F., Barman T., Bodnarik J. G., Hauschildt P. H., Heffner-Wong A., Tamanai A., 2005, ApJ, 623, 585
Fryer C., 2009, APS April Meeting Abstract, p. B4001
Fuller G. M., Fowler W. A., Newman M. J., 1985, ApJ, 293, 1
Fynbo H. O. U. et al., 2005, Nat, 433, 136
Gasques L. R., Brown E. F., Chieffi A., Jiang C. L., Limongi M., Rolfs C., Wiescher M., Yakovlev D. G., 2007, Phys. Rev. C, 76, 035802

Grevesse N., Noels A., 1993, in Prantzos N., Vangioni-Flam E., Casse M., eds, Origin and Evolution of the Elements. Cambridge Univ. Press, Cambridge, p. 15
Gropp W., Lusk E., Skjellum A., 1999, Using MPI: Portable Parallel Programming with the Message-Passing Interface, 2nd edn. MIT Press, Cambridge, MA
Heger A., Langer N., Woosley S. E., 2000, ApJ, 528, 368
Herwig F. et al., 2008, in Nuclei in the Cosmos (NIC X), Proceedings of Science, 023
Hirschi R., Meynet G., Maeder A., 2004, A&A, 425, 649
Hirschi R., Meynet G., Maeder A., 2005, A&A, 433, 1013
Hix W. R., Khokhlov A. M., Wheeler J. C., Thielemann F., 1998, ApJ, 503, 332
Iapichino L., Lesaffre P., 2010, A&A, 512, A27
Iliadis C., D'Auria J. M., Starrfield S., Thompson W. J., Wiescher M., 2001, ApJS, 134, 151
Imanishi B., 1968, Phys. Lett. B, 27, 267
Imbriani G., Limongi M., Gialanella L., Terrasi F., Straniero O., Chieffi A., 2001, ApJ, 558, 903
Imbriani G. et al., 2005, Eur. Phys. J. A, 25, 455
Itoh N., Adachi T., Nakagawa M., Kohyama Y., Munakata H., 1989, ApJ, 339, 354
Itoh N., Hayashi H., Nishikawa A., Kohyama Y., 1996, ApJS, 102, 411
Jaeger M., Kunz R., Mayer A., Hammer J. W., Staudt G., Kratz K. L., Pfeiffer B., 2001, Phys. Rev. Lett., 87, 202501
Jiang C. L., Esbensen H., Back B. B., Janssens R. V., Rehm K. E., 2004, Phys. Rev. C, 69, 014604
Jiang C. L., Rehm K. E., Back B. B., Janssens R. V. F., 2007, Phys. Rev. C, 75, 015803
Käppeler F., Beer H., Wisshak K., 1989, Rep. Prog. Phys., 52, 945
Kondo Y., Matsuse T., Abe Y., 1978, Prog. Theor. Phys, 59, 465
Kunz R., Fey M., Jaeger M., Mayer A., Hammer J. W., Staudt G., Harissopulos S., Paradellis T., 2002, ApJ, 567, 643
Lamb S. A., Howard W. M., Truran J. W., Iben I., Jr, 1977, ApJ, 217, 213
Limongi M., Straniero O., Chieffi A., 2000, ApJS, 129, 625
Maeder A., 2009, Physics, Formation and Evolution of Rotating Stars. Springer-Verlag, Berlin
Mauron N., Josselin E., 2011, A&A, 526, A156
Meynet G., Maeder A., 2003, A&A, 404, 975
Michaud G. J., Vogt E. W., 1972, Phys. Rev. C, 5, 350
Montes F. et al., 2007, ApJ, 671, 1685
Mukhamedzhanov A. M. et al., 2003, Phys. Rev. C, 67, 065804
Nugis T., Lamers H. J. G. L. M., 2000, A&A, 360, 227
Oda T., Hino M., Muto K., Takahara M., Sato K., 1994, At. Data Nucl. Data Tables, 56, 231
Perez-Torres R., Belyaeva T. L., Aguilera E. F., 2006, Phys. Atomic Nuclei, 69, 1372
Peters J. G., 1968, ApJ, 154, 225
Pignatari M., Gallino R., Heil M., Wiescher M., Käppeler F., Herwig F., Bisterzo S., 2010, ApJ, 710, 1557
Prantzos N., Arnould M., Arcoragi J., 1987, ApJ, 315, 209
Raiteri C. M., Busso M., Picchio G., Gallino R., Pulone L., 1991a, ApJ, 367, 228
Raiteri C. M., Busso M., Picchio G., Gallino R., 1991b, ApJ, 371, 665
Rauscher T., Thielemann F., 2000, At. Data Nucl. Data Tables, 75, 1
Rauscher T., Thielemann F., 2001, At. Data Nucl. Data Tables, 79, 47
Rauscher T., Heger A., Hoffman R. D., Woosley S. E., 2002, ApJ, 576, 323
Rogers F. J., Swenson F. J., Iglesias C. A., 1996, ApJ, 456, 902
Spillane T. et al., 2007, Phys. Rev. Lett., 98, 122501
Strieder F., 2008, J. Phys. G: Nuclear Phys., 35, 014009
Strieder F., 2010, J. Phys. Conf. Ser., 202, 012025
Terrasi F. et al., 2007, Nucl. Instrum. Methods Phys. Res. B, 259, 14
The L.-S., El Eid M. F., Meyer B. S., 2000, ApJ, 533, 998
The L., El Eid M. F., Meyer B. S., 2007, ApJ, 655, 1058
Tinsley B. M., 1979, ApJ, 229, 1046
Travaglio C., Gallino R., Arnone E., Cowan J., Jordan F., Sneden C., 2004, ApJ, 601, 864
Truran J. W., Cameron A. G. W., 1971, Ap&SS, 14, 179
Truran J. W., Iben I., Jr, 1977, ApJ, 216, 797
Tur C., Heger A., Austin S. M., 2009, ApJ, 702, 1068
Vink J. S., de Koter A., Lamers H. J. G. L. M., 2001, A&A, 369, 574
Woosley S. E., Weaver T. A., 1986, ARA&A, 24, 205
Woosley S. E., Weaver T. A., 1995, ApJS, 101, 181
Woosley S. E., Heger A., Weaver T. A., 2002, Rev. Mod. Phys., 74, 1015
Xu C., Qi C., Liotta R. J., Wyss R., Wang S. M., Xu F. R., Jiang D. X., 2010, Phys. Rev. C, 81, 054319
Yakovlev D. G., Beard M., Gasques L. R., Wiescher M., 2010, Phys. Rev. C, 82, 044609
Young P. A., Fryer C. L., 2007, ApJ, 664, 1033
Zickefoose J. et al., 2010, Proc. 11th Symp. on Nuclei in the Cosmos, Heidelberg, Germany

APPENDIX A: PARALLEL-PROGRAMMING IMPLEMENTATION

At a particular timestep, the parameters for a 1D spherical shell (or zone) are loaded into memory and a nuclear reaction network is calculated for that zone. This requires the inverse of a square matrix to be calculated, which has dimensions equal to the number of isotopes included in the network. For each timestep there are typically 10^3 zones, dependent on the stellar model and the evolutionary stage of the model, and there are $\sim 10^6$ timesteps per model. Therefore, the post-processing of a single stellar model requires $\sim 10^9$ nuclear network calculations. With the nuclear reaction network specified in Table 1 including $\simeq 1.3 \times 10^4$ reactions, the computational expense involved becomes significant; the typical duration of a single MPPNP run on a uniprocessor is approximately 10–12 months with current serial technology. Therefore, the application of parallel programming is an absolute necessity to allow the calculations to complete over a reasonable time-scale.

The choice of parallelism is a simple master–slave (or WORKQUEUE) strategy where a single, master, processor allocates work to a number of slave processors, which is implemented using the Message Passing Interface (MPI) library routines in FORTRAN (Gropp, Lusk & Skjellum 1999). This is an implementation of parallelism where processors communicate information by passing 'messages' to each other with each processor having access to a local, private memory. The advantage of message passing is the ability to operate on distributed memory resources (such as cluster networks), as well as shared memory resources, and the ability to control explicitly how communications are handled and the parallel behaviour of the program. It is an embarrassingly parallel program,[6] which allows for an efficient parallelization and reduces dramatically the potential communication overhead. This was achieved by distributing 'work' over mass zones for each timestep, which are calculated independently from each other during the post-processing calculations. Here, a single unit of 'work' is defined as the nuclear reaction network calculation (in flops) for all involved species for a single zone at a particular timestep.

The operation of the parallel program is as follows. First, the nuclear reaction rates and other global parameters are broadcasted to each slave so that each processor has the required data available in local memory. Then a loop over timesteps is entered. For each iteration of the loop, a simple first-in first-out (FIFO) scheduler is invoked, which assigns work (in the form of a message containing

[6] An embarrassingly parallel program is one where slave processors are not required to communicate information to each other during the run; the problem can simply be split and allocated in parts to a large number of processors.

the temperature, density and abundances) zone by zone (from the centre to the surface), first to all assigned processors and then to idle processors as they become available for further work.

Load balancing is important to reduce the impact of idle processors on the performance. In MPPNP, a simple load balancing scheme is specified, where the zones are allocated in order from the centre to the surface. This choice is made in lieu with the typical distribution of work over the interior of the star at any particular timestep. The distribution is set by the dynamic network implemented in MPPNP, which adds or removes isotopes from the network calculation depending on the nucleosynthesis flux limits (negligible changes in abundances are ignored to save on unnecessary computation). In general, the dynamic network assigns more isotopes to zones that have higher temperatures (since higher temperatures increase the nuclear reaction rates) and are convective (since the resultant mixing can cause an increase in the abundance of fuel). Therefore, the distribution has a maximum in the centre and decreases with mass coordinate towards the surface, affected by the presence of convection zones. However, this is a general case; it is not unusual to have a non-monotonic distribution of work at particular steps throughout the model evolution, especially at the boundaries of convection zones and where neutron sources are efficient.

The parallel burning step is followed by a serial mixing step. The change in mass-fraction abundance of species i, X_i, over time, t, is calculated using the diffusion equation

$$\frac{\partial X_i}{\partial t} = \frac{\partial}{\partial m_r}\left[D(4\pi r^2\rho)^2\frac{\partial X_i}{\partial m_r}\right], \tag{A1}$$

where m_r is the mass coordinate (at radius r), ρ is the density and D is the diffusion coefficient calculated from MLT. The diffusion coefficient is normally large enough ($\sim 10^{16}$ cm^2 s^{-1} for hydrogen and helium burning) so that all convection zones, over a timestep Δt, act to smooth out immediately any sharp changes in abundance associated with concentrated nuclear burning.

Fig. A1 shows the speed-up factor of MPPNP for a small test run (with 250 zones and 2000 timesteps; a typical stellar model uses $\approx 10^3$ zones and $\sim 10^6$ timesteps) compared to the theoretical laws predicted by Amdahl's and Gustafson's law for a program with a serial fraction of 1 per cent. Amdahl's law,

$$S(p) = \frac{t_s}{t_p} = \frac{t_s}{f t_s + (1-f)t_s/p} = \frac{p}{1+p-1f}, \tag{A2}$$

gives the maximum speed-up, $S(p)$, possible for a program with a fixed amount of work, i.e. the time spent running serial computations is constant. In equation (A2), t_s is the duration of the program with a serial fraction, f, on a uniprocessor and t_p is the parallel duration on a system with p processors. The close fit of this law with MPPNP suggests that the parallelization is close to the ideal case and is not hampered by communication overhead or excessive initialization. However, it would be preferable to achieve a parallelization comparable to Gustafson's law,

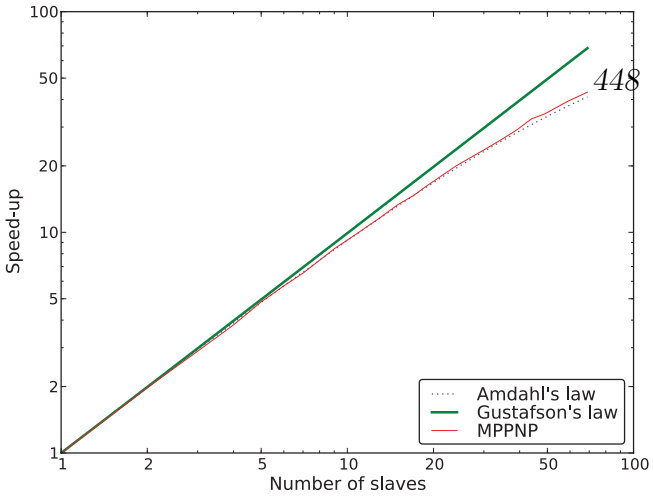

Figure A1. Speed-up factor for MPPNP with respect to those of Gustafson's law and Amdahl's law with a serial fraction of 1 per cent.

$$S(p) = \frac{t_s}{t_p} = \frac{f t_p + p(1-f)t_p}{t_p} = p + f(1-p), \tag{A3}$$

which is the maximum speed-up possible with a constraint on the parallel time, i.e. the time spent running parallel computations is constant. This could be achieved by including more zones (for example, with the adaptive mesh refinement routine), but the improved scaling would come at the expense of an increased workload. In any case, only 250 zones were used in the test case; as the number of slave processors approaches 250, the total number of jobs allocated to each processor approaches unity. In this regime, the time spent by idle processors is likely to increase significantly and the speed-up factor will plateau. The post-processing calculations for each model, using 60 slave processors, took approximately 5–10 d each, depending on the model.

SUPPORTING INFORMATION

Additional Supporting Information may be found in the online version of this article.

Table 7. Yields for all models.

Please note: Wiley-Blackwell are not responsible for the content or functionality of any supporting materials supplied by the authors. Any queries (other than missing material) should be directed to the corresponding author for the article.

This paper has been typeset from a TEX/LATEX file prepared by the author.

PROCEEDINGS OF SCIENCE

NuGrid: *s* process in massive stars

R. Hirschi*[abc], U. Frischknecht[d], M. Pignatari[abe], F.-K. Thielemann[d], M. E. Bennett[ab], S. Diehl[afg], C. L. Fryer[af], F. Herwig[abh], A. Hungerford[ag], G. Magkotsios[aei], G. Rockefeller[ag], F. X. Timmes[ai], and P. Young[ai]

[a] *The NuGrid Collaboration*
[b] *Astrophysics Group, Keele University, ST5 5BG, UK*
[c] *IPMU, University of Tokyo, Kashiwa, Chiba 277-8582, Japan*
[d] *Theoretical Astrophysics Group, University of Basel, Basel, 4056, Switzerland*
[e] *Joint Institute for Nuclear Astrophysics, University of Notre Dame, IN, 46556, USA*
[f] *Theoretical Astrophysics Group (T-6), Los Alamos National Laboratory, Los Alamos, NM, 87544, USA*
[g] *Computational Methods (CCS-2), Los Alamos National Laboratory, Los Alamos, NM, 87544, USA*
[h] *Dept. of Physics & Astronomy, Victoria, BC, V8W 3P6, Canada*
[i] *School of Earth and Space Exploration, Arizona State University, Tempe, AZ 85287, USA*
E-mail: r.hirschi@epsam.keele.ac.uk

The *s*-process production in massive stars at very low metallicities is expected to be negligible due to the low abundance of the neutron source ^{22}Ne, to primary neutron poisons and decreasing iron seed abundances. However, recent models of massive stars including the effects of rotation show that a strong production of ^{22}Ne is possible in the helium core, as a consequence of the primary nitrogen production (observed in halo metal poor stars). Using the PPN post-processing code, we studied the impact of this primary ^{22}Ne on the *s* process. We find a large production of *s* elements between strontium and barium, starting with the amount of primary ^{22}Ne predicted by stellar models. There are several key reaction rate uncertainties influencing the *s*-process efficiency. Among them, ^{17}O(α,γ) may play a crucial role strongly influencing the *s* process efficiency, or it may play a negligible role, according to the rate used in the calculations. We also report on the development of a new parallel (MPI) post-processing code (MPPNP) designed to follow the complete nucleosynthesis in stars on highly resolved grids. We present here the first post-processing run from the ZAMS up to the end of helium burning for a 15 $M_{\odot}$ model.

10th Symposium on Nuclei in the Cosmos
July 27 - August 1 2008
Mackinac Island, Michigan, USA

*Speaker.

1. Introduction

Massive stars are known to produce elements heavier than the iron group via rapid neutron captures during their explosion, *r* process (see for example the contribution by Qian and Kratz et al. 2007 [1]) and also via slow neutron captures (*s* process) during the pre-supernova evolution, forming the so-called weak *s* component. The weak *s* process in massive stars with initial solar like composition is well understood. ^{22}Ne is the main neutron source and it is produced starting from the initial CNO isotopes (The et al. 2000 and 2007 [2, 3], Raiteri et al. 1991 [4, 5], Pignatari et al. in prep.). The weak *s* process, producing mostly elements in the atomic mass range $60 \lesssim A \lesssim 90$, starts at the end of helium burning when the temperature is high enough to activate $^{22}\mathrm{Ne}(\alpha,n)^{25}\mathrm{Mg}$. More massive stars reach higher temperatures at the end of He-burning and therefore burn more ^{22}Ne. Consequently *s*-process production during central helium burning increases with increasing stellar mass. The ^{22}Ne left over from helium burning is the main neutron source during the subsequent carbon shell burning. The carbon shell *s*-process contribution depends on the history of convective zones after the He-core burning and on different nuclear uncertainties (e. g. $^{12}\mathrm{C}(\alpha,\gamma)^{16}\mathrm{O}$). The standard *s*-process production in massive stars depends on the initial metallicity. At low metallicity, the low iron seed abundance, the low ^{22}Ne content and the increasing strength of primary neutron poisons limits the *s*-process efficiency, permitting only negligible production of *s* elements (e. g. Raiteri et al. 1992 [6]).

2. Weak *s* process at low metallicity in rotating stars

At solar metallicity, the main effect of rotation on the *s*-process production is the enlargement of convective helium core due to additional mixing and therefore a behaviour like non-rotating more massive stars [7]. Thus a 25 $M_\odot$ star with rotation behaves like non-rotating stars with masses between 30 and 40 $M_\odot$. Hence the *s*-process efficiency in He-core burning is enhanced in rotating stars (Frischknecht et al. in prep.).

At low metallicity, the impact of rotation is more important. Indeed, at the start of core He-burning, carbon and oxygen are mixed upward into hydrogen rich regions leading to a strong production of nitrogen (see Meynet et al. 2006 [8] and Hirschi 2007 [9]). Part of this primary nitrogen may enter the convective He core and be transformed into primary ^{22}Ne by α-captures. As a consequence, with respect to the non-rotating models, the ^{22}Ne available in the He-core is strongly enhanced. According to Hirschi (2008 [10]), about 1% in mass of the helium core is composed of ^{22}Ne at the *s*-process activation.

We present in Fig. 1 one-zone post-processing runs up to the end of He-burning calculated with the PPN code (see next Sect.) with an initial metallicity of $Z = 10^{-6}$. In order to reproduce the effect of rotational mixing on the helium burning core composition in the one-zone calculation, we replaced 1% in mass of ^{4}He by ^{22}Ne at the start of helium burning. The primary ^{22}Ne enhances the *s* process compared to the non-rotating case, where negligible amounts of *s* elements are produced. The highest nucleosynthesis efficiency is around Sr with overproduction factors ($X_\mathrm{i}/X_\mathrm{ini}$) between thousand and ten thousand. As can be seen in Fig. 1, iron seeds and in general elements lighter than strontium feed the *s* nucleosynthesis in the mass region between strontium (Sr) and barium (Ba). Beyond Ba, the *s* efficiency rapidly falls, depending on the total neutron exposure. The major

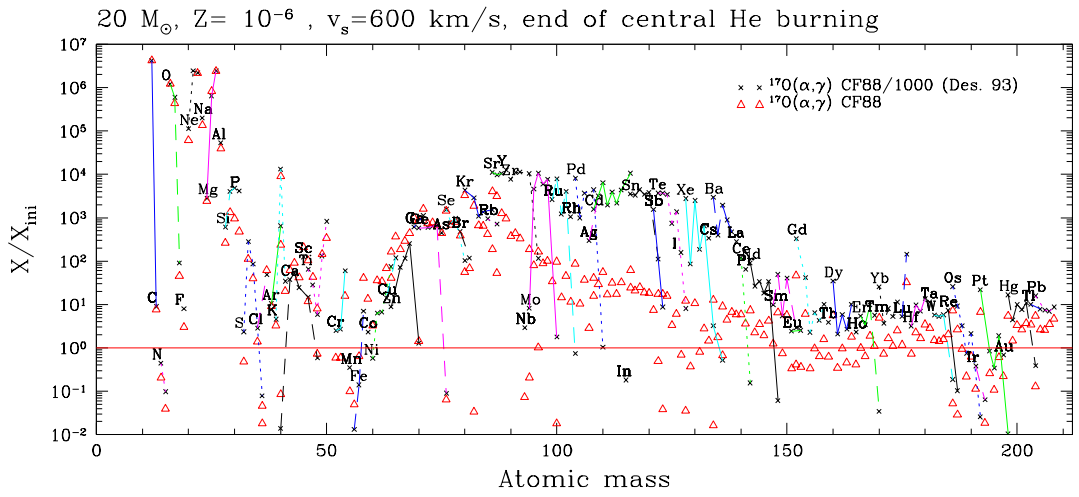

Figure 1: The overproduction factors after He-burning in the one-zone post-processing calculations. Using a low $^{17}O(\alpha,\gamma)$ rate (black crosses) leads to a strong increase of *s*-process overproduction between Sr and Ba. Isotopes with X_i/X_{ini} below the lower limit are not plotted.

neutron poisons are ^{16}O, ^{25}Mg and ^{22}Ne, where ^{16}O is the strongest neutron absorber. Whether or not ^{16}O is an efficient poison depends on the ratio of $^{17}O(\alpha,\gamma)$ to $^{17}O(\alpha,n)$. According to the study of Descouvemont (1993 [11]), the (α,γ) channel should be orders of magnitude weaker than the (α,n) channel, in which case the neutrons captured by ^{16}O are recycled by $^{17}O(\alpha,n)$. On the other hand, using the rates of Caughlan and Fowler (1988 [12]), $^{17}O(\alpha,\gamma)$ is about a factor ten slower than $^{17}O(\alpha,n)$ and a significant fraction of neutrons captured by ^{16}O are not re-emitted. In this case, ^{16}O is the strongest neutron poison. In Fig. 1, we show the importance of the $^{17}O(\alpha,\gamma)$ rate by comparing the isotopic distributions obtained using the rate of Caughlan and Fowler (1988 [12]) (red triangles) and using this same rate divided by a factor 1000 to reproduce the $(\alpha,\gamma)/(\alpha,n)$ ratio suggested by Descouvemont (1993 [11]) (black crosses). The different *s*-process production between the two calculations demonstrates the importance of the $^{17}O(\alpha,\gamma)$ to $^{17}O(\alpha,n)$ ratio for the *s* process at low metallicity. This was also suggested by Rayet and Hashimoto (2000 [13]) in standard *s*-process calculations in massive stars at low metallicity. However, because of the large primary ^{22}Ne production in rotating stars, in the present calculations the impact of the $^{17}O(\alpha,\gamma)$ to $^{17}O(\alpha,n)$ ratio on the *s*-process efficiency is much stronger than in Rayet and Hashimoto (2000 [13]). A better knowledge of these two rates at He-burning temperature is highly desirable in order to obtain more reliable *s*-process calculations at very low metallicity. The strong production of *s* elements between Sr and Ba is in agreement with Pignatari et al. (2008 [14]), where the $^{17}O(\alpha,\gamma)$ rate of Descouvemont 1993 [11] is used and where the amount of primary ^{22}Ne is in agreement with Hirschi 2008 [10]. The boosted *s* process due to primary ^{14}N production may provide a new *s*-process component with important implications for nucleosynthesis at low metallicity. Massive rotating stars may therefore contribute considerable amounts of isotopic abundances between Sr and Ba to the Galactic chemical evolution at halo metallicities, which could provide a possibility to explain the high Sr enrichment and the high Sr/Ba ratio (see Pignatari et al. 2008 [14] for more

details). In order to make a quantitative and more precise statement about the importance of this *s* process occurring in rotating low-metallicity stars, further investigations are needed.

3. Multi-zone parallel (MPI) post-processing code, MPPNP

Although only a few isotopes are crucial for the energy generation in massive stars, many more are important for the nucleosynthesis, for example to determine how much *s* process is made in massive stars. Since it is not necessary to follow many of these species within a stellar evolution calculation, we developed a post-processing network, called PPN, that allows us to follow the complete nucleosynthesis taking place in massive stars. It also enables testing of the importance of various reaction rates and especially the use of the same set of nuclear reactions in different stellar environments. The MPPNP variant uses MPI and is therefore much faster than a serial code. Using MPPNP, we have post-processed a full stellar evolution model of 15 $M_\odot$ at Z$=0.01$ calculated with the Geneva code [15] from the ZAMS up to the end of helium burning with a 400-isotope network up to Ag. The overabundance pattern at the end of the core He-burning phase is shown in Fig. 2. As expected, the weak *s*-process production in a 15 $M_\odot$ star is modest, with overproduction factors up to 10 for *s*-only isotopes between iron and strontium. This is due to the low central temperature reached at the end of the core He-burning phase in a 15 $M_\odot$ star (compared to more massive stars) with a marginal activation of the ^{22}Ne$(\alpha,n)^{25}$Mg during He-burning. We are currently testing MPPNP in the advanced stages and we plan to calculate the full nucleosynthesis for a large range of masses and metallicities. The MPPNP code will also be able to post-process AGB models (see contribution by Pignatari) and another variant of PPN, called TPPNP will follow trajectories of multi-dimensional simulations of supernova explosion and convective-reactive events in stars (see contribution by Herwig).

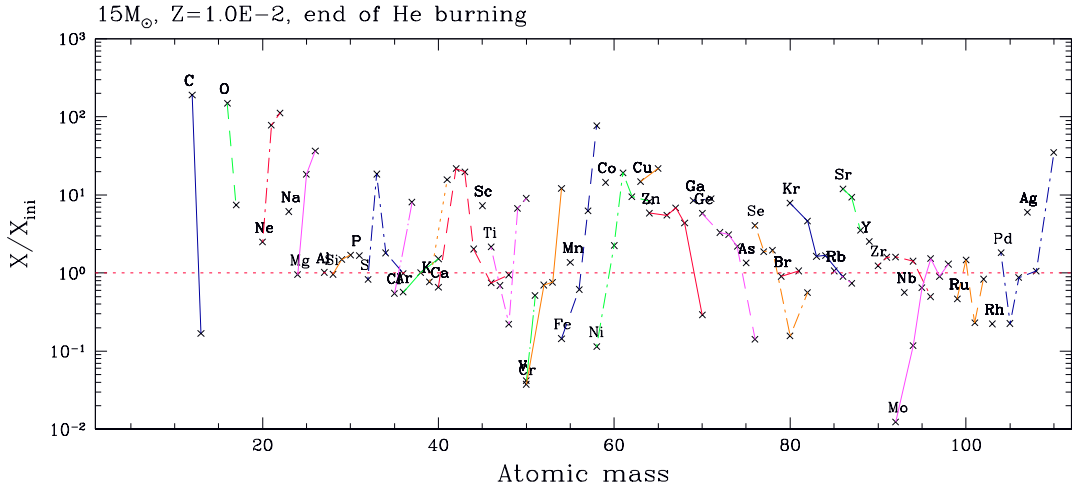

Figure 2: Overproduction factors in the convective core at the end of He-burning. Isotopes with $X_i/X_{\rm ini}$ below the lower limit are not plotted.

References

[1] K.-L. Kratz, K. Farouqi, B. Pfeiffer, J. W. Truran, C. Sneden, and J. J. Cowan, *Explorations of the r-Processes: Comparisons between Calculations and Observations of Low-Metallicity Stars*, ApJ **662** (Jun., 2007) 39–52, [arXiv:astro-ph/0703091].

[2] L.-S. The, M. F. El Eid, and B. S. Meyer, *A New Study of s-Process Nucleosynthesis in Massive Stars*, ApJ **533** (Apr., 2000) 998–1015.

[3] L.-S. The, M. F. El Eid, and B. S. Meyer, *s-Process Nucleosynthesis in Advanced Burning Phases of Massive Stars*, ApJ **655** (Feb., 2007) 1058–1078, [arXiv:astro-ph/0609788].

[4] C. M. Raiteri, M. Busso, G. Picchio, and R. Gallino, *S-process nucleosynthesis in massive stars and the weak component. II - Carbon burning and galactic enrichment*, ApJ **371** (Apr., 1991) 665–672.

[5] C. M. Raiteri, M. Busso, G. Picchio, R. Gallino, and L. Pulone, *S-process nucleosynthesis in massive stars and the weak component. I - Evolution and neutron captures in a 25 solar mass star*, ApJ **367** (Jan., 1991) 228–238.

[6] C. M. Raiteri, R. Gallino, and M. Busso, *S-processing in massive stars as a function of metallicity and interpretation of observational trends*, ApJ **387** (Mar., 1992) 263–275.

[7] R. Hirschi, G. Meynet, and A. Maeder, *Yields of rotating stars at solar metallicity*, A&A **433** (Apr., 2005) 1013–1022, [arXiv:astro-ph/0412454].

[8] G. Meynet, S. Ekström, and A. Maeder, *The early star generations: the dominant effect of rotation on the CNO yields*, A&A **447** (Feb., 2006) 623–639.

[9] R. Hirschi, *Very low-metallicity massive stars:. Pre-SN evolution models and primary nitrogen production*, A&A **461** (Jan., 2007) 571–583, [arXiv:astro-ph/0608170].

[10] R. Hirschi, C. Chiappini, G. Meynet, A. Maeder, and S. Ekström, *Stellar Evolution at Low Metallicity*, in *IAU Symposium*, vol. 250 of *IAU Symposium*, pp. 217–230, 2008.

[11] P. Descouvemont, *Microscopic three-cluster study of 21-nucleon systems*, Phys. Rev. C **48** (Dec., 1993) 2746–2752.

[12] G. R. Caughlan and W. A. Fowler, *Thermonuclear Reaction Rates V*, *Atomic Data and Nuclear Data Tables* **40** (1988) 283.

[13] M. Rayet and M.-a. Hashimoto, *The s-process efficiency in massive stars*, A&A **354** (Feb., 2000) 740–748.

[14] M. Pignatari, R. Gallino, G. Meynet, R. Hirschi, F. Herwig, and M. Wiescher, *The s process in massive stars at low metallicity. effect of primary ^{14}N from fast rotating stars.*, ApJ **L** (2008) accepted, arXiv0810.0182.

[15] P. Eggenberger, G. Meynet, A. Maeder, R. Hirschi, C. Charbonnel, S. Talon, and S. Ekström, *The Geneva stellar evolution code*, Ap&SS (Jun., 2007) 263.

PROCEEDINGS OF SCIENCE

Nucleosynthesis simulations for a wide range of nuclear production sites from NuGrid

F. Herwig[*ab], M. E. Bennett[b], S. Diehl[c], C. L. Fryer[d], R. Hirschi[be], A. Hungerford[d], G. Magkotsios[fg], M. Pignatari[bf], G. Rockefeller[d], F. X. Timmes[g], and P. Young[g]

[a] *Dept. of Physics & Astronomy, Victoria, BC, V8W 3P6, Canada*
[b] *Astrophysics Group, Keele University, ST5 5BG, UK*
[c] *Theoretical Astrophysics Group (T-6), Los Alamos National Laboratory, Los Alamos, NM, 87544, USA*
[d] *Computational Methods (CCS-2), Los Alamos National Laboratory, Los Alamos, NM, 87544, USA*
[e] *IPMU, University of Tokyo, Kashiwa, Chiba 277-8582, Japan*
[f] *Joint Institute for Nuclear Astrophysics, University of Notre Dame, IN, 46556, USA*
[g] *School of Earth and Space Exploration, Arizona State University, Tempe, AZ 85287, USA*
E-mail: fherwig@uvic.ca

Simulations of nucleosynthesis in astrophysical environments are at the intersection of nuclear physics reaction rate research and astrophysical applications, for example in the area of galactic chemical evolution or near-field cosmology. Unfortunately, at present the available yields for such applications are based on heterogeneous assumptions between the various contributing nuclear production sites, both in terms of modeling the thermodynamic environment itself as well as the choice of specifc nuclear reaction rates and compilations. On the other side, new nuclear reaction rate determinations are often taking a long time to be included in astrophysical applications. The NuGrid project addresses these issues by providing a set of codes and a framework in which these codes interact. In this contribution we describe the motivation, goals and first results of the NuGrid project. At the core is a new and evolving post-processing nuclesoynthesis code (PPN) that can follow quiescent and explosive nucleosynthesis following multi-zone 1D-stellar evolution as well as multi-zone hydrodynamic input, including explosions. First results are available in the areas of AGB and massive stars.

10th Symposium on Nuclei in the Cosmos
July 27 - August 1 2008
Mackinac Island, Michigan, USA

[*] Speaker.

1. Introduction

Nuclear astrophysics combines nuclear physics of astrophysical relevance with the simulation of nuclear production sites in stellar evolution and explosions, and ultimately with abundance observations in stars and galaxies and measurements in pre-solar grains. Numerous compilations of yield data, for applications such as chemical evolution of galaxies, have been presented, based on different modeling assumptions. For example, in the area of massive stars the compilation of Woosley & Weaver (1995) provides yields which is based on solving a nuclear network together and in lock-step with the stellar evolution code. A similar approach is applied for AGB star yields [8, 10], although yields based on synthetic models are also still in use [11]. The latter was justified by the significant labour involved in full stellar evolution tracks of the advanced phases of stellar evolution, where most of the interesting nucleosynthesis takes place. It is largely for this reason that we still don't have yield tables that cover low-mass *and* massive stars (including explosive yields) for a meaningful range of metallicities and both light *and* heavy elements with internally consistent physics assumptions, including the nuclear physics data. However, such comprehensive yield data is required, for example in near-field cosmology applications [16, 6].

In addition, new results, for example on the hydroynamic nature of convective boundary mixing (Woodward et al., this vol. and [12]), need to be included in new yield calculations as quickly as possible to make them available for comparison with observations. Finally, the nuclear physics community needs to prioritze their efforts through the ability to run numerical nucleosynthesis experiments in realistic stellar production environments. On the other hand,

In order to address these issues we have pooled capabilities and expertise in the nucleosynthesis grid (NuGrid) collaboration to create a new simulation library and nucleosynthesis code capability. In this paper we describe our approach and report first results, for example from AGB s process and massive star nucleosynthesis. Other results relating to the NuGrid project have been presented at this conference by Hirschi et al., Pignatari et al., Fryer et al., Diehl et al., Hungerford et al. and Rockefeller et al. .

2. NuGrid nucleosynthesis post-processing

We have developed a new post-processing nucleosynthesis (PPN) code, and we are developing a stellar evolution and explosion (SEE) database, including an interface that allows these two components to communicate efficiently. The ultimate goal is to combine these two tools to create the needed comprehensive and internally consistent yields tables. The design goals of the PPN codes are (1) a capability of post-processing a wide range of thermodynamic environments from both 1D stellar evolution codes and trajectories from hydro-simulations (explosions and stellar hydro, both grid and particle), (2) comprehensive yet flexible nuclear physics input, and (3) to match resolution, detail, accuracy and precision of TD simulations, observations and nuclear physics.

The core unit of the PPN code implementation is a nuclear network kernel that consists of a physics package and a solver package. The nuclear network kernel evolves one nuclear network cell over one time step. There are three drivers that use the same network kernel. The single-zone driver (SPPN) is used for simple one-zone network experiments with either analytic, algorthmic or tabulated thermodynamic input. The multi-zone driver (MPPN) post-processes the output of

one-dimensional spherically symmetric stellar evolution codes, while the trajectory driver (TPPN) deals with trace particle data from hydrodynamic simulations.

The nuclear physics package includes most major nuclear data compilations, i.e. Basel reaclib [14], Kadonis [5], NACRE [2], Illiadis et al. (2001, [9]), Cauhglan & Fowler (1988, [4]), the nuclear data online interface Bruslib [1], Oda et al. (1994, [13]) and Fuller et al. (1985, [7]). The network includes NSE with T-dependent partition functions and mass excesses from reaclib and Coulomb screening from Calder et al. (2007, [3]). The network is dynamically built in two steps. In a first configuration step the master set of isotopes out of a maximum of 5180 is selected using simple configuration instructions. Based on this master set the actual network is adjusted dynamically in size for each network kernel calculation, so that the solution in every network cell is performed for the optimal selection of isotopes. The solver package relies at this time on a Newton-Raphson, fully implicit implementation with full precision control and adaptive sub-time stepping. We are also implementing a variable order method for improved accuracy [15]. The multi-zone and trajectory drivers are parallelized through a simple master-slave strategy, implemented in the distributed memory standard MPI. The parallel MPPNP driver has been run on up to 150 cores, although in most practical applications we are running post-processing grids of ~ 250 shells on 60-80 cores. The MPPNP drivers provides three grid options: static, input grid or adaptive grid.

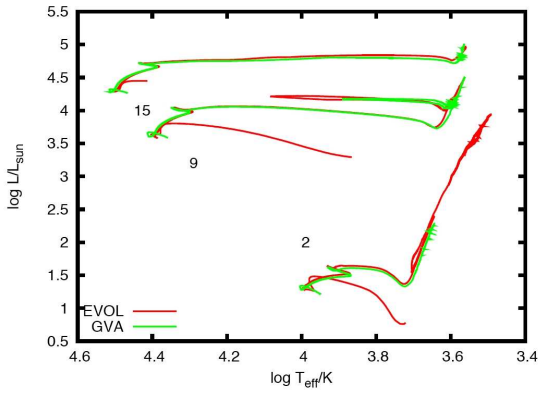

Figure 1: Stellar evolution tracks from EVOL and GVA (Geneva code) for different masses as indicated, without rotation, identical initial composition and an overshoot parameter ($f_{\rm ov} = 0.014$ for EVOL and $\alpha_{\rm ov} = 0.2$ for GVA) that has been choosen so that the width and duration of the main-sequence match.

The interface to the stellar evolution and explosion data is defined through the custom library USEEPP[1] built on top of the platform independent hdf5[2] standard. The SEE database is populated with low-mass tracks with the EVOL code (Pignatari et al., this vol.) and with tracks from the Geneva code (Hirschi et al., this vol.) and the Tycho code [18] for massive stars. Within the physics options implemented in these codes we are calibrating the free parameters to obtain the largest possible internal consistency (Fig. 1). Explosion simulations in the SEE database are provided as described in Fryer et al. (this vol.).

One potential problem with the post-processing approach is the need to exactly match nuclear reactions that produce the majority of the nuclear energy in the stellar evolution and post-processing code. We have a special interface in the physics package to either reproduce exactly the same reaction rate source as used in the stellar evolution code, or to introduce the same subroutine with the same interpolation or fit formula evaluation algorithm as used in the stellar evolution calculation. In addition, we save up to ten control abundances that are primarily linked to the energy produc-

[1] USEEPP = Unified Stellar Evolution and Explosion Post-Processing

[2] http://www.hdfgroup.org/HDF5

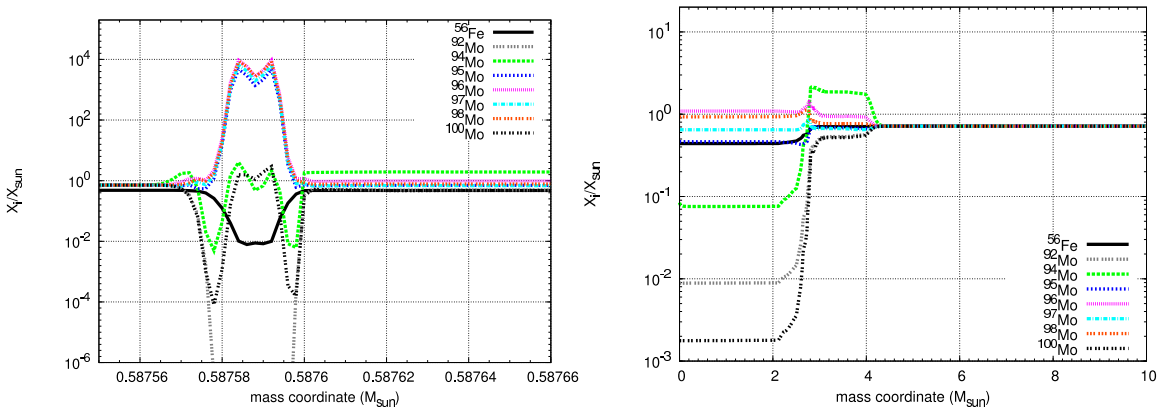

Figure 2: Post-processing results for the Mo isotopes and the s-process seed ^{56}Fe at the end of the interpulse ^{13}C-pocket nucleosynthesis (left) as in Pignatari et al. (this vol.) and in He-core burning in a 15M$_\odot$ model (right) as described in more detail in Hirschi et al. (this vol.)

tion in the USEEPP format, and monitor any differences that may develop between the original and post-processing nucleosynthesis. Another problem may be to correctly map the original stellar evolution or explosion calculation into the post-processing code. Through our USEEPP IO library all thermodynamic and mixing data in all mass zones and all time steps of all tracks are saved, which takes on average 5GB per full stellar evolution track. We are then able to either post-process on the original stellar evolution grid, or accomodate special grid requirements of the nucleosynthesis. Thus, our post-processing approach is accurate with the added benefit of additional grid options, updated nuclear physics and optionally higher-order solvers. The results are as reliable as yields calculated with an extra nucleosynthesis step inlined into the stellar evolution simulations, with a larger network than used for the energy generation feeding into the stellar structure solver [17, 10]. Contrary to the latter approach we can rerun our post-processing with any nuclear phyiscs input at minimal human labour cost. This method is affordable, with a full post-process run of one stellar evolution track sequence (10^5 time steps, ~ 300 pp grid zones) taking 2 days on $\sim 60 \ldots 80$ cores.

We have so far populated the SEE database with both low-mass and massive star tracks (Fig. 1). A major advantage of our approach is the ability to calculate the nucleosynthesis in both regimes with the same MPPNP code and the same nuclear physics data. At solar-like metal content s-process contributions to Mo come from AGB stars. However, as discussed in this volume by Hirschi et al., models of very low metal content with rotation may produce significant amounts of s-process elements between Sr and Ba, including Mo. Fig., 2 demonstrates by example of Mo nucleosynthesis in an AGB and a massive star environment how we will use our NuGrid to investigate nucleosynthesis in a comprehensive and consistent way.

Acknowledgments

FH was supported Marie Curie International Reintegration Grant within the 6$^{\text{th}}$ European Community Framework Programme, grant MIRG-CT-2006-046520. MP ackowledges support through NSF grants PHY 02-16783 (Joint Institute for Nuclear Astrophysics).

References

[1] M. Aikawa, M. Arnould, S. Goriely, A. Jorissen, and K. Takahashi, *BRUSLIB and NETGEN: the Brussels nuclear reaction rate library and nuclear network generator for astrophysics*, A&A **441** (2005), 1195–1203.

[2] C. Angulo, M. Arnould, and Rayet, M. et al., *A compilation of charged-particle induced thermonuclear reaction rates*, Nucl. Phys. **A 656** (1999), 3–183, NACRE compilation.

[3] A. C. Calder, D. M. Townsley, I. R. Seitenzahl, F. Peng, O. E. B. Messer, N. Vladimirova, E. F. Brown, J. W. Truran, and D. Q. Lamb, *Capturing the Fire: Flame Energetics and Neutronization for Type Ia Supernova Simulations*, ApJ **656** (2007), 313–332.

[4] G. R. Caughlan and W. A. Fowler, Atom. Data Nucl. Data Tables **40** (1988), 283, CF88.

[5] I. Dillmann, M. Heil, F. Käppeler, R. Plag, T. Rauscher, and F.-K. Thielemann, *KADoNiS- The Karlsruhe Astrophysical Database of Nucleosynthesis in Stars*, Capture Gamma-Ray Spectroscopy and Related Topics (A. Woehr and A. Aprahamian, eds.), American Institute of Physics Conference Series, vol. 819, March 2006, pp. 123–127.

[6] A. S. Font, K. V. Johnston, J. S. Bullock, and B. E. Robertson, *Chemical Abundance Distributions of Galactic Halos and Their Satellite Systems in a ΛCDM Universe*, ApJ **638** (2006), 585–595.

[7] G. M. Fuller, W. A. Fowler, and M. J. Newman, *Stellar weak interaction rates for intermediate-mass nuclei. IV - Interpolation procedures for rapidly varying lepton capture rates using effective log (ft)-values*, ApJ **293** (1985), 1–16.

[8] F. Herwig, *Evolution and Yields of Extremely Metal-poor Intermediate-Mass Stars*, ApJS **155** (2004), 651–666.

[9] C. Iliadis, J. M. D'Auria, S. Starrfield, W. J. Thompson, and M. Wiescher, *Proton-induced Thermonuclear Reaction Rates for A=20-40 Nuclei*, ApJS **134** (2001), 151.

[10] A. Karakas and J. C. Lattanzio, *Stellar Models and Yields of Asymptotic Giant Branch Stars*, Publications of the Astronomical Society of Australia **24** (2007), 103–117.

[11] P. Marigo, *Chemical yields from low- and intermediate-mass stars: Model predictions and basic observational constraints*, A&A **370** (2001), 194–217.

[12] C. A. Meakin and D. Arnett, *Turbulent Convection in Stellar Interiors. I. Hydrodynamic Simulation*, ApJ **667** (2007), 448–475.

[13] T. Oda, M. Hino, K. Muto, M. Takahara, and K. Sato, *Rate Tables for the Weak Processes of sd-Shell Nuclei in Stellar Matter*, Atomic Data and Nuclear Data Tables **56** (1994), 231–+.

[14] F.-K. Thielemann, M. Arnould, and J.W. Truran, *Reaclib data tables of nuclear reaction rate*, Advances in Nuclear Astrophysics (Gif-sur-Yvette) (E. Vangioni-Flam et al., ed.), Edition Frontières, 1987, p. 525.

[15] F. X. Timmes, *Integration of Nuclear Reaction Networks for Stellar Hydrodynamics*, ApJS **124** (1999), 241–263.

[16] K. A. Venn, M. Irwin, M. D. Shetrone, C. A. Tout, V. Hill, and E. Tolstoy, *Stellar Chemical Signatures and Hierarchical Galaxy Formation*, AJ **128** (2004), 1177–1195.

[17] S.Ẽ. Woosley and T.Ã. Weaver, *The evolution and explosion of massive stars. ii. explosive hydrodynamics and nucleosynthesis*, APJS **101** (1995), 181+.

[18] P. A. Young and D. Arnett, *Observational Tests and Predictive Stellar Evolution. II. Nonstandard Models*, ApJ **618** (2005), 908–918.

PROCEEDINGS OF SCIENCE

Complete nucleosynthesis calculations for low−mass stars from NuGrid

M. Pignatari[*abc], F. Herwig[abd], M. E. Bennett[ad], S. Diehl[aef], C. L. Fryer[af], R. Hirschi[abg], A. Hungerford[af], G. Magkotsios[ach], G. Rockefeller[af], F. X. Timmes[ah], and P. Young[ah]

[a] *The NuGrid Collaboration*
[b] *Astrophysics Group, Keele University, ST5 5BG, UK*
[c] *Joint Institute for Nuclear Astrophysics, University of Notre Dame, IN, 46556, USA*
[d] *Dept. of Physics & Astronomy, Victoria, BC, V8W 3P6, Canada*
[e] *Theoretical Astrophysics Group (T-6), Los Alamos National Laboratory, Los Alamos, NM, 87544, USA*
[f] *Computational Methods (CCS-2), Los Alamos National Laboratory, Los Alamos, NM, 87544, USA*
[g] *IPMU, University of Tokyo, Kashiwa, Chiba 277-8582, Japan*
[h] *School of Earth and Space Exploration, Arizona State University, Tempe, AZ 85287, USA*
E-mail: marco@astro.keele.ac.uk

Many nucleosynthesis and mixing processes of low−mass stars as they evolve from the Main Sequence to the thermal-pulse Asymptotic Giant Branch phase (TP−AGB) are well understood (although of course important physics components, e.g. rotation, magnetic fields, gravity wave mixing, remain poorly known). Nevertheless, in the last years presolar grain measurements with high resolution have presented new puzzling problems and strong constraints on nucleosynthesis processes in stars. The goal of the NuGrid collaboration is to present uniform yields for a large range of masses and metallicities, including low−mass stars and massive stars and their explosions. Here we present the first calculations of stellar evolution and high−resolution, post−processing simulations of an AGB star with an initial mass of 2 $M_{\odot}$ and solar−like metallicity (Z=0.01), based on the post−processing code *PPN*. In particular, we analyze the formation and evolution of the radiative ^{13}C−pocket between the 17th TP and the 18th TP. The *s*-process nucleosynthesis profile of a sample of heavy isotopes is also discussed, before the next convective TP occurrence.

10th Symposium on Nuclei in the Cosmos
July 27 - August 1 2008
Mackinac Island, Michigan, USA

[*] Speaker.

1. Introduction

When He−burning is exhausted in the core, low mass stars (1.5 − 3 $M_{\odot}$) evolve along the AGB. Late on the AGB, recurrent thermal instabilities called Thermal Pulses (TP-AGB phase, [16]) affect shell He−burning history. After TPs (time scale in the order of few hundreds years), the third dredge−up events (TDU) mix He shell material in the envelope, and fresh protons down in the He−intershell. A ^{13}C−pocket is formed in the radiative He intershell phase, where the ^{13}C(α,n)^{16}O neutron source becomes efficient activating slow neutron capture process (s−process, [4]). A marginal contribution is also given by the partial activation of the ^{22}Ne(α,n)^{25}Mg at the bottom of the He intershell (e.g., [8]).
As a result of the TDU enriching the AGB envelope with *s*-process rich material, AGB stars provide most of the s elements beyond Sr observed in the Solar System. In particular, the "main component" between Sr and Pb is produced by solar−like AGB stars, while the "strong component" explaining half of the solar ^{208}Pb is produced by low metallicity AGB stars ([2], and references therein). Carbon is also dredged-up with s elements in the envelope, and eventually the AGB star may become a C-rich star (C(N) star), meaning that carbon is more abundant than oxygen in the envelope.
Spectroscopic observations and composition measurements in presolar grains formed in AGB stars confirm this scenario ([5],[12] ,respectively), and provide important insight to study and understand those stars in more details. In particular, presolar grains carry the isotopic and chemical signature of their parent stars (e.g., [18],[12], [3]), providing a powerful tool to test and constrain stellar models and nuclear physics inputs. The *NuGrid* project (see also Herwig et al. in this volume) has the goal to generate uniform yields for a large range of masses and metallicities also for low−mass stars, and to constrain them with observations. In this proceeding we present the first calculations of stellar evolution and high-resolution, post-processing simulations of a 2 $M_{\odot}$ Z = 0.01 AGB star, based on the post−processing code *PPN*.

2. Post−processing calculations

The main input parameters for the post-processing calculations are given by a 2 $M_{\odot}$ and Z = 0.01 star (EVOL Code, e.g., [10]). The stellar model has been calculated assuming an overshoot parameter f = 0.128 at the bottom of the envelope and f = 0.008 for all the other convective boundaries. The f applied at the base of the convective TP in the He shell (f = 0.008) has been constrained to explain the He/C/O ratio observed in H deficient post-AGB stars of type PG1159 and in WC central stars of planetary nebulae ([17]). The higher overshoot parameter at the bottom of the envelope is calibrated to reproduce the mass of the ^{13}C-pocket needed to reproduce the observed overabundance of *s*-process elements [13]. The post-processing code *PPN* is described in Herwig et al. (this vol.) and includes dynamically all species from H to Bi. Concerning the simulations shown in this proceeding, from the physics package in *PPN* we selected [1] (NACRE compilation) for the main charged particle reactions, [6] (Kadonis compilation) for neutron capture reactions and [15] for unstable isotopes not included in the Kadonis network. We selected [14] and [7] (or terrestrial rates if not available in the previous references) for stellar β-decay rates of light unstable isotopes, and [9] (or terrestrial rates if not available) for β-decay rates of heavy

unstable isotopes (see also Herwig et al. in this volume for more details about the physics package).

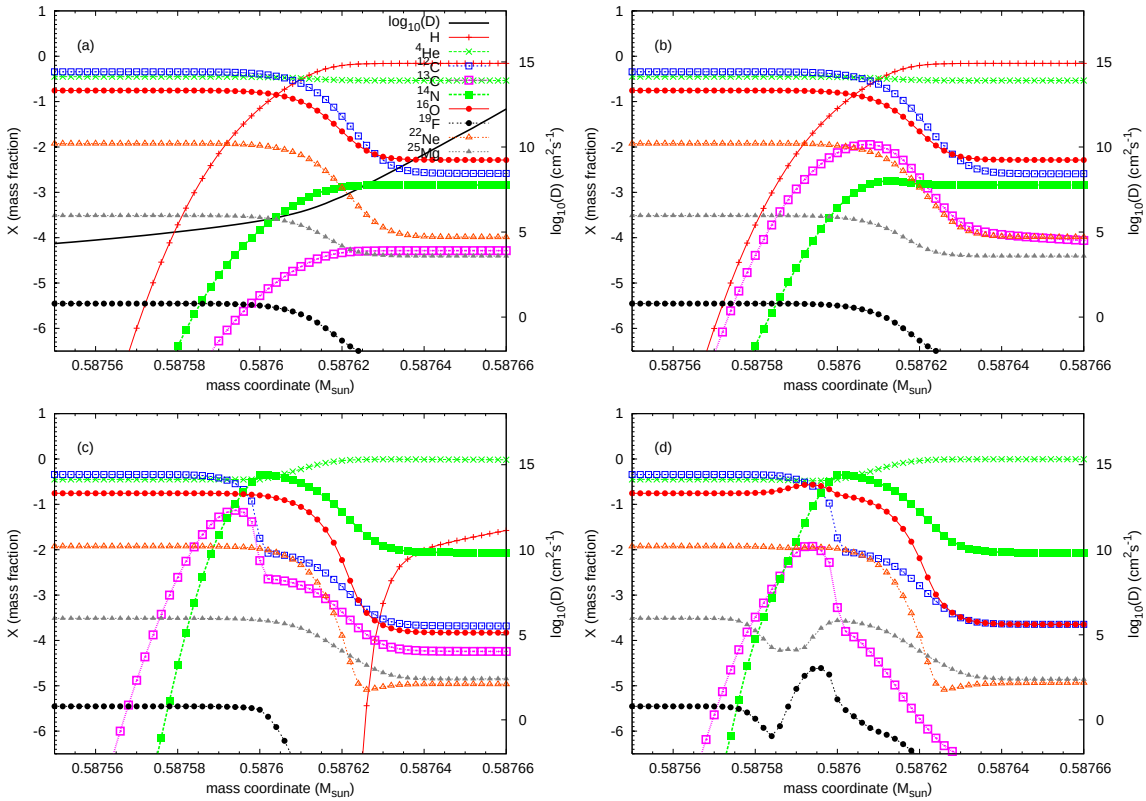

Figure 1: Panel (a,b,c,d): Formation and evolution of the ^{13}C-pocket after the 17th TP for the 2 $M_{\odot}$ Z = 0.01 star. The profile for the mixing coefficient D (it is different from zero only in Panel (a)) and for a sample of light isotopes is provided.

In Fig. 1 we show the formation and evolution of the ^{13}C-pocket between the 17th TP and the 18th TP (interpulse phase of about 70000 yr). In Panel (a) the TDU mixes down in the He intershell protons and envelope material, before the re-activation of the H shell. In Panel (b) the abundant ^{12}C is efficiently capturing protons producing ^{13}C in radiative conditions via the nucleosynthesis channel ^{12}C(p,γ)^{13}N(β^+)^{13}C (e.g., [8]). At the ^{13}C abundance peak, also ^{14}N starts to be produced by the proton capture channel ^{13}C(p,γ)^{14}N. In Panel (c) the ^{13}C-pocket final shape is shown, since protons are fully consumed. The pocket size is $1-2\times10^{-5}$ $M_{\odot}$. Moving outward, a prominent ^{14}N-

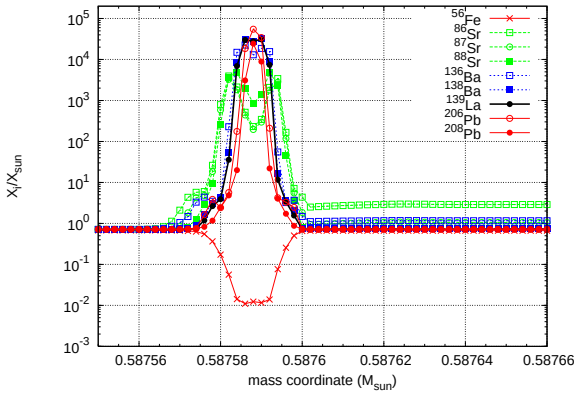

Figure 2: The overabundances of a sample of heavy isotopes has been reported (among them the s-only isotopes ^{86,87}Sr, ^{136}Ba and ^{206}Pb), at the same time-step of Fig. 1, Panel (d).

pocket is formed just after the ^{13}C-pocket, as expected. After about 40000 years, the temperature in the ^{13}C-pocket is high enough to efficiently activate the ^{13}C(α,n)^{16}O reaction, producing neutrons for the *s* process. In Panel (d) we show the ^{13}C-pocket region once ^{13}C has been burnt and the *s* process is not anymore efficient. ^{25}Mg is the main neutron poison in the ^{13}C-pocket, and it has been partially depleted by the neutron flux. In the ^{14}N-pocket, instead, as it is well known ^{14}N(n,p)^{14}C is the main neutron poison and the neutron capture efficiency of ^{25}Mg (and of the main *s*-process seed ^{56}Fe) quickly decreases with increasing the ^{14}N abundance. The final ^{19}F abundance profile basically follows the ^{13}C profile. If ^{13}C is more abundant than ^{14}N, then ^{19}F is depleted by neutron capture and by α capture. In case ^{14}N is more abundant than ^{13}C, ^{19}F can be produced starting from ^{14}N [11].
Finally, in Fig. 2, we report the final overabundance profile in the ^{13}C-pocket region for a sample of isotopes at the Sr neutron magic peak (^{86,87,88}Sr), at the Ba neutron magic peak (^{136,138}Ba, ^{139}La) and at the Pb neutron magic peak (^{206,208}Ba). The *ls* peak species (e.g. Sr, [5]) show a maximum of overproduction of about 5×10^3, while the *hs* peak (e.g. Ba) and the Pb peak show an overproduction of about few 10^4. Sr isotopes show a double peak in coincidence of the ^{56}Fe depletion tails. At 0.58758 $M_\odot$ the ^{13}C abundance is rapidly decreasing and as a consequence a lower amount of neutrons are produced. On the other hand, at 0.587595 $M_\odot$ the poisoning effect of ^{14}N is increasing, until the ^{56}Fe neutron capture efficiency is negligible. The Ba peak and the Pb peak are more produced in the center of the ^{13}C-pocket, where lighter Sr peak elements are feeding *s* nucleosynthesis of heavier elements. The next convective TP will mix the *s*-process rich pocket in all the He intershell, which will be partially dredged up in the envelope by the next TDU event.

The analysis presented Fig. 1 and in Fig. 2 shows part of the capabilities of the *PPN* post-processing code applied to AGB nucleosynthesis calculations. At present, we may calculate the abundances from H to Bi (including isotopic ratios) at any position and at any time in a complete stellar track. Furthermore, in the nuclear network every reaction rate may be automatically chosen between different nuclear sources, or a multiplication factor can be applied or the reaction may be not considered. This opens up possibilities to systematically take into account the effect of nuclear reaction rate uncertainties in our nucleosynthesis calculations.

Acknowledgments

M.P. acknowledges support through NSF grants PHY 02-16783 (JINA). M.P. and F.H. were supported by a Marie Curie International Reintegration Grant MIRG-CT-2006-046520 within the European FP6.

References

[1] C. Angulo, M. Arnould, M. Rayet, P. Descouvemont, D. Baye, C. Leclercq-Willain, A. Coc, S. Barhoumi, P. Aguer, C. Rolfs, R. Kunz, J. W. Hammer, A. Mayer, T. Paradellis, S. Kossionides, C. Chronidou, K. Spyrou, S. Degl'Innocenti, G. Fiorentini, B. Ricci, S. Zavatarelli, C. Providencia, H. Wolters, J. Soares, C. Grama, J. Rahighi, A. Shotter, and M. Lamehi Rachti, *A compilation of charged-particle induced thermonuclear reaction rates.*, Nuclear Physics A **656** (1999), 3–183.

[2] C. Arlandini, F. Käppeler, K. Wisshak, R. Gallino, M. Lugaro, M. Busso, and O. Straniero, *Neutron Capture in Low-Mass Asymptotic Giant Branch Stars: Cross Sections and Abundance Signatures*, ApJ**525** (1999), 886–900.

[3] J. G. Barzyk, M. R. Savina, A. M. Davis, R. Gallino, M. J. Pellin, R. S. Lewis, S. Amari, and R. N. Clayton, *Multi-element isotopic analysis of single presolar SiC grains*, New Astronomy Review **50** (2006), 587–590.

[4] E. M. Burbidge, G. R. Burbidge, W. A. Fowler, and F. Hoyle, *Synthesis of the Elements in Stars*, Reviews of Modern Physics **29** (1957), 547–650.

[5] M. Busso, R. Gallino, D. L. Lambert, C. Travaglio, and V. V. Smith, *Nucleosynthesis and Mixing on the Asymptotic Giant Branch. III. Predicted and Observed s-Process Abundances*, ApJ**557** (2001), 802–821.

[6] I. Dillmann, R. Plag, M. Heil, F. Käppeler, and T. Rauscher, *Present status of the KADoNiS database*, International Symposium on Nuclear Astrophysics - Nuclei in the Cosmos, 2006.

[7] G. M. Fuller, W. A. Fowler, and M. J. Newman, *Stellar weak interaction rates for intermediate-mass nuclei. IV - Interpolation procedures for rapidly varying lepton capture rates using effective log (ft)-values*, ApJ**293** (1985), 1–16.

[8] R. Gallino, C. Arlandini, M. Busso, M. Lugaro, C. Travaglio, O. Straniero, A. Chieffi, and M. Limongi, *Evolution and Nucleosynthesis in Low-Mass Asymptotic Giant Branch Stars. II. Neutron Capture and the s-Process*, ApJ**497** (1998), 388–+.

[9] S. Goriely, *Uncertainties in the solar system r-abundance distribution*, A&A**342** (1999), 881–891.

[10] F. Herwig, S. M. Austin, and J. C. Lattanzio, *Nuclear reaction rate uncertainties and astrophysical modeling: Carbon yields from low-mass giants*, Phys. Rev. C**73** (2006), no. 2, 025802–+.

[11] A. Jorissen, V. V. Smith, and D. L. Lambert, *Fluorine in red giant stars - Evidence for nucleosynthesis*, A&A**261** (1992), 164–187.

[12] M. Lugaro, A. M. Davis, R. Gallino, M. J. Pellin, O. Straniero, and F. Käppeler, *Isotopic Compositions of Strontium, Zirconium, Molybdenum, and Barium in Single Presolar SiC Grains and Asymptotic Giant Branch Stars*, ApJ**593** (2003), 486–508.

[13] M. Lugaro, F. Herwig, J. C. Lattanzio, R. Gallino, and O. Straniero, *s-Process Nucleosynthesis in Asymptotic Giant Branch Stars: A Test for Stellar Evolution*, ApJ**586** (2003), 1305–1319.

[14] T. Oda, M. Hino, K. Muto, M. Takahara, and K. Sato, *Rate Tables for the Weak Processes of sd-Shell Nuclei in Stellar Matter*, Atomic Data and Nuclear Data Tables **56** (1994), 231–+.

[15] T. Rauscher and F.-K. Thielemann, *Astrophysical Reaction Rates From Statistical Model Calculations*, Atomic Data and Nuclear Data Tables **75** (2000), 1–2.

[16] M. Schwarzschild and R. Härm, *Thermal Instability in Non-Degenerate Stars.*, ApJ**142** (1965), 855.

[17] K. Werner and F. Herwig, *The Elemental Abundances in Bare Planetary Nebula Central Stars and the Shell Burning in AGB Stars*, PASP**118** (2006), 183–204.

[18] E. Zinner, *Stellar Nucleosynthesis and the Isotopic Composition of Presolar Grains from Primitive Meteorites*, Annual Review of Earth and Planetary Sciences **26** (1998), 147–188.

The Astrophysical Journal, 727:89 (15pp), 2011 February 1 doi:10.1088/0004-637X/727/2/89

CONVECTIVE–REACTIVE PROTON–^{12}C COMBUSTION IN SAKURAI'S OBJECT (V4334 SAGITTARII) AND IMPLICATIONS FOR THE EVOLUTION AND YIELDS FROM THE FIRST GENERATIONS OF STARS

Falk Herwig[1,10], Marco Pignatari[1,2,3,10], Paul R. Woodward[4], David H. Porter[5], Gabriel Rockefeller[6,7,10], Chris L. Fryer[6,7,10], Michael Bennett[8,10], and Raphael Hirschi[8,9,10]
[1] Department of Physics & Astronomy, University of Victoria, Victoria, BC V8P5C2, Canada; fherwig@uvic.ca
[2] Joint Institute for Nuclear Astrophysics, University of Notre Dame, Notre Dame, IN 46556, USA
[3] TRIUMF, 4004 Wesbrook Mall, Vancouver, BC V6T2A3, Canada
[4] LCSE & Department of Astronomy, University of Minnesota, Minneapolis, MN 55455, USA
[5] Minnesota Supercomputing Institute, University of Minnesota, MN, USA
[6] Computational Computer Science Division, Los Alamos National Laboratory, Los Alamos, NM 87545, USA
[7] Physics Department, University of Arizona, Tucson, AZ 85721, USA
[8] Astrophysics group, Keele University, Lennard-Jones Lab., Keele, ST55BG, UK
[9] Institute for the Physics and Mathematics of the Universe, University of Tokyo, 5-1-5 Kashiwanoha, Kashiwa 277-8583, Japan
Received 2010 February 6; accepted 2010 August 18; published 2011 January 7

ABSTRACT

Depending on mass and metallicity as well as evolutionary phase, stars occasionally experience convective–reactive nucleosynthesis episodes. We specifically investigate the situation when nucleosynthetically unprocessed, H-rich material is convectively mixed with an He-burning zone, for example in a convectively unstable shell on top of electron-degenerate cores in asymptotic giant branch stars, young white dwarfs, or X-ray bursting neutron stars. Such episodes are frequently encountered in stellar evolution models of stars of extremely low or zero metal content, such as the first stars. We have carried out detailed nucleosynthesis simulations based on stellar evolution models and informed by hydrodynamic simulations. We focus on the convective–reactive episode in the very late thermal pulse star Sakurai's object (V4334 Sagittarii). Asplund et al. determined the abundances of 28 elements, many of which are highly non-solar, ranging from H, He, and Li all the way to Ba and La, plus the C isotopic ratio. Our simulations show that the mixing evolution according to standard, one-dimensional stellar evolution models implies neutron densities in the He intershell ($\lesssim$ few 10^{11} cm^{-3}) that are too low to obtain a significant neutron capture nucleosynthesis on the heavy elements. We have carried out three-dimensional hydrodynamic He-shell flash convection simulations in 4π geometry to study the entrainment of H-rich material. Guided by these simulations we assume that the ingestion process of H into the He-shell convection zone leads only after some delay time to a sufficient entropy barrier that splits the convection zone into the original one driven by He burning and a new one driven by the rapid burning of ingested H. By making such mixing assumptions that are motivated by our hydrodynamic simulations we obtain significantly higher neutron densities ($\sim$ few 10^{15} cm^{-3}) and reproduce the key observed abundance trends found in Sakurai's object. These include an overproduction of Rb, Sr, and Y by about two orders of magnitude higher than the overproduction of Ba and La. Such a peculiar nucleosynthesis signature is impossible to obtain with the mixing predictions in our one-dimensional stellar evolution models. The simulated Li abundance and the isotopic ratio ^{12}C/^{13}C are as well in agreement with observations. Details of the observed heavy element abundances can be used as a sensitive diagnostic tool for the neutron density, for the neutron exposure and, in general, for the physics of the convective–reactive phases in stellar evolution. For example, the high elemental ratio Sc/Ca and the high Sc production indicate high neutron densities. The diagnostic value of such abundance markers depends on uncertain nuclear physics input. We determine how our results depend on uncertainties of nuclear reaction rates, for example for the ^{13}C(α, n)^{16}O reaction.

Key words: stars: abundances – stars: AGB and post-AGB – stars: evolution – stars: individual (V4334 Sagittarii) – stars: interiors – hydrodynamics – nuclear reactions, nucleosynthesis, abundances

Online-only material: color figures

1. INTRODUCTION

1.1. Convective–Reactive Phases of Stellar Evolution

In stellar evolution the nuclear timescale is usually much larger than the convective mixing timescale. However, this is not always the case. An example of stellar nucleosynthesis where nuclear reactions and convective mixing occurs on the same timescale are slow neutron capture process branchings (*s* process, Burbidge et al. 1957; Wallerstein et al. 1997) in He-shell flash convection of asymptotic giant branch (AGB) stars, such as the branching at ^{128}I (Reifarth et al. 2004). This situation is comparatively simple to simulate as the rapid nuclear reaction in question, the double-decay of ^{128}I, does not release any significant amount of energy. A post-processing approach of the standard stellar evolution calculation with some one-dimensional treatment of convection, like mixing-length theory (MLT), with time-dependent mixing gives a reasonable approximation of this situation.[11]

[10] NuGrid Collaboration.

[11] Although even in this case multi-dimensional effects of convection have to be taken into account eventually as simulations by Herwig et al. (2006) indicate that the velocity profile at the bottom of the convective shell is flatter compared to the MLT prediction.

The goal of this paper is instead to investigate the situation when rapid nuclear reactions are indeed releasing amounts of energy that are likely to affect the fluid flow, as, for example, in the case of proton capture of ^{12}C in convective He burning. In the fluid dynamics community this mixing regime is sometimes referred to as level-3 mixing, where the flow is altered by attendant changes in the fluid (Dimotakis 2005). We refer to these situations as reactive–convective phases in order to emphasize the fact that the timescales of highly exothermic nuclear reaction and the convective fluid flow timescales are of the same order.

The ratio of the mixing timescale and the reaction timescale is called the Damköhler number:

$$D_\alpha = \frac{\tau_{\rm mix}}{\tau_{\rm react}} \ . \quad (1)$$

MLT is concerned with averaged properties both in time over many convective turnovers and in space over the order of a pressure scale height. In the categories of Dimotakis (2005) diffusion coefficients derived from MLT may describe level-1 mixing (while mixing induced by rotation involves flow dynamics that are altered by mixing processes and labeled in this scheme as level-2 mixing). Therefore, time-dependent mixing through a diffusion algorithm with diffusion coefficients derived from MLT is appropriate for regimes with $D_\alpha \ll 1$. The difficulty of simulating convective–reactive phases in present one-dimensional stellar evolution codes then appears as the inability of MLT (or any similar convection theory) to properly account for the additional dynamic effects introduced through rapid and dynamically relevant nuclear energy release in level-3 mixing associated with Damköhler numbers $D_\alpha \approx 1$.

Convective–reactive episodes can be encountered in numerous phases of stellar evolution, including the He-shell flash of AGB stars of extremely low metal content (e.g., Fujimoto et al. 2000; Suda et al. 2004; Iwamoto et al. 2004; Cristallo et al. 2009), metallicity low-mass stars (e.g., Hollowell et al. 1990; Schlattl et al. 2002; Campbell & Lattanzio 2008), young white dwarfs of solar metallicity (e.g., Iben et al. 1983; Herwig et al. 1999; Lawlor & MacDonald 2003), both rotating and non-rotating Pop III massive stars (Ekström et al. 2008), and more in general, in low metallicity massive stars (Woosley & Weaver 1995). These combustion events are encountered as well in X-ray burst calculations of accreting neutron stars (Woosley et al. 2004; Piro & Bildsten 2007), and accreting white dwarfs (Cassisi et al. 1998) that may be the progenitors of SNe Ia. Convective–reactive events have been found in post red giant branch (post-RGB) stellar evolution models and associated with the horizontal branch anomalies in certain globular clusters (Brown et al. 2001; Miller Bertolami et al. 2008). Finally, again in AGB stars, convective–reactive phases can be found in hot dredge-up (Herwig 2004; Goriely & Siess 2004; Woodward et al. 2008a), a phenomenon that is associated with the treatment of convective boundaries, generally in more massive and lower metallicity AGB stars.

Although convective–reactive phases are quite common in stellar evolution, in particular in the early, low-metellicity universe, we do not currently have a reliable and accurate way of simulating them. In this work, we discuss the case of the He-shell flash with H ingestion in a very late (post-AGB) thermal pulse at solar metallicity. This situation is extremely similar to H ingestion associated with the He-shell flash in AGB stars at extremely low metallicity. The one-dimensional, spherically symmetric stellar evolution approximation is not very realistic in this case, because both the entrainment of H into the He-shell flash convection zone and the subsequent convective transport, mixing, and nuclear burning of hydrogen enriched fluid parcels are inherently a three-dimensional hydrodynamic process. The energy from proton captures by ^{12}C via the ^{12}C$(p,\gamma)^{13}$N reactions is released on the same timescale ($\sim$1–10 minutes for $T = 1.3$–1.05×10^8 K) of the fluid flow of convection (Appendix B), and this energy will add entropy to fluid elements and in turn feed back into the hydrodynamics (Herwig 2001). These highly coupled, multi-dimensional processes are approximated through the MLT, complemented with a time-dependent mixing algorithm. This assumption may not be realistic in the present case (see Sections 3.2 and 4.2).

1.2. Post-AGB Flash Star Sakurai's Object and its Observed Abundance Properties

Sakurai's object is a very late thermal pulse (VLTP) post-AGB object (Duerbeck et al. 2000, and references therein) and has experienced a H-ingestion flash in 1994. The star's observed abundance signatures are highly non-solar, and very unusual for a post-AGB low-mass star (Section 3.2). Nevertheless, there is wide agreement in the literature that the object's distance is 2–5 kpc and that it has a mass of around 0.6 $M_\odot$ (van Hoof et al. 2007, and references therein), pointing to a low-mass star progenitor. Moreover, the high abundance of Li requires the existence of ^{3}He in the envelope (Herwig & Langer 2001), pointing again to a low-mass star progenitor that was not affected by hot bottom burning (HBB). Indeed, HBB occurs at solar metallicity for stars with $M_{\rm ZAMS} \gtrsim 4\,M_\odot$ and destroys ^{3}He in the AGB envelope (Scalo et al. 1975). Another process that could affect the evolution of ^{3}He during the progenitor evolution of Sakurai's object is extra-mixing below the convective envelope during either the RGB or AGB (e.g., Wasserburg et al. 1995; Charbonnel & Zahn 2007; Denissenkov 2010). Sakurai's object potentially serves as an important constraint for theories of such mixing because the observed Li abundance increase during the observations in 1996 as reported by Asplund et al. (1999) can only be modeled in the VLTP if significant amounts of ^{3}He are still present in the envelope at the beginning of the post-AGB evolution.

The light curve of this object was closely monitored as it evolved within approximately 2 yr from the pre-WD location in the HRD back to the AGB location, a much shorter evolution timescale than previously predicted (Herwig et al. 1999). A possible explanation of such a fast born-again evolution of Sakurai's object is that the convective mixing efficiency in the He-shell flash convection zone is smaller by a factor of $\sim$30 compared to the MLT predictions in standard one-dimensional stellar models (Herwig 2001). This modification is motivated by the reasoning that in the convective–reactive regime the fluid flow would be eventually strongly affected by the energy released rapidly on a timescale comparable to the fluid flow velocity. This process, indeed, would locally add buoyancy to the fluid element causing a behavior that is not reflected in the MLT.

Miller Bertolami et al. (2006) have presented a more detailed investigation and emphasize the importance of appropriate time resolution. In addition, they studied the role of overshooting and μ-gradients. Their simulations with exponential, depth-dependent overshooting agree better with observations than tracks computed without any overshooting. μ-gradients appear to have only secondary effects. Confirming the mass dependence of the proton-ingestion born-again evolution first reported by

Table 1
Observed Neutron Capture Signature, Asplund et al. (1999)

[Fe/H] = 0 (−0.63)	1996 April	1996 October
[Y/Fe]	+0.96 (+1.59)	+1.96 (+2.59)
[Ba/Fe]	−0.63 (0.0)	−0.23 (+0.40)
[Ba/Y]	−1.59 (−1.59)	−2.19 (−2.19)

Herwig (2001), Miller Bertolami & Althaus (2007) point out that the initial return light curve of Sakurai's object could be reproduced with a slightly lower mass model than the 0.604 $M_{\odot}$ adopted by Herwig (2001), a high time resolution and their alternative description of convective transport. However, the second heating phase into which Sakurai's object has entered now (van Hoof et al. 2007) seems to be in better agreement with the modified convection models proposed by Herwig (2001).

While the light curve of Sakurai's object has certainly raised doubts about the capability of one-dimensional stellar evolution calculations to reproduce its evolution, in this work we show that the abundance determinations by Asplund et al. (1999) pose a much more stringent constraint on the physics of convective–reactive phases. Asplund et al. determined 28 elemental abundances at four times between 1996 April and October, when the star had cooled to below 8000 K. In particular, among light elements a significant enhancement (at least 0.5 dex) with respect to the solar abundance has been observed for Li, Ne, and P. Beyond iron, Cu, Zn, Rb, and Sr peak elements are significantly enhanced. In addition, there are trends as a function of time that are smaller than the differences to solar. However, for this initial analysis which is not yet based on full hydrodynamic simulations with nuclear burn, we will not discuss those trends in detail.

A few preliminary comments on individual elements may be in order. The observed Li is clearly produced above the meteoritic value. Herwig & Langer (2001) proposed that together with protons ^{3}He is ingested into the He-shell flash convection zone, providing the fuel to produce Li via the reaction chain $^{3}\mathrm{He}(\alpha,\gamma)^{7}\mathrm{Be}(\beta^{+})^{7}\mathrm{Li}$. The first *s*-process peak elements are enhanced by up to 2 dex while Ba and La are not enhanced, causing a ratio of Ba peak to Sr peak elements that is much lower than expected from models and observations of AGB stars (Busso et al. 2001). We can translate the abundances observed by Asplund et al. (1999) into the ratio of the two *s*-process indicator indices *hs* and *ls*. An *s*-process index $s/s_{\odot}$ is the overproduction factor of a group of *s*-process elements with respect to the initial solar value. The index ratio [hs/ls] = [hs/Fe] − [ls/Fe] monitors the distribution of the *s*-process elements, and it is an intrinsic index of the neutron capture nucleosynthesis on heavy elements (Luck & Bond 1991). We have used [ls/Fe] = $\frac{1}{3}$([Sr/Fe]+[Y/Fe]+[Zr/Fe]) and [hs/Fe] = $\frac{1}{2}$([Ba/Fe]+[La/Fe]), where square brackets indicate the logarithmic ratio with respect to the solar ratio (Table 1). For Asplund's October measurements the indices are [hs/Fe]= 0.05 and [ls/Fe]= 1.9, assuming that [Fe/H]= 0.0 for Sakurai's object. We record measurements of ±0.2–0.3 dex as the average approximate index ratio [hs/ls] ∼ − 2 at the end of the observed period. In Figure 1, we compare such ratio with *s*-process theoretical predictions and stellar observations of low-mass AGB stars, which are the progenitor population of the Sakurai's object. In particular, we show that the observed [hs/ls] is a factor of 10 or more lower than in typical AGB stars. Therefore, the nucleosynthesis environment that has generated the abundances observed by Asplund et al. was very different from that encountered in the previous AGB

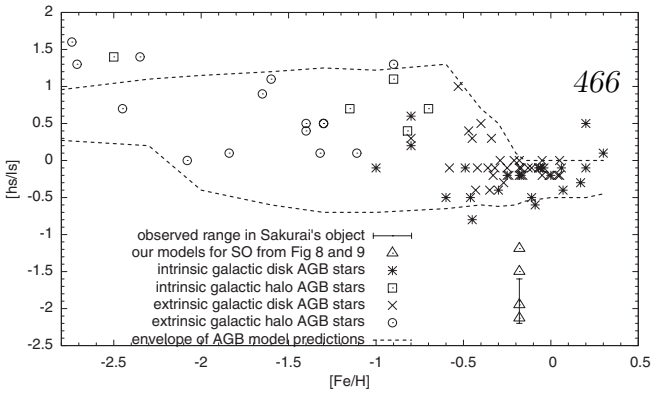

Figure 1. Observed and predicted *s*-process abundance distribution index ratio [hs/ls] for stars with a large range of metallicities. Observations (Tech 1971; Smith 1984; Smith & Lambert 1984, 1985, 1986; Smith & Suntzeff 1987; Smith & Lambert 1990; Smith et al. 1993, 1996, 1997; Abia & Wallerstein 1998; Van Winckel & Reyniers 2000; Zacs et al. 1995, 1998; Začs et al. 2000; Reddy et al. 1999; Kipper et al. 1996; Kipper & Jorgensen 1994; Tomkin & Lambert 1983, 1986; Kovacs 1985; Vanture 1992; A. D. Vanture 2000, private communication; Pereira et al. 1998; Aoki et al. 2000; McWilliam et al. 1995; McWilliam 1998; Norris et al. 1997; Beveridge & Sneden 1994) and model predictions of AGB stars are from Busso et al. (2001). In the figure, the [hs/ls] ratio observations of the Sakurai's object have a certain range, depending on which of the four observations from Asplund et al. are considered, and how the indices are calculated. In general, the ratio is about 2 dex smaller compared to AGB predictions and observations. Our nucleosynthesis results are also included for comparison (see Section 5 for details).

phase. In Figure 1 we also include [hs/ls] from our nucleosynthesis calculations presented in this paper, which successfully reproduce the same ratio measured in the Sakurai's object. Such calculations will be discussed in detail in Section 5.

The abundance pattern of Sakurai's object further distinguishes itself from the AGB stars through the significantly enhanced P, Cu, and Zn. These elements are not usually produced in low-mass stars. Several other elements are reduced, i.e., S, Ti, Cr, and Fe. In particular, Fe is expected to be depleted, since it is the seed for *n*-capture nucleosynthesis. All these abundance signatures appear to be the result of an *n*-capture burst of large *n*-density. Another important feature is the C isotopic ratio $^{12}\mathrm{C}/^{13}\mathrm{C} \sim 3$–4, where the large ^{13}C abundance results from the $^{12}\mathrm{C}(p,\gamma)^{13}\mathrm{N}(\beta^{+})^{13}\mathrm{C}$ reaction channel. ^{13}C is also the main neutron source during the H-ingestion event, which causes the peculiar abundance signature observed by Asplund et al. (see Section 5 for details).

In the following, we will briefly describe the tools we use in this investigation (Section 2) and defer more details to an appendix (Appendix A). Next, we describe the stellar evolution picture of Sakurai's object and show how nucleosynthesis simulations based directly on the output of one-dimensional stellar evolution calculations fail to account for the observed abundance patterns (Section 3). Then, we describe hydrodynamic simulations of entrainment into He-shell flash convection that motivate our modified mixing assumptions (Section 4). We will show how corresponding nucleosynthesis simulations account for the observed abundances, and we discuss the influence of nuclear reaction rate uncertainty (Section 5). The paper ends with a summary and some remarks on implications for the nucleosynthesis in the first generations of stars, including the light-element primary process (LEPP; Section 6). In Appendix A we give additional information on the codes we have used, and in Appendix B we discuss timescales for burning and mixing.

2. SIMULATION CODES

Three different types of simulation codes have been used in this work:

1. a stellar evolution code (EVOL), providing one-dimensional stellar evolution up to the post-AGB and thermodynamic structures for the beginning of the post-AGB He-shell flash event, also known as the VLTP;
2. a multi-zone post-processing nucleosynthesis code (PPN) with complete nuclear network and mixing;
3. a multi-dimensional-hydrodynamical code (PPM) to study how hydrogen is ingested during the VLTP.

We have used the stellar evolution code EVOL to calculate the global evolution of post-AGB stars (Section 3.1) experiencing a VLTP (Blöcker 1995; Herwig 2000; Herwig & Austin 2004). The assumptions and input physics choices are very similar to those in Herwig (2001). Furthermore, we have used structures from the last thermal pulse of the AGB model by Herwig & Austin (2004), and of the VLTP model by Herwig et al. (1999).

For the detailed nucleosynthesis simulations (Sections 3.2 and 5) we have used the PPN code (Herwig et al. 2008). This code allows us to calculate the complete nucleosynthesis along the radial profile of a star according to the structure input from a stellar evolution model in as many zones as required. Nuclear burn steps are alternated with time-dependent mixing steps. Details, including the nuclear physics data information, are given in Appendix A.1.

In order to investigate the hydrodynamic behavior of unprocessed H-rich material entrained into the He-shell flash convection (Section 4), we used Woodward's PPM gas dynamics code with the PPB advection scheme on a Cartesian grid (Woodward et al. 2003, 2007, 2008b). For important code details, see Appendix A.2.

3. THE STELLAR EVOLUTION PICTURE

3.1. Global Stellar Evolution Scenario and Calculation

The VLTP evolution scenario involves a He-shell flash on a single young white dwarf after the end of H-shell burning when the evolution track has just entered the white dwarf cooling curve in the HRD, as, for example, shown in Herwig et al. (1999), and in more detail in Section 3.2.1 of Miller Bertolami et al. (2006). It involves the convective ingestion of all or parts of the small ($\sim 10^{-4}\,M_{\odot}$) remaining unprocessed, and thus H-rich, envelope into the hot ($T = 1$–3×10^{8} K) He-burning flash layers. This He-burning convection zone contains a mass fraction of 20%–40% (depending on convective model assumptions; Herwig 2000; Miller Bertolami et al. 2006) of primary ^{12}C. Protons are rapidly captured by the abundant ^{12}C, on the timescale of convective fluid flows of approximately 5–10 minutes.

The progenitor is a low-mass AGB star for which *s*-process element enhancements are expected at the Sr–Y–Zr peak and at the Ba peak (e.g., Busso et al. 2001). The elements signature observed in Sakurai's object is not typical of the *s*-process in AGB stars. Indeed, according to the observations by Asplund et al. (1999), the ratio of the second peak to the first peak *s*-process elements is [Ba/Y] ~ -2, in contrast to the expected AGB stars ratio $-1 <$ [hs/ls] < 1 at solar-like metallicity (e.g., Busso et al. 2001). This result does not change if we assume a lower than solar metallicity for Sakurai's object of [Fe/H] $= -0.63$ (values between brackets in Table1). Such a choice may be indicated by the sub-solar observed Ba abundance, and indeed, the Ba and La abundance even lead us to assume that there was no significant *s*-process contribution in the previous AGB phase at all.

In any case, the peculiar abundance signatures of Sakurai's object has to originate in the H-ingestion event of the VLTP, and cannot be explained in terms of any nucleosynthesis during the AGB progenitor evolution.

The initial abundance distribution for our post-AGB He-shell flash nucleosynthesis simulations is a combination of light elements (with A < 23) from the intershell abundance of an AGB star at the end of the evolution taken from a $2\,M_{\odot}$ simulation similar to those in Herwig & Austin (2004), and heavier species according to Asplund et al. (2005) with the isotopic ratios from Lodders (2003) scaled to metallicity [Fe/H] $= -0.18$.

The intershell abundances that matter for our simulations are mostly primary He-burning products, so details of the initial abundance are not important. The choice of more recent solar abundances (Asplund et al. 2009; Lodders et al. 2009) would not modify the results presented in this paper.

In the following section, we will discuss the nucleosynthesis according to one-dimensional stellar evolution mixing predictions of the VLTP.

3.2. Nucleosynthesis According to the Stellar Evolution Model

Figure 2 shows the H profile from stellar evolution in the initial phase of the H-ingestion phase for a model like those in Herwig (2001), recalculated with $f_{\rm v} = 30$ and higher time resolution. The proton abundance at any location is the result of mixing and simultaneous burning. The two times correspond to panels (A) and (B) in Figure 4 in Miller Bertolami et al. (2006) and the account of events given in their Section 3.2.1 applies here as well.

At time t_0 the He-shell flash convection zone is about to make contact with the H-rich layers above. The H profile at $m_{\rm r} \sim 0.6042\,M_{\odot}$ is the burning profile of the now extinct H shell. During the late phase of the post-AGB evolution, basically past the "knee" in the HRD, the H shell is inactive, and the He-shell convection can grow into the H-rich layers and mix those protons (and ^{3}He) down into the ^{12}C-rich He-shell flash convection zone. As H is mixed into deeper and hotter regions its lifetime against capture by ^{12}C decreases because the rate of the nuclear reaction ^{12}C$(p,\gamma)^{13}$N increases strongly with temperature. At some depth, in our simulation at $m_{\rm r} = 0.6005\,M_{\odot}$, the mixing timescale equals the nuclear timescale (Damköhler number $Da \sim 1$, Section 1.1) and protons are now reacting rapidly with ^{12}C, thereby releasing for a brief period more energy than the He-shell that is initially driving the flash.

In the stellar evolution simulation we treat time-dependent mixing mathematically as a diffusion process. It is implicitly assumed that on spheres the H abundance is exactly homogeneous, and that the radial mixing efficiency based on the radial mean convective velocity is also exactly homogeneous. This assumption in combination with the strong temperature sensitivity of the p-capture reaction causes the stellar evolution code to predict the shell of peak H-burning energy release to be extremely thin. In the stellar evolution code an entropy step develops that separates the H-ingestion top convection from the He-shell flash convection underneath. A thin radiative zone formally prohibits mixing between the two convection zones. It shows up as a break in the diffusion coefficient line for time t_1 in the top panel of Figure 2. It now depends on the convective boundary mixing assumptions whether or not material from the top convection

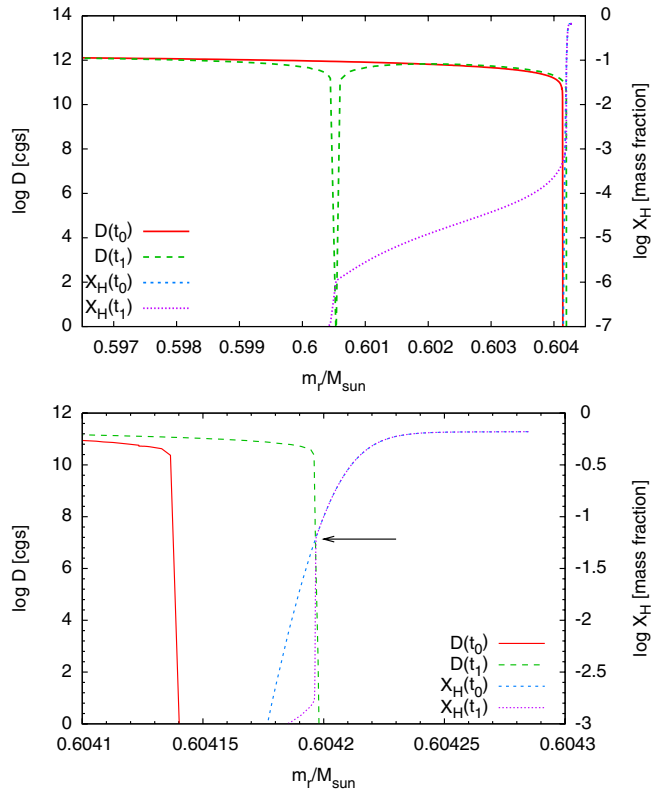

Figure 2. Convective diffusion coefficient and H-abundance profile at the beginning of the H-ingestion flash t_0 and at the time when the split of the convection zone appears at $t_1 = t_0 + 8.58 \times 10^5$ s. Top panel: the outer section of the convection zone showing the location of the split as a deep dip in D; bottom panel: just the interface of the outer boundary of the convection zone. The arrow indicates the H abundance at the position that has been reached by the convection zone at the time t_1. t_0 is at the time of the minimum of the H-burning luminosity at the onset of the H-ingestion event.

(A color version of this figure is available in the online journal.)

zone can mix below and vice versa. These boundary mixing assumptions, i.e., the amount of overshooting appropriate for this situation, is not yet known.

Figure 2 shows that the split of the two convection zones appears already very early when only a small amount of protons has been consumed. We mark the position in the H profile and the corresponding H abundance that has been reached at the time when the split occurs in the lower panel. The good agreement of our evolution simulation with the result by Miller Bertolami et al. (2006, Figure 3 in their work) only means that these calculations properly converge and are precise, but not that they are accurate.

At the time of the split the peak temperature in the now separated top H-burning driven convection zone is $T \lesssim 1.0 \times 10^8$ K. Although the $^{12}C(p,\gamma)^{13}N(\beta^+)^{13}C$ reaction chain is providing plenty of the neutron source isotope ^{13}C, the $^{13}C(\alpha,n)^{16}O$ reaction activation depends on the peak temperature reached in this top convection layer. For $T = 10^8$ K the lifetime of ^{13}C against capture by ^4He (and thus the time-scale of releasing neutrons) is 454 yr, and thus *neutron capture nucleosynthesis is negligible*, considering that the born-again lifetime is only a few years. As a result, these stellar evolution models cannot provide the environment to generate abundance patterns as observed by Asplund et al. (1999).

We have performed a full nucleosynthesis analysis of the stellar evolution model sequence shown in Figure 2, using the MPPNP code (Appendix A.1). The technique for this nucleosynthesis analysis is explained in full detail in Section 5. Indeed no modification of heavy element abundances is seen, in disagreement with the observations by Asplund et al. (1999), and in agreement with the qualitative arguments that these authors made in their original paper.

The Herwig et al. (1999) models show a larger peak-temperature of $T = 1.5 \times 10^8$ K[12] for the H-ingestion driven top convection zone. As discussed in detail in Herwig (2001), those older models are not correctly reproducing the fast luminosity rise time observed in Sakurai's object, and there exists an inverse correlation between the rise time and the depth of the burning zone and split (i.e., convection speed, peak temperature). Models with the higher peak temperature have far too slow rise times and can thus be excluded. For these higher peak temperatures the lifetime of ^{13}C is 0.13 yr. However, even this is not short enough to generate the abundance patterns observed in Sakurai's object (see Section 5 for further discussion).

We conclude from this analysis that a one-dimensional stellar evolution calculation cannot fully account for the mixing conditions in the convective–reactive H-ingestion flash that occurred in Sakurai's object. In this section, we have already hinted at the possible reasons for the discrepancy. We will now have a closer look at what information and guidance we can derive from present three-dimensional hydrodynamic simulations of He-shell flash convection.

4. THE HYDRODYNAMIC PICTURE

4.1. New Simulations

In order to study the hydrodynamic process of entrainment and further mixing of H-rich material from the stable layers into the convection zone we have carried out new gas dynamics simulations of the entire three-dimensional He-shell flash convection domain in 4π geometry (Figure 3). We used the PPM code described in Appendix A.2. We have not included burning of protons with ^{12}C because we restrict the goal of the numerical experiments purely to the investigation of mixing properties during the onset of the H ingestion, which starts when the He-shell flash convection has reached its largest Lagrangian extension.

Herwig et al. (2006) simulated the He-shell flash convection shell as plane-parallel box-in-a-star. They selected an earlier phase of the He-shell flash when the convection had not yet reached its largest extent, and the H-rich layers had not been reached. Therefore, only ∼4.5 pressure scale heights needed to be included in those simulations which made them considerably less demanding than the new simulations. In addition, the previous simulations were only in two dimensions.

The new simulations were performed on a cubical domain with two uniform Cartesian grids of 576^3 and 384^3 respectively (Figure 3).[13] Each simulation realistically represents the abundance mixture in the He-shell flash convection zone and in the stable layer above as different materials with the correct molecular weight ratio. The setup includes an inert white-dwarf-like core and a radiative region below the bottom of the He-shell flash convection zone at 9500 km where the gravitational acceleration is 4.9545×10^7 cm s^{-2}, the density is 1.174×10^4 g cm^{-3},

[12] We have now recalculated those old models with higher resolution and find the peak H-burning location at slightly lower temperature of $T = 1.3 \times 10^8$ K.

[13] The 576^3 calculation took 4 days on 24 workstations at the University of Minnesota's Laboratory for Computational Science & Engineering (LCSE). A movie made from the output of this run may be downloaded from the LCSE Web site http://www.lcse.umn.edu/index.php?c=movies.

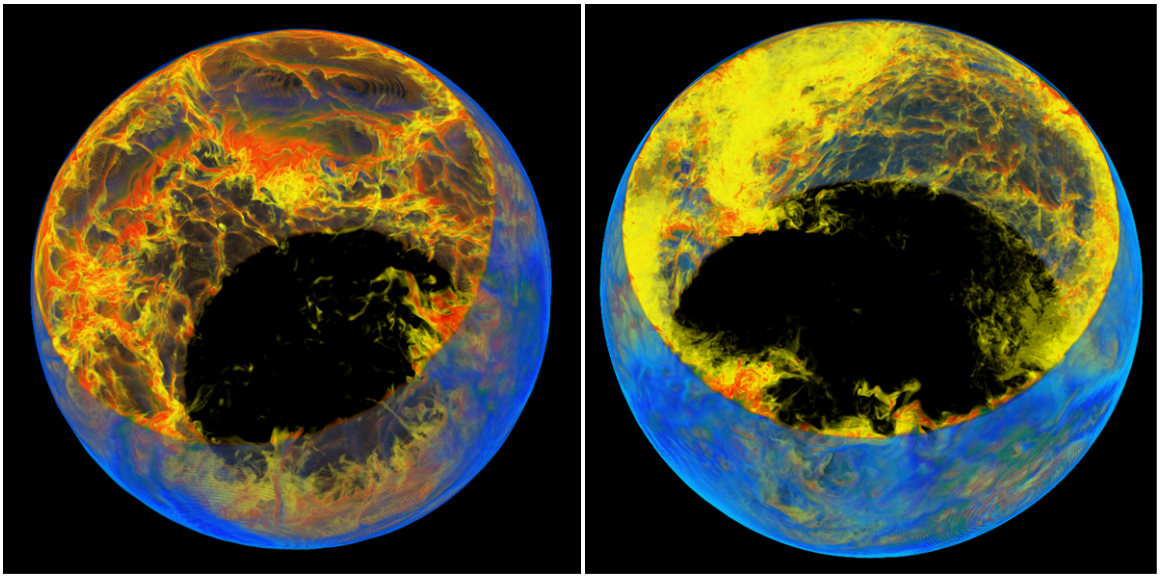

Figure 3. Hydrodynamic picture of H-entrainment into He-shell flash convection near the luminosity peak of the flash. The setup is based on a stellar evolution model corresponding to the situation shortly after time t_0 shown in Figure 2, when the top of the convection zone is just making contact with the H-rich stable layer. Colors indicate abundance of proton-rich material that is originally only in the stable layer above the convection zone that is entrained into the convection zone. Volume fractions of about ∼1% are shown as blue, while concentrations that are close to one are transparent. The lowest concentration yellow blobs that are mixed deep into the convection zone correspond to ∼0.01%. Abundance levels below approximately 5×10^{-5} have been made transparent as well. The left panel shows a snapshot from a 384^3 grid while the right panel image is from a run on a 576^3 grid. Slightly different times are shown and similar but not identical color maps have been used. The PPM simulation is described in more detail in Section 4.1, and the simulation code is described in Appendix A.2.

(A color version of this figure is available in the online journal.)

and the pressure is 1.696×10^{20} g cm^{-1} s^{-2}. At the bottom of the convection zone a luminosity of $4.2 \times 10^7\ L_\odot$ is artificially added in a shell of 1000 km. This heating corresponds to the He burning that drives the flash, and compares as follows to the He-shell flash luminosity in the stellar evolution models shown in Figure 2. In the model at time t_0 the He-burning luminosity is at its peak of $L_{\rm He,0} = 4.75 \times 10^7\ L_\odot$, whereas it drops somewhat once the H-burning flash ignites at t_1 when $L_{\rm He,1} = 4.27 \times 10^7\ L_\odot$. Thus, the three-dimensional hydrodynamic simulations are driven at the nominal heating rate.

The top of the convection zone is at a radius of 30,000 km and surrounded by a radiative shell of thickness 4500 km. The three layers are each polytropes. The adiabatic polytrope that represents the convection zone spans $\sim 9 H_p$. The setup contains two materials. The lighter material represents the H/He mixture in the stable layer above the convection zone. The heavier fluid represents the ^{12}C-rich mixture that occupies the convection zone. We have assumed here that the material in the stable layer below the convection zone has the same molecular weight. The ratio of the molecular weights of the two components is $\mu_{\rm C,O,He}/\mu_{\rm H,He} = 2.26$.

The higher resolution run (Figure 3, right panel) is shown at time 21,653 s. For convective transport the typical radial velocities are of interest. In the shown snapshot the largest radially rms-velocities are found about 4500 km above the bottom of the convection zone around $< v_{\rm rad,ave} >= \sqrt{2 < E_{\rm kin} >} \sim$ 12.5 km s^{-1}. The velocity of individual convective gusts can be significantly higher. Toward the upper boundary of the convection zone the radial velocities decrease to a few km s^{-1}. This is compensated by large tangential velocities > 12 km s^{-1} which stay this high all the way to the convection boundary (Figure 4). The resulting strong radial gradient of the tangential velocities at the top convection boundary is, via Kelvin–Helmholtz instabilities, likely the main mechanism of the entrainment and convective boundary mixing that we observe in these simulations. The information on typical convective velocities together with the radial scale of the convection zone implies a convective turnover timescale of the order ∼3000 s (cf. Appendix B). Therefore, Figure 3 shows the entrainment after ∼7 convective turnovers.[14] When estimating the timescale for H-rich material to enter the convection zone it must be considered that the entrained material is dominantly transported in downflow lanes that are gravitationally compressed as the material descends. This mechanism is reflected in the radial velocities of the H-rich material that has entered the convection zone, which in the snapshot shown exceed 20 km s^{-1}. We note that for this

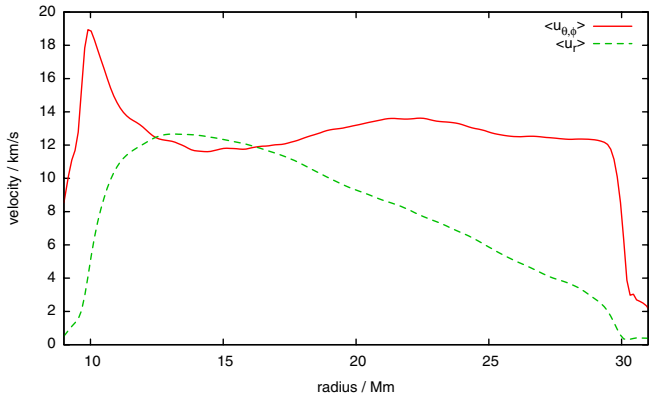

Figure 4. Radial and tangential radially averaged rms-velocities of the 576^3 simulation at the same time as shown (in the right panel) of Figure 3.

(A color version of this figure is available in the online journal.)

[14] We have continued this run for another 14 convective turnovers. However, as will become clear from the following discussion, the omission of proton burning limits the scientific use of that later part of the run to our application. Note that the time step of the three-dimensional simulations is limited to $\Delta t = 5.9 \times 10^{-2}$ s which implies that 300,000 cycles had to be computed to reach the state shown.

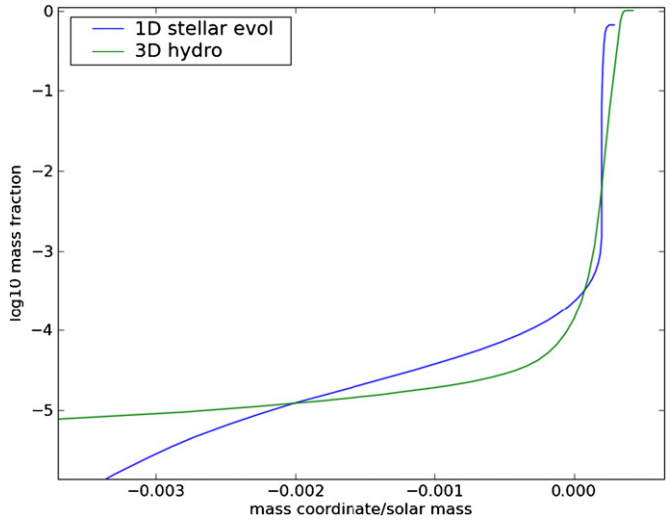

Figure 5. Comparison of entrainment of material from the stable layer above the convection zone into the ^{12}C-rich layer as it is represented in the one-dimensional stellar evolution model with mixing treated as diffusion in the mixing-length picture and in the three-dimensional simulations discussed in this paper. The three-dimensional profile (green line) shows the same data, radially averaged, as in Figure 3 (right panel). The one-dimensional line (blue) is the line labeled t_0 in Figure 2. The mass coordinates have been set to zero in both cases near the top of the convection zone.

(A color version of this figure is available in the online journal.)

component even the radially averaged velocity corresponds to a Mach number $Ma \sim 0.02$ which is much higher than the MLT convective velocity based estimate of $Ma \sim 0.001$.

After some initial transient period the convection assumes a flow pattern that is dominated by large upwelling convective cells that typically occupy a full octant as they emerge at the top convection boundary. These large convective structures can be observed because we simulate the full 4π sphere. Entrainment of the H-rich material from the stable layer into the convection zone is mostly associated with downdraft lanes that form when large cells collide on the surface of the convection zone (Figure 3). Note that the radially averaged profile of the ingested H-rich material from the three-dimensional hydro-simulation is qualitatively very similar compared to the diffusion picture of the one-dimensional stellar evolution (Figure 5), at least close to the upper boundary. Further inward the lines divert from each other systematically as no H is burned in the three-dimensional simulations (this physics is not yet included).

However, the important result of the three-dimensional simulations is that entrainment is rather inhomogeneous and asymmetric, as well as intermittent in locally confined wedges of the star. From the snapshot image of the entrainment it is clear that significant anisotropy of the H abundance is advected into the deeper layers where the burning will eventually take place.

4.2. Implications for the Nucleosynthesis in a Convective Reactive Environment Like Sakurai's Object

We will give a full account of these simulations elsewhere. Here we want to describe a few properties that are relevant for guiding our mixing strategy for the nucleosynthesis simulation of the flash in Sakurai's object. The details of the convective–reactive burning of hydrogen in the He-shell flash convection zone depend on two aspects of the problem that hydrodynamic simulations can address. The first is the process of entrainment. How much is the fuel premixed immediately after the entrainment in the near-boundary layers? Subsequently these H-enriched fluid elements will be carried along with the convective flow to deeper and hotter layers where protons will eventually react with ^{12}C. This leads to the second aspect of the problem, the hydrodynamic feedback of the nuclear energy released. In the one-dimensional simulations this feedback is in the form of a sharp entropy barrier, or a thin shell of positive entropy gradient locally confined to a sphere. In reality, the thickness of this layer will depend on the velocity distribution and the abundance distribution of fluid elements entering the layers hot enough for rapid burning.

We can illustrate the possible outcomes by considering two extreme cases. Assuming first that any entrained material is immediately mixed and that vertical velocities of fluid elements are only deviating negligibly from some average value (obviously, this case is very close to the MLT picture of convection) then all fluid parcels or blobs would release nuclear energy at almost the same radial position inside the convection zone, and thus a very thin burn layer would form, concentrating the entropy jump into a narrow region with large positive entropy gradient, and soon inhibiting any further radial mixing. The other extreme would be a wide range of mixing ratios in blobs of H-enriched material entering the deeper layers with a large range of velocities. Both of these inhomogeneities lead to a broadening of the burning layer. To first approximation a blob (note that this may be a shredded blob in order to conceptually overcome mixing-length concepts) burns at $Da \sim 1$ (Section 1.1). For smaller Da (above the burning layer) the nuclear reaction timescale is longer than the mixing timescale and the blob will rather move further down than burn. For $Da > 1$ we are below the burning layer because now the blob burns faster than it can move further down. Since the burn timescale decreases with depth a range of mixing velocities translates into a spatial range in which $Da \sim 1$. Differently than in the first case, the velocity distribution of blobs leads to a broadening of the burn layer. Distributing the energy released from proton capture over a thicker layer will make the emerging entropy gradient shallower. Mixing across the burn layer will be more efficient. A distribution of levels of H-enrichments in blobs being advected through the burn layer would mean that the H abundance is heterogeneous (patchy) on spheres. Thus, the energy generation and the dynamic feedback may very well be patchy and inhomogeneous on spheres, as well as time variable. At least initially, the inhibiting effect of the burn layer on mixing may as well be time variable and inhomogeneous on spheres.

In other words, an inhomogeneous distribution of fuel abundance in blobs together with a distribution of vertical blob velocities would have the tendency to delay the inhibiting effect of nuclear burning on mixing from the top to the bottom of the convection zone. We leave a detailed quantitative analysis of these processes to a forthcoming investigation. Here we focus on the conceptual guidance we can gain from the hydrodynamic simulations. These do indeed show a significant inhomogeneity of the entrained material all the way down to the bottom of the convection zone (Figure 3), as well as a significant distribution of vertical velocities, including convective gusts up to Mach numbers around $Ma \sim 0.03$.

We conclude from this analysis that the hydrodynamic nature of the convective–reactive phase of H ingestion into the He-shell flash convection zone likely translates into a continued mixing through the burn layer. We therefore hypothesize that mixing is not inhibited at the early stage, as indicated by stellar evolution models, but that instead mixing across the H-burning layer is

possible for a prolonged period. It may stop only at a later time after more H ingestion has taken place. In the next section, we will test this hypothesis through nucleosynthesis simulations that can be compared with the observations of Asplund et al. (1999).

5. NUCLEOSYNTHESIS SIMULATIONS

In this section, we will describe mixing and nucleosynthesis simulations based on the thermodynamic stellar evolution structure of a post-AGB He-shell flash. We describe initially two cases, one that resembles the mixing predicted by stellar evolution (Section 5.2), and one with a mixing prescription that reflects the findings discussed in the previous section (Section 5.3). While the first fails to reproduce key observational features of Sakurai's object, the second one succeeds. We show that high neutron densities in the range $10^{12} < N_n/\mathrm{cm}^{-3} < 10^{16}$ are required to reproduce the observed abundance features, as already pointed out by Asplund et al. (1999). Such a neutron density regime is higher than the classic *s*-process and significantly lower compared to the classic *r*-process.

5.1. General Setup of Nucleosynthesis Simulations

We are using the MPPNP post-processing code (Appendix A.1) to calculate the nucleosynthesis of an He-shell flash peak one-dimensional stellar structure model. We use two structures, one of them shown in Figure 2 for $t = t_0$. The MPPNP code reads the MLT diffusion coefficient as well as the temperature and density structure from the stellar evolution structure model. We post-process this structure with sub-time steps of $\Delta t_{\mathrm{post-processing}} = 63$ s. Thus, the mixing timescale is well resolved, and the numerical splitting of the mixing and the nucleosynthesis operators is justified. The He-shell flash convection zone is spatially resolved with 70–90 zones. The grid is statically refined and provides extra resolution near the ingestion layer at the top of the convection zone, as well as around any split region, should it be included.

The MLT based diffusion coefficient that is read in along with the stellar structure from the stellar evolution output does not show a split because the stellar evolution model is from a time just before the ingestion of H-rich material begins. However, we are providing for an optional split that can be inserted at an arbitrary location and time, by modifying the diffusion coefficient in Eulerian coordinates in the following way:

$$D_{\mathrm{with\ split}} = \frac{D_{\mathrm{MLT}}}{(1. + a_2 \exp(-a_1(m_r - m_{r,\mathrm{split}})^2)} \quad (2)$$

where the split is located at $m_{r,\mathrm{split}}$. When a split is imposed it is chosen to be deep enough so that only very little material can be mixed through, and the split is also very narrow. With $a_1 = 10^4$ and $a_2 = 10^7$ the diffusion coefficient in the convection zone of $D_{\mathrm{MLT}} \sim 5 \times 10^{13}$ cm^2 s^{-1} is reduced to $D_{\mathrm{split,min}} \sim 5 \times 10^6$ cm^2 s^{-1} over a width of $<10^{-4}\,M_\odot$. We emphasize that a_1 and a_2 are free parameters of our simple delayed split model and their particular value is not important at this point. Only further hydrodynamic simulations can possibly determine the mixing properties in this environment. The purpose of the delayed split in terms of the radially averaged nucleosynthesis calculations is further discussed below.

We are solving only for the nucleosynthesis and mixing equations while the T, ρ stratification is assumed to remain unchanged. Protons and ^{3}He are inserted into the top of the convection zone at a rate that is derived from the Lagrangian velocity of the top of the convective boundary, as it moves into the H-rich layers above the convection zone in the stellar evolution model. This velocity is $\dot{M}_{\mathrm{top,conv}} \sim 1.7 \times 10^{-2}\,M_\odot$ yr^{-1}. We are ingesting at a rate of $5.3 \times 10^{-10}\,M_\odot$ s^{-1}.[15] We also add ^{3}He according to the solar H/^{3}He ratio in order to obtain a prediction for Li.

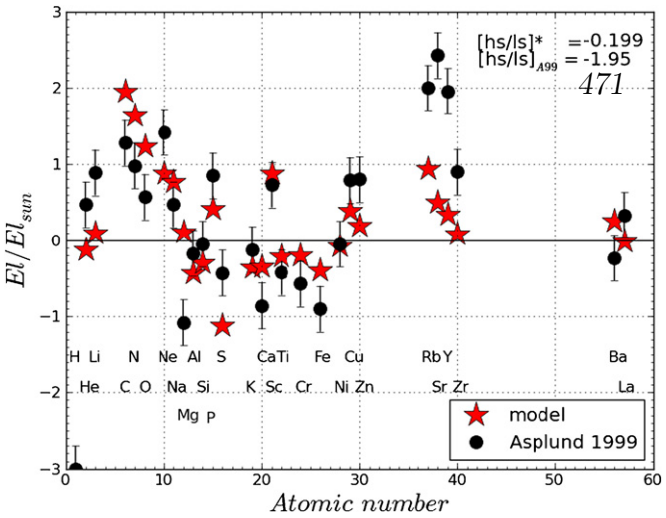

Figure 6. Abundance distribution obtained at the top of the He intershell assuming that the mixing split develops as soon as H is ingested. This case corresponds to the one-dimensional stellar evolution prediction for mixing in the H-ingestion flash. The abundances measured by Asplund et al. (1999) are reported for comparison.

(A color version of this figure is available in the online journal.)

Another constraint is that the total amount of H available for ingestion is limited to the small remaining envelope mass that remains on the pre-formed WD when the star leaves the AGB. For a core mass of 0.6 $M_\odot$ this envelope mass is $\sim 10^{-4}\,M_\odot$ with H and He fractions as expected at the end of the AGB (mostly the initial ratio possibly modified by third dredge-up). In all of the cases discussed here we always find a nucleosynthetic reason to stop a simulation before we run out of fuel.

5.2. Stellar Evolution Mixing Case

In the stellar evolution models the convection zone split due to H-burning activation starts as soon as H is ingested (Section 3.2), and no H or ^{13}C can by mixed below the split coordinate. In Figure 6, we show the abundance distribution prediction at the top of the convection zone for this model in comparison with the observations by Asplund et al. (1999). We have used the (ρ, T, D) stratification (strat-A) from the Herwig et al. (1999) sequence, selecting a model just before the H ingestion starts as a template for this run. The mixing split as described in the previous section is activated immediately as H starts to mix into the convection zone. Peak H burning is located at a higher temperature in the Herwig et al. (1999) sequence compared to more recent models, and therefore this case yields

[15] Specifically, we add every ~6 minutes (every sixth cycle, corresponding roughly to 10 times per convective turnover time) $\Delta X = 5 \times 10^{-4}$ to the mass fraction of H in the uppermost $4 \times 10^{-4}\,M_\odot$ of the convection zone. The baryon numbers are conserved by subtracting the required mass fraction from ^{12}C. The abundances up to ^{23}Na are initialized as described in Section 3.1.

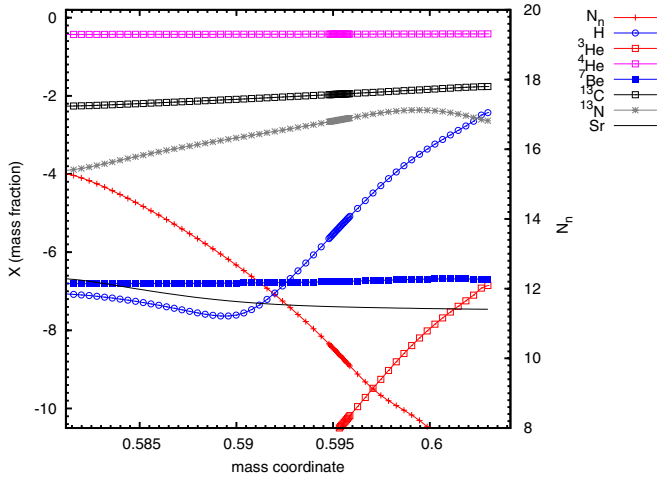

Figure 7. Abundance profiles snapshot (RUN103), just before the mixing split is imposed, demonstrates the simultaneous action of nucleosynthesis and mixing on similar timescales.

(A color version of this figure is available in the online journal.)

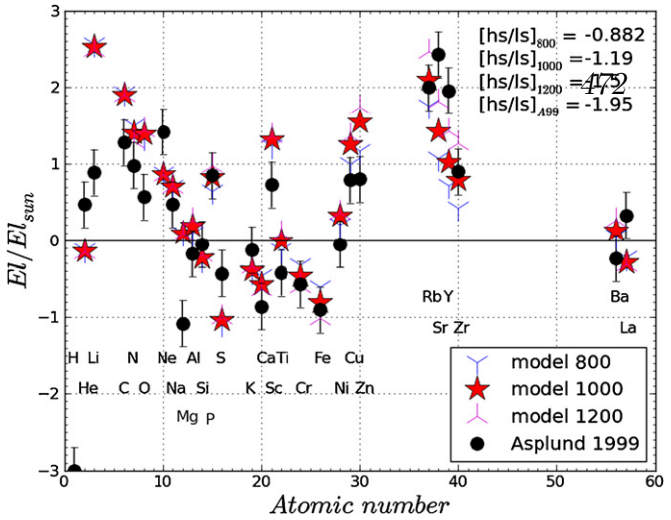

Figure 8. Abundance distribution at step 2000 for different cases with the split starting after 800 minutes (RUN105), 1000 minutes (RUN103), and 1200 minutes (RUN106).

(A color version of this figure is available in the online journal.)

an upper limit of the nucleosynthesis efficiency predicted from one-dimensional models.[16]

Calculations are run for about one year, after which also Ba starts to be produced, in disagreement with observations. The neutron density reaches a value of the order of 10^{11} cm^{-3} at the split coordinate due to the high ^{13}C concentration accumulated via proton capture on ^{12}C. This value is comparable with the neutron density obtained at the bottom of a regular He-shell flash convection zone from ^{22}Ne(α,n)^{25}Mg reaction. Nevertheless, the predicted abundances do not matching the observations.

Li produced initially during the ingestion (see below and Herwig & Langer 2001 for more details) is destroyed on the timescale of ∼1 yr. Stellar models predict that material around and beyond the split expands and cools which reduces the α-capture efficiency depleting Li. But this also reduces the production of heavy elements.

Sc is well reproduced within the uncertainties, in neutron densities higher than in the classic *s*-process. ^{40}Ca is the main seed along the neutron capture path, and Sc is mainly produced as ^{45}Ca which will decay to ^{45}Sc in ∼ 166 days. The production of Sc is subject to nuclear reaction uncertainties, for instance the (n,γ) rates of Ca isotopes, ^{41}Ca(n,p)^{41}K and in particular ^{41}Ca(n,α)^{38}Ar.

The bottom line is that Li observations cannot be reproduced together with a significant *s*-process nucleosynthesis in this simulation. But most importantly, the predicted [hs/ls] ratio is much higher than observed. Therefore, the nucleosynthesis simulation based on the one-dimensional stellar evolution prediction for mixing cannot account for the observed abundance patterns in Sakurai's object, which confirms our findings from Section 3.2.

5.3. Delayed Split Model Motivated by the Hydrodynamic Simulations

We now assume that the split is not created instantaneously by H burning, but mixing continues—at least initially—unrestricted despite the energy generation from H burning (see Section 4.2). We use same background model (strat-A) as in Section 5.2.

^{13}N is still formed in the upper layers where the reaction and the mixing time coincide (Figure 7). ^{13}N decays to ^{13}C on a timescale of ∼10 minutes. During this time ^{13}N will be swept along with the flow, possibly covering a distance of the order 10,000 km. Eventually ^{13}C is mixed to the bottom of the He-shell flash convection zone ($T \sim 2.5$–3.0×10^8 K) and establishes an abundance of ∼1% by mass throughout the He intershell. Neutrons are released via ^{13}C(α,n)^{16}O on the timescale of 1–10 s and neutron densities reach a value of $\sim 10^{15}$ cm at the bottom of the convection zone. The profile for Sr is shown as an example for how the abundance, even of heavy elements, varies inside the convection zone as mixing and production proceed at similar timescales.

The intense neutron burst leads to the formation of the first *s*-process peak elements Rb, Y, Sr, Zr, with Fe as the main seed. The unimpeded mixing between the formation region of ^{13}N and the deeper layers where the neutrons are released must finish before the Ba–La elements are significantly produced, which is not observed. This defines the moment when mixing finally has to be limited, and we then turn on the delayed split. In Figure 8 we show the abundances expected at the top of the He intershell for different split times between 800 minutes and 1200 minutes.

Burning of ^{3}He produces ^{7}Be via the reaction ^{3}He(α,γ)^{7}Be, which will decay later to ^{7}Li. As pointed out by Herwig & Langer (2001), Li destruction is avoided under these conditions, but not because Li is mixed into cooler regions (Cameron–Fowler mechanism). Rather, in this *hot H-deficient ^{3}He burning* all the protons are consumed before ^{7}Be decays to ^{7}Li. Then ^{7}Li is more stable as it is only destroyed through α-captures. In all cases Li is overproduced if we can assume that a sufficient supply of ^{3}He is still available in the envelope when the VLTP begins (cf. Section 1.2).

Mg is more abundant in the simulations by one order of magnitude compared to observations. In all runs Mg is only weakly modified by nucleosynthesis. For this reason, the low observed Mg abundance may be another indicator of a sub-solar initial metallicity of the star, unless there is some observational problem.

[16] As discussed in Section 1.2, this older model did not reproduce the observed light curve, but more recent models (Herwig 2001; Miller Bertolami et al. 2006) predict the split at lower temperature and as a result even less n-induced nucleosynthesis.

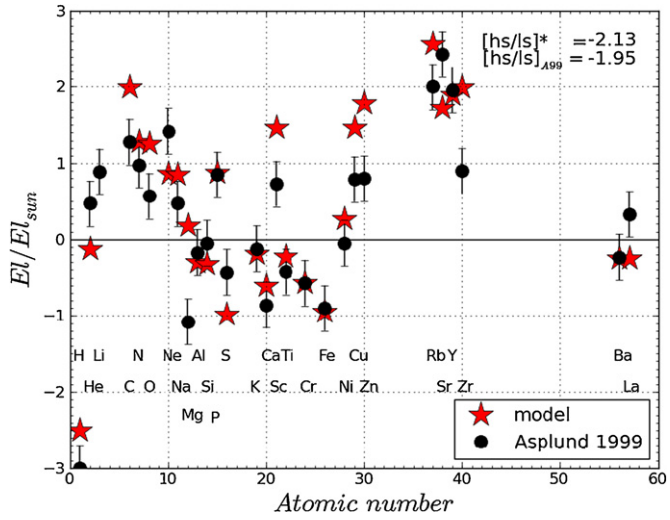

Figure 9. Abundance distribution at the end of the simulations (RUN48/strat-B) after 3000 minutes, when all H- and ^{3}He-ingestion has been ingested.

(A color version of this figure is available in the online journal.)

Despite the differences between these tests and the measurements, the overall abundance trends are similar. In particular all three test cases in Figure 8 have a low [hs/ls] that ranges between −0.9 and −1.5, decreasing with increasing the split delay. In the case with the latest split (at 1200 minutes) [hs/ls] is still ∼0.5 dex higher than observed in Sakurai's object. Light and intermediate elements are not much affected by the split time.

In addition to the split delay time the quantitative model predictions depend on the base stratification and convective mixing coefficient taken from the stellar evolution model. This determines, for instance, how quickly the protons and resulting ^{13}C are mixed, and in turn the neutron density. To test the dependence of the results on this point we present another set of simulations based on the structure (strat-B) at the last thermal pulse in the 2 $M_\odot$ star model sequence by Herwig et al. (model ET14 2006). We have applied a delayed split as for the strat-A model. With this base structure, the measured [hs/ls] is reproduced within the uncertainties (Figure 9). However, now Zr is higher by 1 dex compared to the Asplund et al. measurements. A general overview of the abundance profiles in the He intershell for the most indicative light isotopes and of the elements included in Figure 9 is given in Figure 10, where the split position and the variation in the abundances are shown.

Figure 10 (left upper panel) confirms that the ^{12}C/^{13}C = 6.7 ratio agrees within uncertainties with the observed ratio of ∼3–5.

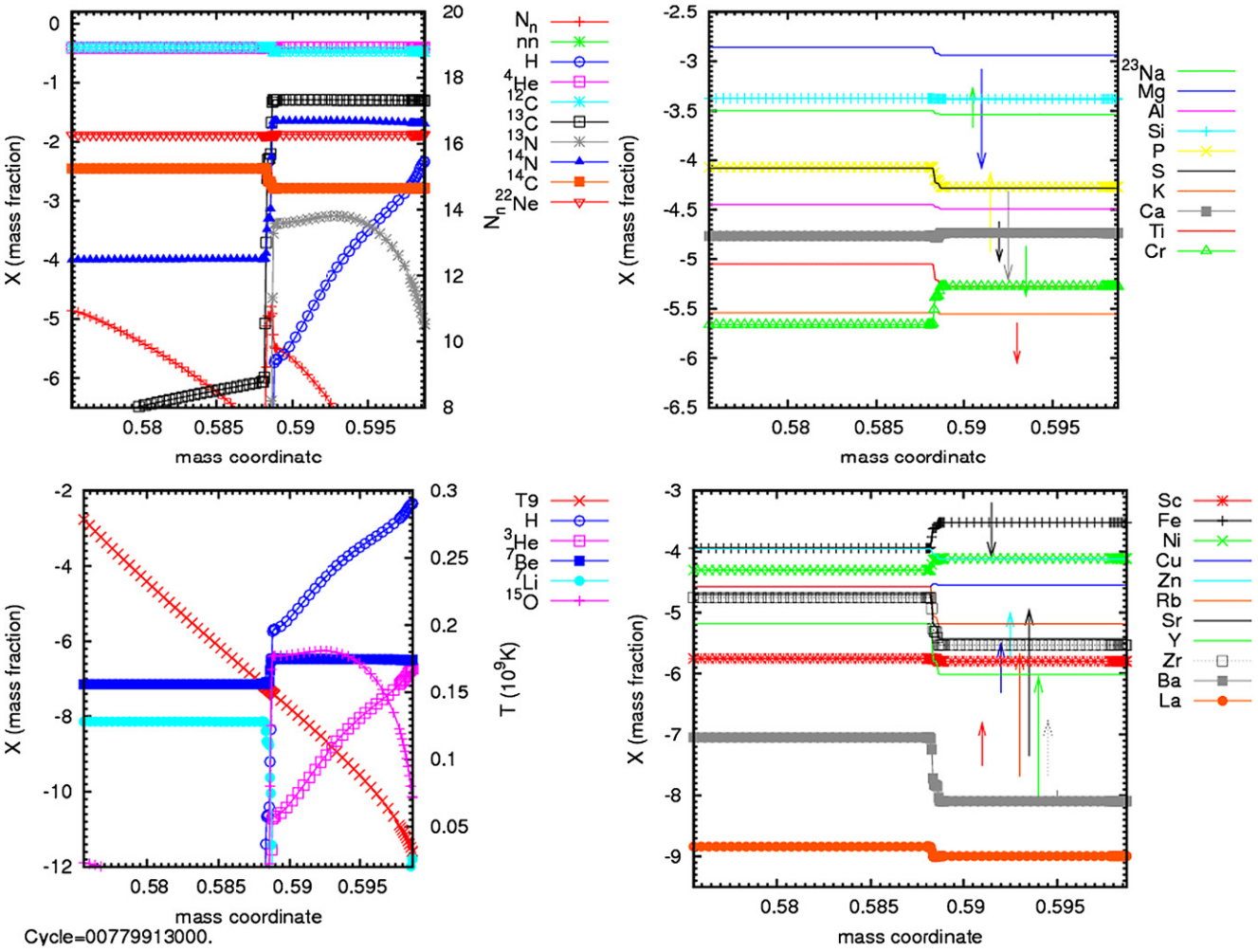

Figure 10. Abundance profile at the end of simulation RUN48 after 3000 minutes, when all H and ^{3}He have been ingested. A split imposed at 950 minutes has prevented further mixing between the He-shell flash driven convection zone (left) and the H-ingestion flash driven convection zone (right). Arrows in the right panels indicate the observed abundances, connecting the solar values with the observed ones.

(A color version of this figure is available in the online journal.)

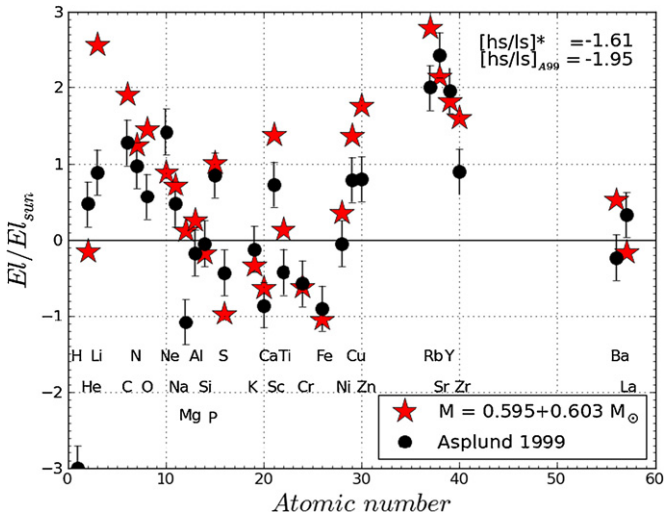

Figure 11. Abundance distribution at step 2000 for a split delay of 1200 minutes, considering mixing of 10% of the deep component with 90% from the component above the split.

(A color version of this figure is available in the online journal.)

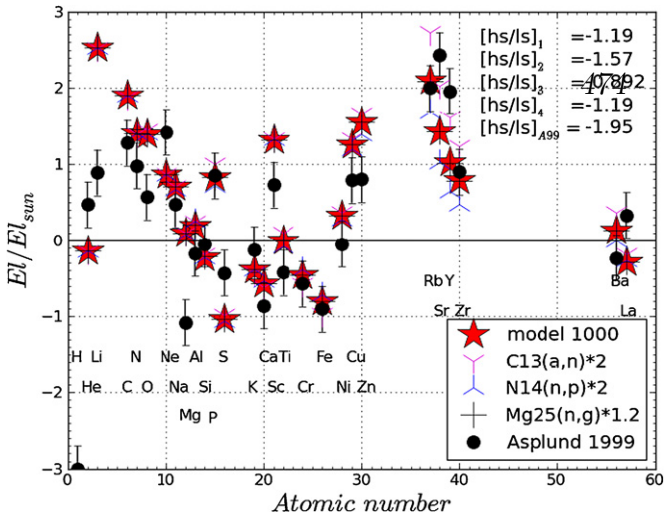

Figure 12. Abundance distribution for different nuclear test at step 2000, from RUN103 (split delay = 1000 minutes) as standard, and RUN107, RUN108, RUN109.

(A color version of this figure is available in the online journal.)

^{7}Be is shown in the lower left panel to be highly abundant, which will feed Li.

This profile view of one of our simulations reveals that the neutron capture nucleosynthesis continues below the split, thereby further modifying chemical abundances. Possibly this further processed material below the split has affected Sakurai's observed surface abundances, through additional, later mixing. H burning at the split must lose efficiency at some point when running out of fuel. This may allow material exchange between the two regions (see also discussion in Asplund et al. 1999). Asplund et al. observed Sakurai's object four different times in 6 months, and these observations show some drastic changes for some elements. It is not the aim of this paper to directly address these abundance trends over the 6 month period, since this level of detail cannot be captured by our modeling approach, but has to await updated multi-dimensional simulations.

However, we may assume, as a working hypothesis, that the He intershell is made of two components, one heavily processed below the split (region 1), and one above the split (region 2) that was affected only by the first ingestion phase. Because of the decreasing of efficiency of the H burning at the split, some material from region 1 is allowed to reach region 2 again and contribute to the observed abundance distribution. Such a two-component model is shown in Figure 11. Starting from the simulation based on stratification strat-A, with a delayed split after 1200 minutes (see Figure 8) 10% of the material is coming from region 1, and 90% from region 2. No significant differences are obtained compared to Figure 8. However, this depends on how much material is mixed from region 1 to region 2. In this specific case, such mixing implies a decrease on [hs/ls], but also an increase in Ba production, not supported from the observations. For this reason, at present we cannot confirm or rule out such a double component scenario.

5.4. Nuclear Reaction Rate Uncertainties

In this nucleosynthesis scenario both H- and He-burning reactions, as well as the *n*-capture reactions including those of short-lived isotopes, are important. Especially, several elemental abundances, for example Ti and Sc, are strongly dependent on s-process branchings which require extra accuracy from the nuclear physics data. As we want to use this case to probe future hydroynamic simulations, we need to assess the influence of nuclear rate uncertainties.

In Figure 12 we show for the model strat-A with a split after 1000 minutes the impact of changing the ^{13}C(α,n)^{16}O and the ^{14}N(n,p)^{14}C reactions by a factor of two. The ^{25}Mg(n,γ)^{26}Mg reaction has been varied by a factor of 1.2. ^{13}C(α,n)^{16}O is the main neutron source and the two neutron capture reactions are important neutron poisons. Among these tests, the [hs/ls] changes between -0.9 and -1.6. In particular, the first peak elements are strongly affected. The Rb abundance changes by 1 dex. Intermediate and light element predictions are only weakly affected by nuclear reaction rate uncertainties. Small errors associated with the CNO cycle rates (e.g., ^{12}C(p,γ)^{13}N and ^{14}N(p,γ)^{15}O) have a marginal impact in our results compared to the other rates that we have considered.

In Figure 12, we only included the impact of varying the neutron capture reaction rates of light neutron poisons. In the short timescale of the neutron burst, the neutron capture process is also expected to show a strong propagation effect in the final abundance distribution beyond iron, due to uncertainties of neutron capture rates along the nucleosynthesis path. In particular, such propagation may be relevant in our case, since Rb, Sr, Y, and Zr production is affected by the error of several low cross sections of isotopes in the mass region between Fe and Sr, acting like bottlenecks in the neutron capture flow (e.g., ^{62}Ni, ^{68}Zn, ^{74}Ge, and ^{78}Se; Pignatari et al. 2010, and reference therein). Another point to consider is that in the high neutron density regime reached in our calculations several unstable isotopes are produced efficiently, and many stable isotopes receive a significant contribution from unstable species from radiogenic decay and/or from decay during the neutron freezeout, when the split is established. For instance, in all the cases presented in Figure 12 most of Y (that is formed by one stable isotope only, ^{89}Y) is produced as ^{89}Sr. The neutron capture rates of unstable species are mostly theoretical, and also their large uncertainty (typically a factor of 2–3) may affect the final isotopic distribution.

None of our simulations seem to be reproducing Sc particularly well. Sc and the elemental ratio Sc/Ca are particularly

sensitive to the neutron density. Indeed, ^{45}Sc is produced as unstable ^{45}Ca via neutron captures on stable Ca species, where ^{40}Ca is the main seed for Sc production. ^{41}Ca is unstable, and has stronger (n,p) and (n,α) than (n,γ) channels. For this reason, the uncertainty in the relative efficiency of the (n,p), (n,α) and (n,γ) channels may affect the total Sc production. Among nuclear uncertainties, another possible explanation for Sc overproduction is that the initial metallicity of Sakurai's object is even lower than what we have used for our simulations ([Fe/H] $= -0.18$). Indeed, a lower initial ^{40}Ca will results in a lower final Sc abundance.

6. CONCLUSIONS

6.1. Summary

We have presented in this paper a multi-physics view of the combustion in a VLTP in a pre-WD. H is mixed convectively into the He-shell flash convection zone. We have discussed the one-dimensional stellar evolution picture, which predicts that early on the energy generation from the ^{12}C(p, γ)^{13}N reaction creates a sharp entropy discontinuity which prohibits mixing. A detailed nucleosynthesis analysis, based on a complete multi-zone treatment of nucleosynthesis with mixing, shows that this one-dimensional structure evolution leads to abundance predictions that are incompatible with the observed abundances in Sakurai's object. Seeking guidance from full three-dimensional hydrodynamic simulations of He-shell flash convection in 4π geometry with entrainment, we obtain reasons to suspect that the burning front is more distributed than predicted in one-dimensional stellar evolution. Fuel will be transported down in down-draft lanes leading to an inhomogeneous distribution of fuel in the burning zone. In addition, vertical down drafts enriched with fuel will populate a velocity distribution. From this information we speculate that mixing of protons and of the neutron source material ^{13}N which later becomes ^{13}C, across the convective H-burning zone, will proceed for much longer than indicated by one-dimensional stellar evolution.

We point out that the main nucleosynthetic signature of convective–reactive burning in this study is the significant overproduction of the first peak elements Sr, Y, and Zr, coupled with a non-efficient production of the second peak elements Ba and La. According to our simulations, neutron densities 10^{12} cm^{-3} $< N_{\rm n} <$ 10^{16} cm^{-3} are required to explain such abundance distribution. More specifically, in Sakurai's object timescale of $\sim$ 2 years between the luminosity peak due to H burning and the Asplund observations, a neutron density peak of $\sim 10^{15}$ cm^{-3} with a delay of $\sim$ 1 day before the complete split activation would qualitatively reproduce the observed [hs/ls] ratio, the Li abundance, and the low ^{12}C/^{13}C ratio. The problems that we encounter in reproducing single elements may be due to the approximations in our model (e.g., for the nucleosynthesis simulations we use parameters from one-dimensional stellar models), to observation problems (e.g., the observed Y/Zr ratio cannot be reproduced by neutron capture nucleosynthesis), or to nuclear physics uncertainties (e.g., Sc).

Nuclear reaction rate uncertainties are shown to have a particularly important effect on some key observables in this non-equilibrium nuclear burning environment.

6.2. Implications for Stellar Evolution and Nucleosynthesis of the First Generations of Stars

One of our main motivations to study convective–reactive phases in stellar evolution is their prevalence in models of the first generation of stars. As reviewed in Section 1.1, convective mixing of protons with the ^{12}C from He burning at He-burning temperatures is frequently encountered in stellar evolution calculations at very low and zero metal content at all masses. This investigation shows that the predictive power of one-dimensional stellar evolution simulations is severely limited for observables that depend on these convective–reactive phases.

Neutron burst nucleosynthesis of the type described in this paper is nevertheless expected to also happen in the convective–reactive H–^{12}C combustion events in the first generation of stars. Indeed, the neutron source ^{13}C is of primary origin, i.e., its abundance is not affected by the metal content in the initial stellar composition. Massive stars at different metallicities may experience H–^{12}C combustion, ingesting protons in the He shell (see discussion in Woosley & Weaver 1995). If enough hydrogen fuel is ingested then Sr, Y, and Zr may be efficiently produced by the primary ^{13}C(α,n)^{16}O neutron source, just as in our simulations presented here. This may be an alternative or complementary explanation for a missing component in the first neutron-peak region of the abundance distribution in both the solar abundance distribution and the metal-poor stars (LEPP Travaglio et al. 2004; Pignatari et al. 2008; Farouqi et al. 2009). In the future we intend to study the speculation that the convective–reactive proton–^{12}C combustion in the convective He shell in massive stars could provide another possible solution for the LEPP.

F.H. acknowledges NSERC Discovery Grant funding. The hydrodynamics simulations were performed by P.R.W. on a cluster of workstations at the University of Minnesota, provided through an NSF equipment grant, NSF-CNS-0708822. The work of C.F. and G.R. was funded in part under the auspices of the National Nuclear Security Administration of the U.S. Department of Energy at Los Alamos National Laboratory and supported by Contract No. DE-AC52-06NA25396. R.H. acknowledges support from the World Premier International Research Center Initiative (WPI Initiative), MEXT, Japan. This work used the SE library (LA-CC-08-057) developed at Los Alamos National Laboratory as part of the NuGrid collaboration; the SE library makes use of the HDF5 library, which was developed by The HDF Group and by the National Center for Supercomputing Applications at the University of Illinois at Urbana-Champaign.

APPENDIX A

CODE DESCRIPTION

A.1. Nucleosynthesis

The PPN physics package allows a flexible combination of nuclear reaction rates and entire compilations of rates. For this study we choose for the main charged particle reactions the compilation by Angulo et al. (1999; NACRE compilation). This choice allows us to be consistent with the original network used to calculate the stellar structures for basic energetic nuclear reactions, i.e., ^{14}N(p,γ)^{15}O, 3-α and ^{12}C(α,γ)^{16}O. Note that the use of more recent rates (e.g., Imbriani et al. 2005; Fynbo et al. 2005; Kunz et al. 2002, respectively) would not change our results, where uncertainties related to physics processes and mixing still has a critical impact. Other charged particle reactions, among the others ^{13}C(α,n)^{16}O, which is the main neutron source during the H ingestion, have more recent measurements (e.g., Heil et al. 2008). However, in this case NACRE rates are consistent with the new rates within their

uncertainty. For instance, we consider a factor of 2 of uncertainty for the $^{13}C(\alpha,n)^{16}O$ rate in the temperature regime that is relevant for the ^{13}C burning (see Section 5 for more details). For neutron capture reactions of stable isotopes we refer to Dillmann et al. (2006; KADoNIS compilation). Stellar β-decay rates and electron captures are from Oda et al. (1994) and Fuller et al. (1985) for many light unstable isotopes, and Goriely (1999) for many heavy unstable isotopes. Rates not included in the previous references are given by the Basel REACLIB compilation. We are solving the complete network in each radial grid point, including all relevant charged particle, n-capture reactions as well as the β-decays. A recursive, dynamic network generation has been integrated into the solver, i.e., the size of the network automatically adapts to the conditions given. If, for example, a neutron source is activated the network will be automatically enlarged to include all heavy and unstable isotopes as needed according to the network fluxes. This dynamic network feature ensures that the network calculation never misses any important isotope or reaction.

In these simulations we are using the multi-zone driver of the PPN code (MPPNP) that allows for the calculation of the complete nucleosynthesis in all of the zones of one-dimensional profiles, e.g., from stellar evolution, of density and temperature. The MPPNP driver employs MPI parallelism to enable efficient calculations on up to 30–50 processors depending on problem sizes. The simulations carried out here involve relatively small grids between 70 and 90 zones. A fully implicit nucleosynthesis step is followed by a mixing step according to the diffusion coefficient taken, for example, from the stellar evolution model. This procedure is repeated for subsequent time steps in order to compute the evolution of the abundance profiles of all species involved. Mixing and network calculations are performed in the operator split mode, which is a good approximation for the post-processing because we choose the post-processing time step to be small enough to resolve the mixing timescale.

A.2. Hydrodynamics

The PPM gas dynamics scheme (Woodward & Colella 1984; Colella & Woodward 1984; Woodward 1986, 2007; Woodward et al. 2008c) has been in use in computational astrophysics for many years. It is incorporated in the community codes VH1 (Blondin & Lufkin 1993), ENZO (Bryan et al. 1995), and FLASH (Calder et al. 2002). The version that we use in this work is described in full in Woodward (2007). Here we have augmented PPM with the PPB moment-conserving advection scheme to treat the entrainment of fluid from above the convection zone during the helium shell flash in an AGB star (see Woodward et al. 2008a). PPB is built upon van Leer's Scheme VI (van Leer 1977), a one-dimensional scheme that conserves the first three moments of the advected distribution in each grid cell. To this scheme we have added a set of very carefully constructed constraints (Woodward 2005), keeping the advected fractional volume of a multifluid constituent of the gas within the range from 0 to 1. These constraints are a considerable improvement over those outlined in Woodward (1986) for a two-dimensional PPB scheme. We have also streamlined the implementation of PPB in three dimensions by eliminating various high-order terms in order to obtain a highly efficient, directionally split scheme (Woodward 2005) that conserves 10 moments of the distribution of the advected fractional volume variable in each cell. PPB is combined with PPM to describe multifluid hydrodynamics by adding the constraint of pressure and temperature equilibrium within each grid cell. At present our code is explicit. Mach numbers in the convective gusts of helium shell flash convection are about 1/30 or less. Consequently, we must take many time steps to follow the flow through an entire circuit of a large convective eddy. We note that such eddies are global in scale, and we follow them by including the entire convection shell in our computational domain. The conclusion that large scales are involved here is similar to the earlier findings of Porter et al. (2000) and Porter & Woodward (2006) for the outer convective envelope of an AGB star. The restricted time step values, from explicit hydrodynamics, and the large domain, arising from the natural scale of the convection, place significant demands on the computation. We address these demands in two ways. First, we exploit a new implementation of our codes aimed specifically at the multicore CPUs found in modern computers (see Woodward et al. 2008b, 2009), which has delivered to our codes roughly a 40× speed-up over performance on single-core platforms from about four years ago (the code performance now stands at 24 Gflop/s/4-core-CPU, scalable to thousands of CPUs, and we obtain sustained performance over 1 Tflop/s on our small local cluster daily). Second, we exploit the fact that explicit computation is roughly as efficient as implicit computation when Mach numbers are around 1/30.

The code scales to hundreds of thousands of processor cores, for which runs with the proper heating rates, the full convection zone, and well resolved entrainment at the convection zone boundary are easily carried out in a single day.

APPENDIX B

TIME AND LENGTH SCALES

The relevant nuclear burning timescale for the H-ingestion problem is the timescale for a proton to be captured by a ^{12}C:

$$\tau_{^{12}C}(p) = \frac{12}{X(^{12}C)\,\rho\,N_a\langle\sigma v\rangle_{^{12}C(p,\gamma)}}\,.$$

For the quantitative evaluation of the relevant timescales we use the pre-ingestion model at time t_0 shown in Figure 2 (Section 3.2). The mass fraction of ^{12}C in that model is $X(^{12}C) = 0.36$ and the density increases from $\rho_{top} = 1.26 \times 10^2$ g cm^{-3} at the top of the convection zone to $\rho_{bot} = 1.0410 \times 10^4$ g cm^{-3} at the bottom of the convection zone. The nuclear reaction rate $\langle\sigma v\rangle_{^{12}C(p,\gamma)}$ depends sensitively on the temperature which increases from $T_{top} = 2.2\times10^7$ K at the top to $T_{bot} = 2.9\times10^8$ K at the bottom of the convection zone. $\langle\sigma v\rangle_{^{12}C(p,\gamma)}$ increases by 12 orders of magnitude across the convection zone.

The location of the peak H burning due to H ingestion takes place where the mixing timescale is the same as $\tau_{^{12}C}(p)$ (Chapter 4 of Arnett 1996). The diffusion coefficient D_{MLT} for convective mixing is derived from the MLT. With an appropriate length scale l a mixing timescale can be obtained. For some properties the MLT mixing-length l_{MLT} should be used: $l_{MLT} = \alpha_{MLT} H_p$ with $\alpha_{MLT} = 1.7$ the mixing-length parameter and H_p the pressure scale height. This MLT mixing timescale is then $\tau_{MLT} = l^2_{MLT}/D_{MLT}$. As can be seen in Figure 13 $\tau_{^{12}C}(p) = \tau_{MLT}$ at $m_r = 0.6024\ M_\odot$, a significantly larger mass coordinate than the location of the peak H burning ($\sim$0.6005 $M_\odot$) calculated in the stellar evolution model, as evident from the H profile at t_1 in Figure 2.

l_{MLT} should not be used to estimate a mixing timescale relevant for rapid nuclear burning, since the rate of p-captures depends only indirectly on P. In fact, in the vicinity of the H-peak luminosity the pressure scale height is $H_P \sim 1.4$ Mm which implies $l_{MLT} \sim 2.4$ Mm. This is much larger than the

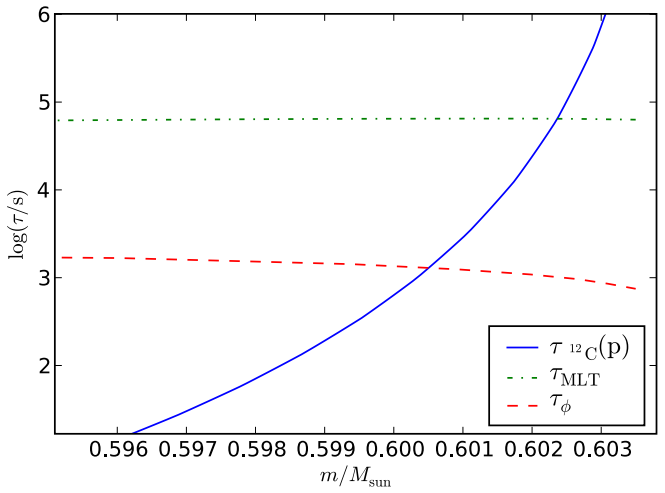

Figure 13. Timescales as a function of the mass coordinate in the convection zone, for proton capture by ^{12}C (blue solid line), as well as the MLT mixing timescale (green dash-dot) and the rate of reaction mixing timescale (red dashed; see the text for details). For this figure the tabulated reaction rate from Angulo et al. (1999) was used.

(A color version of this figure is available in the online journal.)

distance over which the rate of p-capture by ^{12}C (rate of reaction) increases significantly. It is this rate of reaction length scale that defines the width and location of the combustion flame for a given diffusion coefficient. A generalized length for any quantity $\phi = \phi(r)$ may be defined as (Chapman 1961)

$$H_\phi = \frac{1}{\frac{d \ln \phi}{dr}}$$

where H_ϕ is the rate of reaction length scale if we define $\phi = \rho\, \mathrm{N_a} \langle \sigma v \rangle_{^{12}\mathrm{C}(p,\gamma)}$. The rate of reaction mixing timescale is then $\tau_\phi = H_\phi^2 / D_{\mathrm{MLT}}$. As shown in Figure 13, the mass coordinate where $\tau_{^{12}\mathrm{C}}(p) = \tau_\phi$ coincides very well with the location of peak H burning (where as a result the mixing split occurs) at $t = t_1$ in Figure 2.

At this location ($m_r \sim 0.6005\, M_\odot$) the reaction length scale is $H_\phi \sim 330$ km which is the geometric scale of the flame that hydrodynamic simulations including nuclear burn have to resolve. A simulation box that fits the 4π geometry of the entire He-shell flash convection zone needs to have a side length of 50 Mm which corresponds to ~166 flame widths. In order to resolve the flame with at least 10 radial zones an equidistant grid for a H-ingestion flash simulation needs to have a 1660^3 grid.

REFERENCES

Abia, C., & Wallerstein, G. 1998, MNRAS, 293, 89
Angulo, C., et al. 1999, Nucl. Phys. A, 656, 3 (NACRE compilation)
Aoki, W., Norris, J. E., Ryan, S. G., Beers, T. C., & Ando, H. 2000, ApJ, 536, L97
Arnett, D. 1996, Supernovae and Nucleosynthesis: An Investigation of the History of Matter, from the Big Bang to the Present (Princeton, NJ: Princeton Univ. Press)
Asplund, M., Grevesse, N., & Sauval, A. J. 2005, in ASP Conf. Ser. 336, Cosmic Abundances as Records of Stellar Evolution and Nucleosynthesis, ed. T. G. Barnes, III & F. N. Bash (San Francisco, CA: ASP), 25
Asplund, M., Grevesse, N., Sauval, A. J., & Scott, P. 2009, ARA&A, 47, 481
Asplund, M., Lambert, D. L., Kipper, T., Pollacco, D., & Shetrone, M. D. 1999, A&A, 343, 507
Beveridge, R. C., & Sneden, C. 1994, AJ, 108, 285
Blöcker, T. 1995, A&A, 297, 727
Blondin, J. M., & Lufkin, E. A. 1993, APJS, 88, 589
Brown, T. M., Sweigart, A. V., Lanz, T., Landsman, W. B., & Hubeny, I. 2001, ApJ, 562, 368
Bryan, G. L., Norman, M. L., Stone, J. M., Cen, R., & Ostriker, J. P. 1995, Comput. Phys. Commun., 89, 149
Burbidge, E. M., Burbidge, G. R., Fowler, W. A., & Hoyle, F. 1957, Rev. Mod. Phys., 29, 547
Busso, M., Gallino, R., Lambert, D. L., Travaglio, C., & Smith, V. V. 2001, ApJ, 557, 802
Calder, A. C., et al. 2002, ApJS, 143, 201
Campbell, S. W., & Lattanzio, J. C. 2008, A&A, 490, 769
Cassisi, S., Iben, I. J., & Tornambe, A. 1998, ApJ, 496, 376
Chapman, S. 1961, Proc. Phys. Soc., 77, 424
Charbonnel, C., & Zahn, J. 2007, A&A, 467, L15
Colella, P., & Woodward, P. R. 1984, J. Comput. Phys., 54, 174
Cristallo, S., Piersanti, L., Straniero, O., Gallino, R., Domínguez, I., & Käppeler, F. 2009, PASA, 26, 139
Denissenkov, P. A. 2010, ApJ, 723, 563
Dillmann, I., Heil, M., Käppeler, F., Plag, R., Rauscher, T., & Thielemann, F.-K. 2006, in AIP Conf. Ser. 819, Capture Gamma-Ray Spectroscopy and Related Topics, ed. A. Woehr & A. Aprahamian (Melville, NY: AIP), 123
Dimotakis, P. E. 2005, Annu. Rev. Fluid Mech., 37, 329
Duerbeck, H. W., et al. 2000, AJ, 119, 2360
Ekström, S., Meynet, G., Chiappini, C., Hirschi, R., & Maeder, A. 2008, A&A, 489, 685
Farouqi, K., Kratz, K., Mashonkina, L. I., Pfeiffer, B., Cowan, J. J., Thielemann, F., & Truran, J. W. 2009, ApJ, 694, L49
Fujimoto, M. Y., Ikeda, Y., & Iben, I. J. 2000, ApJ, 529, L25
Fuller, G. M., Fowler, W. A., & Newman, M. J. 1985, ApJ, 293, 1
Fynbo, H. O. U., et al. 2005, Nature, 433, 136
Goriely, S. 1999, A&A, 342, 881
Goriely, S., & Siess, L. 2004, A&A, 421, L25
Heil, M., et al. 2008, Phys. Rev. C, 78, 025803
Herwig, F. 2000, A&A, 360, 952
Herwig, F. 2001, ApJ, 554, L71
Herwig, F. 2004, ApJ, 605, 425
Herwig, F., & Austin, S. M. 2004, ApJ, 613, L73
Herwig, F., Austin, S. M., & Lattanzio, J. C. 2006, Phys. Rev. C., 73, 025802
Herwig, F., Blöcker, T., Langer, N., & Driebe, T. 1999, A&A, 349, L5
Herwig, F., Freytag, B., Hueckstaedt, R. M., & Timmes, F. X. 2006, ApJ, 642, 1057
Herwig, F., & Langer, N. 2001, Nucl. Phys. A, 688, 221
Herwig, F., et al. 2008, in Proc. of the 10th Symp. on Nuclei in the Cosmos (NIC X), 23
Hollowell, D., Iben, I. J., & Fujimoto, M. Y. 1990, ApJ, 351, 245
Iben, I., Jr., Kaler, J. B., Truran, J. W., & Renzini, A. 1983, ApJ, 264, 605
Imbriani, G., et al. 2005, Eur. Phys. J. A, 25, 455
Iwamoto, N., Kajino, T., Mathews, G. J., Fujimoto, M. Y., & Aoki, W. 2004, ApJ, 602, 378
Kipper, T., & Jorgensen, U. G. 1994, A&A, 290, 148
Kipper, T., Jorgensen, U. G., Klochkova, V. G., & Panchuk, V. E. 1996, A&A, 306, 489
Kovacs, N. 1985, A&A, 150, 232
Kunz, R., Fey, M., Jaeger, M., Mayer, A., Hammer, J. W., Staudt, G., Harissopulos, S., & Paradellis, T. 2002, ApJ, 567, 643
Lawlor, T. M., & MacDonald, J. 2003, ApJ, 583, 913
Lodders, K. 2003, ApJ, 591, 1220
Lodders, K., Palme, H., & Gail, H. 2009, in Landolt-Börnstein–Group VI Astronomy and Astrophysics Numerical Data and Functional Relationships in Science Technology Volume 4B: Solar System, ed. J. E. Trümper (Berlin: Springer), 4.4
Luck, R. E., & Bond, H. E. 1991, ApJS, 77, 515
McWilliam, A. 1998, AJ, 115, 1640
McWilliam, A., Preston, G. W., Sneden, C., & Searle, L. 1995, AJ, 109, 2757
Miller Bertolami, M. M., & Althaus, L. G. 2007, MNRAS, 380, 763
Miller Bertolami, M. M., Althaus, L. G., Serenelli, A. M., & Panei, J. A. 2006, A&A, 449, 313
Miller Bertolami, M. M., Althaus, L. G., Unglaub, K., & Weiss, A. 2008, A&A, 491, 253
Norris, J. E., Ryan, S. G., & Beers, T. C. 1997, ApJ, 489, L169
Oda, T., Hino, M., Muto, K., Takahara, M., & Sato, K. 1994, At. Data Nucl. Data Tables, 56, 231
Pereira, C. B., Smith, V. V., & Cunha, K. 1998, AJ, 116, 1977
Pignatari, M., Gallino, R., Heil, M., Wiescher, M., Käppeler, F., Herwig, F., & Bisterzo, S. 2010, ApJ, 710, 1557
Pignatari, M., Gallino, R., Meynet, G., Hirschi, R., Herwig, F., & Wiescher, M. 2008, ApJ, 687, L95
Piro, A. L., & Bildsten, L. 2007, ApJ, 663, 1252

Porter, D. H., & Woodward, P. R. 2006, in Implicit Large Eddy Simulation: Computing Turbulent Fluid Dynamics, ed. L. M. F. Grinstein & W. Rider (Cambridge: Cambridge Univ. Press), 370
Porter, D. H., Woodward, P. R., & Jacobs, M. L. 2000, in Annals of the New York Academy of Sciences, Vol. 898, Astrophysical Turbulence and Convection, ed. J. R. Buchler & H. Kandrup, http://www.lcse.umn.edu/convsph
Reddy, B. E., Bakker, E. J., & Hrivnak, B. J. 1999, ApJ, 524, 831
Reifarth, R., Käppeler, F., Voss, F., Wisshak, K., Gallino, R., Pignatari, M., & Straniero, O. 2004, ApJ, 614, 363
Scalo, J. M., Despain, K. H., & Ulrich, R. K. 1975, ApJ, 196, 805
Schlattl, H., Salaris, M., Cassisi, S., & Weiss, A. 2002, A&A, 395, 77
Smith, V. V. 1984, A&A, 132, 326
Smith, V. V., Coleman, H., & Lambert, D. L. 1993, ApJ, 417, 287
Smith, V. V., Cunha, K., Jorissen, A., & Boffin, H. M. J. 1996, A&A, 315, 179
Smith, V. V., Cunha, K., Jorissen, A., & Boffin, H. M. J. 1997, A&A, 324, 97
Smith, V. V., & Lambert, D. L. 1984, PASP, 96, 226
Smith, V. V., & Lambert, D. L. 1985, ApJ, 294, 326
Smith, V. V., & Lambert, D. L. 1986, ApJ, 311, 843
Smith, V. V., & Lambert, D. L. 1990, ApJS, 72, 387
Smith, V. V., & Suntzeff, N. B. 1987, AJ, 93, 359
Suda, T., Aikawa, M., Machida, M. N., Fujimoto, M. Y., & Iben, I. J. 2004, ApJ, 611, 476
Tech, J. L. 1971, A High Dispersion Spectral Analysis of the Ba_II star HD_204075 (zeta _Capricorni) (NBS Monograph 11; Washington, DC: National Bureau Standards)
Tomkin, J., & Lambert, D. L. 1983, ApJ, 273, 722
Tomkin, J., & Lambert, D. L. 1986, ApJ, 311, 819
Travaglio, C., Gallino, R., Arnone, E., Cowan, J., Jordan, F., & Sneden, C. 2004, ApJ, 601, 864
van Hoof, P. A. M., et al. 2007, A&A, 471, L9
van Leer, B. 1977, J. Comput. Phys., 23, 276
Vanture, A. D. 1992, AJ, 104, 1986
Van Winckel, H., & Reyniers, M. 2000, A&A, 354, 135
Wallerstein, G., et al. 1997, Rev. Mod. Phys., 69, 995
Wasserburg, G. J., Boothroyd, A. I., & Sackmann, I.-J. 1995, ApJ, 447, L37
Woodward, P. R. 1986, in Astrophysical Radiation Hydrodynamics, ed. K.-H. Winkler & M. L. Norman (Dordrecht: Reidel), 245
Woodward, P. R. 2005, PPB: the Piecewise-Parabolic Boltzmann Scheme for Moment-Conserving Advection in 2 and 3 Dimensions, LCSE internal report, University of Minnesota, http://www.lcse.umn.edu/PPBdocs
Woodward, P. R. 2007, in Implicit Large Eddy Simulation, Computing Turbulent Fluid Dynamics, ed. F. F. Grinstein, L. G. Margolin, & W. Rider (Cambridge: Cambridge Univ. Press), 130
Woodward, P., & Colella, P. 1984, J. Comput. Phys., 54, 115
Woodward, P., Herwig, F., Porter, D., Fuchs, T., Nowatzki, A., & Pignatari, M. 2008a, in AIP Conf. Ser. 990, First Stars III (Melville, NY: AIP), 300
Woodward, P. R., Jayaraj, J., Lin, P.-H., & Dai, W. 2009, Concurrency and Computation Practice and Experience, 21, 2160
Woodward, P. R., Jayaraj, J., Lin, P.-H., & Yew, P.-C. 2008b, Computing in Science & Engineering, 10, 16
Woodward, P. R., Porter, D. H., Anderson, S., Fuchs, T., & Herwig, F. 2006, J. Phys. Conf. Ser., 46, 370
Woodward, P. R., Porter, D. H., Herwig, F., Pignatari, M., Jayaraj, J., & Lin, P. 2008c, Proc. of the 10th Symp. on Nuclei in the Cosmos (NIC X), 40
Woodward, P. R., Porter, D. H., & Jacobs, M. 2003, in ASP Conf. Ser. 293, 3D Stellar Evolution, ed. S. Turcotte, S. C. Keller, & R. M. Cavallo (San Francisco, CA: ASP), 45
Woosley, S. E., & Weaver, T. A. 1995, APJS, 101, 181
Woosley, S. E., et al. 2004, ApJS, 151, 75
Zacs, L., Klochkova, V. G., & Panchuk, V. E. 1995, MNRAS, 275, 764
Zacs, L., Nissen, P. E., & Schuster, W. J. 1998, A&A, 337, 216
Začs, L., Schmidt, M. R., & Schuster, W. J. 2000, A&A, 358, 1022

Bibliography

Aguilera E. F., Rosales P., Martinez-Quiroz E., Murillo G., Fernández M., Berdejo H., Lizcano D., Gómez-Camacho A., Policroniades R., Varela A., Moreno E., Chávez E., Ortíz M. E., Huerta A., Belyaeva T., Wiescher M., 2006, Phys. Rev. C, 73, 064601

Aikawa M., Arnould M., Goriely S., Jorissen A., Takahashi K., 2005, A&A, 441, 1195

Anders E., Grevesse N., 1989, Geochimica Cosmochimica Acta, 53, 197

Angulo C., Arnould M., Rayet M., Descouvemont P., Baye D., Leclercq-Willain C., Coc A., Barhoumi S., Aguer P., Rolfs C., Kunz R., Hammer J. W., Mayer A., Paradellis T., Kossionides S., Chronidou C., Spyrou K., degl'Innocenti S., Fiorentini G., Ricci B., Zavatarelli S., Providencia C., Wolters H., Soares J., Grama C., Rahighi J., Shotter A., Lamehi Rachti M., 1999, Nuc. Phys. A, 656, 3

Arcones A., Montes F., 2011, ApJ, 731, 5

Arcoragi J., Langer N., Arnould M., 1991, A&A, 249, 134

Arnett W. D., 1972a, ApJ, 176, 681

Arnett W. D., 1972b, ApJ, 176, 699

Arnett W. D., Thielemann F., 1985, ApJ, 295, 589

Arnett W. D., Truran J. W., 1969, ApJ, 157, 339

Asplund M., Grevesse N., Sauval A. J., Scott P., 2009, ARA&A, 47, 481

Asplund M., Lambert D. L., Kipper T., Pollacco D., Shetrone M. D., 1999, A&A, 343, 507

Barrón-Palos L., Aguilera E. F., Aspiazu J., Huerta A., Martínez-Quiroz E., Monroy R., Moreno E., Murillo G., Ortiz M. E., Policroniades R., Varela A., Chávez E., 2006, Nuc. Phys. A, 779, 318

Becker H. W., Kettner K.-U., Rolfs C., Trautvetter H. P., 1981, Zeitschrift fur Physik A Hadrons and Nuclei, 303, 305

Bennett M. E., Hirschi R., Pignatari M., Diehl S., Fryer C., Herwig F., Hillary W., Hungerford A., Richman D., Rockefeller G., Timmes F. X., Wiescher M., 2010, in Nuclei in the Cosmos XI. The effect of 12C + 12C rate uncertainties on the weak s-process component

Bennett M. E., Hirschi R., Pignatari M., Diehl S., Fryer C., Herwig F., Hungerford A., Magkotsios G., Rockefeller G., Timmes F., Wiescher M., Young P., 2010, JPhCS, 202, 012023

Betts R. R., Wuosmaa A. H., 1997, Rep. Prog. Phys., 60, 819

Burbidge E. M., Burbidge G. R., Fowler W. A., Hoyle F., 1957, Rev. Mod. Phys., 29, 547

Busso M., Gallino R., 1985, A&A, 151, 205

Busso M., Gallino R., Lambert D. L., Travaglio C., Smith V. V., 2001, ApJ, 557, 802

Busso M., Gallino R., Wasserburg G. J., 1999, ARA&A, 37, 239

Busso M., Picchio G., Gallino R., Chieffi A., 1988, ApJ, 326, 196

Cameron A. G. W., 1955, ApJ, 121, 144

Cameron A. G. W., 1957, PASP, 69, 201

Cameron A. G. W., 1960, AJ, 65, 485

Caughlan G. R., Fowler W. A., 1988, ADNDT, 40, 283

Chapman B., Jost G., Pas R. v. d., 2007, Using OpenMP: Portable Shared Memory Parallel Programming (Scientific and Engineering Computation). The MIT Press

Chen C., Chu Y., Gruendl R. A., Gordon K. D., Heitsch F., 2009, ApJ, 695, 511

Chieffi A., Limongi M., Straniero O., 1998, ApJ, 502, 737

Chugunov A. I., Dewitt H. E., 2009, Phys. Rev. C, 80, 014611

Chugunov A. I., Dewitt H. E., Yakovlev D. G., 2007, Phys. Rev. D, 76, 025028

Churchwell E., 2002, ARA&A, 40, 27

Churchwell E., Babler B. L., Meade M. R., Whitney B. A., Benjamin R., Indebetouw R., Cyganowski C., Robitaille T. P., Povich M., Watson C., Bracker S., 2009, PASP, 121, 213

Cirne W., Brasileiro F., Paranhos D., Góes L. F. W., Voorsluys W., 2007, Parallel Computing, 33, 213

Clayton D. D., 1968, Principles of stellar evolution and nucleosynthesis. The University of Chicago Press

Clayton D. D., Fowler W. A., Hull T. E., Zimmerman B. A., 1961, Annals of Physics, 12, 331

Clayton D. D., Rassbach M. E., 1967, ApJ, 148, 69

Colella P., Woodward P. R., 1984, J. Comp. Phys., 54, 174

Cooper R. L., Steiner A. W., Brown E. F., 2009, ApJ, 702, 660

Costa V., Pumo M. L., Bonanno A., Zappalà R. A., 2006, A&A, 447, 641

Costantini H., Formicola A., Imbriani G., Junker M., Rolfs C., Strieder F., 2009, Rep. Prog. Phys., 72, 086301

Couch R. G., Schmiedekamp A. B., Arnett W. D., 1974, ApJ, 190, 95

Cowan J. J., Roederer I. U., Sneden C., Lawler J. E., , 2011, r-Process Abundance Signatures in Metal-Poor Halo Stars

Crank J., 1975, The mathematics of diffusion, 2nd edn. Clarendon Press

Crowther P. A., 2007, ARA&A, 45, 177

Cussons R., Langanke K., Liolios T., 2002, Eur. Phys. J. A, 15, 291

Dayras R., Switkowski Z. E., Woosley S. E., 1977, Nuc. Phys. A, 279, 70

de Jager C., Nieuwenhuijzen H., van der Hucht K. A., 1988, A&AS, 72, 259

Demarque P., Sarajedini A., Guo X., 1994, ApJ, 426, 165

Descouvemont P., 1993, Phys. Rev. C, 48, 2746

Diaz-Torres A., 2008, Phys. Rev. Lett., 101, 122501

Diaz-Torres A., Gasques L. R., Wiescher M., 2007, Phys. Lett. B, 652, 255

Diehl R., Halloin H., Kretschmer K., Lichti G. G., Schönfelder V., Strong A. W., von Kienlin A., Wang W., Jean P., Knödlseder J., Roques J., Weidenspointner G., Schanne S., Hartmann D. H., Winkler C., Wunderer C., 2006, Nat, 439, 45

Dillmann I., Heil M., Käppeler F., Faestermann T., Knie K., Korschinek G., Poutivtsev M., Rugel G., Wallner A., Rauscher T., 2008, ArXiv e-prints

Dillmann I., Heil M., Käppeler F., Plag R., Rauscher T., Thielemann F., 2006, in A. Woehr & A. Aprahamian ed., Capture Gamma-Ray Spectroscopy and Related Topics Vol. 819 of American Institute of Physics Conference Series, KADoNiS- The Karlsruhe Astrophysical Database of Nucleosynthesis in Stars. pp 123–127

Eggenberger P., Meynet G., Maeder A., Hirschi R., Charbonnel C., Talon S., Ekström S., 2008, Ap&SS, 316, 43

El Eid M. F., Meyer B. S., The L., 2004, ApJ, 611, 452

El Eid M. F., The L.-S., Meyer B. S., 2009, S. Sci. Rev., 147, 1

Eldridge J. J., Tout C. A., 2004, MNRAS, 353, 87

Esposito S., Mangano G., Miele G., Picardi I., Pisanti O., 2003, Nuc. Phys. B, 658, 217

Ferguson J. W., Alexander D. R., Allard F., Barman T., Bodnarik J. G., Hauschildt P. H., Heffner-Wong A., Tamanai A., 2005, ApJ, 623, 585

François P., Depagne E., Hill V., Spite M., Spite F., Plez B., Beers T. C., Andersen J., James G., Barbuy B., Cayrel R., Bonifacio P., Molaro P., Nordström B., Primas F., 2007, A&A, 476, 935

Freytag B., Ludwig H.-G., Steffen M., 1996, A&A, 313, 497

Fryer C., 2009, APS April Meeting Abstracts, pp B4001

Fuller G. M., Fowler W. A., Newman M. J., 1985, ApJ, 293, 1

Furness J. P., Crowther P. A., Morris P. W., Barbosa C. L., Blum R. D., Conti P. S., van Dyk S. D., 2010, MNRAS, 403, 1433

Fynbo H. O. U., Diget C. A., Bergmann U. C., Borge M. J. G., Cederkäll J., Dendooven P., Fraile L. M., Franchoo S., Fedosseev V. N., Fulton B. R., Huang W., Huikari J., Jeppesen H. B., Jokinen A. S., Jones P., Jonson B., Köster U., Langanke K., Meister M., Nilsson T., Nyman G., Prezado Y., Riisager K., Rinta-Antila S., Tengblad O., Turrion M., Wang Y., Weissman L., Wilhelmsen K., Äystö J., ISOLDE Collaboration 2005, Nat, 433, 136

Gallino R., Arlandini C., Busso M., Lugaro M., Travaglio C., Straniero O., Chieffi A., Limongi M., 1998, ApJ, 497, 388

Gallino R., Busso M., Picchio G., Raiteri C. M., Renzini A., 1988, ApJL, 334, L45

Gasques L. R., Afanasjev A. V., Aguilera E. F., Beard M., Chamon L. C., Ring P., Wiescher M., Yakovlev D. G., 2005, Phys. Rev. C, 72, 025806

Gasques L. R., Brown E. F., Chieffi A., Jiang C. L., Limongi M., Rolfs C., Wiescher M., Yakovlev D. G., 2007, Phys. Rev. C, 76, 035802

Grevesse N., Noels A., 1993, in N. Prantzos, E. Vangioni-Flam, & M. Casse, Origin and Evolution of the Elements Cosmic abundances of the elements.. pp 15–25

Gropp W., Lusk E., Skjellum A., 1999, Using MPI (2nd ed.): portable parallel programming with the message-passing interface. MIT Press, Cambridge, MA, USA

Heger A., Langer N., Woosley S. E., 2000, ApJ, 528, 368

Heil M., Käppeler F., Uberseder E., Gallino R., Bisterzo S., Pignatari M., 2008, Phys. Rev. C, 78, 025802

Herwig F., 2005, ARA&A, 43, 435

Herwig F., Diehl S., Fryer C. L., Hirschi R., Hungerford A., Magkotsios G., Pignatari M., Rockefeller G., Timmes F. X., Young P., Bennet M. E., 2008, in Nuclei in the Cosmos (NIC X) Nucleosynthesis simulations for a wide range of nuclear production sites from NuGrid

Herwig F., Freytag B., Hueckstaedt R. M., Timmes F. X., 2006, ApJ, 642, 1057

Herwig F., Pignatari M., Woodward P. R., Porter D. H., Rockefeller G., Fryer C. L., Bennett M., Hirschi R., 2011, ApJ, 727, 89

High M. D., Čujec B., 1977, Nuc. Phys. A, 282, 181

Hirschi R., 2004, PhD thesis, Université de Genève, Switzerland

Hirschi R., Meynet G., Maeder A., 2004, A&A, 425, 649

Hirschi R., Meynet G., Maeder A., 2005, A&A, 433, 1013

Hix W. R., Khokhlov A. M., Wheeler J. C., Thielemann F.-K., 1998, ApJ, 503, 332

Hollowell D., Iben Jr. I., 1988, ApJL, 333, L25

Iapichino L., Lesaffre P., 2010, A&A, 512, A27+

Iben Jr. I., 1975a, ApJ, 196, 549

Iben Jr. I., 1975b, ApJ, 196, 525

Iliadis C., 2007, Nuclear Physics of Stars. Wiley-VCH Verlag

Iliadis C., D'Auria J. M., Starrfield S., Thompson W. J., Wiescher M., 2001, ApJS, 134, 151

Imbriani G., Costantini H., Formicola A., Vomiero A., Angulo C., Bemmerer D., Bonetti R., Broggini C., Confortola F., Corvisiero P., Cruz J., Descouvemont P., Fülöp Z., Gervino G., Guglielmetti A., Gustavino C., Gyürky G., Jesus A. P., Junker M., Klug J. N., Lemut A., Menegazzo R., Prati P., Roca V., Rolfs C., Romano M., Rossi-Alvarez C., Schümann F., Schürmann D., Somorjai E., Straniero O., Strieder F., Terrasi F., Trautvetter H. P., 2005, Eur. Phys. J. A, 25, 455

Itoh N., Adachi T., Nakagawa M., Kohyama Y., Munakata H., 1989, ApJ, 339, 354

Itoh N., Hayashi H., Nishikawa A., Kohyama Y., 1996, ApJS, 102, 411

Itoh N., Tomizawa N., Wanajo S., Nozawa S., 2003, ApJ, 586, 1436

Jaeger M., Kunz R., Mayer A., Hammer J. W., Staudt G., Kratz K. L., Pfeiffer B., 2001, Phys. Rev. Lett., 87, 202501

Jiang C. L., Esbensen H., Back B. B., Janssens R. V., Rehm K. E., 2004, Phys. Rev. C, 69, 014604

Jiang C. L., Rehm K. E., Back B. B., Janssens R. V. F., 2007, Phys. Rev. C, 75, 015803

Käppeler F., 1999, Prog. Part. Nuc. Phys., 43, 419

Käppeler F., Beer H., Wisshak K., 1989, Rep. Prog. Phys., 52, 945

Käppeler F., Beer H., Wisshak K., Clayton D. D., Macklin R. L., Ward R. A., 1982, ApJ, 257, 821

Kettner K. U., Lorenz-Wirzba H., Rolfs C., 1980, Zeitschrift fur Physik A Hadrons and Nuclei, 298, 65

Kippenhahn R., Weigert A., 1990, Stellar Structure and Evolution

Kozhurina-Platais V., Demarque P., Platais I., Orosz J. A., Barnes S., 1997, AJ, 113, 1045

Krane K. S., 1987, Introductory Nuclear Physics

Kratz K.-L., Farouqi K., Pfeiffer B., Truran J. W., Sneden C., Cowan J. J., 2007, ApJ, 662, 39

Kunz R., Fey M., Jaeger M., Mayer A., Hammer J. W., Staudt G., Harissopulos S., Paradellis T., 2002, ApJ, 567, 643

Lamb S. A., Howard W. M., Truran J. W., Iben Jr. I., 1977, ApJ, 217, 213

Limongi M., Straniero O., Chieffi A., 2000, ApJS, 129, 625

Lodders K., 2003, ApJ, 591, 1220

Lodders K., Palme H., Gail H.-P., 2009, in Landolt-Börnstein - Group VI Astronomy and Astrophysics Numerical Data and Functional Relationships in Science and Technology Volume 4B: Solar System. Edited by J.E. Trümper, 2009, 4.4. Abundances of the Elements in the Solar System. pp 44

Maeder A., 1992, A&A, 264, 105

Maeder A., 2009, Physics, Formation and Evolution of Rotating Stars. Springer-Verlag Berlin Heidelberg

Maeder A., Meynet G., 1987, A&A, 182, 243

Meakin C. A., Arnett D., 2007, ApJ, 667, 448

Meakin C. A., Sukhbold T., Arnett W. D., 2011, Ap&SS, pp 254

Merrill S. P. W., 1952, ApJ, 116, 21

Metcalf M., Reid J., 1990, Fortran 90 explained. Oxford University Press, Inc., New York, NY, USA

Meynet G., Maeder A., 2000, A&A, 361, 101

Meynet G., Maeder A., 2003, A&A, 404, 975

Michaud G. J., Vogt E. W., 1972, Phys. Rev. C, 5, 350

Miller Bertolami M. M., Althaus L. G., 2007, MNRAS, 380, 763

Mocák M., Meakin C. A., Müller E., Siess L., 2011, ArXiv e-prints

Montes F., Beers T. C., Cowan J., Elliot T., Farouqi K., Gallino R., Heil M., Kratz K., Pfeiffer B., Pignatari M., Schatz H., 2007, ApJ, 671, 1685

Mukhamedzhanov A. M., Bém P., Brown B. A., Burjan V., Gagliardi C. A., Kroha V., Novák J., Nunes F. M., Iskoř Š., Pirlepesov F., Šimečková E., Tribble R. E., Vincour J., 2003, Phys. Rev. C, 67, 065804

Neilson H. R., Cantiello M., Langer N., 2010, ArXiv e-prints

Nugis T., Lamers H. J. G. L. M., 2000, A&A, 360, 227

Oda T., Hino M., Muto K., Takahara M., Sato K., 1994, ADNDT, 56, 231

Patterson J. R., Winkler H., Zaidins C. S., 1969, ApJ, 157, 367

Perez-Torres R., Belyaeva T. L., Aguilera E. F., 2006, Phys. Atom. Nuc., 69, 1372

Peters J. G., 1968, ApJ, 154, 225

Pignatari M., Gallino R., Heil M., Wiescher M., Käppeler F., Herwig F., Bisterzo S., 2010, ApJ, 710, 1557

Pignatari M., Gallino R., Meynet G., Hirschi R., Herwig F., Wiescher M., 2008, ApJL, 687, L95

Prantzos N., Arnould M., Arcoragi J., 1987, ApJ, 315, 209

Press W. H., Teukolsky S. A., Vetterling W. T., Flannery B. P., 1992, Numerical recipes in FORTRAN. The art of scientific computing (2nd ed.). Cambridge: University Press, 1992

Pumo M. L., Contino G., Bonanno A., Zappalà R. A., 2010, A&A, 524, A45+

Qian Y., Wasserburg G. J., 2008, ApJ, 687, 272

Qian Y.-Z., Wasserburg G. J., 2007, Phys. Rep., 442, 237

Raiteri C. M., Busso M., Picchio G., Gallino R., 1991, ApJ, 371, 665

Raiteri C. M., Busso M., Picchio G., Gallino R., Pulone L., 1991, ApJ, 367, 228

Rauscher T., Heger A., Hoffman R. D., Woosley S. E., 2002, ApJ, 576, 323

Rauscher T., Thielemann F., 2000, ADNDT, 75, 1

Rauscher T., Thielemann F., 2001, ADNDT, 79, 47

Rogers F. J., Swenson F. J., Iglesias C. A., 1996, ApJ, 456, 902

Rolfs C. E., Rodney W. S., 1988, Cauldrons in the cosmos: Nuclear astrophysics

Scalo J. M., Ulrich R. K., 1973, ApJ, 183, 151

Seeger P. A., Fowler W. A., Clayton D. D., 1965, ApJS, 11, 121

Serminato A., Gallino R., Travaglio C., Bisterzo S., Straniero O., 2009, PASA, 26, 153

Siess L., 2007, A&A, 476, 893

Smartt S. J., Eldridge J. J., Crockett R. M., Maund J. R., 2009, MNRAS, 395, 1409

Spillane T., Raiola F., Rolfs C., Schürmann D., Strieder F., Zeng S., Becker H.-W., Bordeanu C., Gialanella L., Romano M., Schweitzer J., 2007, Phys. Rev. Lett., 98, 122501

Steigman G., 2007, Annual Review of Nuclear and Particle Science, 57, 463

Strieder F., 2008, Journal of Physics G: Nuclear Physics, 35, 014009

Strieder F., 2010, JPCS, 202, 012025

Suda T., Aikawa M., Machida M. N., Fujimoto M. Y., Iben Jr. I., 2004, ApJ, 611, 476

Suess H. E., Urey H. C., 1956, Rev. Mod. Phys., 28, 53

Terrasi F., Rogalla D., de Cesare N., D'Onofrio A., Lubritto C., Marzaioli F., Passariello I., Rubino M., Sabbarese C., Casa G., Palmieri A., Gialanella L., Imbriani G., Roca V., Romano M., Sundquist M., Loger R., 2007, Nuclear Instruments and Methods in Physics Research B, 259, 14

The L., El Eid M. F., Meyer B. S., 2007, ApJ, 655, 1058

The L.-S., El Eid M. F., Meyer B. S., 2000, ApJ, 533, 998

Tinsley B. M., 1979, ApJ, 229, 1046

Travaglio C., Gallino R., Arnone E., Cowan J., Jordan F., Sneden C., 2004, ApJ, 601, 864

Truran J. W., Cameron A. G. W., 1971, Ap&SS, 14, 179

Truran J. W., Iben Jr. I., 1977, ApJ, 216, 797

Tur C., Heger A., Austin S. M., 2007, ApJ, 671, 821

Tur C., Heger A., Austin S. M., 2009, ApJ, 702, 1068

Tytler D., O'Meara J. M., Suzuki N., Lubin D., 2000, Physica Scripta Volume T, 85, 12

Ulrich R. K., 1973, in D. N. Schramm & W. D. Arnett ed., Explosive Nucleosynthesis The s-Process in Stars. pp 139

Vink J. S., de Koter A., Lamers H. J. G. L. M., 2001, A&A, 369, 574

Walter G., Beer H., Kaeppeler F., Penzhorn R., 1986, A&A, 155, 247

Weiss A., Hillebrandt W., Thomas H.-C., Ritter H., 2004, Cox and Giuli's Principles of Stellar Structure. Cox and Giuli's Principles of Stellar Structure, by A. Weiss, W. Hillebrandt, H-C. Thomas, H. Ritter. Cambridge, UK: Princeton Publishing Associates Ltd, 2004.

Wilkinson B., Allen M., 2004, Parallel Programming: Techniques and Applications Using Networked Workstations and Parallel Computers (2nd Edition). Prentice-Hall, Inc., Upper Saddle River, NJ, USA

Williams K. A., Bolte M., Koester D., 2009, ApJ, 693, 355

Woosley S. E., Heger A., Weaver T. A., 2002, Rev. Mod. Phys., 74, 1015

Woosley S. E., Heger A., Weaver T. A., 2002, Rev. Mod. Phys., 74, 1015

Woosley S. E., Weaver T. A., 1986, ARA&A, 24, 205

Woosley S. E., Weaver T. A., 1995, ApJS, 101, 181

Xu C., Qi C., Liotta R. J., Wyss R., Wang S. M., Xu F. R., Jiang D. X., 2010, Phys. Rev. C, 81, 054319

Yakovlev D. G., Gasques L. R., Afanasjev A. V., Beard M., Wiescher M., 2006, Phys. Rev. C, 74, 035803

Young P. A., Fryer C. L., 2007, ApJ, 664, 1033

Zahn J., 1991, A&A, 252, 179

Zinnecker H., Yorke H. W., 2007, ARA&A, 45, 481

Zomaya A. Y. H., 1996, Parallel and distributed computing handbook. McGraw-Hill, Inc., New York, NY, USA